

Smart Innovation, Systems and Technologies 265

A. N. R. Reddy
Deepak Marla
Margarita N. Favorskaya
Suresh Chandra Satapathy *Editors*



Intelligent Manufacturing and Energy Sustainability

Proceedings of ICIMES 2021



 Springer

Smart Innovation, Systems and Technologies

Volume 265

Series Editors

Robert J. Howlett, Bournemouth University and KES International,
Shoreham-by-Sea, UK

Lakhmi C. Jain, KES International, Shoreham-by-Sea, UK

The Smart Innovation, Systems and Technologies book series encompasses the topics of knowledge, intelligence, innovation and sustainability. The aim of the series is to make available a platform for the publication of books on all aspects of single and multi-disciplinary research on these themes in order to make the latest results available in a readily-accessible form. Volumes on interdisciplinary research combining two or more of these areas is particularly sought.

The series covers systems and paradigms that employ knowledge and intelligence in a broad sense. Its scope is systems having embedded knowledge and intelligence, which may be applied to the solution of world problems in industry, the environment and the community. It also focusses on the knowledge-transfer methodologies and innovation strategies employed to make this happen effectively. The combination of intelligent systems tools and a broad range of applications introduces a need for a synergy of disciplines from science, technology, business and the humanities. The series will include conference proceedings, edited collections, monographs, handbooks, reference books, and other relevant types of book in areas of science and technology where smart systems and technologies can offer innovative solutions.

High quality content is an essential feature for all book proposals accepted for the series. It is expected that editors of all accepted volumes will ensure that contributions are subjected to an appropriate level of reviewing process and adhere to KES quality principles.

Indexed by SCOPUS, EI Compendex, INSPEC, WTI Frankfurt eG, zbMATH, Japanese Science and Technology Agency (JST), SCImago, DBLP.

All books published in the series are submitted for consideration in Web of Science.

More information about this series at <https://link.springer.com/bookseries/8767>

A. N. R. Reddy · Deepak Marla ·
Margarita N. Favorskaya ·
Suresh Chandra Satapathy
Editors

Intelligent Manufacturing and Energy Sustainability

Proceedings of ICIMES 2021

 Springer

Editors

A. N. R. Reddy
Department of Mechanical Engineering
Malla Reddy College of Engineering
and Technology
Hyderabad, India

Margarita N. Favorskaya
Reshetnev Siberian State University
of Science and Technology
Krasnoyarsk, Russia

Deepak Marla
Department of Mechanical Engineering
Indian Institute of Technology Bombay
Mumbai, India

Suresh Chandra Satapathy
Kalinga Institute of Industrial Technology
Bhubaneswar, India

ISSN 2190-3018

ISSN 2190-3026 (electronic)

Smart Innovation, Systems and Technologies

ISBN 978-981-16-6481-6

ISBN 978-981-16-6482-3 (eBook)

<https://doi.org/10.1007/978-981-16-6482-3>

© The Editor(s) (if applicable) and The Author(s), under exclusive license to Springer Nature Singapore Pte Ltd. 2022

This work is subject to copyright. All rights are solely and exclusively licensed by the Publisher, whether the whole or part of the material is concerned, specifically the rights of translation, reprinting, reuse of illustrations, recitation, broadcasting, reproduction on microfilms or in any other physical way, and transmission or information storage and retrieval, electronic adaptation, computer software, or by similar or dissimilar methodology now known or hereafter developed.

The use of general descriptive names, registered names, trademarks, service marks, etc. in this publication does not imply, even in the absence of a specific statement, that such names are exempt from the relevant protective laws and regulations and therefore free for general use.

The publisher, the authors and the editors are safe to assume that the advice and information in this book are believed to be true and accurate at the date of publication. Neither the publisher nor the authors or the editors give a warranty, expressed or implied, with respect to the material contained herein or for any errors or omissions that may have been made. The publisher remains neutral with regard to jurisdictional claims in published maps and institutional affiliations.

This Springer imprint is published by the registered company Springer Nature Singapore Pte Ltd. The registered company address is: 152 Beach Road, #21-01/04 Gateway East, Singapore 189721, Singapore

ICIMES-2021 Committees

Conference Committee

Chief Patron

Sri. CH. Malla Reddy, Founder Chairman, MRGI

Patrons

Sri. CH. Mahendar Reddy, Secretary, MRGI

Sri. CH. Bhadra Reddy, President, MRGI

Conference Chair

Dr. V. S. K. Reddy, Principal

Honorary Chairs

Dr. Lakshmi C. Jain, University of Sydney, Sydney, Australia

Dr. Margarita N. Favorskaya, Reshetnev Siberian State University of Science and Technology, Russia

Publication Chair

Dr. Suresh Chandra Satapathy, Professor, KIIT, Bhubaneswar, India

Convener

Dr. S. Srinivasa Rao, Principal, MRCET

Co-convener

Dr. PHV Sessa Talpa Sai, Director, R&D, MRCET

Organizing Chair

Dr. A. N. R. Reddy, HOD, Mechanical Engineering

Organizing Secretary

Dr. Srikar Potnuru, Associate Professor, Mechanical Engineering

Coordinator

Prof. Harish Makena, Assistant Professor, Mechanical Engineering

Editorial Board

Dr. A. N. R. Reddy, Malla Reddy College of Engineering and Technology, India

Dr. Deepak Marla, Indian Institute of Technology Bombay, India

Dr. Margarita N. Favorskaya, Siberian State University of Science and Technology, Russia

Dr. Suresh Chandra Satapathy, KIIT, Bhubaneswar, India

International Advisory Committee

Dr. Lakshmi C. Jain, University of Sydney, Sydney, Australia

Dr. Narayanan Kulathuramaiyer, Universiti Malaysia Sarawak, Malaysia

Dr. Abu Saleh Ahmed, Universiti Malaysia Sarawak, Malaysia

Dr. Shahrol Mohamaddan, Shibaura Institute of Technology, Japan

Dr. Sinin Hamdan, Universiti Malaysia Sarawak, Malaysia

Dr. Jaesool Shim, Yeunagnam University, South Korea

Dr. V. Vasudeva Rao, University of South Africa, South Africa

Dr. Sinin Hamdan, Universiti Malaysia Sarawak, Malaysia

Dr. Amiya Bhaumik, Lincoln University College, Malaysia

Dr. Bhaskar Kura, University of New Orleans, LA, USA

Dr. Devarayapalli K. C., Yeunagnam University, South Korea

Dr. Raja V. Pulikollu, Electric Power Research Institute, North Carolina, USA

Dr. Nguyen Dang Nam, Duy Tan University, Vietnam

Dr. Angel Sanz Anderes, UPM, Madrid, Spain

Dr. S. V. Prabhakar, Yeunagnam University, South Korea

Dr. Yequing Bao, University of Alabama, USA

Dr. Sabastian Franchini, UPM, Madrid, Spain

National Advisory Committee

Dr. G. Balu, DOAD, DRDL, Telangana, India

Dr. K. Vijay Kumar Reddy, Jawaharlal Nehru Technological University, Hyderabad, Telangana, India

Dr. P. K. Jain, Centre for Carbon Materials, ARCI, Hyderabad, Telangana, India
Dr. Susanta Kumar Sahoo, NIT Rourkela, Odisha, India
Dr. K. S. Reddy, Indian Institute of Technology Madras, Tamil Nadu, India
Dr. G. Raghavendra, National Institute of Technology Warangal, Telangana, India
Dr. T. Gangadhar, National Institute of Technology Tadepalligudem, Andhra Pradesh, India
Dr. U. S. Paul Russel, Air India, India
Dr. V. P. Chandra Mohan, National Institute of Technology Warangal, Telangana, India
Dr. P. Narsimha Reddy, Sreenidhi Institute of Science and Technology, Hyderabad, Telangana, India
Dr. Swami Naidu, National Institute of Technology Raipur, Chhattisgarh, India
Dr. Vemuri Laxmi Narayana, Rajamahendri Institute of Engineering and Technology, Andhra Pradesh, India

Industry Advisory Committee

Mr. Uddagiri Vidyasagar, TCS, Hyderabad, India
Mr. Uma Shankar, Farm Division, Mahindra & Mahindra, Zaheerabad, India
Mr. Sunil Maheshwari, Sr. Regional Manager, Adroit Engineering Solutions Pvt. Ltd., India
Mr. Sandeep Arora, Associate Director, Verizon, India
Mr. Bhusan Prasad M., Vice President, Renewable Energy Systems Ltd., India
Mr. Ramana Rao P. V., ADM, SMC Corporation India Pvt. Ltd.
Ramky Enviro Engineers Ltd.

Organizing Committee

Prof. (Dr.) V. Madhusudhana Reddy
Prof. (Dr.) T. Siva Kumar
Prof. (Dr.) T. Lokeswara Rao
Prof. (Dr.) B. Jain A. R. Tony
Prof. (Mr.) D. Damodar Reddy
Prof. (Mr.) Y. Dilip Kumar
Prof. (Ms.) S. Deepthi
Prof. (Ms.) K. Akhila
Prof. (Mr.) O. Y. V. Subba Reddy
Prof. (Mr.) V. Gopal Krishna

Preface

The International Conference on Intelligent Manufacturing and Energy Sustainability (ICIMES-2021) was successfully organized by Malla Reddy College of Engineering and Technology, an UGC Autonomous Institution, during June 18–19, 2021, at Hyderabad. The objective of this conference was to provide opportunities for the researchers, academicians and Industry persons to interact and exchange the ideas, experience and gain expertise in the cutting-edge technologies pertaining to Industry 4.0. research papers were received and subjected to a rigorous peer review process with the help of editorial board, program committee and external reviewers. The editorial committee has finally accepted 21% manuscripts for publication in a single volume with Springer SIST series.

Our sincere thanks to guest of honor and keynote session by Prof. Akihiko Hanafusa—Systems Engineering and Science, Functional Control Systems, Department of Bioscience and Engineering, Shibaura Institute of Technology (SIT), Japan.

We would also like to thank both the keynote session speakers and session chairs:

1. Prof. Nguyen Dang Nam—Electrochemistry—Metallurgy, Associate Editor—Chemical Papers—Springer Publishing, Institute of Fundamental and Applied Sciences, Duy Tan University, Vietnam
2. Prof. Ir. Dr. Andrew Ragai Henry Rigit, Deputy Dean (Industry and Community Engagement), Faculty of Engineering, Universiti Malaysia Sarawak, Malaysia

Our outmost thanks to all our chairs for their immense support.

1. Dr. Shahrol Mohamaddan, Associate Professor, Department of Bioscience and Engineering, College of Systems Engineering and Science, Shibaura Institute of Technology, Japan.
2. Dr. D. K. Charyulu, Research Associate, School of Nano and Materials Science and Engineering, Kyungpook National University, Sangju, Gyeongbuk, South Korea.

3. Prof. Dr. Veeredhi Vasudeva Rao, Professor, Department of Mechanical and Industrial Engineering, University of South Africa, South Africa.
4. Dr. Deepak Marla, Professor, Department of Mechanical Engineering, IIT Bombay, India.
5. Dr. Jose Immanuel R., Assistant Professor, Department of Mechanical Engineering, IIT Bhilai.
6. Dr. G. Raghavendra, Assistant Professor, Department of Mechanical Engineering, NIT Warangal.
7. Dr. Bunil Kumar Balabantaray, Assistant Professor, NIT Meghalaya.
8. Dr. Ajit Behera, Assistant Professor, Metallurgical and Materials Engineering, NIT Rourkela.

We are indebted to the editorial board, program committee and external reviewers who have produced critical reviews in a short time. We would like to express our special gratitude to publication chair and editor, Dr. Suresh Chandra Satapathy, Professor, KIIT, Bhubaneswar, for his valuable support and encouragement till the successful conclusion of the conference.

We express our heartfelt thanks to our Chief Patron Sri. CH. Malla Reddy, Founder Chairman, MRGI, Patrons Sri. CH. Mahendar Reddy, Secretary, MRGI, Sri. CH. Bhadra Reddy, President, MRGI, Conference Chair Dr. V. S. K. Reddy, Convener Dr. M. Murali Krishna, Organizing Chair Professor Dr. A. N. R. Reddy, Organizing Secretary Dr. Srikar Potnuru, and Coordinator Mr. M. Harish, for their valuable contribution to successful conduct the conference. Last, but certainly not least, our special thanks to all the authors without whom the conference would not have taken place. Their technical contributions have made our proceedings rich and praiseworthy.

Hyderabad, India
 Mumbai, India
 Siberian, Russia
 Bhubaneswar, India

Dr. A. N. R. Reddy
 Dr. Deepak Marla
 Dr. Margarita N. Favorskaya
 Dr. Suresh Chandra Satapathy

Contents

1	An Experimental Investigation into the Performance Characteristics of TiO₂/Ethylene Glycol Nanofluid Flowing in a Horizontal Counterflow Heat Exchanger	1
	Thembelani Sithebe and Veeredhi Vasudeva Rao	
2	Calibration of Industrial Fanuc 430iF Series Robot Arm	11
	Mazleenda Mazni, Muhammad Azmi Ayub, and Norhafiza Muhammad	
3	Development of Batch Type Convection Dryer for Fish Cracker Manufacturing	21
	Muhammad Naim Leman, Shahrol Mohamaddan, Ana Sakura Zainal Abidin, Mohamad Syazwan Zafwan Mohamad Suffian, Khairul Fikri Tamrin, Rubiyah Bains, and Akihiko Hanafusa	
4	An Experimental Investigation on Mechanical and Tribological Behaviour of (AZ91D Mg Alloy + Graphene) Metal Matrix Composite	33
	N. Satish Kumar, G. G. Sozhamannan, and V. S. K. Venkatachalapathy	
5	Investigation of Wear and Mechanical Properties of Aluminium Hybrid Composites: Effect of Addition of SiC/B₄C Through Casting Process	45
	S. Sunil Kumar Reddy, C. Sreedhar, and S. Suresh	
6	Effect of Stress on Ferroelectric, Energy Storage and Harvesting Properties of 0.4BZT-0.6BCT Ceramics	57
	Nishchay Saurabh and Satyanarayan Patel	
7	Survey of Nanosensors and Nano-heterostructures	67
	Priya Chaudhary, Sonam Gour, and Amit Rathi	

8	Recognition of Facial Expressions Based on Detection of Facial Components and HOG Characteristics	77
	K. A. Anu and N. Ali Akbar	
9	Optimization of Pneumatic Extrusion Machining Method Process Parameters on Polycaprolactone (PCL) Material	85
	O. Y. Venkata Subba Reddy, A. N. R. Reddy, and V. Venkatesh	
10	A Comparison of Mixing and Displacement Ventilation System in an Office Environment Using Computational Fluid Dynamics . . .	95
	Mohammed Abdul Hameed Khan, Chanfiou Ahmed Mboreha, and Hazem Abdelrahman	
11	Performance Study and Analysis of an UAV Airfoil at Low Reynolds Number	107
	Ramanan Gopalakrishnan, Neela Rajan Rajadurai Ramakrishnan, Bino Prince Raja Dennis, and Anton Savio Lewise Kuzhanthai	
12	Life Cycle Assessment Based Environmental Footprint of a Battery Recycling Process	115
	Arvind Kumar, Abhishek Gupta, Shalini Verma, Akshoy Ranjan Paul, Anuj Jain, and Nawshad Haque	
13	Review on the Structural Components of Floating Photovoltaic Covering Systems	125
	Nagananthini Ravichandran, Nagavinothini Ravichandran, and Balamurugan Panneerselvam	
14	Performance and Emission Test of C.I. Engine Using Biodiesel . . .	135
	P. V. Chandra Sekhara Rao, B. Renuka Swathi, and Aluri Manoj	
15	Evaluation on the Diseased Damage Grading Model of the Fresh Destemmed Chilli Fruits	147
	Quoc-Khanh Huynh, Chi-Ngon Nguyen, Jeng-Rong Ho, Hong-Phuc Vo-Nguyen, and Van-Cuong Nguyen	
16	On the Study and Analyses of “Vertical Farming—The Future of Agriculture” via Various Hydroponic Systems	157
	Tanishi Mathur and Senthil Arumugam Muthukumaraswamy	
17	Design and Analysis of Progressive Tool for Glass Brackets	167
	Nagaveni Thallapalli, K. Laxman Kumar, and S. B. Manikanta Katepalli	
18	Analysis of Strain Hardening Behavior of ARMCO Iron After Severe Plastic Deformation Using K–M Plots	177
	Vindala Poojitha, T. Raghu, and V. Pandurangadu	

19 Optimization of Process Parameters for Friction Stir Spot Welding Using Dissimilar Metals 185
 Pitala Adithya, B. D. Y. Sunil, and C. Labesh Kumar

20 Development of a Preliminary Approach for Automatic Generation of the CAD Model of the Spur Gear 199
 Shubham Agarwal, Gurunandan Jamalpur, Nikhil Tuljapurkar, and Jayakiran Reddy Esanakula

21 Design of a Robot for the Welfare of the Poultry 209
 Rushikesh Hanuman Yede and Skylab Paulas Bhore

22 A Despeckling Filter for Ultrasound Images Based on Cellular Automata Approach 217
 Ankur Bhardwaj, Sanmukh Kaur, Manoj Shukla, and Anand Prakash Shukla

23 Development of a Preliminary Approach for Automatic CAD Model Generation of the IC Engine Piston 227
 Nikhil Tuljapurkar, Gurunandan Jamalpur, Shubham Agarwal, and Jayakiran Reddy Esanakula

24 Temperature Control Methodology for Catalytic Convertor to Reduce Emissions and Catalyst Aging 239
 S. Mithun Vaisnav and Sivanesan Murugesan

25 Solar Powered Autonomous Robotic Car Using for Surveillance 249
 V. Premchandran, M. Karthikkumar, V. Thamizharasan, and E. Sathish

26 Design and Simulation of Hybrid Microsystem and Its Effect on the Environment Using Homer Software 257
 Alok Kumar and Shelly Vadhera

27 Battery Charging Using Solar Photovoltaic System with Maximum Power Point Tracking 267
 Siddharth Samaddar, Ujjwal Rastogi, Soham Tyagi, and Saurabh Mishra

28 Design and Analysis of Hydraulic Machining Fixture for a Drifter Bit of a Top Hammer 277
 Nagaveni Thallapalli, G. Sudheer Kumar Reddy, J. Jaswanth Raju, S. B. Manikanta Katepalli, and Vineela Chippe

29 Inverse Kinematic Analysis of PUMA 560 for Vision Systems 285
 Navya Mohan, Athul Thomas, P. P. Prasanth, M. S. Midhun, and James Kurian

30	Experimental Investigation on Portable Refrigerating Bottle	295
	Shiva Kumar Reddy Devasani, Sudeshna Vodnala, and K. Krishnamurthy	
31	Challenges of Introducing Lean Six Sigma, IoT in Industry 4.0, and Supply Chain Management: A Review	303
	Vedant Kale, Chetan Katke, Shailendra Dayane, and Prashant Thakar	
32	Development of Novel Concrete for Recharging the Ground Water Levels in the Rocklands of Urban Areas	317
	Venu Malagavelli, A. Jagadish Babu, S. Siva Rama Krishna, and V. Suryaprakash Reddy	
33	Vision-Based Real-Time Hand Wash Accuracy Prediction	327
	C. Kavinkumar, S. Tony Geefus, and Prashant R. Nair	
34	Development and Analysis of Efficient Dispatching Rules for Minimizing Flow Time and Tardiness-Based Performance Measures in a Job Shop Scheduling	337
	S. Ashwin, V. Shankaranarayanan, Damien lamy, S. P. Anbuudayasankar, and M. Thenarasu	
35	Vibration Measurement Using a Low-Cost MEMS Accelerometer Kit for the Education	347
	Syed Faizan Shah and Skylab Paulas Bhore	
36	Disease Prediction by Stacking Algorithms Over Big Data from Healthcare Communities	355
	M. Hema Latha, A. Ramakrishna, B. Sudarsha Chakravarthi Reddy, Ch. Venkateswarlu, and S. Yamini Saraswathi	
37	Experimental Investigation on Performance and Emission Characteristics of Mixture of Sunflower and Soybean Biodiesels	365
	Shiva Kumar Reddy Devasani and K. Krishna Murthy	
38	Experimental Study of Nano Additive-Added Biodiesel Blend to Improve the Engine Performance Characteristics.	381
	B. Jayakrishnan and D. Senthilkumar	
39	Detection of Fake and Clone Accounts in Twitter Using Classification and Distance Measure Algorithms.	391
	S. Siva Rama Krishna, K. Umakanth Reddy, T. Anji Reddy, A. Saiteja, and R. Sumanjali	
40	Review of Recent Developments in Sustainable Traffic Management System	401
	Bhawini Sharma and Jai Kumar Maherchandani	

41	Automatic Machine for Round Welding Using Programmable Logic Controller (PLC)	411
	Gautam Gupta, Rajanpreet Singh, and Anant Kumar Singh	
42	Road Surface Quality Monitoring Using Machine Learning Algorithm	423
	Prabhat Singh, Abhay Bansal, Ahmad E. Kamal, and Sunil Kumar	
43	Optimization of Electric Vehicle Ladder Frame Chassis Based on Material and Thickness Parameter Variation Using FEA	433
	Yash Keskar, Sourabh Damkale, and Pankaj Dhattrak	
44	Smart Personal Task Scheduler	443
	N. Sai Swaroop Krishna, A. Krishna Tej, and M. Suchithra	
45	Employee Attrition Prediction Using Machine Learning Comparative Study	453
	Shobhit Aggarwal, Manik Singh, Shivam Chauhan, Mugdha Sharma, and Deepti Jain	
46	Optimising Effect of Resonance by Harmonic Analysis of Ethylene Propylene Diene Monomer (EPDM) Engine Mount	467
	Tripti Khulbe and Vikas Rastogi	
47	Design and Analysis of Multi-Tool Light Agricultural Vehicle	475
	K. Vijay Kumar, Ismail Kakaravada, and Y. Dilip Kumar	
48	Identification of Alzheimer’s Disease Using Various Deep Learning Techniques—A Review	485
	Ragavamsi Davuluri and Ragupathy Rengaswamy	
49	UPQC with AI Techniques for Power Quality Improvement	499
	M. Sharanya, Basavaraja Banakara, and M. Sasikala	
50	Field Investigation of Fundamental Frequency of Structures Using Frequency Domain Vibration Analysis	509
	Saugato Dey, Saikat Kr Shome, and Kalyan Kr Mistry	
51	On the Study and Analysis of Automated Aquaponics System Using AVR Microcontroller	519
	Alka Sathyan, Senthil Arumugam Muthukumaraswamy, and Habibur Rahman	
52	Stack-based Outbound Operation Method for Steel Plate Yard in Shipbuilding	529
	Lebao Wu and Zuhua Jiang	
53	Investigations on Microstructures by Using Friction Stir Processing	539
	Bazani Shaik, G. Harinath Gowd, B. Durga Prasad, and P. Siddik Ali	

54	Comparative Study of Plain and Twisted Ducts in Heat Transfer	549
	M. Udaya Kumar and Gadi Karthik	
55	Performance Evaluation of a Predictive and PID Control Applied to a Didactic Flow Regulation Process	559
	Wilson Guambo, Byron P. Corrales, Luigi O. Freire, and Mauro D. Albarracin	
56	Analysis Factors in the Adoption of Digital Manufacturing Technologies in SMEs	571
	Luisa Maria Tumbajoy and Mariela Muñoz-Añasco	
57	Analysis of Microstructural Features and Corrosion Resistance of Cryogenic Burnished and Hydroxyapatite Powder Burnished Titanium Alloy	581
	Samatham Madhukar, Gyara Ajay Kumar, Dharamkar Sai Suman, Syed Azam Pasha Quadri, and U. Ashok Kumar	
58	Detection of Micro-defects on Metal Screw Surfaces Based on Faster Region-Based Convolutional Neural Network	587
	Mohd Nor Azmi Ab Patar, Muhammad Azmi Ayub, Nur Aainaa Zainal, Muhammad Aliff Rosly, Hokyoo Lee, and Akihiko Hanafusa	
59	Effects of Rotation Speeds on Electrical Submersible Pump Performance Under Two-Phase Flow	599
	Abdulqader Hasan, Salman Shahid, Sharul Sham Dol, Mohamed S. Gadala, Mohd Shiraz Aris, and Mohammed Alavi	
60	Design of Electrical Screwdriver Using Arduino and Planetary Gear System	609
	Rajanpreet Singh, Gautam Gupta, and Gaganpreet Kaur	
	Author Index	619

About the Editors

Dr. A. N. R. Reddy is a Ph.D. in Mechanical and Manufacturing Engineering, currently working as a Professor and HOD of Mechanical Engineering at MRCET Campus. He is a life member of professional associations ORSI, ISTAM, IndACM, ISTE, EWB, SAE India, and ISSMO. He has received many academic excellence and research innovation awards like the Malaysian Government International Student Award ‘Malaysian International Scholarship’. His research interests include Mathematical Modelling, DOE and TRIZ, Bioenergy, Pyrolysis of Biomass, Synthesis of Nanomaterials, Engine Performance Analytics, Applied and Fluid mechanics, Spectrophotometry. Dr. Reddy, as a principle investigator, has successfully completed AICTE, Government of India sponsored research project “Multi-Objective Optimization of Production Process Parameters using Evolutionary Algorithms” and actively guiding Ph.D., PG and UG research projects. Dr. A. N. R. is the organizing chair and editor for Springer book series SIST “Proceedings of Intelligent Manufacturing and Energy Sustainability”.

Dr. Deepak Marla is currently working as an Assistant Professor in the Department of Mechanical Engineering at the Indian Institute of Technology Bombay (IIT Bombay). He has obtained Ph.D. from IIT Bombay and had done his post-doctoral work from the Technical University of Denmark and University of Illinois at Urbana-Champaign. His work is in the domain of micro/nano-manufacturing using advanced techniques that involve lasers, electric discharges, electrochemical reactions, plasmas, and micro-tools. His research focuses on gaining a fundamental insight into these processes through a synergetic use of multi-physics modeling and simulation, and experiments with an eye on addressing critical challenges at the process level.

Dr. Margarita N. Favorskaya received her engineering diploma from Rybinsk State Aviation Technological University, Russia, in 1980 and was awarded a Ph.D. by St. Petersburg State University of Aerospace Instrumentation, St. Petersburg, in 1985. Since 1986 she is working in the Siberian State Aerospace University, Krasnoyarsk, in which she is responsible for the Digital Image and Videos

Processing Laboratory. Presently, she is a Full Professor and the Head of Department of Informatics and Computer Techniques, Siberian State Aerospace University. Her main research interests are in the areas of digital image and videos processing, pattern recognition, fractal image processing, artificial intelligence, information technologies, and remote sensing. She has authored/co-authored more than 130 publications. Margarita Favorskaya is a member of KES International organization and the IPC member of a number of National and International Conferences. She is on the editorial board of *International Journal of Computer and Information Science* and *International Journal of Intelligent Decision Technology*. She has a number of awards from the Ministry of Education and Science of the Russian Federation for significant contribution in educating and training a number of highly qualified specialists over a number of years.

Dr. Suresh Chandra Satapathy is a Ph.D. in Computer Science Engineering, currently working as a Professor of School of Computer Engineering and Dean-Research at KIIT (Deemed to be University), Bhubaneswar, Odisha, India. He held the position of the National Chairman (Educational and Research) of Computer Society of India and also a Senior Member of IEEE. His active research areas include Swarm Intelligence, Machine Learning, Data Mining and Cognitive Sciences. He has more than 150 research publications in reputed journals and conference proceedings. Dr. Satapathy has played an integral role in organizing more than 60 International Conferences in India as the Organizing Chair and edited more than 80 Book Volumes from Springer LNCS, AISC, LNEE and SIST Series as a Corresponding Editor. He is also a part of the Editorial board of *IGI Global*, Inderscience, *Growing Science Journals* and also a Guest Editor for *Arabian Journal of Science and Engineering* published by Springer. He is also the Editor-in-Chief of *IJIDSS* from Inderscience and Associate Editor of *KES Journal* from IOS press. He has been invited to and visited a number of global Universities like University of Leicester, London, NTU, Singapore, Duy Tan University, Vietnam, etc. for delivering lecture and collaboration. Dr. Satapathy was awarded the Leadership in Academia Award in India by ASSOCHAM for the year 2017.

Chapter 1

An Experimental Investigation into the Performance Characteristics of TiO₂/Ethylene Glycol Nanofluid Flowing in a Horizontal Counterflow Heat Exchanger



Thembelani Sithebe and Veeredhi Vasudeva Rao

Abstract This paper presents experimental results on the thermal performance of low volume concentration (0.002%, 0.004% and 0.007%) TiO₂/ethylene glycol nanofluid. Investigations are conducted using a counterflow heat exchanger in the range of fluid temperatures from 30° to 70 °C with Reynolds number ranging from 200 to 700. It is concluded that the non-dimensional heat transfer coefficient Nu increases with Reynolds. Addition of nanoparticles to the base fluid by 0.007% increased the thermal conductivity by 2%. Experimental results show that there is reduction in heat transfer coefficient as a function of temperature that corresponds to the reduction in Prandtl number. Important results are presented in graphical and tabular forms.

1.1 Introduction

During the last couple of decades, researchers all over the world have focused their attention to employ nanofluids as heat transfer medium in thermal systems. Extensive studies have been conducted to identify suitable alternatives to replace heat transfer fluids with much better thermal properties. Tijani and bin Sudirman [1] carried out an investigation into the thermo-physical properties and heat characteristics of water-antifreeze mixed with Al₂O₃/CuO nanofluid as a coolant of a car radiator. They concluded that copper oxide nanofluid had relatively a higher heat transfer performance compared to aluminium oxide nanofluid. Reddy and Rao [2] carried out an experimental investigation on the performance of water-based (TiO₂)

T. Sithebe (✉) · V. V. Rao
University of South Africa, Johannesburg, South Africa
e-mail: sithet@unisa.ac.za

V. V. Rao
e-mail: vasudvr@unisa.ac.za

and ZnO nanofluids in a horizontal concentric tube-in-tube heat exchanger at concentrations of 0.002 and 0.004% (for both oxides) and various Reynolds numbers ranging from 1600 to 6100. It was observed that the convective heat transfer coefficient and effectiveness increase with an increase in volume concentration and Reynolds number. Nusselt number increases with increasing volume concentration of nanofluids and Reynolds number. They presented the variations of heat transfer coefficient in both dimensional and non-dimensional forms as a function of Reynolds number for different volume concentrations of nanofluids. Abdollahi-Moghaddam et al. [3] experimentally investigated the thermal performance (heat transfer coefficient) of water-based CuO nanofluids with low volume concentration (0.03, 0.1, 0.3, 0.5 and 0.7%) of nanoparticles. They also measured the pressure drop in their experiments. They reported 2.8 times improvement in heat transfer when compared to pure water while there is a rise in pressure drop of 1.4 times. Contreras et al. [4] performed experiments on an automotive cooling system using graphene and silver nanoparticles with concentrations of 0.01, 0.05 and 0.1% with a view to determine the thermo-hydraulic performance. Graphene nanofluid achieved better results at 0.05% volume concentration than silver, and this observation was attributed to the fact that graphene has a higher thermal conductivity compared to silver. Devireddy et al. [5] determined the cooling performance of an automotive radiator with ethylene glycol water-based mixture (40:60 volume %) nanofluids with concentrations of 0.1, 0.3 and 0.5%. The experiment was conducted in the range of Reynolds numbers from 4000 to 15,000. The result showed that the heat transfer enhancement is based on the quantity of nanoparticles added to the base fluid. Other experimental studies have been performed by many researchers on performance of nanofluids, and none of them have used the widely used ethylene glycol as a base fluid. This research evaluates the performance of ethylene glycol nanofluid in a mixture of EG (100%) as a base fluid in laminar flow in a counterflow heat exchanger to augment the data base of nanofluid with new knowledge.

1.2 Experimental Test Set-Up

To investigate the performance of EG-based TiO₂ nanofluid, a counterflow heat exchanger is employed. A test rig shown in Fig. 1.1, consisting necessary instrumentation shown in Fig. 1.2, is designed and developed in the laboratory. The rig has two flow circuits—one for the nanofluid and the other for the cold fluid. The nanofluid flows through a closed circuit, and the cold fluid runs through an open circuit. Provision is made to measure inlet and outlet temperatures of both the hot and cold fluids. The rig has the working fluid storage with a heating element, a centrifugal pump, a control valve, flow meter, ball valve to control the flow. The hot working fluid (TiO₂/EG) flows in the inner pipe of diameter 12.7 mm. The reliability and accuracy of the test rig were established through a heat balance test (Eq. 1.5).

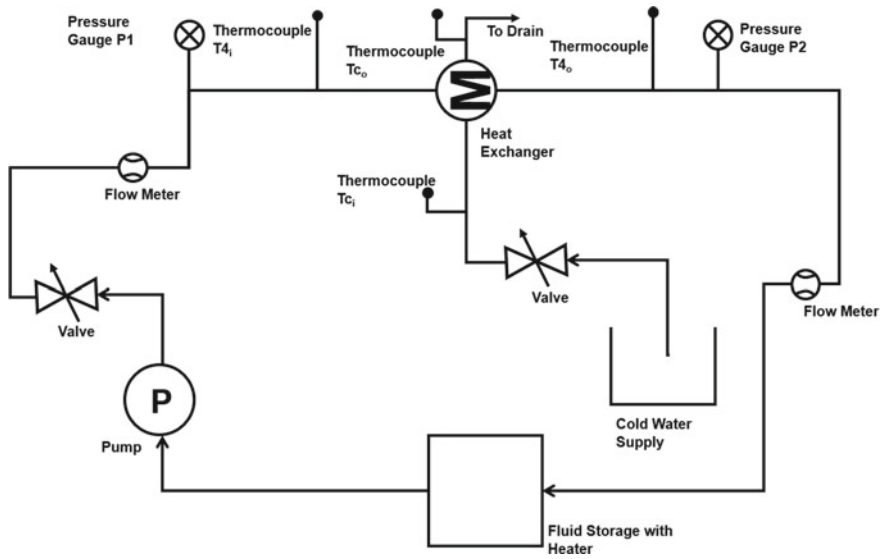


Fig. 1.1 Schematic diagram of the experimental test rig

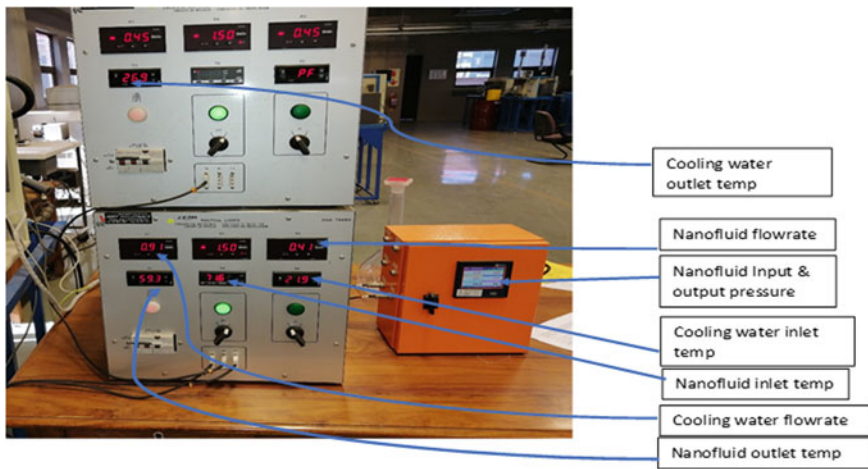


Fig. 1.2 Experimental data acquisition system

Table 1.1 Heat exchanger tube specifications

Item	Value (mm)
Length	740
Inner tube diameter	12.7
Outside diameter	15
Tube thickness	1.15

1.3 Preparation of Nanofluid

The preparation of nanofluids was made through the two-step method as detailed by Yu and Xie [6]. In this method, the dry powder form of TiO₂ nanoparticles (21 nm size) is dispersed into ethylene glycol under homogenic agitation to break down the aggregates of nanopowder. The nanofluid is prepared using ethylene glycol as the base fluid and titanium oxide (TiO₂) nanoparticles with 0.002, 0.004 and 0.007%.

The quantity of nanoparticles is calculated using $\varphi = \frac{\left(\frac{w}{\rho}\right)_{\text{TiO}_2}}{\left(\frac{w}{\rho}\right)_{\text{TiO}_2} + \left(\frac{w}{\rho}\right)_{\text{EG}}}$, where φ is nanoparticle volume fraction, ' ρ ' is density and ' w ' is the weight of nanopowder for the desired volume concentration. The following procedure is used to prepare nanofluid: (1) weight of TiO₂ nanoparticles is accurately measured and mixed with ethylene glycol, and (2) the mixture is put in a homogenizer for 8 h to achieve uniform dispersion. Estimated quantity of TiO₂ is added to 100 ml of base fluid. A surfactant C-TAB (Cetyltrimethylammonium bromide) was added with weight equal to one-tenth weight of TiO₂ nanoparticles.

The thermo-physical properties like thermal conductivity, specific heat, dynamic viscosity and density of nanofluid were evaluated through equations below. The above procedure is repeated for all samples.

1.4 Data Reduction

In this investigation, properties such as thermal conductivity, viscosity, specific heat and density were estimated from the correlations available in the literature: Pak and Cho [7] and Xuan and Roetzel [8] as indicated below.

$$\rho_{\text{nf}} = \varphi \cdot \rho_{\text{np}} + (1 - \varphi) \cdot \rho_{\text{bf}} \quad (1.1)$$

$$(\rho \cdot C_p)_{\text{nf}} = \varphi \cdot (\rho \cdot C_p)_{\text{np}} + (1 - \varphi) \cdot (\rho \cdot C_p)_{\text{bf}} \quad (1.2)$$

where subscripts np, bf and nf refer to nanoparticle, base fluid and nanofluid, respectively. The rate of heat transfer (Q), the heat transfer area (A), the specific heat capacity (C_p) and the temperature difference of the fluids ($\Delta T_{\text{bf}}, \Delta T_{\text{nf}}$) were determined analytically through the use of experimental data in the rig.

$$\text{From } Q = \dot{m}C_p\Delta T \quad (1.3)$$

$$(\dot{m}C_p\Delta T)_{\text{water}} = (\dot{m}C_p\Delta T)_{\text{EG}} \quad (1.4)$$

Equation (1.4) was applied for the validation of the experimental rig.

$$(\dot{m}C_p\Delta T)_{\text{water}} = (\dot{m}C_p\Delta T)_{\text{nf}} \quad (1.5)$$

Equation (1.5) was used to conduct heat balance test. The overall heat transfer coefficient is determined from Eq. (1.6) as quoted by Cengel [9] using the measured inlet and outlet temperatures of the fluid.

$$Q = FUA\Delta T_{\text{im}} \quad (1.6)$$

$$\text{Where } \Delta T = \frac{\Delta T_1 - \Delta T_2}{\ln(\Delta T_1/\Delta T_2)} \quad (1.7)$$

$$\text{And } \Delta T_1 = T_{\text{nf in}} - T_{\text{w out}} \quad \text{and } \Delta T_2 = T_{\text{nf out}} - T_{\text{w in}}$$

$$Q_{\text{av}} = \frac{(\dot{m}C_p\Delta T)_w + (\dot{m}C_p\Delta T)_{\text{nf}}}{2} \quad (1.8)$$

where F is the correction factor.

The Hamilton and Crosser [10] model Eq. (1.9) was employed to determine the effective thermal conductivity of the nanofluid.

$$k_{\text{nf}} = k_{\text{bf}} \left[\frac{K_p + (n-1)K_{\text{bf}} - \varphi(n-1)(K_{\text{bf}} - K_p)}{K_p + (n-1)K_{\text{bf}} + \varphi(K_{\text{bf}} - K_p)} \right] \quad (1.9)$$

where $n = 3/\psi$, in which n is the empirical shape factor and ψ is the sphericity. The sphericity of the particle is defined as the ratio of the surface area of a sphere to the surface area of the particle. The sphericity ψ for sphere is 1 and for cylinder is 0.5 (Table 1.2).

The Reynolds and the Nusselt numbers are obtained from:

$$\text{Re}_{\text{nf}} = \frac{4\dot{m}_{\text{nf}}}{\pi\mu D_h} \quad \text{and} \quad (1.10)$$

Table 1.2 Thermo-physical properties of ethylene glycol TiO₂ nanoparticles at 30 °C

S. No.	Material	Value (mm)	Density (kg/m ³)	Thermal conductivity (W/mK)	Specific heat (kJ/kg K)	Viscosity (mPa s)
1	Ethylene glycol base fluid	740	1109	0.258	2.347	16.1
2	TiO ₂ nanopowder	1.15	4260	11.7	6.89	–

The properties of ethylene glycol were taken from the ASHRAE Handbooks

$$Nu_{nf} = \frac{(\delta/8)Re Pr}{1 + 12.7\sqrt{((\delta/8)Pr^{2/3})}} \left[1 + \left(\frac{d}{L}\right)^{2/3} \right] k. \quad (1.11)$$

where theoretical value of dynamic viscosity can be calculated from Wang et al. [11] in which $\mu_{nf} = \mu_{bf}(1 + 7.3\phi + 123\phi^2)$.

Nusselt number is estimated from $Nu = 0.000972 Re^{1.17} Pr^{1/3}$ adopted from Said and Saidur [12] for $Re < 2000$.

The Prandtl number (Pr) is given by: $Pr = \frac{\mu C_p}{K}$, where μ is the viscosity and C_p is the specific heat.

1.5 Results and Discussion

The experimental data generated in the present investigation is processed, analysed and presented in graphical form in charts. These charts are used to discuss the results and the dependence of heat transfer coefficient on the variables such as Reynolds number, Nusselt number and volume concentration of nanofluids. Measurements of inlet and outlet temperature and pressure of titanium oxide nanofluid and the cooling water were taken for the following flowrates, i.e. 0.2, 0.3, 0.4, 0.5, 0.6 L per minute (LPM), for different nanoparticle volume concentrations of 0.002, 0.004 and 0.007%.

The nanofluid density, thermal conductivity, specific heat and the dynamic viscosity all increase with an increase in the percentage volume of nanoparticles. Thermal conductivity was enhanced by 1.94% at a nanoparticle percentage concentration of 0.007%. Compared with EG, the collisions and interaction between nanoparticles enhance thermal conductivity and reduce the thermal resistance of the nanofluid. As more nanoparticles are added, thermal resistance is further reduced, and thermal conductivity gets more enhanced. The nanoparticle surface area is higher than that of EG at nanoscale. This translates to an enhancement of thermal conductivity in nanofluids. Nanoparticles in nanofluids act like molecules and the Brownian motion effect create a stable suspension.

Figure 1.3 shows the variation of heat transfer coefficient with increase in the percentage of nanoparticles. It is observed that there is a reduction of heat transfer coefficient as the percentage of TiO_2 nanoparticles increases in ethylene glycol base fluid. This reduction can be attributed to the corresponding reduction in the Prandtl number of the fluid.

Figure 1.4 shows the effect of volume/mass flowrate of nanofluids with 0.002%, nanoparticle concentrations on the Reynolds and Nusselt numbers at 30 °C. In this analysis, Reynolds and Nusselt numbers increase with an increase in volume/mass flowrate. This is consistent with Eqs. 1.10 and 1.11, in which the Reynolds number is directly proportional to the mass flowrate and the Nusselt number which is also

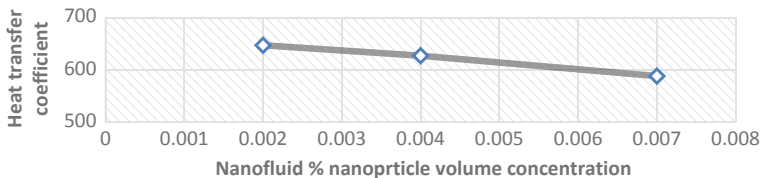


Fig. 1.3 Variation of HTC as a function of volume concentration of TiO₂ nanoparticles at constant temperature of 50 °C and constant nanofluid flowrate of 0.5LPM

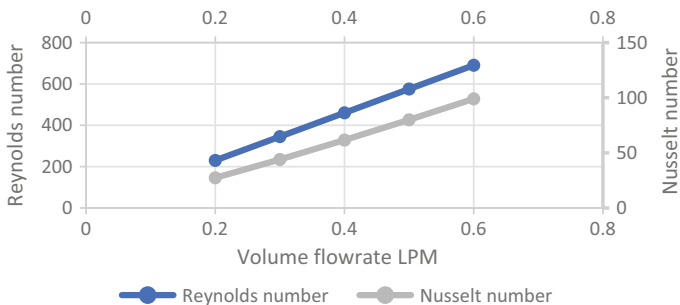


Fig. 1.4 Variation of Reynolds and Nusselt numbers with nanofluid flowrate at constant 0.002% nanoparticle vol. concentration, constant temperature of 30 °C

directly proportional to the Reynolds number. Similar results are observed for 0.004 and 0.007% volume concentration.

Devireddy et al. [5] depicted a relationship in which the Reynolds and Nusselt numbers increase with an increase in nanofluid volume flowrate.

Figure 1.5 shows the typical relation between Reynolds number and Nusselt for EG/TiO₂ nanofluid with 0.002% volume concentration. Figure 1.6 shows the variation of heat transfer coefficient as a function of temperature for 0.002% volume concentration. The trends were very similar for the other concentrations at 0.004% and 0.007%. The overall effect is that the HTC decreases with an increase in temperature of the nanofluids. This observation is in line with the findings of Sundar et al. [13] on nanofluids.

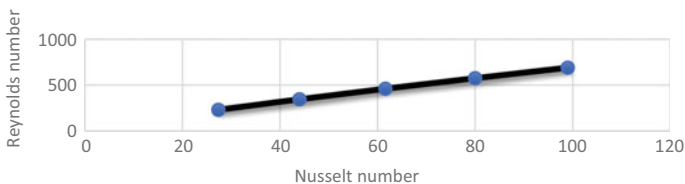


Fig. 1.5 Variation of Reynolds number with Nusselt number at nanoparticle concentration of 0.002% at different flowrates

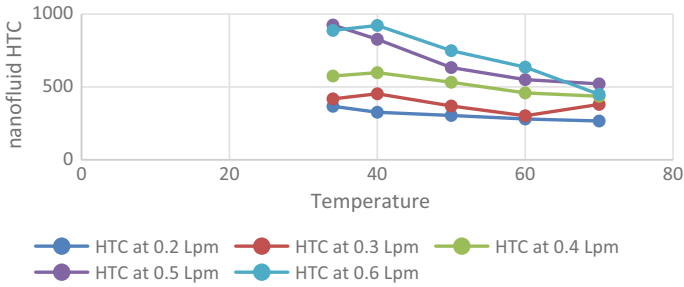


Fig. 1.6 Variation of HTC as a function of temperature at a nanoparticle concentration of 0.002%

1.6 Conclusion

An experimental investigation is conducted on a counterflow heat exchanger using EG-based TiO_2 nanofluids with low volume concentrations. From this investigation and experimental data generated, it is concluded that the Nusselt number increases as a function of Reynolds number for EG-based TiO_2 nanofluids. The HTC decreases with an increase in volume concentration of nanoparticles and temperature of the nanofluid. This observation is consistent with variation of Prandtl number as function of temperature and volume concentration of nanoparticles. More experimental data is needed to draw further conclusions in the range beyond this investigation. Several experiments are underway to increase the level of understanding of the role of various parameters on thermal properties and heat transfer coefficient.

References

1. Tijani, A.S., bin Sudirman, A.S.: Thermos-physical properties and heat transfer characteristics of water/anti-freezing and $\text{Al}_2\text{O}_3/\text{CuO}$ based nanofluid as a coolant for car radiator. *Int. J. Heat Mass Transfer.* **118**, 48–57 (2018)
2. Reddy, M.C.S., Rao, V.V.: Experimental investigation of heat transfer coefficient and friction factor of ethylene glycol water based TiO_2 nanofluid in double pipe heat exchanger with and without helical coil inserts. *Int. Commun. Heat Mass Transf.* **50**, 68–76 (2014)
3. Abdollahi-Moghaddam, M., Motahari, K., Rezaei, A.: Performance characteristics of low concentrations of CuO/water nanofluids flowing through horizontal tube for energy efficiency purposes; an experimental study and ANN modelling. *J. Mol. Liq.* (2018). <https://doi.org/10.1016/j.molliq.2018.08.149>
4. Contreras, E.M.C., Oliveira, G.A., Bandarra Filho, E.P.: Experimental analysis of the thermohydraulic performance of graphene and silver nanofluids in automotive cooling systems. *Int. J. Heat Mass Transf.* **132**, 375–387 (2019)
5. Devireddy, S., Mekala, C.S.R., Veerredhi, V.R.: Improving the cooling performance of automobile radiator with ethylene glycol water based TiO_2 nanofluids. *Int. Commun. Heat Mass. Transf.* **78**, 121–126 (2016)

6. Yu, W., Xie, H.: A review on nanofluids: preparation, stability mechanisms, and applications. *J. Nanomater* **2012**, 1 (2012)
7. Pak, B.C., Cho, Y.I.: Hydrodynamic and heat transfer study of dispersed fluids with submicron metallic oxide particles. *Exp. Heat Transf. Int. J.* **11**(2), 151–170 (1998)
8. Xuan, Y., Roetzel, W.: Conceptions for heat transfer correlation of nanofluids. *Int J Heat Mass Transf* **43**(19), 3701–3707 (2000)
9. Cengel, Y.: *Heat and mass transfer: fundamentals and applications*. McGraw-Hill Higher Education (2014)
10. Hamilton, R.L., Crosser, O.K.: Thermal conductivity of heterogeneous two-component systems. *Ind Eng Chem Fundam* **1**(3), 187–191 (1962)
11. Wang, X., Xu, X., Choi, S.U.: Thermal conductivity of nanoparticle-fluid mixture. *J. Thermophys. Heat Transf.* **13**(4), 474–480 (1999)
12. Said, Z., Saidur, R.: Thermophysical properties of metal oxides nanofluids. *Nanofluid Heat and Mass Transfer in Engineering Problems*, p. 39 (2017)
13. Sundar, L.S., Sharma, K.V., Singh, M.K., Sousa, A.C.M.: Hybrid nanofluids preparation, thermal properties, heat transfer and friction factor—a review. *Renew. Sustain. Energy Rev.* **68**, 185–198 (2017)

Chapter 2

Calibration of Industrial Fanuc 430iF Series Robot Arm



Mazleenda Mazni, Muhammad Azmi Ayub,
and Norhafiza Muhammad

Abstract Robot calibration is a process to enhance the accuracy of robot manipulator through modification of the robot control software. The repeatability motion causes wears and tears to the robot joints that deteriorate the robot accuracy and repeatability. These wears and tears affect the position and orientation of the end-effector at any point in the workspace relative to a fixed known coordinate frame which is a set of three orthogonal right-handed axes X , Y , and Z , called principal axes. To compensate and improve the absolute positioning accuracy of serial link manipulator, a cost-effective measurement system was applied to calibrate the robot using theodolite system. The calibration process was carried out at the point of interaction between the workpiece and the end-effector of the Fanuc 430iF series arm robot. The experimental method of the robot calibrations was explained, analyzed, and evaluated. The analysis of inaccuracies and the sources of errors in the calibration was discussed. The outcome of this calibration procedures has the potential to be used to correct the inaccuracies in specific components of the robot joints and then improve the performance of the robot.

2.1 Introduction

Industrial robots transport objects to multiple locations in the workspace, which is one of their main functions. Positioning accuracy is required by these robots in order to accomplish their tasks [1]. Robot end-effectors can have positioning accuracy anywhere in the workspace relative to a fixed known coordinate frame.

M. Mazni (✉)

Faculty of Mechanical Engineering, Universiti Teknologi MARA Cawangan Johor, Jalan Purnama, 81750 Masai, Johor, Malaysia
e-mail: mazleenda@uitm.edu.my

M. A. Ayub · N. Muhammad

School of Mechanical Engineering, College of Engineering Studies, Universiti Teknologi MARA, 40450 Shah Alam, Selangor, Malaysia
e-mail: muhammadayub@uitm.edu.my

This coordinate frame consists of three orthogonal axes—X, Y, and Z, which are called principal axes. Robot manufacturers usually specify accuracy during the installation and commissioning of their new products. Nevertheless, the accuracy of the positioning system may deteriorate over time due to several factors. In addition to wearing down the robot joints, dislocation of the target in relation to a reference coordinate frame, and changes in the kinematic parameters of the robot manipulator, these factors affect the performance of the robot.

To improve the positioning accuracy, the manipulator of the robot needs to be calibrated and recalibrated periodically from time to time. Robot calibration is a process of improving the accuracy of a robot manipulator by modifying the robot control software [2, 3].

Calibrating a robot is the process of determining the geometrical dimensions and mechanical characteristics of its structure by determining the values of its kinematic and dynamic parameters [4]. The need for robot calibration has arisen in many applications that necessitate off-line programming and situations. This requires multiple robots to share the same applications software. Without calibration, robots which share application programs may experience significant accuracy degradation [5, 6].

Furthermore, robots should be recalibrated due to wears and tears of the robot joints over a certain period. This recalibration procedure should take a fraction of the reprogramming time for calibration to be economically acceptable. There are several different measurement techniques which can be used to perform robot calibration such as using laser [7, 8] or charge-coupled device (CCD) camera techniques, theodolites [9], ultrasonic measurements [10], coordinate-measuring machine (CMM), and machine vision technique [11]. In this paper, theodolite is used for the robot calibration technique. To implement this technique, an experiment will be carried out to determine the position accuracy of the end-effector of industrial Fanuc 430iF series robot link manipulator.

2.2 Calibration Apparatus and Procedure

In this research, calibration equipment consists of a Fanuc 430iF series arm robot, teach pendant controller, and theodolite as shown in Fig. 2.1. The Fanuc 430iF series arm robot is a spherical manipulator which has six revolute joints that give six degrees of freedom movement. Fanuc 430iF series arm robot is designed to perform task in the 3-D space. The end-effector must follow a planned trajectory when manipulating workpieces or performing tasks in a robot work cell. The position and orientation of the tool need to be controlled by each joint and link of the manipulator. The robot system is equipped with servo controller for various industrial applications such as spotting welding applications.

The robots offer high dynamics with large work envelope which easily causes changes in positioning accuracy of the end-effector. Commands are issued to the robot system through the teach pendant. Teach pendants are used to interface robot

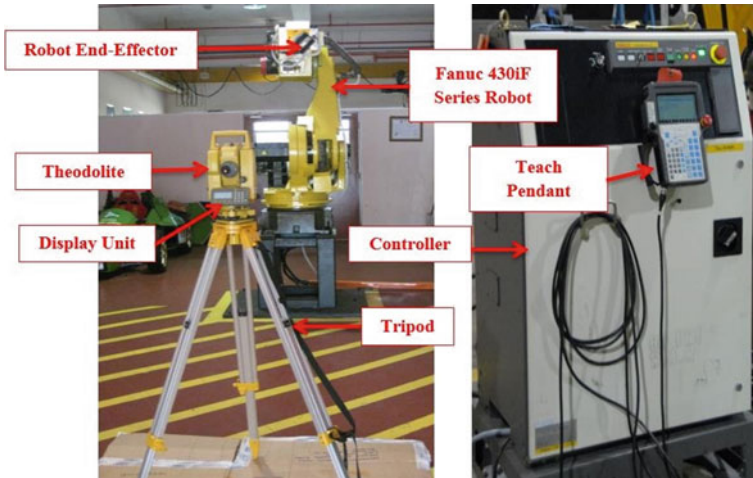
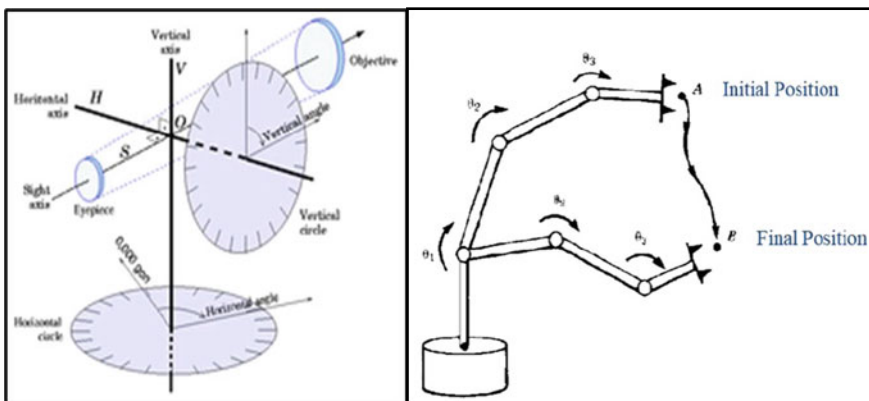


Fig. 2.1 The apparatus used during calibration

software and the operator. Through a cable, the teach pendant is connected to the PC board in the controller. The arm and wrist of the robot can be moved with the keys on the teach pendant [9]. An optional homing bracket allowed automating and customizing the arm’s homing routine through the teach pendant. End-effectors such as grippers and other tools enabled the arm to perform specialized tasks.

A theodolite is a well-established technology for measuring points in three dimensions, and it is used to measure angles in horizontal and vertical directions [9]. Figure 2.2a shows two axes of a theodolite equipped with graduated circles that can be observed under magnifying glasses. It is essential that a theodolite’s



a. The horizontal and vertical axes.

b. Point A (Initial) to point B (Final).

Fig. 2.2 Schematic of experimental procedures

horizontal and vertical axes are perpendicular; otherwise, index errors, horizontal axis errors, and collimation errors will occur. By adjusting the theodolite's mechanism, thus index error, horizontal axis error, and collimation error can be eliminated. Theodolites are mounted on tripod heads for accuracy in leveling and must be vertically positioned above the measuring point.

In order to perform this experimental task, a model with parameters which accurately represent the real robot errors must be developed. Next, specifically chosen features of the robot model accurately reflect the measurements made. Figure 2.2b shows the schematic of the robot manipulator indicated two points of calibration; point *A* and point *B*. Point *A* and point *B* are the initial position and the final position of the end-effector, respectively. The end-effector will be moved by using the controller from point *A* (initial) to point *B* (final). This experimental procedure will be performed repetitively by changing the angle at Joint 1, Joint 2, and Joint 3 as illustrated in Fig. 2.3. Two sets of experimental reading will be taken. The first reading is using theodolite, and the second reading is using the teach pendant. Both readings are important to measure the distance of end-effectors movements from point *A* (initial) to point *B* (final). To reduce the experimental error, the experimental procedure will be repeated twice. The sources of error will be identified.

2.2.1 Results from the Teach Pendant

In this experiment, the difference δf (final position) and δi (initial position) has been calculated to represent the coordinates of movements of the end-effector through space from point *A* (initial) to point *B* (final). Figure 2.3a shows the robot test joint

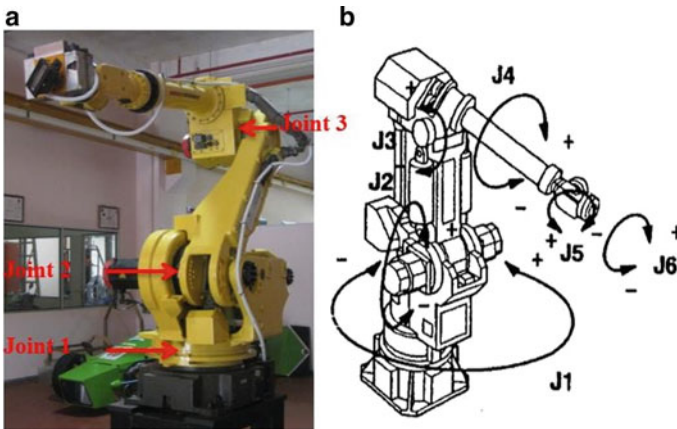


Fig. 2.3 a Robot test joint and b global coordinate system

for the Fanuc 430iF series robot, and the corresponding coordinate system is shown in Fig. 2.3b.

All the calculation result is shown in Tables 2.1, 2.2, and 2.3. A next step in the calculation is to obtain the distance of movements of the end-effector using Eq. 2.1. By using theorem Pythagoras, we can find the distance movements of the end-effector from point A to point B .

Table 2.1 Result calculation of Joint 1

Test	Initial coordinate		Final coordinate		Difference ($\delta f - \delta i$)		Distance, d_i
	X_1	Y_1	X_2	Y_2	δx	δy	
1	1159.484		1119.997		39.487		0.301
	-1.985		300.741		298.756		
	1098.567		1098.414		0.153		
2	1174.745		1174.995		0.25		0.189
	77.348		-112.484		189.832		
	850.877		850.781		0.096		

Table 2.2 Result calculation of Joint 2

Test	Initial coordinate		Final coordinate		Difference ($\delta f - \delta i$)		Distance, d_i
	X_1	Y_1	X_2	Y_2	δx	δy	
1	1439.328		1037.880		401.448		0.490
	15.176		10.935		4.241		
	842.831		562.265		280.566		
2	1021.824		1659.160		637.336		0.073
	10.758		17.468		6.71		
	542.137		895.958		353.821		

Table 2.3 Result calculation of Joint 3

Test	Initial coordinate		Final coordinate		Difference ($\delta f - \delta i$)		Distance, d_i
	X_1	Y_1	X_2	Y_2	δx	δy	
1	1156.218		1176.862		20.644		0.248
	89.433		91.014		1.581		
	1098.414		850.948		247.466		
2	1142.165		1163.646		21.481		0.458
	12.069		12.289		0.22		
	1141.239		684.118		457.121		

Sample Calculation for Joint 1 Tests1:

$$\begin{aligned} \text{Theorem Pythagoras Formula: } d_i &= \sqrt{\delta x^2 + \delta y^2 + \delta z^2} \\ &= (39.487)^2 + (298.756)^2 + (0.153)^2 \quad (2.1) \\ &= 301.354 = 0.301 \end{aligned}$$

2.2.2 Result Taken from Theodolite

The distance of movements for the end-effector through workspace from point A to point B is measured by using the theodolite shown in Fig. 2.4.

Equation 2.2 was used to calculate the angle and the distance movements of end-effectors in 2D by using the theodolite. In this method, the angle of movements and the distance of theodolite from robot were measured as the end-effector was moved through space from point A (initial) to point B (final). The data is shown in Table 2.4.

$$\text{Cosines Rules; } a_i^2 = b^2 + c^2 - 2bc\cos A \quad (2.2)$$

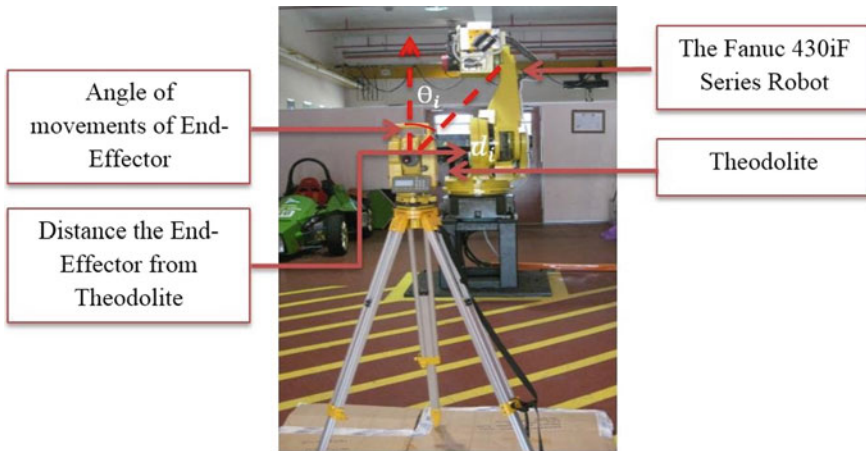


Fig. 2.4 Experimental setup to show the measuring of angle and distance using theodolite

Table 2.4 Experimental result of distance by theodolite

Test joint	Initial, b	Final, c	Angle of movements, Θ	Distance, a_i
1	3.018	3.057	6°	0.320
	2.995	3.009	3°	0.178
2	2.744	3.147	7°	0.540
	3.163	2.516	10°	0.813
3	3.017	2.994	5°	0.263
	3.035	3.019	8°	0.423

Table 2.5 Percentage of errors

Test joint	Via teach pendant, TP	Via theodolite, TH	% of error
Joint 1	0.301	0.320	6.31
	0.189	0.178	6.28
Joint 2	0.490	0.540	10.20
	0.730	0.813	11.34
Joint 3	0.248	0.263	6.05
	0.458	0.423	7.64

2.3 Result Analysis

A comparison was made between the results of the two methods. The percentage of differences between these two readings was evaluated using Eq. 2.3. The difference indicates the static errors of the robot's end-effector. Table 2.5 shows the comparison between two sets of results via teach pendant and via theodolite.

Percentage of error:

$$\%E = \frac{\sum |TP - TH|}{TP} \times 100 \quad (2.3)$$

Figure 2.5a shows the comparison of distance from the results obtained using teach pendant and theodolite. The results indicate that the percentages of error for the three different joint movements are not the same, while Fig. 2.5b is the angle of movements versus the percentage of error of the robot. According to the graph, the percentages of error of the robot joints are closely related to the angle of end-effector movement of robot. This result shows that the angle of movements contributes significantly to the robot positioning errors. These errors are mainly due to the wears and tears at the robot revolute joints which require recalibration for compensating the position accuracy of the end-effector.

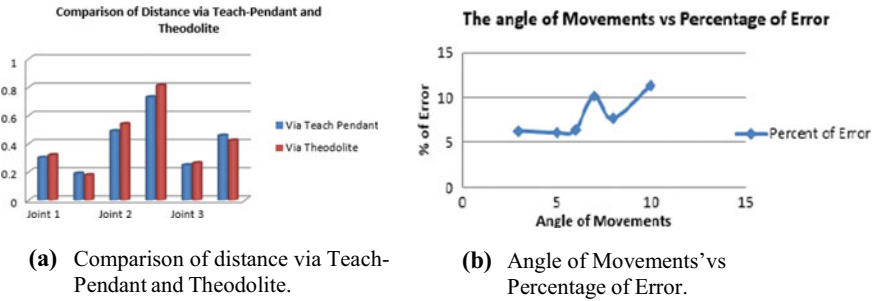


Fig. 2.5 Result analysis

2.4 Conclusion

From the result, it shows that the robot has inherently positioning errors. There are possibilities that the differences percentage at every test joint may be due to the repeatability of movements of the robot itself that causes cumulative wears and tears. The age of the Fanuc is over than 20 years and has been used for tasks such as pick and place, welding, and painting. Since the robot has been in service for over 20 years, the change in joint performance is unavoidable even though there is a monthly maintenance. Wear and fatigue on the robot joints cause the positioning accuracy of the end-effector to deteriorate. The teach pendant and theodolite can also contribute to the errors but very minimal. In conclusion, theodolites can be used for calibration of robots. Furthermore, the calibration results of this robot can be used with other calibration methods such as in references [1] and [2]. By adjusting the robot configuration parameters of the computer controller algorithm, the position accuracy of the robot end-effector could be improved.

References

1. Zhuang, H., Roth, Z.S.: Camera-Aided Robot Calibration. CRC Press (2018)
2. Nubiola, A., Slamani, M., Joubair, A., Bonev, I.A.: Comparison of two calibration methods for a small industrial robot based on an optical CMM and a laser tracker. *Robotica* **32**(3), 447–466 (2014). <https://doi.org/10.1017/s0263574713000714>
3. Schaller, J., Vopat, R., McLane, J.: Robot calibration method. 05 May 2015
4. Blondel, L., Heavener, J.: Robotic calibration method. 04 Jun 2013
5. Alberts, J., Kleinschmidt, S.P., Wagner, B.: Robust calibration procedure of a manipulator and a 2D laser scanner using a 1D calibration target. *ICINCO 2019—Proceedings of the 16th International Conference on Informatics Control, Automation and Robotics*, vol. 1, no. Icinco, pp. 112–119, 2019. <https://doi.org/10.5220/0007946701120119>.
6. Chiwande, S.N., Ohol, S.S.: Comparative need analysis of industrial robot calibration methodologies. *IOP Conf. Ser. Mater. Sci. Eng.* **1012**, 012009 (2021). <https://doi.org/10.1088/1757-899x/1012/1/012009>

7. Driels, M.R., Pathre, U.S.: Robot calibration using an automatic theodolite. *Int. J. Adv. Manuf. Technol.* **9**(2), 114–125 (1994). <https://doi.org/10.1007/BF01750418>
8. Marwan, A., Simic, M., Imad, F.: Calibration method for articulated industrial robots. *Procedia Comput. Sci.* **112**, 1601–1610 (2017). <https://doi.org/10.1016/j.procs.2017.08.246>
9. The Robot Fanuc Series Spot Tool Manual
10. Sultan, I.A., Wager, J.G.: Simplified theodolite calibration for robot metrology. *Adv. Robot.* **16**(7), 653–671 (2002). <https://doi.org/10.1163/15685530260390764>
11. Wang, R., Wu, A., Chen, X., Wang, J.: A point and distance constraint based 6R robot calibration method through machine vision. *Robot. Comput. Integr. Manuf.* **65**, 101959 (2020). <https://doi.org/10.1016/j.rcim.2020.101959>

Chapter 3

Development of Batch Type Convection Dryer for Fish Cracker Manufacturing



**Muhammad Naim Leman, Shahrol Mohamaddan,
Ana Sakura Zainal Abidin,
Mohamad Syazwan Zafwan Mohamad Suffian, Khairul Fikri Tamrin,
Rubiyah Bains, and Akihiko Hanafusa**

Abstract Manual production of fish cracker is inherently inefficient with low productivity. Mechanisation and automation of the drying process which constitutes a major process would contribute to increase production. In this study, a batch type convection dryer for fish cracker with a capacity of 2 kg was developed. The prototype with a dimension of 89-cm length, 72-cm width and 60-cm height consists of a drying chamber, moving tray, transmission system, heating element and control system. A moving tray concept was applied for the machine design. The maximum temperature that can be reached in the chamber without load is 40.0 °C. Two different air velocities of 1.5 m/s and 2.0 m/s were applied in both simulation and experimental study. The higher air velocity was observed to shorten the time

M. N. Leman

Department of Mechatronics Technology, Industrial Training Institute, 94300 Kota Samarahan, Sarawak, Malaysia

M. N. Leman · S. Mohamaddan (✉) · A. Hanafusa

Department of Bioscience and Engineering, College of Systems Engineering and Science, Shibaura Institute of Technology, Fukasaku 307, Saitama 337-8570, Japan
e-mail: mshahrol@shibaura-it.ac.jp

A. Hanafusa

e-mail: hanafusa@shibaura-it.ac.jp

S. Mohamaddan · A. S. Z. Abidin · M. S. Z. M. Suffian · K. F. Tamrin

Department of Mechanical and Manufacturing, Faculty of Engineering, Universiti Malaysia Sarawak, 94300 Kota Samarahan, Sarawak, Malaysia
e-mail: zaasakura@unimas.my

M. S. Z. M. Suffian

e-mail: mmsyazwan@unimas.my

K. F. Tamrin

e-mail: tkfikri@unimas.my

R. Bains

Department of Chemical and Energy Sustainability, Faculty of Engineering, Universiti Malaysia Sarawak, 94300 Kota Samarahan, Sarawak, Malaysia
e-mail: ruby@unimas.my

taken to heat the overall drying chamber. It was observed that the air velocity is higher when the tray rotates close to the fan inlet at the angle of 135° . The simulation results are consistent with the experiment in terms of temperature profile and air velocity. As a result, the dryer has successfully improved the drying hygiene and maintain the quality of fish cracker produced.

3.1 Introduction

Fish cracker is one of the famous crispy food products in South-East Asian countries. The manufacturing is mostly carried out in the small-scale industry [1]. In Malaysia, the processing industries are widely available at the coastal areas. This is due to the high-seafood supply, high temperature and windy conditions that contribute to the sustainability of the industries. In fish cracker industries, most of the production processes are conducted by using semi-automated machines such as grinding, mixing and slicing [2]. In current practice, slices of fish cracker are arranged in one layer on the ground by using a drying board, locally known as *pemidai*. The fish cracker on the board is exposed under the sunlight to be dried. The method can be considered as the most convenient and practical due to the minimum operating cost.

However, the existing method is considered unhygienic and subjected to unpredictable weather conditions which limit the production of fish cracker in high volumes [2]. By using *pemidai*, the fish cracker pieces are exposed to dust and may be contaminated with dirt from the surrounding. Besides, the fish cracker slices are also exposed to animals and insects such as birds and flies. With the current conditions, the quality level of the fish cracker produced is considered low and dirt. Besides, the contaminated fish cracker may cause illness to the consumers and not recommended for international export.

Many types of food dryer have been developed focussing on different types of products such as potato [3, 4], okra [5], guava [6], ginger [7], chilli [8], biscuit [9], tomato [10], pistachio nut [11], sorghum [12], peach [13], seaweed [14], grain [15, 16], mango [17], white mulberry [18], locust bean [19], etc. However, the development and study of dryer related to fish cracker can be considered limited. The objective of this study was to mechanise and automate the drying process of the fish cracker slices based on a batch type convection dryer. The methodology adopted which includes design, fabrication and its evaluation are discussed in the following section.

3.2 Materials and Method

A morphological approach was utilised to generate all design ideas through sketching, and the Pugh selection matrix was used to select the best concept. In this section, the final conceptual design of the dryer is presented with control system design, computational fluid dynamic (CFD) analysis and no-load experiment.

3.2.1 Drying Chamber and Moving Tray Design

The cabinet type drying chamber was selected for the final design as shown in Fig. 3.1. The drying chamber was designed in the form of rectangular shape with a dimension of 89-cm length, 72-cm width and 60-cm height. The estimated total volume is $384,480 \text{ cm}^3$. The chamber consists of five walls made of a 3-mm thick transparent polycarbonate sheet to reduce heat loss through the walls. It was selected because the material was not brittle, can withstand high temperature, lightweight, low-thermal conductivity and able to trap heat for a certain time duration [3].

The chamber consists of a square air inlet with a dimension of 12.5 cm^2 positioned at the back wall. This provision allows air generation by the cooling blower fan to flow inside the chamber. At the centre of the top wall, five outlet holes were provided with a total area of 137.5 cm^2 . The outlets allow proper air and heat circulation inside the chamber. The outlets were designed to release moist air out of the drying chamber during the drying process. A pair of doors with a dimension of 45-cm height and 66-cm width each was fixed in front of the drying chamber structure for loading and unloading the fish cracker slices.

Figure 3.2 shows the moving tray design for the dryer consisting of four units of rectangle buckets with trays. The size of each bucket was 70-cm length, 25-cm width and 2.6-cm height, whilst the size of each tray was 69.60-cm length, 24.60-cm width and 2.6-cm height. Two units of couplings set with plate and holder were utilised to hang the buckets. The main material used for the bucket design was aluminium alloy. For the tray design, perforated stainless steel was utilised because the material suitable for food processing machine due to the anti-corrosion property.

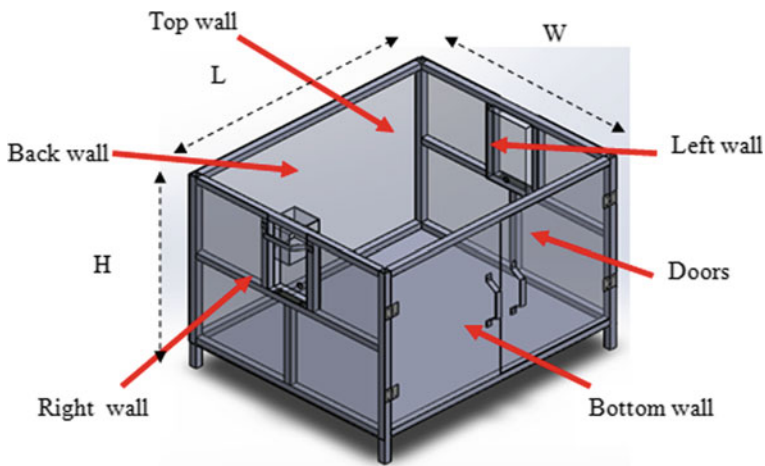


Fig. 3.1 The conceptual design of drying chamber

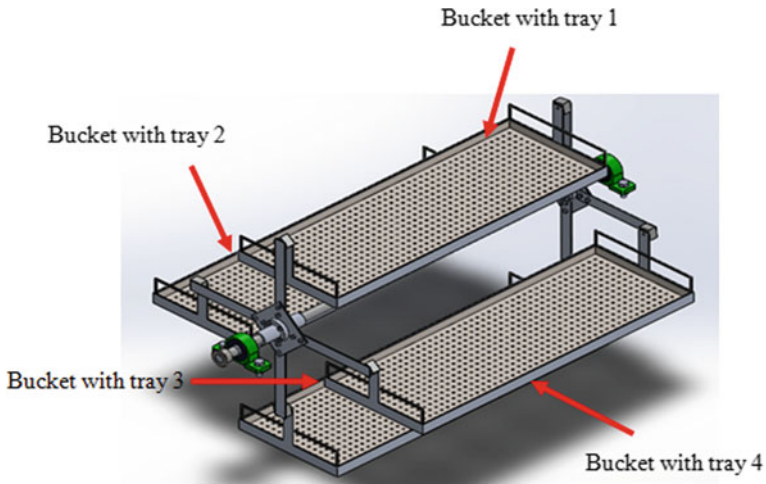


Fig. 3.2 The conceptual design of moving tray

The anti-corrosion property is important since the fish cracker was arranged on the tray during the drying process. Besides, small holes were design on the tray to allow airflow to pass over the fish cracker during the drying process. Two units of pillow block bearings were fitted at both ends of the shaft to support and assist shaft rotation. The bearings then were bolted to the structure frame. The minimum diameter of the shaft size was calculated based on a free body diagram by using the equation given in [4]. Based on the calculation, the minimum diameter size of the shaft was 1.19 cm. However, in the moving tray design, a 2 cm shaft was chosen for the tray design in order to compensate for additional loading mass of the fish cracker.

3.2.2 *Transmission System*

The designed transmission system consists of 24 V DC gear motor with 1/8 HP and 2 units of 17 teeth sprockets with ratio 1:1. A roller chain was utilised to transmit the rotational energy from the motor to the shaft. The length of the chain was calculated by using equation given by Kushwaha et al. [5]. Based on the calculation, the selected length of the roller chain in the design was 77 cm.

3.2.3 Heating Element, Fan Size and Air Vent

The size of the heating element was selected based on the calculated sensible heat, evaporation heat during drying and heat loss through five walls of the dryer. The heat energy was calculated by using equations given by Modi et al. [6]. According to Kumar [7], the ideal temperature to dry the fish cracker was in the range of 40–50 °C. In this study, 40 °C was selected as the final temperature and the basis for heating element selection. The ambient temperature was assumed to be 29 °C.

The total wattage of heating element selected in the design was 2300 W. The 400 W element was arranged perpendicularly to the fan inlet to reduce air humidity when the air was blown into the chamber. The other 1900 W element was arranged at the bottom wall of the drying chamber. An electronic thermostat was installed to regulate the temperature inside the drying chamber to maintain it with the desired set point. The fan size for the dryer was selected by using the energy balance equation. The inlet energy was equal to the total amount of energy inside the drying chamber. The inlet energy of the fan and the area of air vent areas was calculated by using equations given by Mohanraj and Chandrasekar [8]. Based on the calculation, a 24 V DC 8.6 W cooling blower fan with 70.62 cubic per minute (CFM) was selected for the dryer and the air vent area size was 137.5 cm².

3.2.4 Control System Design

The control panel was designed for mounting all switches, knobs and displays of the dryer. The panel was divided into five sub-controls namely the main, motor, fan, emergency and automatic switches. The activation and deactivation of the overall system in the control panel were based on the main switch. Motor and fan switches were used to switch on or off the motor and fan, respectively. The automatic switch was used to provide auto signal to the controller in order to control overall system in the dryer automatically. An emergency switch was provided on the control panel for the safety purpose to shut off the whole system if any undesirable condition happens during the machine operation [9]. The OMRON PLC series model CP1E was selected as the main controller for the system.

3.2.5 CFD Analysis and No-Load Experiment

The computational fluid dynamic (CFD) was utilised to simulate the temperature profile and air flow inside the drying chamber. The mass, momentum and energy conservation based on Navier Stroke and energy equation were applied in the simulation study. The $k-\epsilon$ turbulence model was also applied in the analysis. The numerical finite volume method was used to solve the equations and to build

numerical model based on unstructured 3D mesh by tetrahedral cells. The main procedure involves in the analysis were simplified drying chamber geometry, mesh generation, setup all boundary condition, run solver and finally evaluate the results. The geometry configuration for the simulation is displayed in Fig. 3.3a.

The simulation was performed in a steady state condition. The symmetrical plane was selected to analyse the velocity and temperature profile inside the drying chamber since the fan inlet and air outlet were designed to be symmetrical in the drying chamber. In the analysis, the temperature and air velocity were measured by the sensor probe of the software tool via coordinate system. The tray inside the chamber was designed to move in rotary movement with 8 difference angles of rotation including 0° , 45° , 90° , 135° , 180° , 225° , 270° and 315° as shown in Fig. 3.3b. The selected angles cover wide range of the camber area. However, in the simulation analysis, the tray was assumed to be in a static condition.

The maximum temperature that can be reached inside the chamber without load was evaluated using the no-load testing. A digital temperature and humidity metre model UNI-T UT333 were utilised for the data collection. The reading was taken every 1 min manually after switching on the heating element and fan, respectively, until 360 min, by using timer clock. Two levels of air velocity of 1.5 and 2.0 m/s were selected as the parameter to perform the testing. The air velocity above the tray was measured manually by using a digital hot wire anemometer model BENETECH GM8903.

3.3 Results and Discussion

A newly developed prototype of fish cracker dryer is shown in Fig. 3.4. The prototype is 89-cm length, 72-cm width and 60-cm height (similar to the initial design). The prototype consists of five main parts namely the drying chamber, moving tray, transmission system, heating element and control system. During the machine

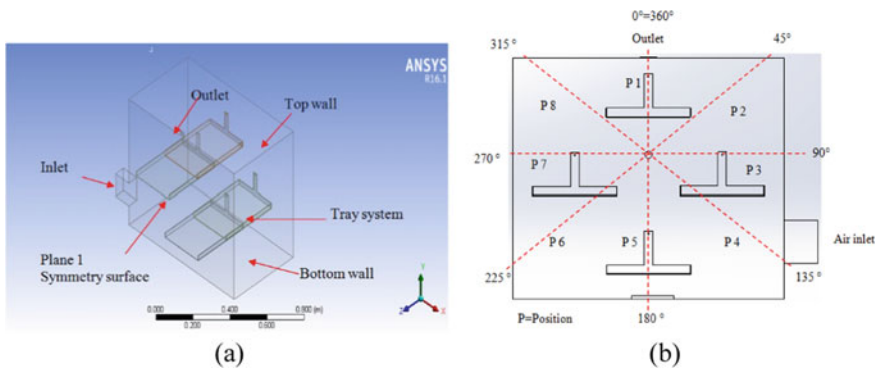


Fig. 3.3 a The arrangement of transmission system, b position and angle of tray rotation

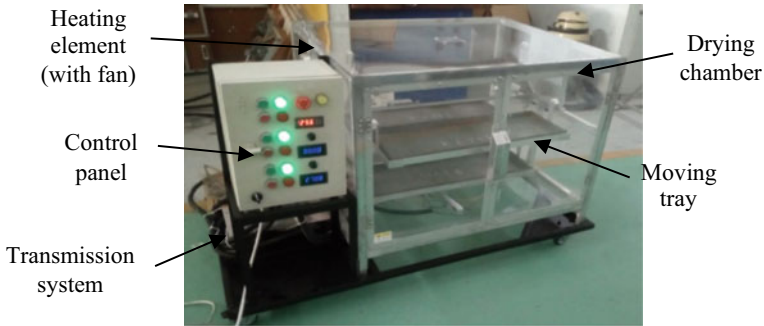


Fig. 3.4 The main components of the drying machine prototype

operation, the slices of fish cracker were arranged on the four-unit bucket trays. The transmission system was utilised to rotate the trays every 2 min in the anti-clockwise rotation. The heating element was used to raise the temperature inside the drying chamber and to evaporate the water from the fish cracker slices. The vapour produces from the evaporation process was removed together with air flow stream generated by the fan to the dryer outlet. The process was continued until the moisture of the fish cracker can be considered low and suitable for packaging. The capacity of the dryer was set to be 2 kg at one drying cycle.

Figure 3.5 shows the simulation results of the dryer focussing on the temperature profile. The light blue colour region indicates that the air from the fan starts to flow into the drying chamber. The temperature was considered low because the area was exposed and cooled by the airflow and external air surrounding. In the light green and yellow colour regions, the airflow starts to distribute inside the chamber. In this region, the airflow starts to absorb heat, and the chamber temperature was reduced. The red colour region indicates that the air does not reach the area, and the airflow does not affect the chamber temperature. The simulation results showed that the temperature inside the drying chamber decreased when the air velocity increases. It is because the higher-velocity air flow absorbed more heat from the drying chamber. Consequently, the amount of heat inside the chamber was reduced, and hence, the temperature drops.

Based on the sensor probe that was positioned above each tray, the temperature readings for all positions were in the range of 38 °C to 40 °C for both air velocities. The maximum temperature differences above the tray for all positions were about 1.1 and 1.2 °C for the air velocities of 1.5 m/s and 2.0 m/s, respectively. The differences were obtained by calculating the difference between the maximum and minimum temperature above the tray for both air velocities inside the chamber. However, the difference was considered small, and it can be assumed that the trays inside the chamber achieved reasonable uniformity of temperature profile. This was supported by a previous research carried out by [9], which stated that the tray inside the chamber will achieve reasonable temperature uniformity if the differences of temperatures between the trays are small. The uniformity of the temperature inside

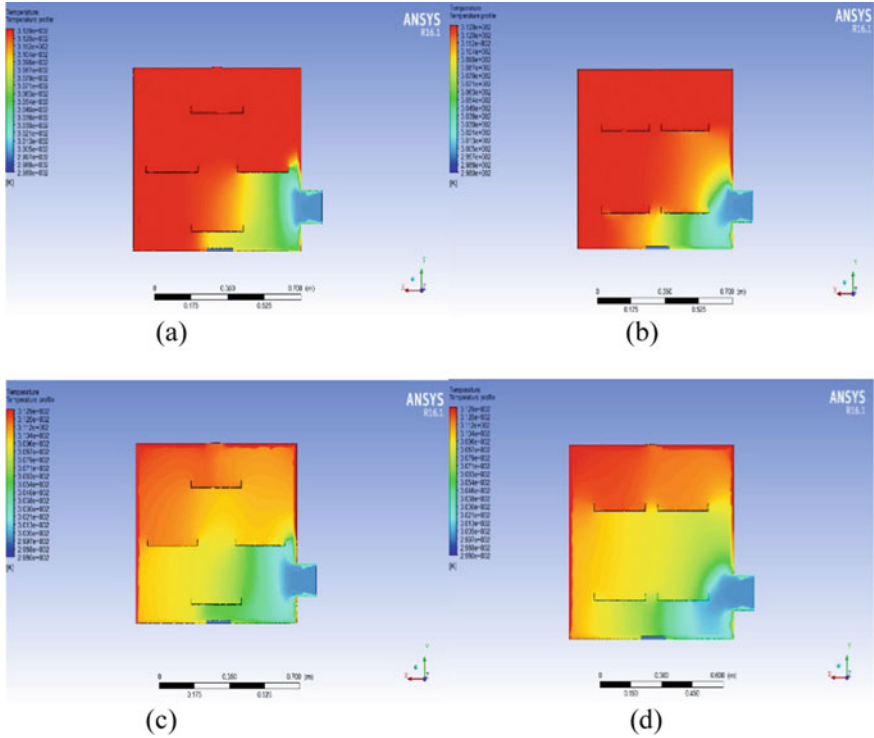


Fig. 3.5 Temperature profile at position $0^\circ = 360^\circ, 90^\circ, 180^\circ$ and 270° for **a** 1.5 m/s, **c** 2.0 m/s, and $45^\circ, 135^\circ, 225^\circ$ and 315° for **b** 1.5 m/s, **d** 2.0 m/s

the chamber is important to ensure that the heat can be transferred uniformly to the fish cracker slices and to assist the heat transfer for the evaporation process. In addition, the uniformity of heat assisted the fish cracker slices to dry evenly on all trays.

Table 3.1 shows the comparison of air velocities within the drying chamber between 1.5 m/s and 2.0 m/s air inlet velocity. The results show that when the air velocity of the inlet inside the chamber increases, the air velocity above the tray also increases. It was observed that the air velocity was higher when the tray rotates close to the fan inlet at the angle of rotation of 135° (Position 4). The air velocities of air inlet recorded at both positions were 0.31 m/s and 0.37 m/s (simulation) and 0.32 m/s and 0.38 m/s (experiment) for air velocities of 1.5 and 2.0 m/s, respectively. The air velocity recorded was lower at rotation angles of $45^\circ, 225^\circ, 270^\circ$ and 315° . It is because the moving tray is far away from the fan inlet.

Besides, the airflow starts to distribute from the small area of the fan inlet to the large chamber area. However, the air velocity increases slightly when the tray reaches the chamber outlet at an angle of tray rotation of $0^\circ = 360^\circ$ (Position 1). The air velocities recorded at this position were 0.088 m/s and 0.120 m/s (simulation)

Table 3.1 Comparison of air velocities between simulation and experimental results

Tray position	Angle of rotation (°)	Air inlet velocity 1.5 m/s			Air inlet velocity 2.0 m/s		
		Sim.	Exp.	Error (%)	Sim.	Exp.	Error (%)
Pos. 1	0 = 360	0.088	0.090	0.002	0.120	0.130	0.010
Pos. 2	45	0.045	0.050	0.005	0.089	0.090	0.001
Pos. 3	90	0.090	0.092	0.002	0.080	0.081	0.001
Pos. 4	135	0.310	0.320	0.010	0.370	0.380	0.010
Pos. 5	180	0.075	0.080	0.005	0.098	0.100	0.002
Pos. 6	225	0.010	0.020	0.010	0.023	0.024	0.001
Pos. 7	270	0.082	0.083	0.001	0.089	0.095	0.006
Pos. 8	315	0.047	0.048	0.001	0.075	0.076	0.001

and 0.090 m/s and 0.130 m/s (experiment) at the air velocities of 1.5 m/s and 2.0 m/s, respectively. It is because the air is forced to flow from the large area of the chamber to the outlet hole with a small diameter. Based on the results, the moisture of fish cracker is assumed to be removed faster when the tray reaches the position angles of 135° and 360°. At these positions, the tray rotates close to fan inlet and chamber outlet. The higher air velocity increased the rate of mass transfer from fish cracker slices during the drying process. In addition, the higher air velocity also helps to carry more moisture out from the drying chamber to reduce the chamber humidity. The lower humidity is important so that the air able to pick up more moisture from the fish cracker slices during the drying process.

In the drying application, the temperature, velocity and humidity of the drying air condition have significant effects on the drying process [10]. However, in this simulation and experiment, only the temperature and air velocity of the drying air was analysed. Figure 3.6 shows the experimental temperature readings without load inside the drying chamber with two different air inlet velocities of 1.5 m/s and 2.0 m/s. The graph shows that the times taken to heat up the entire chamber from ambient temperature of 29 °C to achieve the steady state condition are approximately 21 and 23 min, respectively. With the higher velocity of airflow inside the drying chamber, a lower temperature inside the chamber was recorded. The heat energy inside the chamber was absorbed by the airflow stream circulating inside the chamber. A higher velocity of airflow inside the chamber will bring about a lower temperature in the drying chamber. The results were consistent with the previous research conducted in [4, 11].

3.4 Conclusions

In this study, a batch type convection dryer for fish cracker with a capacity of 2 kg was successfully developed. The cabinet type with moving tray system was selected as the concept design. The simulation was carried out at a constant temperature of

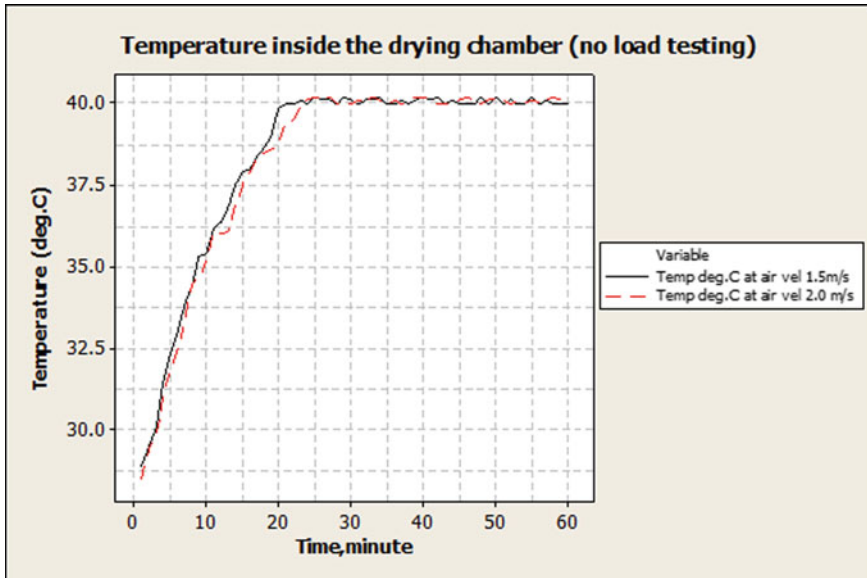


Fig. 3.6 Experimental temperature inside the drying chamber at air velocity of 1.5 m/s and 2.0 m/s

40 °C with two different air velocities of 1.5 m/s and 2.0 m/s. The CFD simulation results showed that the designed chamber achieves a reasonable uniformity of temperature profile. It is because the differences in temperature above the tray are considered small where the values of which recorded are 1.2 °C for both air velocities. The patterns of the air velocity show that when air velocity inside the chamber increases, the velocity above the tray also increases. The no-load experiment with two level of air velocity of 1.5 m/s and 2.0 m/s was conducted to the dryer. It was found that the maximum temperature in the chamber was 40.0 °C. The time taken to heat the overall chamber with air velocity of 1.5 m/s and 2.0 m/s until achieved in steady state condition was around 21 min and 23 min, respectively. The highest air velocity recorded above the tray occurs when the tray rotates approximately at position 1 and 4 with angle of tray rotation 135° and 0°/360°. At this position, heat and mass transfer on the fish slices are at the highest than the others positions. The CFD results were consistent with the experimental study. The closed drying chamber improved the hygiene of the fish cracker drying process. In addition, moving tray enables the fish cracker to dry evenly. The prototype is currently applied for the community project with bigger volume.

Acknowledgements This research is funded by Ministry of Higher Education Malaysia through Research Acculturation Grant Schemes [Grant no: RAGS/TK01(4)/1318/2015(12)]. The authors would like to thank Universiti Malaysia Sarawak (UNIMAS) for providing facilities for this research.

References

1. Taewee, T.K.: Cracker “Keropok”: a review on factors influencing expansion. *Int. Food Res. J.* **18**(3), 855–866 (2011)
2. Mohamaddan, S., Mohd Mohtar, A.M.A.A., Junaidi, N., Mohtadzar, N.A.A., Mohamad Suffian, M.S.Z.: Development of Keropok Keping drying machine for small & medium enterprises (SMEs). *Mater. Sci. Eng.* **114**, 1–6 (2016)
3. Darvishi, H., Asl, A.R., Asghari, A., Najafi, G., Gazori, H.A.: Mathematical modeling, moisture diffusion, energy consumption and efficiency of thin layer drying of potato slices. *J. Food Process. Technol.* **4**(3), 4–9 (2013)
4. Veleşcu, I., Tenu, I., Carlescu, P.: Experimental study of drying behaviour of potato. *Lucrări Ştiinţifice.* **56**(1), 107–112 (2013)
5. Kushwaha, H.L., Srivastava, A.P., Singh, H.: Development and performance evaluation of an okra seed extractor. *Res. J. Appl. Sci. Eng. Technol.* **3**(9), 1–13 (2005)
6. Modi, S.K., Durgaprasad, B., Basavaraj, M.: An experimental study on drying kinetics of guava fruit (*Psidium Guajava L*) by thin layer drying. *J. Environ. Sci. Toxicol. Food Technol.* **9**(1), 74–80 (2015)
7. Kumar, S.K.S.: Analysis of ginger drying inside a natural convection indirect solar dryer: an experimental study. *J. Mech. Eng. Sci. (JMES)* **9**, 1671–1685 (2015)
8. Mohanraj, M., Chandrasekar, P.: Performance of a forced convection solar drier integrated with gravel as heat storage material for chili drying. *J. Eng. Sci. Technol.* **4**(3), 305–314 (2009)
9. Olufemi, A., Fatukasi, S.O., Awotunde, O.W.: Design and development of a domestic biscuit cabinet tray dryer. *J. Eng. Res. Appl.* **4**(3), 13–20 (2014)
10. Santos-Sánchez.: Effect of rotating tray drying on antioxidant components, color and rehydration ratio of tomato saladette slices: *LWT. Food Sci. Technol.* **46**(1), 298–304 (2012)
11. Ghazanfari, A., Tabil, L.: Evaluating a solar dryer for in-shell drying of split pistachio nuts. *Drying Technol. Int. J.* **21**(7), 1357–1368 (2014)
12. Susanti, D.Y., Joko, N.Y.K., Mariyam, S.: Drying characteristics of crackers from sorghum using tray dryer in different drying air velocities. *J. Adv. Agric. Technol.* **3**(4), 258–264 (2016)
13. Golisz, E., Jaros, M., Kalicka, M.: Analysis of convection drying process of peach. *Tech. Sci.* **16**(4), 333–343 (2013)
14. Fudholi, A., Othman, Y.M., Ruslan, M.H., Yahya, M., Zaharim, A., Sopian, K.: The effects of drying air temperature and humidity on the drying kinetics of seaweed. *Recent Res. Geogr. Geol. Energy Environ. Biomed.* 129–133 (2011)
15. Ezekoye, B.A., Enebe, O.M., State, E.: Development and performance evaluation of modified integrated passive solar grain dryer. *Pacific J. Sci. Technol.* **7**(2), 185–190 (2006)
16. Wilson, K.K.: Design, development and evaluation of a continuous-flow mixing grain drayer. Master Thesis (2011)
17. Akoy, E.O.M.: Experimental characterization and modeling of thin-layer drying of mango slices. *Int. Food Res. J.* **21**(5), 1911–1917 (2014)
18. Akpinar, E.K.: Mathematical modelling and experimental investigation on sun and solar drying of white mulberry. *J. Mech. Sci. Technol.* **22**, 1544–1553 (2008)
19. Adamade, C.A., Olaoye, J.O.: Performance evaluation of a dryer for processed. Locust Bean Condiments. *Agroresearch.* **14**(2), 103–112 (2014)

Chapter 4

An Experimental Investigation on Mechanical and Tribological Behaviour of (AZ91D Mg Alloy + Graphene) Metal Matrix Composite



N. Satish Kumar, G. G. Sozhamannan,
and V. S. K. Venkatachalapathy

Abstract Main focus of this research work is to analyze the impact of mechanical behaviour (hardness) and tribological behaviour (wear properties) of Graphene reinforced Magnesium alloy (AZ91D) consisting of metal matrix compound. During this analysis, 1% reinforcement found in Graphene molecules by weight to the Mg alloy (AZ91D) to generate a compound by applying the technique of bottom poured stir casting. Wear analysis technique (wear and frictional coefficient) has been incorporated on the DUCOM pin and on the setup of disc tribometer, with the utilization of metal matrix composite (MMC). For experimental designs, Taguchi's optimization technique has been incorporated. To study the wear resistance phenomenon of the MMC, "Smaller the better" criteria have been taken into consideration as an objective model. The operating parameters like applied load (30 N, 40 N, 50 N), disc rotating time (4, 6, 8 min) and disc rotational speed (500, 650, 800 RPM) are optimized through analysis of variance (ANOVA) along with signal to noise ratio analysis. From the statistical study of ANOVA, finally, it is concluded from the observation that tribological behaviour is significantly affected by rotational time and the load applied on the disc.

4.1 Introduction

Most frequently used alloys with magnesium have a high-frequency utilization in several industries like metallurgical, electrical, motor vehicle, air craft and chemical industries now-a-days. This is associated with other things with an advancement of

N. Satish Kumar (✉) · G. G. Sozhamannan · V. S. K. Venkatachalapathy
Department of Mechanical Engineering, Sri Manakula Vinayagar Engineering College,
Pondicherry University, Puducherry 605107, India
e-mail: smvec@smvec.ac.in

dependency amongst tensile strength (160–365 MPa), density (1.74 g/cm^3) and modulus of elasticity (45 GPa). Comparatively, Mg alloy tensile strength and density are high with other alloys. Furthermore, in magnesium, electrical and thermal conductivity are reasonably good and its damping capacity is also high [1, 2]. Several manufacturing industries uses Mg alloys (i.e. AZ91D) because of their versatile exceptional corrosion resistance quality with low weight and heavy strength. Apart from metals like steel, copper and aluminium, magnesium and its alloys are choosing as a metal in all future applications like aerospace, automotive, electronics, bio-medical and sports [3]. In metal matrix composites (MMC's), reinforcement material is added to base material in some percentage to advance the physical and mechanical features of the final product. Metal matrix compounds contain matrix materials like copper, aluminium, magnesium, etc., to deliver low weight and high-strength criteria preferably used in aerospace applications [4]. AZ91D is the most extensively used Mg compound for the structural applications of aerospace. Several reinforcements are implemented for the enhancement of distinct properties of compounds under various methods. In general priority of reinforcements for magnesium compounds were graphite, boron carbide, silicon carbide, etc., in the mode of whiskers, fibres and particles. Graphene is one of the highly effective reinforcements because of its exceptional properties of mechanics like Young's modulus 0.5 to 1 TPa, specific surface area $2630 \text{ m}^2 \text{ g}^{-1}$ and tensile strength (130 GPa) [5, 6]. Mg metal matrix compounds are made by various methods like solid, semi-solid and liquid states. Along with these techniques of liquid processing, the simple and economical are stir casting only [7]. Casting samples preparation addressed in this paper describes the hardness as well as wear characteristics of Mg alloy AZ91D embedded with 1.0% weight of graphene nano-particles formed by the process of bottom poured stir casting. The size of the casting $300 \times 100 \times 15 \text{ mm}$ can be made by the requirement of base metal 750 gms and reinforcement material like graphene 1% weight (i.e. 7.5 gms) is added to the base metal to get MMC.

4.2 Experimental Work

4.2.1 Materials

Preparation of the MMC sample has been taken place with the utilization of AZ91D alloy like the compound and the graphene particles with 1.0% (by weight) as the strengthening (Table 4.1). The graphene powder particle size has been taken in the range of 37–54 μm . The chemical combination of the Mg alloy (AZ91D) is depicted in Table 4.2.

Table 4.1 Comparison of hardness before and after reinforcement

Test no.	Magnesium alloy (AZ91D)		Magnesium alloy (AZ91D) + Graphene	
	Load (kgf)	Hardness No. (HB)	Load (kgf)	Hardness No. (HB)
1	579	79	579	85
2	1158	103	1158	110
3	1750	104	1750	111

Table 4.2 Chemical composition (fraction—percentage by weight) of the AZ91D

Mg	Al	Zn	Mn	Si	Cu	Fe	Be
Remainder	9.15	0.6	0.24	0.03	0.01	0.01	0.0001

4.2.2 Composites Processing Phenomenon

The stir casting method of combining reinforcement into the compounds of liquid metals with the utilization of mechanical stirrer. The process of stir casting has been included for production of the Mg metal matrix compounds (MMC) with the bottom pouring stir casting machine (Fig. 4.1). Mg alloy (AZ91D) is melted when the metals are in liquid state with the usage of electric induction furnace maintaining hotness in the range of 700–750 °C and with stirrer circling speed 450–500 RPM and 1% (weight) graphene. For the removal of moisture content and the elimination of casting defects, first the die is pre heated at 300 °C temperature, and then liquid metal is poured in to the die.

4.3 Hardness Testing

The hardness of magnesium alloy (AZ91D) and fabricated of MMC by adding graphene as a reinforcement at weight percentage of 1.0 by doing bottom poured stir casting process. At different loads by using Brinell Hardness Tester with 5 mm

Fig. 4.1 Bottom poured stir casting machine

ball indenter diameter taken to find base metal and reinforcement material as shown in Figs. 4.2 and 4.3. By comparing with before and after reinforcement, the hardness will be increased as shown in Table 4.1.

4.4 Testing of the MMC's

4.4.1 Tribological Behaviour (Wear Test)

Evaluation of dry sliding wear results in the MMC-pin specimens can be done with the use of a pin-on-disc tribometer as shown in Fig. 4.4. The E-30 steel material has been placed the role of the counter-face disc. For the wear test, a collection of specimens ($8\phi \times 35$) was equipped to maintain the ASTM G-99 standards. The cleaning of specimens has been done through ultrasonic with the usage of ethanol solution for a period of 10 min before conducting the wear tests. The conduction of dry sliding tests can be done with the variation of three parameters like normal load, rotational time and rotational disc speed, and rest of the parameters kept fixed. The operating parameters are displayed in Table 4.3. An electronic weighing machine (least count = 1×10^{-3} g) is used to test the weights of the worn-out pins pre and post conduction every test run. During the wear test, weight loss observed in the wear rate of tested specimens are displayed in Fig. 4.5.

EDM wire cut technique with 10×10 mm square cross section with 30-mm height is used to prepare wear specimens as depicted in Fig. 4.5. Rotating disc and specimen surface end are polished with new emery paper for the elimination of

Fig. 4.2 AZ91D alloy metal



Fig. 4.3 AZ91D + graphene metal



Table 4.3 L9 orthogonal array of Taguchi matrix for the results of wear test

Test no.	Time (min)	Load (N)	Rotational speed (R.P.M)	Coefficient of friction (μ)	S/N Ratio
1	4	30	500	0.21	13.5556
2	6	30	650	0.22	13.1515
3	8	30	800	0.26	11.7005
4	6	40	500	0.28	11.0568
5	8	40	650	0.31	10.1728
6	4	40	800	0.29	10.7520
7	8	50	500	0.27	11.3727
8	4	50	650	0.28	11.0568
9	6	50	800	0.26	11.7005

Fig. 4.4 Wear testing machine

scratches on the specimen. The rotating disc was properly cleaned using acetone after the end of each test for the removal of dust particles from the disc. The wear rate along with raw materials (AZ91D) friction coefficient stir casted specimen is determined with the performance of Taguchi's L9 Orthogonal array.

4.4.2 Taguchi's Method

The design of experiments (DoEs) is one of the statistical tools applied in the enrichment of production and process. This statistical tool specifies the knowledge of predictive information regarding complex, multivariable approach with some experiments. It is purely based on three important aspects—quality loss function, orthogonal array and signal to noise ratio (S/N). By Minitab[®] 17 software experimental designs and generation of ANOVA for the S/N has been done.

The main goal of this study is reducing the wear rate, as a result S/N for “smaller the better” has been considered. Usage of the S/N ratio leads to detect the best

Fig. 4.5 Wear testing samples



probable collection of operating parameters to get the required responses. The S/N ratio for “smaller the better” can be acquired using Eq. (4.1).

$$S/N = -10 \log \left(\frac{1}{n} \sum_{i=1}^n Y_i^2 \right) \tag{4.1}$$

4.5 Results and Discussion

Tribological behaviour (frictional coefficient) of MMC generally magnesium alloys are high strength because of less density when compared to other metals like aluminium, copper, etc. Dry sliding wear behaviour of AZ91D-graphene compounds was inspected using Taguchi’s L9 Orthogonal array. Investigational study of AZ91D graphene compounds coefficient is displayed in Table 4.3. The experiential data of frictional coefficient has been resolved implementing the S/N ratio response criteria. Table 4.4 reveals that the parameter has high influence for wear properties is disc revolving time followed by disc rotational speed and normal load. The graphical details are also depicted in Fig. 4.6. Tribological behaviour (wear rate) of MMC Dry sliding wear behaviour of graphene (AZ91D) compounds were estimated through Taguchi’s L9 orthogonal array. Investigational observation of graphene—AZ91D compounds wear rate is displayed in Table 4.5. The experiential data of wear rate that has been estimated by employing the S/N ratio response analysis. Table 4.6 reveals that the highly dominating parameter for the wear

Table 4.4 Response table for signal to noise ratios smaller is better

Level	Time	Load	Speed
1	11.79	12.80	12.00
2	11.79	10.66	11.46
3	11.08	11.38	11.38
Delta	0.89	2.14	0.61
Rank	2	1	3

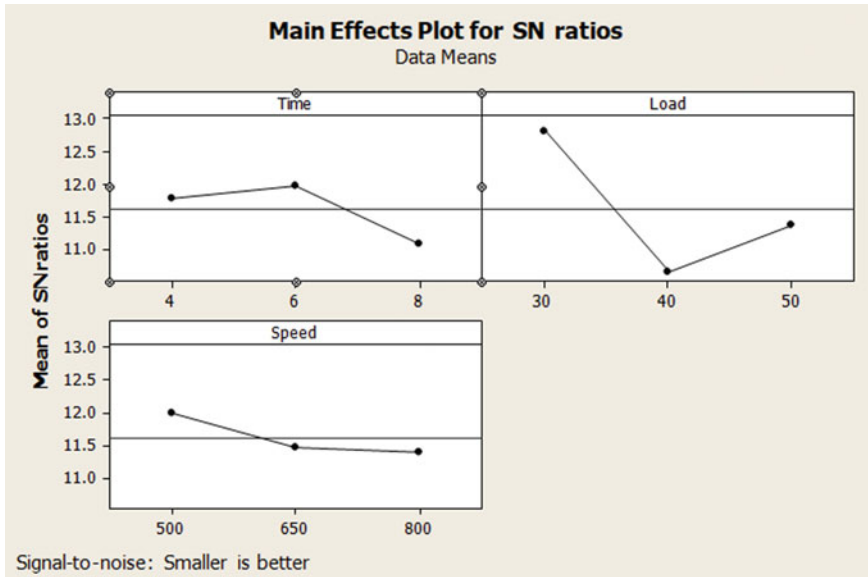


Fig. 4.6 Frictional coefficient for S/N ratio

Table 4.5 L9 orthogonal array of Taguchi matrix for wear test results

Test no.	Time (min)	Load (N)	Rotational speed (R.P. M)	Wear rate (mm ³ /m)	S/N ratio
1	4	30	500	0.00235	52.5786
2	6	30	650	0.00303	50.3711
3	8	30	800	0.00395	48.0681
4	6	40	500	0.00298	50.5157
5	8	40	650	0.00458	46.7827
6	4	40	800	0.00187	54.5632
7	8	50	500	0.00331	49.6034
8	4	50	650	0.00199	54.0229
9	6	50	800	0.00347	49.1934

features is the disc rotational time, followed by disc rotational speed and normal load. The graphical information is also depicted in Fig. 4.7.

4.5.1 Analysis of Variance (Frictional Co-efficient)

Graphene (AZ91D) based compounds produced by adopting the method bottom poured stir casting that reveals the reduction of friction coefficient. AZ91D

Table 4.6 Response table for signal to noise ratios smaller is better

Level	Time	Load	Speed
1	53.72	50.34	50.90
2	50.03	50.62	50.39
3	48.15	50.94	50.61
Delta	5.57	0.60	0.51
Rank	1	2	3

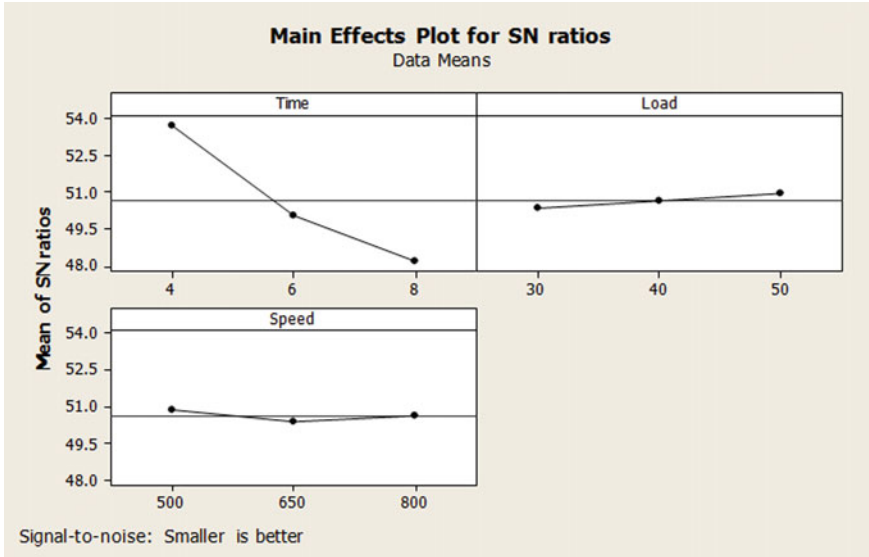


Fig. 4.7 Wear rate for S/N Ratio

represents coefficient of friction values and are enhanced when the load is increased. Decrement of wear rate with the raise of rotational speed observed because of the deviation in the contact time between specimen and disc [8].

The oxide layer opposes the action of sliding wear on the specimen surface which results low wear rate and identical outcomes were stated [9, 10]. This oxide layer acts as additional safeguard on the specimen surface, thus it resulted in significant decline in wear rate [11, 12]. Augment in sliding time, exclusion of matrix causes the rigid particles of graphene protruded from the surface. These graphene particles are highly offer resistance to sliding wear, thus decrement in wear rate is noticed for the increment of rotational speed.

Table 4.6 displays the outcome of ANOVA for friction value coefficients for Mg alloy (AZ91D), from the observation of results through ANOVA, it is noticed that high-impact factors over friction coefficient of graphene-AZ91D compound were load, time and rotational disc speed. With this study, it is being concluded that load

Table 4.7 Analysis of variance for coefficient of friction, using adjusted SS for tests

Source	DF	Seq SS	Adj SS	Adj MS	F	P	%
Time	2	0.0011556	0.0011556	0.0005778	3.25	0.235	14.05
Load	2	0.0061556	0.0061556	0.0030778	17.31	0.055	74.86
Speed	2	0.0005556	0.0005556	0.0002778	1.56	0.390	6.75
Error	2	0.0003556	0.0003556	0.0001778			4.32
Total	8	0.0082222					

has high impact on coefficient of friction. Table 4.7 displays the time (14.05%), load (74.86%) and rotational speed (6.75%) with high significance on friction coefficient of AZ91D material. R^2 value for stir cast process is 95.68%.

4.5.2 Analysis of Variance (Wear Rate)

ANOVA applied for the wear characteristics of wear rate of graphene-(AZ91D) compound fabricated by the process of stir cast are determined in Table 4.8. From Table 4.8, it is noticed that time (82.81%) have significant contribution comparatively with other two parameters namely rotational speed (3.12%) and load (1.56%). Hence, no communications result on the wear behaviour of Mg composites. R^2 value for stir cast process is 87.01%.

4.5.3 Micro Structural Examination

Figure 4.8 represents the SEM of wear tested AZ91D + graphene composites fabricated by stir cast processed samples which helped in analyzing the material deduction phenomenon of the composite specimens during wear test. The SEM of the worn out MMC is shown in Fig. 4.8a–d. All the wear tested SEM images shown here are of maximum sliding speed and maximum load. From Fig. 4.8c, it is clearly observed that the metal and matrix are de-bonded such that the specific wear rate decreased largely at higher speeds. All composite samples contain micro cracks

Table 4.8 Analysis of variance for wear rate, using adjusted SS for tests

Source	DF	Seq SS	Adj SS	Adj MS	F	P	%
Time	2	0.0000053	0.0000053	0.0000027	6.40	0.135	82.81
Load	2	0.0000001	0.0000001	0.0000000	0.10	0.908	1.562
Speed	2	0.0000002	0.0000002	0.0000001	0.19	0.839	3.125
Error	2	0.0000008	0.0000008	0.0000004			12.5
Total	8	0.0000064					

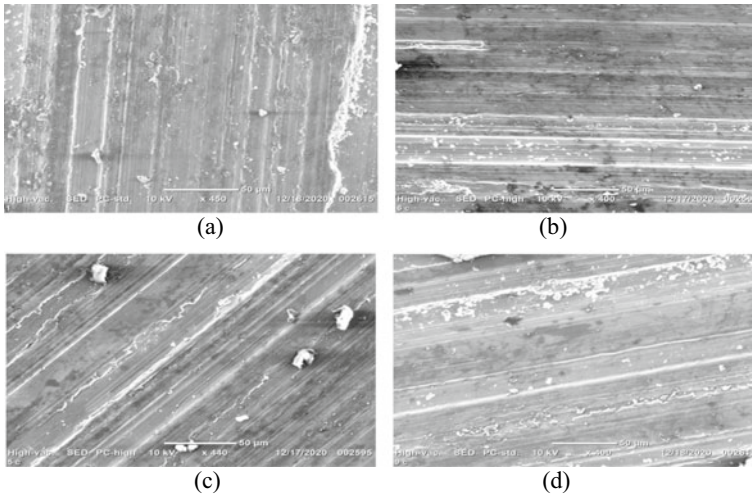


Fig. 4.8 SEM images of worn out surfaces of AZ91D-graphene composites

and grooves which are due to the rubbing action of the composite sample with the disc. All the wear tested samples come across with the presence of micro grooves which was observed in the literature as well [13]. A higher applied load indicates the metal fracture, and large de-bonding and wear debris are observed from Fig. 4.8a,b,d in turn its lead to higher material removal rate. From all Fig. 4.8a–d, it is clearly understood that load is transmitted to the metal because of the good linkage between matrix and reinforcement.

4.6 Conclusions

The motive of this study is to analyze the mechanical and wear behaviour of the Mg alloy AZ91D-1.0% graphene composites were fabricated through bottom poured stir casting route.

- Mechanical properties (hardness) can be found by using Brinell hardness tester for AZ91D magnesium alloy were decreased when compared to composite material like AZ91D/Graphene. A high hardness of 85 HB is obtained at the load of 571 kgf.
- The three parameters, i.e. normal load, rotational speed and rotational time influence the wear behaviour of the composite. The disc revolving time is the highly influencing parameter, followed by the disc rotational speed and normal load.

- The ANOVA represents the normal load and revolving time have the significant impact on the MMC's wear behaviour, with and adverse effect of rotational speed.
- The worn out composite samples showed that the material removal mechanism is due to the de-bonding of metal from the matrix, and such that small grooves and voids were took place.

References

1. Cizek, L., et al.: Structure and properties of the selected magnesium alloys. In: 10th International Scientific Conference "Achievements in Mechanical & Materials Engineering", Zakopane (2001)
2. Luo, A.: Magnesium: current and potential automotive applications. *J. Mater.* (2002)
3. Mordike, B.L., Ebert, T.: Magnesium: properties—applications—potential. *Mater. Sci. Eng A*. **302**, 37–45 (2001)
4. Aatthisugan, I., Razal, A., Rose, D., Selwyn, J.: Mechanical and wear behaviour of AZ91D magnesium matrix hybrid composite reinforced with boron carbide and graphite. *J. Magnes. Alloys*. **5**, 20–25 (2017)
5. Aravindan, S., Rao, P.V., Ponappa, K.: Evaluation of physical and mechanical properties of AZ91D/SiC composites by two step stir casting process. *J. Magnes. Alloys*. **3**(1), 52–62 (2015)
6. Narayanasamy, P., Selvakumar, N.: Tensile, compressive and wear behaviour of self-lubricating sintered magnesium based composites. *Trans. Nonferrous Metals Soc. China* **27**, 312–323 (2017)
7. Al-maamari, A., Iqbal, A.A., Nuruzzaman, D.: Wear and mechanical characterization of Mg-Gr self-lubricating composite fabricated by mechanical alloying. *J. Magnes. alloys*. **7**, 283–290 (2019)
8. Yang, J.B., Lin, C.B., Wang, T.C., Chu, H.Y.: The tribological characteristics of A356.2Al alloy/Gr(p) composites. *Wear* **257**, 941–952 (2004)
9. Deaquino-Lara, R., Soltani, N., Bahrami, A., Gutierrez-Castaneda, E., García-Sánchez, E., Hernández-Rodríguez, M.: Tribological characterization of Al7075-graphite composites fabricated by mechanical alloying and hot extrusion. *Mater. Des.* **67**, 224–231 (2015)
10. Lokesh, T., Mallik, U.S.: Dry sliding wear behaviour of Al/Gr/SiC hybrid metal matrix composites by Taguchi techniques. *Mater. Today Proc.* **4**, 11175–11180 (2017)
11. Akhlaghi, F., Zare, B., Idaki, A.: Influence of graphite content on the dry sliding and oil impregnated sliding wear behaviour of Al2024-graphite composites produced by in-situ powder metallurgy method. *Wear* **266**, 37–45 (2009)
12. Prabhakar, S.N., Radhika, N., Raghu, R.: Analysis of tribological behavior of aluminum/B4C composites under dry sliding motion. *Proc. Eng.* **97**, 994–1003 (2014)
13. Zhang, L., Wang, Q., Liao, W., Guo, W., Li, W., Jiang, H., Ding, W.: Microstructure and mechanical properties of the carbon nanotubes reinforced AZ91D magnesium matrix composites processed by cyclic extrusion and compression. *Mater. Sci. Eng.* **689**, 427–434 (2017)

Chapter 5

Investigation of Wear and Mechanical Properties of Aluminium Hybrid Composites: Effect of Addition of SiC/B₄C Through Casting Process



S. Sunil Kumar Reddy, C. Sreedhar, and S. Suresh

Abstract Aluminium is a binary alloy has a larger importance to engineering industries with excellent wear resistance and stiffness that have been designed for lightweight and higher strength applications in the automobile sectors. To synthesis the hybrid metal matrix composite, silicon carbide is chosen as primary reinforcement varied at different weight fraction (1, 2, 3, 4 wt%) with a constant boron carbide of 3 wt% used in the present study was carried through liquid metallurgy technique. The composites were then subjected to mechanical and wear properties study. The effect of reinforcement particles by increasing various weight fractions have been investigated and characterized mechanical and wear properties. The 4 wt% of SiC/B₄C reinforced composites tends to increases hardness and tensile strength to 29.7% and 20% as compared to the base alloy.

5.1 Introduction

Aluminium is used in a variety of industries because it is the essential aspect in a wide range of products encompassing of most industrial goods and structural components. However, due to their low wear resistance, their applications are minimal. A metal matrix is made up of two parts such as metal and secondary as reinforcement. Metal matrix composites with at least three constituents are known as hybrid composites. Aluminium metal matrix composites (AMMC) alloys are corrosion-resistant and suitable for industrial applications. AMMCs are commonly used for low-cost parts with high-material efficiency. In structural and functional high applications, aluminium composites are often used in the army, sports and manufacturing industry. High-silica content in boron, widespread incidentally with the same strength as SiC, is present in the boron carbide. The glasses are made of ceramic solid clay at elevated temperatures. Baradeswaran and Perumal [1] studied

S. Sunil Kumar Reddy (✉) · C. Sreedhar · S. Suresh
Department of Mechanical Engineering, Siddharth Institute of Engineering and Technology,
Puttur, India

the effect of B_4C on Al 7075 composites, both mechanically and tribologically. Mechanical properties and wear behaviour were tested on T6 heat treated samples. Hardness value improved with increasing B_4C particles due to increased strain energy. Increasing reinforcing particles to enhance increased tensile toughness. Improvement in flexural strength indicates that composites possess enough ductility. The wear rate decreased with increase in reinforcing particles because the contact of matrix area with reinforcement was reduced. The presence of iron and oxygen in the EDAX analysis confirmed that the transfer of ferrous from counter faces and oxidation reaction, respectively. However, the mechanical and wear behaviour of as casted composites are not reported. Ramanathan et al. [2] evaluate the effect of aluminium matrix hybrid composites at different weight percentage of silica particles and keeping fly ash particles contents as constant. Addition of reinforcing particles offers more resistance to particle deformation due to which the micro and macro hardness increases. The tensile strength of the composites increases owing to strengthening mechanism on the other hand presence of hard ceramic particles reduces ductility. Gomez et al. [3] revealed lightweight aluminium (6061) alloys with SiC and B_4C as reinforcements were many factors to take the residential or commercial properties of the MMC into consideration. Significant as hard steel, SiC and Al_2O_3 are equivalent to 3.20 as well as 3.96 g/cm^3 reinforcement will improves the material strength. The conclusion is that 10% of B_4C is the endorsed amount of support content in order to achieve optimal strength and stability. It also has excessive mechanical reigns and better weathering. Naher et al. [4] deliberated the fabrication and heat treatment process in a crucible up to 800°C . The reinforcement was then added to the Al matrix with SiC particles treated upto 400°C . Once the mixed composite has been finished, around $700\text{--}800^\circ\text{C}$ have been plastered into a metal mould. The prepared compound is machined to the necessary form and size after design. Umanath et al. [5] conducted the wear behaviour of T6 heated on the AA6061 alloy improved with silica lubricant and particles of aluminium oxide produced by casting dispersion. The effect of volume fraction, applied load, rotational speed and counter-face hardness on wear behaviour of the composites was analysed through pareto chart, normal probability chart optical and scanning electron micrograph. The limits of the factors were decided by the trial experiments. The results revealed that all the above-mentioned factors were contributed towards the wear rate. In the interface reaction layer, the XRD spectrum unveiled aspects such as Al, Si, C and O. The porosity of the composites increases with a volume fraction increase but it resists delamination process hence wear rate reduces. The worn surfaces of hybrid composites were rougher than unreinforced aluminium alloy which indicated abrasive wear mechanism. The hypothesis of this research is as follows:

- Fabrication was performed through a liquid metallurgy route.
- To identify mechanical properties of Al7075-SiC- B_4C hybrid composites.
- To determine and understand the tribological characteristics for both Al alloy and aluminium hybrid composites.
- To identify surface morphology was carried out through SEM analysis.

5.2 Materials and Methods

5.2.1 Materials

The matrix used in the research work is Aluminium (7075) as base alloy and chemical composition is represented in Table 5.1. In the present investigation, silicon carbide (SiC) is taken as primary reinforcement, and boron carbide is chosen as secondary reinforcement obtained from Indian scientific business (India) Pvt. Ltd., Tirupati at a fragment size of 50 nm. The chemical composition of reinforcement particles is labelled in Tables 5.2 and 5.3.

5.2.2 Fabrication of Aluminium Hybrid Composites

5.2.2.1 Heat Treatment of Aluminium Matrix

Aluminium 7075 bars were sliced into pieces and immersed in 10% sodium hydroxide (NaOH) solution at a 100 °C temperature for 15 min and then cleaned with methanol solution. The alloy was then dried and melted in the furnace.

5.2.2.2 Preparation of Strengthening Particulates

The reinforcements (SiC and B₄C) are pre-heated to 800 °C and maintained at that temperature for about one hour using a muffle furnace to remove the volatile surface impurities, moisture, gases related to powder agglomeration and to improve the wettability between the matrix.

Table 5.1 Chemical composition of Al 7075 matrix

Al 7075	Ti	Si	Mn	Zn	Cr	Fe	Others	Al
% composition	0.045	0.049	0.06	5.7	0.18	0.3	0.030	Reminder

Table 5.2 Chemical composition of nano-SiC

Al 7075	SiC	Si	B	C	SiO ₂	Fe
% composition	98.79	0.34	80.1	0.2	0.5	0.07

Table 5.3 Chemical composition of B₄C

Al 7075	Si	Fe	C	Ca	F
% composition	0.5	0.1	18.1	0.3	0.025

5.2.2.3 Casting and Melting of Fabricated Samples

Table 5.4 represents the different compositions of aluminium hybrid composites as follows:

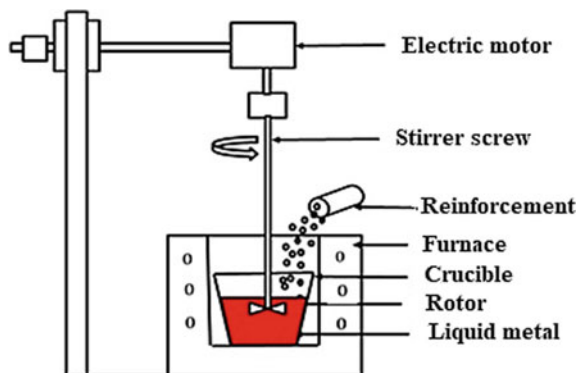
5.2.3 Preparation of Aluminium Hybrid Composites

Al 7075 alloy is incorporating with silicon carbide as primary reinforcement varied at different weight fraction (1, 2, 3, 4 wt%) with a constant boron carbide as 3 wt% were utilized. A stir casting approach was used to create enhanced hybrid composite pieces, which are also illustrated in Fig. 5.1. Whilst an electric oven was used. SiC/B₄C powders were pre-heated to 800 °C in a separate muffle furnace for 2 h to remove the hydroxide and other gases. The Al 7075 has been heated in a sink. For 10 min, they were melted extensively in the heat oven at roughly 700 °C to melt. The heating SiC then and the B₄C powder contributed slowly to the Al 7075. During mixing, an additional 1% of the magnesium is employed to increase the weight of the aluminium and to create a more reliable liquid metal bath. The lightweight aluminium-coated stainless-steel strainer approximately 10 min and at 400 rpm, respectively [6]. After placing the solution, it kept a substantial blend of slurry. The fluid steel is then placed into the moulds to produce it both the correct

Table 5.4 Volume fraction of aluminium hybrid composites

S. No.	Al 7075 (%)	SiC (%)	B ₄ C (%)
1	100	0	0
2	96	1	3
3	95	2	3
4	94	3	3
5	93	4	3

Fig. 5.1 Stir casting setup



shape and the size. The slurry has been placed in pre-heated steel moulds. The specimen was allowed to warm up at 530 °C two hours, then cool down for 4 h (at room temperature) and later heat again is prepared by insertion of 175 °C temperature at 8 h drain under environmentally friendly settings. The composite material sampling was developed on the basis of ASTM samples and all are polished using 200, 400 and 600 grit emery paper for microstructural analysis.

5.3 Results and Discussions

5.3.1 Tensile Strength

The test results are shown in Fig. 5.2, which indicates a difference in the strength of the traction with the increase in weight of SiC and B₄C particles according to ASTM E 08-8 standards. The tensile strength increases from 267 to 300 MPa when reinforced using SiC/B₄C reinforcement fragments, according to the experimental results. In a lightweight aluminium matrix, the accessibility of interbreed support pieces increases resistance to fracture initiations resulting in an improved tensile strength [7]. The highest composite tensile resistance increased by 12.35%, whilst the supports increased dramatically to 4%.

5.3.2 Microhardness

The microhardness of the Al alloy and aluminium hybrid composites at different weight fractions were observed in Fig. 5.3. As the number of strengthening particles increases, the toughness of the composites often increases. A larger number of

Fig. 5.2 Graphical representation of tensile strength versus wt% of (SiC/B₄C) hybrid composites

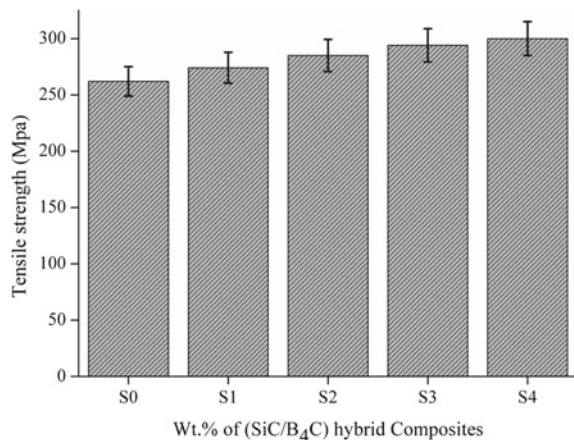
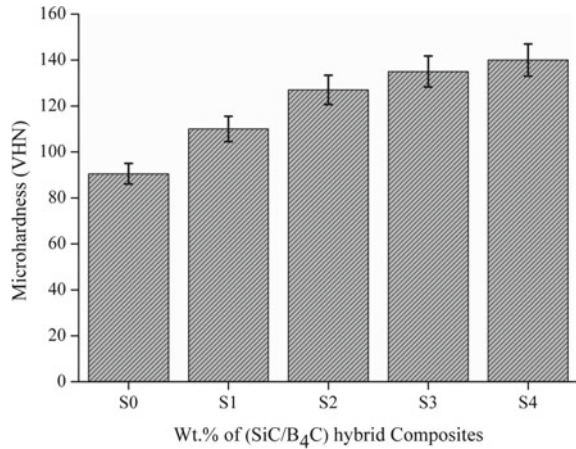


Fig. 5.3 Microhardness versus wt% of (SiC/B₄C) composites



strengthening bits can contribute to strengthening the composite. However, the microhardness enhanced from VHN 90.6 to VHN 140 by increasing the support fraction from SiC/B₄C particles strengthening to 0% to 4% [8]. In comparison with the unreinforced Al7075 aluminium alloy, an increase in 54.52% in Vickers microhardness is seen in compounds.

5.3.3 Wear Behaviour

Dry sliding wear was calculated based using pin-on-disc methods that were determined by the ASTM G-99 process. Each sample's dimensions were taken as 30 mm diameter, and the length of 6 mm was cut out by turning with a lathe tool. A pin positioned a set centre vertically on a rotating metallic piece and revolving on EN 31 steel disc [9].

5.3.3.1 Effect of Load on the Wear Rate

The influences of load on wear rate with a variation of the sliding velocity are shown in Fig. 5.4a, b. The graphs showing the wear rates of the hybrid composites at various load applied such as 20 N, 30 N and 40 N with two sliding speeds such as 2 m/s and 4 m/s, respectively. Every composite used for this investigation exhibit wear rate as a function of its loading rates at two sliding speeds. The pin gets extremely hot as the load is higher there is a significant amount of deformation occurring with the aluminium on the countertop [10]. Through assessment of 40 N loads, the hard surface is going to start wearing the aluminium

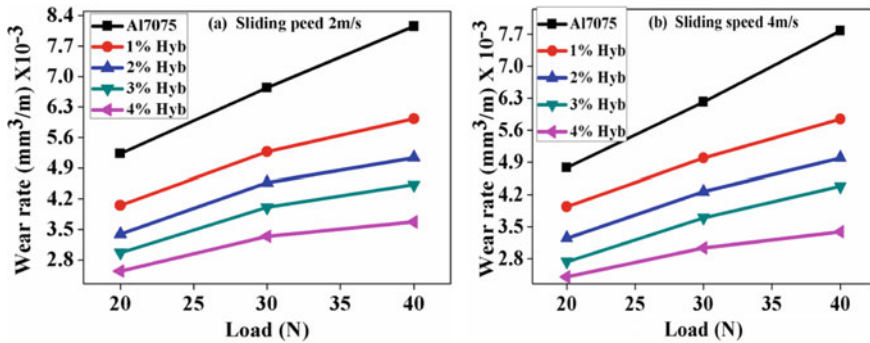


Fig. 5.4 Wear rate versus load

matrix. Then, the new SiC crystals are exposed to the worn iron surface. Such ultra-fine particles are responsible for regular inter-region interaction between the interfaces.

5.3.3.2 Effect of Applied Load on C.O.F

The various loading types of aluminium-based alloys on the pure aluminium alloys are seen in Fig. 5.5a, b. From Figure, friction coefficient would reduce the addition of reinforcement percentage composition increases. The coefficient of friction value decreases with growing the moving speed and reduces as the loads start to rise. This graph shows that the friction coefficient decreases as the linear velocity increases from 2 to 4 m/s. It observes a substantial decrease in the coefficient of friction as sliding speed is enhanced. Due to the weak particle reinforcements in the composite materials, they have cracked on the mating surface areas. The COF is decreased as the metal contact gets smaller and more constraints are used, resulting in less metal interaction between the reinforcements and the matrix [11].

5.3.4 Worn Surface Analysis

An SEM investigation was conducted to validate the wear test results. SEM studies were also utilized to identify the major wear mechanisms under a particular loading condition as well as the transition from one wear mechanism to another due to the change in test conditions. The scanning electron micrography (SEM) studies show visual evidence of particle pull-out and wear debris formation. When the sample and counter are available, regular and tangential loads pass through the contact points. The lower surface's asperities are subjected to relative motion resulting from the force applied to the lower surface. Initially, the pin and disc are rougher than the

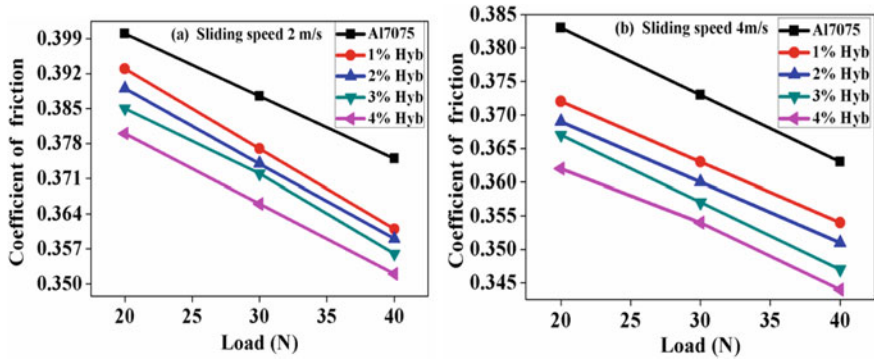


Fig. 5.5 Coefficient of friction versus load

smooth surface. The points of contact between the two surfaces are primarily at these locations. The drawback of plastic distortion on the soft surface effectively exists because of repeated loading activity, which aspects wear debris in Fig. 5.6d. Whilst alloys are softer than other metals used in impact wrenches, the wear debris can reach the smoother metal surface more quickly, forcing the weaker material on the surface to expand and break [12]. A small amount of projected particle fragments acts as debris, ploughing the softer surface on the specimen (Fig. 5.6b). In the case of hybrid composites, the broken reinforcements and the sharp asperities on the disc surface readily abrade the soft matrix surface of the composite specimen, causing it to wear faster. The grooves were positioned parallel to the countertop's counter surface, so the applied load was uniform across the surface un-fractured reinforcement particulates present in debris form also plough the specimen and disc surface, thus developing wear tracks along the surface of the hybrid composites (Fig. 5.6c). This worn-out debris acts as third-party abrasive particulates leading to crack formation. As a result of crack formation in the pin, small flakes of material are removed by delamination. An increase in wear rate with an increase in the reinforcement content is validated by the SEM micrograph of the composite pins. Scanning electron microscopy images of the base alloy ligaments show severe delamination, which results in the large removal of metal from the pin surface. The loss of ceramics in the Al 7075 alloy leads to an effortless removal of steel from the surface, and thus, the wear price is more significant. To conclude, it can be inferred that delamination was the leading wear mechanism in the Al 7075 alloy. The delamination and adhesion wear were minimized by using reinforcements from 1 to 4% (Fig. 5.6b, d). There is ample evidence that in the case of particulate reinforced composites, the alumina and silicon carbide particulates were strongly bonded with the Al 7075 core, protecting the bottom layer against delamination, which in turn minimized the wear rate. Also, the addition of 1–4% silicon carbide to the matrix resulted in a change in wear mechanism from delamination wear to abrasive wear type and the formation of mild wear tracks with the addition of reinforcements (Fig. 5.6a–e). Therefore, experimental values can be confirmed that the Al7075/4%

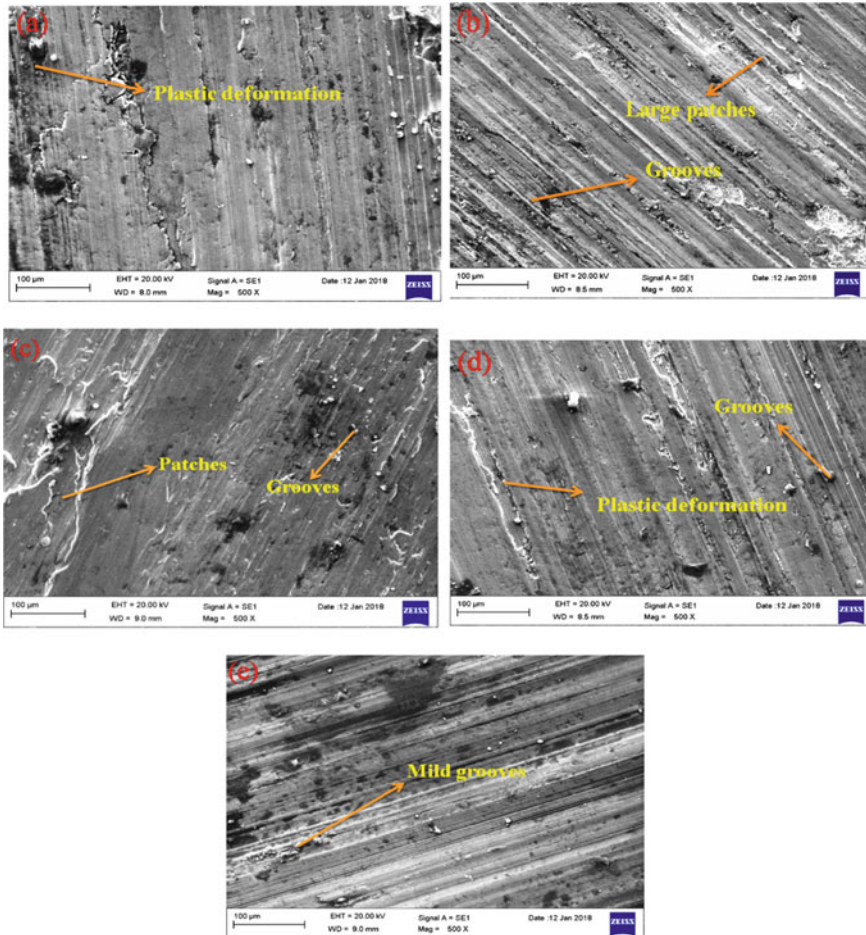


Fig. 5.6 Surface morphology of **a** 7075 Al alloy, **b** 7075/1% (SiC/B₄C), **c** 7075/2% (SiC/B₄C), **d** 7075/3% (SiC/B₄C) and **e** 7075/4% (SiC/B₄C) composite materials

SiC/4% B₄C composite strengths, minimized wear rate at all load and weight percentage of reinforcements.

5.4 Conclusions

The SiC/B₄C nanoparticles were produced utilizing the stir casting process in the form of 0, 1.0, 2.0, 3.0 and 4.0 wt% aluminium 7075 reinforced nanoparticles. Composites were invented and explored with mechanical and wear characteristics. The following conclusions have been reached from the experimental results.

- Aluminium with SiC and B₄C at different compositions were successfully fabricated through stir casting process.
- The enhancement of reinforcement particles substantially influenced the mechanical properties of the composites Al 7075 and reinforcement.
- Tensile strength and microhardness are higher for the addition of 4% (SiC-B₄C) reinforced with Al 7075 alloy in comparison to as-cast alloy. The improvement of tensile strength is attributed to the presence of high silica and boron content.
- Wear loss and coefficient of friction were reduced by the addition of SiC and boron carbide particles. The presence of hard ceramic particularly in hybrid composite was found to have more influence on the wear properties due to the presence of reinforcement particles.
- Enhancement of wear resistance of materials is due to increased hardness. Hence, 7075/4% (SiC/B₄C) composite material is more favourable in automobile sectors.

Acknowledgements The authors are thankful the laboratories utilized at the Siddharth Institute of Engineering and Technology in Mechanical Department at Puttur, India.

References

1. Baradeswaran, A., Perumal, A.E.: Study on mechanical and wear properties of Al 7075/ Al₂O₃/graphite hybrid composites. *Comp. Part B Eng.* **56**, 464–471 (2014)
2. Ramanathan, S., Vinod, B., Anandajothi, M.: Investigation of fatigue strength and life prediction for automotive safety components of V-notched and un-notched specimen part I: utilization of waste materials into raw materials. *Trans. Indian Inst. Met.* **72**, 2631–2647 (2019)
3. Gomez, L., Busquests Mataix, D., Amigo, V., Salvador, M.D.: Analysis of boron carbide aluminum matrix composites. *J. Comp. Mater.* **43**, 987–995 (2009)
4. Naher, S., Brabazon, D., Looney, L.: Simulation of the stir casting process. *J. Mater. Proc. Tech.* **143**, 567–571 (2003)
5. Umanath, K., Selvamani, S., Palanikumar, K.: Friction and wear behavior of Al6061 alloy (SiC_p+ Al₂O₃) hybrid composites. *Inter. J. Eng. Sci. Tech.* **3**, 5441–5451 (2011)
6. Vinod, B., Ramanathan, S., Anandajothi, M.: Constitutive equation and processing maps of Al-7Si-0.3 Mg hybrid composites: a novel approach to reduce cost of material by using agro-industrial wastes. *Silicon* **11**, 2633–46 (2019)
7. Walker, J., Rainforth, W., Jones, H.: Lubricated sliding wear behavior of aluminum alloy composites. *Wear* **259**, 577–589 (2005)
8. Poovazhagan, L., Kalaichelvan, K., Rajadurai, A., Senthilvelan, V.: Characterization of hybrid silicon carbide and boron carbide nanoparticles-reinforced aluminum alloy composites. *Procedia Eng.* **64**, 681–689 (2013)
9. Siva Prasad, D., Shobab, C., Ramanaiah, N.: Investigations on mechanical properties of aluminum hybrid composites. *J. Mater. Res. Tech.* **3**, 79–85 (2014)
10. Radhika, N., Subramanian, R., VenkatPrasat, S., Anandavel, B.: Dry sliding wear behavior of aluminum/alumina/graphite hybrid metal matrix composites. *Indust. Lubr. Trib.* **64**, 359–366 (2012)

11. Du, X., Zhang, Z., Wang, W., Wang, H., Fu, Z.: Microstructure and properties of B₄C-SiC composites prepared by polycarbosilane-coating/B₄C powder route. *J. Eur. Cer. Soc.* **34**(5), 1123–1129 (2014)
12. Pul, M.: Effect of sintering on mechanical property of SiC/B₄C reinforced aluminum. *Mater. Res. Exp.* **6**, 016541 (2018)

Chapter 6

Effect of Stress on Ferroelectric, Energy Storage and Harvesting Properties of 0.4BZT-0.6BCT Ceramics



Nishchay Saurabh and Satyanarayan Patel

Abstract In the present work, the effect of uniaxial stress on ferroelectric properties, energy storage and harvesting is studied for the $0.4\text{Ba}(\text{Zr}_{0.2}\text{Ti}_{0.8})\text{O}_3$ - $0.6(\text{Ba}_{0.7}\text{Ca}_{0.3})\text{TiO}_3$ (0.4BZT-0.6BCT) ceramics. Therefore, hysteresis loops were measured at different uniaxial compressive stress and temperature. The ferroelectric parameters (maximum polarization, remanent polarization, hysteresis loss and coercive electric field) decrease with an increase in stress. This is because the uniaxial compressive stress depolarizes 0.4BZT-0.6BCT by switching dipole in the energetically favorable direction (generally away from the electric field or poled direction). The maximum recoverable energy storage was found as 73.7 kJ/m^3 at 100°C and 80 MPa . Results show that the uniaxial compressive stress increases the stored energy density by 22% and stored energy efficiency from $\sim 20\%$ to $\sim 38\%$ at 22°C . The maximum energy harvesting was obtained as 100 kJ/m^3 when the cycle was operated between 5 – 160 MPa and 0.75 – 2 kV/mm at 22°C .

6.1 Introduction

Many efforts have been made to efficiently use ferroelectric/pyroelectric materials for waste heat/vibration to useful energy conversion [1, 2]. In this context, recently, lead-free ferroelectric materials were extensively explored as compared to lead-containing materials [3]. This is because lead is a hazardous material. Hence, it is essential to shift materials free from lead, but the major challenge was obtaining similar ferroelectric/pyroelectric properties as lead-based material. In this direction, BaTiO_3 , $\text{Na}_{0.5}\text{Bi}_{0.5}\text{TiO}_3$, $\text{K}_{1/2}\text{Na}_{1/2}\text{NbO}_3$, etc., and their solid solutions were developed [3, 4]. Among all of these, BaTiO_3 -based materials show the potential to

N. Saurabh · S. Patel (✉)

Department of Mechanical Engineering, Indian Institute of Technology Indore, Khandwa Road, Simrol, Indore, Madhya Pradesh 453552, India
e-mail: spatel@iiti.ac.in

N. Saurabh
e-mail: phd2001203003@iiti.ac.in

replace lead-based material because of high dielectric, piezoelectric and pyroelectric properties with relatively easy fabrication [2, 5]. Thus, BaTiO₃-based material can be a vital solution for sensing, actuator, energy harvesting and storage [5]. They show high spontaneous polarization in the temperature range of 248–473 K and can be used to convert waste heat to electricity [6–8].

In this direction, efficient energy harvesting requires a high pyroelectric effect in the material with a wide operating temperature range [9]. The conversion of energy through linear piezoelectric or pyroelectric material can yield only a small amount of electricity [10]. Hence, an Olsen cycle-based energy harvesting can give higher energy conversion density. Olsen cycle uses temperature-dependent polarization electric field (*P-E*) hysteresis loop for energy conversion density [11–13]. However, stress-dependent *P-E* loops can also be used for energy conversion. These stress-dependent energy conversion cycles are known as the modified Olsen cycle [14]. Stress-dependent energy conversion cycles showed better energy harvesting capabilities [14, 15]. Olsen cycle-based energy harvesting in Ba_{0.85}Zr_{0.15}TiO₃ was obtained as 42 kJ/m³ under a cycle of 24–70 °C and 0.25–1.25 kV/mm [15]. Nevertheless, the electromechanical-based cycle shows a high energy conversion density of 78 kJ/m³ under a cycle of 5–160 MPa and 0.25–1.25 kV/mm [15]. Moreover, a solid solution of 1-*x*Ba(Zr_{0.2}Ti_{0.8})O₃-*x*(Ba_{0.7}Ca_{0.3})TiO₃ is seen to give a very high piezoelectric and pyroelectric coefficient [5, 9]. It has been seen that 0.5Ba(Zr_{0.2}Ti_{0.8})O₃-0.5(Ba_{0.7}Ca_{0.3})TiO₃ has a large quality factor, better figures of merit and outstanding energy harvesting values [16]. 0.4Ba(Zr_{0.2}Ti_{0.8})O₃-0.6(Ba_{0.7}Ca_{0.3})TiO₃ ferroelectric material showed a strain of 0.10% and piezoelectric coefficient of 295 pm/V [17]. Thus, it is beneficial to use 1-*x*Ba(Zr_{0.2}Ti_{0.8})O₃-*x*(Ba_{0.7}Ca_{0.3})TiO₃-based compositions for energy conversion or storage applications.

In this work, energy storage and harvesting is studied in 0.4Ba(Zr_{0.2}Ti_{0.8})O₃-0.6(Ba_{0.7}Ca_{0.3})TiO₃ (0.4BZT-0.6BCT) ferroelectric ceramics. The stress-dependent *P-E* loops were recorded for energy harvesting or storage at various temperatures. The effect of temperature and stress on the ferroelectric parameters and energy storage is studied. A modified Olsen cycle was used to calculate the energy conversion density.

6.2 Materials and Method

0.4Ba(Zr_{0.2}Ti_{0.8})O₃-0.6(Ba_{0.7}Ca_{0.3})TiO₃ (0.4BZT-0.6BCT) ceramic was fabricated by conventional solid-state reaction route. For this purpose, precursor materials (purity > 99%) CaCO₃, BaCO₃, ZrO₂ and TiO₂ were used as starting powder. The powders were weighed according to stoichiometric ratio and milled for 5 h using a ball mill. Then, milled powder was calcined at 1300 °C for 2 h in the air using a muffle furnace. The calcined powder was again milled, and a uniaxial hydraulic press was used to obtain a cylinder sample of 10 × 6 mm². To obtain a higher density sample, cold isostatic press was used at ~300 MPa for 90 s and sintered at 1500 °C for 2 h under normal atmospheric conditions. Afterward, the sample was

grounded and sputtered on both sides with silver paste for polarization–electric field (P - E) measurement. The P - E loops are recorded with the help of a modified Sawyer–Tower circuit. The applied electric field was varied as ± 2 MV/m (Trek Model 610E, Trek Inc.) at 1 Hz. P - E loops are measured at 5–160 MPa (steps 20 MPa) and various temperatures with the help of a screw-driven load frame (Z010, Zwick GmbH & Co. KG, Germany). The final sample dimension was $\sim 6 \times 6$ mm². Here, 5 MPa is used as contact stress to make a proper contact between sample and load frame to measure the P - E loop.

6.3 Results and Discussions

The P - E hysteresis loop is plotted under various temperatures and uniaxial compressive stress (σ_{xx}). Figure 6.1a, b shows the P - E hysteresis loop at 22 °C and 100 °C for different σ_{xx} . Figure 6.1a shows that as σ_{xx} increases from 5 to 160 MPa, polarization decreases. The direction of applied σ_{xx} is parallel to the applied electric

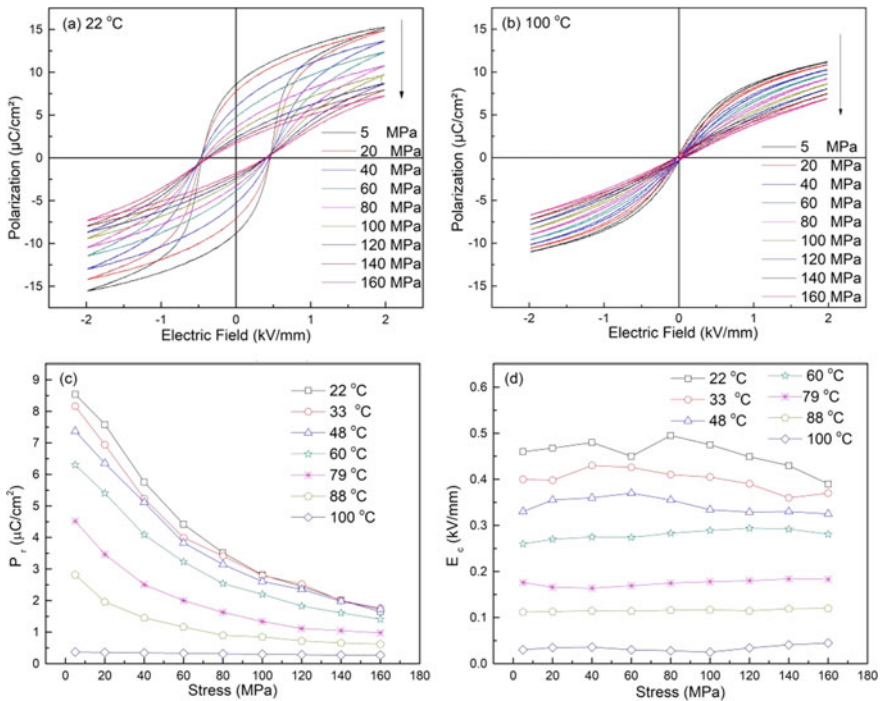


Fig. 6.1 Ferroelectric hysteresis loop under the various stress conditions at **a** 22 °C and **b** 100 °C. Effect of uniaxial compressive stress on the **c** remanent polarization (P_r) and **d** coercive electric field (E_c) at different operating temperatures

field. As the compressive stress increases, dipoles try to switch in the direction of favorable energy.

The direction of favorable energy is usually away from applied σ_{xx} . On the other hand, the electric field aligns dipoles in its direction. This conflict of applied σ_{xx} and electric field counteract each other. Thus, as shown in Fig. 6.1a, b, the value of polarization decreases with increased uniaxial stress. Figure 6.1a, b also shows that as the temperature increases from 22–100 °C, the hysteresis loop becomes thinner (similar P - E loops are also recorded at an intermediate temperature which is not presented here). This narrowing can be the effect of the thermal relaxation of domains by reducing ferroelectric switching. Figure 6.1c shows the effect of temperature and uniaxial stress on remnant polarization (P_r). The highest value of P_r is obtained as 8.5 $\mu\text{C}/\text{cm}^2$ at 22 °C and 5 MPa. The P_r decreases with an increase in temperature (22–100 °C) and stress (5–160 MPa). This is because σ_{xx} causes pinning of domain. As the stress field increases, fewer domains are available for reorientation, which decreases P_r and narrowing the hysteresis loop. Temperature also affects the ferroelectric switching, thus reducing P_r and hysteresis area with an increase in temperature. However, the coercive electric field (E_c) remains almost constant with stress, as seen in Fig. 6.1d. However, E_c decreases from 0.45 kV/mm to 0.05 kV/mm with an increment of temperature from 22 to 100 °C at 5 MPa. These values of the low E_c show the soft ferroelectric nature of the material [14].

6.3.1 Energy Storage Performance

Figure 6.2a represents the schematic diagram for recoverable energy storage density and energy loss. The shaded area in the schematic (Fig. 6.2a) represents recoverable energy storage, and the area within P - E loop shows energy loss. Recoverable energy storage density can be obtained as [18]

$$U = \int_{P_1}^{P_2} EdP. \quad (6.1)$$

where U is the recoverable energy storage density, E is the applied electric field, and P_1 and P_2 are the starting and end limits of polarization. The value of U increases from 50 to 68 kJ/m^3 as the temperature increases from 22 to 100 °C at 5 MPa, as shown in Fig. 6.2b. Further, U increases with stress up to 60 MPa when the temperature is below 60 °C and up to 80 MPa for above 60 °C. Beyond 60 MPa, the decrease in maximum polarization surpasses the reduction in P_r ; therefore, the energy storage density decreases. An increase in energy storage density occurs due to domain pinning in ferroelectric materials and the domains' thermal agitation. Hence, fewer domains are available for switching and improve the U . In Fig. 6.2c, the energy loss density is depicted, which shows a decreasing trend with increasing temperature and stress. The value of energy loss decreases

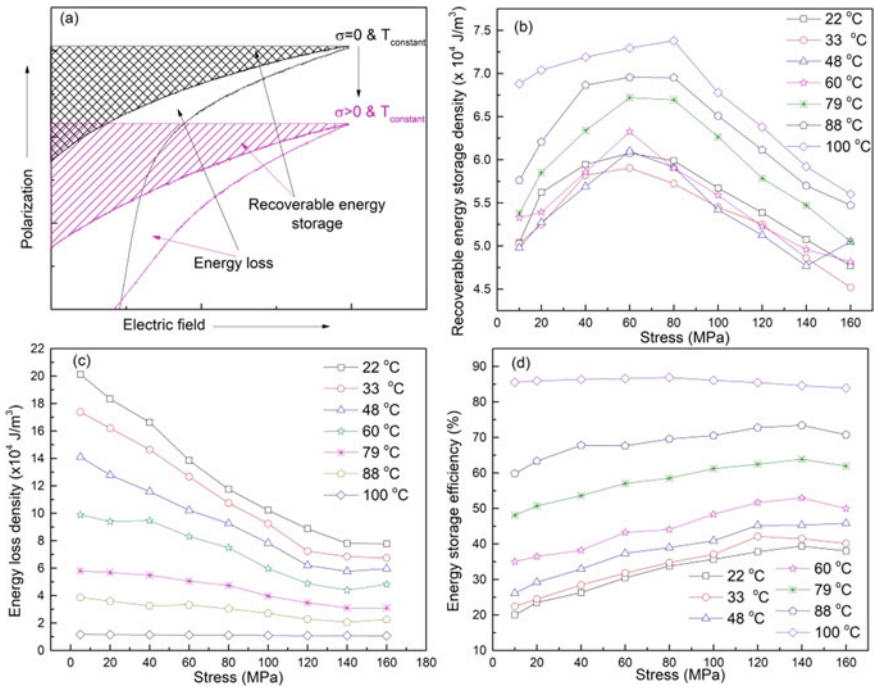


Fig. 6.2 **a** Schematic for improved energy storage density via compressive stress, **b** recoverable energy storage density, **c** energy loss density and **d** energy storage efficiency as a function of applied stress at different operating temperatures

from 200 to 100 kJ/m^3 as the temperature increases from 22 to 100 °C at 5 MPa stress. Similarly, energy loss decreases from 200 to 78 kJ/m^3 as the stress increases from 5 to 160 MPa at 22 °C. This decrement of energy loss is due to the narrowing of the *P-E* hysteresis loop with increased temperature and stress, as discussed above. Figure 6.2d shows the energy storage efficiency variation with temperature and stress. Energy efficiency can be obtained by the ratio of *U* and total energy (sum of *U* and energy loss density). The energy storage efficiency increases from 20 to 85% with an increase in temperature from 22 to 100 °C.

6.3.2 Energy Harvesting

Figure 6.3a shows a schematic diagram for energy harvesting for the modified Olsen cycle. The various steps in the modified Olsen cycle-based electromechanical energy harvesting are as follows:

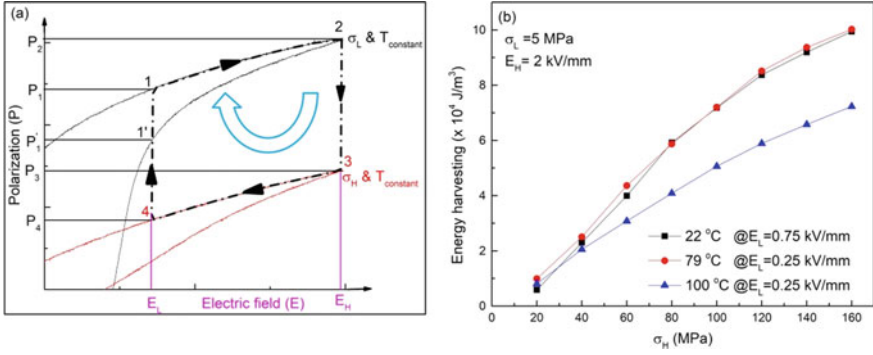


Fig. 6.3 **a** Schematic of the mechanical energy conversion cycle. **b** Mechanical energy conversion density versus uniaxial stress under various applied temperatures

Process 1–2: It is the process in which the electric field is increased from E_L to E_H at constant stress σ_L . This increase in electric field orients the dipoles in the electric field direction, and thus, the polarization increases from P_1 to P_2 .

Process 2–3: The stress on the material increases from σ_L to σ_H , keeping E_H as fixed, which decreases the polarization of material from P_2 to P_3 . This depolarization of material produces a depolarization current in a material.

Process 3–4: In this process, keeping σ_H as fixed, the electric field decreases from E_H to E_L , which reduces the polarization P_3 to P_4 . This process also produces a depolarization current.

Process 4–1: The stress supplied is removed from σ_H to σ_L at constant electric field E_L .

The area under the process 1-2-3-4-1 is the energy harvested from the modified Olsen cycle. The area under the process 1'-1-2 provides the loss present in the cycle. However, if a unipolar hysteresis loop is used or material is poled before starting the next cycle, loss (1'-1-2) is minimized. Hence, in the present work, area under the 1-2-3-4-1 is considered for energy harvesting. Apart from the hysteresis loss, other losses, i.e., leakage current, friction and other irreversible processes also present in the cycle, which reduce the actual energy harvesting capacity. The mathematical equation to calculate the energy harvesting is given by [8]

$$N_D = \oint E dD. \quad (6.2)$$

where N_D is the energy harvested per cycle, E is the electric field applied, and dD is the change in polarization between σ_L and σ_H . Figure 6.3b shows the energy harvesting of the 0.4BZT-0.6BCT material as a function of σ_{xx} at different temperatures. At a constant temperature of 22 °C and lower stress (σ_L) fixed at 5 MPa, energy harvesting increases from 10 to 100 kJ/m³ with increase in higher stress (σ_H) from 20 to 160 MPa (@0.75–2 kV/mm). However, at a higher cyclic

Table 6.1 Comparison of mechanical energy harvesting and related parameters for various ceramics

Material	T (°C)	$\sigma_L - \sigma_H$ (MPa)	$E_L - E_H$ (kV/mm)	N_D (kJ/m ³)	$N_D/\Delta\sigma$ ($\sigma_1 - \sigma_2$)	$N_D/\Delta E$ ($E_1 - E_2$)	References
0.5BZT-0.5BCT	–	5–160	0–2	221	1.42	110.5	[19]
PIC 151 PZT	–	0–200	0.2–2	526	2.63	292.22	[20]
Pb(Mn _{1/3} Nb _{2/3})O ₃ -32PbTiO ₃	80	2–28	0–1.5	160	6.15	106.6	[21]
Ba _{0.85} Zr _{0.15} TiO ₃	23	5–160	0.25–1.5	78	0.41	62.4	[15]
PKI-552	–	0–1 ton	0.1–2.5	348	–	145	[14]
0.4BZT-0.6BCT	22	5–160	0.75–2	100	0.64	80	This work

temperature of 100 °C, energy harvesting increases from 10 to 72 kJ/m³ with increase in σ_H from 20 to 160 MPa (@0.25–2 kV/mm). As discussed above, the decrease in energy harvesting is because of the decreased ferroelectric domain switching at a higher temperature. The energy harvesting at 22 and 79 °C has a similar value as seen in Fig. 6.3b. This is an effect of variation in the E_L at 22 and 79 °C. The E_L is kept as 0.25 MV/m and 0.75 MV/m for energy harvesting at 22 and 79 °C, respectively. Hence, it can be said that the effect of temperature on energy harvesting can be neutralized by varying the E_L value. Table 6.1 shows the various lead-based and lead-free ferroelectric ceramics used for electromechanical energy harvesting density with their operating parameters. It shows that the 0.4BZT-0.6BCT is also a potential candidate for energy harvesting at constant cycle temperature (T).

6.4 Conclusions

0.4BZT-0.6BCT ferroelectric ceramic is fabricated via conventional mixed-oxide route technique, and polarization–electric field (P - E) ferroelectric hysteresis loops were recorded at various σ_{xx} and temperatures. The applied compressive stresses drastically decrease the hysteresis parameter (P_{max} , P_r and E_c) and increase energy storage density. The energy storage increases from 50.4 to 60.8 kJ/m³ as σ_{xx} increases from 5 to 60 MPa at 22 °C. Additionally, σ_{xx} improves the energy storage efficiency from 20 to 30.5% at similar working conditions. The compressive stress reduces hysteresis loss which increases energy storage density and efficiency. The mechanical energy harvesting is obtained as 100 kJ/m³ when the cycle operates between 5–160 MPa and 0.75–2 kV/mm at a constant temperature of 22 °C. The normalized per MPa and kV energy harvesting is comparable with the literature. 0.4BZT-0.6BCT can be a suitable candidate for enhanced mechanical energy harvesting at lower applied stress and electric field.

Acknowledgements S. Patel acknowledges Florian Weyland for providing the sample; Dr. Nikola Novak and Dr. Rahul Vaish for measurement. S. Patel also acknowledges the financial support received by Science and engineering research board (SERB) for Start-up Research Grant (No. SRG/2020/000188).

Conflicts of Interest The authors declare that they have no known competing financial interests or personal relationships that could have influenced the work reported in this paper.

References

1. Kishore, R.A., Priya, S.: A review on low-grade thermal energy harvesting: materials, methods and devices. *Materials* **11**(8), 1433 (2018)
2. Bowen, C.R., Taylor, J., LeBoulbar, E., Zabek, D., Chauhan, A., Vaish, R.: Pyroelectric materials and devices for energy harvesting applications. *Energy Environ. Sci.* **7**(12), 3836–3856 (2014)
3. Akram, F., Kim, J., Khan, S.A., Zeb, A., Yeo, H.G., Sung, Y.S., Song, T.K., Kim, M.-H., Lee, S.: Less temperature-dependent high dielectric and energy-storage properties of eco-friendly BiFeO₃-BaTiO₃-based ceramics. *J. Alloys Compd.* **818**, 152878 (2020)
4. Shrout, T.R., Zhang, S.J.: Lead-Free Piezoelectric Ceramics: Alternatives for PZT? Progress in Advanced Dielectrics: World Scientific, pp. 295–327 (2020)
5. Acosta, M., Novak, N., Rojas, V., Patel, S., Vaish, R., Koruza, J., Rossetti Jr, G., Rödel, J.: BaTiO₃-based piezoelectrics: fundamentals, current status, and perspectives. *Appl. Phys. Rev.* **4**(4), 041305 (2017)
6. Li, S., Nie, H., Wang, G., Liu, N., Zhou, M., Cao, F., Dong, X.: Novel AgNbO₃-based lead-free ceramics featuring excellent pyroelectric properties for infrared detecting and energy-harvesting applications via antiferroelectric/ferroelectric phase-boundary design. *J. Mater. Chem. C.* **7**(15), 4403–4414 (2019)
7. McKinley, I.M., Lee, F.Y., Pilon, L.: A novel thermomechanical energy conversion cycle. *Appl. Energy.* **126**, 78–89 (2014)
8. Nguyen, H., Navid, A., Pilon, L.: Pyroelectric energy converter using co-polymer P (VDF-TrFE) and Olsen cycle for waste heat energy harvesting. *Appl. Therm. Eng.* **30**(14–15), 2127–2137 (2010)
9. Shen, M., Li, W., Li, M.-Y., Liu, H., Xu, J., Qiu, S., Zhang, G., Lu, Z., Li, H., Jiang, S.: High room-temperature pyroelectric property in lead-free BNT-BZT ferroelectric ceramics for thermal energy harvesting. *J. Eur. Ceram. Soc.* **39**(5), 1810–1818 (2019)
10. Pilon, L., McKinley, I.M.: Pyroelectric energy conversion. *Annu. Rev. Heat Transfer.* **19** (2016)
11. Olsen, R., Bruno, D., Briscoe, A.J., Dullea, J.: Cascaded pyroelectric energy converter. *Ferroelectr.* **59**(1), 205–219 (1984)
12. Olsen, R.B., Bruno, D.A., Briscoe, J.M.: Pyroelectric conversion cycles. *J. Appl. Phys.* **58** (12), 4709–4716 (1985)
13. Olsen, R.B., Evans, D.: Pyroelectric energy conversion: hysteresis loss and temperature sensitivity of a ferroelectric material. *J. Appl. Phys.* **54**(10), 5941–5944 (1983)
14. Patel, S., Chauhan, A., Vaish, R.: Enhanced energy harvesting in commercial ferroelectric materials. *Mater. Res. Express.* **1**(2), 025504 (2014)
15. Patel, S., Yadav, H., Kumar, M.: Effect of uniaxial stress on energy harvesting, storage and electrocaloric performance of BZT ceramics. *J. Korean Ceram. Soc.* 1–8 (2021)

16. Bijalwan, V., Erhart, J., Spatz, Z., Sobola, D., Prajzler, V., Tofel, P., Maca, K.: Composition driven (Ba, Ca)(Zr, Ti)O₃ lead-free ceramics with large quality factor and energy harvesting characteristics. *J. Am. Ceram. Soc.* **104**(2), 1088–1101 (2021)
17. Ehmke, M.C., Glaum, J., Hoffman, M., Blendell, J.E., Bowman, K.J.: In Situ X-ray Diffraction of Biased Ferroelastic Switching in Tetragonal Lead-free (1-x)Ba(Zr_{0.2}Ti_{0.8})O_{3-x} (Ba_{0.7}Ca_{0.3})TiO₃ Piezoelectrics. *J. Am. Ceram. Soc.* **96**(9), 2913–2920 (2013)
18. Sun, Z., Wang, Z., Tian, Y., Wang, G., Wang, W., Yang, M., Wang, X., Zhang, F., Pu, Y.: Progress, outlook, and challenges in lead-free energy-storage ferroelectrics. *Adv. Electron. Mater.* **6**(1), 1900698 (2020)
19. Patel, S., Chauhan, A., Rojas, V., Novak, N., Weyland, F., Rödel, J., Vaish, R.: Thermomechanical energy conversion potential of lead-free 0.50Ba(Zr_{0.2}Ti_{0.8})O₃-0.50 (Ba_{0.7}Ca_{0.3})TiO₃ bulk ceramics. *Energy Technol.* **6**(5), 872–882 (2018)
20. Patel, S., Chauhan, A., Vaish, R.: Analysis of high-field energy harvesting using ferroelectric materials. *Energy Technol.* **2**(5), 480–485 (2014)
21. Patel, S., Moghal, A.A.B., Madhar, N.A., Chauhan, A., Vaish, R.: Cyclic piezoelectric energy harvesting in PMN-PT single crystals. *Ferroelectricity* **481**(1), 138–145 (2015)

Chapter 7

Survey of Nanosensors and Nano-heterostructures



Priya Chaudhary, Sonam Gour, and Amit Rathi

Abstract In this paper, we have studied various types of sensors like chemical sensors, electrochemical sensors, biosensors, optical sensors, and mass-sensitive sensors. These sensors measure the temperature, velocity liquid level, displacement, pressure, vibrations, force radiation, chemical species, and strain at the nanoscale. Then, we have also reviewed different subsequent parameters like accuracy, precision, linearity, resolution, and hysteresis which are using for their characterization. In this paper, we have also discussed the applications of nano-heterostructure in various fields like biomedical, optoelectronic, etc., which are made by using various nanomaterials like Si, Si-Ge, GaAs, AlGaAs, InP, InGaAs, AlGaN, CdS, AlInGaP, ZnS, ZnSe, CdSe, SiC, GaN, and HgCdTe.

7.1 Introduction

Nanosensors have been distinguished by the Dr.-Rudolf Eberle Innovation Award of the German State of Baden-Württemberg in 1995. Nanosensor is a brand of atomic force microscopy and scanning probe microscopy known as AFM and SPM [1, 2]. Sensor is the device that includes transduction element, recognition element, and the signal processor accomplished of reversibly and continuously reporting chemical or physical information as shown in Fig. 7.1 [1].

Modern sensor consists of some basic features which are as follows. The first feature is that the sensors must be directly got in touch with the investigated subject.

P. Chaudhary · S. Gour · A. Rathi (✉)

Department of Electronics and Communication, Manipal University Jaipur, Jaipur, Rajasthan, India

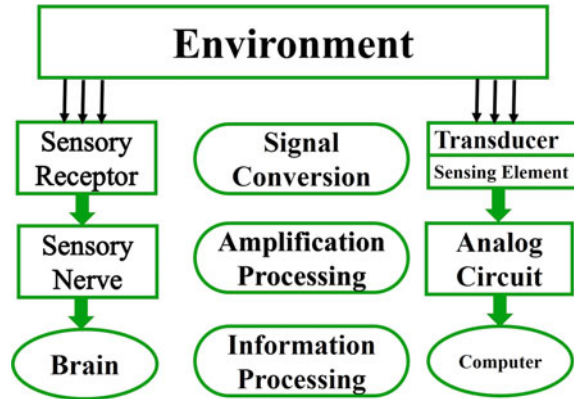
P. Chaudhary

Department of Electronics and Communication, Arya Institute of Engineering and Technology, Jaipur, Rajasthan, India

S. Gour

Department of Electronics and Communication, Arya College of Engineering and Research Center, Jaipur, Rajasthan, India

Fig. 7.1 Communication through sensors



The second feature is that the sensor has to convert electric information to the electric signal. The third feature is that the sensor has to respond quickly and also operates on repeated cycles continuously [3, 4]. The other feature is that the sensor has to be small and also inexpensive.

For biosensors, molecules are defined by their size of dimension, namely by the so-called steric recognition. The second part of the chemical sensors is called a transducer that is the device which allows the transformation of real concentration value or non-electric into an electric quantity such as current, voltage, or resistance [1].

There are several types of transducers and the two main representative bonds are the following, energy conversion transducer, where the principal of the energy conversion is that sensors produce the electrical energy. None of these classes of the sensor is able to function without any external voltage supply. A transducer transforms environmental properties and conductivity, or on the other hand second type of representative is resistive transducer, the resistivity of electrically conducting materials alterations relating to changes in physical quantity. According to their operation mode, there are many categories of sensors.

7.2 Classification of Sensor

Here, nanosensors are classified according to their structure and application. Five types of nanosensors are discussed below, namely (i) Chemical sensor (ii) Electrochemical sensor (iii) Biosensor (iv) Optical sensor (v) Mass-sensitive sensor.

7.2.1 Chemical Sensor

The first category of these sensors is the chemical sensor, namely the device which converts chemical information such as concentration of precise sample components

into the logically beneficial signal. The chemical sensor contains basically two fundamental units that are (1) receptor, (2) transducer. In the first unit receptor that is shown in Fig. 7.2, chemical information is changed into the energy form that is noticed by a transducer. Because of this, an electrochemical sensor is a kind of chemical sensor [4, 5]. Indeed, in continuation to the chemical sensors, second category of the sensors is the electrochemical sensors. This group of chemical sensors is the largest group.

They can be employed to identify the bulk of general toxic gases in a broad diversity of safety applications [1].

7.2.2 Electrochemical Sensors

These sensors function by reacting with gas and generating an electrical signal that is relative to the analyte concentration as shown in Fig. 7.3 [1]. A classic electrochemical sensor is composed of a sensing electrode, or it is known as a working electrode and conversely, a counter electrode which is separated by a slim layer of electrode.

Depending on the chemical reactivity of the target, this composition of electrode light and the material of the sensing electrode are preferred. These sensors are compact and need very small power. They show outstanding compatibility and linearity and usually have a long life, normally one to three years [1].

7.2.3 Biosensor

The third category of the sensors is called biosensors. A chemical sensor is a sensor, in which a biochemical mechanism is utilized by the recognition system [6]. As an example of biosensors, the results from the research that is taken and obtained by a

Fig. 7.2 Idealized scheme depicting chemiresistors and receptors (chemical sensor)

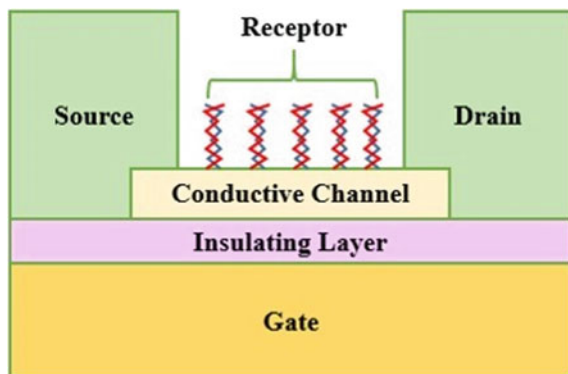
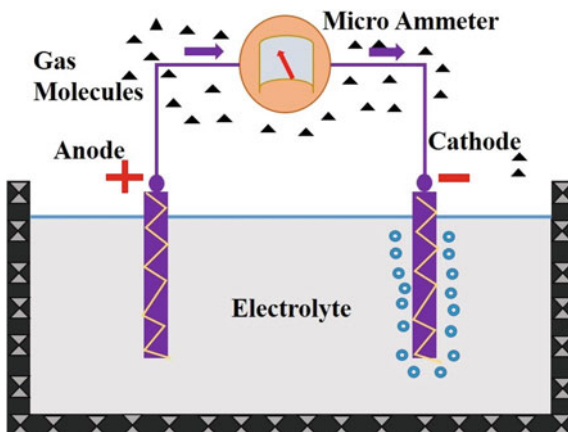


Fig. 7.3 Electrochemical sensors



group of researchers with the United States Department of Energy at Berkeley who has discovered a technique in that RNA or DNA assays can be read, evaluated without the requirement to explore chemical classification or complicated instrumentation [7].

This biosensing approach is depending on the electrostatic repulsion wherein objects with similar electrical charges construct one other. The most astonishing thing about the electrostatic recognition system is that—it needs nothing more than the nude eyes to announce results that presently need chemical leveling and confocal laser scanner [8]. Biosensors are employed to observe the level of glucose in the patients with diabetes, treatment of wastewater, analysis of food, and applications of environment and drug discovery [9].

7.2.4 Optical Sensor

This category of sensors can be categorized into two main subgroups. The first subgroup is called proximity sensors, which are useful to detect object's presence in a variety of industries, mobile phones, electronic applications, and retail mechanizations. When a proximity sensor is positioned near a phase, it can detect out-of-paper circumstances in a printer or darken the screen of a mobile phone to save battery life [1, 10]. The second subcategory of the optical sensors is known as an ambient light sensor as shown in Fig. 7.4, which will make available accurate detection of light for ambient brightness and are employed normally in LCD backlight control in smartphones, panels, or LCD TVs applications [1]. The method to change the optical signal is by employing an electro-optical sensor that is the electronic detector that changes the light or converts light into the electrical signal.

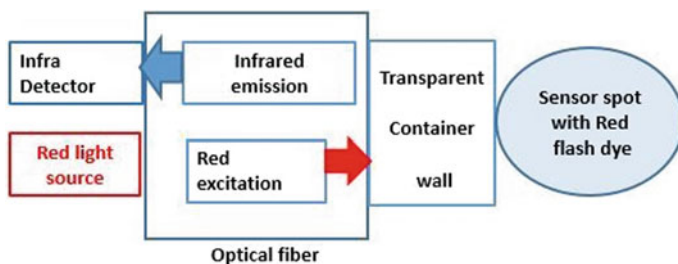


Fig. 7.4 Optical sensors [5]

There are many components of light like the wavelength, the polarization, the intensity, and the phase, which can be sensed. The light interaction with the matter can be calculated by absorbance, luminescence, reflectance, and others [1, 11–13].

7.2.5 Mass-Sensitive Sensor

By sensing the mass, these sensors can find out unlike molecules. There are numerous types of these sensors as shown in Fig. 7.5 [3]. The first subcategory of mass-sensitive sensors is the cantilever sensors. In this subcategory, the displacement of the beam on a cantilever surface is related to a beam length and the applied force. The customization of the cantilever surface can be done by permitting differential stress to propagate as an analyte of interest is bound to its target on the modified surface [1].

The second subcategory of the mass-sensitive sensor is the so-called quartz crystal microbalance, or briefly, QCM. QCM is an ultra-sensitive mass sensor which relies on the quartz crystal that is oscillated at its resonance frequency as a result of the piezoelectric effect. Upon exclusion or adding of small masses or

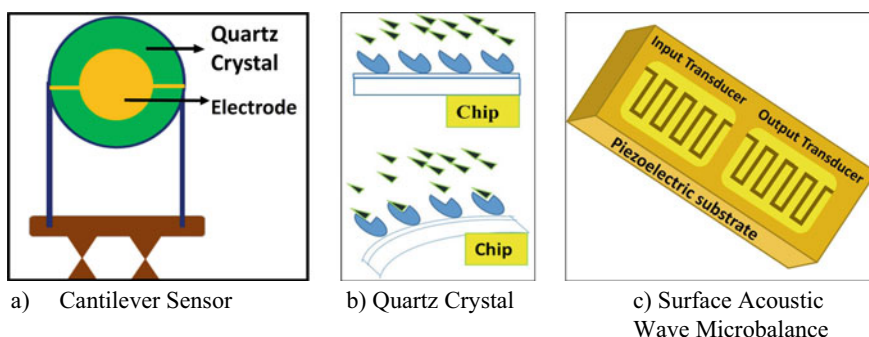


Fig. 7.5 Different types of mass-sensitive sensors

surface molecules, there the quartz crystal resonance is disrupted; therefore, the change occurs in the calculated frequency. In the frequency, the prop changes are then altered throughout a physical relationship to transform in mass [1]. The third subcategory of mass-sensitive sensors is called surface acoustic wave or, briefly, SAW. A sensor acoustic wave is a wave which is going along with the surface of the material showing elasticity with an amplitude that characteristically declines exponentially with a dip into the substrate. When the propagation of acoustic wave takes place throughout the surface of the material, it makes the changes to the features of propagation that influences the amplitude or the velocity of the wave. We can monitor the changes in velocity by determining the frequency and able to correlate it to equivalent physical quantity that can be measured [4, 8]. In summary, there are a large variety of sensors, but the basic analysis and parameters that characterize the sensors are common to all sensors. A comparison of all these nanosensors is shown below in Table 7.1.

7.3 Parameters for Sensors Characterization

To describe a sensor, various parameters are given away. Authentication of sensing results is satisfied by characterizing one or grouping of the subsequent parameters [1]. Accuracy is the primary parameter. Accuracy means how close a calculated value is to the real value. The precision is the second parameter that is significant for the sensing validation. Precision is how scattered the results are around an average value. Characteristics of selectivity decide whether the sensor can react

Table 7.1 Comparison of the mechanism of nanosensors and their applications

S. no.	Sensors	Mechanism	Application
1	Chemical sensor	Chemical information is converted by the device into analytically valuable signal	To identify the bulk of general toxic gases in a broad diversity of safety applications
2	Electrochemical Sensor	The gas reaction takes place, and electric signal is generated	To sense the existence of poisonous gases like H ₂ S, SO ₂ , and O ₂ variation in air
3	Bio sensor	Biological component is combined by the device with the physical chemical detector component	Treatment of wastewater, analysis of food, and applications of environment and drug discovery
4	Optical sensor	Transform light signals into electronic signals	LCD backlight control in smart phones, panels or LCD TVs, and notebook applications
5	Mass-sensitive sensor	It can find out unlike molecules by sensing its mass	To detect various body hormones

selectively to the cluster of the analyte, or even especially, to the single analyte. Linearity is the additional feature. Ideal sensors are planned to be linear or linear to a number of a simple mathematical function of the measurement, classically logarithmic [1, 4]. An additional characteristic of the sensors is called resolution. This requirement is the negligible noticeable incremental change of input parameter that can be detected in the output signal. Hysteresis refers to the feature that a transducer has been incapable to replicate authentically in the opposite way of operation [11]. Hysteresis is the main problem for sensing applications because two signals might be achieved for a similar concentration, such as, based on the directionality of the concentration [1].

7.4 Nano-heterostructures and Their Applications

Nano-heterostructures are composite structures. These structures are made by the grouping of two and more nanomaterial components with precise interfacial contacting [2]. Nanostructures are used to design different nanosensors. To construct nanosensors and nano-heterostructure, nanomaterials and the composition of nanomaterial are used for various applications. Some semiconductor nanomaterials like Si, Si-Ge, GaAs, AlGaAs, InP, InGaAs, AlGaN, CdS, AlInGaP, ZnS, ZnSe, CdSe, SiC, GaN and HgCdTe, etc., show tremendous applications in palm pilot, computer, cell phone, laptops, pagers, mobile terminals, traffic signal, satellite dishes, fiber networks, TV remote, car tail lights, CD player, and airbags. These nanomaterials define the behavior of quantum confinement of the size 1–20 nm range. If semiconductor material size is concentrated at the nanoscale, the chemical or physical properties of nanomaterial change radically. Semiconductor conductivity and optical properties like refractive index and coefficient of absorption can be changed. Nanomaterials and nano-heterostructure devices are continuously in research, and they have applications in several fields like electronic devices at the nanoscale, optical sources (LEDs and LASER technology), solar cells, waveguides, automobile parts, chemical sensors and biosensors, super absorbent, and substances [14].

7.4.1 *Nano-heterostructures in Optoelectronics*

Heterostructures are designed to solve the problem of parameters control in semiconductor devices: bandgap, charge carrier's effective mass and mobility, refractive indices, energy spectrum of electron, etc. Development in nano-heterostructures has caused extraordinary changes in daily life. Heterostructure electronic is broadly used in several areas of human civilization. This is unthinkable in today's world without a double heterostructure laser-based telecommunication system, a heterostructure light-emitting diode, a heterostructure-based bipolar transistor, and a

low noise-based high electron mobility transistor for high-frequency applications such as satellite television. Solar cells with heterostructures are employed in both terrestrial and space applications [15].

7.4.2 *Nano-heterostructure in Biomedical*

Inorganic nano-heterostructures are developed for biomedicine applications. And applications in diagnostics and imaging fields are also taken into account, including in vivo tests. Nano-heterostructures are especially used in cancer therapy and diagnosis. By compositions of various nanodomains, nano-heterostructure gives better results. Because of these multifunctional nano-heterostructures, these are used in contemporary therapy and diagnosis. In single-system nano-heterostructure, two and more nanoscale domains occur, and due to this, it accomplishes different roles at the same period, like enable both imaging and tumor mass treatment. Therapy and diagnosis are commonly called theranostic. To eradicate the bacterial infection, theranostic nano-heterostructures are employed [16].

7.5 Conclusion

Various types of nanosensors are discussed and characterized based on energy sources and materials. Optical nanosensors are useful for absorption, luminescence, fluorescence, light scattering and also for chemicals monitoring inside the cell. Optical sensors work effectively and maintain their own sensitivity to the property they measure. In electromagnetic nanosensors, electrode light is used for composing and sensing the electrode material. Also, sensors that depend on nanoparticles are used for the detection of DNA and biomolecules. And different nanomaterials-based nano-heterostructure are employed in various applications like NHS for optical sources to achieve high optical gain for high output power and NHS for biomedical application.

References

1. Coursera Education for everyone: Nanotechnology and Nanosensor Part 1, Technion Israel Institute of Technology. <https://www.coursera.org/learn/nanotechnology1>
2. Saleh, A.J., Joon, J., Aminur, M.: *Sensors* **9**, 2289 (2009)
3. Khorasaninejad, M., Shi, Z., Zhu, A.Y., Chen, W.T., Sanjeev, V., Zaidi, A., Capasso, F.: Achromatic metalens over 60 nm bandwidth in the visible and metalens with reverse chromatic dispersion. *Nano Lett.* (2017)
4. Vijaya Lakshmi, U., Srividya Devi, P.: *Sensors and its smart applications*. *Int. J. Sci. Eng. Res.* (IJSER) ISSN (Online): 2347–3878

5. Sasaki, K., Shi, Z.Y., Kopelman, R., Masuhara, H.: Three-dimensional ph microprobing with an optically-manipulated fluorescent particle. *Chem. Lett.* **25**, 141 (1996)
6. Mehrotra, P.: Biosensors and their applications—a review. *J. Oral Biol. Craniofac. Res.* **6**(2), 153–159 (2016)
7. Pant, M., Ray, K., Sharma, T.K., Rawat, S.: *Soft computing: theories and applications*. Springer Science and Business Media LLC, Proceedings of SoCTA 2016, vol. 2
8. Gründler, P.: *Chemical sensors*. Chem. Texts **3** (2017)
9. Azosensors: Biosensor Technology: Advantages and Applications (2013) <https://www.azosensors.com/article.aspx?ArticleID=402>
10. Yuepeng, Lv., Duan, S., Wang, R.: Review structure design, controllable synthesis, and application of metal-semiconductor heterostructure nanoparticle. *Prog. Nat. Sci. Mater. Int.* **30** (1), 1–12 (2020)
11. Wang, Y., Tong, M.M., Zhan, D., Gao, Z.: *Sensors* **11**, 19 (2011)
12. Riyaj, M., Singh, A.K., Rathi, A., Kattayat, S., Kumar, S., Dalela, S., Alvi, P.A.: High pressure affects on optical characteristics of AlGaAs/GaAsP/AlGaAs nano-heterostructure. *Optik* **181**, 389–397 (2019)
13. Riyaj, M., Vijay, J.P., Khan, A.M., Kattayat, S., Kaya, S., Ayaz Ahmad, M., Kumar, S., Alvi, P.A., Rathi, A.: Band dispersion and optical gain calculations of staggered type GaAs_{0.4}Sb_{0.6}In_{0.7}Ga_{0.3}As/GaAs_{0.4}Sb_{0.6} nano-heterostructure under electric field and [100] strain. *Superlattices Microstruct.* **150**, 106694 (2021)
14. Suresh, S.: *Semiconductor nanomaterials, methods and applications: a review*. *Nanosci. Nanotechnol.* **3**(3), 62–74 (2013)
15. Zhores, I.: Nobel lecture: the double heterostructure concept and its applications in physics, electronics, and technology. *Rev. Mod. Phys.* **73**, 767 (2001)
16. Quarta, A., Piccirillo, C., Mandriota, G., Corato, R.D.: Nanoheterostructures (NHS) and their applications in nanomedicine: focusing on in vivo studies. *Materials (Basel)* **12**(1), 139 (2019)

Chapter 8

Recognition of Facial Expressions Based on Detection of Facial Components and HOG Characteristics



K. A. Anu and N. Ali Akbar

Abstract People were able to convey intentions and feelings through non-verbal languages such as gestures and facial expressions. However, recognizing facial expressions is a very difficult task. Numerous factors such as light, posture, and distortion can cause complications. The proposed system is a good method for facial emotion detection problems. The system, which considers the elements of the face, will help to predict emotions from an image. Then histogram of oriented gradient (HOG) is used to encode these facial elements as features. A linear support vector machine is then used to identify facial expressions. The final results of this experiment show the accuracy of our prediction.

8.1 Introduction

Facial emotions are the process of perceiving human feelings from facial expressions. The human brain automatically recognizes emotions and has now developed software that can detect emotions as well. Facial recognition is attracting more attention because it can be used in many cases to detect lies, medical evaluations, etc. In fact, the generally accepted prediction is that computing will return to the background, weave the fabric of our everyday spaces, and project the individual into the foreground. To achieve this goal, many strategies need to be developed to strengthen emotional psychology. There are two important ways to recognize the shape of a face, based on appearance and geometry. Externally, Gabor filters are described the local binary model for the face. Geometry is considered by the points, and these points can be considered as geometric shapes.

In this paper, we introduce a good strategy-based approach to dealing with facial expression detection problems. Given a face image, the process detects the face first and then, removing the facial components. A histogram-oriented gradient (HOG) is

K. A. Anu (✉) · N. Ali Akbar

Department of Computer Science and Engineering, Government Engineering College, Thrissur, Kerala, India

e-mail: akbar@gectcr.ac.in

then created to encode these components on the face and convert them into a single vector. This function vector is used for linear SVM training.

Our work is similar to the previous work entitled “emotional recognition via facial expressions” [1]. However, there are still differences between our work and the past. Previous work included feature descriptions on whole face, and they examined various features including HOG, LBP, and LTP. This work analyzes facial features and works with HOG to define objects and facial features. Previous work has focused on the problem of facial expression detection and registration errors. Our study paid attention to the facial features that make up the facial feature recognition.

Jang et al. [2] developed a form of face-to-face contact for learning for sensory processing. The dataset used are multi-PIE dataset, CK+ dataset, and audience dataset. The viewer’s attention is focused when he or she focuses on and explores aspects of the facial expression and feeds it online. The network makes decisions about facial features based on features obtained from visual fixations. Pukhrambam et al. [3] introduce support vector machine for recognizing human face expressions. The facial expressions of one person representing a certain type of feeling are not always unique. As a result, facial expressions that represent emotions not only may differ from one person to another but also from one person to another for different conditions of the same effect. Most approaches to recognizing emotional impact should address the problem of face localization, facial expression, and training as well as the conflicting process of the learning process used. The component of the face, i.e., the eye and mouth parts, is removed. After the production is completed, the resulting components are trained. SVM classifier is used to distribute the category of facial expressions.

8.2 Method

8.2.1 Problem Definition

Humans were able to convey intentions and emotions through non-verbal languages like gestures and facial expressions. However, facial expression recognition is a difficult task. Numerous factors like lighting, pose, and deformation could cause to the complexity. So our aim is to build an effective appearance-based system to manage the facial expression recognition problems by using the detection of facial components and HOG features.

8.2.2 Overview of Proposed System

A face recognition technology is a technology that can identify or analyze a person through video sources or digital photographs [4]. There are many ways to make a

face-to-face system work, but they generally work by considering the selected face recognition and images in the database. It is described as an application based on biometric artificial intelligence. It can distinguish a person by examining the process based on the facial features and appearance of the person, although it is primarily a computer application. Recently, there have been many uses of the Internet and other technologies such as robotic technology. It works as a safety access control and security system and can be compared to other biometrics such as fingerprint detection system or iris detection system. It has recently become popular as a tool to identify its identity and market.

System comprises three blocks. The first block is to identify the face then extract the components from face. The next block is to encode the components of face using HOG. The final block is to work on an SVM classifier. Figure 8.1 shows the proposed architecture of the system.

8.2.2.1 Face Perception and Extraction of Facial Components

This section begins by using Viola–Jones to detect the face. Once the face is exposed, scars, eyes, nose, and mouth will be removed. We can first look at the objects and remove the objects depending relative position of those elements. The face-to-face images and databases we use are facial expressions, and we know how many are beyond the eyes. We also have shortcomings so that we can expand the available eye areas.

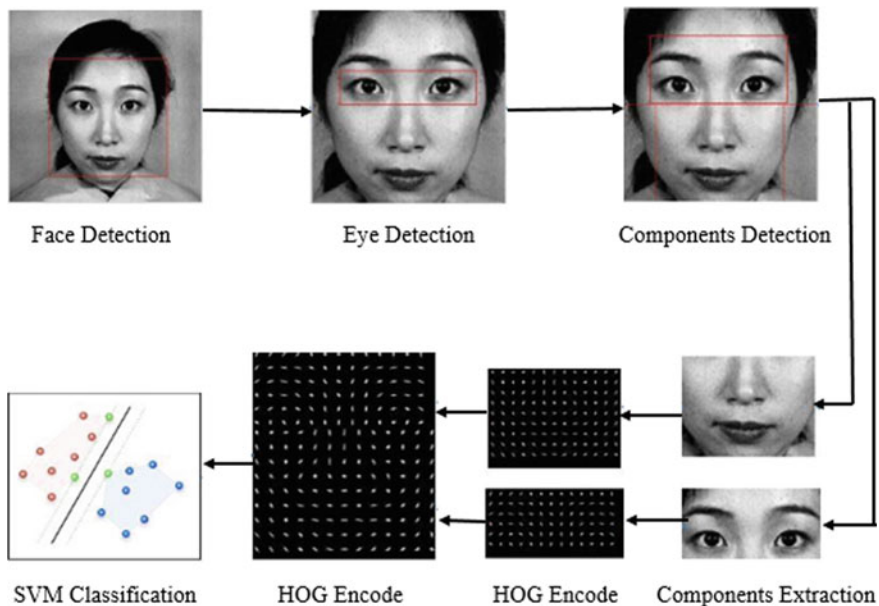


Fig. 8.1 Proposed Architecture

8.2.2.2 HOG—Histogram-Oriented Gradient Feature

Different models are introduced, including SIFT, Gabor filter, local binary patterns (LBP) and HOG. Considering the HOG buildings are at very risk. We encourage you to use the HOG function to fix those facial features. The visual field of computers is well-received and is used in many search applications. The idea is that the dynamics and aggressive nature of the environment can reflect the shape and form of objects.

Compared to other functions such as LBP and Gabor filtering, HOG facial knowledge is very useful. The shape of HOG's essential components forms facial expressions. Therefore, HOG is required to modify these front parts we use. In our experiments, we set the cell size to 8 by 8, the number to 9, and the translation size from 0 to 180.

8.2.2.3 SVM Classifier

Support vector machine (SVM) is widely used in many style detection operations. It is believed that there is a great deal of difference between SVM units. In the study, we train SVMs using the features we proposed to classify facial expressions [5]. In general, SVM builds a hyperplane to identify a large area. The distance between the hyperplane and the training information in any class is huge, and it helps for the ideal distinction. Training is provided with labeled samples:

$$D = \{(X_i, Y_i) | X_i \in R^n, Y_i \in \{-1, 1\}\}_{i=1}^p \quad (8.1)$$

The SVM is used to detect small errors in the samples.

$$w \cdot x - b = 0 \quad (8.2)$$

For the input vector x_i , the classification is obtained by calculating the connection distance between the input vectors. The first SVM is a binary classification. However, we can adopt a unified strategy for multi-class placement. We use LIBSVM in our experiments.

8.3 Experiments and Results

8.3.1 Dataset

The system uses the most commonly used databases: JAFFE and Cohn-Kanade dataset. The JAFFE dataset has 213 images.

There are 10 topics and 7 themes for each topic. Each topic has about twenty pictures, and each expression includes two or three pictures. These seven



Fig. 8.2 Seven expressions from one subject

expressions are anger, joy, disgust, sadness, surprise, fear, and neutral. The second image shows seven details on a single topic. The Cohn-Kanade database contains 123 articles and sequences of 593. Figure 8.2 shows seven expressions from one subject.

8.3.2 Analysis of Results

Table 8.1 shows the performance of our method.

8.3.3 Evaluation Measures

The performance metrics for the evaluation are precision, recall, *F1*-score, and accuracy.

- **Precision** can be calculated by,

$$\text{Precision} = \text{TP} / (\text{TP} + \text{FP})$$

i.e.,

$$\text{Precision} = \frac{\text{No. of images predicted correctly}}{\text{Total no. of images predicted}}$$

- **Recall** can be calculated by,

$$\text{Recall} = \text{TP} / (\text{TP} + \text{FN})$$

Table 8.1 Performance evaluation

Method	Precision	Recall	<i>F1</i> -score
HOG + SVM	0.90	0.88	0.89

i.e.,

$$\text{Recall} = \frac{\text{No. of images predicted correctly}}{\text{Total no. of images}}$$

- **F1-score** can be calculated by,

$$F1 = \frac{\text{Precision} * \text{Recall}}{\text{Precision} + \text{Recall}}$$

- **Accuracy** can be calculated by,

$$\text{Accuracy} = (\text{TP} + \text{TN}) / (\text{TP} + \text{FP} + \text{TN} + \text{FN})$$

Figure 8.3 shows the prediction of percentage of emotion on happy, anger, and disgust images.

```
+ Code + Text
▶ Instructions for updating:
Colocations handled automatically by placer.
2020-06-30 06:23:43.525817: I tensorflow/core/platform/cpu_feature_gu
2020-06-30 06:23:43.528818: I tensorflow/core/platform/profile_utils/c
2020-06-30 06:23:43.529025: I tensorflow/compiler/xla/service/service
2020-06-30 06:23:43.529059: I tensorflow/compiler/xla/service/service
WARNING:tensorflow:From /usr/local/lib/python3.6/dist-packages/tensor:
Instructions for updating:
Use tf.cast instead.

PREDICTING ON HAPPY IMAGE...
anger: 44.1%
calm: 9.5%
happiness: 46.4%

PREDICTING ON DISGUST IMAGE...
anger: 60.5%
calm: 17.5%
happiness: 21.9%

PREDICTING ON ANGER IMAGE...
anger: 49.3%
calm: 3.5%
happiness: 47.1%
```

Fig. 8.3 Percentage of emotion prediction

8.4 Conclusion and Future Work

In this paper, we have suggested an effective way of recognizing facial expressions. First part of the work is face detection and facial component extraction. Instead of using the whole face, first grab and remove the facial features. Facial expressions are movements of the facial muscles, and these movements or subtle changes can be expressed in the form of emotional HOGs. Here used HOG to encode the facial components. Coded functions are used to train linear SVMs. By the help of SVM, we can easily classify the facial expressions. The results of the experiment of the two databases, JAFFE and Cohn-Kanade extended datasets, show that the proposed method can achieve optimal performance. Understanding of facial expression recognition is a very difficult matter. Necessary efforts should be made to improve the level of implementation. Our future work will focus on developing more performance in the wild environment with more subtle expressions like “contempt.”

References

1. Kwong, J.C.T., Felan Carlo, C., Garcia, P.A., Abu, R., Reyes, R.S.J.: Emotion recognition via facial expression: utilization of numerous feature descriptors in different machine learning algorithms. In: TENCON 2018–2018 IEEE Region 10 Conference, pp. 2045–2049. IEEE (2018)
2. Jang, J., Cho, H., Kim, J., Lee, J., Yang, S.: Facial attribute recognition by recurrent learning with visual fixation. *IEEE Transactions on Cybernetics*, vol. 49, no. 2, pp. 616–625 (2018)
3. Pukhrambam, M., Das, A., Saha, A.: Facial components extraction and expression recognition in static images. In: 2015 International Conference on Green Computing and Internet of Things (ICGCIoT), pp. 726–731. IEEE (2015)
4. Salunke, V.V., Patil, C.G.: A new approach for automatic face emotion recognition and classification based on deep networks. In: 2017 International Conference on Computing, Communication, Control and Automation (ICCUBEA), pp. 1–5. IEEE (2017)
5. Xie, S., Hu, H.: Facial expression recognition using hierarchical features with deep comprehensive multipatches aggregation convolutional neural networks. *IEEE Transactions on Multimedia*, vol. 21, no. 1, pp. 211–220 (2018)

Chapter 9

Optimization of Pneumatic Extrusion Machining Method Process Parameters on Polycaprolactone (PCL) Material



O. Y. Venkata Subba Reddy, A. N. R. Reddy, and V. Venkatesh

Abstract Polycaprolactone (PCL) is an auspicious material for bone repair and bone replacement due to similar naturally occurring inorganic components. In this work, the polycaprolactone (PCL) scaffolds are manufactured using pneumatic extrusion method and scanning electron microscopy (SEM) images of the manufactured scaffolds can be produced to display the interior of the scaffold struts and the profile of in vitro release can be done to reveal the biocompatibility of the scaffolds. In order to confirm the performance of the manufactured composite scaffolds for the required strength of bone loadbearing regions, the UTM tests are carried out, and after this, the Taguchi optimization technique was applied to the numerical data derived from the experiments with the concept of the L9 orthogonal array. From this, it was determined that 40% porosity scaffold, 30 and 90 filament angle, 0.5 mm nozzle diameter is a sophisticated design compatible with the structure and function of the natural bone trabecular part. Taken together these results show that PCL scaffolds can be manufactured easily using 3D printing technology and can be a possible solution as implantable material for bone tissue engineering application.

9.1 Introduction

Biomedical engineering (BME) will interface advanced engineering technological into medical sciences in treatment and diagnosis. BME will be used in engineering design application, concepts, and principle into the medical and biological fields in therapeutics and diagnostics. It directs to solve engineering and medical diagnostics issues. BME is one of the interdisciplinary approaches. This progression leads to

O. Y. Venkata Subba Reddy (✉) · A. N. R. Reddy
Mechanical Engineering, MRCET, Hyderabad 500010, India
e-mail: oyvsreddy@mrcet.ac.in

V. Venkatesh
Mechanical Engineering, AITS, Rajampet 516126, India

© The Author(s), under exclusive license to Springer Nature Singapore Pte Ltd. 2022
A. N. R. Reddy et al. (eds.), *Intelligent Manufacturing and Energy Sustainability*,
Smart Innovation, Systems and Technologies 265,
https://doi.org/10.1007/978-981-16-6482-3_9

the enlargement of biocompatible prostheses. This is possible to accomplish by using advanced technology called as bioprinting. Bioprinting is an advanced technology where biological matter will be produced by using biomaterials, cells, etc., in a layer-by-layer process [1].

Human being contains lot of natural bone tissues which is in complex with precise structures. The ideal bone tissue engineering scaffold design requires the implants structures to conform to the anatomical structure of natural bone tissues [2, 3]. Meanwhile, it also requires good biological compatibility, bone tissue integration ability, and good bone-bonding ability and suitable mechanical property [4]. In order to meet the needs of new bone tissue ingrowth, bone tissue engineering scaffold must be designed with mutual penetration of porous structure [5–11]. Three-dimensional porous structures are benefit for cells adhesion, migration, and proliferation and provide the necessary living space, providing transmission channels for nutrients, metabolism, and metabolic products [10, 11]. A large number of studies have shown that the ideal macropore size of a scaffold composed of bone tissue is about 300–900 μm , and the porosity is between 60 and 95% [12–16]. A major problem in the manufacture of bone tissue scaffolds is that traditional porous scaffold manufacturing methods [17], such as foaming (chemical foaming and physical foaming), particle leaching, and electrostatic spinning, cannot accurately reach the pores in most cases rate [18, 19].

Three-dimensional printing or rapid prototyping is also known as additive manufacturing (AM). It is a class of technology which construct the physical complex objects directly from computer-aided design model by reducing the material wastage where the printing is going to be done by adding materials layer by layer in order to get the original shape. Many researchers worked on SLS, FDM, SLA, LOM.

To achieve compressive strength as that to biological bone, swelling and degradation rate, narrow pore size distribution of interconnectivity pores within, polymers are chosen in bone tissue engineering. Polycaprolactone (PCL) is found to be an effective composite scaffold in the applications of bone grafting.

In this work, polycaprolactone-based scaffolds are manufactured with different porosity and nozzle diameter using 3DP pneumatic extrusion technique to mimic in different composition variations and pore morphology in trabecular bone regions. The printed scaffolds are subjected to uniaxial compression to determine the relationship of the porosity of the scaffold, the nozzle diameter and the compressive module, and the yield stress. This study is focused specifically on the following considerations:

- Demonstrating the feasibility of integrating porosity into 3DP polymer scaffolds;
- Identifying the relationship between design criteria for uniform scaffolds (porosity, nozzle diameter) and mechanical properties (yield stress, compressive modulus);

- Investigation on the effects of incorporation of porosity gradients of the compressive properties of scaffolds;
- Analysis of compressive properties in porosity gradient of scaffolds designed to replicate the anatomy of trabecular bones.

Additionally, improvements in porosity and strain were measured after recovery of scaffold. Those findings were later adapted for different gradients of porosity and nozzle diameter to suit the strength of trabecular bone region of 3–30 MPa.

9.2 Experimentation

Pneumatic extrusion is an advanced technique to extract melted polymer or polymer composite at constant temperature. The amount of pneumatic energy will be regulated by pressure regulator. This attachment was connected to a 3-axis system which will be controlled by a Ramps1.4 shield with Arduino Mega 2560. Required *G* and *M* codes were written to get precise control over linear motion and extrusion process. Temperature-controlled heater was controlled with instruction written in *G* and *M* codes.

9.3 Methodology

In this, pneumatic extrusion/micro-syringe method was employed to manufacture scaffolds of polycaprolactone (PCL) to fabricate nine 3D cylindrical scaffolds of dimensions 15 mm diameter, 10 mm height as per the Taguchi design of experiments of L9 orthogonal array.

9.3.1 Process Parameters

- **NOZZLE DIAMETER**

The diameter of the nozzle of the extrusion chamber can be varied to vary the diameter of the filament being extruded. Nozzle diameter/filament nozzle has a profound effect on the mechanical properties of the scaffolds. The different nozzle diameters selected are as follows: 0.3 mm, 0.4 mm, 0.5 mm. A point worth notifying is that, the nozzle diameter and the filament diameter cannot be the same as many factors affect this parameter. Some of them being pull of the gravity causing the filament to compress under its own weight, velocity of filament being extruded.

- **POROSITY**

Porosity is nothing but the percentage of empty space within the scaffold fabricated. As the scaffolds need to maintain certain interconnected porosity to allow the cell proliferation and flow of the body fluids through these pores causing the cells to adhere themselves to the walls of the scaffolds. Even with the variation in the pore size, the cell proliferation rate varies and the controls the osteoblastic or the osteoclastic process to be carried out. A flexibility is available with the software utilized to generate the scaffolds that it itself varies or adjusts the porosity as per the demand. So, here three porosity levels were selected to study the scaffolds for its mechanical properties. The porosity levels are as follows: 40, 50, and 60%.

- **LAYER ANGLE OF THE FILAMENTS**

Angle of the filament can be varied that way these filaments are arranged in a scaffold can vary from layer to layer. For instance, if the selected pair of angles are $(0^\circ, 90^\circ)$, then the first layer has its filaments maintained at 90° with the filaments of the second layer. Some of the pairs of the angles are $(0^\circ, 90^\circ)$, $(30^\circ, 90^\circ)$, and $(60^\circ, 90^\circ)$ (Fig. 9.1).

- **LAYER HEIGHT**

It is the distance from the base or surface to the point of extrusion of the scaffold filament, and here it is maintained constant. Some of the other parameters that are maintained constant are extrusion velocity, room temperature at which these scaffolds are extruded.

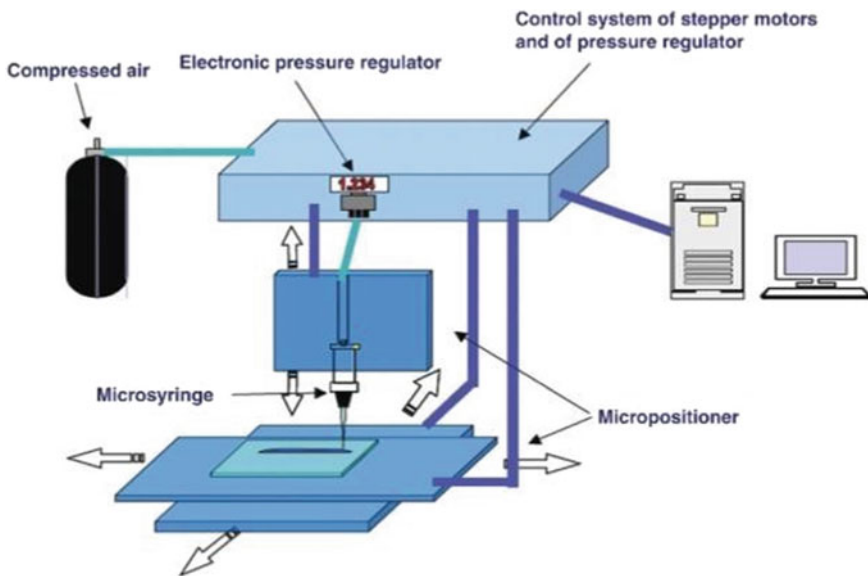


Fig. 9.1 Schematic elucidating the micro-syringe method

9.3.2 Design of Experiments

Design of experiments (DoE) techniques enable designers to determine the factors that affect individually and interactively that show impact on the output of the design. It also provides a deep insight of interaction in between design elements. In this study, Taguchi method is used in order to generate the orthogonal array experiments. It provides minimum experiments for optimizing the experimental results. Signal-to-noise ratios are logarithmic functions of desired output, serve as objective functions in optimization, and also help in data analysis and prediction of optimum results (Tables 9.1 and 9.2).

The above experimental plan was taken for the fabrication of the scaffolds in order to minimize the number of experiments and to have good results. These scaffolds were fabricated by 3D printing technique called pneumatic extrusion method/extrusion by micro-syringe.

9.3.3 Tests Done Over the Scaffolds

All these scaffolds were tested for SEM and UTM tests. The SEM tests were done at the Yogi Vemana University, Kadapa. From the SEM tests, it was to make it clear about the composition of the scaffolds; that is, they were of polycaprolactone

Table 9.1 Machining process parameters with levels

S. no.	Process parameter	Levels		
		Level 1	Level 2	Level 3
1	Porosity(%)	40	50	60
2	Angle of filament layer	0	30	60
3	Nozzle diameter	0.3	0.4	0.5

Table 9.2 Experimental plan

S. no.	Porosity (%)	Angle of filament layer	Nozzle diameter
1	40	0	0.3
2	50	30	0.4
3	60	60	0.5
4	40	30	0.5
5	50	60	0.3
6	60	0	0.4
7	40	60	0.4
8	50	0	0.5
9	60	30	0.3

(PCL). Later, the SEM analysis was done to collect the microstructural images of the scaffolds. Later these scaffolds were tested for the mechanical strength for compressive strength under a UTM machine at VIT, Vellore. The capacity of the machine was 5kN.

9.4 Optimization of Results

Later these results of compressive strength obtained from UTM tests were optimized by using Taguchi’s optimization techniques. The strength of trabecular bone area region was compared with the scaffold compressive strength (Fig. 9.2; Table 9.3).

$$\text{Yield Strength(YS)} = 514.3 - (1600 * P) - (1.100 * A) - (557 * d) + (1567 * (P * P)) - (0.00593 * (A * A)) + (733 * (d * d)) + (3.444 * P*)$$

In the above work, Taguchi optimization techniques were used with the combination of independent parameters like porosity of 60%, printing angle of 60°/90°, and nozzle diameter if 0.5 mm. After completion of scaffold development by using UTM compressive strength was measured for all the samples. Scaffold with 40% porosity, printing angle 0/90°, and 0.3 mm nozzle diameter has least compressive strength. Similarly, scaffold with 50% porosity, 30°/90° printing angle, and 0.4 mm nozzle diameter has optimal compressive strength. Scaffold-04 with 40% porosity, 30°/90° printing angle, and nozzle diameter 0.5 mm is compatible with trabecular bone (Fig. 9.3).

Fig. 9.2 SEM image of the developed scaffold

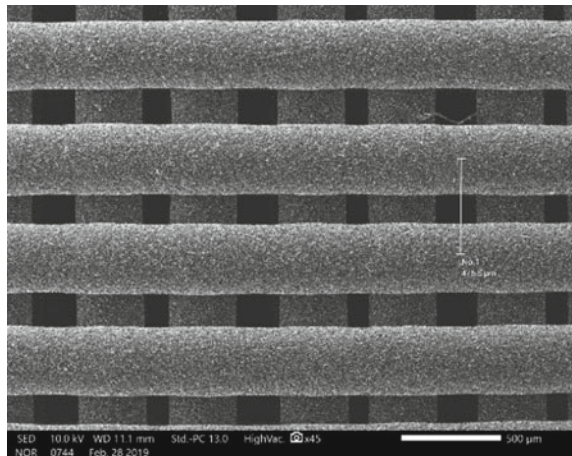


Table 9.3 Optimum results

Level	Porosity (%)	Angle of filament (°)	Nozzle diameter (mm)
1	24	16	28.67
2	15.33	29.33	14
3	38	32	34.67
Delta	22.67	16	20.67
Rank	1	3	2

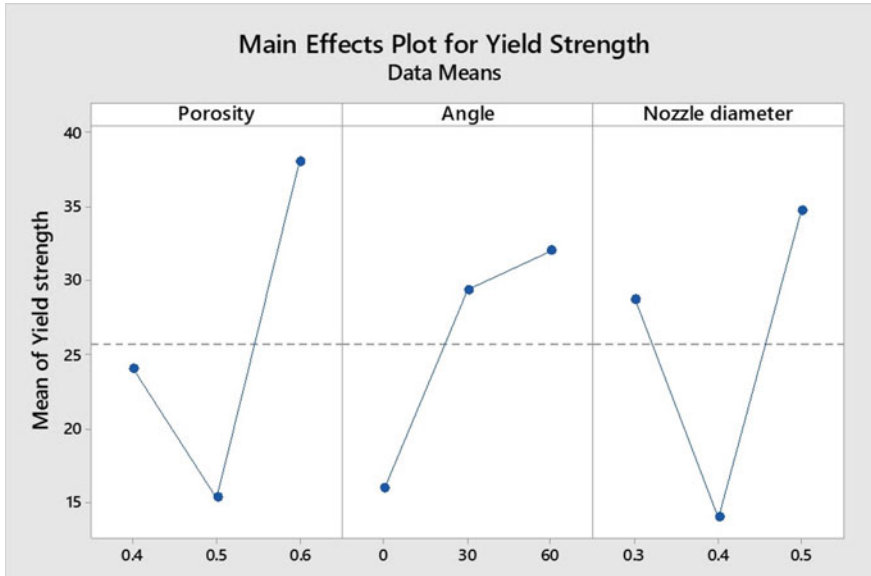


Fig. 9.3 Main effects plot for means

9.5 Conclusion

In this work, bone scaffold was fabricated by using extrusion method with PCL material, which is a bioactive material. In the process of scaffold development, temperature and pressure were precisely controlled with temperature controller and digital pressure regulator. Later the compressive strength test of bone scaffold performed on universal testing machine and analyzed the results. The results are obtained in the form of stress–strain relationship for the scaffold material, and yield strengths of these scaffolds were compared with the compressive strength of the trabecular bone areas of the body. This is an optimization study that compares the compressive strengths of the bone scaffolds and the trabecular bone regions.

According to the results of this study, the scaffold sample 4 with 40% porosity, 30°, 90° column angles of struts, and 0.5 mm nozzle diameter proved to be the best-optimized scaffold for the trabecular bone regions for bone tissue engineering applications.

References

- Guillemot, F., Mironov, V., Nakamura, M.: Bioprinting is coming of age: report from the international conference on bioprinting and biofabrication in Bordeaux (3B'09). *Biofabrication* **2**(1) (2010). <https://doi.org/10.1088/1758-5082/2/1/010201>
- Mironov, V., Boland, T., Trusk, T., Forgacs, G., Markwald, R.R.: Organ printing: computer-aided jet-based 3D tissue engineering. *Trends Biotechnol.* **21**(4), 157–161 (2003). [https://doi.org/10.1016/S0167-7799\(03\)00033-7](https://doi.org/10.1016/S0167-7799(03)00033-7)
- Murphy, S.V., Atala, A.: 3D bioprinting of tissues and organs. *Nat. Biotechnol.* **32**(8), 773–785 (2014). <https://doi.org/10.1038/nbt.2958>
- Abeykoon, C., Martin, P.J., Kelly, A.L., Brown, E.C.: A review and evaluation of melt temperature sensors for polymer extrusion. *Sensors Actuators A Phys.* **182**, 16–27 (2012). <https://doi.org/10.1016/j.sna.2012.04.026>
- Zein, D., Hutmacher, W., Tan, K.C., Teoh, S.H.: Fused deposition modeling of novel scaffold architectures for tissue engineering applications. *Biomaterials* **23**(4), 1169–1185 (2002). [https://doi.org/10.1016/S0142-9612\(01\)00232-0](https://doi.org/10.1016/S0142-9612(01)00232-0)
- Lin, C.Y., Kikuchi, N., Hollister, S.J.: A novel method for biomaterial scaffold internal architecture design to match bone elastic properties with desired porosity. *J. Biomech.* **37**(5), 623–636 (2004). <https://doi.org/10.1016/j.jbiomech.2003.09.029>
- Schek, R.M., Wilke, E.N., Hollister, S.J., Krebsbach, P.H.: Combined use of designed scaffolds and adenoviral gene therapy for skeletal tissue engineering. *Biomaterials* **27**(7), 1160–1166 (2006). <https://doi.org/10.1016/j.biomaterials.2005.07.029>
- Pfister, R.L., Laib, A., Hübner, U., Schmelzeisen, R., Mülhaupt, R.: Biofunctional rapid prototyping for tissue-engineering applications: 3D bioplotting versus 3D printing. *J. Polym. Sci. Part A Polym. Chem.* **42**(3), 624–638 (2004). <https://doi.org/10.1002/pola.10807>
- Khalil, S., Nam, J., Sun, W.: Multi-nozzle deposition for construction of 3D biopolymer tissue scaffolds. *Rapid Prototyp. J.* **11**(1), 9–17 (2005). <https://doi.org/10.1108/13552540510573347>
- Khalil, S., Sun, W.: Biopolymer deposition for freeform fabrication of hydrogel tissue constructs. *Mater. Sci. Eng. C* **27**(3), 469–478 (2007). <https://doi.org/10.1016/j.msec.2006.05.023>
- Elloumi-Hannachi, M., Yamato, Okano, T.: Cell sheet engineering: a unique nanotechnology for scaffold-free tissue reconstruction with clinical applications in regenerative medicine. *J. Intern. Med.* **267**(1), 54–70 (2010). <https://doi.org/10.1111/j.1365-2796.2009.02185.x>
- Jakab, K., Neagu, A., Mironov, V., Markwald, R.R., Forgacs, G.: Engineering biological structures of prescribed shaped using self-assembling multicellular systems. *Proc. Natl. Acad. Sci. U. S. A.* **101**(9), 2864–2869 (2004). <https://doi.org/10.1073/pnas.0400164101>
- Mironov, V., Viscontini, R.P., Kasyanov, V., Forgacs, G., Drake, C.J., Markwald, R.R.: Organ printing: Tissue spheroids as building blocks. *Biomaterials* **30**(12), 2164–2174 (2009). <https://doi.org/10.1016/j.biomaterials.2008.12.084>
- Norotte, C., Marga, F.S., Niklason, L.E., Forgacs, G.: Scaffold-free vascular tissue engineering using bioprinting. *Biomaterials* **30**(30), 5910–5917 (2009). <https://doi.org/10.1016/j.biomaterials.2009.06.034>
- Ozbolat, T., Hospodiuk, M.: Current advances and future perspectives in extrusion-based bioprinting. *Biomaterials* **76**, 321–343 (2016). <https://doi.org/10.1016/j.biomaterials.2015.10.076>

16. Horvath, L., Umehara, Y., Jud, C., Blank, F., Petri-Fink, A., Rothen-Rutishauser, B.: Engineering an in vitro air-blood barrier by 3D bioprinting. *Sci. Rep.* **5** (2015). <https://doi.org/10.1038/srep07974>
17. Almeida, C.R., Serra, T., Oliveira, M.I., Planell, J.A., Barbosa, M.A., Navarro, M.: Impact of 3-D printed PLA- and chitosan-based scaffolds on human monocyte/macrophage responses: unraveling the effect of 3-D structures on inflammation. *Acta Biomater.* **10**(2), 613–622 (2014). <https://doi.org/10.1016/j.actbio.2013.10.035>
18. Bertassoni, L.E., et al.: Direct-write bioprinting of cell-laden methacrylated gelatin hydrogels. *Biofabrication* **6**(2) (2014). <https://doi.org/10.1088/1758-5082/6/2/024105>
19. Ehsan, S.M., Welch-Reardon, K.M., Waterman, M.L., Hughes, C.C.W., George, S.C.: A three-dimensional in vitro model of tumor cell intravasation. *Integr. Biol. (United Kingdom)* **6** (6), 603–610 (2014). <https://doi.org/10.1039/c3ib40170g>

Chapter 10

A Comparison of Mixing and Displacement Ventilation System in an Office Environment Using Computational Fluid Dynamics



Mohammed Abdul Hameed Khan, Chanfiou Ahmed Mboreha,
and Hazem Abdelrahman

Abstract An indoor space resembling a 4-occupant office room was modeled to evaluate the airflow characteristics of the Mixing and Displacement Ventilation system under different air supply rates. The room was created with box-shaped occupants seated in front of the table. The occupants along with the PCs placed on the table served as the heat sources in the domain. The supply airflow rate considered for the study was 6, 9, and 12 ACH. Three-dimensional CFD simulations were performed using the Fluent Solver. The airflow pattern, air velocity distribution, and temperature distribution showcased that the obtained flow-field is a strong function of the ventilation strategy being implied in the room. For identical air supply rates, the displacement ventilation system showcased a cooler sensation to the occupant.

10.1 Introduction

A ventilation system incorporated in a building is responsible for human comfort. An effective ventilation system improves the state of wellbeing, on the other hand, an ineffective ventilation system can be detrimental to human health. The location of the inlet, outlet, amount of air supplied, air-velocity, temperature, humidity, number of occupants in the room, furniture, etc., influences the thermal comfort.

M. A. H. Khan (✉)

Aurora's Scientific and Technological Institute, Hyderabad, India
e-mail: aehod@asti.edu.in

C. A. Mboreha

Key Laboratory of Aircraft Environment Control and Life Support, MIIT,
Department of Aeronautical Engineering, Nanjing University of Aeronautics
and Astronautics, Nanjing City, China

H. Abdelrahman

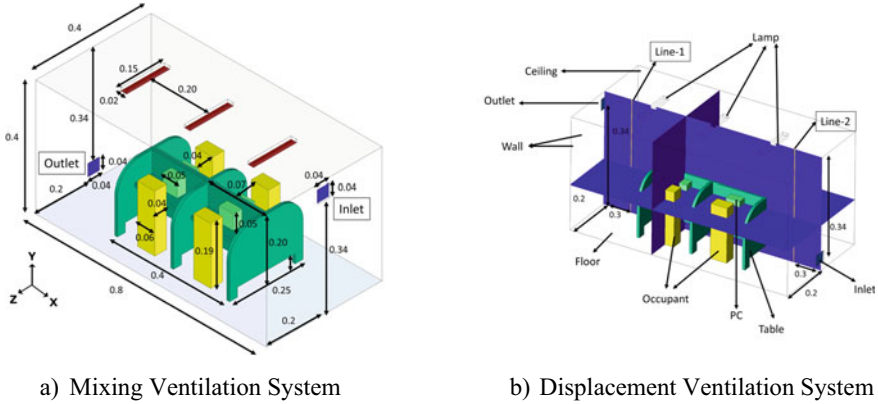
Faculty of Engineering, Ain Shams University, Cairo, Egypt

The most common type of ventilation systems used in indoor spaces is “mixing ventilation system” and “displacement ventilation system.” Both of these ventilation systems have their own merits and demerits. The mixing ventilation system supplies air at high velocity into the room from the inlet situated close to the ceiling. The fresh air mixes with the air present in the room and exits from the outlet located near the floor [1]. The displacement ventilation system supplies fresh air from the inlet located near the floor. This fresh air displaces the existing room air, encounters heat sources, and rises upward in the room [2, 3]. Numerous studies (experimental and numerical) reported the comparison of the mixing and displacement ventilation system. The studies investigated the thermal comfort, indoor air quality in offices, classroom, retail shops, industrial workshop, space capsules, tutorial rooms [4–7], effects of the cooling ceiling in a ventilated room [8], air quality in single-person patient ward [9], air-quality and air conditioning performance in a partitioned room [10], and removal effectiveness during vacuuming session [11]. To the author’s best knowledge, previous studies demonstrated the two ventilation systems (mixing and displacement) airflow characteristics with fixed boundary conditions in larger room sizes. The present study numerically investigates the airflow characteristics in a scaled-office room equipped with the two most commonly used air-diffusion systems (mixing and displacement) functioning at different ACH (air change hour). A validated CFD code will be employed to analyze the airflow pattern in the room, evaluate air velocity and temperature at different levels of the room.

10.2 Geometry Description

The model of the office room used for the investigation is illustrated in Fig. 10.1. A four seat-table is placed in the center region of the room. According to Topp et al. [12], a box-shaped mannequin representing an occupant is sufficient for studying the global air flow of the room. Therefore, four box-shaped mannequins are placed near the table. Seats are not created in the model, the box-shaped mannequin represented an occupant seated at their respective desk. To replicate an office scenario, a personal computer (PC) is placed on the desk for the occupant to perform the office job. Three lamps are mounted on the ceiling to illuminate the room.

Two CAD models of the office room are created using Creo Parametric software. The first model is incorporated with the mixing ventilation system, and the second model is incorporated with the displacement ventilation system. Figure 10.1a illustrates the dimensions used for modeling the office room. The length, breadth, and height of the room are based on Chen et al.’s experimental study [13]. In the experimental study, the authors used an empty room for their investigation. For the present research, the room is created with “furniture” and “occupants” to depict an office environment. Figure 10.1a represents the office room with a “mixing ventilation system,” and Fig. 10.1b represents the office room with a “displacement ventilation system”. The difference between the two models is the placement of the inlet and outlet, and the rest of the dimensions is identical.



a) Mixing Ventilation System

b) Displacement Ventilation System

Fig. 10.1 Room model with mixing and displacement ventilation system

10.3 Numerical Scheme

The CFD solver ANSYS Fluent is employed to investigate the flow characteristics. This solver works on the principle of the “Finite Volume Method,” a discretization technique well-suited for numerical experiments in several engineering fields [14]. The presence of low-speed incompressible flow in the computational domain required the utilization of a pressure-based coupled algorithm [15] to solve the governing equations. The coupled algorithm solves the momentum and pressure-based continuity equations simultaneously. The airflow in the indoor environment is driven by two major factors, one is the air-diffusion system, and the second is the buoyancy. In buoyancy-driven flow, the heat sources in the room vary the density of air (lighter air moving upward and heavier air moving down); therefore, the flow is induced due to the gravity force acting on these density variations. To model the buoyancy characteristics, a gravity force of 9.81 m/s is included in the numerical scheme. Incompressible ideal gas law is adapted to compute the density of air in the domain using the following equation:

$$\rho = \frac{P_{op}}{\frac{R}{M_w} T} \quad (10.1)$$

where R is the universal gas constant, M_w is the molecular weight of the gas, P_{op} is the operating pressure and T is the temperature. The pressure at the middle height of the domain is considered to be the operating pressure [16]. The energy and species transport equations are used to quantify the temperature and humidity in the room. For spatial discretization, the second-order upwind scheme was adapted for the momentum, turbulence, and energy equations. The pressure values were interpolated using the Pressure Staggering Option scheme (PRESTO!). The convergence was satisfied when the residuals reached below 10^{-4} and the average velocity in the breathing zone was constant with the iterations.

The realizable k - ϵ model proposed by Shih et al. [17] is used for turbulence modeling [18]. The transport equations for k and ϵ in the steady-state form are:

$$\frac{\partial}{\partial x_j} (\rho k u_j) = \frac{\partial}{\partial x_j} \left[\left(\mu + \frac{\mu_t}{\sigma_k} \right) \frac{\partial k}{\partial x_j} \right] + G_k + G_b - \rho \epsilon - Y_M + S_k \quad (10.2)$$

And

$$\begin{aligned} \frac{\partial}{\partial x_j} (\rho \epsilon u_j) = \frac{\partial}{\partial x_j} \left[\left(\mu + \frac{\mu_t}{\sigma_\epsilon} \right) \frac{\partial \epsilon}{\partial x_j} \right] + \rho C_1 S \epsilon - \rho C_2 \frac{\epsilon^2}{k + \sqrt{\nu \epsilon}} \\ + C_{1\epsilon} \frac{\epsilon}{k} C_{3\epsilon} G_b + S_\epsilon \end{aligned} \quad (10.3)$$

where

$$C_1 = \max \left[0.43, \frac{\eta}{\eta + 5} \right], \quad \eta = S \frac{k}{\epsilon}, \quad S = \sqrt{2 S_{ij} S_{ij}}$$

In the above equations, G_k represents the generation of turbulent kinetic energy due to mean velocity gradients, G_b represents the generation of turbulent kinetic energy due to buoyancy, Y_m represents fluctuating dilatation in compressible turbulence to the overall dissipation rate. C_2 and $C_{1\epsilon}$ are constants. σ_k and σ_ϵ are the Prandtl numbers for k and ϵ , respectively. S_k and S_ϵ are user-defined source terms.

10.4 CFD Validation

The experimental study performed by Chen et al. [13] was considered to demonstrate the accuracy of the numerical scheme. Air at a velocity of 0.225 m/s (corresponding to 10 ACH) was supplied in the room. The supplied air exited from the outlet located on the wall near the floor. During this journey, the x -velocity of air was measured at three locations along with the height of the room. Detailed dimensions of the room and the location of the poles used to measure the velocity can be found in [13]. Figure 10.2 illustrates that CFD obtained results are consistent with the reported experimental results. Therefore, the numerical scheme has demonstrated accuracy and is valid to be used for the consequent simulations.

10.5 Boundary Conditions and Grid Independence Study

The boundary conditions are presented in Table 10.1. The supply velocity (m/s) varied with the amount of air supplied in the room. The supplied temperature is constant for both the ventilation systems.

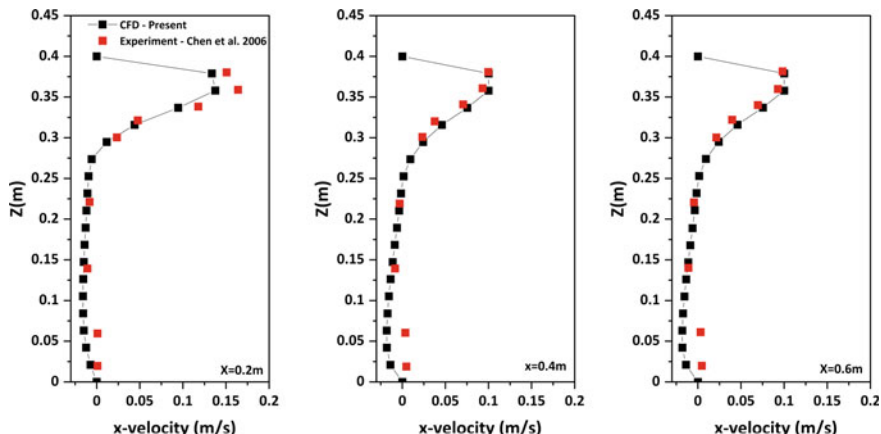


Fig. 10.2 Comparison of present-CFD and experimental x-velocity

Table 10.1 Boundary condition

Boundary type (Velocity inlet)	Value		
Air change hour	6	9	12
Supply air velocity (m/s)	0.13	0.2	0.27
Supply air temperature (K)	292.65		
Boundary type (Outflow)	Value		
Exhaust outlet	Outflow boundary		
Boundary type (Wall)	Value		
Ceiling (K)			300
Floor (K)			300
Lamp (K)			319.15
Occupant (K)			303.45
PC (K)			313.15
Wall (K)			297.15
Table (K)			Adiabatic wall

A three-dimensional unstructured grid discretized the fluid domain into tetrahedral elements. The advanced size functions; Proximity and Curvature, were used to capture refined grid near the wall boundaries, curved regions, and small features of the geometry. The tetrahedral cells were converted into polyhedral cells in the ANSYS Fluent. The polyhedral cells are less sensitive with improved grid quality and offer numerical stability with a reduction in the computational time required for convergence [19]. The generated grid corresponds to a Y^+ value of less than 5 at all the wall boundaries of the domain. Therefore, enhanced wall treatment is utilized to resolve the boundary layer.

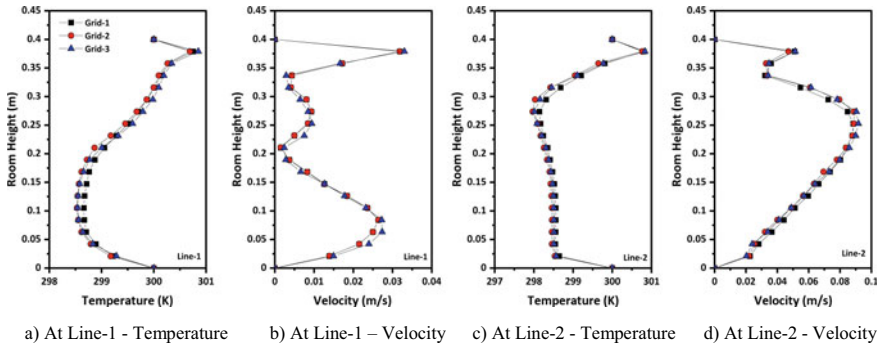


Fig. 10.3 Effect of grid-refinement on the temperature and velocity

Three grid sizes of 0.7, 0.8, and 1 million cells are tested to evaluate the variation of velocity and temperature in the room with a mixing ventilation system supplying air at 6ACH. The velocity and temperature are measured at two lines along with the height of the room. Figure 10.1b shows the position of Line-1 and Line-2. Figure 10.3 illustrates the effect of grid-refinement on the velocity and temperature distribution, for the three grid sizes. The flow variables differ minutely with grid refinement. Due to this insignificant difference in the flow parameters, Grid-2 is considered for the subsequent simulations.

10.6 Results and Discussion

Figures in this section depict the global airflow movement in the office environment with the help of CFD obtained velocity vectors on the cut-section planes illustrated in Fig. 10.1b. The black-colored arrows on the vector graphic illustrate the direction of the air velocity vectors. The airflow movement in all three cases (ACH 6, 9, 12) is identical, the major difference is in the distance of the throw of supplied air. The supply air jet in ACH-12 (due to high velocity) travels further in comparison with ACH-6 and 9. Therefore, the velocity vectors of ACH-12 are used to illustrate the airflow movement in the office room.

Figure 10.4 illustrates the airflow pattern on the cut-section plane $Z = 0$ m. The **mixing ventilation system** (Fig. 10.4a) supplies air from the inlet near the ceiling. Due to buoyancy, the jet flow (cool-air) moves in a downward direction to impact the table. In this process, occupant-1 and occupant-3 face a high risk of the draft. The thermal plume of occupant-1 and 3 moves up to reattach with the oncoming supply jet. The thermal plume of occupant-2 and 4 moves to the ceiling, impinges the wall to travel downwards, and exits from the outlet. In the **displacement ventilation system** (Fig. 10.4b), the supplied air travel along the floor surface, to impinge occupant 1 and 3, followed by occupant 2 and 4. The temperature of the air

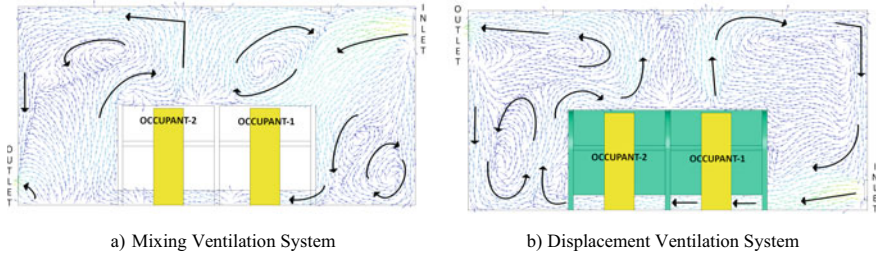


Fig. 10.4 Velocity vector on cut-section plane $Z = 0$ m

gets reduced due to its interaction with the occupant body (ankle). Therefore, the air after crossing occupant-2 and 4 rises upward with the occupant's thermal plumes, reaches the ceiling, and exits from the outlet. The thermal plume of occupant-1 and 3 impinges the ceiling and directs to the right-side walls, and latter moves down to reattach the inlet air.

Plane $X = -0.1$ m (Fig. 10.5) shows that the thermal plumes of the occupant impinge the ceiling and travel downward along the surface of the wall behind the occupants. Therefore, the air behind the occupants forms a circulation zone. The air in the circulation region becomes older and may have a high concentration of contaminants. Both the ventilation systems (mixing—Fig. 10.5a and displacement—Fig. 10.5b), showcased an identical airflow pattern; however, in the displacement ventilation system, there exists a circulation zone below the table. This is because the supplied air rises upwards with the occupant thermal plume and impacts the surface of the table to circulate.

The airflow pattern in the occupant breathing zone is illustrated in Fig. 10.6. In **the mixing ventilation system** (Fig. 10.6a), the desk of occupant 1 and 3 have fresh air supplied from the inlet. A certain quantity of fresh air impacts the table and divides it into two identical paths. The first path is behind occupant 1 and 2. The second path is behind occupant 3 and 4. The air surpasses occupant-1 and 3 to enter the desk region of occupant 2 and 4, respectively. The thermal plumes from the floor raise upward and reach the desk of occupant-2 and 4. Therefore, the air near occupant-2 and 4 is mixed with the incoming fresh air (from the right) and the thermal plumes (from the left). Due to this, the air in this region loses its freshness. This indicates that the occupants seated farther from the inlet location are prone to unrefresh and contaminated air. In **the displacement ventilation system** (Fig. 10.6b), the air is supplied at the occupant ankle level ($Y = 0.01$ m). Therefore, the cut-section ($Y = 0.16$ m) represents the air that traveled upward either due to its interaction with the obstacles (table) or due to buoyancy (with the thermal plume). The vector plot reveals that the air impacts the table and redirects to enter the zone of occupant 1 and 2. Because of its lesser travel time, this air (near occupant 1 and 2) is free from contaminants and may be considered as fresh air. Plane $Z = 0$ m (Fig. 10.4b) revealed that the supplied air travels along the floor surface, crosses the occupant 2 and 4, and rises upward to enter into the occupant-2 and 4 desks regions.

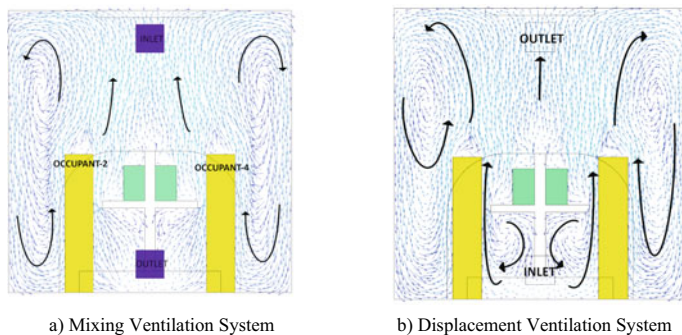


Fig. 10.5 Velocity vector on cut-section plane $X = -0.1$ m

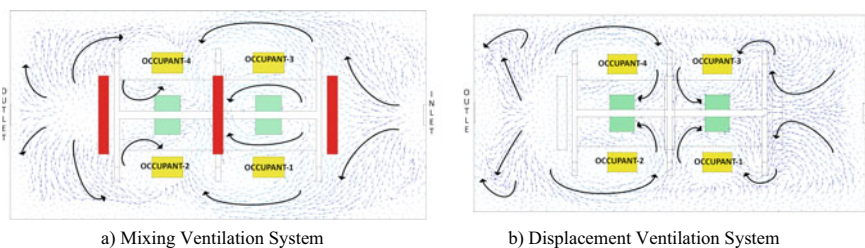


Fig. 10.6 Velocity vector on the cut-section plane $Y = 0.16$ m

In addition to this, the plane $Y = 0.16$ (Fig. 10.6b) reveals that the rising air flows in the space behind the occupant 2 and 4. This flow pattern indicates that the air in the vicinity of occupant-2 and 4 is unfresh and may possess a high-contaminant concentration.

Figure 10.7 illustrates the average velocity at different levels of the occupant body (Ankle-0.01 m, Knee-0.05 m, Stomach-0.1 m, Breathing-0.16 m, and Occupant standing position-0.21 m). For ACH-6, the mixing ventilation system showcases a high air velocity from the ankle to the occupant standing position. For ACH-9 and 12, the mixing ventilation system showcases high-air velocity from the knee to the occupant standing position. The displacement ventilation system showcases, a high-air velocity at the ankle level (for ACH-9 and 12), and at the rest of the levels, the displacement ventilation system possesses lower air velocity in comparison with the mixing ventilation system. Figure 10.8 illustrates the average temperature on the different occupant body levels. At ACH-6, 9, and 12, the displacement ventilation system demonstrates low temperature in all the occupant levels. However, at the standing position, the temperature of the mixing ventilation (at ACH 9 and 12) is slightly lower than that of the displacement ventilation system. Furthermore, the occupants in the displacement ventilation system will show dissatisfaction in the ankle and knee levels.

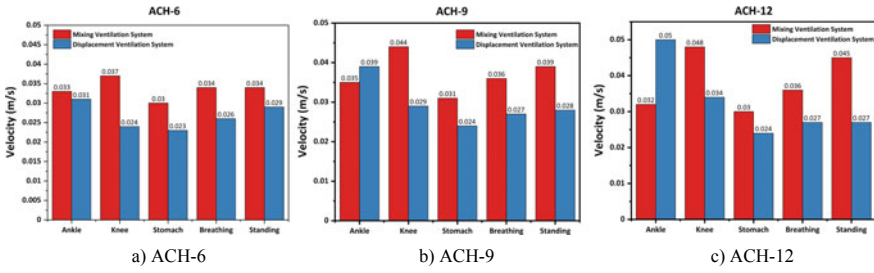


Fig. 10.7 Average velocity—occupant body levels

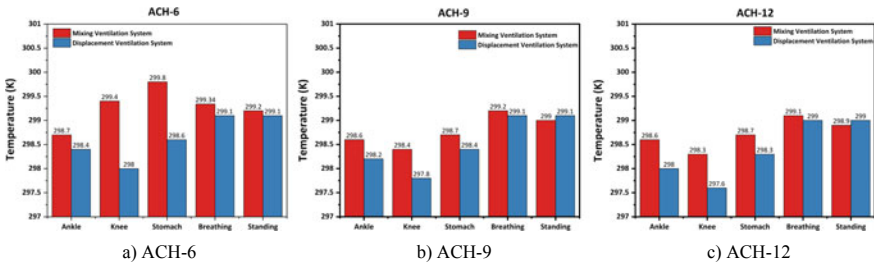


Fig. 10.8 Average temperature—occupant body levels

10.7 Limitations and Future Work

The present work demonstrated the airflow pattern in a scaled room model used by Chen et al. [13] for their experimental investigation. The Future work will focus on full-sized room geometry (with a similar office setting used in this research) to evaluate and compare the airflow pattern with that of a scaled room. Although the computational cost to evaluate the airflow pattern in the realistic room will be extremely high, an identical flow pattern will illustrate the possibility to allow the researchers to use scaled rooms for their investigations (provided the objective of their study is to identify the airflow movement).

10.8 Conclusion

The vector plots revealed that the airflow pattern in the office room is a function of the ventilation system being employed. The path of the supplied air in the office room varied according to its interaction with the obstacles (table), and occupants. As mentioned in the literature, the occupant thermal plumes (buoyancy effects) contributed to the airflow movement in the room. For a ventilation system, the change in supply rate has showcased a variation in the throw of air near the inlet,

whereas the air further away from the inlet possessed an identical flow pattern. The study revealed that the occupants seated closer to the inlet have fresh air surrounding them, whereas the occupants seated further are surrounded with unfresh air. The average velocity and temperature in the occupant activity zone determined the draft and thermal sensation. The mixing ventilation system showcased a higher average air velocity, therefore, a high-draft sensation, and the displacement ventilation system showcased a lower air temperature in comparison with the mixing ventilation system.

References

1. Ameen, A., Cehlin, M., Larsson, U., Karimipناه, T.: Experimental investigation of ventilation performance of different air distribution systems in an office environment-heating mode. *Energies* **12**(10) (2019). <https://doi.org/10.3390/en12101835>
2. Awbi, H.B.: *Ventilation Systems: Design and Performance*, 1st Ed. Taylor & Francis Group, Routledge (2019)
3. Cao, G., Awbi, H., Yao, R., Fan, Y., Sirén, K., Kosonen, R., Zhang, J.J.: A review of the performance of different ventilation and airflow distribution systems in buildings. *Build. Environ.* **73**, 171–186 (2014). <https://doi.org/10.1016/j.buildenv.2013.12.009>
4. Lin, Z., Chow, T.T., Fong, K.F., Tsang, C.F., Wang, Q.: Comparison of performances of displacement and mixing ventilations. Part II: indoor air quality. *Int. J. Refrig.* **28**(2), 288–305 (2005). <https://doi.org/10.1016/j.ijrefrig.2004.04.006>
5. Lin, Z., Chow, T.T., Fong, K.F., Wang, Q., Li, Y.: Comparison of performances of displacement and mixing ventilations. Part I: thermal comfort. *Int. J. Refrig.* **28**(2), 276–287 (2005). <https://doi.org/10.1016/j.ijrefrig.2004.04.005>
6. Deng, X., Gong, G.: Comparison of mixing and displacement ventilation under limited space air stability conditions in a space capsule. *Microgravity Sci. Technol.* **32**(4), 749–759 (2020). <https://doi.org/10.1007/s12217-020-09802-2>
7. Shan, X., Zhou, J., Chang, V.W.C., Yang, E.H.: Comparing mixing and displacement ventilation in tutorial rooms: students' thermal comfort, sick building syndromes, and short-term performance. *Build. Environ.* **102**, 128–137 (2016). <https://doi.org/10.1016/j.buildenv.2016.03.025>
8. Qiu-Wang, W., Zhen, Z.: Performance comparison between mixing ventilation and displacement ventilation with and without cooled ceiling. *Eng. Comput. (Swansea, Wales)* **23**(3), 218–237 (2006). <https://doi.org/10.1108/02644400610652965>
9. Yin, Y., Xu, W., Gupta, J., Guity, A., Marmion, P., Manning, A., Gulick, B., Zhang, X., Chen, Q.: Experimental study on displacement and mixing ventilation systems for a patient ward. *HVAC R Research* **15**(6), 1175–1191 (2009). <https://doi.org/10.1080/10789669.2009.10390885>
10. Ahn, H., Rim, D., Lo, L.J.: Ventilation and energy performance of partitioned indoor spaces under mixing and displacement ventilation. *Build. Simul.* **11**(3), 561–574 (2018). <https://doi.org/10.1007/s12273-017-0410-z>
11. Chakroun, W., Alotaibi, S., Habchi, C., Ghali, K., Ghaddar, N.: Comparison of removal effectiveness of mixed versus displacement ventilation during vacuuming session. *Build. Environ.* **155**(Feb), 118–126 (2019). <https://doi.org/10.1016/j.buildenv.2019.03.047>
12. Topp, C., Nielsen, P., Sorensen, D.: Application of computer simulated persons in indoor environmental modelling. *ASHRAE Trans.* **108**(2), 1084–1089 (2002)

13. Chen, F., Simon, C.M., Lai, A.C.: Modeling particle distribution and deposition in indoor environments with a new drift-flux model, vol. 40, pp. 357–367 (2006). <https://doi.org/10.1016/j.atmosenv.2005.09.044>
14. Eymard, R., Gallouët, T., Herbin, R., Eymard, R., Gallouët, T., Herbin, R., Volume, F., Lions, M.J.L.: Finite volume methods to cite this version: HAL Id: Hal-02100732 (2019)
15. Alsaad, H., Voelker, C.: Performance assessment of a ductless personalized ventilation system using a validated CFD model. *J. Build. Perform. Simul.* **11**(6), 689–704 (2018). <https://doi.org/10.1080/19401493.2018.1431806>
16. Zhao, R., Gosselin, L.: Natural ventilation of a tall industrial building: investigation on the impact of modeling assumptions (2014)
17. Shih, T.-H., Liou, W.W., Shabbir, A., Yang, Z., Zhu, J.: A new $K-\epsilon$ eddy viscosity model for high reynolds number turbulent flows. *Comput. Fluids* **24**(3), 227–238 (1995). [https://doi.org/10.1016/0045-7930\(94\)00032-T](https://doi.org/10.1016/0045-7930(94)00032-T)
18. Makhoul, A., Ghali, K., Ghaddar, N.: Thermal comfort and energy performance of a low-mixing ceiling-mounted personalized ventilator system. *Build. Environ.* **60**(2013), 126–136 (2013). <https://doi.org/10.1016/j.buildenv.2012.11.016>
19. Son, C.H.: Computational fluid dynamics ventilation study for the human powered centrifuge at the international space station, pp. 1–9 (2012)

Chapter 11

Performance Study and Analysis of an UAV Airfoil at Low Reynolds Number



Ramanan Gopalakrishnan, Neela Rajan Rajadurai Ramakrishnan,
Bino Prince Raja Dennis, and Anton Savio Lewise Kuzhanthai

Abstract The design and analysis of airfoil of an UAV at a low Reynolds number has been discussed in this paper. The new airfoil designs are being hampered by the aerodynamic attributes at low Reynolds number flows. The first step is to identify the design of the wing and the requirements for the analysis and then to formulate all the related concepts. Based on literature survey, analysis is piloted with four main design parameters using design concepts. Selection of airfoil is done using 2-dimensional computational fluid dynamic (CFD) analyses. Later, the verification of Xfoil is conducted by comparing the in hand wind tunnel data with the results of the Xfoil. The demerit of Xfoil compels us to use a 3-dimensional CFD analysis tools along with fluent so as to overcome it. Considering the lift and stability and requirements of the airfoil at various stall patterns, GEMINI and NACA0012 are considered for the wing and tail airfoils, respectively.

11.1 Introduction

We can notice a rise in the technology of large and small unmanned aerial vehicle (UAV) in European and Indian market. The commercial and general purpose aircrafts design and the design principles of a UAV are similar in many ways [1]. This UAV design has been successfully used in the industry over the years. This also benefited the country's economy by increasing the employments in the country, and it is predicted to rise in the coming 20 years [2]. The cost-effectiveness and the multidisciplinary optimizations of the UAV design have been carried out frequently. Recently in the field of UAV wing studies, major focus areas are

R. Gopalakrishnan (✉)

Aeronautical Engineering, ACS College of Engineering, Bangalore, Karnataka 560074, India

N. R. R. Ramakrishnan · A. S. L. Kuzhanthai

Aeronautical Engineering, Noorul Islam Centre for Higher Education, Kumaracoil, Tamilnadu 629180, India

B. P. R. Dennis

Aeronautical Engineering, SJC Institute of Technology, Bangalore, Karnataka 562101, India

inflatable and retractable wings [3]. This process will cover analysis and design of the wing by computerized control system. High-lift airfoil design philosophy that was presented by author gives the importance of low Reynolds number regime in which small UAV's operate. Kontogiannis et al. studied about light weight UAV aircraft is to operate as survey plane capable of carry all sorts of equipment's. This kind of UAV's is also equipped with FPV systems for making its control easier and accurate [4]. Anyoji et al. designed airfoil shape for high lift to drag ratio under the pre-mentioned conditions such as analysis of flow fields and aerodynamic characteristics of the Ishii airfoil [5]. Raja et al. proved that large UAVs have proven to be successful as entry-level military survey platforms; there exist a need for smaller, platoon-level unmanned aircrafts [6]. Pelletier et al. presented some of the results of an experimental inspection on low Reynolds number and aerodynamics of small and low-aspect-ratio wings. Nowadays, there is large need of micro-aerial vehicles (MAVs) has surfaced [7]. Ramanan et al. presented issues such as the thickness, camber, and surface pro les, related to the design of low Reynolds number airfoils are investigated [8].

To overcome the issues encountered in NACA 0012 and CLARK Y, the 2 well-known airfoils that were currently proposed on low Reynolds number airfoil S1223, and a modified airfoil UF, are compared under different Reynolds numbers and various angles of attacks. Shukla et al. explained that excellent design requires knowledge of all the flow characteristics. The question of how these features differ from the expected traditional analytical methods for rotorcraft was raised for the low Reynolds number of many UAV rotors [9]. Lafountain et al. gave the instructions to his students about tools and methodology that can be used in aircraft design. Pre junior students of the state of the art morphing technology were inspired by flying techniques of birds and introduced the integrated aircraft design [10].

Mosquera et al. designed an aerodynamic design of a low-cost UAV that were able to perform aerial survey over volcanic environments. Its main purpose was to transfer real time volcanic data to a remote location, in order to prevent the volcanic eruptions and also to prevent the pilots from these dangerous places [11]. Its main mission is to transmit period volcanic information to a distant location, so as to help to forecast volcanic eruptions, furthermore as avoiding the exposition of pilots and scientists to those dangerous flight conditions. Elangovan et al. have given the variation of missile dimensions, which tracks trajectories that the other tractability and values, which is allotted for commercial services [12]. This work in the main aims to gift this standing of style and analysis in UAV development through a scientific review with a descriptive study is planned. Ranges of the Reynolds variety vary from 2.5×10^5 to 10.32×10^5 . Associate approach to low Reynolds variety surface style is delineated and 4 kinds of cases square measure given and mentioned. Finally, the general approach involves exploitation the planning and Xfoil for analysis.

11.2 Methodology

The design of UAVs could be a multidisciplinary method that begins with the definition of the necessities and specifications which are typically a list of the foremost essential mission characteristics like the payload, the endurance, the altitude, and also the speed [1]. In turn, this can have direct influence done with the craft performance and stability, and hence, its assignment capabilities. In essence, the assignment of planning contains the guidance of physical parameters to change the mechanics. From Table 11.1, the craft specifications square measure selected for style of UAV. The design method started to use find out the required flying conditions, in addition because the varied data to meet mission needs. As per previous study, a grade is generated for every parameter in this work [2]. To initiate the look method, the physical parameters are initially identified. There are 2 sorts of parameters, dimensional, and style. In the wing and tail, the dimensional parameters are really important to study the design. From study, it was revealed within the optimization method, exploit the look parameters to be discovered [3].

11.2.1 Critical Performance Parameters

The most essential information for wing and tail design is the relationship between the lift coefficient and its corresponding angle of attack. The reason is primarily ruled by the airfoil choice and also the plan form. To link the sectional Cl of a second airfoil, new method ways are developed to 3D wings of finite span mistreatment lifting line theory [2]. It's tried to be fairly correct for straight wings in regions before stall. Apart from estimation of drag and the connection between drag and vary in determinant of parameter is crucial and endurance of the aircraft also. Still, it should be noted that for telemetry flight change it is additionally restricted by the radius of the signal strength of transmitter and also the endurance cannot last on the far side its battery length. Some circumstances for stability parameters are that the tendency of the level to come to its initial position once a disturbance, square measure is studied. It was studied from previous study that the tasks for the

Table 11.1 Aircraft specifications

Parameter	Specifications
Configuration	Pusher, high-wing
Take-off/recovery	Hand launched take off and Belly assisted landing
Altitude and cruising speed	2000 ft; 13–15 m/s
Designated task	short range surveillance
Maneuverability	Turning radius of <1 km
Range and endurance	Range of <4 km radius base, 10 min endurance time
Payload	Total aircraft weight <1 kg with camera and data logger

assorted parameters higher velocity studied. Tables 11.2 and 11.3 show the chosen data for wing and tail airfoils. Analysis is going to be targeted on wing section alone. For tail sections, the scope of this project solely needs them to satisfy the perform of pitch and yaw management, additionally on maintain flight stability.

11.3 Airfoil Analysis Results and Discussion

For the planning and analysis, Xfoil is associate interactive program used for subsonic isolated airfoils. This is widely received as a reputable tool [8] for coupling viscous and inviscid conditions. The most purpose of corroborative Xfoil is to increase the restricted library of device information within the best manner. Supported literature study solely has information of a couple of airfoils and is proscribed number at intervals [6]. Also this, integrating a wider vary device can improve the credibleness of the ultimate choice. At last, given Xfoil's comparatively short computation time, mechanics information was produced rapidly through totally different airfoils.

Table 11.2 Selected data for wing airfoils

Parameters	Clark Y	E197	GEMINI	NACA 2415
Max C_l	2.18	2.57	1.64	1.72
Max $\frac{C_l}{C_d}$	68	68	62	60
C_l versus $\alpha = 5^\circ$	0.82	0.76	0.8	0.75
$\frac{C_l}{C_d}$ versus $\alpha = 5^\circ$	68	55	55	54
Stall angle	11	13	14	14

Table 11.3 Selected data for tail airfoils

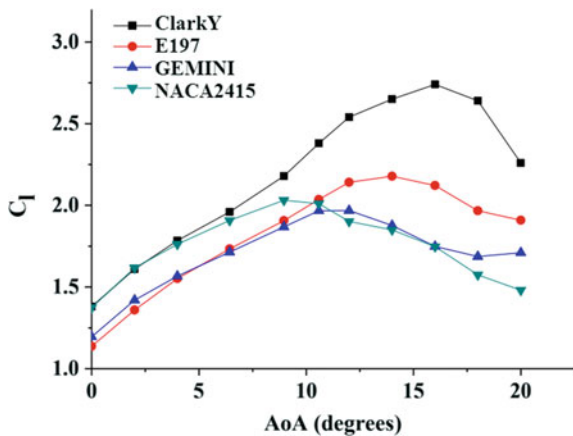
Parameters	NACA64A-010	SD8020	NACA009	NACA0012
Max C_l	0.7	0.92	0.84	1
Max $\frac{C_l}{C_d}$	35	45	42	45
C_l versus $\alpha = 5^\circ$	0.6	0.6	0.6	0.6
C_l versus $\alpha = 5^\circ$	0.08	0.08	0.08	0.08
$\frac{C_l}{C_d}$ versus $\alpha = 5^\circ$	35	45	42	45
Stall angle	6	10	10	10
Stall pattern	Moderately gentle	Moderately sharp	Moderately sharp	Moderately sharp

Data from obtainable literature are going to be compiled and compared with the plots from Xfoil below identical painter range. This can be distributed for four totally different airfoils at $Re = 10^5$ wherever real information is available and information were found [7, 8]. They are Clark Y, GEMINI, NACA64-A-10 and SD8020. From the analysis, graphs were planned, and so it's determined that the slope of the raise curves generated by Xfoil is fairly correct. The best deviation belongs to Clark Y, with a percentage of 4.91%. Further this, with exceptions to NACA0009. It is also seen that viscous formulations are well documented in software as drag estimations area unit correct at values before stall the stall patterns for the wing candidate's area unit well approximated too [9].

To additional justify further of Xfoil to match and dissimilarity information of various airfoils, the trends for the elevate plots are observed. Figures 11.1 and 11.2 represent the lift and drag coefficient results with various angle of attack values of the four chosen airfoils. It's determined that in terms of stall angles, lift coefficient terms reach most for Gemini airfoil, and additionally the order is that the same for both the particular and Xfoil information [10]. Figure 11.3 shows the lift and drag coefficient for various angle of attack of shortlisted tail airfoils. With the results from Xfoil verified that to be a reputable information generator, information is generated for four airfoils, doubling the scale of data at hand [11]. To begin, the desired lift coefficient for the finite wing must be determined. Clark Y produces a lot of stall angle than different airfoils. For one kilogram UAV cruising at a speed of 15 m/s, lift coefficient value is 0.589. Using lifting line theory earlier, in addition as introducing an element of 1.1, the minimum sectional mountain pass is decided as 0.694 [12].

When examining all features, GEMINI airfoil provides the most effective overall result. All of the airfoil fulfills the least sectional C_l . But E197 comes shut but it loses out slightly over the stall pattern that is decisive for brief range RC flight. C_d follows an almost vertical trend, constant drag for variable wing loadings which can aid within the design of propulsion system [13]. The GEMINI selected as wing

Fig. 11.1 C_l versus alpha for short listed wing airfoils



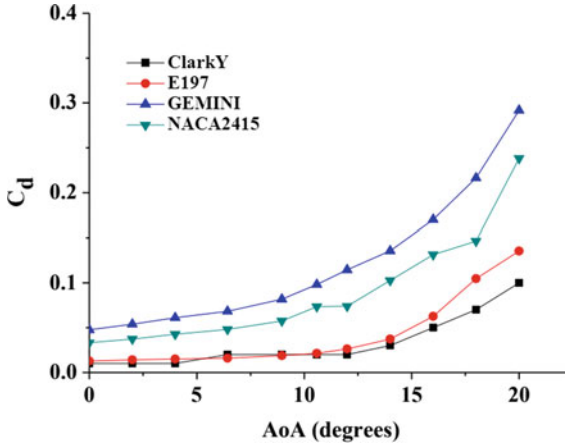


Fig. 11.2 C_d versus alpha for shortlisted wing airfoils

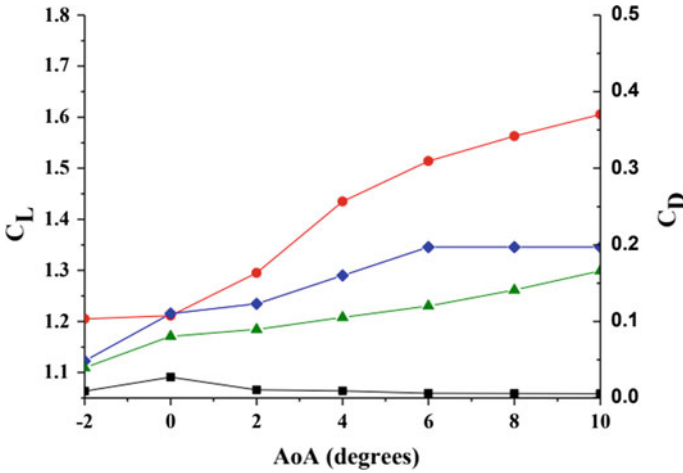


Fig. 11.3 C_l/C_d versus alpha for shortlisted tail airfoils

airfoil to use the lifting line theory and for all the tail airfoils hand-picked, and they are ready to fulfil the steadiness criteria higher than. SD8020 and NACA0012 each present themselves to be possible choices for tail airfoil [14]. NACA0012 is chosen as an appropriate airfoil for tiny UAV which may turn out most lift coefficient because of angle of attack that is 0.0123 per degree.

11.4 Conclusion

In this work, the selected airfoils designed model results are obtained, and the performance results are calculated both by numerically and analytically. The result from Xfoil data will clearly indicate that low Reynolds number airfoil can be designed to meet the maximum lift coefficient which will be much higher than that of airfoil selected as a reference. Using computational fluid dynamics simulation, low Reynolds number airfoil design is carried out which helped authors to study airfoil flow properties at different angle of attack. From above analysis, it is concluded that the Gemini and NACA0012 airfoil is give better aerodynamic performance because it gives more variations in lift coefficient than that of all the airfoils that were referred.

References

1. Chao, H., Cao, Y., Chen, Y: Autopilots for small unmanned aerial vehicles: a survey. *Int. J. Control, Autom. Syst.* **8**(1), 36–44 (2010)
2. Newcome, L.R.: *Unmanned aviation: a brief history of unmanned aerial vehicles*. American Institute of Aeronautics and Astronautics (2004)
3. Kay, N.J., Richards, P.J., Sharma, R.N.: Influence of turbulence on cambered and symmetrical airfoils at low Reynolds numbers. *AIAA J.* **58**(5), 1913–1925 (2020)
4. Kontogiannis, S.G., Ekaterinaris, J.A.: Design, performance evaluation and optimization of a UAV. *Aerosp. Sci. Technol.* **29**(1), 339–350 (2013)
5. Anyoji, M., Nonomura, T., Aono, H., Oyama, A., Fujii, K., Nagai, H., Asai, K.: Computational and experimental analysis of a high-performance airfoil under low-Reynolds-number flow condition. *J. Aircr.* **51**(6), 1864–1872 (2014)
6. Raja, B.P.D., Ramanan, G., Samuel, D.G: Computational analysis of blended winglet model performance by varying cant angle. *J. Comput. Theor. Nanosci.* **16**(2), 467–471 (2019)
7. Pelletier, A., Mueller, T.J.: Low Reynolds number aerodynamics of low-aspect-ratio, thin/flat/cambered-plate wings. *J. Aircr.* **37**(5), 825–832 (2000)
8. Ramanan, G., Krishnan, P.R., Ranjan, H.M.: An aerodynamic performance study and analysis of SD7037 fixed wing UAV airfoil. *Mater. Today: Proc.* (2021)
9. Shukla, D., Komerath, N.: Multirotor drone aerodynamic interaction investigation. *Drones* **2** (4), 43 (2018)
10. Lafountain, C., Cohen, K., Abdallah, S.: Use of XFOIL in design of camber-controlled morphing UAVs. *Comp. Appl. Eng. Edu* **20**(4), 673–680 (2012)
11. Elangovan, R.R., Vijayakumar, K.R., Ramanan, G.: Computational analysis of base drag reduction for a subsonic missile projectile at different flow velocity conditions. *Int. J. Veh. Struct. Syst. (IJVSS)* **12**(5) (2020)
12. Bravo-Mosquera, P.D., Botero-Bolivar, L., Acevedo-Giraldo, D., Cerón-Muñoz, H.D.: Aerodynamic design analysis of a UAV for superficial research of volcanic environments. *Aerosp. Sci. Technol.* **70**, 600–614 (2017)
13. De, S., Guida, D.: Control design for an under-actuated UAV model. *FME Trans.* **46**(4), 443–452 (2018)
14. Hann, R., Hearst, R.J., Sætran, L.R., Bracchi, T.: Experimental and numerical icing penalties of an S826 airfoil at low Reynolds numbers. *Aerospace* **7**(4), 46 (2020)

Chapter 12

Life Cycle Assessment Based Environmental Footprint of a Battery Recycling Process



Arvind Kumar, Abhishek Gupta, Shalini Verma,
Akshoy Ranjan Paul, Anuj Jain, and Nawshad Haque

Abstract South Asian countries are facing a problem of transport vehicle emission. Electric vehicle with low or even a zero-emission is seen as a potential solution for the tail pipe emission. The environmental impact of lithium-ion battery has been undertaken in this study. One battery pack used in three-wheel electric rickshaws chosen as a case. It has nominal capacity of 3.69 kWh which is considered which is able to be used up to 40,000 km of driving distance for 400 cycles for a period of 3 years. This study reveals the environmental footprint associated with the lithium-ion battery production, use and recycling phases. The result shows that the production phase generates higher impact compared with other phases. In this use phase, electricity losses due to battery charging also cause environmental impact. Valuable materials are recycled in the end-of-life waste management phase contributing benefits and earning environment credits.

12.1 Introduction

Rapid growth of population in South Asian countries and the increase in their gross domestic product have increased vehicle ownerships. There is an exponential growth in the ownership of vehicle in India. Only 4% of the total vehicle ownership is for 3-wheelers, which includes Auto, Tempos and E-rickshaw [1]. However, vehicular air pollution can only be successfully managed by replacing the conventional fuel-driven vehicles with battery-operated electric vehicles (EV). India

A. Kumar · A. Gupta (✉) · S. Verma · A. R. Paul · A. Jain
Department of Applied Mechanics, Motilal Nehru National Institute of Technology
Allahabad, Prayagraj, India
e-mail: arpaul@mnnit.ac.in

A. Jain
e-mail: anujjain@mnnit.ac.in

N. Haque
Commonwealth Scientific and Industrial Research Organization (CSIRO), Clayton, VIC,
Australia

has set a target to 100% EV sales by 2030 [2]. Lots of batteries are required for these EVs. Battery contributes approximately 50% of the total cost of the electric vehicle purchase cost. If the battery materials are not effectively recycled, the cost of battery cannot be managed.

Currently lithium-ion battery (LIB) is one of the most important energy storing devices (electro-chemical device). LIB is used to power the electric vehicle nowadays.

A lithium-ion battery is made up of anode material, cathode material, electrolyte, separator and binder with other components. Depending on the type of anode materials, the lithium-ion batteries are classified in categories like Lithium Iron Phosphate (LFP), Lithium Nickel–Cobalt–Manganese Oxide (NMC), Lithium Manganese Oxide (LMO) [3]. If the spent lithium-ion battery is disposed to the landfill before recovering the valuable battery materials, it may leach to the underground water bodies, resulting in serious environmental pollution. Recycling of the lithium-ion battery has several advantages as it reduces battery cost, environment pollution and energy consumption. This study used European electricity mix as the GWP depends upon the type and sources of electricity for the production phase of any product/process [4].

In India, the market of lithium-ion batteries is expected to grow in the future with a projection of about 6–7 million of electric vehicles on Indians roads [2]. Annual lithium-ion battery market in India is estimated to increase from 2.9 GWh in 2018 to 132 GWh in 2030. Considering the future projection of increase in the number of electric vehicles, the number of traction battery will also increase and so will the environmental impact.

In this present study, environmental footprint of a battery upto recycling process has been carried out. For this assessment, Lithium Manganese Oxide–Lithium Nickel Manganese Cobalt Oxide (LMO–NMC) type of lithium-ion battery is selected.

12.2 LMO-NMC Battery

12.2.1 Battery Cell Materials

India does not have the abundance of lithium metal (a critical metals). Presently, Indian battery manufacturers rely on importing battery pack from abroad. Due to increase in lithium-ion battery market in India that leads to a rise of volume of spent batteries. If this spent battery is discarded, this would cause in environment pollution. Moreover, the rare earth metals would be lost forever. Figure 12.1 shows the battery material for the production of a battery cell.

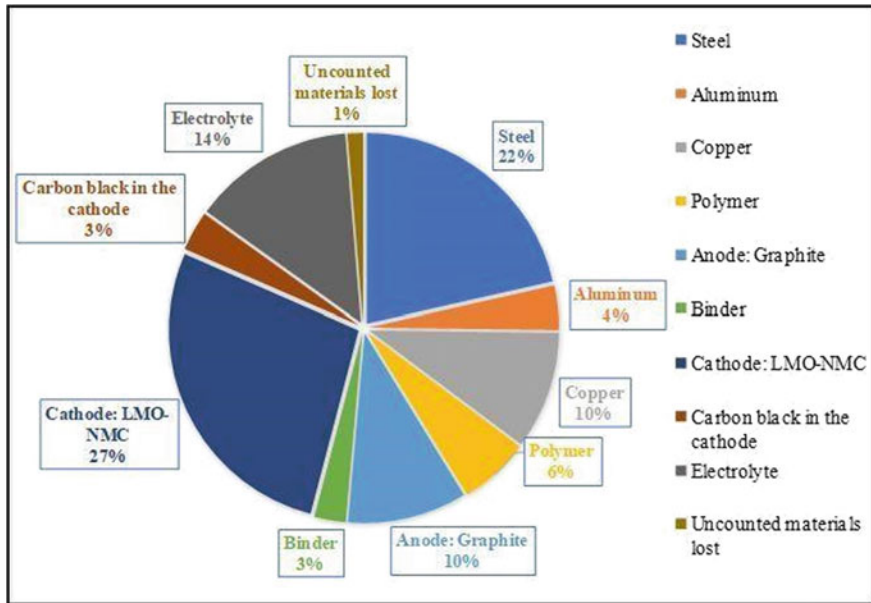


Fig. 12.1 Key material per battery cell. Source Cusenza et al. [5]

12.2.2 Battery Recycling

For battery recycling process, UMICORE process has applied. The process includes recovering metals by using acids and base solutions, as well as pyrolysis, smelting and refining using high temperatures [6].

12.3 Life Cycle Analysis of LMO–NMC Battery

12.3.1 Goal and Scope Definition

The goal of this study is to find out the environmental footprint of the lithium-ion battery. Lithium Manganese Oxide-Lithium Nickel Manganese Cobalt Oxide (LMO–NMC) battery is considered for the study. The processes considered are the battery production phase, use phase and end-of-life phase recycling phase [5]. The goal of recycling is mainly to reuse the resource avoiding the new extraction of virgin materials.

12.3.2 System Boundary

The system boundary is taken as ‘cradle-to-grave’ that includes recycling phase. The environmental impact of the battery is associated with production phase (raw material extraction, material production, battery cell and assembly), use phase (electricity needed to charge that lithium-ion battery) and recycling phase. The detailed system boundary is illustrated in Fig. 12.2. Figure 12.2 illustrates the unit process associated with system boundary. The functional unit is considered as ‘per kWh of battery energy capacity’.

12.3.3 Life Cycle Inventory Assessment

The process data input and output for each system were collected from the prior work done by Ellingsen et al. [4] (NMC battery), Majeau-Bettez [7] (NMC battery), Philippot [8] (NCA (Lithium Nickel–Cobalt–Aluminium Oxide) battery) and Cusenza [9] (LMO–NMC battery). Majority of the data used in this study is from the Cusenza [9] (LMO–NMC battery). In the production phase, the production of LMO–NMC batteries takes place in China. Hence, the electricity mix of China is used. In the use/operation phase, battery needs to be replaced after the use of 3 years or 40,000 km for this study. We used a 3-wheeler electric rickshaw which having the rechargeable lithium-ion battery. During use phase, the battery requires electricity for charging. Other details are given in Tables 12.1 and 12.2.

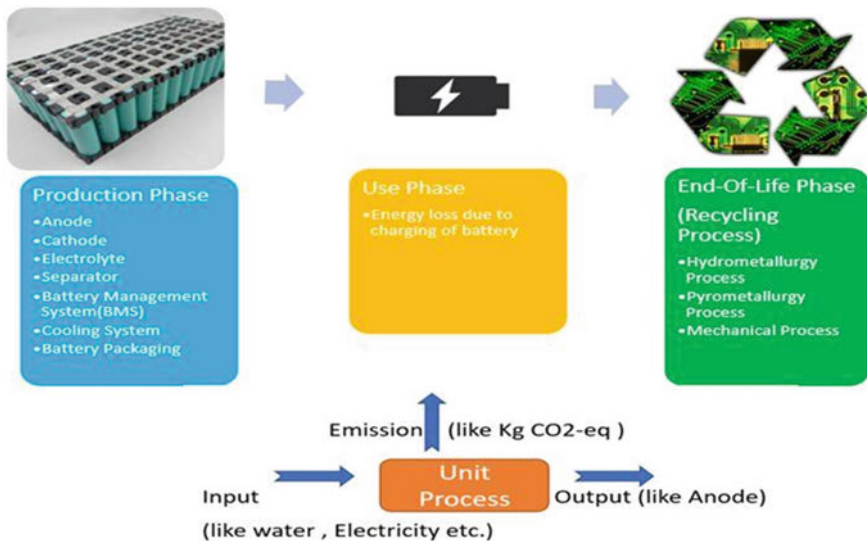


Fig. 12.2 System boundary

Table 12.1 Battery capacity

Vehicle type	3-Wheeler (E-rickshaw)
Battery type	LMO–NMC
Rated capacity	3.69 (kWh)
Battery weight	45 (kg)
Battery energy density	82 (Wh/kg)

Table 12.2 Battery life

3 Wheeler electric rickshaw	LMO–NMC
Battery first life	
Total distance with 1 eV battery (km)	40,000
Average consumption (kWh/km)	0.2 (Assumption)
Total energy (First life) (kWh)	8000
Battery second life	
Tot kWh second life	0
Tot kWh EV + Second life	8000

For the modelling of the end-of-life phase (recycling phase), the half of the battery was treated by the pyro-metallurgy process, and the rest half was treated by the hydrometallurgy process. This study considers the available life cycle datasets of the Ecoinvent database [10].

12.4 Life Cycle Impact Assessment and Interpretation

The life cycle impact assessment method was based on the product environmental footprint (PEF) which provides a large set of environmental impact categories [11]. Life cycle environmental impact is based on per kilogram of battery pack and per kWh of energy capacity (functional unit) basis. For the present study, the value of GWP for the production phase 216.2 kg CO₂ per kWh, for the use phase 94.2 kg CO₂ equivalent per kWh and for the recycling phase –17.18 kg CO₂ equivalent per kWh (negative value indicates of the recycling phase contributing to the environment credit).

In comparison with Ellingsen et al. [4], production phase GWP was equal to 172 kg CO₂ per kWh (NMC battery). In this study, it is approximately equals to 216 kg CO₂ per kWh (LMO–NMC battery). The difference in the GWP of the production phase is attributed to the type of electricity selected in the present study, i.e. electricity grid mix 1–60 kV, consumption mix (grid mix-Asia and the Pacific) for the battery production. To reduce the impact of GWP during the production phase, one needs to use the cleaner energy source. Table 12.3 represents environment impact due to production, use and recycling phase of study.

Total battery production phase environment footprint is shown in Fig. 12.3. As shown in Fig. 12.3, global warming potential environment impact category—

Table 12.3 Environmental impact of total battery with each phase contribution

Impact category	Unit	Production phase	Use phase	Recycling phase
		Impact per kWh	Impact per kWh	Impact per kWh
Global warming potential (GWP)	kg CO ₂ eq/unit	216.21	94.123	-17.181
Acidification terrestrial and freshwater (ACTF)	mol H+ eq/unit	2.50	0.867	-1.1466
Ecotoxicity freshwater (EcoF)	CTU eq/unit	184.43	23.253	-175.841
Eutrophication freshwater (EuF)	kg P eq/unit	0.112	3.03E-05	-0.06976
Eutrophication marine (EuM)	kg N eq/unit	0.205	0.103	-0.0694
Eutrophication terrestrial (EuT)	mol N eq/unit	1.95	1.133	-0.406
Land use	Pt/unit	330.183	140.2	-822.694
Ozone depletion (OD)	(kg CFC11 eq/unit)	0.0004	1.92E-09	6.26E-08
Resource use, energy carriers (Res-En)	(MJ/unit)	2450.82	1227.56	-222.441
Resource use, mineral and metals (Res-M)	(kg Sb eq/unit)	0.00578	4.664E-06	-46.23
Water scarcity (Water-S)	(m ³ depriv./unit)	241.127	8.796	6210.86

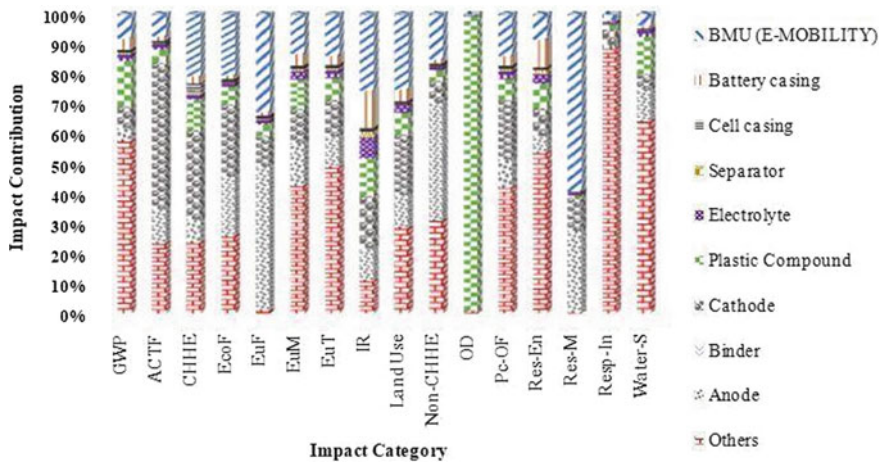


Fig. 12.3 Total battery production phase environment footprint. Abbreviations used: GWP (Global Warming Potential), ACTF (Acidification terrestrial and freshwater), CHHE (Cancer Human Health Effects), EcoF (Ecotoxicity Freshwater), EuF (Eutrophication Freshwater), EuM (Eutrophication Marine), EuT (Eutrophication Terrestrial), IR (Ionizing Radiation), Land Use, Non-CHHE (Non-Cancer Human Health Effects), OD (Ozone Depletion), Pc-OF (Photochemical-Ozone Formation), Res-En (Resource Use-Energy Carriers), Res-M (Resource Use-Minerals and Metals), Resp-In (Respiratory Inorganics), Water-S (Water-Scarcity)

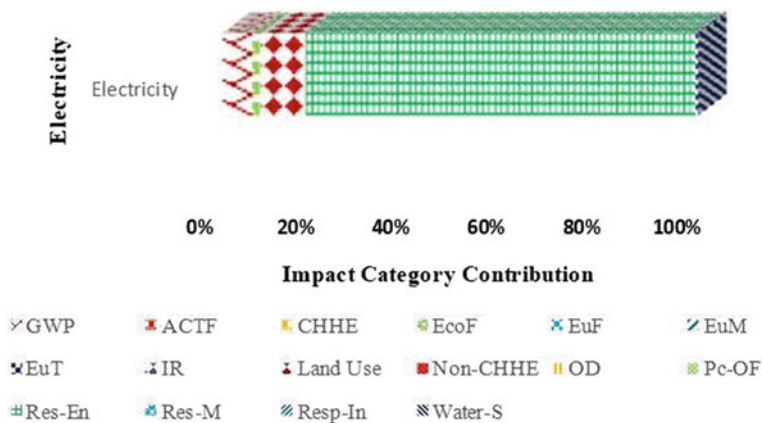


Fig. 12.4 Total battery use phase environment footprint (Abbreviation used: similar to Fig. 12.3)

majority of the contribution in this environment category is due to the others (which consist of the electricity used for the production of the lithium-ion battery). Anode, cathode, separator, binder, battery casing, cell casing and electrolyte production are contributing impact on total global warming potential.

Figure 12.4 indicates electricity resource use and its environment impact in different categories. If the cleaner and greener sources of renewable energy are utilized for charging the electric rickshaw (E-rickshaw) battery, the environment footprint would be decreased further.

Total battery recycling phase environment footprint is shown in Fig. 12.5. Here, the negative value of the impact category corresponds to the material credit due to

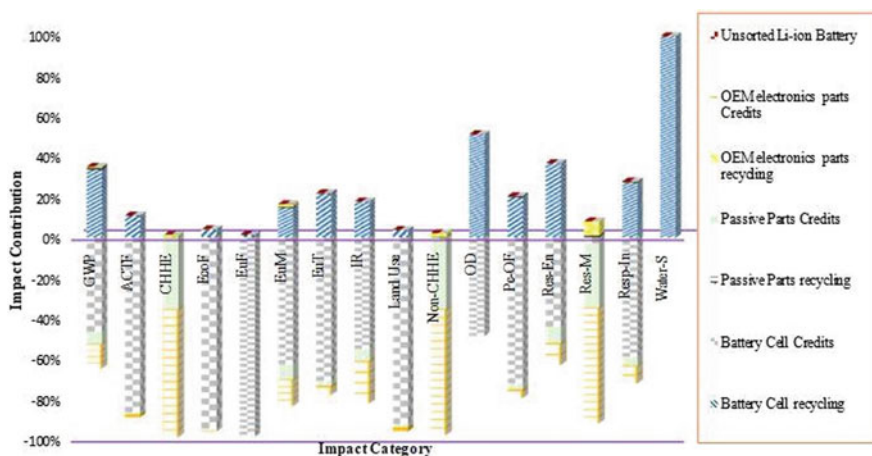


Fig. 12.5 Total battery recycling phase environment footprint (Abbreviations used: Similar to Fig. 12.3)

the recycling process. As shown in Fig. 12.5, OEM electronics, parts, passive parts and battery cell parts generate negative impact contribution on the environmental impact categories. As shown in Fig. 12.5 unsorted Lithium-ion battery, OEM electronics parts recycling, passive parts recycling and battery cell recycling process, however, would generate some positive impact on the environmental impact.

12.5 Conclusions

This assessment was carried out for lithium-ion battery per kWh basis. Major conclusions from this study are:

- This study confirms that the production phase of the lithium-ion battery (LMO–NMC) is generating higher environmental impact. The electricity used for cell assembly is generating higher impact in the production phase.
- Due to the electricity losses in the battery, charging of battery generated higher impact during use phase.
- Various rare metals with the battery cell material were recycled at the end-of-life waste phase which would significantly benefit the environment.

Based on these conclusions, several recommendations are made for the battery manufacturers to ensure a sustainable future for the planet:

- Battery component like anode, cathode and separator, etc., are required to be designed in a manner that can be easily disassembled at the end-of-life and recycled. As a result, recycling rate would be increased.
- The electricity used in manufacturing of battery packs during the production phase generates higher global warming potential (GWP). Thus, low-carbon intensive electricity that can reduce the GWP.
- In case of recycling phase, collection efficiency of the battery packs is low. Hence, the battery manufacturing industry and regulatory authorities need consideration on how to increase the collection efficiency of the end-of-life battery packs.

References

1. NITI AAYOG Global mobility summit move (2018)
2. India's energy storage mission: a make-in-India opportunity for globally competitive battery manufacturing. NITI Aayog and Rocky Mountain Institute (2017). <https://www.rmi.org/Indias-Energy-Storage-Mission>
3. Hao Han, M., Zhexuan, J.S., Zongwei, L., Fuquan, Z.: GHG emissions from the production of lithium-ion batteries for electric vehicles in China. *Sustainability* **9**, 504 (2017)
4. Ellingsen, L.A.W., Majeau-Bettez, G., Singh, B., Srivastava, A.K., Valøen, L.O., Strømman, A.H: Life cycle assessment of a lithium-ion battery vehicle pack. *J. Indus. Ecol.* (2013)

5. Silvestri, L., Forcina, A., Arcese, G., Bella, G.: Recycling technologies of nickel-metal hydride batteries: an LCA based analysis. *J. Clean. Prod.* **273**, 123083 (2020)
6. UMICORE.: Battery recycling—our recycling process (2018). <http://csm.unicore.com/en/recycling/battery-recycling/our-recycling-process>
7. Majeau-Bettez, G., Hawkins, T.R., Stromman, A.H.: Life cycle environmental assessment of lithium-ion and nickel metal hydride batteries for plug-in hybrid and battery electric vehicles. *Environ. Sci. Technol.* **45**, 4548–4554 (2011)
8. Maeve, P., Garbine, A., Elixabete, A., Van Mierlo, J., Messagie, M.: Eco-efficiency of a lithium-ion battery for electric vehicles: influence of manufacturing country and commodity prices on GHG emissions and costs. *Batteries* **5**, 23 (2019)
9. Cusenza, M.A., Bobba, S., Ardente, F., Cellura, M., Di Persio, F.: Energy and environmental assessment of a traction lithium-ion battery pack for plug-in hybrid electric vehicles. *J. Clean. Prod.* **215**, 634–649 (2019)
10. Ecoinvent—the world’s most consistent and transparent life cycle inventory database. <https://www.ecoinvent.org/>
11. PEFCR.: Product environmental footprint category rules for high specific energy rechargeable batteries for mobile applications, February (2018)

Chapter 13

Review on the Structural Components of Floating Photovoltaic Covering Systems



**Nagananthini Ravichandran, Nagavinothini Ravichandran,
and Balamurugan Panneerselvam**

Abstract The alarming increases in the utilization of fossil fuels in the energy sector had led to serious environmental threats in the last two decades. To meet the noticeable rise in energy demand, while maintaining the sustainability of the environment, power generation from renewable energy resources is the recent highly preferred technology. Among these, floating photovoltaic (FPV) systems are becoming increasingly competitive. Admittedly, high-efficient power production from underused surfaces of water sources is the reason for increased investment by global nations. Thus, it is necessary to analyze the structural components of FPV systems making them unaffected by external sources deterring uninterrupted power supply. This study provides insights into FPV technology in mitigating the evaporation rate on installed water bodies and discussing the key elements involved designing an FPV system with comparisons of real-time design examples.

13.1 Introduction

Gaseous emissions due to power generation from fossil fuels are polluting the atmosphere gradually, which not only diminishes the purity of the air but also affects human health. In order to combat climate change, moving toward clean energy, while generating affordable electricity is necessary [1]. Moreover, with the large demand for energy sources and the unbalanced increase in the cost of fossil fuels, the focus is now moving toward renewable energy sources (RES) [2]. Power

N. Ravichandran (✉)
Power Electronics and Drives, Dindigul, India

N. Ravichandran
Department of Structures for Engineering and Architecture, University of Naples Federico II,
Naples, Italy
e-mail: nagavinothini.ravichandran@unina.it

B. Panneerselvam
Department of Civil Engineering, M. Kumarasamy College of Engineering, Karur,
Tamil Nadu, India

generation through RES plays a significant role in transforming the fossil fuel-based power sector toward zero-carbon green energy from the solar, wind, hydro, and geothermal-based generated power [3]. The worldwide traction on RES is increasing gradually to maintain sustainability and to pass on a pollution-free environment to the future generation. As per the statistics provided by the International Renewable Energy Agency, the global renewable energy generation capacity has increased by 7.40% which is equal to 176 GW from 2018 to 2019 [1]. Out of the total renewable energy production worldwide, 47% accounts for the power generated from hydroelectric power plants (HEPP) with a generating capacity of 1190 GW [2]. Followed by HEPP, wind energy and solar photovoltaic systems share an equal amount of power generating capacities which totally contribute 90% of the newly installed systems of renewable energy production mainly from China, India, Japan, and the Republic of Korea [1].

Sunlight being the major source of energy production, power generation through PV panels is receiving worldwide attention. With the continuous decrease in the cost of PV systems and increase in their efficiency, the generation of electricity from solar PV tend to contribute major solutions to the energy demand faced by the world [1, 3]. Also, the availability of technically advanced silicon panels and an effective way of generating power even in lowlight conditions motivate the consumers for self-power generation [3]. However, the unavailability of land for the installation of large-scale land mounted PV systems is the major drawback for this sector especially in densely populated countries like India. Such barriers to the installation of the solar PV systems hinders the development of sustainable energy production that helps in reducing fossil fuel usage. Thus, achieving the target solar energy production just through land mounted and rooftop PV systems is quite challenging. One of the alternative solutions is FPV, also called floatovoltaics or floating solar PV (FSPV) or floating solar covering system (FSCS).

This advancement in the solar technology of placing the PV panels on the water surface experiences higher annual energy yield than the ground or roof-mounted solar PV system [4–6]. This highly efficient technology has been facing real-time implementation since 2007, from then it is showing a dramatic growth with increased efficiency [7, 8]. The major highlight of the FPV system which is making them particularly beneficial in comparison with land mounted and rooftop-mounted systems is the automatic cooling of the panels. The optimum temperature of the PV panel is maintained, while placing them in direct contact with water that helps in increasing the efficiency of the panels considerably. The other significant environmental impact of placing PV panels on the water is the reduction in evaporation, which helps in saving the freshwater for domestic, hydropower generation, and agricultural purposes [9, 10]. Thus, these systems exist harmonically with the water bodies without any issues concerning land usage, but also provides a supplementary benefit of saving the water lost by evaporation in the arid and semi-arid regions of the country.

Studies revealed that covering the water surface has the potential to mitigate water loss through evaporation by 90% compared to the uncovered water surface [11]. The FPV technology will address this issue in a better way by increasing solar

power production and preserving the water for future use. Experimental investigations had also proved that the FPV system is technically feasible and economically viable for even covering the total water surface area of a reservoir [12, 13].

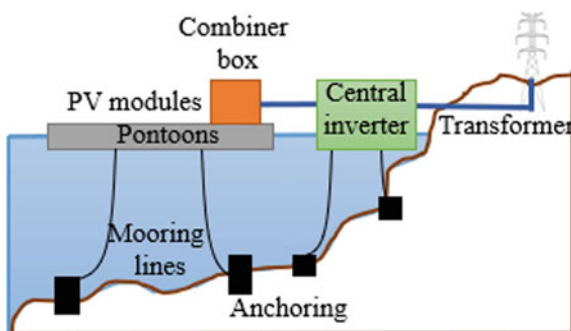
Despite the availability of several studies on this new technology, a detailed overview on all the design factors of FPV to be considered throughout the design process is not readily available in the literature. The design of floating PV systems differs with respect to the size and shape of the water surface under consideration. Another major parameter is the depth of the reservoir which changes the mooring forces and subsequently affects the design of the PV system. Thus, a suitable solar PV system should be selected for a particular location based on the detailed study on several factors that affects the the power production. This study presents a detailed review of the key structural elements of this emerging FPV systems. This detailed overview of the FPV design elements will provide a clear understanding of the advantages and disadvantages associated with the deployment of FPV modules in standing water bodies.

13.2 Key Structural Elements of FPV System

In order to avoid land acquisition for PV projects, the idea of installing PV panels on the water resources has emerged from 2007 and there is an evident growth in this technology all over the world due to its significance. Apart from special arrangements required to make the system float and support PV arrays, inverters, and combiner boxes on the water surface with a mooring system, the FPV system is quite similar to the conventional PV system. Problems due to corrosion and harsh wave conditions arise only in the FPV systems deployed in oceans [8, 14, 15] and these issues can be avoided considerably in the FPV systems deployed in freshwater reservoirs [9, 16].

The main parameters required to design a suitable FPV plant for any water storage system includes the type of PV panel, slope direction of panels, meteorological conditions of the site, support system, and moorings. The major key design elements of FPV systems are shown in Fig. 13.1.

Fig. 13.1 Key design elements of FPV system [7, 8]



13.2.1 PV Panel Support Systems

Solar PV panels are placed on a floating structure called a pontoon. It is usually made up of fiber-reinforced plastic (FRP), high-density polyethylene (HDPE), medium-density polyethylene (MDPE), polystyrene foam, hydro-elastic floating membranes or ferro-cements to provide enough buoyancy and stability to the total system. Less dense materials with density close to the a density of water are usually preferred. The pontoons are designed in such a way to withstand the vertical load, horizontal wind forces, wind uplift, water drift, and live loads. Considering the elasticity of the less dense materials, a minimum thickness of 4.0 mm is required to ensure good structural performance [13].

For high stiffness and good load-bearing capacity, the upper side of the pontoon is divided into portions called gutters. The PV panel is positioned on these gutters by means of vertical metal elements as the support structure, as shown in Fig. 13.2a. These metal structures are also used to position the panels with optimum tilt. The gutters also serve as a place to position the electrical wires made of polyurethane (PU) in order to avoid water contact [15]. A single pontoon can be suitably designed to accommodate two PV panels with space for personnel access (around 0.50 m) in between, as shown in Fig. 13.2b, and the adjacent pontoons can be connected with each other by means of bolts (Fig. 13.2c), metal chains or cables. The floating platforms in the 500 kW and 2 MW FPV systems installed in India used HDPE pontoons over which the PV modules are mounted using steel and aluminum bars.

Flexible coupling made up of MDPE or rubber straps attached to the pontoon are helpful to track the system to a particular extent and provide a relative motion between them whenever there is a drift in the water level [13]. Elastic joints are always preferred as flexible couplings rather than chains. These elastic joints are closed during full reservoir conditions and open to cover longitudinal slopes when the reservoir is empty. For deployment of larger FPV systems, it is advantageous to introduce a central electrical coupling which is a string of microinverters to support the electrical output of a number of panel rows on either side. This electrical coupling increases the reliability of the system by minimizing the losses with desired array scalability [15, 18].

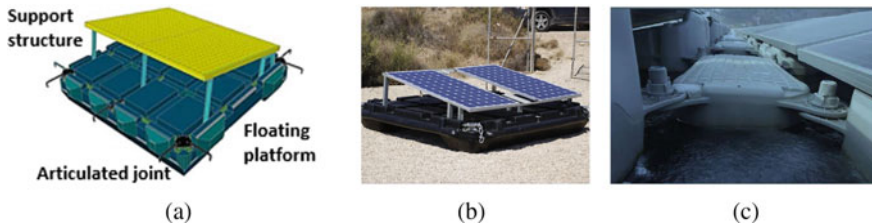


Fig. 13.2 Types of pontoon systems **a** PV panels fixed to the pontoon [10], **b** Single pontoon with chain interconnection [13], and **c** Pontoon interconnection using bolts [17]

As an alternative to pontoons, polyethylene rafts of 8–12 m length are also used to support the PV panels as shown in Fig. 13.3a. The raft structure can be suitably designed to support 6–10 PV panels with space for catwalks as shown in Fig. 13.3b. The number of panels accommodated by the raft increases with the increase in the angle of the inclination of the panel. However, the better yield of PV panel can be achieved only through a lower angle of inclination, and this results in the increase in the cost of the raft structures per kWh. Studies revealed that the raft type structure has higher reliability than the former structures due to its ability to uniformly distribute the stress developed due to waves and wind forces. These rafts can withstand wind loads up to 140 km/hour and also allow trackers, reflectors as well as cooling mechanisms [16, 19]. For water bodies with a surface area of less than 200 m², rubber mats are also being used as a covering system which is economical and simple in design with the additional advantage of higher yield than normal FPV due to its direct contact with water [3]. The FPV plant with a rubber mat as a floating platform is shown in Fig. 13.4.

Despite the several advantages of FPV systems, it is also important to observe the impact of FPV installation on the water bodies. Some of the physical changes in the water surface after installation of panels is the reduction in the wind speed,



Fig. 13.3 **a** Polyethylene rafts supporting 9 PV modules, **b** raft with catwalks [17, 19, 20]



Fig. 13.4 FPV plants with rubber mats as floating platform [21]

reduction in thermal energy and the increase in vapor pressure up to saturated vapor pressure (due to the change in temperature between the water surface and floating deck) [10, 16, 22]. In this condition, covering the entire reservoir with FPV panels may tend to have a negative impact on the ecosystem as well as the efficiency of the FPV system due to the changes in the evaporative cooling of the water body. So, the area of the FPV plant should be determined suitably considering its negative impact on hydrochemical characterization of water [9].

13.2.2 Mooring and Anchoring

Anchoring the floating deck with proper technique is essential for an FPV system as the drift in water level, and the action of wind load can damage the floating platform and the mooring cables [17, 20, 23]. Various types of mooring systems suggested for FPV plants include gravity type, anchor-tension type, semi-rigid type, tension-type, and modified type [4]. The type of the mooring system is selected based on the water level and soil type at the location. Among these types, the anchor tension type is widely used, which can be further classified as (i) bank anchoring, (ii) bottom anchoring, and (iii) pile anchoring.

In bank anchoring system, the outer edge of pontoons is connected to the bollards present in the ridge of the embankment by means of aluminum spread bar, cables, shackles chain, and ropes at certain intervals (see Fig. 13.5a). The total structure (along the perimeter/central mooring) is anchored by using reinforced concrete (RC) piles. This bank anchoring system with nylon ropes is used in the 500 kW FPV system in Wayanad, India [24]. A similar arrangement with concrete blocks is also used in the 2 MW FPV system installed in Vishakhapatnam, India [25]. In the case of irrigation canals and small ponds, the floating bed is connected through cables or chains to the wall of the reservoir as shown in Fig. 13.5b. In locations with low-water depths and fewer environmental forces, moorings made up of nylon polyester or nylon nautical rope or chain is sufficient. But in the case of sites with larger water depth and extreme weather conditions, there exists a high probability of mooring cable failure and foundation collapse, which in turn affects the stability of the floating platform [14, 17]. In such conditions, moorings with elastic joints which are capable of contraction and expansion according to various environmental conditions are the better solution [4].

In order to reduce the material degradation in elastic moorings, Titanium hybrids are used due to their good corrosive resistance. In a submerged PV system, the lightweight flexible thin-film modules eliminate the heavyweight and large stress on pontoon/metal rafts in the floating platforms. Therefore, a simple mooring system to avoid the dislocation of panels by the water force is sufficient as shown in Fig. 13.5c. Figure 13.5d shows the pile anchoring system in which the piles are

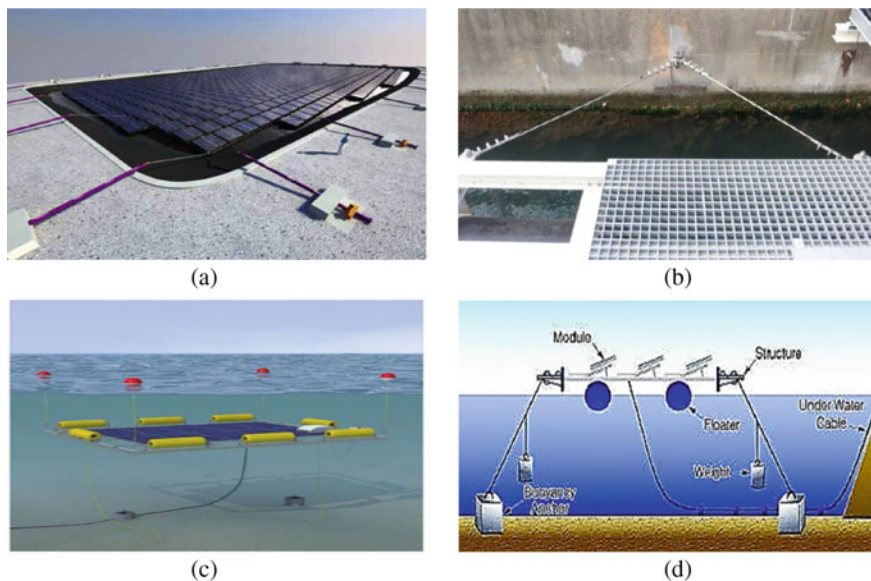


Fig. 13.5 **a** Anchoring at the reservoir bank, **b** anchoring at reservoir embankment, **c** mooring system for submerged PV, **d** pile anchoring system [9, 20, 23, 26]

drilled to the bottom of the water bodies. This system has the potential to handle various water depths, but it is expensive compared to other types of systems [1, 9].

13.3 Conclusion

The floating photovoltaic installation had grown tremendously in the last three years with the global installed capacity of 1314 MW. India being in the development stage has increased its FPV implementation from kW to MW scales in the last five years. With proper technological development in the FPV sector, India has the potential to implement up to 280 GW of capacity with its available water resources. This study presents the overview of various structural components of FPV systems. The paper discussed also compares the design requirements essential in the early stage of the FPV system, such as a suitable floating platform to place the PV panels and mooring support for smoother and uninterrupted operation of the system. In addition, the key design elements elaborated in the study will aid in the design and deployment of FPV systems in reservoirs all over the world. The advantages of the FPV system being established based on the present study, the future investigations by the research group will be focused on the performance assessment of a model FPV system in reservoirs.

References

1. IRENA.: Renewable capacity statistics 2020, Abu Dhabi (2020)
2. BP.: BP statistical review. Stat. Rev. World Energy. 1–56 (2018)
3. Acharya, M., Devraj, S.: Floating solar photovoltaic (FSPV): a third pillar to solar PV sector? TERI Discuss. Pap. ETC India Proj. New Delhi Energy Resource Institute, 68 (2019)
4. Kim, S.H., Yoon, S.J., Choi, W.: Design and construction of 1MW class floating PV generation structural system using FRP members. *Energies* **10** (2017)
5. Nagananthini, R., Nithya, G., Bhuvanesh, S.: Economic analysis of bi-directional net-meters with orientation and positioning of solar module. In: Proceedings 2019 International Conference on Advanced Computing and Communication Engineering ICACCE 2019, pp. 4–6 (2019)
6. Sahu, A., Yadav, N., Sudhakar, K.: Floating photovoltaic power plant: a review. *Renew. Sustain. Energy Rev.* **66**, 815–824 (2016)
7. Nagananthini, R., Nagavinothini, R., Balamurugan, P.: *Floating Photovoltaic Thin Film Technology—A Review*. Springer Singapore (2020)
8. Nagananthini, R., Nagavinothini, R.: Investigation on floating photovoltaic covering system in rural Indian reservoir to minimize evaporation loss. *Int. J. Sustain. Energy.* **0**, 1–25 (2021)
9. Haas, J., Khalighi, J., de la Fuente, A., Gerbersdorf, S.U., Nowak, W., Chen, P.J.: Floating photovoltaic plants: ecological impacts versus hydropower operation flexibility. *Energy Convers. Manag.* **206** (2020). <https://doi.org/10.1016/j.enconman.2019.112414>
10. Redón Santafé, M., Torregrosa Soler, J.B., Sánchez Romero, F.J., Ferrer Gisbert, P.S., Ferrán Gozálviz, J.J., Ferrer Gisbert, C.M.: Theoretical and experimental analysis of a floating photovoltaic cover for water irrigation reservoirs. *Energy* **67**, 246–255 (2014)
11. Taboada, M.E., Cáceres, L., Graber, T.A., Galleguillos, H.R., Cabeza, L.F., Rojas, R.: Solar water heating system and photovoltaic floating cover to reduce evaporation: experimental results and modeling. *Renew. Energy.* **105**, 601–615 (2017)
12. Armstrong, A., Page, T., Thackeray, S.J., Hernandez, R.R., Jones, I.D.: Integrating environmental understanding into freshwater floatovoltaic deployment using an effects hierarchy and decision trees. *Environ. Res. Lett.* **15** (2020)
13. Ferrer-Gisbert, C., Ferrán-Gozálviz, J.J., Redón-Santafé, M., Ferrer-Gisbert, P., Sánchez-Romero, F.J., Torregrosa-Soler, J.B.: A new photovoltaic floating cover system for water reservoirs. *Renew. Energy.* **60**, 63–70 (2013)
14. Nagavinothini, R., Chandrasekaran, S.: Dynamic analyses of offshore triceratops in ultra-deep waters under wind, wave, and current. *Structures* **20**, 279–289 (2019)
15. Trapani, K., Millar, D.L.: The thin film flexible floating PV (T3F-PV) array: the concept and development of the prototype. *Renew. Energy.* **71**, 43–50 (2014)
16. Dörenkämper, M., Wahed, A., Kumar, A., de Jong, M., Kroon, J., Reindl, T.: The cooling effect of floating PV in two different climate zones: a comparison of field test data from the Netherlands and Singapore. *Solar Energy* **214**, 239–247 (2021)
17. Cazzaniga, R.: *Floating PV structures*. Elsevier Inc. (2020)
18. Choi, Y.-K., Lee, N.-H., Lee, A.-K., Kim, K.-J.: A study on major design elements of tracking-type floating photovoltaic systems. *Int. J. Smart Grid Clean Energy.* **3**, 70–74 (2014)
19. Cazzaniga, R., Cicu, M., Rosa-Clot, M., Rosa-Clot, P., Tina, G.M., Ventura, C.: Floating photovoltaic plants: performance analysis and design solutions. *Renew. Sustain. Energy Rev.* **81**, 1730–1741 (2018)
20. Chandrasekaran, S., Nagavinothini, R.: Tether analyses of offshore triceratops under wind, wave and current. *Mar. Syst. Ocean Technol.* **13**, 34–42 (2018)
21. Ocean sun, Norway. <https://oceansun.no/our-products/>
22. Ravichandran, N., Ravichandran, N., Panneerselvam, B.: Performance analysis of a floating photovoltaic covering system in an Indian reservoir. *Clean Energy* **5**(2), 208–228 (2021). <https://doi.org/10.1093/ce/zkab006>

23. Chandrasekaran, S., Nagavinothini, R.: Tether analyses of offshore triceratops under ice force due to continuous crushing. *Innov. Infrastruct. Solut.* **4** (2019)
24. Kerala State Electricity Board (KSEB).: <http://kseb.in>
25. (GVSCCL), SMARTNET. <https://smartnet.niua.org/users/greater-visakhapatnam-smart-city-corporation-limited>
26. Cazzaniga, R., Rosa-Clot, M., Rosa-Clot, P., Tina, G.M.: Integration of PV floating with hydroelectric power plants. *Heliyon.* **5**, e01918 (2019)

Chapter 14

Performance and Emission Test of C.I. Engine Using Biodiesel



P. V. Chandra Sekhara Rao, B. Renuka Swathi, and Aluri Manoj

Abstract The most efficient primary drivers are diesel engines. In order to safeguard the global environment and long-term security of energy, alternative fuels with equivalent qualities to petroleum-based fuels need to be developed. Contrary to the rest of the globe, India's demand for diesel fuels is around 6 times that of petrol hence it is logical to look for alternatives to mineral diesel. Bio generated fuels present the developing nations with a viable answer to the double crises of depletion and degradation of fossil fuels in the environment. Due to the worldwide emphasis on the reduction of greenhouse gases (GHGs) and a clean development mechanism (CDM), bio-fuels are given additional emphasis. The usage of vegetable oil increases the usage of gasoline and Brake-specific fuel consumption (BSFC). It is injected in droplets to compensate for the insufficient mixing of fuel. CI engine is performed without substantial problems of long-term operation and durability. However, the transesterification step requiring chemical and process heat inputs adds significant processing costs. Vegetable oils can be crucial to decentralised power production for irrigation and electricity in rural and remote parts of developing nations where grid electricity is not accessible. Different types of vegetable oils in these remote places are cultivated/produced locally, however, owing to logistics challenges in rural locations they cannot be processed chemically. Hence, using heated or blended vegetable oils as petroleum fuel substitutes is an attractive proposition. Given this fact, Jatrophan oil on engines, typically used for agriculture and irrigation, and the decentralising generation of electricity, was used for a number of engine experiments in the current research. In order to minimise different operating issues, heating and mixing were utilised to reduce the viscosity of Jatrophan oil.

Please note that the LNCS Editorial assumes that all authors have used the western naming convention, with given names preceding surnames. This determines the structure of the names in the running heads and the author index.

P. V. C. S. Rao (✉) · B. R. Swathi · A. Manoj
Rajiv Gandhi University of Knowledge Technologies, Basar, Telangana 504107, India
e-mail: chandrasedkhararao@rgukt.ac.in

14.1 Introduction

Biodiesel is a liquid biofuel made from vegetable oils or animal fats and an alcohol that may be used in diesel engines alone or in combination with diesel oil. Diesel fuel mixtures are denoted as “Bx” whereby “x” represents the proportion of biodiesel in the mixture. “B5”, for example, refers to a mixture of 5% *Jatropha* oil and 95% diesel fuel, therefore, “B100” refers to pure *Jatropha* oil. Vegetable oils, animal fats and short chain alcohols are the biodiesel production raw materials. Palm, sunflower, rape seed and soya beans are the most commonly used oils for global production of biodiesel. Methanol is the most common alcohol consumption. Transesterification was undertaken by Duffy and Patrick early in 1853. The famous German inventor Dr. Rudolph Diesel published life for diesel engines started in 1893, after a paper entitled “The theory and building of a rotary heat engine”. Initially, Diesel created a vegetable oil engine. Transesterified vegetable oil was named “biodiesel” to indicate its usage as a diesel fuel. Biodiesel is typically produced by reactions to the yield of methyl or ethyl esters (biodiesel) and glycerine by vegetable oil or animal fat using methanol and ethanol in a catalyst presence [1–3].

Biofuels, obtained from renewable energy sources, are non-toxic, biodegradable, free from sulphur and carcinogenic compounds. Biodiesel is a plant-based product that includes oxygen in its molecules which makes it cleaner than petroleum and diesel fuel. Vehicle emissions from biodiesel contain less hazardous gases such as carbon monoxide, sulphur dioxide and aromatic content than the use of diesel petroleum. It also functions as an excellent lubricant and promotes the autonomy of motors. It's also more accurate than diesel with a greater flash-point [4, 5]. Other biodiesel advantages such as diesel include the mobility of liquidity, conveniently accessible, renewability, increased combustion efficiencies. Increasing NO_x emissions, greater cloud and pour points are all the disadvantages of biodiesel. Certain elements of diesel engines, particularly elastomers, might potentially be dissolved. The benefits of biodiesel still surpass the downsides which make it a preferred alternative to petroleum derived diesel. Given the increased viscosity of vegetable oils and other biologically produced fuel that causes the fuel to be burned improperly, it is necessary that they lower the viscosity that may be generated by mixtures [6, 7]. Table 14.1 shows the properties of diesel and biodiesel.

Table 14.1 Properties of biodiesel and diesel

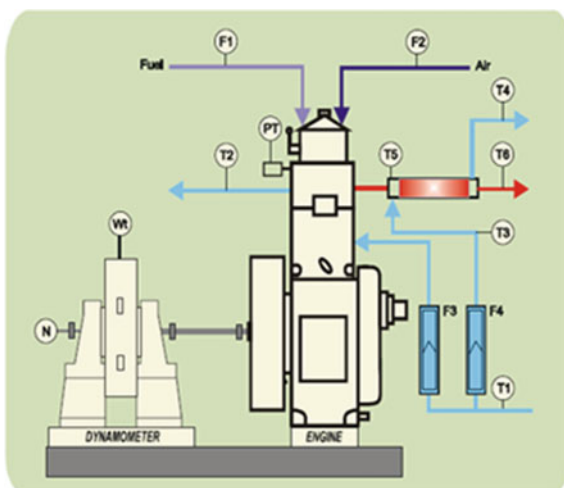
Name of the blend	Calorific value (kcal/kg)	Calorific value (kJ/kg)	Density (kg/m ³)
Biodiesel	10,650	44,580	813
Diesel	10,765	45,000	850

14.2 Experimental Setup and Experimentation

The experimental setup including the engine, subsystems, instrumentations and controls is described. The test rig was equipped with instruments for obtaining performance, emissions and in-cylinder pressure of the engine at different operating conditions. The product used is research engine test setup 1 cylinder, 4 strokes, multi-fuel (computerised) as shown in Fig. 14.1, The utilised engine is Type 1 cylinder, 4 stroke, water cooled, stroke 110 mm, bore 87.5 mm. Capacity 661 cc, and the diesel mode is set to Power 3.5 KW, Speed 1500 rpm, CR range 12:1–18:1. Injection variation is 0–25° BTDC Petrol mode with Power 4.5 KW at 1500 rpm, Speed range at 1200–1800 rpm, CR range at 6:1–10:1, Spark variation at 0–70° BTDC. The dynamometer is loaded with type of eddy current, water cooled, with loading unit and a universally joined propeller shaft. The air box is MS fabricated with orifice metre and manometer, and the fuel tank type is duel compartment with 15 L capacity. The purpose of gas analyzer (AVL Di 444) is to measure the relative volume of certain gases such as carbon monoxide (CO), carbon dioxide (CO₂), hydro carbons (HC), oxygen (O₂) and nitric oxide (NO) in the exhaust volume of certain motor vehicles. The initial warm up phase usually takes 7 min and after that leak check is carried out and HC residue test is performed. The configuration of gas analyzer is 13.2 mm for 1 or 2 measured values, 5.4 mm for 3, 4 or 5 measured values and 4.2 mm for 6, 7 or 8 measured values.

In a specific diesel gas, the AVL 437C smoke metric assesses the capacity of air pollution. Devices that shield light sources or cells are utilised to assess the characteristic impedance of the fluorescence emission track. The actual length is $0.430 + 0.005$ m, $0.430 - 0.005$ m. Light differentiation within the chamber on the photocell is minimised by the employment of matt black light traps, from reflections or diffused light. The light source is a mass of incandescent colour at 2800–3250 k.

Fig. 14.1 Schematic arrangement



A photocell is the recipient. When a totally opaque plate placed opposite the photocell is between 0.9 and 1.1 s, the reaction time of the electrical circuit shown by the time within the indicator reaches 90% in full scale. The temperature is kept at 100 ± 5 °C at $100-5$ °C in the measuring chamber by a suitable temperature sensor attached to the regulator.

14.3 Results and Discussion

14.3.1 Engine Torque

The results of the engine's torque, at different compression ratios, are shown in Fig. 14.2. As load increases torque increase linearly. It has observed that at compression ratio 18 diesel has more torque than B10 by 1.4% at full load.

14.3.2 Brake Power

B10 has lower CV than diesel so for the same amount of energy fuel consumption is more for B10 than diesel. As the fuel consumption increases brake power increases and it has observed from Fig. 14.3 that BP of B10 is greater than diesel at full load by 1.12% at CR16.

14.3.3 Effect of Air Fuel Ratio

The variation of *A/F* ratio with respect to load at different CRs is shown in Fig. 14.4, and it is observed that at CR18 B10 has more *A/F* ratio than diesel by 1.5% at full load.

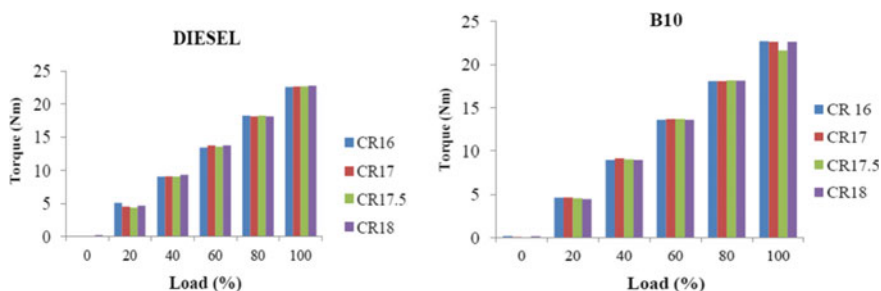


Fig. 14.2 Engine torque for diesel and B10

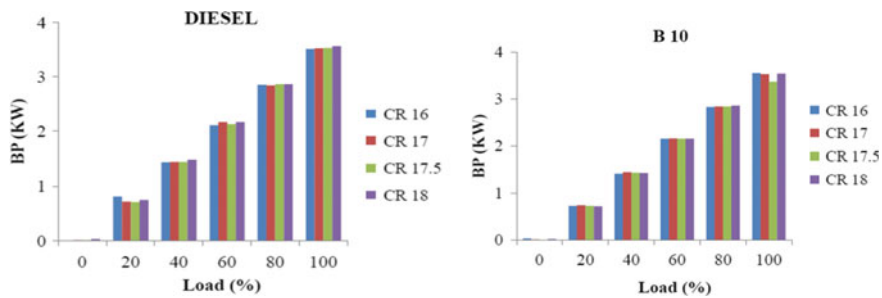


Fig. 14.3 Brake power for Diesel and B10

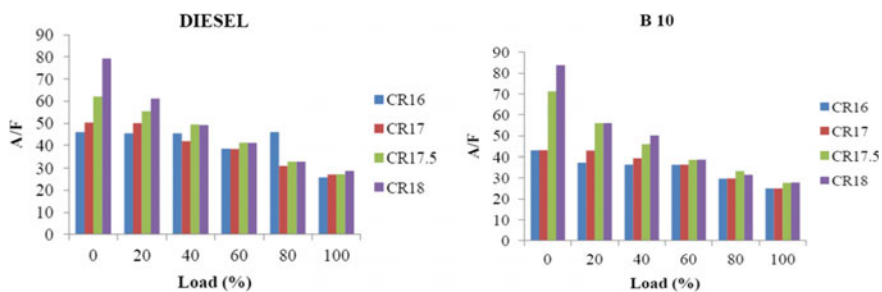


Fig. 14.4 Air fuel ratio for diesel and B10

14.3.4 Effect of Indicated Mean Effective Pressure

There is linear variation in graph for pure diesel from load to load. As CR increases the pressure inside the cylinder increases as shown in Fig. 14.5. SFC is more for B10, and it is observed from the following graphs at CR18 B10 has higher IMEP than diesel by 4.27% at full load.

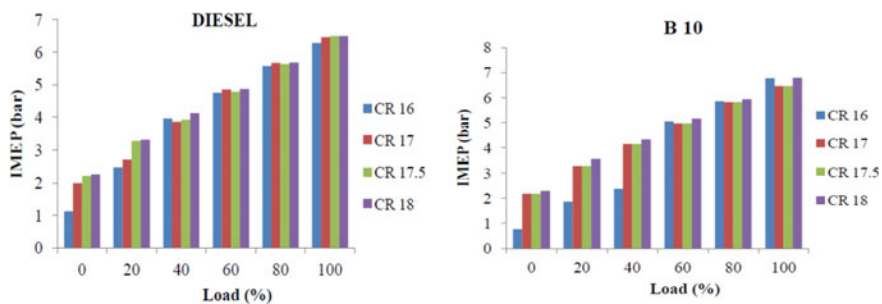


Fig. 14.5 Effect of IMEP on diesel and B10

14.3.5 Effect of Indicated Thermal Efficiency

Indicate thermal efficiency is the ratio of IP to total power it has observed from the Fig. 14.6 that at CR18 B10 has more indicate thermal efficiency than diesel by 5.95% at full load.

14.3.6 Effect of Mechanical Efficiency

Mechanical efficiency is defined as the ratio of BP to IP. As we know that B10 has less CV than diesel and its SFC will be less than the diesel. The amount of increase in IP is more than the increase in BP so total ratio will be less for B10 compared to diesel and it has observed from Fig. 14.7 that at CR17 diesel has more mechanical efficiency than B10 by 1.05% at full load.

14.3.7 Effect of Specific Fuel Consumption

Specific fuel consumption is more for diesel during the initial loading condition, and for B10 the specific fuel consumption is minimum when compared with diesel. As the load goes on increases, the specific fuel consumption remains almost constant for B10 and also for the pure diesel as shown in Fig. 14.8.

14.3.8 Effect of Volumetric Efficiency

During the initial loading B10 at CR17 has the maximum volumetric efficiency, whereas the pure diesel has the minimum volumetric efficiency at the initial

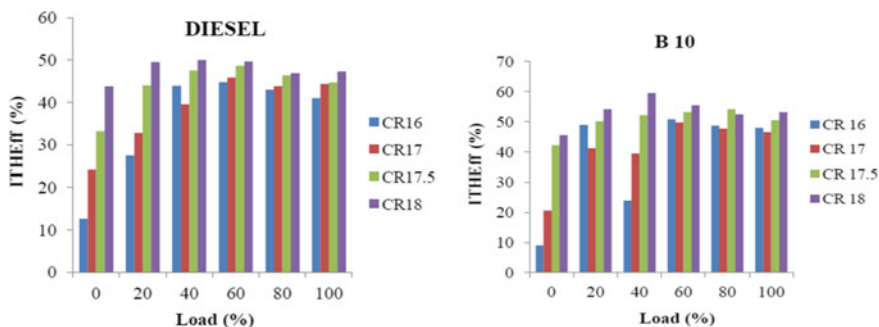


Fig. 14.6 Effect of indicated thermal efficiency

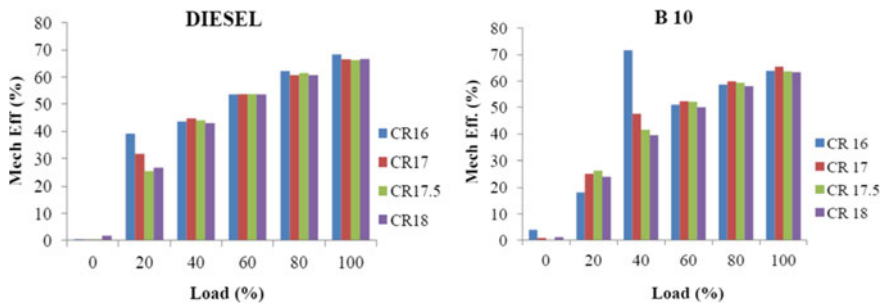


Fig. 14.7 Effect of mechanical efficiency on diesel and B10

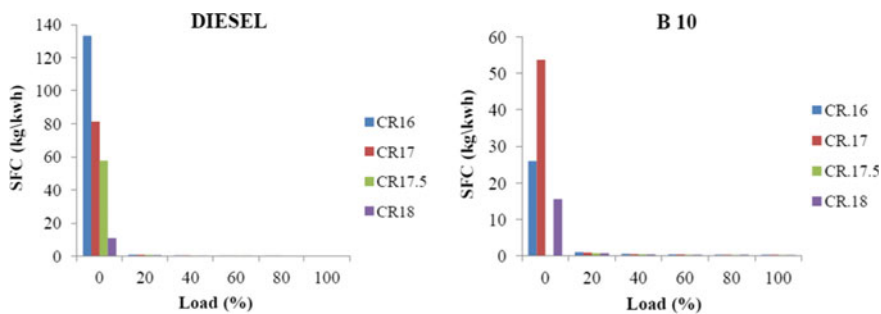


Fig. 14.8 Effect of SFC on diesel and B10

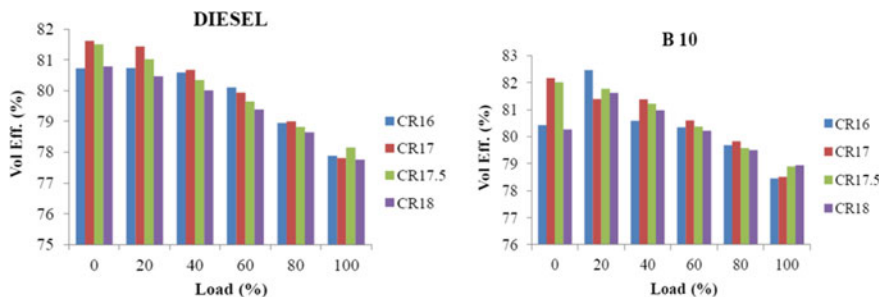


Fig. 14.9 Effect of volumetric efficiency on diesel and B10

loading. As the load increases the volumetric efficiency of B10 along with the pure diesel decreases. From Fig. 14.9, it is observed from the following graphs that B10 at CR18 has more volumetric efficiency than the diesel by 1.18% at full load.

14.3.9 Smoke

The smoke emissions for diesel fuel and B10 are almost constant throughout the process at various loads. The smoke emission for B10 is directly proportional to the load as shown in Fig. 14.10.

14.3.9.1 NO_x Emission

B10 produces lesser NO_x when compared to diesel at given loads as shown in Fig. 14.11. CR 16 has least NO_x than any other compression ratio. B10 produces lesser NO_x when compared to Bharat Standard (BS)-VI which is 0.080.

14.3.9.2 CO₂ Emission

At ¾ of peak load pure biodiesel produces maximum % volume of CO₂ emissions as shown in Fig. 14.12.

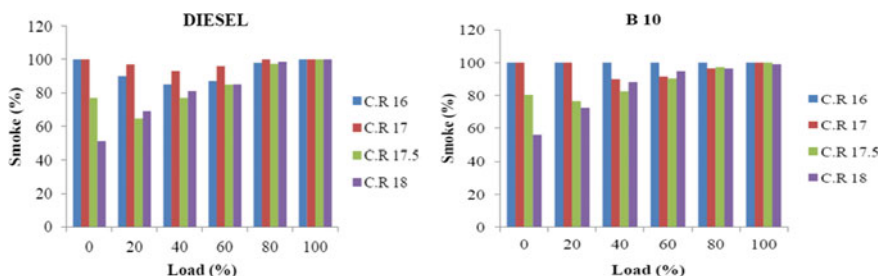


Fig. 14.10 Variation of smoke for diesel and B10

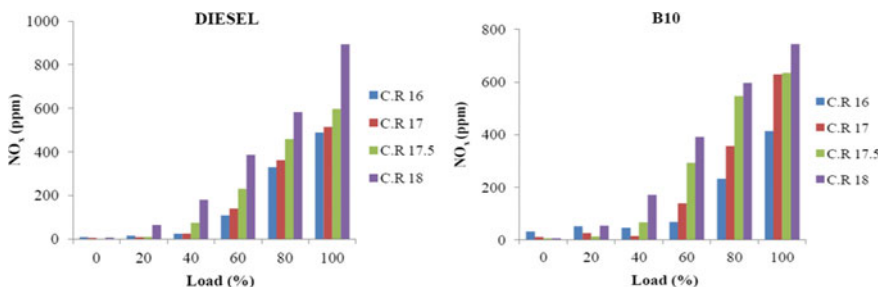


Fig. 14.11 Variation of NO_x for diesel and B10

14.3.9.3 CO Emission

CO emission is nearly equal for both diesel fuel and B10 at given loads. CR 18 produces least amount of CO than other compression ratios as shown in Fig. 14.13, which is also comparable low to the BS-VI (2020) which is 0.50.

14.3.9.4 HC Emission

B10 and diesel have maximum HC emission at lower load. At peak load B10 and diesel have almost same minimum HC emissions. Amongst all compression ratios CR 18 produces less amount of HC emissions as shown in Fig. 14.14, which is also comparable low to the BS-VI (2020).

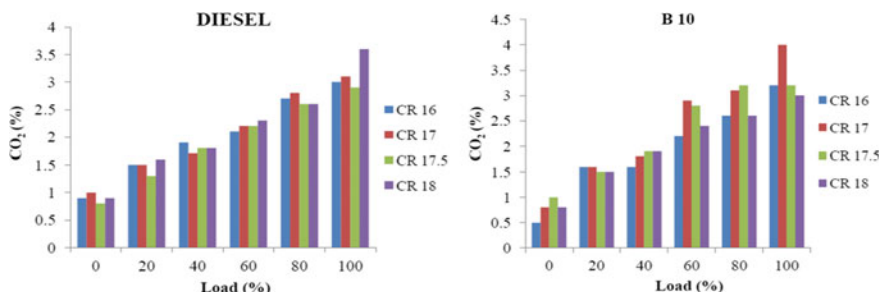


Fig. 14.12 Variation of CO₂ for diesel and B10

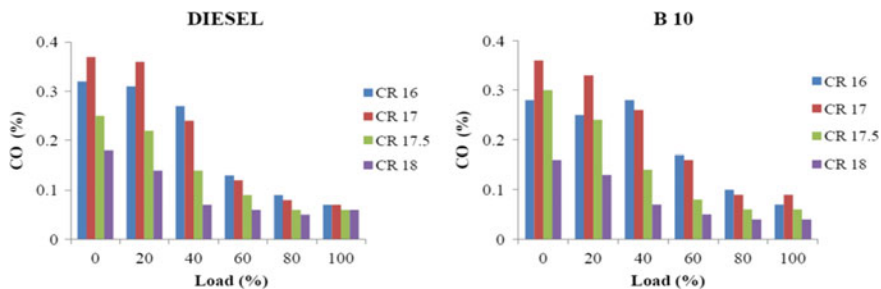


Fig. 14.13 Variation of CO emission with load for diesel and B10

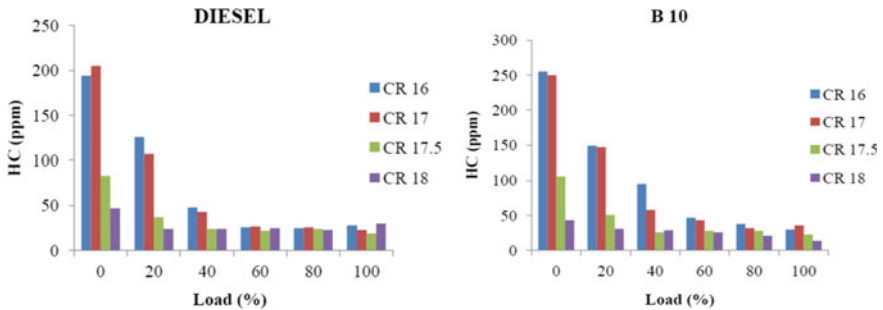


Fig. 14.14 Variation of HC emission with load for diesel and B10

14.4 Conclusions

This study uses *Jatropha* biofuel to evaluate motors' performance and emission testing at a steady speed and compare them with diesel fuel. Brake power for biofuel B10 is more compared to diesel at different compression ratios. The SFC value for biofuel B10 is less than the diesel this is because of lower heating value of *Jatropha* biofuel. Engine exhaust gas emissions CO, HC in B10 are less compared to Diesel because of the improved combustion due to the more oxygen content in biofuel. It is observed that at CR18 diesel has more torque than B10 by 1.4% at full load. Brake power is one of the main properties of performance, and it has observed from the above results that BP of B10 is greater than diesel at full load by 1.12% at CR16. Indicate power is the amount of energy produced inside the cylinder, and it is observed from graphs shown in the above chapters at CR18 B10 has higher IMEP than diesel by 4.27% at full load. Mechanical efficiency is the ratio of BP to IP and from graphs shown in above chapters, it has observed that at CR17 diesel has more mechanical efficiency than B10 by 1.05% at full load. Emissions mainly depend upon the content of oxygen and amount of combustion as B10 has more amount of O₂ it emissions are in less amount compared to diesel.

References

1. Suresh, M., Jawahar, C.P., Richard, A.: A review on biodiesel production, combustion, performance, and emission characteristics of non-edible oils in variable compression ratio diesel engine using biodiesel and its blends. *Renew. Sustain. Energy Rev.* **92**, 38–49 (2018)
2. Seraç, M.R., Aydın, S., Yılmaz, A., Şevik, S.: Evaluation of comparative combustion, performance, and emission of soybean-based alternative biodiesel fuel blends in a CI engine. *Renew. Energy* **148**, 1065–1073 (2020)
3. Baweja, S., Trehan, A., Kumar, R.: Combustion, performance, and emission analysis of a CI engine fueled with mustard oil biodiesel blended in diesel fuel. *Fuel* **292**, 120346 (2021)

4. Nagappan, B., Devarajan, Y., Kariappan, E., Philip, S.B., Gautam, S.: Influence of antioxidant additives on performance and emission characteristics of beef tallow biodiesel-fuelled CI engine. *Environ. Sci. Pollut. Res.* **28**, 12041–12055 (2021)
5. Karishma, S.M., Dasore, A., Rajak, U., Verma, T.N., Rao, K.P., Omprakash, B.: Experimental examination of CI engine fueled with various blends of diesel-apricot oil at different engine operating conditions. *Mater. Today: Proc.* (2021)
6. Ellappan, S., Rajendran, S.: A comparative review of performance and emission characteristics of diesel engine using eucalyptus-biodiesel blend. *Fuel* **284**, 118925 (2021)
7. Ajith, B.S., Math, M.C., Patel, G.M., Parappagoudar, M.B.: Engine performance and exhaust emissions of *Garcinia gummi-gutta* based biodiesel–diesel and ethanol blends. *SN Appl. Sci.* **3**(5), 1–11 (2021)

Chapter 15

Evaluation on the Diseased Damage Grading Model of the Fresh Destemmed Chilli Fruits



Quoc-Khanh Huynh, Chi-Ngon Nguyen, Jeng-Rong Ho,
Hong-Phuc Vo-Nguyen, and Van-Cuong Nguyen

Abstract An automatic grading system is necessary for fresh destemmed chilli fruits. In previous works, a CNN model has been built to identify the diseased damages that appeared on the fruit's body, and a flipping mechanism has been designed to entirely recognition by rotating the fruits. This work focussed on evaluating and implementing the CNN model to classify the diseased damaged ones on the grading model. The training data set was updated to enhance the success rate of the recognition process. Tests were carried out on 1320 fruits, in which there were 920 non-damaged fruits and 400 damaged fruits. The total testing time is 6600, and the success grading rate was found out at an average of 92%. In addition, the limitation and the causes of errors were also clarified to determine the improvement for future works.

Q.-K. Huynh · C.-N. Nguyen · V.-C. Nguyen (✉)
College of Engineering Technology, Can Tho University, Can Tho City, Vietnam
e-mail: nvcuong@ctu.edu.vn

Q.-K. Huynh
e-mail: hqkhanh@ctu.edu.vn

C.-N. Nguyen
e-mail: ncngon@ctu.edu.vn

J.-R. Ho
Department of Mechanical Engineering, National Central University, Taoyuan City, Taiwan,
Republic of China
e-mail: jrho@ncu.edu.tw

H.-P. Vo-Nguyen
School of Medicine, Can Tho University of Medicine and Pharmacy, Can Tho City, Vietnam
e-mail: vnphuc@ctump.edu.vn

15.1 Introduction

The destemming process will increase the fresh chilli product's value in the agriculture product chain [1, 2]. Several destemming processes have been designed and tested [3–5], and it is required to develop an automatic grading system for enhancing the quality of the processing processes. Computer vision and neural networks were recently employed to identify objects and output the appropriate signals to control the actuators [6–9]. They are proved to have strong ability in the fruit grading application [10].

In a previous study, a CNN model was built to identify the damages that appeared on the fresh chilli fruit and obtained a success rate of 90% [11]. Types of damages that could be identified are shown in Fig. 15.1. Because the camera can capture from one direction of view, so a flipping mechanism has been designed to grip and rotate the fruits including damages from downside to upside in order to check the entire body [12]. This mechanism obtained the average success flipping rate at 96.3% with the fruit broken rate at approximately 2%. Both the CNN model and the flipping mechanism have been tested independently. Due to various influencing factors during operation, the performance of the recognition model when embedded in the flipping system will be affected and tend to decline. Therefore, it is required to be evaluated in detail to adjust and ensure acceptable performance.

This study focussed on evaluating the classification ability of the CNN model in the flipping mechanism. The CNN model was also re-trained to match the current working condition, and also to enhance the identification ability in comparing to previous work described in [11]. In addition, this contribution is also a technical solution to classify the fresh destemmed chilli fruit, reduce costs in comparison with manual grading, and improve the agricultural product quality for Mekong Delta farmers. Tests were carried out to examine the working of the grading model.

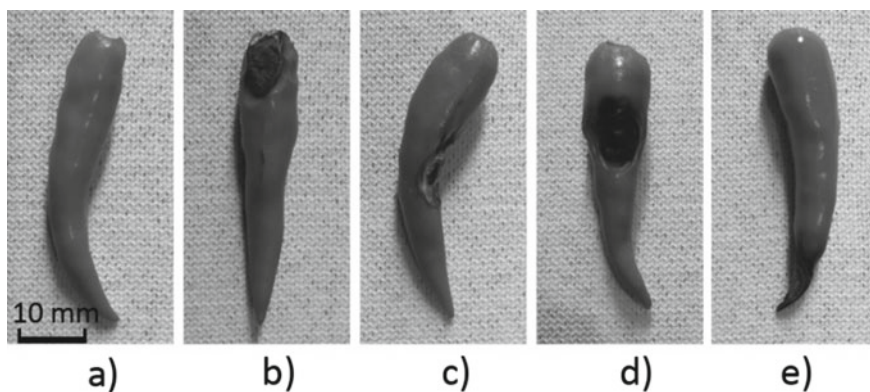


Fig. 15.1 Damaged and non-damaged fruit types **a** Non-damaged, **b** head-damage, **c** side-view-damage, **d** mid-damage, **e** tail-damage

15.2 Materials and Methods

15.2.1 The Grading Model

This grading model had been introduced in [12]. The description is reused here in Fig. 15.2. It consisted of a timing belt, a flipping roller, and some other parts. The timing belt was controlled and rotated by a stepper motor, whilst the flipping roller was driven by the friction between its outer diameter and the outer surface of the timing belt. Grooves on the flipping roller were designed in form of an involute curve.

The general view of the grading model is described in Fig. 15.3. To obtain a clear observation of the model when capturing the general view, the cover which ensures the balance of light was removed.

Fig. 15.2 Working principle of the grading model

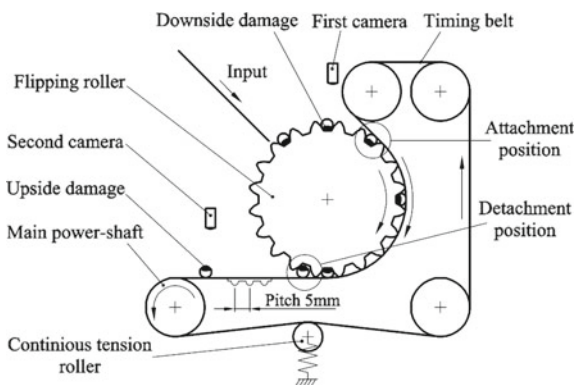
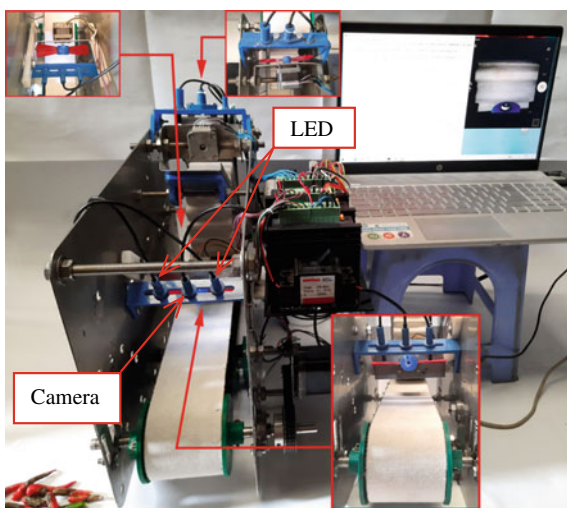


Fig. 15.3 General view of the grading model



To reduce the reflectivity, a white flexible adhesive tape (Urgo trademark) was used to overlay the outer surface both of the timing belt and the flipping roller. As shown in Fig. 15.1, the overlay layer played a role as a white background with less light reflection.

15.2.2 CNN Model Training

The CNN model is presented in Fig. 15.4. A 32×64 pixel grayscale image was transformed to a 2048×1 vector through the convolution layers (Conv32, 64, 128, 256) and a flatten layer, then it was inputted to the neural network. The neural network contained one input layer with 2048 neurons, two hidden layers with 90 neurons in each one, and one output layer with 3 neurons. Because the main target was to classify the damaged fruits, so the number of output neural was decreased from six in previous work to three in this work. They correspond to three cases that occurred in the system:

- O_0 : Damage. CNN returns this output if the fruit is found and damages were recognized on its body;
- O_1 : Non-damage. Fruit is found but there aren't any damages on the body;
- O_2 : Non-data. There is no fruit found on the target area of the camera.

Both training and validation data set were updated by adding images captured when fruits were placed directly on the real system as in Fig. 15.1.

The original data set which including a total of 22,860 images was diversified by 4 methods: enlarge, stretch, rotate 45° and mirror. The final one contains 114,300 images in the size of 32×64 pixels.

The CNN structure is shown in Fig. 15.4. The training data set and parameters are presented in Table 15.1. The training process was done online by Jupyter notebook tool. It was stopped at 70 epochs because after that the training and validation accuracy did not improve significantly.

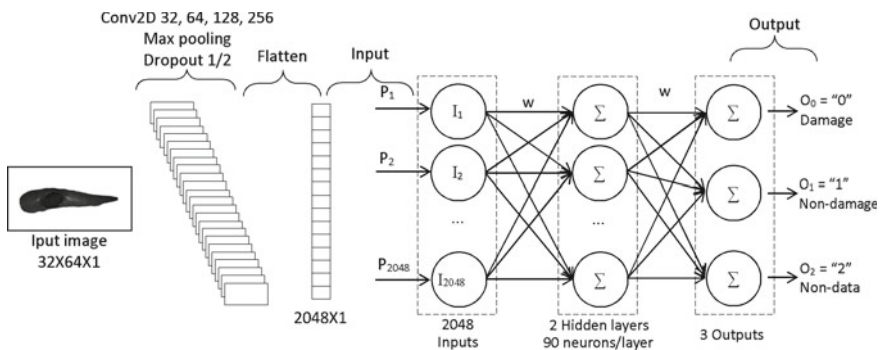


Fig. 15.4 CNN model

Table 15.1 CNN model parameters

	Non-fruit (Non-data)	Non-damaged	Damaged fruit
No. of training images	6150	5034	5146
No. of validation images	2460	2012	2058
Image diversify method	Enlarge, stretch, rotate 45°, mirror		
Total images in data set	114,300 Gy-scale images in size of 32 × 64 pixels		
Training tool/Training time	Jupyter notebook (online)/9 h 30 min		
No. of epochs	70		
Batch size	115		

15.3 Results

15.3.1 Testing Method

A simple code was written to test the grading model, and the testing flowchart is shown in Fig. 15.5. After booting in Python, connecting to Arduino Uno R3, and powering the grading system, the start position of the flipping roller was set by sending “0” or “1” to Arduino until the camera could observe the target area in the middle of the roller’s groove. Whilst the first and the second pushing motor were adjusted by sending “3” and “5” until they approach the appropriate positions.

After setting the start positions, the “S” key was inputted to begin the identification and grading process. The main motor rotates sequentially 50 mm each step to feed chilli to the target area of the cameras. Two images were captured by the first and second cameras. Then, they were converted to grayscale, flattening to the one-column vector, and inputted to compare with the pre-defined *h5* model. If the return value of the image identification was “0”, the damages were recognized and the corresponding pushing motor was activated to push chilli away from the conveyor. Otherwise, the fruit is kept on and moved forward.

Testing fruits are chosen to have a smooth, less curved shape, have a length within 50 ± 5 mm, and a maximum diameter within 9 ± 1 mm.

Two adjustable LED lights were attached beside each camera to fully self-illuminate. In addition, a cover was also added to obtain stable light balance, avoiding outside ambient light. When capturing the general view in Fig. 15.3, the cover was removed for easy viewing inside components.

The CNN model in this study was originally designed and trained to recognize the damaged red chilli fruits. However, in real production, there is a certain percentage of green ones which is also necessary to be classified, so the experiment was expanded to evaluate the performance of the model.

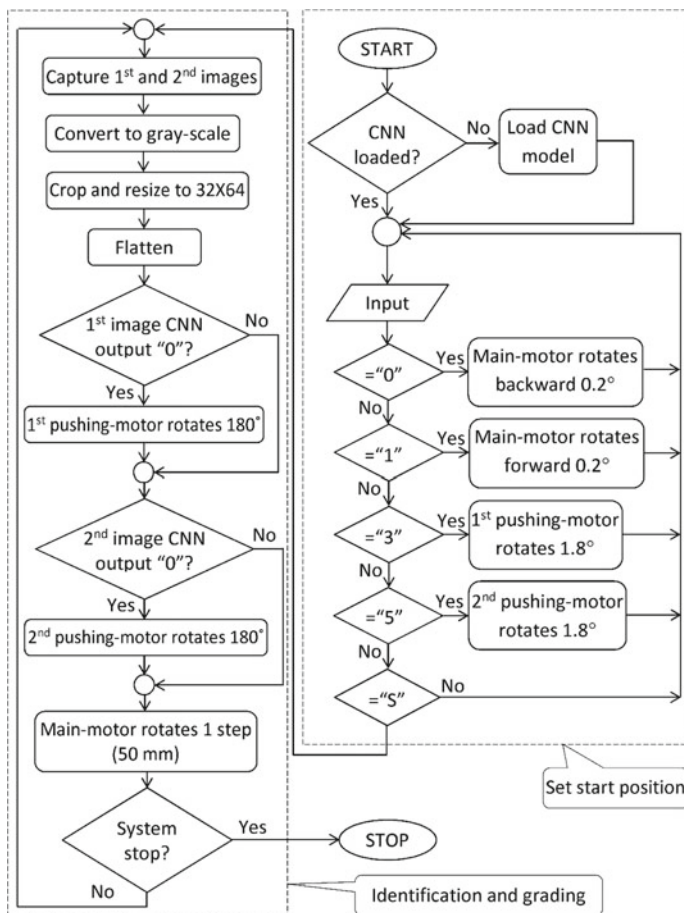


Fig. 15.5 Testing process flowchart

15.3.2 Test Results

The test was carried out in a total of 920 red and 400 green chilli fruits. Each one was tested 5 times, and the total of the test times is 6600.

Chilli is fed manually one by one into a trough, in every batch of 20 fruits. The results are checked at the output. The identification is called “Success” if the damaged fruit is pushed off and the non-damaged one remains on the conveyor belt at the output. Conversely, if the non-damaged fruit is pushed off or the damaged one is left on the conveyor, the identification is called “Fail”. Before running the test, the start position is set as in the video at <https://youtu.be/wN42u4m2Vmw>. A test of 20 fruits is shown at <https://youtu.be/4syjzoGU8Hg>. Test results are recorded and presented in Table 15.2.

Table 15.2 Test results

		No. of fruit	Test/ Fruit	No. of test	Success	Success rate (%)	
Red fruits	Damaged	470	5	2350	2234	95.06	92.87
	Non-damaged	450	5	2250	2038	90.58	
Green fruits	Damaged	200	5	1000	913	91.30	90.05
	Non-damaged	200	5	1000	888	88.80	

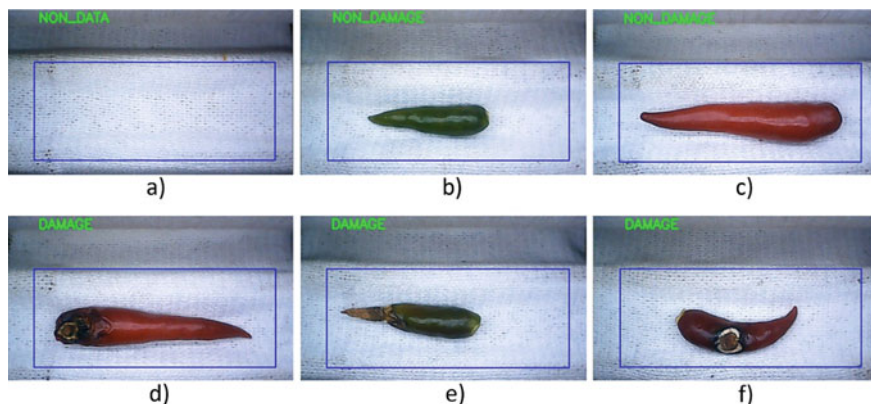


Fig. 15.6 Testing results of different types of fruit **a** No fruit, **b** non-damage green, **c** non-damage red, **d** head-damage, **e** tail-damage, **f** mid-damage

The success rate was found at an average of 95.06% in red damaged fruits, higher than 90.58% in red non-damaged ones. This difference was also found with a little lower in the green group. This could be explained by the misidentification from the concave and convex area on the non-damaged body to be the damaged area.

The average success rates in both damaged and non-damaged green chilli were found at 90.05%, lower than 92.87% in the red group. And the lowest recognition rate was 88.8% appeared in the green non-damaged group.

The screenshot of the identification process was captured and presented in Fig. 15.6 with return values in the text line at the top of the screen. Figure 15.6a was taken when no fruit was found, Fig. 15.6b, c for non-damage green and red chilli and Fig. 15.6e, f for damaged fruits.

15.4 Discussions

Because the success rate in the group of damaged fruits is higher than that in the non-damaged ones, the sorting method that should be used is to detect the damaged chilli fruits and push them away from the conveyor belt. This will ensure the highest quality of the finished product.

There were approximately 4% of cases, the motors rotated but the fruit was not pushed away from the belt. This is because the actuator didn't work properly, so these cases were also considered as success identification. This problem could be solved by enlarging the falling gap of the fruits.

In the previous study, the average recognition success rate was 90% [11], and the effective flipping rate was 96.3% [12], so the overall success rate was 86.67%. This study has improved the CNN model and enhanced the overall success rate to 92.02%.

The rotary pushing mechanism required space for equipment installation right above the fruit, thus the camera must be inclined at a certain small angle. This would lead to a small portion of the fruit's body being invisible and unrecognized. A linear pushing mechanism such as a pneumatic cylinder could overcome this problem.

In this identification test, the distance between adjacent fruits (or the outside pitch of the flipping roller) was chosen at 50 mm—far enough to avoid the impacts of the pushing mechanism. However, this would reduce productivity, and need to be considered in further improvement.

Although this study focussed on classifying red ripen chilli fruits, the experiment was also expanded with green ones to meet the diverse requirements of the market.

15.5 Conclusions

A CNN model has been built and improved to identify the damages caused by diseases in the fresh destemmed chilli fruits. And a grading model has been developed which allows identifying the whole fruit's body by rotating and flipping them. The experiments showed that the CNN model has a strong ability in recognition, and the overall grading success rate was up to 92.02%. This grading model is efficient, useful, and has an acceptable level of success. The real-time and continuous working conditions will be carried out in further studies to meet the requirements of the industrial processing process.

Acknowledgements Quoc-Khanh Huynh was funded by Vingroup Joint Stock Company and supported by the Domestic Master/Ph.D. Scholarship Programme of Vingroup Innovation Foundation (VINIF), Vingroup Big Data Institute (VINBIGDATA), code VINIF.2019.TS.33 and VINIF.2020.TS.109. The authors also would like to thank Thanh-Binh Bui, Thanh-Hieu Do, Van-Luan Khuu, Minh-Vuong Le, Dr. Quoc-Bao Truong, Dr. Chanh-Nghiem Nguyen, and Dr. Huu-Cuong Nguyen for their enthusiastic participant in this research.

References

1. An, N.-T.-T., Loc, V.-T.-T.: Financial efficiency of chili farmers in the Mekong delta. *Can Tho Univ. J. Sci.* **48D**, 87–95 (2017)
2. Loc, V.-T.-T.: Assessment of agri-product value chains in the Mekong delta: problems and solutions. *Can Tho Univ. J. Sci.* **2**, 100–111 (2016)

3. Kodali, N.B.: System and method of processing procedure. USPTO, Patent No. US9185930B2 (2015)
4. Herbon, R., et al.: Engineering a machine to remove stems from chile peppers-a critical need for the new Mexico chile industry. In: American Society of Agricultural and Biological Engineers Annual International Meeting, pp. 775–785 (2009)
5. Herbon, R.P., et al.: Designing a high volume chile de-stemming machine. In: ASABE Meeting Presentation. ASABE (2010)
6. Nturambirwe, J.F.I., Opara, U.L.: Machine learning applications to non-destructive defect detection in horticultural products. *Biosys. Eng.* **189**(1), 60–83 (2020)
7. Tang, Y., et al.: Recognition and localization methods for vision-based fruit picking robots: a review. *Front. Plant Sci.* **11**(510), 1–17 (2020)
8. Taujuddin, N.S.A.M., et al.: Detection of plant disease on leaves using blobs detection and statistical analysis. *Int. J. Adv. Comput. Sci. Appl. (IJACSA)* **11**(8), 5 (2020)
9. Tunio, N., et al.: Detection of infected leaves and botanical diseases using Curvelet transform. *Int. J. Adv. Comput. Sci. Appl. (IJACSA)* **10**(11) (2019)
10. Tian, H., et al.: Computer vision technology in agricultural automation —a review. *Inf. Process. Agri.* **7**(1), 1–19 (2020)
11. Quoc-Khanh, H., et al.: Identification of the damages caused by diseases on fresh destemmed chili fruits. In: The 12th IEEE International Conference on Knowledge and Systems Engineering, pp. 126–130. IEEE (2020)
12. Quoc-Khanh, Huynh et al.: Design of Chili Fruit Flipping Mechanism for Identification of the Damages Caused by Diseases. In: Choudhury, S., Gowri, R., Sena Paul, B., Do DT. (eds) *Intelligent Communication, Control and Devices. Advances in Intelligent Systems and Computing*, vol. 1341. Springer, Singapore (2021)

Chapter 16

On the Study and Analyses of “Vertical Farming—The Future of Agriculture” via Various Hydroponic Systems



Tanishi Mathur and Senthil Arumugam Muthukumaraswamy

Abstract With every passing year, there is an exponential rise in human population. Due to this, the challenge of not having enough cultivable land is becoming a rising issue. It is also predicted that most of the world’s population that currently lives in rural areas will have shifted into urban cities. This will lead to an increase in urbanization and a further reduction in arable lands for agricultural purposes. As a solution to these issues, this paper proposes the idea of vertical farming and Hydroponics in specific. Hydroponics uses a fraction of the space required for traditional farming, uses 90% less water, and can reap practically organic produce all year round. This paper reviews the process of vertical farming, its benefits, and its different types. A detailed methodology that can be adopted to create a hydroponic system has been suggested. In this paper, Lettuce, Basil, and Kale have been used as primary examples.

16.1 Introduction

Scientists predict that by the year 2050, the world’s population will have reached 9.7 billion people out of which 80% of them will be living in urban cities [1]. It has also been reported that in the last 40 years the earth has lost about a third of its arable land, largely due rise in urbanization and industrialization. One of the biggest challenges faced by the governments of different countries is to find an efficient and sustainable method to meet the growing demand for food within these circumstances [2].

It was reported that in 2020, 690 million people were left hungry, and this number is expected to keep rising in the coming years [3]. Furthermore, with the increasing effects of global warming and climate change, regions that were previ-

T. Mathur (✉) · S. A. Muthukumaraswamy
Heriot-Watt University, Dubai, United Arab Emirates
e-mail: mt107@hw.ac.uk

S. A. Muthukumaraswamy
e-mail: m.senthilarumugam@hw.ac.uk

ously ideal for the growth of certain crops no longer have the climactic conditions to cater to the growth of those specific crops. The most practical and realistic method to integrate agriculture and cultivation into modern cities are by adopting vertical farming and making it a core part of any city's planning and structure.

16.2 Literature Review

16.2.1 Vertical Farming

Vertical farming is the process of growing fruits and vegetables on vertically inclined surfaces for agricultural purposes. This method uses controlled environment agriculture (CEA) technology to operate. CEA consists of artificial control on light, humidity, and temperature. It artificially creates the optimum conditions for plant growth using new and innovative technology. Vertical farms are highly diverse in nature as they can be massively scaled up by installing them in buildings and empty warehouses or be scaled down by installing them in shipping containers or PVC pipes. The main purpose of vertical farming is to bring agriculture into cities, while using a fraction of the land required otherwise [2].

There are three versions of vertical farming that can be seen today. The first and most widely used version refers to the construction of tall structures with several levels of growing beds, often lined with artificial lights. Such farms have been springing up all over the world, either in new structures or old repurposed buildings. The second version is smaller in scale and is done on rooftops of buildings or warehouses. The third version is the visionary multi-story building proposals. Many have proposed this idea over the past decade; however, none of them have been physically built to date [4].

Vertical farming is still considered to be a relatively new concept and is not accepted very widely. However, many countries such as the USA, Singapore, China, and UAE have started investing in it as they recognize the potential of this innovation.

16.2.2 Benefits of Vertical Farming

Vertical farming is a fast-growing concept due to its modern approach and large number of benefits. The major advantages in adopting vertical farming are as follows:

- It provides food security in a way horizontal farming could never achieve. It gives higher produce in less area, while using up to 90% less water as compared to traditional methods.
- Being fully indoor it remains unaffected by climate change and global warming. Any kind of reep can be produced at any time of the year by artificially recreating the required environment.

- With the population growing at an exponential rate, it is the perfect way to shift agriculture to cities, while using a mere fraction of land required otherwise.
- These crops would be grown in a soilless and controlled environment without the use of pesticides or insecticides making them effectively organic and a better choice for human consumption.
- Traditional farming methods do more harm to the ecosystem as compared to good. Vertical farming can not only end that but also help reduce CO₂ emissions.
- It is great for economies of countries that lie in hot or arid regions as they can produce crops locally giving rise to a new industry in their country.

For these reasons, it can be justified that vertical farming is an extremely powerful tool in the agricultural sector moving forward [4].

16.2.3 Methods Used in Vertical Farming

Vertical farming is an extremely vast topic with many different methods and systems available within it. Each method has its own set of benefits, challenges, and requirements. The most adopted vertical farming methods seen today are hydroponics, aquaponics, and aeroponics.

16.2.3.1 Hydroponics

Hydroponics is the process of growing plants in a soilless media. A simple hydroponic system consists of two levels. The top level holds the plant, and the bottom level consists of the nutrient-rich water reservoir. The water from the reservoir is periodically pumped to the plant roots and oxygenated according to the plant requirements.

Research on hydroponics began to develop in the 1800s, as botanists and plant nutritionists started working on determining efficient methods to produce healthy food without relying on access to natural resources [5].

The concept of growing plants in water isn't very new; however, its' commercial introduction and acceptance are very recent [6]. Hydroponics is a relatively low-maintenance technique that gives a good yield. It is not a very labor-intensive method of growing. It requires no external pesticides or insecticides as the whole system is soilless in nature. Hydroponics uses 90% less water as compared to traditional farming methods and provides an easier method to control and monitor EC and PH levels of plant beds [7].

16.2.3.2 Aquaponics

Aquaponics is a hybrid bio-system that integrates aquaculture (fish farming) and hydroponics. This method uses nutrient-rich waste from fish tanks to fertilize

hydroponic production beds. In turn, the hydroponic beds act as biofilters and remove chemicals such as nitrates and ammonia from the fish water [4]. Aquaponics is a self-sufficient system that can help combat the drawbacks of hydroponics. However, it is still at an experimental stage and is not very widely used for commercial purposes as aquaponic systems are quite complex to build and require intensive management [8].

With all the benefits aquaponics brings it is, however, still in an experimental stage and is not very widely used for commercial purposes. This is because aquaponic systems are quite complex to build, require intensive management and skilled labor [9].

16.2.3.3 Aeroponics

Aeroponics is a huge step forward from hydroponics. It is defined as an enclosed air and water/nutrient ecosystem that facilitates rapid plant growth with little water, direct sunlight, and without soil or media. The main difference between hydroponics and aeroponics is that hydroponics functions within a soilless (water-based) media and aeroponics require no media. Plants grown by this method are misted or sprayed with the required amounts of water. It uses 95% less water than is normally required. In this process, plants grow upward with their roots suspended in the air. This technique is still in the research phase. It is currently being done on a small scale; however, a lot more research and experimentation are required before we can see this method become a part of society [4].

16.3 Methodology

It's quite clear from the explanations above that although hydroponics isn't a perfect system its positives quite strongly outweigh its negatives. It is the most widely used vertical farming system today. Aquaponics and aeroponics are both great techniques and help combat a couple of the challenges that may arise in hydroponics. However, they are unresearched fields that require more time, experimentation, and skilled labor. Therefore, in Sect. 16.3 of this paper, we have discussed the methodology behind creating a hydroponic system. Table 16.1 explains the effect of each parameter on the growth of plants.

16.3.1 *Choice of Crop*

The starting point for any hydroponic system is deciding on which crop or plant needs to be grown. All other factors such as temperature and humidity conditions, soil pH, and type of setup are determined by this. For the growth of any crop, three

Table 16.1 Effect of various parameters on plant growth

Parameter	Effect on plant growth
Type of system	The appropriate system can effectively speed up the growth of plants
Lighting	Optimum lighting is required for plants to conduct photosynthesis at the required rate
Temperature	Inappropriate temperatures can cause plant damage or even prevent germination
PH value/Electrical conductivity	Measuring these values allow growers to efficiently monitor plant growth and provide them with the right amount of nutrients

things need to be kept in mind, namely, environmental needs, reproductive cycle, and harvesting. Hydroponics works extremely well when growing leafy greens, herbs, certain fruits, and vegetables. In this paper, we have specifically focused on the requirements to create an ideal environment for Lettuce, Basil, and Kale. The comparison between the growth cycles for these crops has been presented in Table 16.2 [10].

16.3.2 Type of Hydroponic Systems

Once the plant has been selected, it is important to identify which type of system can best fit its requirements. This is also determined by how complex a system is being built. The most used hydroponic systems are Deep Water Culture (DWC), Nutrient Film Technique (NFT), Deep Flow Technique (DFT), and Ebb and Flow.

- Deep Water Culture (DWC)—This is the most basic type of hydroponic system, in which well-rooted plants are mounted on net pots on a floating plate in the water reservoir. The net pot is filled with a substrate to stabilize the plant. The roots hang directly in a nutrient solution which, with the assistance of an air pump, is well oxygenated. Plants in this system remain unaffected, even in the event of a power failure [11].
- Nutrient Film Technique (NFT)—This system is characterized by a permanent flow of nutrients in a thin “film” around the roots. A pump transports the nutrient solution on an inclined plane, where the roots lie and are continuously watered and supplied with nutrients which helps prevent the accumulation of nutrients. No substrate is used to provide roots with unhindered access to water [11].

Table 16.2 Crop growth cycle

Crop	Germination	Seedling	Transplant
Lettuce	Day 1–7	Day 7–10	Day 42–56
Basil	Day 1–14	Day 14–21	Day 56–77
Kale	Day 1–7	Day 7–14	Day 42–56

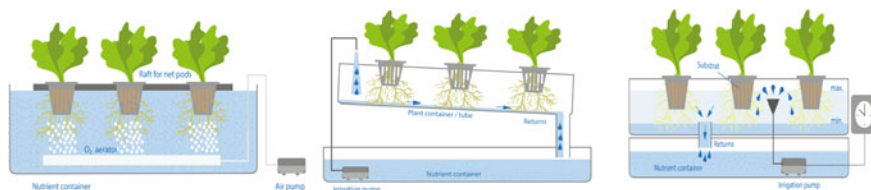


Fig. 16.1 Deep water culture, nutrient film technique and ebb and flow systems

- Deep Flow Technique (DFT)—This system is just a variant of NFT. Instead of the thin nutrient film, this system surrounds roots with approximately 4 cm high-nutrient solution. The advantage of this system is that in the case of a power outage the roots are not left dry [11].
- Ebb and Flow—This system uses a pump to flood the plant level with nutrient solution. On switching off the pump, the excess water is returned to the reservoir via the overflow. To prevent plant roots from drying out, a residual amount remains in the top layer. With the help of a timer, the ebb-tide rhythm can be altered according to the plants' requirements. The system is simple and requires little care [11] (Fig. 16.1).

For the growth of herbs such as basil and green leafy vegetables such as lettuce and kale growers usually opt for DWC, NFT, or DFT. However, even among these methods, DFT is superior. This is because DFT overcomes the challenges of NFT by protecting the plants in the event of a power failure and unlike DWC, DFT allows the roots access to air and does not drench them in water completely.

16.3.3 Lighting

Different plants have different lighting requirements. Some hydroponic systems use both natural and artificial light for plant growth and some use artificial lighting alone. The lighting used in such systems is known as grow lights. Grow lights provide a spectrum that is more tailored to the needs of the plants being cultivated. Depending on the type of plant being cultivated, the stage of cultivation, and the photoperiod required by the plants the manufacturing of grow lights can be adjusted [12].

Plants require sunlight for photosynthesis and proper growth. Complex compounds in leaves known as chlorophyll-a and chlorophyll-b only absorb blue and red light from the sun for photosynthesis. Due to this reason when providing plants with artificial lights, they only emit blue and red light. Table 16.3 shows the effect of different ratios of blue and red light on different aspects of plant growth [13].

Grow lights typically come in different ratios of red and blue LEDs. Different ratios help contribute to different aspects of a plants' growth. The following table

Table 16.3 Effect of different grow light ratios on plant growth

Ratio	Germination energy (%)	Germination rate (%)	Chlorophyll content (Scores)
Type of system	47	89	22.8
Lighting	42	81	19.5
pH value/Electrical conductivity	57	88	20.7

shows the effect of different ratios of blue and red light on different aspects of growth in Lettuce, Basil, and Kale (the effect is very similar on all three).

16.3.4 Temperature

One of the main factors that affect plant growth, be it traditionally or using hydroponics is temperature. Each plant and crop require a certain temperature for it to be grown and harvested. Temperatures in hydroponic systems can be controlled by the use of miniature fans. More complex systems have chiller and HVAC systems of their own. These temperatures can be maintained and controlled by creating an automated system using different sensors within the system itself. Table 16.4 shows the temperature requirements for Lettuce, Basil, and Kale, respectively.

16.3.5 pH of Nutrient Solution

One of the main factors that need to be monitored and controlled constantly, while growing plants is the pH of the nutrient solution. pH is a measure of acidity, which matters because nutrients are available at different levels of acidity. pH is represented by a scale of 0 to 14, where 0 is most acidic and 14 is most basic. pH is short for “potential hydrogen” because hydrogen ions (H⁺) and hydroxide ions (OH⁻) are what makes a solution acidic or basic in nature.

pH levels inform growers of the nutrient availability, hardness, and deficiencies in the water source. For optimal plant growth range within which plants are grown is 5.5–6.5 as most essential nutrients required for plant growth lie in that range [14].

One of the biggest advantages of hydroponics is the fact that there is minimal nutrient wastage. Hydroponics is a closed-loop system in which the solution is constantly circulated throughout the system. The solution is replenished with nutrients periodically and is usually changed once every 2–3 weeks. It is also extremely easy to dispose of expired nutrients as they are simply made up of chemicals and other elements which cause no harm to the environment.

Table 16.4 Temperature requirement for different plants

Crop	Temperature range (F)	Ideal temperature
Lettuce	47–75	65
Basil	55–80	70
Kale	45–85	65

Table 16.5 EC and PPM for different plants

Crop	EC (S/m ² /mole)	PPM
Lettuce	1.0–1.6	500–800
Basil	1.4–2.4	700–1200
Kale	1.6–2.5	800–1250

16.3.6 Electrical Conductivity

Electrical conductivity (EC) is a measure of electric current that can be passed through water. Pure water has zero EC. When nutrients are added to water for the purpose of hydroponics its EC increases. In moderation, EC helps create an osmotic pressure within plants which allows them to retain water for longer periods. However, if the EC is too high the plants become limp and are unable to absorb enough water causing them to get dehydrated. Due to this reason, it is extremely important to always monitor and control EC value. EC is commonly converted into a count of the ions in the water using parts per million. This is done by converting the EC into a value based on the ions contained in the solution. Table 16.5 describes the required EC levels for Lettuce, Basil, and Kale [15].

16.4 Conclusion

The concept of vertical farming and its benefits have been discussed in this paper. The different methods to grow in vertical farms have been described. A deep dive was taken into the methodology behind creating the ideal environment for a hydroponic system. It consists of Choice of Crop, Type of System, Lighting, Temperature, pH of nutrient solution, and Electrical Conductivity. Each factor has its own role to play and varies with different types of plants. Hydroponics and vertical farming are the future of agriculture. Its efficient use of space and materials makes it extremely sustainable and beneficial for mankind.

References

1. 5 Reasons why vertical farming is the future of humankind. In: Earth Buddies (2021). Available: <https://earthbuddies.net/vertical-farming/>. 03 Jan 2021
2. What you should know about vertical farming. In: The Balance Small Business (2021). Available: <https://www.thebalancesmb.com/what-you-should-know-about-vertical-farming-4144786>. Accessed 03 Jan 2021

3. Overview.: World Bank (2021). Available: <https://www.worldbank.org/en/topic/agriculture/overview#:~:text=Analyses%20in%202016%20found%20that,more%20than%2025%25%20of%20GDP>
4. Al-Kodmany, K.: The vertical farm: a review of developments and implications for the vertical city. *Buildings* **8**(2), 24 (2018)
5. Controlled Environment Agriculture (CEA): Hydroponics. In: *FreshBox Articles* (2021). Available: <http://freshboxfarms.com/articles/controlled-environment-agriculture-cea-hydroponics/>
6. Harris, D.: *Hydroponics: a practical guide for the soilless grower* (1992)
7. Hedenblad, E., Olsson, M.: urban growth analysis of crop consumption and development of a conceptual design to increase consumer adoption of vertical greenhouses (2017)
8. Diver, S.: *Aquaponics—Integration of Hydroponics with Aquaculture*. National Sustainable Agriculture Information Service (2006)
9. What is the aquaponics system? definition, benefits, weaknesses. In: *Youmatter* (2021). Available: <https://youmatter.world/en/definition/aquaponics-sustainable-benefits-system/>
10. Zipgrow.com (2021). Available: <https://zipgrow.com/wp-content/uploads/QuickCropsGuide.pdf>
11. Hydroponic: Various hydroponics systems. In: *Hydroponic-urban-gardening.com* (2021). Available: <https://www.hydroponic-urban-gardening.com/hydroponics-guide/various-hydroponics-systems/>
12. Grow light.: In: *En.wikipedia.org* (2021). Available: https://en.wikipedia.org/wiki/Grow_light
13. <https://www.thespruce.com/hydroponic-gardens-nutrient-film-technique-1939220>. Accessed 02 Apr 2021
14. p. Hydroponics and p. Hydroponics, “pH Level In Soil And Hydroponics. In: *Aqua Gardening* (2021). [Online]
15. What is EC? Electrical conductivity in hydroponics | CANNA UK, *Canna-uk.com* (2021). Available: <https://www.canna-uk.com/electrical-conductivity>

Chapter 17

Design and Analysis of Progressive Tool for Glass Brackets



Nagaveni Thallapalli , K. Laxman Kumar ,
and S. B. Manikanta Katepalli 

Abstract In this project, the design of an automobile sheet metal component is done which is used as a bracket for an automobile handlebar. The main aim is to prevent burr at the edges, with optimum cutting clearance, straightness, and no bend marks, wrinkling formation, thinning at the bend region. To achieve this, the operations involved are blanking, notching, bending, and piercing operation where it has been done in a progressive way of tooling rather than eight stage tools. The number of parts per stroke is two numbers (LH + RH). For obtaining this sheet metal component, a progressive tool with eight stations is required, where the above operations are performed on the strip in a progressive way and feed has been from left side of the press. Analysis has been carried out on the punches of the press tool using Ansys 18.1. Software. The press tool has been designed using NX.10 Software. Finally, the deformation, stresses acting on the press tool has been calculated. Punches are made of D2 Steel material. As the result, lowest stress 13 MPa is in bending punch 1 and highest stress 538 MPa is in parting off punch is compared with ultimate tensile strength of D2 steel 600 MPa which is within acceptable limits.

17.1 Introduction

In most of the engineering industries, products are produced in mass. Braces and clamps keep the chaselware in place and prevent it from moving and wobbling. Another reason for the use of glass brackets is that they connect transparent panels to be connected to handrails and posts without destroying the chasels. Press tools are special tools custom-designed to produce a specific component out of sheet metal. The main objective of the progressive press tool design is to lower manu-

Present Address:

N. Thallapalli (✉) · K. L. Kumar · S. B. M. Katepalli
Department of Mechanical Engineering, University College of Engineering,
Osmania University, Hyderabad, Telangana 500007, India
e-mail: nagaveni.t@uceou.edu

facturing costs while maintaining quality and increased production. Progressive press operating may be a mechanical operating of metals during which the latter is subjected to plastic deformation in a cold state.

Progressive press operating is split into sheet stamping and cold die forging. Advantages of stamping are high strength, good dimensional accuracy, surface finish, and relatively low cost. Progressive press tool is a device which the sheet metal can be converted into required shape by various press operations such as piercing, blanking, bending, and notching. Piercing is an operation in a die which cuts out a slug (usually scrap) in sheet or plate material, blanking is the operation of cutting or shearing a piece out of stock to a predetermined contour, notching is the operation of cutting out of various shapes from the edge of a strip, blank or part, and bending is an operation in which permanently deform sheet or strip metal along a straight in v or U shapes. The most common cutting processes are performed by applying a shearing force, that is when a great enough shearing force is applied, the shear stress in the material will exceed the ultimate shear strength and the material will fail and separate at the cut location. Magesh and Mani Kandan [1] research has proposed that it is necessary to assign tolerances to the functional dimensions and the tool performance can be judged by the dimensional quality. Nozari et al. [2] deliberated about the use of progressive die in mass production in sheet metal components, their advantages, and different types of operations performed. Rai et al. [3] research has mainly focused on possible causes for burr formation and methods to prevent it. Dilip Kumar et al. [4] the research carried out for determining the spring back along with thinning effect of aluminum sheet metal during L-bending operation. Hogman [5] research has proposed that due to high strength and mechanical properties enhance the safety level even if the thickness of the steel sheet is reduced. Wang and Bourne [6] discuss an integrated system for the design and production of sheet metal parts and identified important features for the sheet metal bending process.

Press tools for the press operating are classified in keeping with the sort of operation performed; with reference to technological options, there are distinguished easy, compound, and progressive tools. A progressive tool encompasses a series of operations. At every station, associate operation is performed on the workpiece throughout a stroke of the press. Between the strokes, the metal strip is transferred to successive station. A finished workpiece is created at every stroke of the press. Whereas the piercing punch cuts a hole within the stroke, the blanking punch blanks out a little of the metal within which a hole had been pierced at a previous station [7].

17.2 Problem Statement

The aim of this project is to design progressive tool to manufacture a glass bracket with required dimensional accuracy consistently over a period of time to meet production requirements by adopting the cropping operations in 1st stage and

parting off in eighth stage completely in eight-stage progressive tool. This project also involves the theoretical deflection calculation of piercing die and notching and edge bend die. The idea of this project is to evaluate and analyze the forming process before developing the tools and could help to avoid expensive mistakes. To see the effects of punch deformation on the forming and cutting of sheet metals, stresses, and spring backs of the component. The following considerations are made: availability of facilities and maximum safety of operators, minimize possible cost, to minimize the time, tool should be able to accommodate minor changes if required. The main objective of this study is to design and analysis of the progressive press tool for a glass bracket and producing more than one component in each stroke to increase the productivity. To calculate the required cutting, forming force and pad force and press tonnage required and the static structural analysis of punch and die are obtained.

17.3 Design and Analysis

17.3.1 Progressive Tool Design

A die is having a series of stations that perform one press after the other operation in series. A progressive tool develops a part as the work stock goes into the die and the last operation isolates the part. Progressive tool supplies a productive way to convert raw coil stock into a finished product with lower handling.

17.3.2 Properties of the Glass Bracket Material

AISI 1015 is a standard grade cold-rolled steel. It is composed of the following properties (Tables 17.1 and 17.2).

Table 17.1 Properties of glass bracket material

Elastic modulus	205 GPa
Poisson's ratio	0.29
Tensile strength	600 GPa
Yield strength	325 GPa
Thermal expansion coefficient	$1.2 \times 10^{-5}/k$
Mass density	7879 kg/m ³
Hardening factor	0.85 N/A

Table 17.2 Chemical composition of AISI 1015 cold-rolled steel

Carbon (C)	Manganese (Mn)	Phosphorous (Ph)	Sulfur (S)	Iron (Fe)
0.13–0.18%	0.30–0.60%	0.04%	0.05%	Remaining

17.3.3 Design Procedure for Glass Bracket

Press Tool Design Calculations

(1) Shear force calculation in Tons (T):

$$F_{sh} = \frac{K * L * T * S}{1000} \text{ tons} \quad (17.1)$$

where $K = 1$, L = Length of cut (mm), T = Thickness of stock (mm) S = Shear strength of stock material (kg/mm^2), L = Perimeters of contours at each stage.

(2) Bending force calculation in Tons (T):

$$P = \frac{C}{3} * B * T * T_s \text{ N/mm}^2 \quad (17.2)$$

Stagewise Load Calculation

The stagewise load calculation is calculated by using standard formula, and loads are calculated from stage-1 to stage-8. The cold-rolled steel material is used in progressive tool, and the ultimate tensile strength of cold-rolled steel is 420 N/mm^2 (Table 17.3).

Total force = sum of forces in all stages = 104.32 Tons. Considering stripping force as 0.15 times of total force. Stripping force = $0.15 \times 104.32 = 15.6$ tons.

Therefore, tool tonnage = $104.32 + 15.6 = 120$ tons.

Press capacity = $1.3 \times \text{tool tonnage} = 1.3 \times 120 = 156$ tons.

Component Design

Figures 17.1 and 17.2 depict the final view of glass bracket 3D model and the two-dimensional drawing of the component in the NX.10 software. In NX Unigraphics software, there is a module which is called progressive die wizard. In this module, the progressive press tool can be generated step by step. In this progressive die wizard first step is intermediate stages, unfold and bend and of the

Table 17.3 Stages of operations and load calculations

Stages	Operations performed	Perimeter (mm)	Thickness (mm)	Force (Tons)
1	Cropping operation	242	1.5	9.08
2	Piercing	25.7	1.5	1.619
3	Piloting	31.48	1.5	1.98
4	Notching 1	267.2	1.5	16.83
5	Notching 2	209.7	1.5	13.2
6	Bending 1	6	1.5	0.25
7	Bending 2	37	1.5	1.5
8	Part off	122.55	1.5	7.7

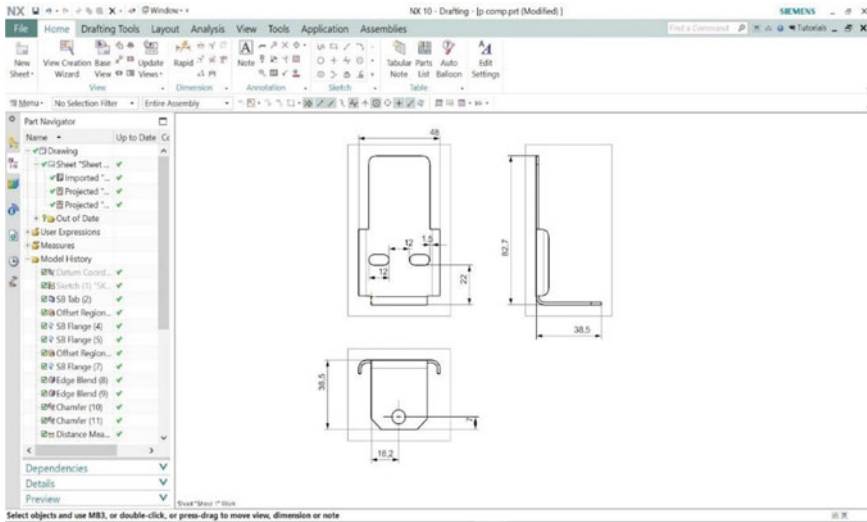


Fig. 17.1 Final component (2D view)

component. The second step is initializing project and blank generator. The third step is blank layout. The fourth step is scrap design. The next steps are strip layout, force calculations, die design, punches design, and remaining parts can be designed. Till strip layout it is designed in this progressive die wizard.

17.3.4 Scrap Design and Final Strip Layout

Figure 17.3 shows the scrap layout design of the glass bracket component.

This strip layout is generated in progressive die wizard module which is present in NX.10 software. The final strip layout shows the eight stages of progressive press tool operations cropping, piercing, piloting, notching, bending, and parting off. By using strip layout, we can design progressive tool.

17.3.5 Progressive Press Tool

The assembly orientation (i.e., front view) of the progressive press tool is shown below which is made in NX.10 software (Fig. 17.4).

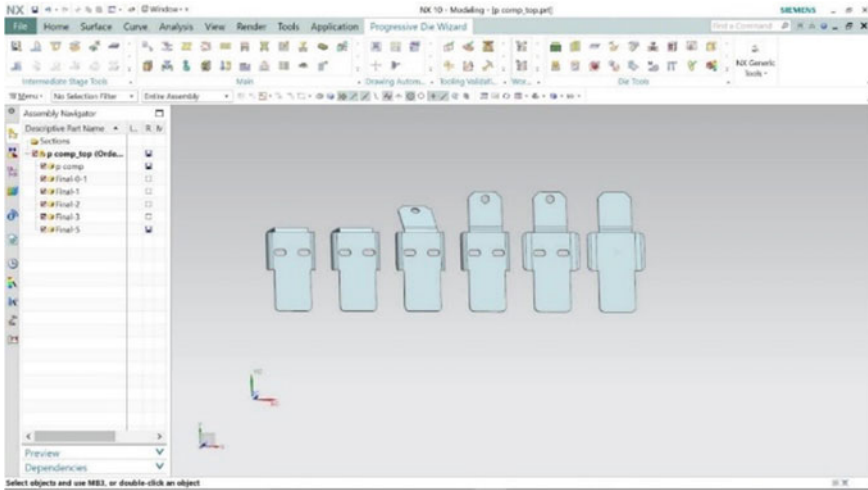


Fig. 17.2 First step

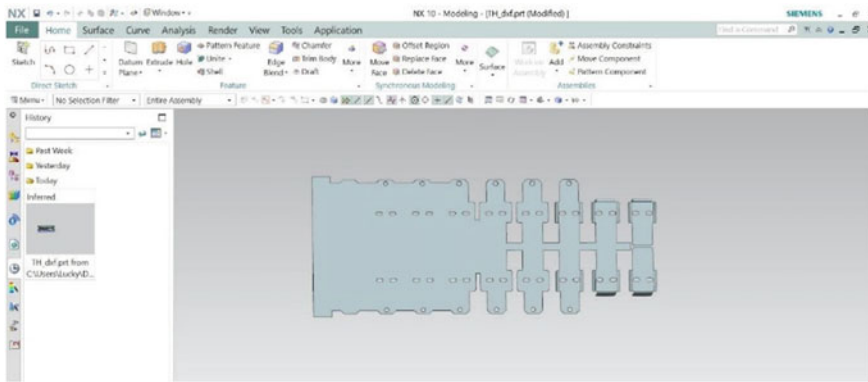


Fig. 17.3 Final strip layout

17.3.6 Analysis of Progressive Press Tool Components

Analysis is the final phase in the designing. In analysis, the components are checked for the mechanical strength and the functionality. In this project, the selected components of tool analyzed manually and finally analyzed by the static analysis using the analysis tool of Ansys and SolidWorks simulation. The version is used SolidWorks simulation 16.0 and Ansys 18.1, finite element analysis of the progressive press tool components. In this FEA analysis, static structural analysis and the press tool components are meshed with coarse element size, and then in the next

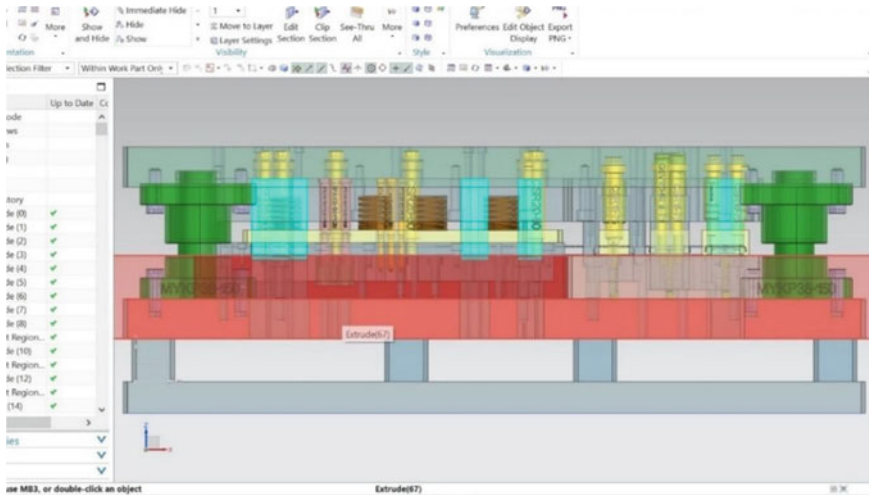


Fig. 17.4 Front view of progressive tool

step, components are given fixed support at one end and force is applied on the other end. The stresses and deformations are shown in the results.

17.3.7 Theoretical Analysis of the Progressive Press Tool Components

Considering the value of the forces on various punches, we are calculating the values of stresses and deformation on the punches. These values are later compared with the value of ultimate strength of tool material to assure no failure takes place [8]. Stage 1-Cropping Operation

$$\text{Stress} = \frac{\text{Force}}{\text{Area}} = \frac{90888}{764} = 199 \text{ MPa} \tag{17.3}$$

$$\text{Deformation} = \frac{FL}{AE} = \frac{90,888 * 90}{764.9 * 205 * 100} = 0.041 \text{ mm} \tag{17.4}$$

Similarly, the values of stresses and deformation for other stages are as follows using the same formula as above. For bending 1, we need to analyze the buckling load as follows (Table 17.4).

Table 17.4 Theoretical results

S. No.	Stage operation	Stress (MPa)	Deformation (mm)
1	Cropping	199	0.041
2	Round piercing	306.7	0.134
3	Oblong piercing	294.2	0.12
4	Notching 1	135.4	0.059
5	Notching 2	138.99	0.061
6	Parting off	392.64	0.27
7	Bending 1	2.38	0.001
8	Bending 2	9.33	0.0041

Table 17.5 Theoretical and analysis comparison

Component	Deflection (mm)		Stress (MPa)		Remarks
	Theoretical	Analytical	Theoretical	Analytical	
Round piercing punch	0.134	0.090	306	325	Acceptable
Oblong piercing punch	0.12	0.097	294.2	307	Acceptable
Cropping punch	0.041	0.089	199	303	Acceptable
Notching punch 1	0.059	0.061	135	117	Acceptable
Notching punch 2	0.061	0.037	138	167	Acceptable
Bending punch 1	0.001	0.002	2.38	13.98	Acceptable
Bending punch 2	0.0041	0.01	9.33	37.86	Acceptable
Parting off punch	2.7	0.16	392	538	Acceptable

17.4 Results

Considering the forces on the punches of D2 steel material, the theoretical and analytical calculations are worked out. The ultimate tensile strength of D2 steel (600 MPa) is taken as the reference for the acceptability. The results of the FEM analysis will be summarized and compared with the analytical results in Table 17.5; it can be clearly seen during the operation of the machine tool, the allowable working stresses and deflections are within the acceptable limit. Analytical results of deformation and stress of static structural analysis are done in Ansys 18.1 (Fig. 17.5).

The deformation and stresses for other punches, i.e., cropping, notching punches, bending punches, parting off punches, have been analyzed in Ansys 18.1, and its values are shown in Table 17.5.

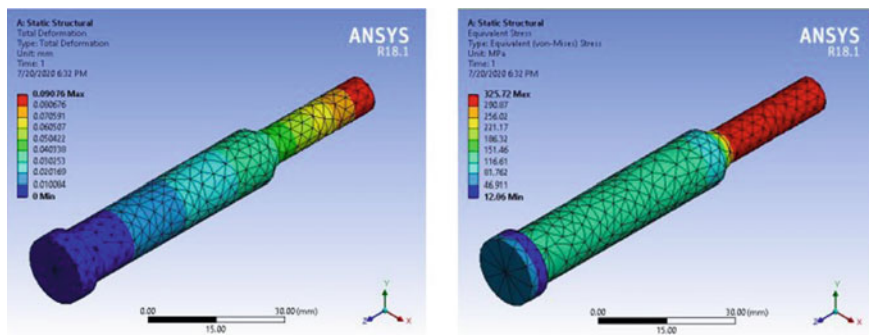


Fig. 17.5 Deformation and stress of round punch analysis

17.5 Conclusions

In this project, the eight-stage progressive tool is designed for the production of bracket component and this bracket component is used in vehicle handlebar and component sheet thickness is 1.5 mm, clearance of 0.36, and material of the component used is cold-rolled D2 steel. The force required to operate tool is calculated using standard formula, and based on these forces, the thickness of the plate is calculated, All the components are drafted, modeled, and analyzed, the component is assembled, and a bill of material is made; the following conclusions can be derived from the thesis. The entire tool has designed, drafted, and analyzed using AutoCAD 2019, Unigraphics. The calculated tonnage required for producing component is 156 tons; hence, press selected to carry the operation is 160 tons, the calculated press tool shut height is 350 mm and recommended press mechanical press 160 tons and sizes (900 × 1500) mm. The stagewise load calculation is done according to the dimension of the component and calculated stagewise load values are 90,888 N, 16,191 N, 19,832 N, 168,361 N, 132,142 N, 5040 N, 14,100 N, and 77,206 N. The structural analysis was also done on different elements of press tool by using analysis software ANSYS as shown in the results and discussions. The cycle time stagewise tool for different operations like piercing, notching, bending, and parting off is 16 secs as per industry and cycle time of progressive press tool is 10.7 secs therefore increase in productivity by 20 percentage. By the comparison of theoretical and analysis results, the lowest stress 13 MPa is in bending punch 1 and highest stress 538 MPa is in parting off punch which is compared with ultimate tensile strength of D2 steel 600 MPa which is in acceptable limits. Future scope of work: For each stroke, this press tool produces two pieces at a time. This can multiply to four pieces each stroke by varying the die length along the bolster plates. With increasing modern technology in presses, the press tonnage capacity can also be increased and automatic hydraulic press tonnage is used to operate manually.

References

1. Magesh, S., Mani Kandan, S.: Design, fabrication and tolerance analysis of progressive tool review. *Int. J. Inno. Res. Sci. Eng. Technol.* **6**(5) (2017)
2. Nozari, M., Shojaie, A.A., Raiss, S.: Study and priority the designing stages of progressive die by DFSS methodology (IDOV model). *Journal IISN: 0061-1069. German Journals* (2002)
3. Rai, P.K., Mohammad, A., Jafri, H.Z.: Causes prevention of defects (burr) in sheet metal component. *Int. J. Inno. Res. Sci. Eng. Technol.* **3**(4) (2013)
4. Dilip Kumar, K., Appukuttan, K.K., Neelakantha, V.L., Naik, P.S.: Experimental determination of spring back and thinning effect of aluminum sheet metal during L-bending operation. *Journal IISN: 0261-3069. German Journals* (2011)
5. Hogman, B.: Design and analysis of progressive press tool using material steel for press tools. *Journal IISN: 0161-2069. German Journals* (2008)
6. Wang, C.H., Bourn, D.A.: *Design and Manufacturing of Sheet Metal Part: Using Features to Aid Process Planning and Resolve Manufacturability Problems*. Published by Carnegie Mellon University (1994)
7. Chavan, H.A., Wani, V.P.: Design and analysis of progressive tool for an automobile component. In: 2nd International Conference on new frontiers in engineering, science and technology (NFEST), vol. 1240, pp. 18–22 (2019)
8. Ostergaard, D.E.: *Advanced Die Making*. McGraw-Hill Book Company (1986)

Chapter 18

Analysis of Strain Hardening Behavior of ARMCO Iron After Severe Plastic Deformation Using K–M Plots



Vindala Poojitha, T. Raghu, and V. Pandurangadu

Abstract In this study, ARMCO iron sheets were subjected to severe plastic deformation through a potential sheet material processing technique called constrained groove pressing. This single phase polycrystalline material is imposed to effective strains of ~ 3.48 and ~ 4.64 after 3rd cycle and 4th cycle of constrained groove pressing process, respectively. Uniaxial tensile tests were carried out on all deformed ARMCO iron sheet samples at room temperature. During this tensile loading performed at a constant strain rate, an attempt was made to study the strain hardening behavior by identifying different stages of strain hardening using Kocks–Mecking (K–M) plots. It is shown that there is an increment in strain hardening rate in these deformed materials with increasing constrained groove pressing cycles. In both the deformed conditions, stage-III is prominently appeared. This stage is estimated to mark the development of dislocation cell structures, where dislocation activity explains strain hardening behavior during various cycles of severe plastic straining.

18.1 Introduction

The field of material science and technology revolves around the correlation between chemical composition, process, structure, and property. Over the years, through different conventional methods like alloying, metal forming process, and heat treatments improved properties were possible. However, for engineering materials with superior mechanical properties grain size had played a vital role. Grains based on its sizes can be categorized as coarse grains, fine grains, ultra-fine grains, and nano-grained. Due to its unique properties achieved, research around processing of ultrafine grained and nano-grained materials has significantly grown for quite some time.

V. Poojitha (✉) · V. Pandurangadu
Jawaharlal Nehru Technological University Anantapur, Ananthapuramu,
Andhra Pradesh 515002, India

T. Raghu
Defence Metallurgical Research Laboratory, Kanchanbagh, Hyderabad 500058, India

Severe plastic deformation (SPD) is currently one of the most trending processes in tailoring ultra-fine/nano-grained microstructures. Its processing involves imposition of severe plastic straining and high hydrostatic pressure resulting in tremendous grain refinement [1]. This extreme straining is carried out without any change in the overall dimensions of the specimen, making it a unique characteristic feature of SPD processes. There are numerous methods that demonstrate the working principle of SPD processing such as equal channel angular pressing (ECAP) [2], high pressure torsion (HPT) [3], twist extrusion (TE) [4] for bulk materials and accumulative roll bonding (ARB) [5], constrained groove pressing (CGP) [6] for sheet material processing. For optimized processing conditions and good service life during structural applications, work hardening behavior of these deformed materials can be an essential factor. Although the work hardening behavior of bulk SPD processed materials is widely studied [7–9], similar information on constrained groove pressed BCC materials is scarce. In the present study, constrained groove pressed ARMCO Fe is subjected to tensile testing in order to understand its strain hardening characteristics with increasing plastic strains using K–M approach.

18.2 Experimental Procedure

ARMCO iron sheets in their as-received condition are processed through CGP technique using a die set up, consisting of a pair of grooved dies and ungrooved dies. Figure 18.1 illustrates the respective CGP process consisting of four steps in each cycle. In the first step, a sheet specimen is pressed between the groove dies (Fig. 18.1b), while in the second step it is pressed in the ungrooved dies (Fig. 18.1c). Prior to further pressings, sample is rotated by 180° in order to maintain similar strains in the other regions of the specimen (Fig. 18.1d). In the next two steps, sample is again deformed between the grooved and ungrooved dies as shown in Fig. 18.1e, f. This results in completion of one cycle in CGP process, imposing an effective strain of 1.16 throughout the sample. However, in this study ARMCO iron sheets are successfully processed upto three and four cycles of CGP using a hydraulic press, inducing an effective strain of 3.48 and 4.64 respectively. On these severely strained samples, a room temperature tensile testing is performed at a constant strain rate (Fig. 18.2). Further, through a standard procedure, the attained stress–strain data is utilized to get the required K–M plots for the analysis.

18.3 Results and Discussions

In Kocks–Mecking (K–M) approach, the strain hardening behavior in polycrystalline materials can be described using change of strain hardening rate (θ) with the effective true stress ($\sigma - \sigma_{ys}$). With θ in K–M plots, differential variation of complex structure with stress and strain during plastic deformation is reflected [11, 12].

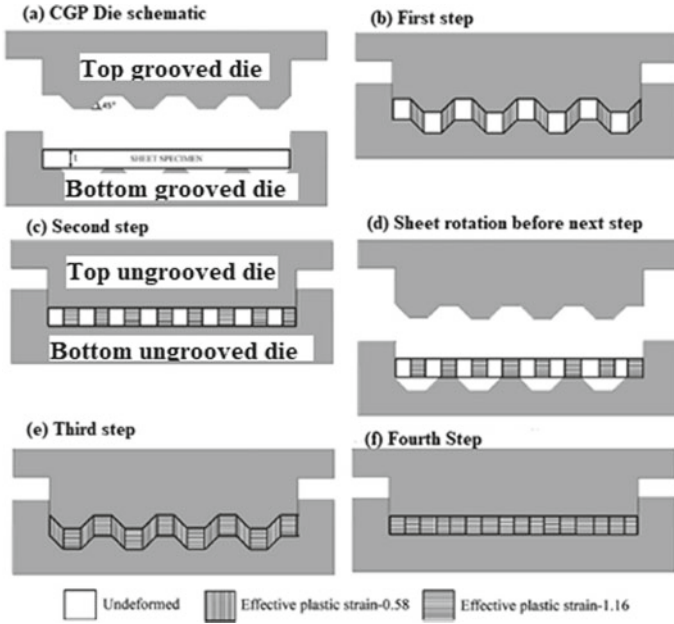
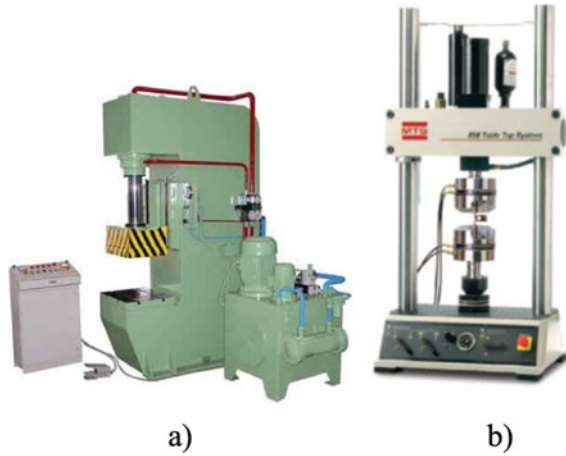


Fig. 18.1 Schematic of CGP process [10]

Fig. 18.2 a Hydraulic press
 b Tensile testing equipment



Strain hardening curves of cubic materials are generally composed of five stages, from stage-I to stage-V. These emphasize on the mechanism during plastic deformation in terms of dislocation activities. Stage-I is called as easy glide, and its occurrence is limited to single crystal materials. Hence, strain hardening in polycrystalline materials may start from stage-II. This is known as linear hardening

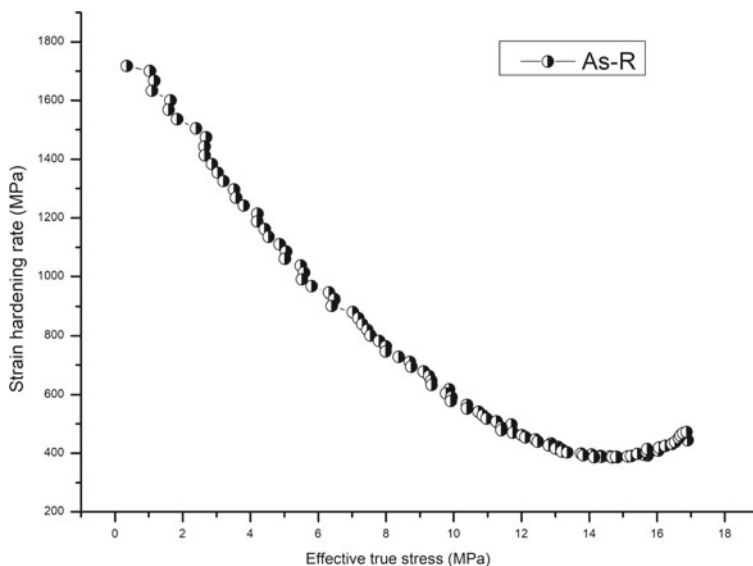


Fig. 18.3 K–M plot of the as-received ARMCO iron

(athermal hardening) stage having tangled dislocations resulting in high strain hardening rate. Further changes in dislocation density determine the consequent stages in strain hardening curves.

The strain hardening behavior of as-received ARMCO iron is explained through the K–M plot as shown in Fig. 18.3. The K–M plot of the as-received ARMCO iron exhibited a rapid decrease in work hardening rate with the increasing true stress. This trend corresponds to stage-III behavior with a starting work hardening rate of ~ 1717 MPa. At certain higher stresses when stage-III reaches a saturation level, a constant strain hardening rate is observed, indicating the existence of stage-IV. Subsequently, a sudden increase in θ is seen which marks the development of stage-V. Figure 18.4a, b illustrates the K–M plots of 3rd cycle and 4th cycle CGP processed samples. Irrespective of CGP cycles, stage-II is not seen in deformed ARMCO iron, but stage-III strain hardening behavior is clearly evident. Unlike the undeformed condition, the deformed ARMCO iron is initially demonstrated a rapid decline in work hardening rate, whereas a gradual decrease was observed at higher stress values. It can be seen that stage-IV and stage-V behavior is not observed in CGP processed ARMCO iron as found in its as-received condition.

The initial strain hardening rate increases significantly by ~ 8.5 times reaching $\sim 14,599$ MPa after 3rd cycle (Fig. 18.4a). It indicates the need of larger activation energy for plastic flow because of the obstruction created to the movement of dislocations [13]. If dislocations could move without any obstacles, there would be practically zero strain hardening rate in the material [14]. As shown in (Fig. 18.4b),

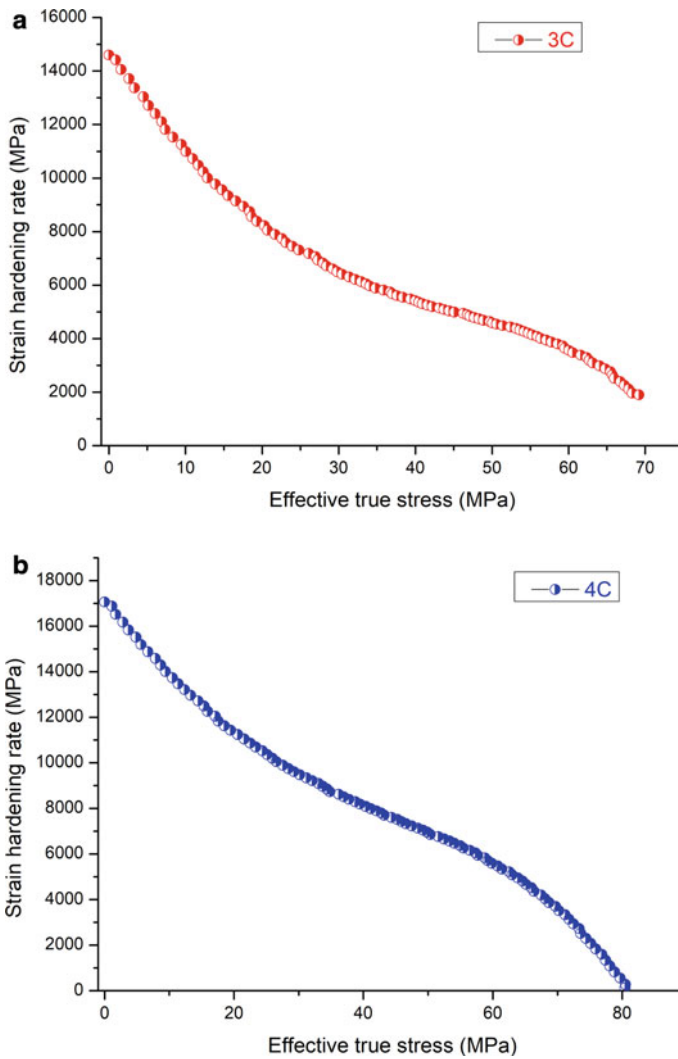


Fig. 18.4 K–M plot of the **a** 3rd cycle **b** 4th cycle CGP processed ARMCO iron

after 4th cycle strain hardening rate further increased to $\sim 17,000$ MPa. This rise in strain hardening rate can be attributed to the enhancement in dislocation density in the severe plastically deformed sheet materials [12].

18.4 Conclusion

1. Constrained groove pressed ARMCO iron revealed strain hardening behavior showing a continuous decrease in strain hardening rate with increasing stress, which indicates stage-III of the Kocks–Mecking plots.
2. The Kocks–Mecking plots exhibited high initial strain hardening rate with every increase in CGP cycles. The initial strain hardening rate after third cycle and fourth cycle of CGP resulted in $\sim 14,599$ MPa and $\sim 17,000$ MPa, respectively, apparently showcasing the likeliness of increased resistance to dislocation motion.
3. Analysis of the strain hardening rate–true stress data in the K–M plot is inferred to be suitable for understanding the hardening behavior in CGPed ARMCO iron as it can be an indicative of sub-grain structure development in highly strained structure.

Acknowledgements The authors acknowledge financial aid provided by Defence Research Development Organization (DRDO) for this work.

References

1. Langdon, T.G.: The principles of grain refinement in equal-channel angular pressing. *Mater. Sci. Eng. A* (2007)
2. Horita, Z., Furukawa, M., Langdon, T.G., Nemoto, M.: Equal-channel angular pressing (ECAP): a novel method for microstructural control. *Materia Japan* (1998)
3. Vorona, D., Sharafutdinov, A.V., Krasilnikov, N.A.: High strength and ductility of nanostructured Al alloy 2024 subjected to high pressure torsion. In: *Solid State Phenomena* (2006)
4. Varyukhin, V., Beygelzimer, Y., Synkov, S., Orlov, D.: Application of twist extrusion. *Mater. Sci. Forum* (2006)
5. Kamikawa, N., Huang, X., Tsuji, N., Hansen, N., Minamino, Y.: EBSD and TEM characterization of ultrafine grained high purity aluminium produced by accumulative roll-bonding. *Mater. Sci. Forum* (2006)
6. Shin, D.H., Park, J.J., Kim, Y.S., Park, K.T.: Constrained groove pressing and its application to grain refinement of aluminum. *Mater. Sci. Eng.: A* (2002)
7. Simsir, C., Karpuz, P., Gür, C.H.: Quantitative analysis of the influence of strain hardening on equal channel angular pressing process. *Comput. Mater. Sci.* (2010)
8. Beygelzimer, Y., Toth, L.S., Jonas, J.J.: Some physical characteristics of strain hardening in severe plastic deformation. *Adv. Eng. Mater.* (2015)
9. Malygin, G.A.: Mechanism of strain hardening and dislocation-structure formation in metals subjected to severe plastic. In: *Physics of the Solid State* (2006)
10. Satheesh Kumar, S.S., Raghu, T.: Structural and mechanical behaviour of severe plastically deformed high purity aluminium sheets processed by constrained groove pressing technique. *Mater. Des.* (2011)
11. Choudhary, B.K., Christopher, J., Isaac Samuel, E.: Applicability of Kocks–Mecking approach for tensile work hardening in P9 steel. *Mater. Sci. Technol.* (2012)
12. Satheesh Kumar, S.S., Raghu, T.: Tensile behaviour and strain hardening characteristics of constrained groove pressed nickel sheets. *Mater. Des.* (2011)

13. Luo, J., Mei, Z., Tian, W. and Wang, Z.: Diminishing of work hardening in Electro formed polycrystalline copper with nano-sized and uf-sized twins. *Mater. Sci. Eng.* (2006)
14. Rollett, A.D., Kocks, U.F.: A review of the stages of work hardening. In: *Solid State Phenomena*. Trans Tech Publications (1993)

Chapter 19

Optimization of Process Parameters for Friction Stir Spot Welding Using Dissimilar Metals



Pitala Adithya, B. D. Y. Sunil, and C. Labesh Kumar

Abstract Welding the steels using aluminum have greater applications, and this combination will help to decrease the overall weight of assembled units. Two metals with dissimilar thickness will be aligned in lapped position wherein a spot weld, it is performed using non-consumable pin profiled tool. Welding is performed based on the friction generated by the rotating tool on the dissimilar metals. This heat generated during the friction helps the dissimilar metals AA6062 with the structural steel ST1020 to join which are taken with thickness of 0.3, 0.5 and 0.7 mm with a rotating tool made of ‘H13’ material and pin profile is taper at the end. Three parameters with three levels have been used to perform joining operation. Minitab software is used for design of experimentation, and ANOVA is utilized for the validation of larger the better.

19.1 Introduction

Friction stir spot welding, i.e., “FSSW” is process of joints which are developed in the state of solid at TWI Limited in the year 1991. FSSW is the technology which has raised curtains for many other innovations and joining techniques. FSSW is the welding process which comes into frame when there is a concept of two dissimilar metals as there would be huge difference in the thermal conductivity of these metals. FSSW uses a tool which is non-consumable, and this is plunged and even rotated into two work pieces with the interface. The joining of two different materials using FSSW has been performed. In industries, FSSW is mainly used to join aluminum alloys which are rolled, casted and even extruded. ST1020 is used as it reduces the body weight and has many applications in the aerospace and automobile industry. FSSW is used for the aluminum alloy with the butt joints with a thickness which are ranging from 0.3 to 75 mm, and these have been joined suc-

P. Adithya (✉) · B. D. Y. Sunil · C. L. Kumar
Department of Mechanical Engineering, Institute of Aeronautical Engineering, Dundigal,
Hyderabad 500043, India
e-mail: bdy.sunil@iare.ac.in

cessfully in a single pass. These factors are again dependent on machine power, work piece material and structural stiffness. Other materials such as MG, TI, CU and steel alloys have also been successfully joined. Plastics and the other different composites have been analyzed and studied based on the availability of metal matrix.

19.2 Literature Survey

The heat generated during the process when tool penetrates into the work piece creates a medium which ensures that work material sticks without melting the pin on the tool. This is quite similar to FSSW where the joining metals like steel is a challenge. The FSSW procedure has become such popular in welding due to high tendency toward the hardness and melting point of the steel [1]. This process uses combination of aluminum and carbon fiber plastics which are welded by the usage of FSSW process. This project uses only two factor which are plunge depth and dwell time which determine the strength of the weld performed and those factors can be used which give the desired optimum results [2]. The FSSW process is used for welding of aluminum alloy as well structural steel which makes the tensile strength to be even more effective which makes the high melting point. The metallurgical bonding is utilized which makes the sleeve-affected zone even more affective. This ensures the mechanism for the strength which ensures dislocation of the welding strength [3]. The process utilized in this is refilled friction spot welding which is mainly used to resolve the keyhole problem. The light metals usually face this problem due to the hook defect, and this type of welding ensured there is no method which makes the improvement in the properties of nanosheets [4]. The FSSW is utilized to join the different alloys of the AL5083 metal and then the microstructure and behavior at the corrosion are analyzed and studied in order to ensure the proper usage of the welded metal. This focusses mainly on the zones which are affected by the application of FSSW, and the corrosion rate decreased due to the usage of modern FSSW welding [5]. The metals used are C10100 and A15083 which are the combination of copper and aluminum. Effect of puncturing and piercing of tool which is used as aluminum in the alloy top layer and copper alloy on the same layer at the bottom which are formulated by variation of FSSW process parameters like rotational speed of the tool, plunge depth and dwell time [6]. This mainly studies about the generation of energy and the temperature distribution which describe the strength of the weld based on the microstructural study. The usage of FSSW process is similar, but both the projects are entirely different in their case studies [7]. The metals used are C10100 and A15083 which are the combination of copper and aluminum. The effect of puncturing and piercing the tool which is used as aluminum in the alloy top layer and copper alloy on the same layer at the bottom which are formulated by variation of FSSW process parameters like rotational speed of the tool, plunge depth and dwell time [8]. The shear tests with regards to the lap are used in finding the mechanical performance of shear test

for the lap where the tool which has square pin produces the joints which are stronger [9]. Friction stir forming is the process which is different from friction stir welding as the joint is formed by mechanical interlocking of the two constituents. This is formed by plasticizing of one of materials by usage of FSW [10]. The different aluminum alloys are AA6063 and AA5052 with the flow rate which has to be with in the spot which increases with depth for the penetration of the tool. FSSW on dissimilar factors such as materials and thicknesses which are produced with differences in penetration depth of the tool [11]. In this process of FSSW, shoulder applies a pressure toward the downward surface which leads to plasticization in the vicinity of work piece and the pin. This is a bit similar to our process which generates the heat through the friction, and this paper focusses mainly to investigate the model which is based on the effects of profiles at different tool pin based on temperature, power consumed and stir zone of welding [12].

19.3 Design and Analysis

The tools structure as well as design pins were designed in the “SOLIDWORKS” (Version 2018) as per the dimensions. The “MINI TAB SOFTWARE” is used for the experimentation design. The validation of the results for larger the better and analysis is done by the usage of “ANOVA” (Fig. 19.1).

The rotational as well as the force for the downward in order to make sure that the welding tool is used for heat generated by the force of friction. The thermo-couples are utilized in order to make sure that the tool is maintained at 900° and the work piece is maintained at 700°.

19.3.1 Tool Material

The material which is used for the tool is the chromium steel tool which is utilized by the hot-work which are generally classified into the ‘H’ group steels by the

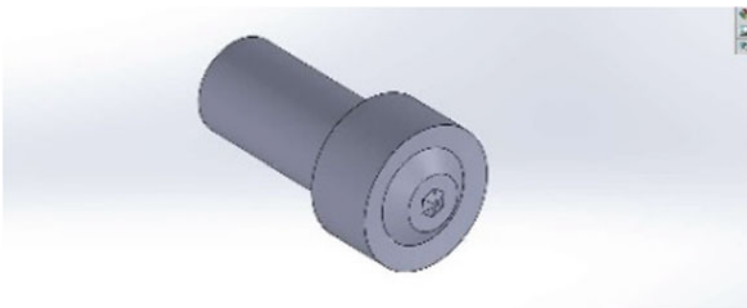


Fig. 19.1 3D Model of tool in solid works

classification systems of the AISI. The tool material utilized is H13 grade of chromium which has various applications and the mechanical properties of H13 tool is considered at 20° temperature (Fig. 19.2; Tables 19.1 and 19.2).

Fig. 19.2 H13 steel tool



Table 19.1 Chemical properties

Element	Content (%)
Cr	4.75–5.50
Mo	1.10–1.75
Si	0.80–1.20
V	0.80–1.20
C	0.32–0.45
Ni	0.3
Cu	0.25
Mn	0.20–0.50
P	0.03
S	0.03

Table 19.2 H13 mechanical properties

Properties	Metric	Imperial
Tensile strength, ultimate (@20 °C/68 °F, varies with heat treatment)	1200–1590 MPa	174,000–231,000 psi
Tensile strength, yield (@20 °C/68 °F, varies with heat treatment)	1000–1380 MPa	145,000–200,000 psi
Reduction of area (@20 °C/68 °F)	50.00%	50.00%
Modulus of elasticity (@20 °C/68 °F)	215 GPA	31,200 KSI
Poisson's ratio	0.27–0.30	0.27–0.30

19.3.2 Work Piece Material

The material of the work piece is AL alloy 6062 which is the metal as it is predominant which includes the elements such as copper, magnesium, silicon, tin, zinc and manganese. These alloys are mostly used in the aerospace manufacturing which would be lighter as these have magnesium at high percentage (Fig. 19.3 and Table 19.3).

In this section, there are five major areas where the analyzing of the process is done using the simulation software ANOVA.

19.3.3 Method and Materials

The work material that is used in the FSSW is AI6062 and ST1020 with different thicknesses such as 0.3, 0.5 and 0.7 mm were used. The dimensions of the material are 150 mm of length and 20 mm of width. The rotating tool material is 'H13' to achieve high strength whose pin profile is taper at the end. The capacity of the welded joint is tested by the automated testing machine. CNC lathe and CNC



Fig. 19.3 Aluminum alloy 6062 sheets

Table 19.3 Composition of Al 6062

Elements	Content (%)
Mg	0.8–1.2
Si	0.4–0.8
Cu	0.15–0.4
Cr	0.04–0.14

milling machine are utilized in the tool manufacturing. Heat treatment is performed on the tool in order to withstand at high temperatures. The welding is done by placing aluminum at the top of steel as shown below (Figs. 19.4, 19.5 and 19.6).

19.3.4 Process Parameters

The process of FSSW involves very complexity in the material movement and also deformation of huge plastic. There are some major factors which are to be considered in a proper manner in order to affect the FSSW process such as geometrical parameters include rotational speed of the tool, load applied and speed of the welding. The other welding parameters such as circular motion of the tool, load applied on the tool, speed of weld and the size of the joint has the major effect on

Fig. 19.4 Aluminum placed at the top of steel

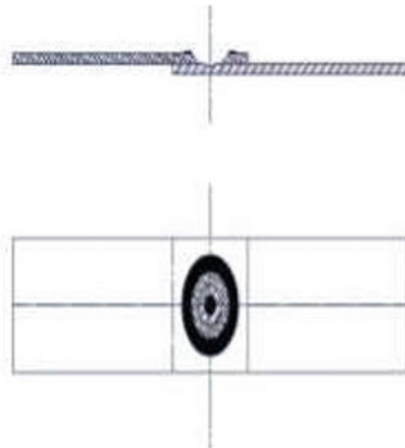


Fig. 19.5 Structure of the hexagonal tool



Fig. 19.6 Machine setup with the tool



the properties of welding. The plastic deformation and high temperature would be extreme simply causes the great alter in the base metal during the process of welding. The mechanical properties of the metal are defined by the area of the joint and the maximum stress which the weld can withstand. The penetration depth of the tool is defined in mm, the rotational rate is defined in rpm, the length of dip is defined in seconds and the tool dip speed is defined in mm/min. The axial force for the tool is defined in KN which is simply to overcome the possibilities for the failure and also would reduce the possible defects. The desired tensile strength of the weld was expected to be around 4 KN (Table 19.4).

19.4 Results and Discussion

The results for the two different thicknesses are performed by using ANOVA and the results are below.

Table 19.4 Parameters

Thickness	Tool rotational speed	DWELL time	Plunge depth
0.5 * 0.5	1200	24	0.6
0.5 * 0.5	1400	26	0.7
0.5 * 0.5	1600	28	0.8
0.7 * 0.7	1200	24	0.85
0.7 * 0.7	1400	26	0.95
0.7 * 0.7	1600	28	1.2

19.4.1 The Result for Thickness $0.5\text{ mm} \times 0.5\text{ mm}$ is as Follows

See Figs. 19.7, 19.8 and Tables 19.5, 19.6, 19.7 and 19.8.

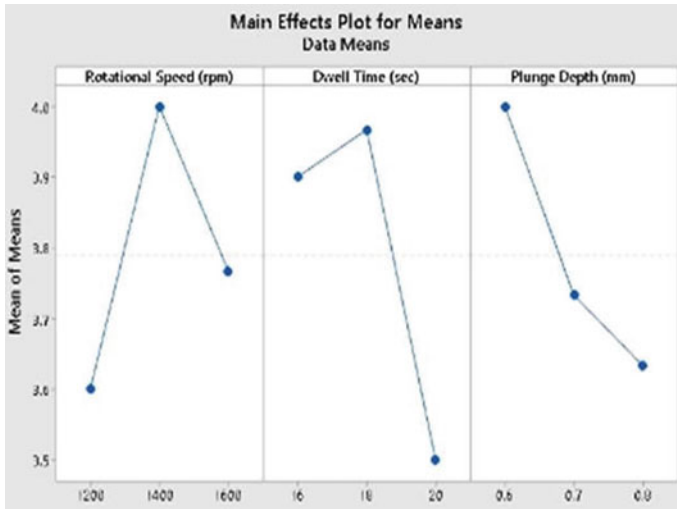


Fig. 19.7 Means main effects plots



Fig. 19.8 SN ratios main effects plot

Table 19.5 Signal to noise ratios response table

Level	Rotational speed	DWELL time	Plunge depth
1	11.09	11.81	12.03
2	12.04	11.95	11.42
3	11.49	10.86	11.16
Delta	0.95	1.09	0.87
Rank	2	1	3

Table 19.6 Means response table

Level	Rotational speed	DWELL time	Plunge depth
1	3.600	3.900	4.000
2	4.000	3.967	3.733
3	3.767	3.500	3.633
Delta	0.400	0.467	0.367
Rank	2	1	3

Table 19.7 SNRA1 response table

Rotational speed	DWELL time	Plunge depth	Strength	SN RAI
1200	16	0.6	4.0	12.0412
1200	18	0.7	3.6	11.1261
1200	20	0.8	3.2	10.1030
1400	16	0.7	4.1	12.2557
1400	18	0.8	4.1	12.2557
1400	20	0.6	3.8	11.5957
1600	16	0.8	3.6	11.1261
1600	18	0.6	4.2	12.4650
1600	20	0.7	3.5	10.8814

Table 19.8 Variance analysis

Source	D.F	Adj SS	Adj MS	F-value	P-value
Rotational speed	2	0.24222	0.12111	3.52	0.221
Dwell time	2	0.38222	0.19111	5.55	0.153
Plunge depth	2	0.21556	0.10778	3.13	0.242
Error	2	0.06889	0.03444		
Total	8	0.90889			

19.4.2 The Result for Thickness $0.7\text{ mm} \times 0.7\text{ mm}$ is as Follows

See Figs. 19.9, 19.10 and Tables 19.9, 19.10, 19.11 and 19.12.

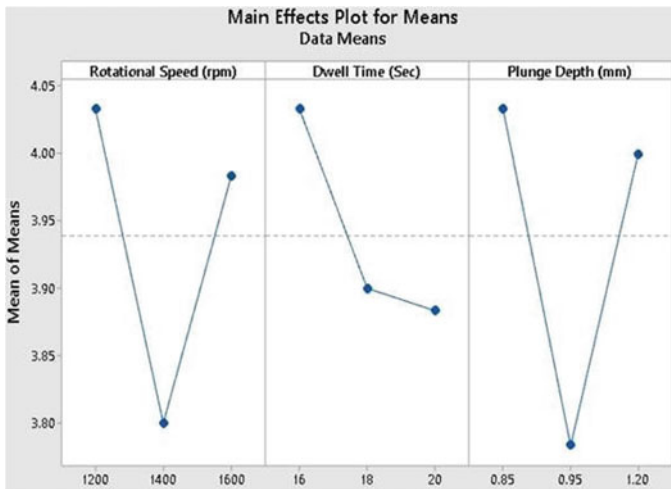


Fig. 19.9 Means main effects plot



Fig. 19.10 SN ratios main effects plot

Table 19.9 Signal to noise ratios response table

Level	Rotational speed	DWELL time	Plunge depth
1	12.11	12.11	12
2	11.59	11.81	11.55
3	11.99	11.77	12.03
Delta	0.51	0.34	0.55
Rank	2	3	1

Table 19.10 Means response table

Level	Rotational speed	DWELL time	Plunge depth
1	4.033	4.033	4.033
2	3.800	3.900	3.783
3	3.983	3.883	4.000
Delta	0.233	0.150	0.250
Rank	2	3	1

Table 19.11 SNRA1 response table

Rotational speed	DWELL time	Plunge depth	Tensile strength
1200	16	0.85	4.10
1200	18	0.95	3.80
1200	20	1.20	4.20
1400	16	0.95	3.90
1400	18	1.20	3.70
1400	20	0.85	3.80
1600	16	1.20	4.10
1600	18	0.85	4.20
1600	20	0.95	3.65

Table 19.12 Variance analysis

Source	D.F	Adj SS	Adj MS	F-value	P-value
Rotational Speed	2	0.09056	0.04528	0.71	0.584
Dwell Time	2	0.11056	0.05528	0.87	0.535
Plunge depth	2	0.04056	0.02028	0.32	0.758
Error	2	0.12722	0.06361		
Total	8	0.36889			

19.5 Conclusion

1. The friction stir spot welding will continue its impact in the welding of lighter metals as it reduces the body weight with respect to the MIG, TIG and fastenings.
2. The observations for the experimentations are taken as three parameters namely rotational speed of the tool (RPM), plunge depth (MM) and the dwell time (SEC) which are taken at three different levels of the experimentation from which the best strength for the weld is determined.
3. L9 orthogonal array is used to solve this problem, and the best result is obtained on a level basis. The greater the better value for the tensile strength is considered as the best level from the experimentation.
4. There are three different dimensions which are taken with respect to 0.5 mm * 0.5 mm and 0.7 * 0.7 mm, and the contributions are found out for each and every factor. The best tensile strength for both these welds is found out by using Minitab software.
5. The strength of the joint would be maximum for 0.5 mm * 0.5 mm when RPM is 1600, dwell time is 18 s and plunge depth is 0.6 mm at level 7. The strength of the joint would be maximum for 0.7 mm * 0.7 mm when RPM is 1600, dwell time is 18 s and plunge depth is 0.85 mm at level 7 (The other parameter at level 3 is not considered here as time taken is more).

References

1. Labesh Kumar, C., Bharathiraja, G., Jayakumar, V.: Friction Stir spot welding of AI6062/ St1020 metals with dissimilar thicknesses. In: AIP Conference Proceedings, vol. 2317(1) (2021)
2. Dong, H., Tang, Z., Li, P., Wu, B., Hao, X., Ma, C.: Friction stir spot welding of 5052 aluminum alloy to carbon fiber reinforced polyether ether ketone composites. In: Materials and Design, vol. 201, ScienceDirect (2021)
3. Li, P., Chen, S., Dong, H., Ji, H., Li, Y., Guo, X., Yang, G., Zhang, X., Han, X.: Interfacial microstructure and mechanical properties of dissimilar aluminum/steel joint fabricated via refilled friction stir spot welding. *J. Manuf. Process.* **49**, 385–396 (2020)
4. Wang, S., Wei, X., Xu, J., Hong, J., Song, X., Yu, C., Chen, J., Chen, X., Lu, H.: Stengthening and toughening mechanisms in refilled friction stir spot welding of AA2014 aluminum alloy reinforced by graphene nanosheets. *Materials and Design*, vol. 186, ScienceDirect (2020)
5. Bagheri, B., Abbasi, M., Abdollahzadeh, A., Omidvar, H.: Advanced approach to modify friction stir spot welding process. In: *Metals and Materials International*, vol. 26, pp. 1562–1573, Springer (2019)
6. Labesh Kumar, C., Jayakumar, V., Bharathiraja, G.: Optimization of welding parameters for friction stir spot welding of AA6062 with similar and dissimilar thickness. In: *Materials Today Proceedings*, vol. 19, Part 2, pp. 251–255 (2019)
7. Shen, Z., Ding, Y., Gerlich, A.P.: Advances in friction stir spot welding. In: *Critical Reviews in Solid State and Material Sciences*, vol. 45, pp. 457–534 (2019)

8. Padhy, G.K., Wu, C.S., Gao, S.: Friction stir based welding and processing technologies processes, parameters, microstructures and applications. *J. Mater. Sci. Technol.* **34**, 1–38 (2018)
9. Liu, F.C., Hovanski, Y., Miles, M.P., Sorensen, C.D., Nelson, T.W.: A review of friction stir welding of steels: tool, material flow, microstructure, and properties. *J. Mater. Sci. Technol.* **34**, 39–57 (2018)
10. Siddharth, S., Senthilkumar, T.: Study of tool penetration behaviour in Dissimilar Al5083/ C10100 friction stir spot welds. In: *Procedia Engineering*, Volume 173, Pages 1439 - 1446 (2017)
11. Haghshenas, M., Gerlich, A.P.: Joining of automotive sheet materials by friction-based welding methods. *Eng. Sci. Technol.* **21**, 130–148 (2018)
12. Sunil, B.D.Y., Kumar, C.L.: Friction surfacing of stainless steel on low carbon steel for corrosion resistance application-an experimental approach. ISSN (P): 2249-6890; ISSN (E): 2249-8001 vol. 7(5), pp. 123–144 (2017)

Chapter 20

Development of a Preliminary Approach for Automatic Generation of the CAD Model of the Spur Gear



Shubham Agarwal, Gurunandan Jamalpur, Nikhil Tuljapurkar, and Jayakiran Reddy Esanakula

Abstract The spur gear is an extensively used machine part where transmission of power is required between the shafts. The need for better spur gear is always there for the present market. Hence, there is a constant strive among the researchers to improve the design and productivity of the spur gear. In this regard, companies are looking forward to develop an advanced system for the design and development of the spur gear. A knowledge-based system can facilitate automating the design process with much more effectiveness. Hence, a knowledge-based system is required to address design and CAD modeling issues automatically. This paper presents an attempt to develop a preliminary approach for generating the spur gear automatically by CAD software based on the minimum design requirements inputs. Advanced modeling techniques like the parametric modeling technique is used to reach the target. Further, the proposed approach has proven itself as the better than the traditional approach where human is involved in CAD model generation.

20.1 Introduction

Automotive industries, shipbuilding, aerospace industries, industrial and architectural designs are some of the fields where computer-aided design (CAD) is extensively used as a tool. The comprehensive engineering method of 3D models and/or 2D sketches of physical parts is commonly done with CAD and is also used throughout engineering applications. Hence, this requires customization so that their effectiveness can be enhanced. The lack of skilled professionals available for CAD modeling and the complexity of design make modeling a time-consuming process. Alternate processes are being researched by the companies and the professionals too.

Shubham Agarwal, Gurunandan Jamalpur and Nikhil Tuljapurkar contribute equally to this work.

S. Agarwal · G. Jamalpur · N. Tuljapurkar · J. R. Esanakula (✉)
Department of Mechanical Engineering, Sreenidhi Institute of Science and Technology,
Hyderabad, Telangana 501301, India

To customize and improve CAD/CAM effectiveness and efficiency is the need of today's generation. A knowledge-based system (KBS) for engineering and design is important for fulfilling this requirement. The problem statement/task can be regenerated in no time when compared to humans with the usage of parametric modeling. The dimension-driven parametric modeling technique allows for automated reuse of existing design processed based on engineering analysis.

20.1.1 Spur Gear

The tooth profile of spur gear is such that they are cut parallel to the axis of the shaft. Because of this parallel profile of the tooth, they are generally used only in the case of parallel shafts. The tooth profile is shaped in the form of an involute curve which remains identical along the entire width of the gear. Generally, shafts are subjected to radial loads when spur gears are used. Figure 20.1 represents the nomenclature of spur gear. The CAD modeling of the spur gear is an elaborate and time-consuming process, and the specifications are constantly changing according to the customer's choice. Hence, automated modeling is very much essential. This can be achieved by the parametric modeling technique which is an advanced modeling technique of the CAD. Many researchers suggested using specialized methods such as KBS to reduce the time of modeling, even though it is an evolving discipline, the automatic generation of a KBE framework based on general knowledge will have the most drastic effects. This paper proposes a KBS for developing the CAD model of spur gear to reduce CAD modeling time.

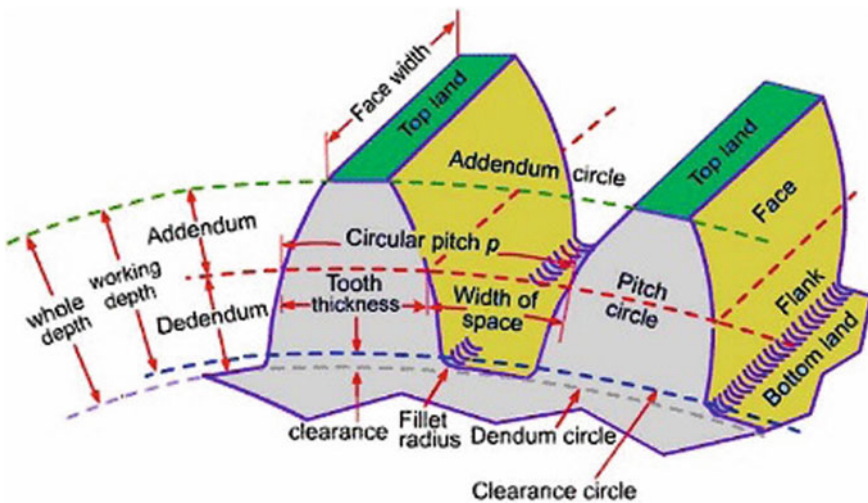


Fig. 20.1 Nomenclature of the spur gear [1]

20.1.2 Knowledge-Based Engineering (KBE)

The blend of CAD techniques and artificial intelligence (AI) technologies are well represented by an engineering method KBE. This provides advantages for customized or various design automation solutions [2–4]. The objective of the KBE system is to capture the product and process its information/data. It also involves simulating the engineering design process system and then uses the model to automate all or part of it. The internal representation of the product design process is the computer-generated product model. It includes information on both the product and the processes used to make the part. The focus is to provide complete product representational information which is captured in the product model. To capture the best design practices and engineering expertise into a corporate knowledge base should be the objective/intention of the KBE system [3].

20.1.3 SolidWorks API

The application programming interface (API) is a mechanism that allows various programs to communicate with one another. It is accomplished by embedding a programming language code within another application. Hundreds of functions are included in the API and can be accessed via visual basic for applications (VBA), VB.NET, Visual C#, Visual C++ 6.0 and Visual C++/CLI. These functions give direct access to SolidWorks features like drawing a line, adding an existing part into a part text and checking a surface's parameters. By writing special scripts, it is possible to automate the modeling and assembly of components using the SolidWorks API. SolidWorks API is a hierarchical tree-like framework that encompasses all of the program's features [5–7].

20.1.4 Visual Basic Language

Microsoft first introduced Visual Basic (VB) in 1991 as a third-generation programming language. It is a beginner-friendly programming language that allows us to quickly create graphical user interface (GUI) windows applications. Furthermore, VB is an effective engine for creating macros in all Microsoft applications. As a result, VB has evolved into a versatile method for creating various programming codes for a variety of applications, including SolidWorks [8].

20.1.5 Macros

A macro is a rule or pattern in computer science that specifies how a certain input sequence should be mapped to an output sequence according to a given process. To boost the design automation process, engagement with the model environment is critical. CAD systems have API interfaces that enable users to communicate with the model environment using macros. And, with the need for data sharing through technologies from different disciplines to solve real-world problems. In certain instances, a complex algorithm must be implemented to execute an efficient calculation that is not available in commercial applications [9].

20.1.6 Parametric Modeling Techniques

One of the most advanced CAD modeling approaches is the parametric modeling technique which provides approaches to traditional 2D drawings. It enables the reuse of pre-existing procedures to carry out quick design changes based on engineering rules that are already in place [10].

20.2 Literature Review

Macro programming can be blended with parametric modeling techniques for one's use to generate effortless and accurate solid shape modeling [4]. As these tools are of great help to minimize the complexities that come up during the time of modeling, these can be used widely for producing CAD-enabled modeling of spur gear [3]. Moreover, these tools facilitate the automation of CAD modeling, particularly for already existing tasks that can be automated and simplified with the help of a predefined algorithm/code [5]. With the help of computer-aided manufacturing, Cockerham and Waite [11] and Sun et al. [12] proposed a fully integrated series of steps for generating the design of spur gear. Modeling the tools and products using parametric modeling techniques were presented by Myung et al. [13]. These techniques facilitated the reduction of the CAD modeling time and led to a faster rate of production. A new process was shown by Yangshou et al. [14] for generating the dynamic gear model for performing structural analysis on it. Similarly, Kumar et al. [15], Dheeraj et al. [16] and Jayakiran et al. [17–20] developed a framework for optimized design on the SolidWorks platform which uses the knowledge-based system for CAD modeling and manufacturing.

A form of artificial intelligence (AI) technique known as knowledge-based system was designed to collect human expert knowledge to promote decision making. This form of computer software helps to increase the probability of generating sustainable modeling and simulation software within the given inputs and

specifications [21–24]. Even though much effort was put into developing parametric modeling of materials, little effort was put into spur gear. As a result, the authors assume that in the current market and research environment, a dedicated automated CAD modeling system for producing a spur gear is necessary, as the spur gear is an essential part of any energy transmission system through the shaft. To conclude, a lot of significant contribution was made toward the CAD modeling and manufacturing using the parametric modeling techniques to reduce the time for modeling and also lead to faster production rates with desired inputs. With the use of virtual basics (VB) as a development tool, SolidWorks can generate the CAD model. Analyzing geometrical information which is available in the predefined text data, an automated CAD model can be acquired.

20.3 Methodology for Modeling and Automation

Most commercial CAD software today is aimed at developing part models of components using a traditional approach and accepting input data in text format related to the model. Besides, a computer program [3, 11] can be used to feed this text input. This method was used to feed the input data in this article. This software can be written in a variety of programming languages, including VBA, C++, Lisp and others [17]. VBA is regarded as the most practical of these languages. The programming editor in SolidWorks CAD applications is VBA. As a result, the developers chose SolidWorks as the CAD program for designing the proposed method to produce spur gear automatic CAD model. Additionally, macro code is used to generate the spur gear CAD model since it allows for the automated creation of the CAD model.

20.3.1 Generating Graphical User Interface

The user can create and develop their GUI with the support of VB in SolidWorks. Figure 20.2 is the GUI that was created for the generation of the CAD model of the spur gear. Figure 20.3 shows the button that was created for the generation of the CAD model of the spur gear. The GUI was developed in such a way that it should be able to collect the required data from the user and should transfer the same inputs to the logical algorithm for performing the design calculations.

20.3.2 Program Development for Design Calculations

As presented earlier, the proposed system enables logical computation methods. This function aids the system in performing design calculations. Calculating the

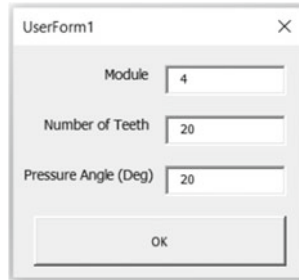


Fig. 20.2 GUI for spur gear

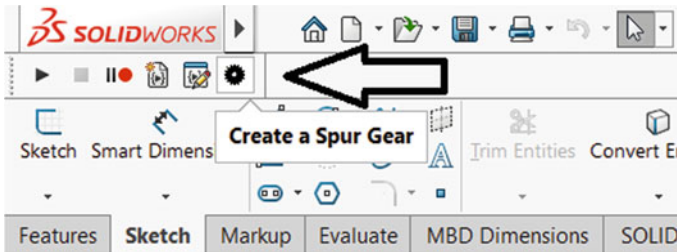


Fig. 20.3 Button for CAD model generation of the spur gear

appropriate dimensions manually using typical empirical methods is difficult and time-consuming. Computer software for design calculations is being developed in an attempt to address this complexity. This computer program will perform all detailed designs and computes for the spur gear geometrical dimensions. The program's output data will be transmitted to the SolidWorks software, which will produce a CAD model based on the computed geometrical parameters. As a result, design and modeling tasks are automated. Figure 20.4 shows the process flowchart of the proposed system.

20.4 Results

A sample result that was generated by the developed KBS is shown in this section. Generally, 150–200 h are required if the complete design calculations and the CAD modeling is done manually for spur gear [3]. But with the help of the proposed approach, the total time required for the complete modeling process is 15 s when it was executed on SolidWorks 2020. When compared to the traditionally generated CAD models and the approach given in the literature [3, 7], the proposed approach produces the same CAD model with very close dimensional accuracy. The sample

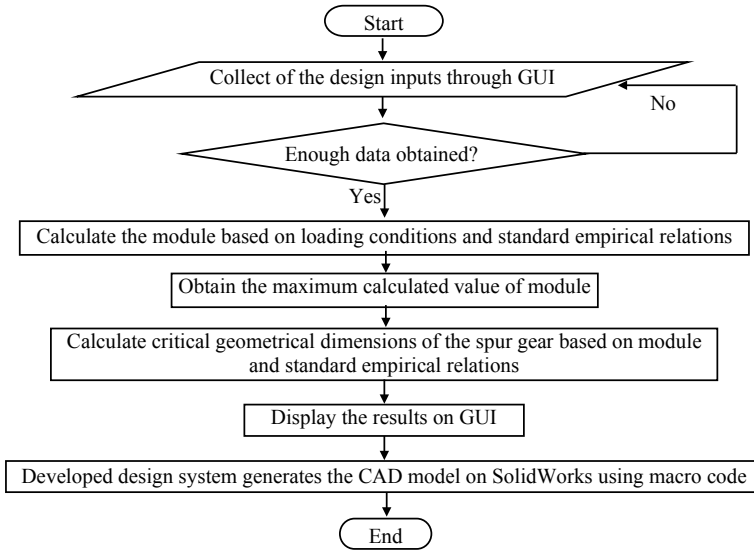


Fig. 20.4 Process flowchart of the proposed system

Table 20.1 Sample inputs for the proposed system

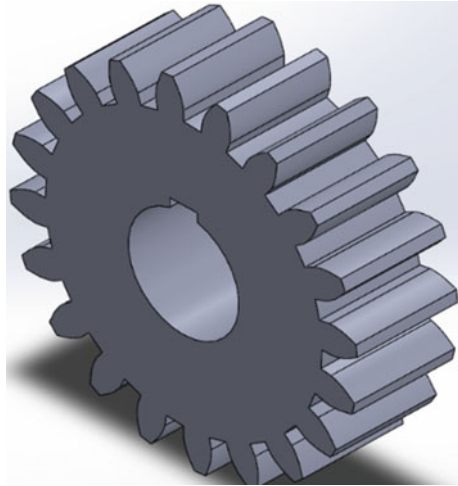
Parameter	Input data
Module	4
Number of teeth	20
Pressure angle	20°

Table 20.2 Spur gear dimensions (Output data)

Parameter	Output data
Diametrical pitch	0.25
Addendum	4
Dedendum	5
Addendum circle diameter (mm)	88
Dedendum Circle diameter (mm)	70
Base circle diameter (mm)	75.175
Pitch circle diameter (mm)	80

input data for the proposed system is given in Tables 20.1, and 20.2 presents the output data (spur gear dimensions) from the proposed system. Figure 20.5 shows the output (spur gear) of the proposed system.

Fig. 20.5 CAD model of the spur gear



20.5 Conclusion

A KBS for generating a CAD model of spur gear is proposed in the paper. This developed system uses VB and SolidWorks redevelopment technologies. This system reuses the design procedure with the help of parametric modeling technology. The proposed design procedure can be used on any computer which has access to SolidWorks. The proposed system is a user-friendly tool and handy to use. This system has also proved to run faster and generate a CAD model of a spur gear in comparison to the traditional approaches.

References

1. <http://mechanicallec.blogspot.com/p/machine-design-gear-drive-terminologies.html>, accessed on 15 April 2021
2. Reddy, E.J., Sridhar, C.N.V., Pandu Rangadu, V.: Knowledge based engineering: notion, approaches and future trends. *Am. J. Intell. Syst.* **5**, 1–17 (2015)
3. Jayakiran Reddy, E., Pandu Rangadu, V.: Development of knowledge based parametric CAD modeling system for spur gear: an approach. *Alexandria Eng. J.* **57**, 3139–3149 (2018)
4. Jayakiran Reddy, E., Sridhar, C.N.V., Pandu Rangadu, V.: Research and development of knowledge based intelligent design system for bearings library construction using solidworks API. *Adv. Intell. Syst. Comput.* **385**, 311–319 (2016)
5. Jayakiran Reddy, E., Venkatesu Naik, J., Rajendra, D., Pandu Rangadu, V.: Online knowledge-based system for CAD modeling and manufacturing: an approach. *Adv. Intell. Syst. Comput.* **910**, 259–268 (2020)
6. Jayakiran Reddy, E., Reddy, G.K., Rajendra, D.: Design of lifting tackle for armor plate of sinter machine. *Int. J. Tech. Phys. Probl. Eng.* **13**, 23–28 (2021)

7. Jayakiran Reddy, E., Rajendra, D., Venkatesu Naik, J.: Developing an automation system for generating the CAD model of Spur Gear. *Int. J. Mech. Prod. Eng. Res. Dev.* **10**(3), 8479–8488 (2020)
8. Jayakiran Reddy, E., Sridhar, C.N.V., Pandu Rangadu, V.: Development of web-based knowledge-based system for CAD modeling and manufacturing. *Mater. Today: Proc.* **5**, 27241–27247 (2018)
9. Jayakiran Reddy, E., Pandu Rangadu, V., Ramachandra, R., Naga Prasad Naidu, V.: Development of a constraint-based approach for Knowledge-Based System for CAD modeling. *Adv. Sci. Eng. Med.* **10**, 357–361 (2018)
10. Jayakiran Reddy, E., Rama Chandra, R.: Development of an intelligent system for the design of a two wheeler IC engine connecting rod. *Int. J. Eng. Sci. Invention* **6**, 67–74 (2017)
11. Cockerham, G., Waite, D.: Computer-aided design of spur or helical gear train. *Comput. Aided Des.* **8**(2), 84–88 (1976)
12. Sun, B., Qin, G., Fang, Y.: Research of standard parts library construction for solidworks by visual basic. In: *International Conference on Electronic & Mechanical Engineering and Information Technology*, pp. 2651–2654 (2011)
13. Sehyun, M., Soonhung, H.: Knowledge-based parametric design of mechanical products based on configuration design method. *Expert Syst. Appl.* **21**, 99–107 (2001)
14. Yangshou, X., Kang, H., Tao, W., Qi, C., Rui, X.: Dynamic modelling and analysis of the microsegment gear. *Shock Vibration*, 13 pages (2016)
15. Kumar Yogeesh, D., Chandrasekaran, M., Eriki Ananda, K., Jayakiran Reddy, E.: Optimization of vibration reduction by De-Coupling method in power train of trucks. *ARPN J. Eng. Appl. Sci.* **11**, 6423–6427 (2016)
16. Thuniki, D., Ravikiran, M.S.S.R., Esanakula, J.R., Venkateswara Rao, B.: Design, modification and analysis of 3 ton electrical overhead travelling crane rope drum. *IOP: Mater. Sci. Eng.* **1057**, 1–10 (2021)
17. Jayakiran Reddy, E., Raju, G.N., Sai, G.A.: Development of a preliminary system for automatic generation of CAD model of the Universal Coupling. *Int. J. Mech. Prod. Eng. Res. Dev.* **10**(3), 8701–8710 (2020)
18. Jayakiran Reddy, E., Sridhar, C.N.V., Pandu Rangadu, V.: Knowledge—based parametric modeling for bolts, nuts and bearings using solidWorks. *Int. J. Appl. Eng. Res.* **10**, 16111–16120 (2015)
19. Jayakiran Reddy, E., Sridhar, C.N.V., Pandu Rangadu, V.: Development of KBS for CAD modeling of a two wheeler IC engine connecting rod: an approach. *Adv. Intell. Syst. Comput.* **530**, 597–606 (2016)
20. Jayakiran Reddy, E., Sridhar, C.N.V., Pandu Rangadu, V.: Development of KBS for CAD modeling of industrial battery stack and its configuration: an approach. *Adv. Intell. Syst. Comput.* **530**, 607–618 (2016)
21. Singh, A., Singh, I., Kalsi, S.: FEM analysis of human CAD model in standing posture while travelling. *Int. J. Mech. Prod. Eng. Res. Dev.* **9**, 29–35 (2019)
22. Jayakiran Reddy, E., Venkatachalapathi, N., Pandu Rangadu, V.: Development of an approach for Knowledge-based system for CAD modelling. *Mater. Today: Proc.* **5**, 13375–13382 (2018)
23. Jayakiran Reddy, E., Bala Raju, A., Bhanodaya Kiran Babu, N.: Enhancing the existing 3 ton electrical overhead travelling crane rope drum by adopting reverse engineering. *IOP: Mater. Sci. Eng.* **1057**, 1–10 (2021)
24. Jayakiran Reddy, E., Bhanodaya Kiran Babu, N., Bala Raju, A.: Reverse engineering technique for enhancing the EOT crane rope drum. *IOP: Mater. Sci. Eng.* **1057**, 1–10 (2021)

Chapter 21

Design of a Robot for the Welfare of the Poultry



Rushikesh Hanuman Yede and Skylab Paulas Bhore

Abstract This paper is on the design of an automatic robot for the welfare of the poultry. The poultry farming is a growing segment of the agriculture in India. The poultry farming creates significant air pollution. To reduce the environmental impacts of the poultry farming, a waste management is considered as the effective method. The implementation of a waste management in the poultry farm incurs the physical contacts between the birds and the personnel and leads to the spread of different diseases. To resolve these problems, an automatic robot is designed. The robot continuously maneuvers on the floor. The underneath tool scrubs the floor and makes the litter and bird waste upside down. Therefore, the odor and the time required to dry the waste reduce. In addition, the bird movement and the production rate are increased.

21.1 Introduction

Poultry farming is a growing sector within the agriculture domain in our country. It is usually classified into organized and unorganized industrial sector. The requirements of organized and unorganized sectors are different. The organized sub-sector follows all the rules tested by various corporations throughout their productions. Poultry farming is principally divided into two kinds of business models, viz broiler production and egg production. More than 80% of boiler production output is produced in the organized sector [1]. The various methods are used in broiler production to keep birds in the poultry farming like intensive and unconfined poultry, layer poultry, organic, yarding methods, etc. Usually, intensive poultry farming is used for a larger variety of poultry birds with high stocking density [2]. According to the Worldwatch Institute, “Around 74% of total poultry meat and 68% of total poultry eggs area unit created from intensive poultry farming

R. H. Yede (✉) · S. P. Bhore

Product Development Lab, Department of Mechanical Engineering, Motilal Nehru National Institute of Technology Allahabad, Prayagraj, Uttar Pradesh, India
e-mail: skylabpbhore@mnnit.ac.in

method” [2]. This method is economical considering factors such as land, feed, labor, and alternative resources and increases the production. In India, the poultry farming business is fully controlled by the farmer. It ensures continuous production throughout the year. However, some disadvantages of this method are generating health risks and environmental threats.

The characterization of wastes and their main elements such as ways of disposals, water quality impact, chemical and microbiological dynamics, etc. [3]. Characterization of wastes is principally because of three factors viz. poultry litter, poultry manure, and dead birds. Poultry litter refers to the material utilized by the poultry for bedding throughout the assembly cycle. The litter material is typically wood, packing, wheat straw, peanut hulls, or rice hulls. Generally, during the broiler production, the accumulating manure is mixed with the litter. The production of litter is influenced by age and breed of chickens, the density of confinement, feed conversion rate, feed volume, type and amount of litter, wet content of litter, floor surface, weather conditions during litter accumulation, and organic matter.

There is a huge amount of various gases trapped inside poultry litter and manure like carbon (C), ammonia (NH₃), nitrate (NO₃), chlorine (Cl), phosphorus (P), potassium (K), etc. The compositions of various gases in poultry litter and poultry manure are given in Tables 21.1 and 21.2.

The main reason of bad odor spread in the poultry and its surrounding is due to the trapped gases [4]. The magnitude of the environmental impact of poultry farming depends on production practices, particularly on manure management practices. The lack of awareness and the capital cost are two factors that affect the implementation of manure management practices [5–24].

The manure management practices are implemented through the collection of poultry litter (once a week in the dry season and twice in a week in the rainy season)

Table 21.1 Composition of gases in poultry litter (g in kg of litter) [3]

Gases	Reported mean	Range
Carbon (C)	376.0	277.0–414.0
Ammonia (NH ₃)	4.6	0.10–20.10
Nitrate (NO ₃)	0.20	0.0–0.70
Chlorine (Cl)	12.7	6.0–50.0
Phosphorus (P)	14.30	8.0–25.8
Potassium (K)	20.70	13.0–45.70

Table 21.2 Composition of gases in poultry manure (g in kg of manure) [3]

Gases	Reported mean	Range
Carbon (C)	290	223–327
Ammonia (NH ₃)	14.40	0.210–29.90
Nitrate (NO ₃)	0.40	0.03–1.50
Chlorine (Cl)	24.50	6.0–60.0
Phosphorus (P)	20.70	13.5–34.0
Potassium (K)	20.90	12.5–32.5

and stored in the bags or dumped in the separate compartment. The collection of poultry litter is difficult in intensive and free-range poultry farming methods because birds roam over entire shed area. Therefore, the poultry farmer tries to dry the mixture of poultry manure and poultry litter on the floor by frequent scrubbing and making the litter upside down manually with local tools. It leads to contact between poultry birds and human, and diseases may spread from human to the birds. In this paper, a design of robot is proposed to address the above problem. The objectives are to design a robot so as to free out trapped gases in poultry litter and manure and to increase movement of birds. The robot scrubs the floor and make the litter upside down for quick dry. In addition, it prevents human–birds contact.

21.2 Methodology

The concept generation is an important stage for designing a new product. As per the poultry farmers' requirement, there is a need of automatic device (or robot) which performs the routine work such as scrubbing the floor and make the litter upside down. To define the specification of robot, the information on the nature of the shed, the density of birds in a shed, the path of a robot, a general obstacle in the path of a robot, etc., are collected.

The shed is a place where the birds are kept. The dimensions of a shed are helpful to decide a path of the robot during its operation. In addition, the information on the roughness of a floor helps to decide the traction of the wheels of a robot. The extra care on the change of floor surface characteristics due to poultry litter is considered. Traction is an important factor in the selection of wheel and type of drive given to wheel. There are four major types of robot wheel available such as standard, caster ball, Mecanum, and Omni wheel. In this work, a 6-inch standard wheel was selected (see Fig. 21.1b).

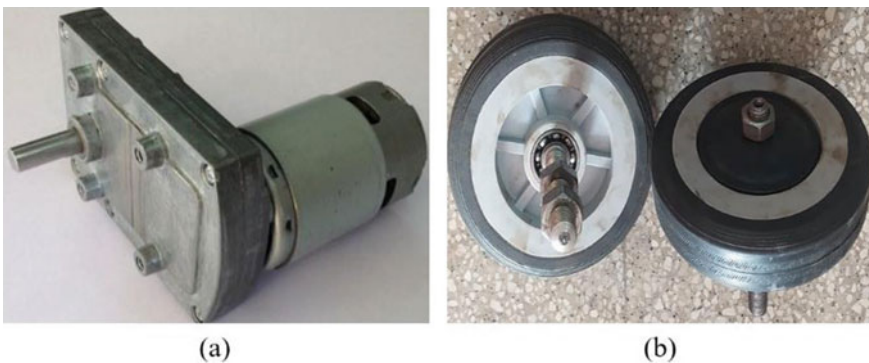


Fig. 21.1 Actual components **a** Motor. **b** Front wheels

The wheels are driven by means of a motor. The selection of motor speed and torque is obtained as follows,

$$\text{Rotational speed (RPM)} = \frac{\text{Robot, speed}}{\text{wheel circumference}}$$

$$\text{Torque} = \frac{\text{Mass of robot} \times \text{Accel. due to gravity} \times \text{Radius of wheel} \times \text{Coefficient of friction}}{\text{Number of wheel to be drive}}$$

In the above relation, the robot speed is fixed on the value of the maximum and minimum speed of the bird. The obtained motor speed and torque are 100 rpm and 5 Nm, respectively. However, the motor with 8Nm torque is selected considering safety factor and the market availability (see Fig. 21.1a).

A tool is designed to scrub the floor and to make the litter on the floor upside down. A shaft with curved blade arrangement is proposed as shown in Fig. 21.2. A shaft is driven by separate motor with sufficient torque to perform the task. The spacing between two blades and the geometry of curved blades is finalized based on initial prototypes.

To design an automatic robot, various electronic components such as microcontroller, distance sensor (ultrasonic sensor), servo motor, and motor controller are required. The microcontroller used in a present robot is Arduino UNO with ATmega328P microcontroller chip. It has 5 V operating voltage, 32 KB flash memory, and 14 digital pins out of which 6 pins provides pulse width modulation (PWM) output, 16 MHz frequency and 7 to 12 V input voltage, and 6 analog input pins (see Fig. 21.3a). Distance sensor is used to measure the distance of the robot from the wall of a shed. It is an ultrasonic sensor (HC-SR04 module) with

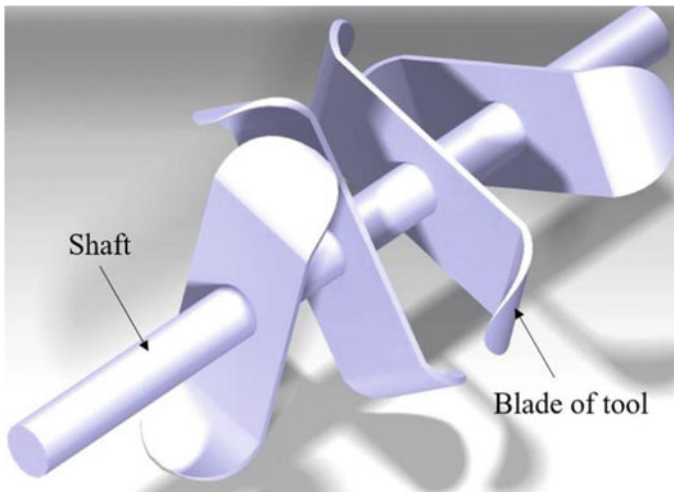


Fig. 21.2 CAD model of tool

specification, viz 5 V (DC) voltage, 15 mA operating current, and 40 Hz frequency. It measures distance in the range of 0.02–4 m (see Fig. 21.3b). The servo motor is used for rotating an ultrasonic sensor through 90° when the measured distance is less than the turning radius of a robot. It has a specification of 0.1765 Nm stall torque, 0.1 s/60° operating speed, 5 V operating voltage, and the mass 9 g (see Fig. 21.3c). The motor controller is used for connecting a microcontroller and the motor (see Fig. 21.3d).

A program in Arduino IDE software is written (see Fig. 21.4a). The above components are wired and interfaced with personal computer for testing. A detail flowchart is shown in Fig. 21.4b.

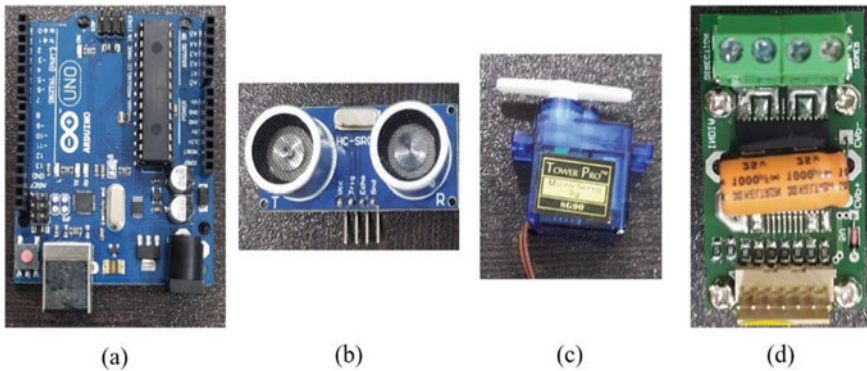


Fig. 21.3 Electronic components **a** Arduino UNO. **b** Ultrasonic sensor. **c** Servo motor. **d** Motor controller



Fig. 21.4 **a** A program in Arduino IDE software. **b** A detailed flowchart of a program

21.3 Result and Discussion

After following the methodology given in Sect. 21.2, an automatic robot is designed and developed. The dimensions of the robot are $400 \times 350 \times 200$ (L \times B \times H) mm³. A 3D CAD model of the automatic robot is developed in CATIA -V5 software. The rendered image of the robot is shown in Fig. 21.5.

The program in the microcontroller (Arduino UNO) allows the user to enter floor area. The robot automatically maneuvers on the floor area.

The robot moves in forward direction by means of DC motor and ultrasonic sensor continuously measures the distance of robot from boundary of poultry farm. When it reaches below the turning radius of robot, then it will stop at that point. Then, servo motor turns 90 degree in clockwise direction. Ultrasonic sensor above servo motor decides distance between wall and robot. If distance is above turning radius, then robot can take U-turn in clockwise direction and if not, it takes anti-clockwise U-turn. After completion of U-turn, it moves in forward direction. Robot repeats the above steps to cover the whole farm area.

The tool attached to the robot constantly rotates and scrubs the floor. It makes the litter on the floor upside down. Therefore, the trapped gases come out and reduces the dry time and the odor. According to the study, 6–7 days are required to dry a bird waste and the other litters on the floor. When the present automatic robot is used in the poultry, the time reduces to 2–3 days.

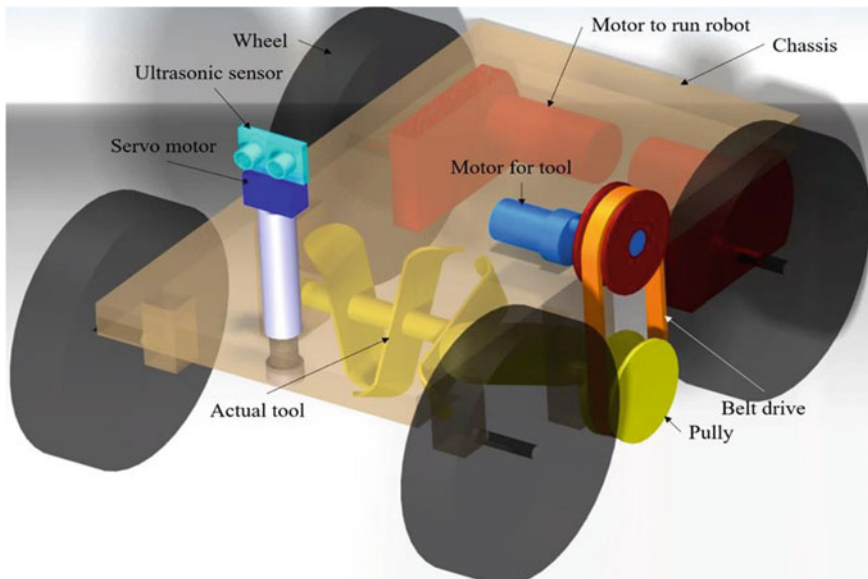


Fig. 21.5 Isometric view of automatic robot

According to the personal interaction with the local poultry farmers, nearly 45–50 days are required to grow the broiler birds from 300 g to 3 kgs in normal condition. When an automatic robot is used, the movement of the birds on the floor happens frequently. Therefore, the birds consume more grains and gain the required weight within 40–42 days. This helps a farmer to produce 2–3 more batches per year.

The main advantage of the automatic robot is that it reduces the human interaction with the birds and resulting diseases. Due to the removal of trapped gases from the bird waste and the other litters on the floor, the spread of the bird diseases is significantly reduced.

21.4 Conclusions

The poultry farming is a growing segment in the agriculture domain in India. The environmental impact due to poultry farming especially air pollution is high near to a poultry farm. The manual tool to make wastes upside down is a conventional method that can consume more time and leads to the spread of diseases from humans to poultry birds. To overcome these issues, an automatic robot is designed for the poultry farms. The automatic robot is found to be more effective in improving the air quality, the birds welfare, and production rate.

References

1. National action plan of poultry farming.: <https://dahd.nic.in/sites/default/files/Seeking-Commentson-National-Action-Plan-Poultry-2022> by 12–12–2017.pdf (2012)
2. Poultry Farming—Garden Pool.: <https://gardenpool.org/facts/poultry-farming>
3. Edwards, D.R., Daniel, T.C.: Environmental impacts of on-farm poultry waste disposal, biological and agricultural engineering department. *Biores. Technol.* **41**, 9–33 (1992)
4. Pelletier, N.: Environmental performance in the US broiler poultry sector: life cycle energy use and greenhouse gas, ozone depleting, acidifying and eutrophying emissions, science-direct. *Agric. Syst.* **98**, 67–73 (2008)
5. Maheshwar, S.: Environmental Impacts of Poultry Production. *Poult Fish Wildlife Science* (2013)
6. Rodić, V., Perić, L., Đukić-Stojčić, M., Vukelić, N.: The Environmental Impact of Poultry Production, Institute for Animal Husbandry, Belgrade-Zemun Biotechnology in Animal Husbandry, vol. 27(4), pp. 1673–1679 (2011)
7. Baxevanou, C., Fidaros, D., Bartzanas, T., Kittas, C.: Energy Consumption and Energy Saving Measures in Poultry. *Energy Environ. Eng.* **5**(2), 29–36 (2017)
8. Akers, J.B., Harrison, B.T., Mather, J.M.: Drying of poultry manure—an economic and feasibility study. In: *Managing Livestock Wastes. Proc. 3rd Int. Symp. on Livestock Wastes.* ASAE, St Joseph, MI, pp. 473–477 (1975)
9. Ammerman, C.B., Henry, P.R., Vijchulata, P.: Influence of cage layer manure on tissue mineral levels of finishing steers. In: *Livestock Waste: A Renewable Resource. Proc. 4th Int. Symp. on Livestock Wastes.* ASAE, St Joseph, MI, pp. 63–65 (1980)

10. Atkinson, G., Dietz, S., Neumayer, E.: Handbook of Sustainable Development. Edward Elgar, Cheltenham (2007)
11. Bolan, N.S., Szogi, A.A., Chuasavathi, T., Seshadri, B., Rothrock, M.J., Panneerselvam, P.: Uses and management of poultry litter. *World's Poultry Sci. J.* **66**, 673–698 (2010)
12. Akhtar, A.Z., Greger, M., Ferdowsian, H., Frank, E.: Health professionals' roles in animal agriculture, climate change, and human health. *Am. J. Prev. Med.* **36**(2), 182–187 (2009)
13. Are, K.S., Adelana, A.O., Fademi, I.O.O., Aina, O.A.: Improving physical properties of degraded soil: Potential of poultry manure and biochar. *Agric. Nat. Resources* **51**(6), 454–462 (2017)
14. DEFRA.: Consultation on 1.1.1 Sector Guidance Note IPPC SG8: Integrated Pollution Prevention and Control (IPPC), Secretary of State's Guidance for the A2 Rendering Sector. DEFRA Publications, UK (2008)
15. Arogo, J., Westerman, P.W., Heber, A.J., Robarge, W.P., Classen, J.J.: Ammonia in animal production—a review. Paper number 014089, 2001 presented at the ASAE Annual Meeting July 30–August 1, 2001, Sacramento, USA. American Society of Agricultural and Biological Engineers (2001)
16. Bowman, A., Mueller, K., Smith, M.: Increased animal waste production from concentrated animal feeding operations: potential implications for public and environmental health. Occasional Paper Series, No. 2. Omaha, USA, Nebraska Centre for Rural Health Research (2000)
17. Gvartyan, G., Cunningham, D.L., Van Tienhoven, A.: Filial imprinting, environmental enrichment, and music application. Effect on behaviour and performance of meat strain chicks. *Poult. Sci.* **68**(2), 211–217 (1989)
18. De Boer, I., Van Der Togt, P., Grossman, M., Kwakkel, R.: Nutrient flows for poultry production in the Netherlands. *Poult. Sci.* **79**, 172–179 (2000)
19. Delgado, C., Rosegrant, M., Steinfeld, H., Ehui, S., Courbois, C.: Livestock to 2020: The Next Food Revolution. International Food Policy Research Institute, Washington, DC (2020)
20. IEEP.: The environmental impacts of trade liberalization and potential flanking measures. Stage 1 of a Report to DEFRA. London, Institute for European Environmental Policy (2005)
21. Nachman, K.E., Graham, J.P., Price, L.B., Silbergeld, E.K.: Arsenic: a roadblock to potential animal waste management solutions. *Environ. Health Perspect.* **13**(9), 1123–1124 (2005)
22. University of Maryland.: Broiler production and the environment. College Park, MD, USA, College of Agriculture and Natural Resources, University of Maryland (available at http://ag.udel.edu/iseq/images/EB_368_Poultry_Regs_book_6%2027%2006.pdf) (2006)
23. Tao, J., Mancl, K.: Estimating manure production, storage size, and land application area. Fact Sheet Agriculture and Natural Resources AEX-715–08, The Ohio State University Extension (2008)
24. Singh, P., Mondal, T., Sharma, R., Mahalakshmi, N., Gupta, M.: Poultry waste management. *Int. J. Curr. Microbiol. App. Sci.* **7**(08), 701–712 (2018)

Chapter 22

A Despeckling Filter for Ultrasound Images Based on Cellular Automata Approach



Ankur Bhardwaj, Sanmukh Kaur, Manoj Shukla,
and Anand Prakash Shukla

Abstract In the medical profession, ultrasound imaging for clinical recognition is far better suggested than any other imaging mode because of its adaptability, suitability, safety, and viability. The images that are taken and then preprocessed as part of the procedure are crucial in medical diagnosis. Different types of noise can be added to the images during the uploading process. The more deteriorated the image, the more difficult it is to better isolate the required components, recognize them, and examine edge clarity. In this study, a comparison is made between several filters such as Gaussian, Kuan, Lee, guided, and anisotropic filters, as well as the proposed filter, which is based on the cellular automata principle. Developing the proposed filter using the cellular automata approach yields superior results in terms of image parameters accessible for consideration.

22.1 Introduction

Ultrasound imaging is a non-invasive method for diagnosing a variety of diseases. It provides real-time photographs of human organs such as the liver, kidneys, heart, uterus, stomach, and many others. Despite its cost-effectiveness and utility, speckle noise, Gaussian noise, and environmental noise render it ineffective. The previous one not only lowers image quality but also imposes certain limitations on disease diagnosis. It is up to the expert who applied their expertise to assess the result of the US imaging. When ultrasound images are recorded or displayed on a computer,

A. Bhardwaj (✉) · M. Shukla
Computer Science and Engineering Department, ASET, Amity University, Noida, India
e-mail: mkshukla@amity.edu

S. Kaur
Electronics and Communication Engineering Department, Amity University, Noida, India
e-mail: skaur2@amity.edu

A. P. Shukla
Department of Computer Science and Engineering, KIET Group of Institutions,
Ghaziabad, India

noise may also distort them. Noise is a common factor that degrades image quality and resolution. The noise in the photographs appears to obscure the fine details. Noise may appear in images because of some physical issue with the imaging systems. It is possible for the noise to be additive or multiplicative in nature. If the classification is done for noise removal based on the nature, additive noise is much easier to reduce than multiplicative noise because it is image dependent. Speckle is a type of multiplicative noise that can be found in a variety of imaging systems that are consistent or systematic. Speckle noise is caused by the constructive and destructive interference of scattered ultrasound waves returning from within the body after striking the body part for which they were intended [1]. The consistency of the captured image, as well as the details of fine lines and edges, suffers as a result of this speckle noise.

22.2 Related Study

In the medical field, speckle noise is a type of underlying quality in ultrasonic imaging. It is responsible for the resolution of the collected image and changes that produce depletion, resulting in a value of diagnosis error in the computing modality [2]. As a result, it is becoming increasingly vital to reduce speckle noise in the first phase, preprocessing, so that ultrasonic imaging can be used for medical purposes. As a result, despeckling the image becomes a primary feature, and noise is removed from the image [3], all while maintaining the required features. The resulting noise disrupts signals returning from objects that are typically smaller than a single image-processing element. Due to the noise present, it is difficult to visualize the image. Goodman [4] provided a statistical property analysis for the speckle noise, which aided in the denial, acceptance, and consideration of the laser speckle to a large extent. Goodman devised a way for overcoming speckle noise using several filtering (linear) methods, which improved image quality. This statistical property that occurs because of noise was extremely useful in identifying differences between different types of tissues [5]. The consequence of [4] was improved in [5]. The most prevalent approaches in the field were detailed, as well as a collection of innovative techniques and hybrid methods that have become more important in speckle filtering and provide novel solutions to typical difficulties in US pictures. Salazar et al. [6] investigated despeckling methods and their implications on legal metrology for healthcare services that are primarily concerned with human safety. Mei and Hu [7] offer an ultrasound speckle filtering approach for filtering tissue-dependent complex speckle noises in ultrasound pictures while maintaining various edge properties. Alex [8] introduces the notion of marker inpainting on medical pictures created using several modalities, which is critical for processing the pictures for a variety of applications. Speckle noise is an intrinsic and well seen problem in medical pictures, particularly in ultrasound pictures. It changes the

margins, small details, and other organ properties that are necessary for interpretation. The requirement for despeckling 2D ultrasound images is investigated in this study by comparing the performance metrics for inpainting using a fast-marching algorithm on speckled and despeckled 2D ultrasound images. Latif et al. [9] suggested a convolutional neural network (CNN) model using a Mendeley Breast Ultrasound dataset, followed by another CNN model for classifying ultrasound images into benign and malignant groups. Rotman et al. [10] suggested a method for compressing and despeckling ultrasonic images at the same time, based on the optimization of quantization parameters applied to the coding transform coefficients.

22.3 Despeckling Filters

- (i) **Bilateral Filter:** A bilateral filter is an irregular method capable of minimizing noise through the application of an averaging filter in images while preserving the edges. The objective of this filter is to blur the photographs captured to edit them while maintaining sharp borders [11]. It alters the magnitude of each pixel by taking a weighted average of nearby pixels' magnitudes, with the weight depending on a Gaussian distribution. This feature is dominating because it makes it easier to record instinct about a creature's behavior, apply it to a specific application requirement, and execute it [12].
- (ii) **Anisotropic Diffusion:** This filter aims to reduce picture noise while preserving crucial components of the image's content, such as edges, lines, and small details that seem to be important for completely interpreting an image [13]. It is the equivalent of processing and constructing a multiscale single representation, with the end result being an image made up of multiple indistinct representations that rely on the diffusion procedure.
- (iii) **Kuan Filter:** It works well to despeckle the SAR image used in image processing. The despeckling algorithm is well known, despite the presence of many local statistical filters. It performs efficiently within the same area of SAR pictures as the border specified with retribution [14].
- (iv) **Lee Filter:** This filter smooths down the image's dominating noise [15] in proportion to the scene of the image and so has an additional component. The Lee filter's function is determined by the standard deviation of the filtered images, which is calculated within each of the filter's individual windows.
- (v) **Median Filter:** The margins must be preserved while the noise is removed. This filter utilizes a type of digital filter with nonlinear algorithms to erase pixels from an image [16]. This method is quite effective at preserving the photographs' important information.

22.3.1 Cellular Automata

Ulam [17] created the term “cellular automata” to describe an individual dynamical system. The parameters of space and time are referred to as discrete systems. The lattice (cells) in this case has a set number of states that are organized in the pattern. Any number can be used to set the grid’s dimensions. At each given time, the state of a particular lattice is solely determined by itself and the adjoining cells one step ahead. The state of a cell is created by a transformation rule, which may be thought of as a mathematical function that changes and updates in real time.

A 2D deterministic CA can be understood and described as a set of three tuples:

$$R = (S : N; \delta) \quad (22.1)$$

where ‘ S ’ is a state set that is not empty. The usage of a ball described by a metric $N(x_0, y_0)$ is a common technique to define neighborhood $N \in \mathbb{Z}^2$. ‘ δ ’ is a transition function that, according to the deterministic rule, clashes with the current state of the specified cell and its neighbors and returns the assigned cell’s next state. There are two sorts of neighborhood variety:

- (i) **Von Neumann Neighborhood:** It’s a diamond-shaped approach with its neighbor, as shown in Fig. 22.1a, and it is utilized to define a cell set with a defined surrounding cell range (x_0, y_0) that effects the square grid of 2D CA.

$$N(x_0, y_0) = (x, y) : |x - x_0| + |y - y_0| \leq r \quad (22.2)$$

- (ii) **Moore Neighborhood:** The square shape pattern is used to traverse over the pixel in this type, even the set of specified neighboring cells (x_0, y_0) are used for definition. The 2D CA which gets affected is shown in Fig. 22.1b and is defined as:

$$N(x_0, y_0) = (x, y) : |x - x_0| \leq r, |y - y_0| \leq r \quad (22.3)$$

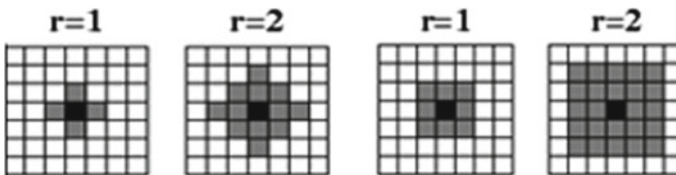


Fig. 22.1 a Von Neuman. b Moore neighborhood

22.4 Quality Parameters for Images

(i) Mean Square Error (MSE): This looks for any differences in grade between a taken image (R) and a processed (noise-free) image (S) of size $M \times M$ [18]. It is written as

$$SE = \frac{1}{M^2} \sum_{i,j=0}^{M-1} (R_{i,j} - S_{i,j})^2 \quad (22.4)$$

MSE is used to scale the image standard, but it cannot work on its own because it does not correlate well enough with the non-cognitive standards. As a result, multiple quality metrics and observable approaches must be compared.

(ii) Signal-to-Noise Ratio (SNR): With the noise in the background, this detects the amount of required signal. The background noise becomes less noticeable as the proportion rises [19]. It is measured in decibels (dB) as follows:

$$SNR = 10 \log_{10} \left(\frac{\sigma^2}{\sigma_e^2} \right) \quad (22.5)$$

where σ^2 is the initial image variance and σ_e^2 be error variance.

(iii) Peak Signal-to-Noise Ratio (PSNR): PSNR is the parameter for statistical quality measurement which is the ratio of the maximum strength to the noise effect of a signal that affects the reliability of its presentation. This can be [20] given as

$$PSNR = 10 \log_{10} \left(\frac{L^2}{MSE} \right) \quad (22.6)$$

where L is the captured (original) image's maximum intensity. The image quality improves when the PSNR value rises, and vice versa.

22.5 Proposed Algorithm

A digital image is shown as a matrix with R rows and C columns, with either gray or color. It is possible that each cell corresponds to the image pixel and the cells' obtainable status to the gray or color values of the corresponding pixel can be represented in a two-dimensional cellular automata mesh. The value was first set to the pixel values of the input image. The state or gray level of the cell depends on the states or gray levels of the adjacent cells. In this case, the boundary value has been stabilized; only non-boundary cells can apply the new rule. We used ultrasound images on a grayscale to denoise the Moore neighborhood.

Let $\{N1(t), N2(t) \dots Nn(t)\}$ contains n samples of pixel element in Moore neighborhood, the current automata cell, at any time t . $\{Ni1(t), Ni2(t), \dots, Nin(t)\}$ is the sorting form for statistical result. Where the minimum is $Ni1(t)$ and the maximum intensity is $Nin(t)$. The mid-pixel value will be changed discreetly with time $t + 1$. The transition rule δ can be represented for cellular automats as:

$$N(t+1) = \frac{1}{n - 2[\alpha n]} \sum_{j=[\alpha n]+1}^{n-[\alpha n]} N_j(t) \quad (22.7)$$

Here $[\cdot]$ represents the highest integer part and $0 \leq \alpha < 0.5$.

Equation (22.7) has been modelled to reflect the proposed filter. This equation clearly shows the percentage of the summary samples in the Moore neighborhood. When the value is about 0.5, it finds the average of mask surrounded cells and moves to the average of next pixels when close to 0.5. Both the least and maximum pixel values are omitted to illustrate the output of the proposed filter.

All processes in a cellular automaton runs in parallel. We consider a temporary image identical to the simulation input image and then maintain the pixels processed. The output of each iteration is further replicated to the original image in a temporary image.

ALGORITHM:

1. *CREATE IMAGE Y -> SIZE[X]*
2. *Read picture X for i=2 to row-1 and j=2 to col-1 X(i,j)*
3. *Sort the pixels next to each other in ascending order.*
4. *Remove the least and maximum values.*
5. *Measure the average of the pixels on the left.*
6. *In Y, assign the estimated mean value Y(i,j)*
7. *end for*
8. *Assigned the value of Y to X.*

In this case, 'X' is used as the filtering input image. Initially, we render the temporary picture 'Y,' which is identical to 'X.' After that, for each pixel in image X, here we arranged all pixels in the Moore neighborhood in ascending order based on their intensity, ignoring the boundary pixels. Next, in the sorted list, remove both the maximum and least strengthen values.

Calculate the average of the intensity values of the leftover pixels. Following that, the measured value is copied to temporary image Y. After the process is completed, the values obtained from Y are copied back to image X.

22.6 Results and Discussion

On brachial plexus pictures, the proposed filter is applied and simulated in Matlab 2018. On different levels of speckle noise, the quality of images determined by mean square error, mean structured similarity index, signal-to-noise ratio, peak signal-to-noise ratio, and square root mean square error ranges from 0.01 to 0.1. Tables 22.1 and 22.2 demonstrate a comparison of four well-known despeckling filters with a proposed filter based on the cellular automata concept (Figs. 22.2 and 22.3).

Despeckling ultrasound medical imaging is one of the biggest and most challenging digital healthcare enterprises. The quality of the ultrasound image obtained determines the complete diagnosis. The proposed cellular automata filter is utilized to despeckle medical ultrasound images in this research. After examining a vast number of existing filters, a transition function for the proposed filter was created. The proposed filter was created in Matlab 18 and evaluated for ultrasonic nerve segmentation [21] on over 100 ultrasound pictures of the brachial plexus. This filter has been proven to operate well and offer better results. Tables 22.1 and 22.2 show how the suggested filter preserves the edges by examining at the values of MSSIN. It performs admirably in terms of PSNR when compared to other filters.

Table 22.1 Comparison of filters at the noise level 0.01 on image 1

Feature/ Filters	Median filter	Anisotropic diffusion	Kuan	Lee	Proposed filter
MSE	59.29	70.07	93.27	45.83	18.492
SNR	12.671	11.219	8.735	14.907	70.989
SRMSE	7.699	8.37	9.657	6.769	4.3
PSNR	30.44	29.71	28.47	31.55	35.494
MSSIN	0.962	0.965	0.975	0.97	0.999

Table 22.2 Comparison of filters at the noise level 0.05 on image 1

Feature/ Filters	Median filter	Anisotropic diffusion	Kuan	Lee	Proposed filter
MSE	206.46	1537.67	169.1	111.8	56.829
SNR	1.834	-15.6065	3.569	7.165	61.238
SRMSE	14.368	39.213	13	10.57	7.538
PSNR	25.02	16.3	25.88	27.68	30.619
MSSIN	0.878	0.611	0.922	0.921	0.999

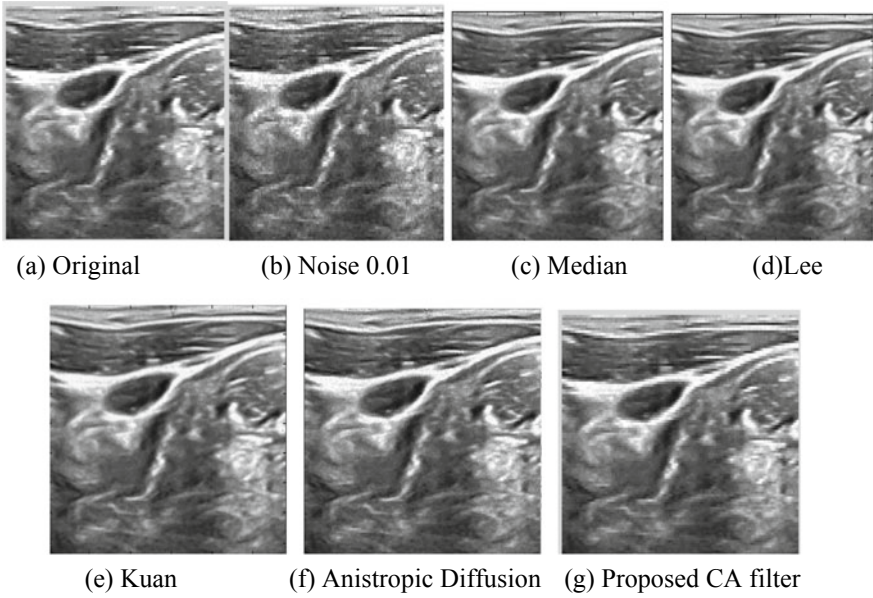


Fig. 22.2 Results of various filters for Image 1 at 0.01 noise density

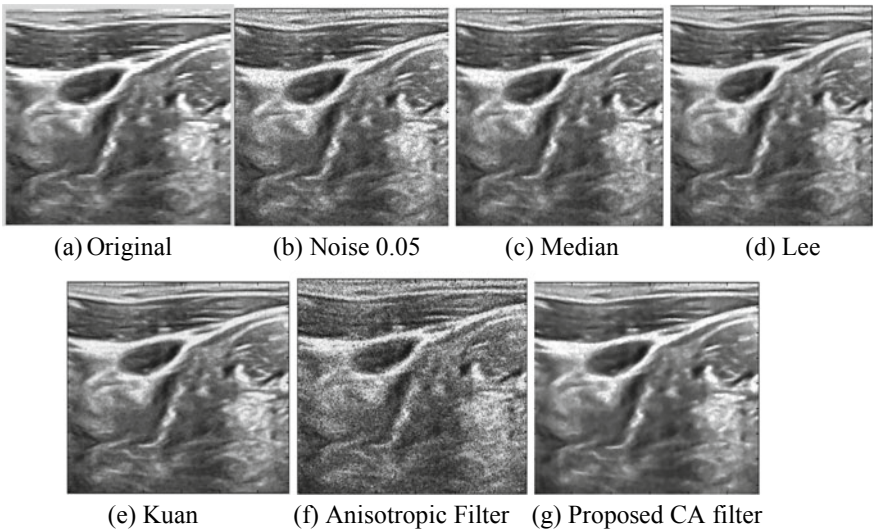


Fig. 22.3 Results of various filters for Image 1 at 0.05 noise density

22.7 Conclusion

One of the most significant and difficult tasks in the world of digital healthcare is despeckling medical ultrasound images. The quality of the ultrasound image obtained determines the overall diagnosis. The proposed cellular automata filter is proposed in this research for despeckling medical ultrasound images. After studying many existing filters, a transition function for the proposed filter was created. This filter has been found to function effectively and deliver a higher-quality outcome both qualitatively and quantitatively. In future, we could apply the concept of cellular automata as a combination of different filters to improve the results based on other parameters also.

References

1. Zhou, S.K., Rueckert, D., Fichtinger, G.: Handbook of Medical Image Computing and Computer Assisted Intervention. Academic Press (2019)
2. Godman, J.W.: Some fundamental properties of speckle. *Jl. Opt. Soc. Am.* **66**(11), 1145–1149 (1976)
3. Gupta, N., Shukla, A.P., Agarwal, S.: Despeckling of medical ultrasound images: a technical review. *Int. J. Inf. Eng. Electron. Bus.* (2016)
4. Goodman, J.W.: Statistical Properties of Laser Speckle Patterns. *Laser Speckle and Related Phenomena*. Springer Berlin Heidelberg, pp. 9–75 (1975)
5. Wagner, F., Smith, S.W., Sandrik, J.M., Lopez, H.: Statistics of speckle in ultrasound B-scans. *IEEE Trans. Sonic Ultrason.* **30**, 156–163 (1983)
6. Duarte-Salazar, C.A., Castro-Ospina, A.E., Becerra, M.A., Delgado-Trejos, E.: Speckle noise reduction in ultrasound images for improving the metrological evaluation of biomedical applications: an overview. *IEEE Access* **8**, 15983–15999 (2020)
7. Mei, K., Hu, B., Fei, B., Qin, B.: Phase asymmetry ultrasound despeckling with fractional anisotropic diffusion and total variation. *IEEE Trans. Image Process.* **29**, 2845–2859 (2019)
8. Alex, D.M., Chandy, D.A.: Evaluation of inpainting in speckled and despeckled 2D ultrasound medical images. In: 2020 Advanced Computing and Communication Technologies for High Performance Applications (ACCTHPA), pp. 221–225. IEEE (2020, July)
9. Latif, G., Butt, M.O., Al Anezi, F.Y., Alghazo, J.: Ultrasound image despeckling and detection of breast cancer using deep CNN. In: 2020 RIVF International Conference on Computing and Communication Technologies (RIVF), pp. 1–5. IEEE (2020, October)
10. Rotman, S.N., Friedman, Z., Porat, M.: Simultaneous compression and de-speckling of medical ultrasound images. In: 2019 IEEE International Ultrasonics Symposium (IUS), pp. 1448–1450. IEEE
11. Zhang, M., Gunturk, B.: A new image denoising method based on the bilateral filter. In: 2008 IEEE International Conference on Acoustics, Speech and Signal Processing. IEEE (2008)
12. Zhang, M., Gunturk, B.K.: Multiresolution bilateral filtering for image denoising. *IEEE Trans. Image Process.* **17**(12), 2324–2333 (2008)
13. Perona, P., Malik, J.: Scale-space and edge detection using anisotropic diffusion. *IEEE Trans. Pattern Anal. Mach. Intell.* **12**(7), 629–639 (1990). <https://doi.org/10.1109/34.56205>
14. Kuan, D.T., et al.: Adaptive noise smoothing filter for images with signal-dependent noise. *IEEE Trans. Pattern Anal. Mach. Intell.* **2**, 165–177 (1985)

15. Yommy, A.S., Liu, R., Wu, S.: SAR image despeckling using refined Lee filter. In: 2015 7th International Conference on Intelligent Human-Machine Systems and Cybernetics, vol. 2. IEEE (2015)
16. Nixon, M., Aguado, A.: Feature Extraction and Image Processing for Computer Vision. Academic press (2019)
17. Ulam, S.: Some ideas and prospects in biomathematics. *Ann. Rev. Biophys. Bioeng.* **1**(1), 277–292 (1972)
18. Gupta, M., Taneja, H., Chand, L.: Performance enhancement and analysis of filters in ultrasound image denoising. *Procedia Comput. Sci.* **132**, 643–652 (2018)
19. Yu, Y., Acton, S.T.: Speckle reducing anisotropic diffusion. *IEEE Trans. Image Process.* **11** (11), 1260–1270 (2002)
20. Hore, A., Ziou, D.: Image quality metrics: PSNR vs. SSIM. In: 2010 20th International Conference on Pattern Recognition, pp. 2366–2369. IEEE (2010, August)
21. <https://www.kaggle.com/c/ultrasound-nerve-segmentation/data>

Chapter 23

Development of a Preliminary Approach for Automatic CAD Model Generation of the IC Engine Piston



Nikhil Tuljapurkar, Gurunandan Jamalpur, Shubham Agarwal,
and Jayakiran Reddy Esanakula

Abstract The traditional CAD modeling approaches for IC engine pistons are tedious because of the complexity in geometry and design calculation. A little change in size or shape of IC engine assembly will cause an extensive chain reaction in calculating the associate modifications because of different interrelated plan issues. Therefore, the CAD model of the piston should be changed in order to match the modification(s) of the IC engine. The CAD modeling techniques, like parametric modeling, offer the answers for these issues. This paper presents a framework for generating the CAD model of an IC engine piston by using SolidWorks. A dedicated GUI was developed in the CAD software for helping the design engineers to feed the input data. The presented framework uses the reuse of the design information.

23.1 Introduction

Automotive industries, shipbuilding, aerospace industries, industrial, and architectural designs are some of the fields where computer-aided design (CAD) is extensively used as a tool. The comprehensive engineering method of 3D models and/or 2D sketches of physical parts is commonly done with CAD and is also used throughout engineering applications. Hence, this requires customization, so that their effectiveness can be enhanced. The lack of skilled professionals available for CAD modeling and the complexity of design make modeling a time-consuming process. Alternate processes are being researched by the companies and the professionals too. Customizing and improving CAD/CAM effectiveness and efficiency are the need of today's generation. A knowledge-based system (KBS) for

Nikhil Tuljapurkar, Gurunandan Jamalpur and Shubham Agarwal contribute equally to this work.

N. Tuljapurkar · G. Jamalpur · S. Agarwal · J. R. Esanakula (✉)
Department of Mechanical Engineering, Sreenidhi Institute of Science and Technology,
Hyderabad, Telangana 501301, India

engineering and design is important for fulfilling this requirement. The problem statement/task can be regenerated in no time when compared to humans with the usage of parametric modeling. The dimension-driven parametric modeling technique allows for automated reuse of existing design processed based on engineering analysis.

23.1.1 IC Engine Piston

The piston is one of the important components of internal combustion (IC) engine. It is the traveling part enclosed inside a cylinder and sealed by piston rings. Mostly it is used in reciprocating engines, reciprocating pumps, gas compressors, hydraulic cylinders, and pneumatic cylinders. The objective of the piston and/or connecting rod in an engine is to pass force from the expanding gas in the cylinder to the crankshaft. Usually, the aluminum alloy piston is used for passenger vehicles, and steel or cast-iron pistons are used for commercial vehicles. Figure 23.1 shows the cut section of the IC engine piston.

The CAD modeling of the IC engine piston is an elaborate and time-consuming process, and the specifications are constantly changing according to the power or IC engine needs. Hence, automatized modeling is very much essential. This can be

Fig. 23.1 Cut section of the IC engine piston [1]



achieved by the parametric modeling technique which is an advanced modeling technique of the CAD. Many researchers suggested that by using specialized methods such as KBS, one can reduce the time of modeling. Even though it is an evolving discipline, the automatic generation of a knowledge-based engineering (KBE) framework based on general knowledge will have the most drastic effects. This paper proposes a KBS for developing the CAD model of the IC engine piston to reduce CAD modeling time.

23.1.2 Knowledge-Based Engineering (KBE)

The blend of CAD techniques and artificial intelligence (AI) technologies is well represented by an engineering method called KBE. This provides advantages for customized or various design automation solutions [2–4]. The objective of the KBE system is to capture the product and process its information/data. It also involves simulating the engineering design process system and then uses the model to automate all or part of it. The internal representation of the product design process is the computer-generated product model. It includes information on both the product and the processes used to make the part. The focus is to provide complete product representational information which is captured in the product model.

23.1.3 SolidWorks API

The application programming interface (API) is a mechanism that allows various programs to communicate with one another. It is accomplished by embedding a programming language code within another application. Hundreds of functions are included in the API and can be accessed via Visual Basic for Applications (VBA), VB.NET, Visual C#, Visual C++ 6.0, and Visual C++/CLI. These functions give direct access to SolidWorks features like drawing a line, adding an existing part into a part text, and checking a surface's parameters. By writing special scripts, it is possible to automate the modeling and assembly of components using the SolidWorks API. SolidWorks API is a hierarchical tree-like framework that encompasses all of the program's features [5–7].

23.1.4 Visual Basic Language

Microsoft first introduced Visual Basic (VB) in 1991 as a third-generation programming language. It is a beginner-friendly programming language that allows us to quickly create graphical user interface (GUI) windows applications. Furthermore, VB is an effective engine for creating macros in all Microsoft applications.

As a result, VB has evolved into a versatile method for creating various programming codes for a variety of applications, including SolidWorks. Programmers will use ActiveX dynamic connection libraries (ActiveX DLLs) to connect VB with various Windows applications [8]. It also can add additional menus, tools, and toolbars to the application's environment.

23.1.5 *Macros*

A macro is a rule or pattern in computer science that specifies how a certain input sequence should be mapped to an output sequence according to a given process. To boost the design automation process, engagement with the model environment is critical. CAD systems have API interfaces that enable users to communicate with the model environment using macros and with the need for data sharing through technologies from different disciplines to solve real-world problems. In certain instances, a complex algorithm must be implemented to execute an efficient calculation that is not available in commercial applications. It also helps to use a computational algorithm to generate geometrical entities and operations [9].

23.1.6 *Parametric Modeling Techniques*

One of the most advanced CAD modeling approaches is the parametric modeling technique which provides approaches to traditional 2D drawings. It enables the reuse of preexisting procedures to carry out quick design changes based on engineering rules that are already in place [10].

23.2 Literature Review

Macro programming can be blended with parametric modeling techniques for one's use to generate effortless and accurate solid shape modeling [4]. As these tools are of great help to minimize the complexities that come up during the time of modeling, these can be used widely for producing CAD-enabled modeling [3]. Moreover, these tools facilitate the automation of CAD modeling, particularly for already existing tasks that can be automated and simplified with the help of a predefined algorithm/code [5]. A system was built for developing various parts of automobile chassis, cylindrical, and seed plate by Liu et al. [11], Luo et al. [12], and Dun et al. [13], respectively, wherein they used SolidWorks as a basis for developing CAD model and developing tool such as Virtual Basic (VB) were used. Modeling the tools and products using parametric modeling techniques were presented by Myung et al. [14]. These techniques facilitated the reduction of the CAD

modeling time and led to a faster rate of production. A new process was shown by Yangshou et al. [15] for generating the dynamic CAD models for performing structural analysis on it. Similarly, Kumar et al. [16], Dheeraj et al. [17], and Jayakiran et al. [18–21] developed a framework for optimized design on the SolidWorks platform which uses the knowledge-based system for CAD modeling.

A form of artificial intelligence (AI) technique known as knowledge-based system was designed to collect human expert knowledge to promote decision making. This form of computer software helps to increase the probability of generating sustainable modeling and simulation software within the given inputs and specifications [22–25]. Even though much effort was put into developing parametric modeling of materials, little effort was put into IC engine pistons. As a result, the authors assume that in the current market and research environment, a dedicated automated CAD modeling system for producing an IC engine piston is necessary. To conclude, a lot of significant contribution was made toward the CAD modeling and manufacturing using the parametric modeling techniques to reduce the time for modeling and also lead to faster production rates with desired inputs. With the use of VB as a development tool, SolidWorks can generate the CAD model. Analyzing geometrical information which is available in the predefined text data, an automated CAD model can be acquired.

23.3 Methodology for Modeling and Automation

Most commercial CAD software today is aimed at developing part models of components using a traditional approach and accepting input data in text format related to the model. Besides, a computer program [5, 13] can be used to feed this text input. This method was used to feed the input data in this article. This software can be written in a variety of programming languages, including VBA, C++, Lisp, and others [19]. VBA is regarded as the most practical of these languages. The programming editor in SolidWorks CAD applications is VBA. As a result, the authors chose SolidWorks as the CAD program for designing the proposed method to produce an automatic CAD model of an IC engine piston. Additionally, macro code is used to generate the CAD model of the IC engine piston since it allows for the automated creation of the CAD model. The novelty of the proposed system is the blending of the macro code into a parametric modeling technique, and the system is powered with the dedicated KBS. As this proposed system is a preliminary approach, the developed KBS works only for the IC engine piston. From the literature, it is found that no researcher has worked on developing a KBS which works on blending the macro code with a parametric modeling technique. Additionally, it is also understood from the literature that no researchers tried to develop a KBS for developing the CAD model of the IC engine piston. Hence, the proposed approach is the novel one in addressing the development of a KBS for generating the CAD modeling of the IC engine piston.

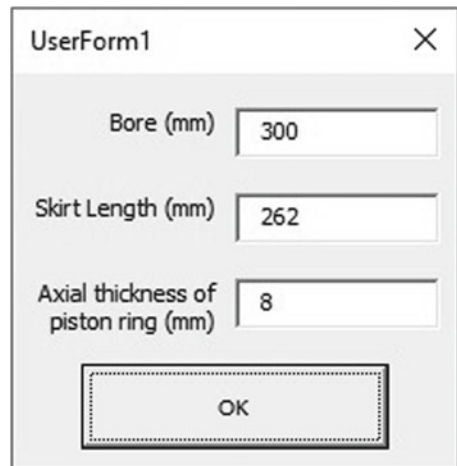
23.3.1 *Generating Graphical User Interface*

The user can create and develop their GUI with the support of VB in SolidWorks. Figure 23.2 is the GUI that was created for the generation of the CAD model of the IC engine piston. Figure 23.3 shows the button that was created for the generation of the CAD model of the IC engine piston. The GUI was developed in such a way that it should be able to collect the required data from the user and should transfer the same inputs to the logical algorithm for performing the design calculations.

23.3.2 *Program Development for Design Calculations*

To compute the design calculation of the IC engine piston, a logical computing algorithm was developed. Calculating the appropriate dimensions manually using typical empirical methods is difficult and time consuming. So, the developed logical computing algorithm helps in design calculation. Computer software for design calculations is being developed in an attempt to address this complexity. This computer program performs all the detailed designs and computes geometrical dimensions of the IC engine piston. The program's output data will be transmitted to the SolidWorks software, which will produce a CAD model based on the computed geometrical parameters. As a result, design and modeling tasks are automated. Figure 23.4 shows the process flowchart of the proposed system.

Fig. 23.2 GUI for the piston



The image shows a graphical user interface window titled "UserForm1". It contains three input fields for numerical data: "Bore (mm)" with the value 300, "Skirt Length (mm)" with the value 262, and "Axial thickness of piston ring (mm)" with the value 8. Below these fields is a button labeled "OK". The window has a standard title bar with a close button (X) in the top right corner.

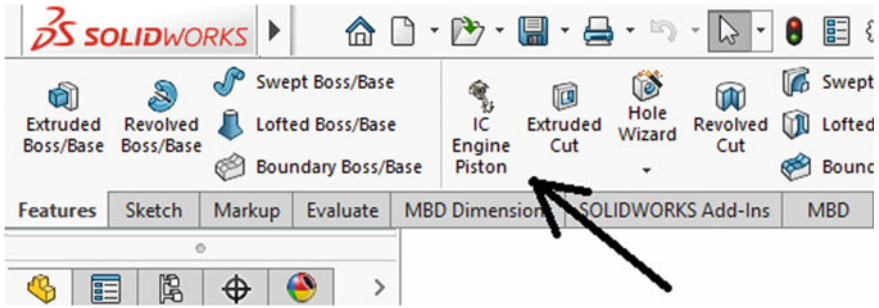


Fig. 23.3 Button for CAD model generation of the piston

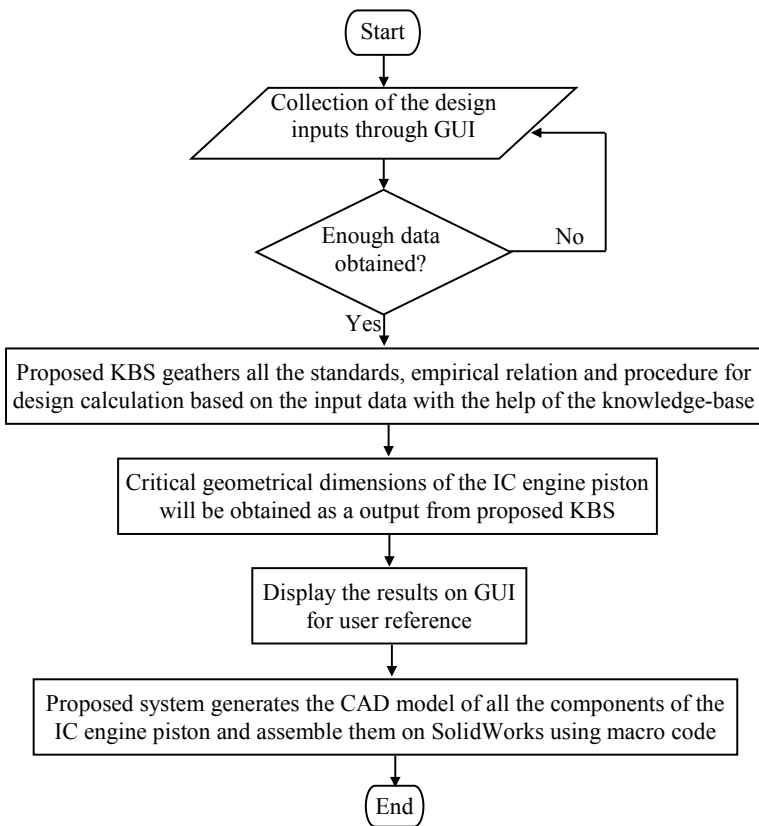


Fig. 23.4 Process flowchart of the proposed system

Table 23.1 Sample inputs for the proposed system

Parameter	Input data (mm)
Bore	300
Skirt length	262
Axial thickness of piston ring	8

23.4 Results

A sample result that was generated by the developed KBS is shown in this section. Generally, 220–345 h are required if the complete design calculations and the CAD modeling are done manually for the IC engine piston [20]. But with the help of the proposed approach, the total time required for the complete modeling process is 13 s when it was executed on SolidWorks 2020. When compared to the traditionally generated CAD models, the proposed approach produces the same CAD model with very close dimensional accuracy. The sample input data for the proposed system is given in Table 23.1. Based on these inputs, the proposed system has generated the IC engine piston, piston pin, piston rings, and IC engine piston assembly which are shown in Figs. 23.5, 23.6, 23.7, and 23.8, respectively.

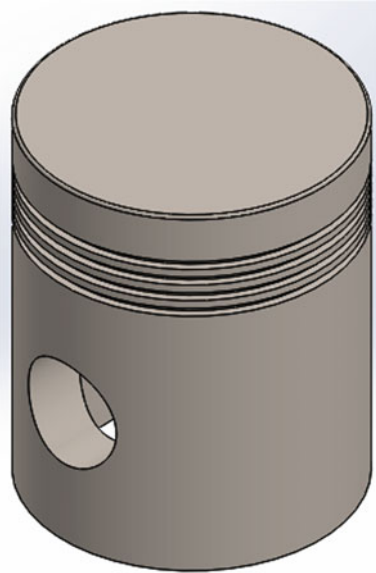
Fig. 23.5 IC engine piston

Fig. 23.6 Piston pin

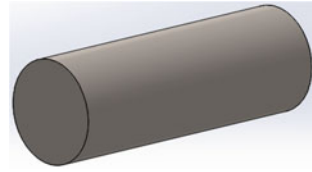


Fig. 23.7 Piston ring

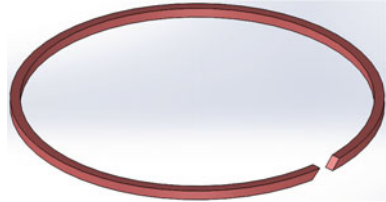
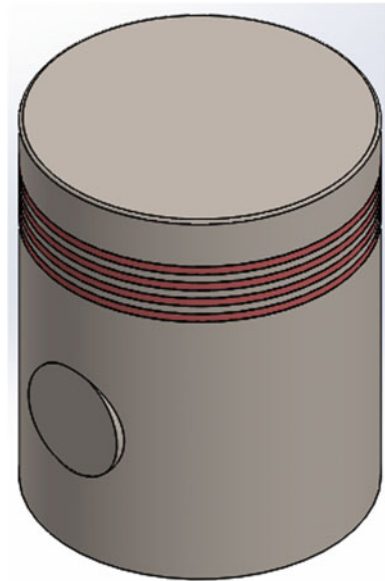


Fig. 23.8 CAD model of the IC engine piston assembly



23.5 Conclusion

A KBS for generating a CAD model is proposed in the paper. This technique reuses the design procedure with the help of parametric modeling technology. This design procedure and parametric modeling technique can be used on any computer which has access to SolidWorks making CAD modeling a user-friendly tool and handy to use. This system has also proved to run faster and generate a CAD model of an IC engine piston in comparison with the traditional approaches.

References

1. <https://x-engineer.org/automotive-engineering/internal-combustion-engines/ice-components-systems/internal-combustion-engine-piston/>, accessed on 17 April 2021
2. Reddy, E.J., Sridhar, C.N.V., Pandu Rangadu, V.: Knowledge based engineering: notion, approaches and future trends. *Am. J. Intell. Syst.* **5**, 1–17 (2015)
3. Jayakiran Reddy, E., Pandu Rangadu, V.: Development of knowledge based parametric CAD modeling system for spur gear: an approach. *Alexandria Eng. J.* **57**, 3139–3149 (2018)
4. Jayakiran Reddy, E., Sridhar, C.N.V., Pandu Rangadu, V.: Research and development of knowledge based intelligent design system for bearings library construction using solidworks API. *Adv. Intell. Syst. Comput.* **385**, 311–319 (2016)
5. Jayakiran Reddy, E., Venkatesu Naik, J., Rajendra, D., Pandu Rangadu, V.: Online knowledge-based system for CAD modeling and manufacturing: an approach. *Adv. Intell. Syst. Comput.* **910**, 259–268 (2020)
6. Jayakiran Reddy, E., Reddy, G.K., Rajendra, D.: Design of lifting tackle for armor plate of sinter machine. *Int. J. Tech. Phys. Probl. Eng.* **13**, 23–28 (2021)
7. Jayakiran Reddy, E., Rajendra, D., Venkatesu Naik, J.: Developing an automation system for generating the CAD model of Spur Gear. *Int. J. Mech. Prod. Eng. Res. Dev.* **10**(3), 8479–8488 (2020)
8. Jayakiran Reddy, E., Sridhar, C.N.V., Pandu Rangadu, V.: Development of web-based knowledge-based system for CAD modeling and manufacturing. *Mater. Today: Proc.* **5**, 27241–27247 (2018)
9. Jayakiran Reddy, E., Pandu Rangadu, V., Ramachandra, R., Naga Prasad Naidu, V.: Development of a constraint-based approach for Knowledge-Based System for CAD modeling. *Adv. Sci. Eng. Med.* **10**, 357–361 (2018)
10. Jayakiran Reddy, E., Rama Chandra, R.: Development of an intelligent system for the design of a two wheeler IC engine connecting rod. *Int. J. Eng. Sci. Invention* **6**, 67–74 (2017)
11. Liu, G.T., Yan, G., Yang, H.M.: A parametric design research on the parts of automobile chassis applied solidworks. *Comput. Knowl. Technol.* **7**(1), 245–249 (2011)
12. Luo, X.J., Liu, D.F., Yi, W.: Research of cylindrical cam CAD/CAM system based on SolidWorks. *Mod. Manuf. Eng.* **7**, 54–59 (2011)
13. Dun, G.Q., Chen, H.T.: SolidWorks API methods of modeling for seed plate based on visual basic. *Soybean Sci.* **31**(4), 630–637 (2012)
14. Sehyun, M., Soonhung, H.: Knowledge-based parametric design of mechanical products based on configuration design method. *Exp. Syst. Appl.* **21**, 99–107 (2001)
15. Yangshou, X., Kang, H., Tao, W., Qi, C., Rui, X.: Dynamic modelling and analysis of the microsegment gear. *Shock Vibration*, 13 pages (2016)
16. Kumar Yogeesh, D., Chandrasekaran, M., Eriki Ananda, K., Jayakiran Reddy, E.: Optimization of vibration reduction by De-Coupling method in power train of trucks. *ARPN J. Eng. Appl. Sci.* **11**, 6423–6427 (2016)
17. Thuniki, D., Ravikiran, M.S.S.R., Esanakula, J.R., Venkateswara Rao, B.: Design, modification and analysis of 3 ton electrical overhead travelling crane rope drum. *IOP: Mater. Sci. Eng.* **1057**, 1–10 (2021)
18. Jayakiran Reddy, E., Raju, G.N., Sai, G.A.: Development of a preliminary system for automatic generation of CAD model of the Universal Coupling. *Int. J. Mech. Prod. Eng. Res. Dev.* **10**(3), 8701–8710 (2020)
19. Jayakiran Reddy, E., Sridhar, C.N.V., Pandu Rangadu, V.: Knowledge—based parametric modeling for bolts, nuts and bearings using solidWorks. *Int. J. Appl. Eng. Res.* **10**, 16111–16120 (2015)
20. Jayakiran Reddy, E., Sridhar, C.N.V., Pandu Rangadu, V.: Development of KBS for CAD modeling of a two wheeler IC engine connecting rod: an approach. *Adv. Intell. Syst. Comput.* **530**, 597–606 (2016)

21. Jayakiran Reddy, E., Sridhar, C.N.V., Pandu Rangadu, V.: Development of KBS for CAD modeling of industrial battery stack and its configuration: an approach. *Adv. Intell. Syst. Comput.* **530**, 607–618 (2016)
22. Singh, A., Singh, I., Kalsi, S.: FEM analysis of human CAD model in standing posture while travelling. *Int. J. Mech. Prod. Eng. Res. Dev.* **9**, 29–35 (2019)
23. Jayakiran Reddy, E., Venkatachalapathi, N., Pandu Rangadu, V.: Development of an approach for Knowledge-based system for CAD modelling. *Mater. Today: Proc.* **5**, 13375–13382 (2018)
24. Jayakiran Reddy, E., Bala Raju, A., Bhanodaya Kiran Babu, N.: Enhancing the existing 3 ton electrical overhead travelling crane rope drum by adopting reverse engineering. *IOP: Mater. Sci. Eng.* **1057**, 1–10 (2021)
25. Jayakiran Reddy, E., Bhanodaya Kiran Babu, N., Bala Raju, A.: Reverse engineering technique for enhancing the EOT crane rope drum. *IOP: Mater. Sci. Eng.* **1057**, 1–10 (2021)

Chapter 24

Temperature Control Methodology for Catalytic Converter to Reduce Emissions and Catalyst Aging



S. Mithun Vaisnav and Sivanesan Murugesan

Abstract Internal combustion engines consume rich mixture during engine start-up to warm up the catalytic converter, which is most efficient while operating at 600–800 °C temperature range. The overall life of the catalytic converter is highly dependent on operating temperature, since noble metals are used for construction. Though modern vehicles are equipped with advanced technology to warm up the catalyst, it does not have a dedicated heat management system for the catalyst. With latest statutory pollution test requirements, the eventual lifespan of a vehicle equipped with factory-fitted catalytic converter remains uncertain. Hence, a dedicated thermal management system is necessary for the catalytic converter, which should be economical and compatible with existing vehicles for retro-fitment. This paper focuses on the quest of reducing automotive emissions through technological advancement. A potential solution for emission reduction is proposed by employing more stringent control on the catalyst's operating temperature, also improving its life.

24.1 Introduction

The objective of the study is to develop an electronic model of a simple and lightweight electronic thermal management system for the catalytic converter. For the study, an existing car in the market with emission values for different catalytic converter temperatures was chosen. The necessary programming codes for its efficient, controlled working were written. The effective working of the program was ensured by simulating the code at different conditions. Suitable modifications were made to standardize the validated design for a suitable group of similar vehicles. The scope can be widened by horizontally deploying this for other categories of vehicles, thus also enhancing the overall impact of the research.

S. M. Vaisnav · S. Murugesan (✉)
Department of Mechanical Engineering, Amrita School of Engineering,
Amrita Vishwa Vidyapeetham, Coimbatore, India
e-mail: m_sivanesan@cb.amrita.edu

From the literature reviewed, it can be seen that (a) improving conduction helps cooling but conventionally delays initial warm-up [1, 1], so there has to be a balanced trade-off; (b) phase changing materials (PCMs) are effective but add to cost [3, 3], thus not desirable for economical applications; (c) including additional components to manage this indirectly leads to emissions due to added weight [5–7]; (d) for effective emission control and catalyst life enhancement, both warm-up and cooling have to be optimized [8–10].

These voids can be filled in by combining strengths of each method like initially working in electronic insulation mode during warm-up period and then switching to rapid heat transfer mode as desired. This projects the need for a dedicated closed-loop integrated electronic system. Hence, existing cooling systems like engine coolant can be extended economically to achieve proper trade-off with help of electronic control.

24.2 Methodology

The best methods from the literature review were combined to achieve desired results. Concerned emission data for the research was studied. A suitable vehicle for the analysis was selected. The selected vehicle was tested initially for emission values in factory-fitted stock form. The programming code was developed and then simulated to ensure no loose ends were there in the blocks. The obtained data was sorted and analyzed for optimization possibility study. The blocks in the code were restructured in a manner that horizontal deployment shall be possible by minor modifications.

From the referred literature, favorable methods are merged by picking the advantages while also eliminating the shortcomings. For cost-effectiveness, temperature control is integrated using the engine's cooling system. For rapid and efficient control, a temperature-based electronic control was designed for the valves.

24.2.1 System Design

The important factors considered for designing the system are (a) less weight, so as to not affect the power-to-weight ratio of the vehicle; (b) affordability—so, it will be economical for retro-fitment; (c) modularity—thus, it can be manufactured on a common platform; (d) repairability, to ensure long life by simply replacing failed parts; and finally (e) effectiveness, to achieve the main goal of less emissions.

Before starting the product and system design, some important decisions were made regarding scope of the research and availability of infrastructure to carry out the desired experiments. It was decided to reduce additional hardware as much as possible to keep the weight and cost down. Only stock materials were to be used, and a standard software with license was zeroed in.

24.2.2 Vehicle Selection

Mahindra Maxximo LCV (Light Commercial Vehicle) was chosen based on test data availability. Its important specifications are as mentioned in the table below. A base test was conducted on the subject vehicle to obtain emission data, using which the optimal temperature range for catalytic convertor operation was deduced (Table 24.1).

24.2.3 Preliminary Test Data

The result of base test performed on the subject vehicle is taken as reference values for future comparison. From the below graph, it can be seen that the optimal operating temperature for the selected vehicle is in the range of **250–350 °C**. This range is considered for all further calculations within this work (Fig. 24.1).

24.2.4 Algorithm

Based on the desired effect, the following algorithm is developed as a basic skeleton. LP is low point, meaning lower cutoff limit for the temperature. HP is high point, meaning higher cutoff limit for the temperature. T1 is the temperature measured by the exhaust gas temperature (EGT) sensor.

When T1 exceeds 850 °C, the HP valve will be closed with LP valve opened. The vice versa will happen if T1 decreases below 650 °C. The entire system is enclosed in a loop for continuous monitoring and desired alteration. If the

Table 24.1 Specifications of the selected vehicle (Mahindra Maxximo LCV)

Description	Specification
Engine and gearbox	909 cc, 2-Cyl, common rail direct injection
Max. power	18.4 kW (24.7 hp) @ 3600 rpm
Max. torque	55 Nm (5.61 kg-m) @ 2200 rpm
Gearbox	4 speed + 1 reverse
Compression ratio	18.5: 1
Payload	850 kg
GVW	1815 kg

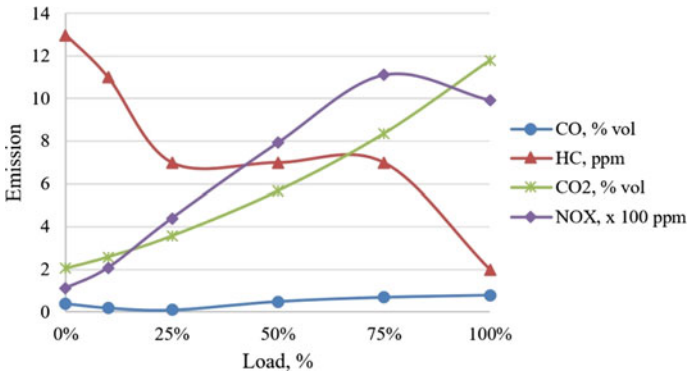


Fig. 24.1 Base test results for the selected vehicle (Mahindra Maxximo LCV)

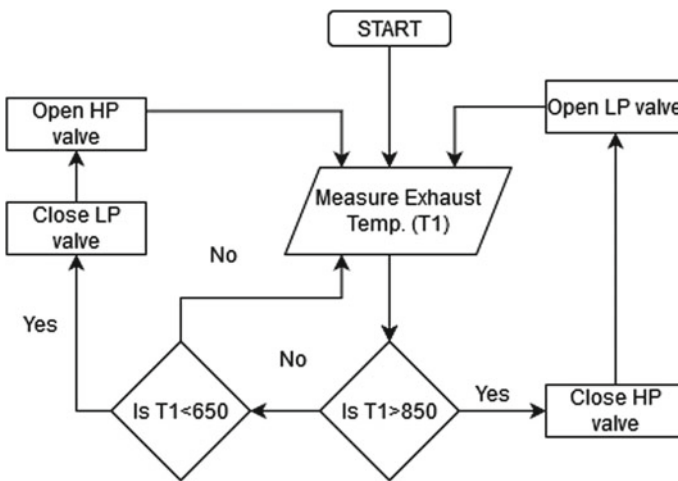


Fig. 24.2 Algorithm for closed-loop control of catalytic converter temperature

operating temperature is already in optimal level, no action will be taken. Thus, it is ensured that the system performs its intended task only if the situation demands (Fig. 24.2).

24.3 LabVIEW Model

The proposed model was simulated in LabVIEW software to obtain better insights and ensure desired results are affected. The following is the internal circuit design of the LabVIEW model used for simulation (Fig. 24.3).

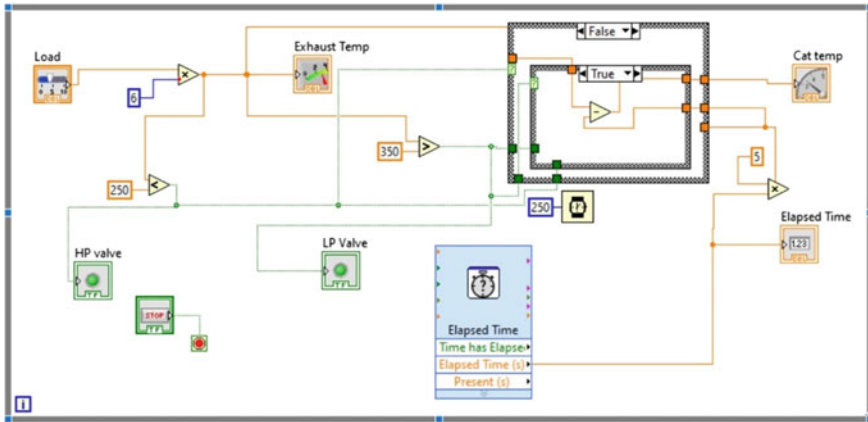


Fig. 24.3 LabVIEW circuit for closed-loop control of catalytic converter temperature

24.3.1 Features of the Model

A time delay is added to make the simulation more understandable for the naked eye. The entire circuit is placed in an infinite loop, so once started the simulation keeps running continuously unless intervened. A STOP button is provided to stall this loop, thus stalling the simulation also. The engine load can be provided as user input. The exhaust temperature varies accordingly.

24.3.2 Simulation

The LabVIEW model created was simulated for different values of exhaust temperature. The results were found to be in accordance with the desired effects. Small improvements were made to run the simulation more smoothly. In the working terminal, input is engine load in %, exhaust temp. is user input temperature in deg. Celsius, Cat temp. is current operating temperature of the catalytic converter, and LP and HP valves are as explained in the previous heading (Fig. 24.4).

24.4 Python Coding

The electronic control device has to be programmed appropriately to reach the objective. Embedded Python was chosen as the language for coding for the following benefits. It is light size and has wide applications. Many devices can run on Python code, e.g., pyboard, Raspberry Pi, etc. Simple structures reduce the

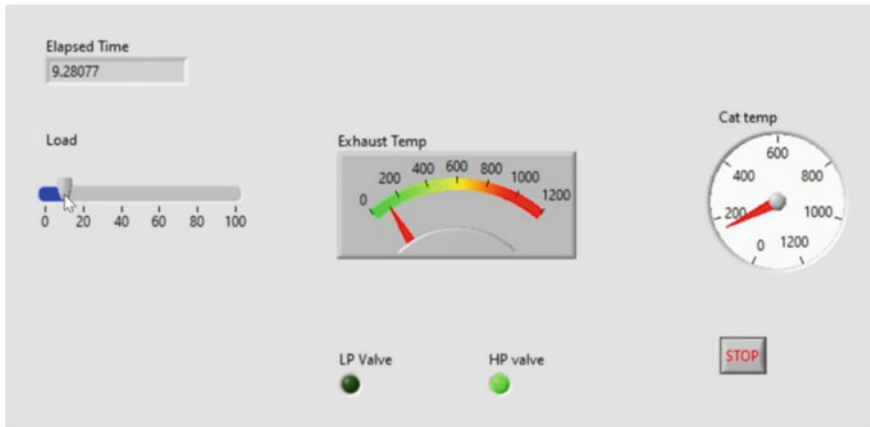


Fig. 24.4 Simulation console for the temperature control program in LabVIEW window

complexity against length of the program. Python code is easy to understand so can be horizontally deployed, as well as easy to debug for repairs and correction. Modularity and extension are possible. It comes with the ability to optimize further for continuous upgradation. Economical hardware is available to satisfy the affordability factor.

24.4.1 Blocks in the Program

The entire code can be split into blocks for better understanding. The library block contains required predefined functions. The constant block comprises assumed values for convenient simulation. Input block obtains desired user-defined values. Function block is for execution of necessary commands. The condition block contains comparators required for closed-loop control. Loops are for continuous monitoring and control. Finally, the output block is to print the required data among various parameters.

24.4.2 User Inputs

The program is written for universal application and hence requires the below mentioned inputs from the user for more accurate results: input exhaust temperature (as measured by the sensor) in deg. C; lower and higher optimum temperature for the catalytic convertor in deg. C; convection coefficient (h) of the particular coolant used in $W/m^2 K$; specific heat (C_p) of that coolant in $kJ/kg K$; mass flow rate of coolant for the selected engine (in $g/sec.$, sensor output data); surface area of the

canister in sq. m (taken from Ansys geometric modeler); frequency of calculation (in milliseconds); no. of time steps to be run (in nos.); and name for writing the log file (.txt).

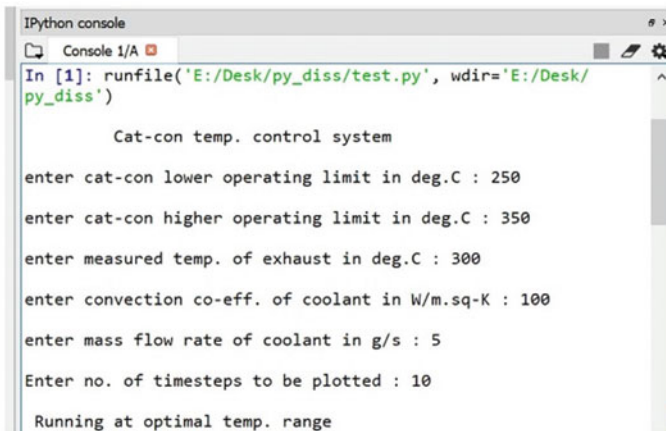
24.4.3 Running the Program

Opening (or) closing time for valve operation, valve opening (or) closing binary (Boolean), temperature comparator output (binary), timesteps, and temperature for each timestep are computed using standard formulae. As the loop monitors continuously as a closed-loop controller, there are 3 cases:

)If working temperature entered is less than optimal, it opens the low point (LP) valve to allow hot coolant from the engine radiator line to flow into the canister continually, until the temperature enters the optimal range again. The HP valve is closed.

)If working temperature entered is higher than optimal, it opens the high point (HP) valve to allow cold coolant from the engine radiator line to flow into the canister continually, until the temperature enters the optimal range again. The LP valve is closed.

)If working temperature entered is within the optimal range, both HP and LP valves are kept closed, and no other action is taken. This ensures no unnecessary action is taken, thus reducing fluid pumping losses (Fig. 24.5).



```

IPython console
Console 1/A
In [1]: runfile('E:/Desk/py_diss/test.py', wdir='E:/Desk/py_diss')

      Cat-con temp. control system

enter cat-con lower operating limit in deg.C : 250
enter cat-con higher operating limit in deg.C : 350
enter measured temp. of exhaust in deg.C : 300
enter convection co-eff. of coolant in W/m.sq-K : 100
enter mass flow rate of coolant in g/s : 5
Enter no. of timesteps to be plotted : 10

Running at optimal temp. range
  
```

Fig. 24.5 Python output terminal for the temperature control program

24.5 Conclusions

The control system for maintaining optimal operating temperature of the catalytic convertor is designed and simulated. The factors considered while designing were selected by studying the gaps in technology from the literature reviewed. The data used for the program was obtained from the base test results of the vehicle selected for this study. The preliminary simulation was performed in LabVIEW software for better understanding of the designed system since it provides a live visual representation. The controller was then programmed in Python language using the software called Spyder, and its working was found to match with the objectives of this work. Thus, using this control system it is possible for more stringent control over the operating temperature of the catalytic convertor, which in turn aids in emission control. The designed system is also easy to modify by altering the program for standardization to suit various vehicles, thereby enhancing its application.

24.5.1 Future Scope

The accuracy of the controller can be improved by loading lookup tables for ' C_p ' and ' h ' values of the coolant for different temperatures and Reynold's number (Re). This can be achieved using a Python library called Pandas (Fig. 24.6).

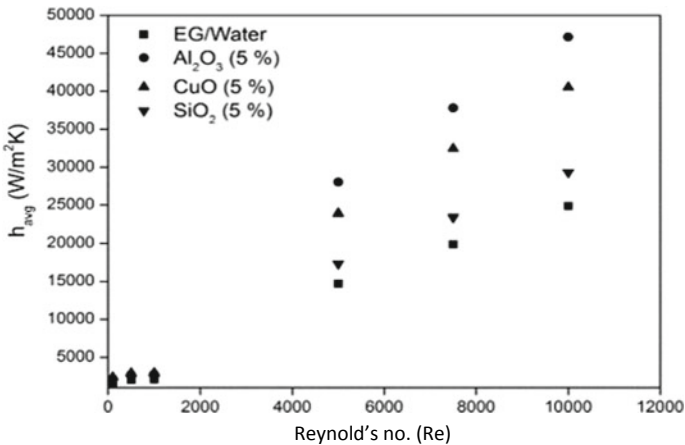


Fig. 24.6 ' h ' versus ' Re ' for different coolants

Acknowledgements The experiment was carried out at Amrita Automotive Research and Testing Centre (AARTC) to acquire the base test data.

References

1. Gasser, I., Rybicki, M., Wollner, W.: Optimal control of the temperature in a catalytic converter. *Comput. Math. Appl.* **67**(8), 1521–1544 (2014)
2. Yusufa, A.A., Inambaoa, F.L.: Effect of cold start emissions from gasoline-fueled engines of light-duty vehicles at low and high ambient temperatures : recent trends. *Case Stud. Thermal Eng.* **14**, 100417 (2019)
3. Mahadeven, G., Sendilvelan, S.: Temperature analysis of dynamic catalytic convertor system with pre-catalyst in a multi cylinder S.I. engine to reduce lightoff time. *Int. J. Heat Technol.* **35**(1), 97–102 (2017)
4. Kizer, T.L., Hills,F., Borroni-Bird, C.E., Hills, R.: Combination Catalytic Convertor and Heat Exchanger That Maintains Catalyst Substrate Within Efficient Operating Temperature Range. United States Patent No.5,987,885 (1999)
5. Lee, S., Bae, C.: Design of a heat exchanger to reduce the exhaust temperature in a spark-ignition engine. *Int. J. Thermal Sci.* **47**(4), 468–478 (2007)
6. Hosoi, A., Morita, A., Suzuki, N.: Thermal analysis of the exhaust line focused on the cool-down process. *SAE Int. J. Engines* **7**(1), 32–42 (2014)
7. Vasava, M.S., Jotaniya, P.V.: Experimental investigation of automotive exhaust system using liquid jet cooling device. *Int. J. Sci. Res. Dev.* **3**(3), 1507–1509 (2015)
8. Lee, S., Bae, C.: Effects of Engine Operating Conditions on Catalytic Converter Temperature in SI Engine. SAE Technical Paper Series, 2002-01-1677 (2002)
9. Rathod, N., Panage, R., Rathod, W.S.: Design and performance analysis of a three way catalytic converter. *Int. J. Res. Sci. Innov. (IJRSI)* **5**(6), 178–183 (2018)
10. Gao, J., Tian, G., Sorniotti, A.: Ahu Ece Karci, Raffaele Di Palo: review of thermal management of catalytic converters to decrease engine emissions during cold start and warm up. *Appl. Therm. Eng.* **147**, 177–187 (2018)

Chapter 25

Solar Powered Autonomous Robotic Car Using for Surveillance



V. Premchandran, M. Karthikkumar, V. Thamizharasan,
and E. Sathish

Abstract Life is a problem-solving workbook. In today's technological world, new technology is being invented on a daily basis. Robotics is the most appropriate technology for surveillance purposes in order to identify the occurrence of related events. As we all know, robots are capable of performing surveillance tasks with a high level of integration while using a surveillance device. To develop long-range portable assistive-aided car system for user. This project presents a reconfigurable sensor network for structural monitoring of a user. In this project, we have built an all in one voice control car using custom mode PCB. This robotic car can perform as Bluetooth voice control robot, self-balancing robot, and obstacles avoidance robot. This robots batteries are powered using a solar panel. This robot can be useful for Industrial automated equipment carriers. This robot can be used for surveillance. All this things are done by Arduino UNO microcontroller.

25.1 Introduction

Nowadays, industries are becoming modern, and they automated the technology to perform various risky jobs. This robot is helpful to minimize the life risk of the humans and the animals. With the advancement of wireless communication technology in robots, there are several possibilities. A surveillance robot is an intelligent device which does not have any particular design or a device which can perform only a particular task [1]. The design of the robot can be changed according to the task to be performed in a particular area. A robot begins with a mechanical structure capable of communicating with its surroundings, such as a wheeled platform, arm, or other construction [2]. A supervision robot is deliberate to assist humans in

V. Premchandran (✉) · M. Karthikkumar · V. Thamizharasan
Department of Electronics and Communication Engineering, Erode Sengunthar Engineering
College, Erode, Tamil Nadu, India

E. Sathish
Department of Electronics and Instrumentation Engineering, Erode Sengunthar Engineering
College, Erode, Tamil Nadu, India

almost any important or insignificant activity where the ease of use makes the human's life easier [3, 4]. In military, the surveillance robot is used in order to reduce the human death rate. Robot can perform even a hard or heavy or risky task easily as per the design of the robot [5, 6].

25.1.1 Solar Cell

Silicon wafer of mono-crystalline is used to make a solar cell. Solar cell, also known as a photovoltaic cell, is a device that uses the photovoltaic effect to convert solar energy into electricity. Photovoltaics is a subject of technology and research concerned with the use of solar cells to generate solar energy. The word solar cell is often used to refer to devices that are expressly designed to harvest energy from sunlight, whereas the word photovoltaic cell is worn when the basis is unknown.

Solar modules are made up of cell assemblies that can be connected together to form photovoltaic arrays.

25.2 Existing System

In existing system need a Bluetooth device to control the robotic car. We can easily control the robotic car using the Bluetooth device, and it includes and high quality camera, and it can 360° we can monitoring any angle from the robot. This system automatically avoids the obstacles, and it stop when it face an obstacles. This robot can be controlled by voice control android app name as Arduino controller. The voice will be used to direct the robot's movement, and the robot will respond to commanding individuals by generating sounds of human voice in response to each verbal instruction [7, 8]. The suggested system would be built around a microcontroller that will be linked to a smart android phone through Bluetooth to receive voice commands [9]. It contains an infrared sensor that detects obstructions in the way of ROBOT's journey. It force to move in a specific direction in order to avoid the impediment in its way [10]. Inverted pendulum theory underpins the concept of self-balancing robot with two-wheel. This kind of robot have piqued the curiosity of researchers and engineers all around the world since it is built on a control system that uses efficient microcontrollers and sensors to stabilize an unstable system [11].

Another ongoing project will be based on a microcontroller that will be connected to a smart android phone during Bluetooth unit to receive voice commands. A function on the android phone converts the voice command to a message, which is then sent to the microcontroller used for robot enlargement control. Following the receipt of the data, the robot responds to the order by undertaking lawful development to the suitable heading as directed by the voice command. The robot will use an SD card module in conjunction with an SD card that has a few pre-recorded person voice the same as a sound record used for the improvement of the machine's

talking framework. Following receipt of each order, the robot behave in accordance with instructions and able to speak in a variety of sentences.

25.3 Proposed System

In this paper, the proposed system is made automated using IR sensor, to function as a line following robot. And also HC-05 Bluetooth module is added for voice control purpose. Including ultrasonic sensor is used in this system to avoid obstacles. The system is enriched with solar tracking system makes energies the project maximum energy as shown in Fig. 25.1. All sub-module is connected with micro-controller using Arduino UNO board, and through this, the proposed system is automated. This is also includes four wheels along DC motor and all other needed supported components.

25.3.1 Speech Recognition Process

The textual content was transmitted to the Arduino through Bluetooth via cell phone handsets with built-in microphones to process the signal, and the robot moved in accordance with the voice command instructions. According to the commands provided to L293D, the robot could move left, right, forward, and backward. From the Arduino Uno, which provided feedback in response to the user’s command. If the user said “autonomous,” the robot began travelling on its own without colliding with something. The ultrasonic sensor, which was able to detect the obstacle, led the avoidance of the obstacle. The microcontroller was then instructed to travel in such a way that the robot did not encounter the obstacle.

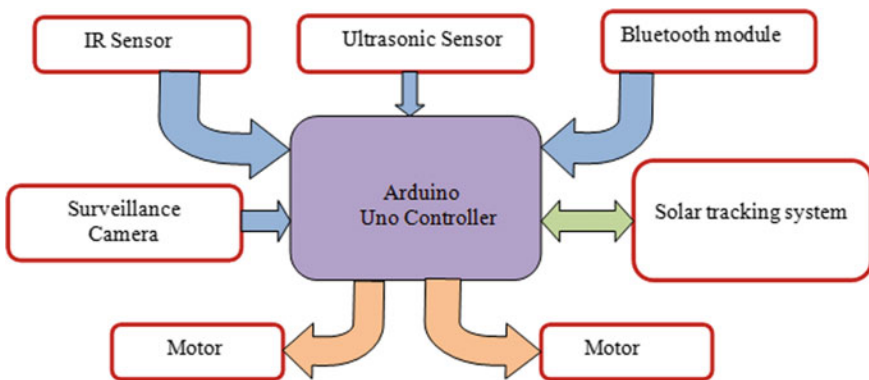


Fig. 25.1 General block diagram of proposed system

25.3.1.1 Methodologies

The proposed system has following methodologies for function in two mode,

- (i) Automatic mode
In this mode, this system will function in automatic mode by using IR sensor signal (as line following robot). This could be mainly required in industrial purpose.
- (ii) Voice control mode
In this mode, this system will function in voice control mode by using blue tooth sensor signal. This mode could be mainly used for surveillance purpose.

25.3.2 Solar Tracking System

Solar tracking system is to gather maximum amount of power supply by means of tracking the solar panel.

As soon as the system is switched on, the solar panel comes to the initial position, i.e., towards east. There are four LDR which is set each in 45° to keep tracking of the sun from sun rise to sun fall. As soon as the light falls on the first LDR, the signal will be sent to microcontroller. This in turn controls the stepper motor position, i.e., first quarter 0° – 45° .

As the sun rises when the sun light fall on the second LDR, i.e., second quarter 45° – 90° , automatically first LDR is put off and the second one gets on. The signal from the second LDR goes to the IC and in turn goes to the stepper motor to change its position, i.e., 45° – 90° . The same process goes on till the sun falls down. So as shown in Fig. 25.2, we are able to track the sun continuously. The electric energy thus obtained from the solar cell goes to a storage cell/battery, and it is stored. When this energy is needed, it is obtained by using an inverter. It is also programmed, regarding the time of load on and load off. Here the load is water pump for irrigating the field.

25.4 Result and Discussion

In this proposed system, a prototype robot is developed with four wheels, a surveillance camera, IR sensor, ultra sonic sensor, Bluetooth sensor, Arduino uno microcontroller, solar panel, four LDRs, and a stepper motor, and the operation is tested (Fig. 25.3). The created robot able to move in any direction in based on voice command obtained via android phone and Bluetooth from the user. The robot will go left, right forward, and backward using voice commands. Through android mobile app we control proposed robot and using Arduino IDE software more than voice command is programmed in proposed system. The voice command

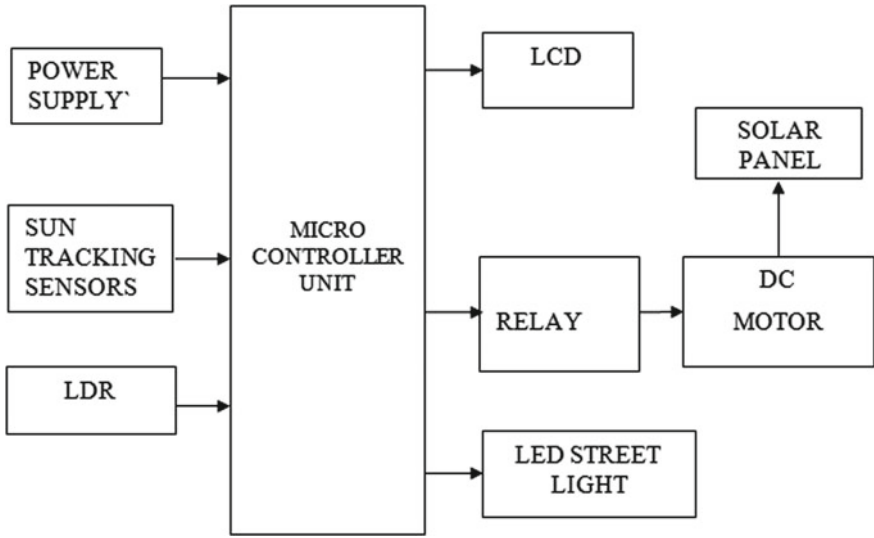


Fig. 25.2 Solar tracking system block diagram



Fig. 25.3 Working model of proposed system

“Autonomous” causes the robot to drive completely autonomously without touching any obstacles, by using ultrasonic sensor including this IR sensor is added to make robot as line following robot. By using surveillance camera, the developed robot is well performed in surveillance function also, with this surveillance camera robot is moved anywhere.

25.5 Comparison

Here proposed system is compared with “DESIGN AND IMPLEMENTATION OF A SELF BALANCING ROBOT” in this, system can do only one function as a self-balancing, “DESIGN AND IMPLEMENTATION OF A VOICE CONTROLLED ROBOT” in this system can do only one function as a voice control and “OBSTACLES AVOIDING ROBOT” in this system can do only one function as a Obstacles avoiding. Whereas proposed system can perform self-balancing, obstacles avoiding and voice controlling along with surveillance using a HD camera shown in Table 25.1.

Comparatively proposed system is performing all the operation (four different operation), while all other is performing single operation as either self-balancing, obstacles avoiding, voice controlling and surveillance, so proposed system better than other compared system. Similarly in Table 25.2, proposed system obstacle

Table 25.1 Comparison of proposed system with other system

System	Functionality	Update
Solar powered autonomous robotic car using for surveillance (Proposed system)	This project performing a self-balancing robot Obstacles avoiding robot and voice controlling robot	It also used for surveillance using a HD camera
Design and implementation of a self-balancing robot	This project performs only as a self-balancing robot	It can do only one function as a self-balancing robot
Design and implementation of a voice controlled robot	This project perform only as a voice controlled robot	It can do only one function as a voice controlled robot
Obstacles avoiding robot	This project perform only as a obstacles avoiding robot	It can do only one function as a obstacles avoiding robot

Table 25.2 Comparison of obstacle detection

S.No	Approach	Obstacles detecting angle (in degree)	Obstacles detecting distance (in cm’s)	Action
1	Proposed system	45	450	Avoiding obstacle in front, right, left successful
2	Self-balancing robot	30	350	Avoiding obstacle in front, successful right, left partially successful
3	Voice controlled robot	15	300	Avoiding obstacle in front successfully
4	Obstacles avoiding robot	30	350	Avoiding obstacle in front, successful right, left partially successful

detection is compared with other system, and it gives distinguish result than other in terms of detecting angle and detecting distance. So, proposed system is better than other compared system.

25.6 Conclusion

The main goal of a solar tracking device is to collect as much energy as possible by tracking the solar panel. As soon as the system is switched on, the solar panel comes to the initial position, i.e., towards east. There are four LDR which is set each in 45° to keep tracking of the sun from sun rise to sun fall. As soon as the light falls on the first LDR, the signal will be sent to microcontroller.

The solar powered autonomous robotic car using for factory and industrial automation. Sensors are helpful to all these operations, and it have multipurpose. This can workable as Bluetooth voice control robot, and it can be work as an obstacles avoiding robot. It get the sufficient power via solar panel for its functions.

References

1. Abdullahi, Z.H., Muhammad, N.A., Kazaure, J.S., Amuda, F.A.: Mobile robot voice recognition in control movements. *Int. J. Comput. Sci. Electron. Eng. (IJCSEE)* **3**(1), 11–16 (2015)
2. Alexenko, T., Biondo, M., Banisakher, D., Skubic, M.: Android-based speech processing for eldercare robotics. In: *IUI '13 Companion Proceedings of the Companion Publication of the 2013 International Conference on Intelligent User Interfaces Companion*, pp. 87–88, March 2013
3. Badadhe, V.A., Deshmukh, P., Bhujbal, S., Bhandare, P.: sBOT: a face authenticated and speech controlled robot. *Int. J. Adv. Res. Electron. Commun. Eng. (IJARECE)* **2**(2), 160–167 (2013)
4. Cvjetkovic, V., Matijevic, M.: Overview of architectures with Arduino boards as building blocks for data acquisition and control systems. In: *13th International Conference on Remote Engineering and Virtual Instrumentation (REV)*, pp. 56–63, Feb 2016
5. “LM340, LM340A and LM78xx Wide V IN 1.5-A Fixed Voltage Regulators”, February 2000, Revised July 2016. Available on <http://www.ti.com>
6. “Ultrasonic Ranging Module HC-SR04” available on www.micropik.com 11. “Micro SD Memory Card interface for 5V MCU” available on www.researchdesignlab.com
7. Arulananth, T.S., Baskar, M., Hari babu, P., Divya Sree, R., Sanjana, R., Bhavana, S.: IR Sensor based obstacle detection and avoiding robot. *PalArch's J. Archaeol. Egypt/Egyptol.* **17** (12) (2020). Available on www.micropik.com
8. Lita, I., Oprea, S., Cioc, I.B., Visan, D.A.: Wireless technologies for distributed sensor networks used in measurement and automation systems. In: *31st International Spring Seminar on Electronics Technology*, 2008. ISSE '08, pp. 303–307, May 2008
9. Rashid, H., Ahmed, I.U., Osman, S.B., Newaz, Q., Rasheduzzaman, M., Taslim Reza, S.M.: Design and implementation of a voice controlled robot with human interaction ability. In: *International Conference on Computer, Communication, Chemical, Materials and Electronic Engineering, IC4ME2-2017*, 26–27 Jan 2017

10. Chandra Kumar, R., Saddam Khan, M., Kumar, D., Birua, R., Mondal, S., Parai, M.: Obstacle avoiding robot—a promising one. *Int. J. Adv. Res. Electr. Electron. Instrum. Eng.* **2**(4) (2013)
11. Ashfaque Shakil Shaon, A.K.M., Bhowmik, S., Bhawmick, B.K., Das, P., Das, N.K.: Design and implementation of a self-balancing robot. In: *International Conference on Mechanical Engineering and Renewable Energy 2017 (ICMERE2017)* 18–20 Dec 2017

Chapter 26

Design and Simulation of Hybrid Microsystem and Its Effect on the Environment Using Homer Software



Alok Kumar and Shelly Vadhera

Abstract The main objective of this research paper is to suggest the best alternative option for continuous power supply in the institute campus Nalanda College of Engineering, Chandi, Bihar in a cost-effective way. In this paper, four different hybrid combinations of solar photovoltaic, fuel cell generator, wind turbine generator, diesel generator, battery, and external grid have been studied. It has been observed that the solar PV-fuel cell battery hybrid system is the best alternative to replace the external grid system to supply continuous power in the campus. Among all four cases studied using hybrid power system optimization software, the levelized cost of ₹11.69 per unit is obtained providing a sustainable source of electricity for a greener future.

26.1 Introduction

Due to the rapid increase in population and urbanization, the consumption of electricity is increasing day by day. As we know, the fossil fuel resources are limited and may exhaust after a few decades [1]. By using fossil fuel for electricity generation, it emits harmful gases that pollute our environment and causes problem like ozone layer depletion, greenhouse effect. So to overcome such a problem, we need alternate sources of energy. Such sources are solar photovoltaic, fuel cells, wind, geothermal, biomass, tidal energy, small hydropower plant, etc. The advantage of using renewable energy sources is they are pollution-free, easily accessible, and inexhaustible [2]. A single renewable energy source is not sufficient for supplying continuous electricity to the load for 24 h. In such a scenario, hybrid

A. Kumar (✉)

School of Renewable Energy and Efficiency, NIT Kurukshetra, Haryana, India

e-mail: alok_31910125@nitkr.ac.in

S. Vadhera

Department of Electrical Engineering, NIT Kurukshetra, Haryana, India

e-mail: shelly_vadhera@nitkr.ac.in

© The Author(s), under exclusive license to Springer Nature Singapore Pte Ltd. 2022

A. N. R. Reddy et al. (eds.), *Intelligent Manufacturing and Energy Sustainability*,

Smart Innovation, Systems and Technologies 265,

https://doi.org/10.1007/978-981-16-6482-3_26

energy systems are employed to get continuous supply to the load. In a developing country like India where a large population lives in villages but 24-h power supply in a day is still a challenge in India there is a lot of power cut issues especially in villages area due to power shortage [3]; so, it needs of time to generate electricity by using a renewable-based hybrid system to fulfill their load requirement [4] in a sustainable way. This work emphasizes the use of the hybrid form of the renewable energy system to power the institutional building located in the rural parts of India. Homer software [5] had been made use of to perform many different functions to accessing the best and effective system.

26.2 Load Profile of Study Area

The selected area Nalanda College of Engineering Chandi, Nalanda is located in the state of Bihar, India, and its latitude is $25^{\circ} 19.2' N$ and longitude is $85^{\circ} 24.7' E$. The per-day average energy consumption of this institute is about 1010.80 kWh and the daily peak is about 125 kWh, annually.

26.3 Resources of Study

The data of solar radiation and wind speed for this selected location has been obtained from NASA's surface meteorology and solar energy website. The detailed annual average data of solar radiation and wind speed [6, 7] is shown in Figs. 26.1 and 26.2, respectively. The daily horizontal solar radiation is approximately 4.96 kWh/m^2 . The monthly average temperature is $24.71^{\circ} C$, and the monthly average wind speed is 2.78 m/s .



Fig. 26.1 Monthly average solar global horizontal irradiance



Fig. 26.2 Monthly average wind speed data

26.4 Economical Modeling

In this section, four different cases are studied to determine the most economical and feasible hybrid system.

26.4.1 Case: 1. N.C.E Campus Connected to Solar PV-Fuel Cell-Battery Hybrid System

Here, the N.C.E campus is connected to a hybrid system comprising of solar PV, fuel cell, and battery [8, 9]. This system is depicted schematically in Fig. 26.3.

The costs associated with this hybrid system are as follows:

Net present cost = ₹49,942,200, Capital cost = ₹40,376,000, Operating cost = ₹826,076.

The individual capital cost of solar PV is ₹15,750,000, and the life of the PV panels is considered as 25 years. Cost of the reformer is ₹420,000, and the life of the reformer is considered as 25 years. Cost of the fuel cell generator is ₹18,900,000, and cost of the battery is ₹2,625,000 and its life is considered as 10 years, after that, we need to replace the battery system. The cost of the converter is ₹2,625,000 and its life is considered as 15 years. The cost of a hydrogen gas storage cylinder is ₹56,000 and its life is considered as 25 years [10, 11]. The following data were entered as input in the HOMER software for simulation and optimization.

Per unit capital cost of all the components of the system, operation cost and maintenance cost, replacement cost, size of components, lifetime, and location of the proposed system. For sensitivity analysis, multiple inputs are given in some specific cases. After the completion of the optimization process, the solar photovoltaic—fuel cell—battery hybrid system came out as the best solution. The optimal system comprises of 90 kW PV panels, a 90 kW fuel cell generator, 125 kWh

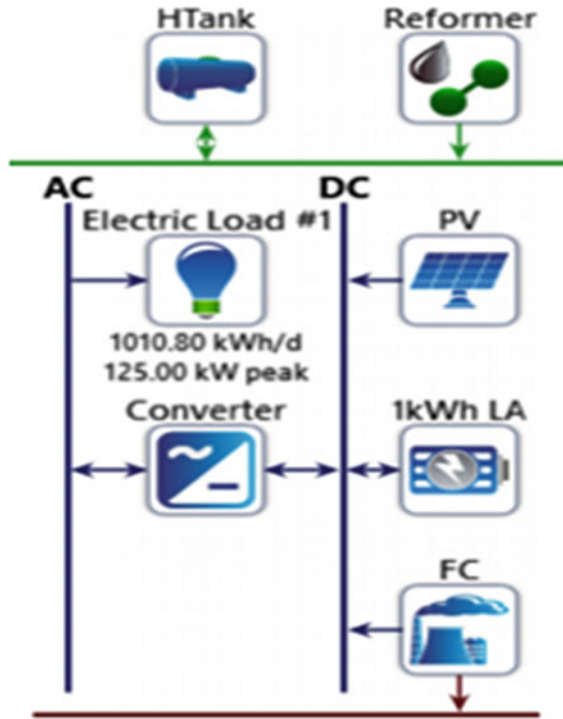


Fig. 26.3 Schematic diagram



Fig. 26.4 Monthly electric production by solar PV-fuel cell-battery

battery reformer, 20 kg/h of capacity, and a converter of 125 kW capacity for the load control strategy in this case. The total annual electricity production 417,841 kWh/yr of which 159,576 kWh/yr produce by solar pv and 258,265 kWh/yr by fuel cell. The total consumption 368,906 kWh/yr and excess electricity 28,822 kWh/yr. production detail is shown in Fig. 26.4.

26.4.2 Case: 2. N.C.E Campus Connected to Solar PV-Fuel Cell-Wind Turbine-Battery Hybrid System

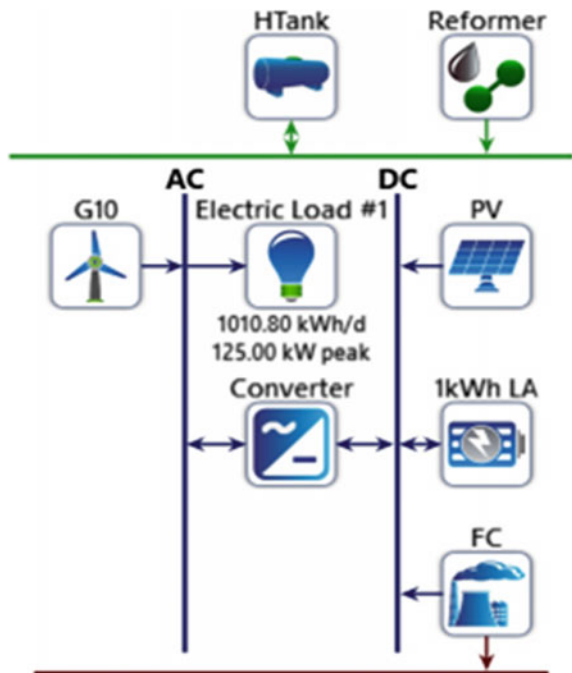
Here, the N.c.e campus is connected to a hybrid system comprising solar PV, fuel cell, wind turbine, and battery [12, 13]. The schematic diagram of the hybrid system is shown in Fig. 26.5.

After the completion of the optimization process, the optimal system comprises of 90 kW PV panels, 90 kW fuel cell generator, 125 kWh battery, reformer 20 kg/h of capacity, converter of 125 kW capacity, and wind turbine of 10 kW capacity for the load control strategy in this case. The total annual electricity production 418,030 kWh/yr of which 159,576 kWh/yr produce by solar pv, 257,663 kWh/yr by fuel cell, and 791 kWh/yr by wind turbine. The total consumption 368,906 kWh/yr and excess electricity 29,059 kWh/yr production detail is shown in Fig. 26.6.

26.4.3 Case: 3. N.C.E Campus Connected to the Grid

Here, the N.C.E campus is connected to an external grid. South Bihar power distribution Ltd is the electricity supplier in Nalanda, Bihar. The schematic diagram of the hybrid system is shown in Fig. 26.7.

Fig. 26.5 Schematic diagram of the hybrid system



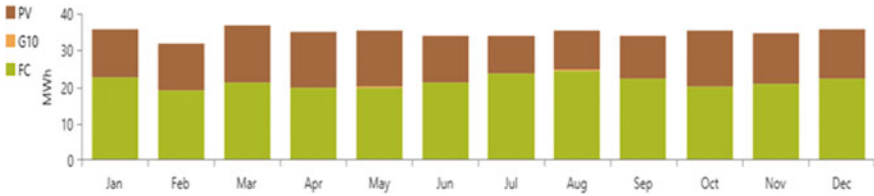
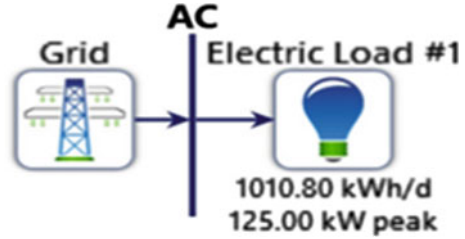


Fig. 26.6 Monthly electric production by solar PV-fuel cell-wind turbine-battery system

Fig. 26.7 Schematic diagram of the system



The net present cost of the system is ₹29,907,150. The operating cost of the system is 2,582,594, and the cost of electricity (COE) is ₹7/kW. The electricity generated by the grid to supply the campus load is shown in Fig. 26.8.

26.4.4 Case: 4. N.C.E Campus Connected to Solar PV-Diesel Generator-Battery Hybrid System

Here, the N.C.E campus is connected to a solar photovoltaic-diesel generator-battery hybrid system [13]. The schematic diagram of the hybrid system is shown in Fig. 26.9.

The optimal system comprises 90 kW PV panels, 80 kW diesel generator, 150 kWh battery, and converter of 55 kW capacity for the load control strategy in this case. The total annual electricity production 415,775 kWh/yr of which 141,845 kWh/yr produce by solar PV and 273,929 kWh/yr by diesel generator. The total



Fig. 26.8 Monthly electric productions by grid for campus demand

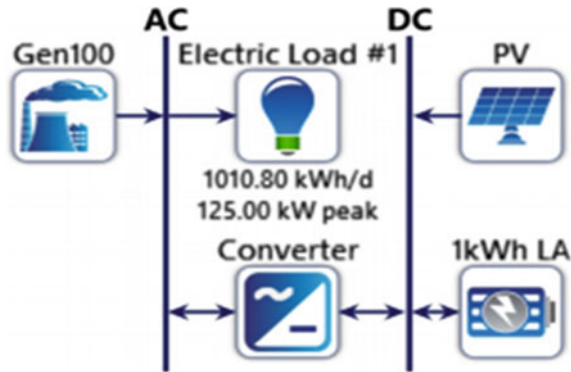


Fig. 26.9 Schematic diagram of the hybrid system

consumption 368,889 kWh/yr and excess electricity 32,856 kWh/yr. production detail is shown in Fig. 26.10.

26.5 Cost Comparison and Effect on Environment

26.5.1 Cost Comparison

The cost summary of all the cases is given in Table 26.1. Levelized COE (Cost of electricity) is lowest in case 3, but the operating cost is cheapest in case: 1 and its cost of electricity (COE) is ₹11.69/kWh.

26.5.2 Environmental Impact

Burning of fossil fuel to supply energy that emits harmful gases [14] unburned carbon and particulate matter that pollute our environment. These emissions can be



Fig. 26.10 Monthly electric production by solar PV-diesel generator-battery hybrid system

Table 26.1 Cost comparison for different cases in Rs

Cost	Case:1	Case:2	Case:3	Case:4
NPC (net present cost)	49,942,200	53,631,920	29,907,150	115,165,600
Operating cost	826,076	842,460	2,582,594	8,019,724
Total system cost	40,376,000	43,876,000	29,907,150	22,295,000
Levelized COE (cost of electricity)	11.69	12.55	7.00	26.96

Table 26.2 Emission in kg/year

Emission	Case:1	Case:2	Case:3	Case:4
Carbon dioxide	0	0	233,171	217,637
Carbon monoxide	0	0	0	1,481
Unburned hydrocarbon	0	0	0	59.9
Particulates matter	0	0	0	5.92
Sulfur dioxide	0	0	1,011	533
Nitrogen oxides	0	0	494	118

reduced to improvement to our energy supply system [15], by using solar PV plants and other cleaner sources of energy. The emission details of all the cases are shown in Table 26.2.

26.6 Conclusion

In this paper, simulations for an economically feasible hybrid system for institutional building (N.C.E Chandi) located in rural parts of India are led by using the different hybrid combinations. The result shows that the external grid meets the daily and yearly load demand at the cost of electricity (COE) ₹7/kwh, which is less when compared to all other cases but the external grid emits harmful gases and also grid has 3–5 h of a power cut on the daily basis at the location N.C.E Chandi, Nalanda so the best alternate option to replace the external grid is the solar PV-Fuel cell- Battery hybrid system, that can fulfill load demand at the cost of 11.69/kWh, that is less when compared to all cases except the external grid and the operating cost of this system is less than all other cases, this hybrid system is based on renewable energy so, there is no emission of any harmful gases overcome the main disadvantage of this hybrid system is high capital cost.

References

1. Shafiee, S., Topal, E.: When will fossil fuel reserves be diminished? *Energy Policy* **37**(1), 181–189 (2009)
2. Kumar, A.A.: A study on renewable energy resources in India. In: 2010 International Conference on Environmental Engineering and Applications. IEEE
3. Singh, A.: Power sector reform in India: current issues and prospects. *Energy Policy* **34**(16), 2480–2490 (2006)
4. Erdinc, O., Uzunoglu, M.: Optimum design of hybrid renewable energy systems: overview of different approaches. *Renew. Sustain. Energy Rev.* **16**(3), 1412–1425 (2012)
5. Lilienthal, P.: HOMER® micropower optimization model. National Renewable Energy Lab. (NREL), Golden, CO (United States) (2005)
6. NREL.: Solar radiation data. 2021 [cited 2021 April 10]; Solar data]. Available from: <https://www.nrel.gov/grid/solar-resource/renewable-resource-data.html>
7. Resources, N.p.o.w.e. Nasa prediction of worldwide energy resources. 2021 [cited 2021 April 11]; Available from: <https://power.larc.nasa.gov/>
8. Silva, S., Severino, M., de Oliveira, M.: Sizing and optimization of hybrid photovoltaic, fuel cell and battery system. *IEEE Lat. Am. Trans.* **9**(1), 817–822 (2011)
9. Hossain, K.K., Jamal, T.: Solar PV-hydrogen fuel cell system for electrification of a remote village in Bangladesh. In: 2015 International Conference on Advances in Electrical Engineering (ICAEE). IEEE
10. Mehrjerdi, H.: Peer-to-peer home energy management incorporating hydrogen storage system and solar generating units. *Renew. Energy* **156**, 183–192 (2020)
11. Sharaf, O.Z., Orhan, M.F.: An overview of fuel cell technology: fundamentals and applications. *Renew. Sustain. Energy Rev.* **32**, 810–853 (2014)
12. Nelson, D., Nehrir, M., Wang, C.: Unit sizing of stand-alone hybrid wind/PV/fuel cell power generation systems. In: IEEE Power Engineering Society General Meeting. IEEE (2005)
13. Rodríguez-Gallegos, C.D., et al.: A siting and sizing optimization approach for PV–battery–diesel hybrid systems. *IEEE Trans. Ind. Appl.* **54**(3), 2637–2645 (2017)
14. Perera, F.: Pollution from fossil-fuel combustion is the leading environmental threat to global pediatric health and equity: solutions exist. *Int. J. Environ. Res. Public Health* **15**(1), 16 (2018)
15. Barbir, F., Veziroğlu, T., Plass, H., Jr.: Environmental damage due to fossil fuels use. *Int. J. Hydrogen Energy* **15**(10), 739–749 (1990)

Chapter 27

Battery Charging Using Solar Photovoltaic System with Maximum Power Point Tracking



Siddharth Samaddar, Ujjwal Rastogi, Soham Tyagi,
and Saurabh Mishra

Abstract This research paper involves available solar energy conversion to useful electrical energy, which is utilized for battery charging to procure maximum power from SPV. The state variables of the solar photovoltaic panel such as voltage, current, and power are utilized for battery charging. Maximum power point tracking technique is utilized for harnessing maximum available solar energy. MPPT is used for the best utilization of the SPV panels to improve efficiency of solar module. At MPP, battery as a load is charged, and solar energy is stored in the it. Optimal operating point of the system used to perform tracking through DC-DC boost converter. The converter is used to control the switching action of IGBT by controlling duty ratio. Perturb and Observe (P&O) algorithm is used in this work. The battery performance in terms of state of charge (SoC), battery current, and voltage is verified for different irradiance in MATLAB/SIMULINK platform.

27.1 Introduction

The energy demand has skyrocketed over the years as the world is becoming more technologically advance and autonomous. This has created problem in demand and supply of energy [1]. The mounting demand cannot be met with non-renewable sources of energy alone due to its limited supply and negative impact on the environment. Renewable forms of energy have to be employed to meet the excess demand. Alternatives such as solar, wind, and hydropower energy can be utilized. Out of these solar energy is an attractive alternative [2, 3]. Compared to the other forms of renewable sources solar energy is an attractive alternative. It is, abundant, low cost, and easy to convert to other forms of energy. Solar photovoltaic (PV) panels is extensively used to generate electricity. PV systems are categorized into stand-alone and utility-interactive systems. The former is disconnected from utility grid and is essential for power supply in remote regions. It comprises of

S. Samaddar · U. Rastogi (✉) · S. Tyagi · S. Mishra
Department of Electrical Engineering, Delhi Technological University, Delhi, India
e-mail: saurabhmishra@dtu.ac.in

energy storage elements such as rechargeable batteries that continuously supplies the load during low irradiation condition. However, PV arrays have major drawbacks [4, 5]. Firstly, energy conversion efficiency from solar to electrical is low. Secondly, the IV curve of PV array is highly nonlinear in nature and is a function of temperature and degree of irradiation [6]. PV panel efficiency decreases if the load impedance and source impedance of solar panel are unequal [7], leading to inefficient operation of solar array as the system is not running at optimal point. The equalization is accomplished by connecting a control unit between solar panel and battery. The control mechanism is called MPPT [8]. The block has a control algorithm to continuously track MPP by examining the voltage at output and PV array current to ascertain the optimal operating point of the system [9–11]. This point is used to perform the tracking action by the boost converter by controlling the switching action of the IGBT with the duty cycle. Thus, improving the efficiency of extracting power from the PV array [12]. In the paper, Sect. 27.1 includes the introduction, Sect. 27.2 consists of the system schematic, Sect. 27.3 elaborates simulations result, and Sect. 27.4 concludes paper.

27.2 System Schematic

See Fig. 27.1.

27.2.1 Solar Panel

PV cells are mounted on a structure called solar module, and these are inter-connected in series–parallel combination forming solar panel which are usually used in road signals, railway signals, etc. When two or more panels are inter-connected, they form arrays which has an application in solar power generation. The governing equation and figure are given (Table 27.1).

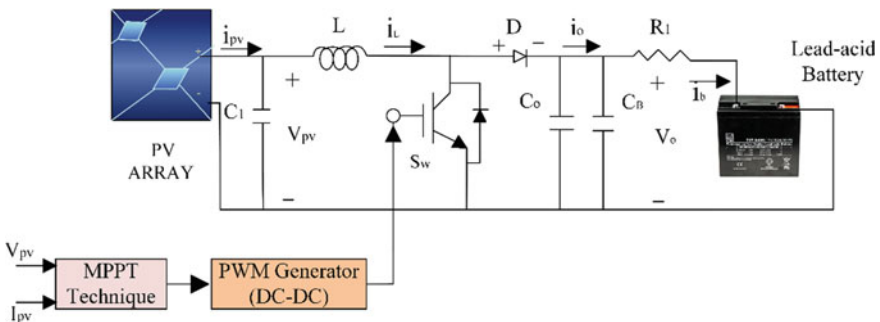


Fig. 27.1 Simulation model of the proposed charger

Table 27.1 PV array parameters

Parameters	Specification
Module name	Canadian solar
Max power (P_{max})	90 W
Max power voltage (V_{mp})	18 V
Max power current (I_{mp})	5 A
Open circuit voltage (V_{oc})	22 V
Short circuit current (I_{sc})	5.4 A
Cells per module	36
No. of parallel strings	1
No. of series connected PV modules	1

27.2.2 Boost Converter

It is a power converter which scale up voltage using switch mode supply in which the magnitude of voltage at output is greater than magnitude of voltage at input. Its input current is continuous by nature and provides lower current and higher voltage. Some of its applications are regenerative braking of DC motors, power supplies, portable devices, etc. The governing equations of duty cycle (D), inductor (L), and capacitor (C_o) with a system efficiency (eff) of 98% are given (Table 27.2):

$$D = 1 - \left(\frac{V_{in_{min}} * \text{eff}}{V_o} \right) \tag{27.1}$$

$$L = V_{in_{min}} * \left(\frac{V_o - V_{in_{min}}}{f * \Delta I * V_o} \right) \tag{27.2}$$

$$C_o = I_o * \left(\frac{V_o - V_{in_{min}}}{f * \Delta I * V_o} \right) \tag{27.3}$$

Since switching frequency of the power converter is high it produces ripples in solar array output parameters. Thus, an electrolytic capacitor C_1 is utilized across the solar array at input of converter to eliminate the ripples. When the switch S_w

Table 27.2 Boost converter parameters

Parameters	Specification
Input capacitance (C_1)	47 μ F
Input inductance (L)	925.33 μ H
Maximum input voltage (V_{pv_max})	16.14 V
Maximum input power (P_{pv_max})	84.57 W
Output capacitance (C_o)	127.48 μ F
Maximum output voltage (V_{out})	33.59 V
C_B	0.1 μ F
R_1	10 Ω

(IGBT) is closed, the magnetic field across the inductor expands and consumes energy. But when switch opens the current through inductor decreases due to reduction in magnetic field, and it dissipates energy. Due to this, the inductor will generate very large voltage across it which is then used to charge output capacitor C_0 through diode D to a voltage greater than input voltage V_{pv} .

27.2.3 Maximum Power Point Tracking

The voltage of photovoltaic array corresponding to maximum output is called maximum power point, varying with change in irradiance. Hence, we need an efficient method for tracking maximum power the entire day for efficient utilization of the system. MPPT is used for this purpose. The underlying principle of this method is centered on maximum power transfer theorem which states that in an electrical circuit the output power achieves maximum value when the source impedance of circuit is equal to the load impedance. Therefore, we keep input impedance of power converter constant irrespective of the load. The input impedance is a function of load impedance and duty cycle.

In order to achieve this, a MPPT control mechanism can be used in which the voltage at input and converter current acts as input to the control mechanism and then a MPPT algorithm is employed to produce a variable duty cycle (D) to convert to PWM signal using a DC-DC PWM generator which is then fed as input control signal to converter switch (S_w).

Figure 27.2 shows the algorithm used in the Perturb and Observe technique. It needs instantaneous voltage $V(k)$ and current $I(k)$ as input for solar cell. It also needs to store the voltage and current before the previous perturbation. Using this, it can calculate whether the current perturbation is positive or negative and therefore can decide in which direction the next perturbation should be. However, this technique has a potential drawback. If the perturbation, i.e., ΔD is large then there is high probability that the algorithm will miss the MPP which will cause high oscillation in the current and voltage waveform. While, if the perturbation is too small, then the system will take more time to reach MPP. This method is more robust when system is much closer to maximum power point [2–13]. Switching frequency is 32.5 kHz.

27.2.4 Lead Acid Battery

Here lead acid battery is used for battery charging. It uses lead peroxide (PbO_2), sponge metallic lead (Pb), and sulfuric acid (H_2SO_4) as an electrolyte to convert chemical energy into electrical energy. It is used in automobiles because of its high cell voltage and lower cost. Some advantages are large current capability, tolerant of overcharging, internal impedance is low, shelf-life is indefinite if stored without electrolyte, highest value of reusability, etc. (Table 27.3) [2].

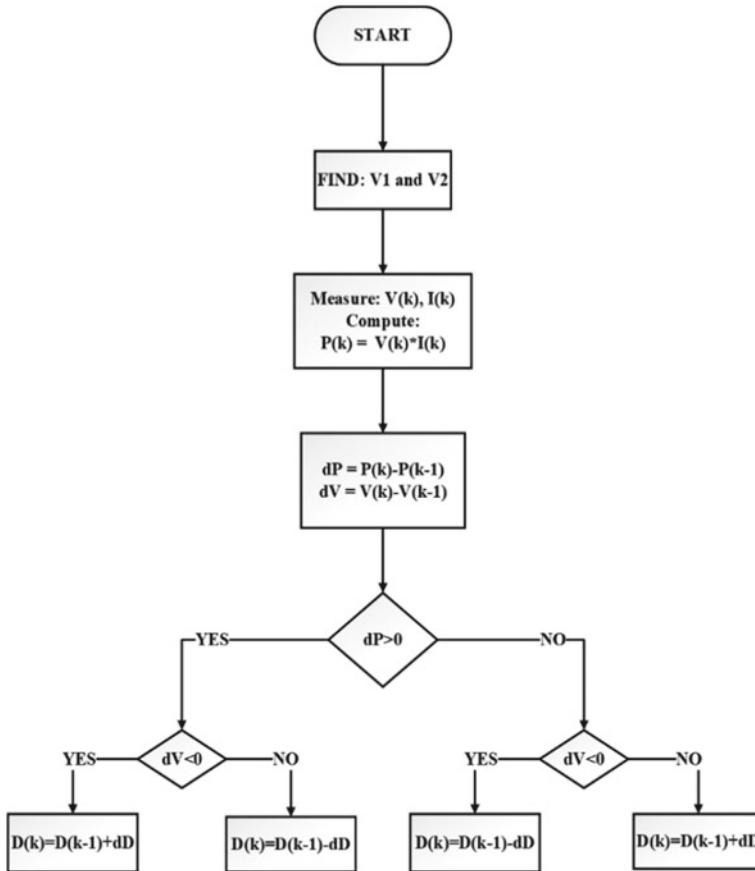


Fig. 27.2 Perturb and observe flowchart

Table 27.3 Battery parameters

Parameters	Specification
Nominal voltage	12 V
Rated capacity	20 Ah
Initial state of charge	45%

27.3 Simulation Results

The model is simulated at various levels of solar irradiation to evaluate dynamic response of the proposed battery charger. The ambient temperature is considered constant at 25 °C. Proposed model has been simulated in MATLAB/SIMULINK. Figure 27.1 shows the proposed battery charger which comprises of a boost converter, a solar panel and a MPPT algorithm to operate the system. Figure 27.3 depicts the variable input irradiation of the PV panel varying from 900 to 1000 W/m².

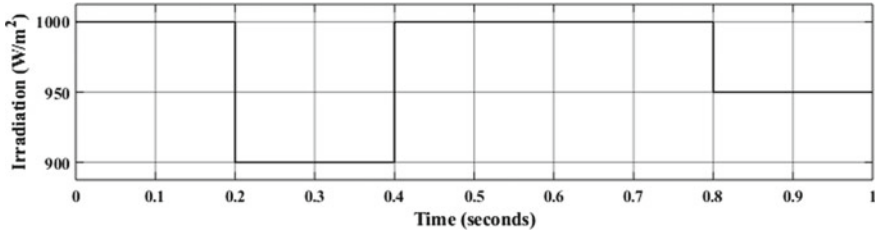


Fig. 27.3 Input irradiance of solar array

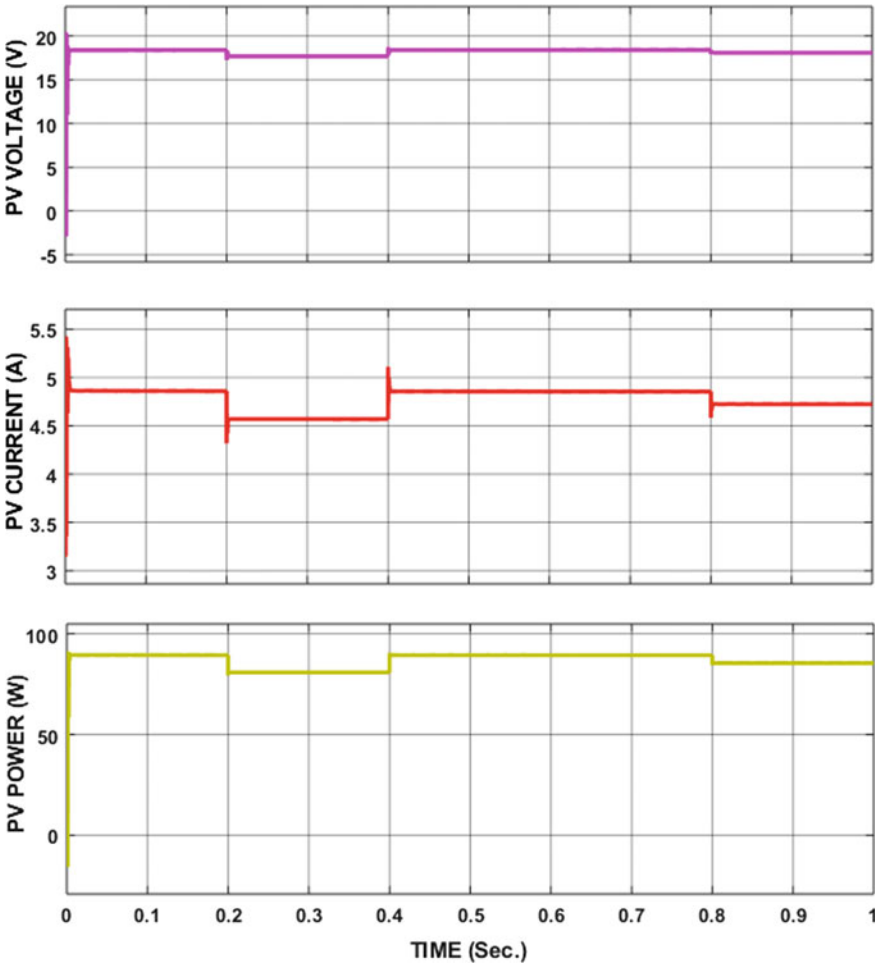


Fig. 27.4 Voltage, current, and power of solar panel

In Fig. 27.4 V_{pv} , i_{pv} and P_{pv} parameters of solar PV panel are shown. The maximum power is 90 W at 1000 W/m^2 . Duty cycle used to ascertain duty ratio is 0.5675. The maximum input voltage and input current are nearly matching with the PV array voltage and current parameters, respectively, after applying MPPT algorithm which properly optimized the solar array output power for all magnitude of irradiation. Hence, MPP is achieved.

Figure 27.5 shows the output parameters (V_o , i_o , P_o) and inductor current (i_L) of the converter. Since power converter has operated in continuous conduction mode

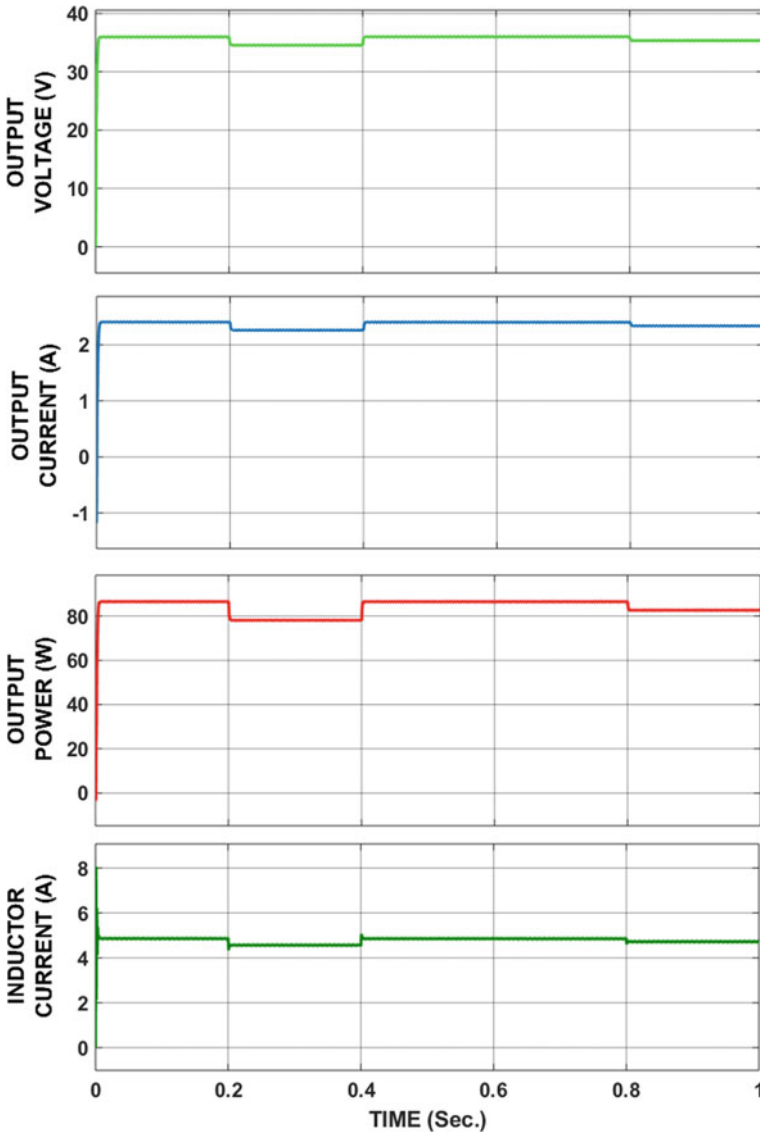


Fig. 27.5 Output voltage, output current, output power, and inductor current of boost converter

(CCM), stress on converter component reduces. The output voltage is nearly constant at around 34 V which is stepped up from input voltage of 16.14 V by converter. When active switch S_w is turned ON, diode which is a passive switch becomes reverse bias, and as a result, there is a charging of the inductor by the input voltage V_{pv} between the time interval from 0 to 0.2 s at irradiation of 1000 W/m^2 .

But when the switch S_w gets turned off between the interval from 0.2 to 0.4 s, then the diode will become forward bias, and there will be release of energy from the inductor at irradiation of 900 W/m^2 . Both input and inductor energy will deliver power to battery through the diode. A RC filter circuit is employed on the input of battery to flatten the battery current and limit any current transient at battery side.

Figure 27.6 shows SOC, i_b and V_B parameters under a variation in irradiation. Under all irradiance levels, SOC is increasing smoothly at 45% level which signifies that battery is charging with small ripples in the battery current of around 4–5% that helps in the storage performance of the battery [3]. The battery voltage is also increasing steadily to a maximum voltage of 11.98 V with a small voltage ripple of around 1–2%.

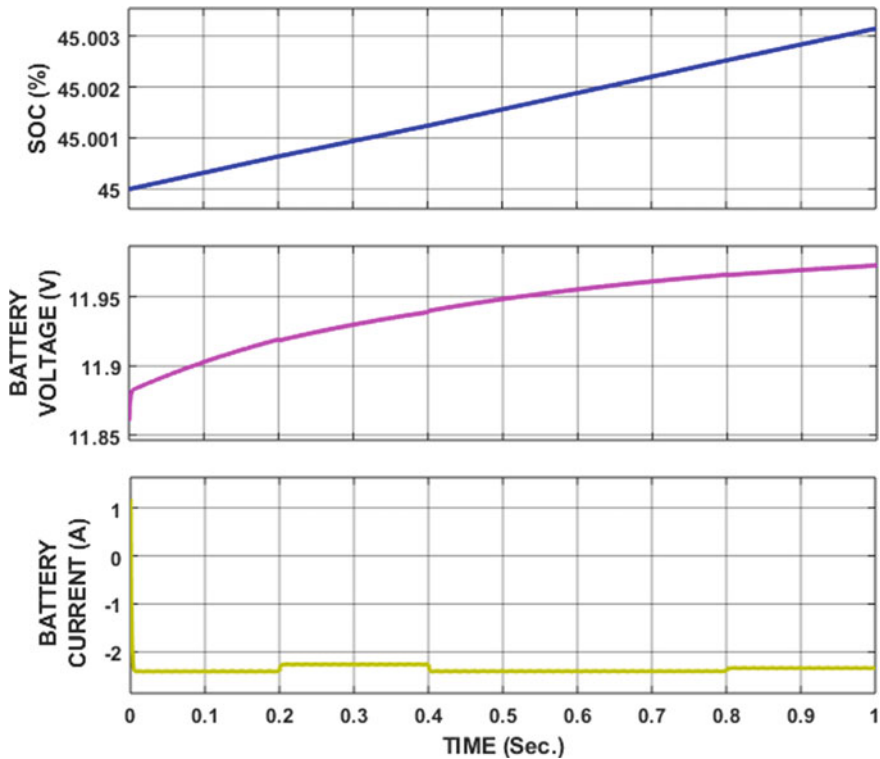


Fig. 27.6 State of charge, voltage, and current of lead acid battery

27.4 Conclusion

The paper has presented effective solar powered charging system of battery with maximum utilization of solar energy and obtained maximum power from SPV using P & O MPPT algorithm. The operating point optimally performed the tracking through the use of DC-DC boost converter. The lead acid battery was not over charged. The proposed system results have been verified to be effective and shows the dynamic response at different irradiance levels. The battery performance has been verified in terms of battery current, battery voltage and SOC for different irradiations. The simulation results show that power converter operates in continuous conduction mode (CCM).

Acknowledgements We hereby acknowledge ICIMES Publisher, annexed sponsors and Delhi Technological University for providing a good platform to showcase our findings. We would also like to express our sincere gratitude and appreciation for making the research work accomplished by providing opportunity and support during crisis of pandemic.

References





1. Ramesh, N., Vanitha, V., Reshmi, R.: Hybrid solar and wind based battery charging controllers. *Innovation in a Power and Advance Computing Technology (i-PACT)*, India, Vellore, vol. 2, pp. 1–5 (2019)
2. Surekha, P., Ashok Kumar, L., Sumathi, S.: Wind energy and solar PV conv. System. In: *Introduction to Theory, Role of Soft Computing Technique and Modeling with MATLAB/SIMULINK*
3. Rokonzaman, M., Mishu, M., Shamimul Islam, M., Haider, M.H.E.: Designing of MPPT solar charged controllers in Matlab/Simulink GUI Environment. In: *Conf paper on University Tenaga National (UNITEN), Military Institute of Science and Technology and Daffodil International University*, Feb 2017
4. Hawke, B.: Basic calculations of boost converters power stages. *Low powered DC/DC Applications*, SLVA372C, Jan 2015
5. Martin, D.C., dos Santos, W.M.: Digital MPPT techniques for PV panel with the singled voltage sensors. In: *Proc. Scottsdale, AZ*, pp. 1–8 (2012)
6. Luo, F.L., Ye, H.: *Advance DC/DC Converter*. CRC Press, Chapter 3 (2003)
7. Mandal, K.K., Roy, K.: Hybrid optimization algorithms for micro-grid management connection systems. *Front. Energies* **8**(3), 305–315 (2014)
8. Enrique, J.M., Duran, E.: Theoretical assessment of the MPPT efficiency of photovoltaic facilities with different converter topologies. *Sci. Direct: Solar Energy* **81**(1), 231–238 (2007)
9. Fie, L., Yong, K., Shanshu, D.: Variable stepped size INC MPPT methods for photovoltaic system. *IEEE Trans. India Elect.* **56**(7), 2622–2629 (2008)
10. Veldman, E., Verzijlberg, R.A.: Distributed grid impact of smart electrical vehicles charged from different perspective. *IEEE Trans. Smart Grids.* **6**, 333–343 (2015)
11. Mahdavi, J., Toliyat, H.A.: Applications of states space average method for slide mode of control of PWM DC/DC converter. *IEEE Ind. Appl. Soc.* (Oct 1998)

12. Lyden, S., Haque, M., Mouka, P.I.: Model and parameters estimations of PV cells. In: 22nd Australian Univ. Power Engineering Conf. (AUPEC), Indonesia, Bali, vol. 14, pp. 63–70 (2014)
13. Chapman, P.L., Eram, T.: Comparison of PV arrays MPPT technique. *IEEE Trans. Energy Conv.* **22**(2), 439–449 (2007)

Chapter 28

Design and Analysis of Hydraulic Machining Fixture for a Drifter Bit of a Top Hammer



Nagaveni Thallapalli , G. Sudheer Kumar Reddy,
J. Jaswanth Raju , S. B. Manikanta Katepalli ,
and Vineela Chippe 

Abstract Jigs and fixtures are special production tools which are used to make the standard machine tool and more adaptable for different operations to be done. Jigs and fixtures are the economical ways to produce a component in mass production. The present work deals with the design of machining fixture for drilling operation for a drill bit of top hammer which is termed as drifter bit. Without jigs and fixtures, this component machining is carried out by manual indexing, setting the work piece for every single component, etc. Therefore, to meet the present production requirement, the time required has to be reduced by using a fixture that can hold the component on a 5-axis machine. A hydraulic fixture is designed for good manufacturability and assembly, and proper fixture elements and hydraulic elements are selected. Model is developed in Creo 4.0. Deflection and von miss stresses are predicted by using ANSYS 17.2 software. Total equivalent stress of the structure is 9.816 N/mm^2 . At the required cutting force, the maximum deflection obtained is 10 microns. The actual permissible limit is 15 microns. So, the obtained value is within the permissible limits for the required cutting force.

28.1 Introduction

Design of jigs and fixtures is the first step for any manufacturing industry. For any component to produce in mass amounts, it is necessary to use jigs and fixtures. Jigs and fixtures are used for tool guiding and work holding purposes. The quality of the component or part in the manufacturing is directly dependent on the quality and type of jigs and fixtures used. A jig or a fixture is designed so that it can do the job

N. Thallapalli · G. Sudheer Kumar Reddy · J. Jaswanth Raju (✉) ·
S. B. Manikanta Katepalli · V. Chippe
Department of Mechanical Engineering, University College of Engineering,
Osmania University, Hyderabad, India
e-mail: nagaveni.t@uceou.edu

perfect and less tedious. A jig is a machine tool component which not only holds the component but also guides the tool during the operation while performing. Whereas, a fixture is used only for holding the component while the operation is carried out. Fixture is a production tool that locates, holds and supports the part securely while machining. Nee et al. [1] presents a feature-based classification scheme for fixtures using a 3D solid modeller, a feature extractor and an object-oriented expert system shell. While designing a fixture, the main considerations are clamping force, cutting force, machining force and clamping concepts [1]. Pachbhai et al. [2] studied a clamping system which uses high-pressure liquids to power clamps and hold a work piece in place. Hydraulically clamped fixtures have many advantages over manually clamped fixtures. In most cases, these benefits reduce costs for manufacturers allowing them to justify the initial investment for a hydraulic clamping system [2]. Lokhande et al. [3], this simple design of drilling fixture assembly enables to perform such operation with accuracy and repeatability by attaching U-CAM fourth axis attachment on vertical machining centre (VMC) [3]. Kashyap et al. [4] in their paper, finite element analysis and optimization in fixture, proposed with minimizing deformation of the work piece due to machining loads about fixing support positions, especially in thin castings [4]. The use of jigs and fixtures is to minimize cycle time, effort required in setting the machine, maintain dimensional tolerances in production, reduce rejection rate, faster production of components, reduce operator fatigue, use manpower since even semi-skilled labour can perform the operation and finally to reduce the cost of the single component in a whole. The important considerations while designing a fixture are: study the geometry and size. Study the machine type which is used. Check for the possibility to use any type of automation on the machine. Check for the positioning of clamping the locating elements on the machine. Design the fixture such that the clamping force should not deform the component and also withstand the cutting forces. The indexing devices are to be located for reducing the cost of fixture design. The fundamental principles of fixtures are: locating points, fool proof, reduction of idle time, weight of fixture, materials of fixtures and clamping device [5]. Hydraulic clamping rod piston are used for clamping the component along with expanding collect in the fixture. Clamping rod piston works under a pressure of 70 bar. The clamping force is calculated as per standards. According to the maximum cutting force estimated for the component, suitable clamps are selected [6]. A hydraulic system is nothing but use of pressurized fluids to transfer on energy. In this case, this technique is used for clamping of the work piece firmly on to the fixture. When compared to clamping devices used manually, the hydraulic clamps are far more advantageous. Hydraulic clamping permits makers to place a lot of intelligence into the fixture eliminating human error and manufacturing a lot of stable, predictable processes regardless of who the operator is or what production shift your machine runs. The major advantages of hydraulic clamping system are: more productivity, consistent clamping forces, repeatable clamp location, eliminates human error, faster, ergonomic efficiency, improved part stability, flexibility and precise clamping load applied on the component [7].

28.2 Problem Definition

The product shown in Fig. 28.1 is a 3D representation of a drifter bit which is generally used for long hole drilling in mines, for underground water mining and various other purposes. A study is done on the component so that all the dimensions of the clamping surfaces and for holes like the front-flush hole and side-flush holes which are required for the passage of the compressed fluid. The main aim of the paper is to design a fixture for cone drilling for improving accuracy during machining, reducing machining time of component, reduce loading and unloading time. The other purposes are minimizing the labour charges, number of setups and lead time required. The above fixture is designed for Mazak Variaxis 500 Vertical Machining Centre where all the holes can be done within a single setting of the component in the machine. The component details are given in Table 28.1 which gives a brief description of the material and operation to be performed. The drilling has to be done on the drifter bit at various rows, and around 360 degrees of the workpiece.

28.3 Design Methodology

28.3.1 Preliminary Design Using CREO

Preliminary design of the component deals with the supporting structure of the component and also designing of the one-way hydraulic valve so that the assembly can be fixed on to the machine rigidly. Considering of different cutting forces are the key for designing of the parts and force transmission of the hydraulic power to the clamping and locating elements. The values of different cutting forces are given in the Table 28.2.



Fig. 28.1 Drifter bit

Table 28.1 Specifications of drifter bit material and operation

Component name	Drill bit of top hammer
Component material	En 36c (Forged steel)
Input condition	Forged Part
Density	8100 kg/mm ³
Hardness	38–42 HRC
Operation	Drilling three types of holes of dias of 11 mm, 9 mm, 6 mm
Drifter bit material composition	(0.14–0.18)C%; (0.40–0.6)Mn%; (0.025–max)P%; (0.015–max)S% (0.2–0.35)Si%; (3–3.75)Ni%; (0.9–1.1)Cr%; (0.15–0.25)Mo%

28.3.2 Design and Analysis of the Hydraulic Fixture

Designing of the hydraulic fixture: in a hydraulic fixture, the location and clamping is done with the help of hydraulic power. For fast loading and unloading and also for high force that can be used with the help of this type of technique. In this fixture, a connecting rod is connected to a piston which is actuated using hydraulic pressure. Due to the linear movement of the connecting rod, a radial displacement of collet is occurred [8]. This is due to the internal taper provided in the collet and the rod. Due to the radial displacement, the collet gets in contact with the component present and holds the component. After holding the component, the hydraulic line can be removed to start the drilling process. The brief assembly representation of the components is given in Fig. 28.2.

28.3.3 Analysis of the Hydraulic Fixture Assembly

The analysis is done basically with the help of CAE software known as Ansys mechanical. The prerequisites of the analysis are that to import the assembly into the software in the form of step file. After importing the assembly file, the contact

Table 28.2 Input parameters

Hole diameter (mm)	11	9	6
Cutting velocity (m/min)	17.26	16.956	16.014
Material removal rate (mm ³ /min)	7123.875	4450.95	2402
Cutting power (KW)	0.296	0.185	0.1
Thrust force (KN)	1.611	1.318	0.878
Torque (N-m)	5.4	2.95	1.124
Clamping force (KN)	2.41	1.977	1.317
Work support force (KN)	3.61	2.96	1.9755

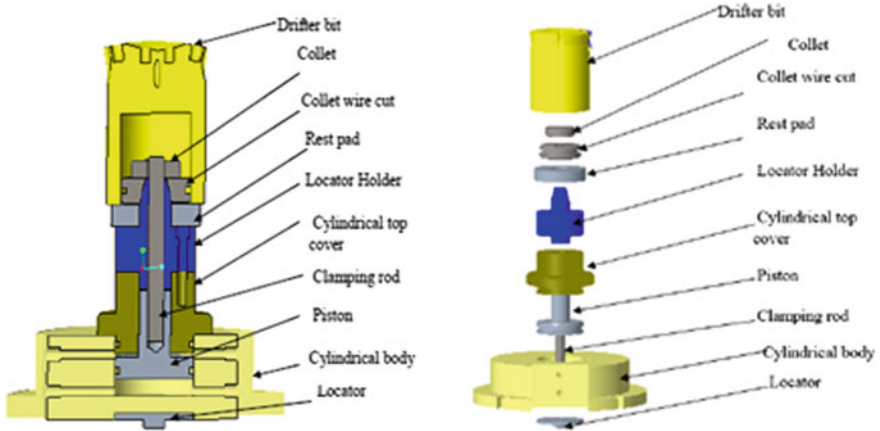


Fig. 28.2 3D representation of hydraulic machining fixture

Table 28.3 Materials used in hydraulic fixture and their composition

Component name	Material assigned	Material composition
Cylinder body	E 19	(0.35–0.45)C%, (0.1–0.35)Si%, (0.5–0.8)Mn%
		(0.035)P%, (0.05)S%, (0.9–1.5)Cr%
		(0.2–0.4)Mo%, (-)Ni%
Locator	E19	
Piston	E19	
Cylinder top Cover	E19	
Locator Holder	E19	
Rest Pad	E19	
Collet	E8	
		(0.36–0.44)C%, (0.1–0.4)Si%, (0.6–1)Mn%, (0.05)P%
		(0.005)S%, (-)Cr%, (-)Mo%, (-)Ni%
Clamping Rod	E8	

type between the components in the assembly are to be given. After giving the boundary conditions, the material of each of the components is assigned as given in the Table 28.3.

Table 28.3 includes the details of each material given to different parts and also their material compositions. Ansys generally gives the contact type as bonded in which there would be no separation and no sliding relation between the components. But the relations are to be changed to no separate contact to the translation components in the assembly. After giving the contacts in the assembly, the boundary conditions are to be given. As we can see from the Table 28.2 that a maximum force of 3.61 KN is applied on the periphery of the body [9]. Cylinder

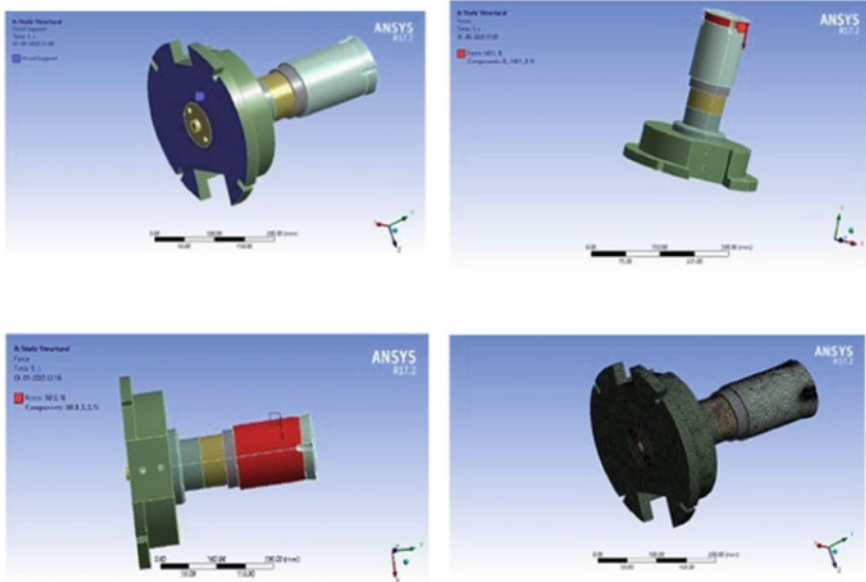


Fig. 28.3 Boundary conditions and meshing

body fixed on machine bed and clamps arrest the rotation ‘Y’ moment of the component. Since the maximum thrust force acting 1611 N is applied on the top surface in the negative y direction. The mesh is created on the geometry a hexagonal dominant mesh is created and a total nodes of 146,960 were created, and total elements of 186,484 were created (Fig. 28.3).

28.4 Results and Discussion

Equivalent stress fixture assembly with component is loaded with force 1611 N is acting on the component is shown in Fig. 28.4, and fixed support is given at base of the cylindrical body of a fixture because fixture is clamped on the work table of Mazak Variaxis machine, ref. the following Fig. 28.4. From analysis result, maximum stress developed for a given load 1611 N is 2.438 N/mm².

Total deformation fixture assembly with component is loaded with force 1611 N is acting on the component is shown in Fig. 28.4, and fixed support is given at base of the cylindrical body of a fixture because fixture is clamped on the work table of Mazak Variaxis machine, ref. the following Fig. 28.4. From analysis result, the red colour indicates that maximum deformation developed for a given load 1611 N is 2 microns.

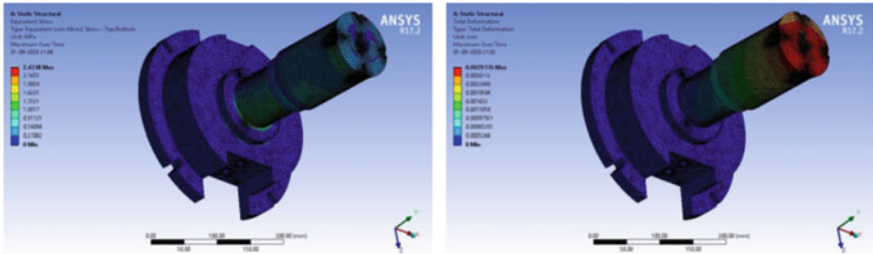


Fig. 28.4 Equivalent stress and total deformation with 1611 N

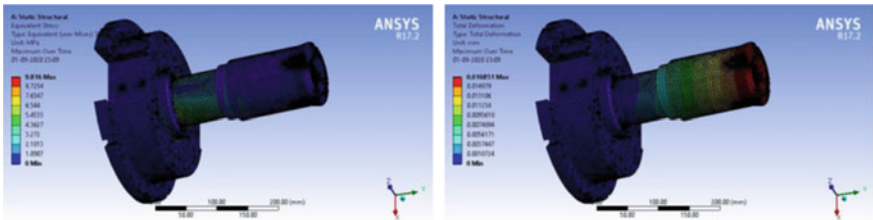


Fig. 28.5 Equivalent stress and total deformation 3610 N

Equivalent stress fixture assembly with component loaded with force 3610 N is acting on the component is shown in Fig. 28.5, and fixed support is given at base of the cylindrical body of a fixture because fixture is clamped on the work table of Mazak Variaxis machine, ref. the following Fig. 28.5. From analysis result, maximum stress developed for a given load 3610 N is 9.816 N/mm^2 .

Total deformation fixture assembly with component is loaded with force 3610 N is acting on the component is shown in Fig. 28.5, and fixed support is given at base of the cylindrical body of a fixture because fixture is clamped on the work table of Mazak Variaxis machine, ref. the following Fig. 28.5. From analysis result, the red colour indicates that maximum deformation developed for a given load 3610 N is 10 microns.

28.5 Conclusions

A hydraulic fixture is designed for good manufacturability and assembly and proper fixture elements and hydraulic elements are selected.

Fixture elements are developed in CREO 4.0. Deflection and von misses stresses are predicted by using ANSYS 17.2 software as follows.

Maximum stress developed for a given load 1611 N is 2.438 N/mm^2 , and maximum deformation developed for a given load 1611 N is 2 microns. Maximum stress developed for a given load 3610 N is 9.816 N/mm^2 , and maximum deformation developed for a given load 3610 N is 10 microns. Total equivalent stress of the structure is 9.816 N/mm^2 . At the required cutting force, the maximum deflection obtained is 10 microns. The actual permissible limit is 15 microns. So, the obtained value is within the permissible limits for the required cutting force. So the structure is safe.

Acknowledgements The author would like to acknowledge the support and contributions of the officials in Epiroc drill tools India, cherllapally, Hyderabad.

References

1. Nee, A.Y.C., Senthil Kurnar, A., Prombanpong, S., Pua, K.Y.: A feature-based classification scheme for fixtures. *CIRP Annals* **41**(1), 189–192 (1992)
2. Pachbhai, S.S., Raut, L.P.: Design and development of hydraulic fixture for machining hydraulic lift housing. *Int. J. Mech. Eng. Robot. Res* **3**, 204–214 (2014)
3. Lokhande, N.G., Tembhurkar, C.K.: Design of angular drilling fixture and analysis of cutting forces during drilling on cylindrical surfaces. *J. Appl. Mech. Eng.* **1**(2) (2012)
4. Kashyap, S., DeVries, W.R.: Finite Element Analysis and Optimization in Fixture Design, vol. 18, pp. 193–201 (1999)
5. Joshi, P.H.: *Jigs and Fixture Design Manual*, 3rd edn. S.Chand publication, Delhi (2017)
6. CMTI: *Machine Tool Design Handbook*. Tata McGraw-Hill, New Delhi (1982)
7. Sen, G.C., Bhattacharyya, A.: *Principles of Machine Tools*, 2nd edn. New central book agency, Calcutta (2009)
8. Dhulia, J.K., Maniar, N.P.: Design, modelling and manufacturing of 16 cylinder hydraulic fixture with automated clamping system. *J. Phys. IOP Publishing*. **1240**(1), 012–036 (2019)
9. Vamshikrishna, G., Gurudatta, K.S.S., Ravindrannair, P., Equbal, M.I.: Design and analysis of hydraulic fixture for WABCO body housing. In: Shunmugam, M., Kanthababu, M. (eds.) *Advances in Simulation, Product Design and Development. Lecture Notes on Multidisciplinary Industrial Engineering*. Springer, Singapore (2020). <https://doi.org/10.1007/978-981-32-9487-5-64>

Chapter 29

Inverse Kinematic Analysis of PUMA 560 for Vision Systems



Navya Mohan, Athul Thomas, P. P. Prasanth, M. S. Midhun,
and James Kurian

Abstract Robust techniques for pose estimation are crucial for robotic manipulators which enable efficient object grasping for industrial applications. The determination of the manipulator joint parameters is very complex and cumbersome. Simulation of these reduces the complication involved in understanding the analysis and implementation behind robotic kinematics. This paper discusses the kinematics of the PUMA 560 robot manipulator for appropriate actions using MATLAB/Simulink in its vision-enabled robotic workspace. The 2D image is processed to estimate the position and orientation vectors which activate the 6R manipulator for further actions. A graphical user interface (GUI) using MATLAB Robotics toolbox is integrated through which one can emulate robotic movements. The graphically represented results can be analysed easily as they are accurate, efficient and suitable for real-time application.

29.1 Introduction

Pose estimation is widely used in robotic industry, automatic manufacturing sectors and aerospace industry and has become a vital part in vision systems [1–5]. In vision systems, it captures the RGB image of a target and processes the image to

N. Mohan (✉) · A. Thomas · P. P. Prasanth · M. S. Midhun · J. Kurian
Department of Electronics, Cochin University of Science and Technology,
Kochi, Kerala 682022, India
e-mail: navyamohan@cusat.ac.in

A. Thomas
e-mail: athulthomas@cusat.ac.in

P. P. Prasanth
e-mail: prasanth.imsl@cusat.ac.in

M. S. Midhun
e-mail: midhunms@cusat.ac.in

J. Kurian
e-mail: james@cusat.ac.in

estimate position and orientation parameters of the object in its coordinate system. Images so obtained are preprocessed to reduce noise and distortions. In order to achieve efficient and effective motion of the end effector to manipulate the identified objects, joint angles have to be determined using the suitable inverse kinematic solutions [6–9], which produce the desired motion in each joint. Therefore, the real-time vision module should provide accurate feedback of joint variables to the manipulators analogous to the end effector position.

Modelling and simulation using MATLAB Robotics toolbox [10] will ease the process of designing and inspecting the robots' joint angles in the real world. For robot programmers, simulation is important in allowing them for estimating and predicting the behaviour of a robotic system in addition to verifying and optimizing the algorithms.

The proposed work performs the simulation of the robotic manipulators so that it is possible to investigate, visualize and test the robot set-up before making it a reality. The proposed work uses PUMA 560 which is modelled using the MATLAB Robotic toolbox to understand its position control using the inputs from the vision module.

The PUMA 560 is an industrial robot arm with six degrees of freedom and all rotational joints [11–13]. Robotic manipulator, PUMA 560 in its vision-enabled workspace for picking its task from the conveyor belt is shown in Fig. 29.1. In order to actuate the manipulator, we have to apply suitable transformation to the image frame from the camera so that end effector can be properly aligned to pick the object.

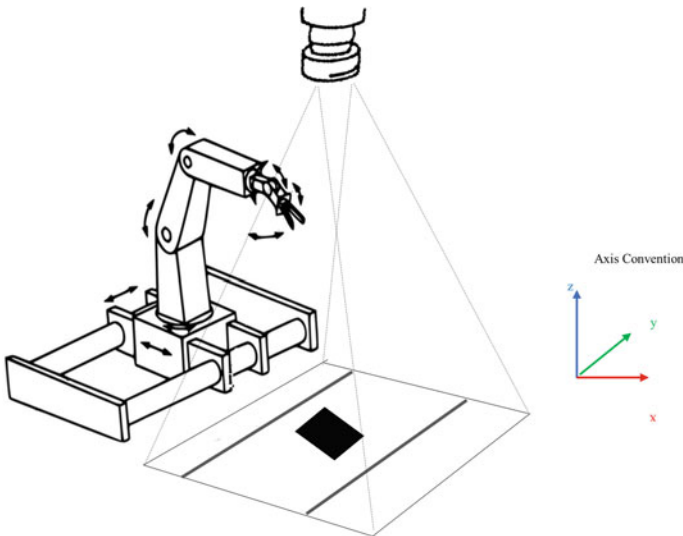


Fig. 29.1 Pictorial representation of robotic manipulator in its vision-enabled workspace

It is necessary to preprocess the image, then to identify the object as well as its pose and finally determine the kinematics for simulating the robotic systems. These steps are organized in this paper as follows. In Sect. 29.2, we have discussed the methodology adopted to determine the angle of each joint of PUMA 560 using MATLAB toolbox. In Sect. 29.3, we have discussed our results. In Sect. 29.4, we summed up the approach and presented some of the suggestions for the future research work.

29.2 Methodology

The proposed work consists of two modules—Pose estimation module and kinematic modelling module. Position and orientation coordinates are determined using the vision set-up in the former module, while the latter module determines the joint space coordinates of the PUMA 560 for accomplishing its task.

Most of the works accomplished by robots need visual feedback to move around its workspace to identify and locate the desired tools by avoiding obstacles in its path. The relationship between the given point in the visual scene and its corresponding point in the image can be obtained by mathematical modelling. The coordinates of objects can be transformed using the operations—translation, rotation and scale which are described by a set of parameters. The vision-based pose estimation module determines these linear transformations (which is the combination of any of these three operators).

The description of the object's pose must be made in relation to world coordinate frame. Given the coordinates of the object in the camera coordinate frame, it is possible to determine its coordinates in the robot coordinate frame by applying suitable transformation matrixes as in the Eq. (29.1).

$${}^I T_R = {}^C T_R * {}^I T_C \quad (29.1)$$

where ${}^I T_R$ = transformation matrix of image frame with respect to robotic base frame.

${}^C T_R$ = transformation matrix of camera with respect to robotic base frame.

${}^I T_C$ = transformation matrix of image with respect to camera coordinates

$${}^I T_C = f(p_x, p_y, p_z, \theta)$$

p_x, p_y, p_z are the position coordinates, and θ is the orientation of object with respect to the camera frame.

Once the transformation is determined, it is necessary to obtain the joint angles for a desired trajectory or to position the end point of the robot. The inverse kinematic modelling module manipulates the pose and computes the corresponding

joint parameters. The inverse kinematics problem is solved and simulated by using Robotics toolbox for MATLAB.

29.2.1 Vision-Based Pose Estimation Technique

Multiple objects can remarkably intricate the recognition of each entity in an image. Real-time views of the entity that has to be recognized are distracted by the scene clutter. Likewise in any image analysis, it is mandatory to perform basic operations like generating a binary image, removing the noise, image sharpening and smoothing.

Thresholding operation is done to change the image into a binary. In order to ensure that the image is noise free, dilation operation was performed. Erosion operation was also performed to close small holes in the object. Centroid extraction is done after this.

The centroid coordinates corresponding to the object in binary image are the arithmetic mean of all boundary coordinates as described in the equation below:

$$\bar{x} = \frac{1}{N} \sum_{i=1}^N x_i \quad (29.2)$$

$$\text{and } \bar{y} = \frac{1}{N} \sum_{i=1}^N y_i \quad (29.3)$$

where x_i and y_i are the x and y coordinates along the boundary of the object, and N is the total number of boundary coordinates.

Robot manipulator needs orientation of the object of interest to take desired actions. The orientation of geometric objects is extracted using visual information. This is accomplished by determining the major axis of the ellipse around the geometric object in the segmented binary image. The orientation is the angle between this major axis and the horizontal line.

29.2.2 Inverse Kinematic Modelling of PUMA 560

The conversion of the position and orientation of a manipulator end effector from Cartesian space to joint space is called as inverse kinematics problem. Inverse kinematics uses the kinematic equations to determine the motion of a robot to reach a desired position. Finding solutions to the inverse kinematics problem is computationally complex and generally takes a quantum of time in the real-time control of manipulator structures.

Given the pose of the object under the vision set-up, in order for the manipulator to grasp the object from its position, the joint angles need to be properly activated. Tasks to be accomplished by a manipulator are in the Cartesian space, while actuators perform in joint space. The conversion between these coordinate frames is implemented using Eq. (29.1). Modelling of such a system is proposed in this work using PUMA 560.

The inverse kinematic transformation feeds the reference values corresponding to an assigned end effector. A six-axis 6-R robot system for a “pick and place” operation is designed and developed using MATLAB/Robotics toolbox as shown in Fig. 29.2. Forward kinematics is applied to move the manipulator to its desired position (Denavit–Hartenberg (D–H) parameters).

Denavit–Hartenberg (D–H) parameters are necessary to calculate forward kinematics in serial robot manipulator. Initial step to find the serial link robot manipulator forward kinematics is to find the link description, and the next step involves finding the D–H convention after the frame attachment and finally finds the forward kinematics. Forward kinematics is a 4×4 matrix in which 3×3 of

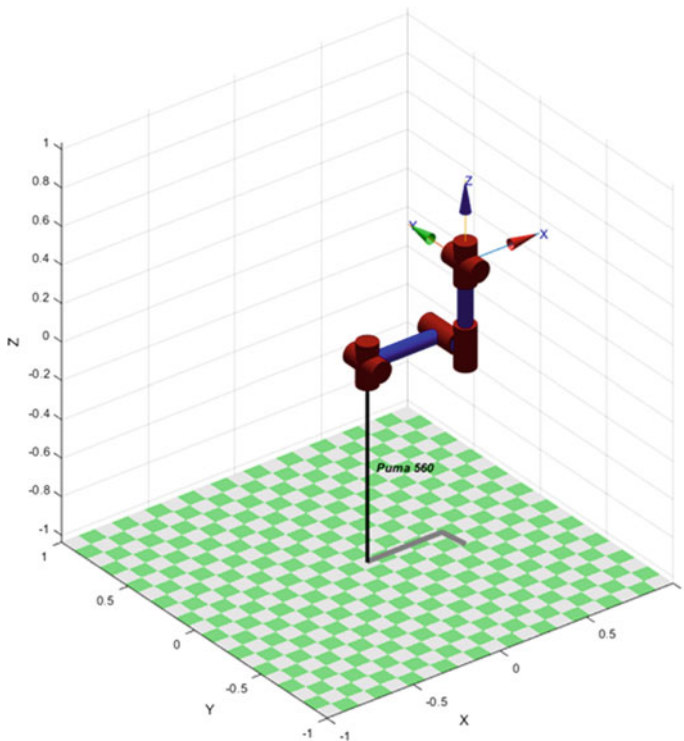


Fig. 29.2 Visual model of PUMA 560 in MATLAB

them shows the rotation matrix, 3×1 of them is the position vector, and last four cells are scaling factor. PUMA 560 is an example of the class of all revolute six-axis robot manipulators with DH parameters as shown in Table 29.1.

29.3 Results and Discussions

Experimentation to determine the pose and subsequently find the transformation matrices with respect to the robot manipulator base was done on a total of five classes each of JPEG format. Evaluation was done on 18 images from each class which is rotated from 0 to 180° with a span of 10° . A set of images from a class which is used for determining the pose parameters are shown in Fig. 29.3.

The orientation and position coordinates of the set of images have been obtained as shown in Table 29.2.

The orientation is estimated for the rotation angles from 10° to 180° , and its error plot is shown as in Fig. 29.5. The plot shows that determined orientation values are very close to the actual values, and the maximum error obtained is for 0.64.

The inverse kinematics problem is calculation of joint variables (displacement and angles), when the position and orientation of the end point are known. The main objective of the inverse kinematics problem is to calculate the $q = h^{-1}(X)$, where q is the joint space variable, and $q = [q_1, q_2, \dots, q_n]$ and X are the position and orientation of the endpoint of manipulator. The inverse kinematic solution of the

Table 29.1 DH parameters for PUMA 560 robot

Link	a (m)	b (m)	α (deg)	Θ (deg)
1	0	0	-90	θ_1
2	0.432	0.149	0	θ_2
3	0.02	0	90	θ_3
4	0	0.432	-90	θ_4
5	0	0	90	θ_5
6	0	0.056	0	θ_6

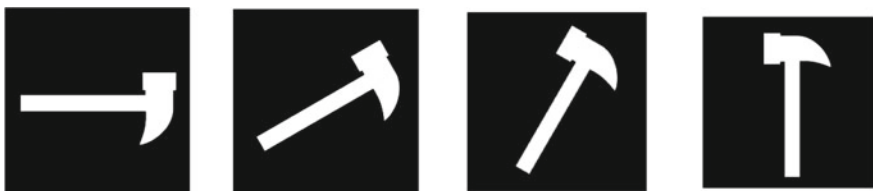


Fig. 29.3 Examples of a few images used for pose estimation

Table 29.2 Position and orientation determined for the images

Object orientation	Position coordinates determined	Orientation determined (degrees)
30°	(358.16, 289.23)	29.42
60°	(341.68, 267.29)	59.41
90°	(233.44, 173.56)	89.37
120°	(289.23, 259.84)	119.42
150°	(267.30, 276.32)	149.42
180°	(173.56, 218.55)	179.32

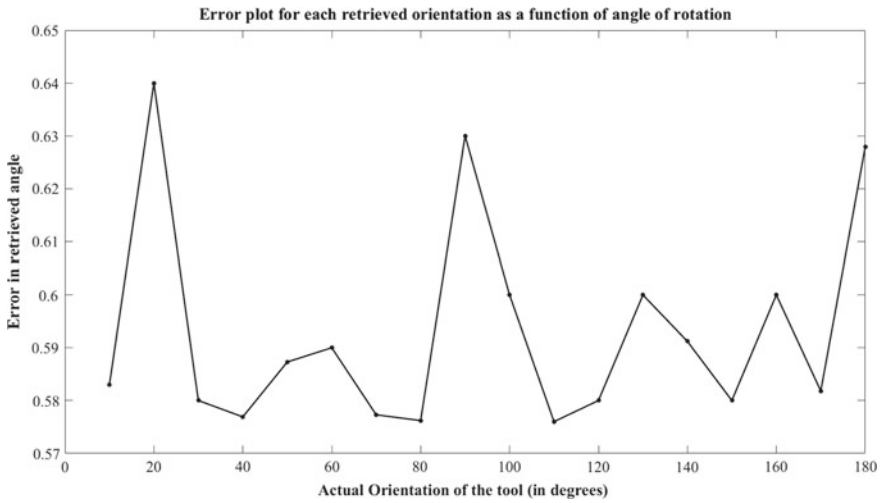


Fig. 29.5 Error plot for each retrieved orientation as a function of actual orientation

PUMA 560 was determined for position coordinate (289.23, 259.84) and angle 119.42°. The joint angles (q) for the above position are obtained as

$$3.3893 \quad 2.1349 \quad 0.1425 \quad 2.1903 \quad 0.2832 \quad 2.3675$$

Once the joint angles are determined, it is possible to apply forward kinematics and verify if it has taken the actual position as in Fig. 29.6. The transformation matrix for the joint angles as well as for the above pose is determined using the above joint angles as shown below.

$$T = \begin{bmatrix} -1 & 0 & 0 & 0.5182 \\ 0 & 0.4912 & 0.8710 & 0.2858 \\ 0 & 0.8710 & -0.4912 & 0.1 \\ 0 & 0 & 0 & 1 \end{bmatrix}$$

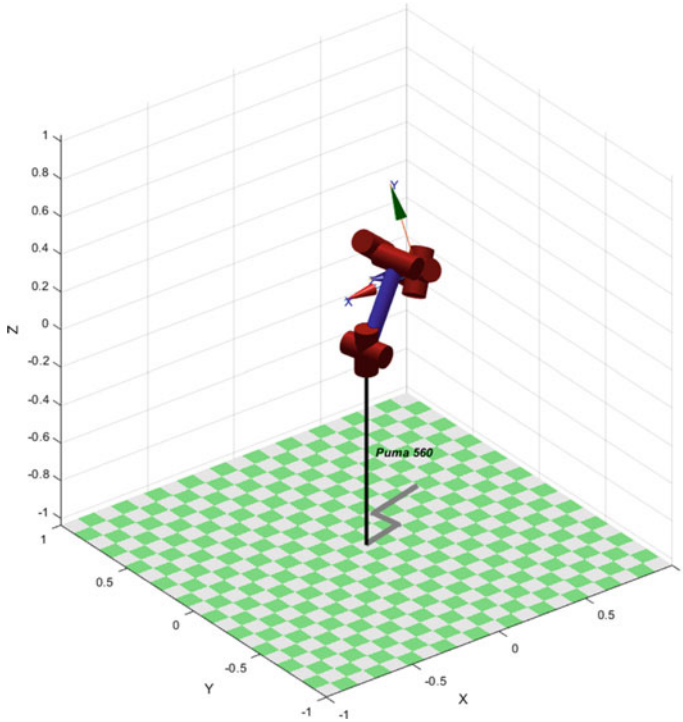


Fig. 29.6 PUMA 560 in MATLAB for position coordinates (289.23, 259.84) and orientation 119.42°

29.4 Conclusion

An algorithm is presented for determining the pose of objects from vision module and activating the robotic manipulator to complete its action. Orientation determination is a difficult problem as multiple representations exist for the same physical orientation, and the proposed work has attempted to achieve it with less error. In addition, a visual model of the PUMA 560 is plotted using the real-time input from the vision modules. Such a visualization of robotic manipulators provides an insight into the kinematics of the robotic link structures which indirectly reflects the motion of end effectors and yields a theoretical basis for the specific development and control strategy of the manipulator.

References

1. Abbas, Q., Ibrahim, M.E.A., Jaffar, M.A.: Video scene analysis: an overview and challenges on deep learning algorithms. *J. Multimed. Tools Appl.* (2017)
2. Sheth, S., Kher, R., Shah, R., Dudhat, P., Jani, P.: Vision automatic sorting system using machine vision. *Academia. Edu*, no. November 2016 (2010). <https://doi.org/10.13140/2.1.1432.1448>
3. Volpe, R., Sabatini, M., Palmerini, G.B.: Pose and shape reconstruction of a noncooperative spacecraft using camera and range measurements. *Int. J. Aerospace Eng.* **2017**(4535316), 13 (2017)
4. Dhakshina Kumar, S., Esakkirajan, S., Bama, S., Keerthiveena, B.: A microcontroller based machine vision approach for tomato grading and sorting using svm classifier. *Microprocess. Microsyst.* **76**, 103090 (2020)
5. Kanjanawanishkul, K., Chupawa, P., Nuantoon, T.: Design and assessment of an automated sweet pepper seed sorting machine. *Eng. Agric. Environ. Food* **11**, 196–201 (2018)
6. Atique, M.U., Sarker, R.I., Ahad, A.R.: Development of an 8DOF quadruped robot and implementation of Inverse Kinematics using Denavit–Hartenberg convention. *Heliyon* **4** (2018)
7. Fu, K.S., Gonzalez, R.C., Lee, C.S.G.: *Robotics: Control, Sensing, Vision and Intelligence (CAD/CAM, Robotics, and Computer Vision)*. McGraw-Hill, New York, NY, USA, 198
8. Lenarcic, J., Husty, M.: *Latest Advances in Robot Kinematics*. Springer (2012)
9. Siciliano, B., Khatib, O.: *Springer Handbook of Robotics*. Springer (2008)
10. Corke, P.: Faculty of Built Environment and Engineering, School of Engineering Systems, Queensland University of Technology (QUT), pp. 142–145, 164–168 (2011)
11. Cheng, Y.L., Zhu, S.Q., Liu, S.G.: Inverse kinematics of 6R robots based on the orthogonal character of rotation sub-matrix. *Robot* **30**(2), 160–164 (2008)
12. Rodriguez, R., Cardozo, T., Ardila, D.L., Cuellar, C.A.: A consistent methodology for the development of inverse and direct kinematics of robust industrial robots. *ARPN J. Eng. Appl. Sci.* **13**, 293–300 (2018)
13. González-Palacios, M.A.: The unified orthogonal architecture of industrial serial manipulators. *Robot. Comput. Integr. Manuf.* **29**(1), 257–271 (2013)

Chapter 30

Experimental Investigation on Portable Refrigerating Bottle



Shiva Kumar Reddy Devasani, Sudeshna Vodnala,
and K. Krishnamurthy

Abstract There is a tremendous rise in pollution in recent times due to the increased use of sophisticated equipment in many domestic and industrial applications. There is a considerable increase in dangerous emissions like chlorofluorocarbons (CFCs) due to the use of refrigerants. On the other hand, the increasing demand for refrigeration systems in transportation emphasizes portable refrigeration systems. The portable refrigeration works with electricity to provide the cooling effect. This system is free from emissions. In this work, a mobile refrigeration system is designed and developed on a bottle. The developed model is a bottle that is thermally insulated and has a Peltier module and batteries for the electric power supply. It has a digital temperature controller for displaying the temperature of the fluid. Various characteristics of the developed portable refrigeration model have been studied. It is observed that the optimum condition is obtained when the device is working with the power supply of 10.5 W.

30.1 Introduction

Refrigeration is a process of providing a cooling effect by reducing temperature below ambient temperature. Heat is absorbed from the refrigeration space and rejected to the surroundings in different types of refrigeration systems. However, all these systems involve heating and cooling of refrigeration space and surroundings.

Patil et al. [1] capitulated the evolution of thermoelectric refrigeration over the past decades. It was said that thermoelectric refrigeration was more efficient than the conventional refrigeration process when implemented in portable refrigeration systems. Analysis was done over various research works carried out by different

S. K. R. Devasani (✉) · S. Vodnala
Mechanical Engineering Department, Bachelor of Technology, VNR VJIET,
Hyderabad, India

K. Krishnamurthy
Mechanical Engineering Department, VNR VJIET, Hyderabad, India
e-mail: krishnamurthy_k@vnrvjiet.in

people in the field of thermoelectric refrigeration. Chavan and Dhawde [2] this paper explained that a new type of cooling was developed by implementing thermoelectric refrigeration systems. Thermoelectric cooling was more effective than conventional cooling processes. Its efficiency was more due to its smaller size and absence of moving elements. Bismuth telluride is the most used thermoelectric element in these systems; less cost, longer working life, etc., were the advantages of these systems. Rakesh et al. [3] in this study, the advantages of thermoelectric systems were stated. It was reported that these systems have more extended durability, low maintenance cost, and no hazardous gas emissions, eliminating pollution. The disadvantages were the low coefficient of performance and high cost for large-scale applications. It was also stated that better strategies to improve the effectiveness of heat transfer and to use better thermoelectric materials could improve the performance of the systems. Totala et al. [4] developed a thermoelectric heating and cooling device. This device was incorporated to heat and cool the ambient air, which was being circulated by a blower. This device had cooled the ambient air from 32 °C to 22 °C in 10 min. By using a high-performance thermoelectric cooling module, this device was further made compact. Employing recirculation pipes around the heat sink and high-speed blowers increased the system's effectiveness and extent of cooling. Chang et al. [5] had experimented on the performance of a thermoelectric cooling module. They studied the effect of input current and heating power on the working of the thermoelectric cooling module. Analysis was done by applying a thermal resistance network. It was found that the input current to the cooling module was inversely proportional to the thermoelectric cooling resistance and directly proportional to the heat sink resistance. The heating power of the heat source was inversely proportional to the heat sink resistance and directly proportional to the thermoelectric cooling resistance. Maaspuro [6] was studied and simulated the working of a thermoelectric cooling module. An active cooling module consisting of a thermoelectric module, a heat sink, and a fan was used. A setup was constructed and experimented with, and simulation tools were used to study the cooling process. Finite element method tools were used to study the heat transfer. It was reported that the device could be made accurately for a limited range of current. However, the device's accuracy was decreased with an increase in the range of the input current. Shah et al. [7] were analyzed and studied various thermal insulating materials and provided for the selection of insulating material based on thermal conductivity, temperature, and other factors that might limit application. Lavanya et al. [8] were experimented and compared two Peltier modules, TEC1-12,730 and TEC1-12,706, and reported that TEC1-12,730 module was having more efficiency relative to others. TEC1-12,730 achieved lower temperature, which was higher relative to TEC1-12,706, and TEC1-12,730 obtained stable condition in less time than TEC1-12,706. A study was conducted on the evaluation of water cooler thermo-electric refrigerator. The inner temperature of the thermo-electric system was reported to be varying for different flow rates. The inner temperature was reported to be inversely proportional, and the coefficient of performance was found to directly proportional to the flow rates. It was concluded that due to the energy consumption factor, the

thermoelectric refrigeration can be used in specific applications effectively [9]. Fadzly et al. [10] worked on determining how the refrigeration and heat pumps utilize the thermoelectric principles. The results have shown that the designed prototype has achieved desired result with optimized energy consumption. Chinguwa et al. [11] designed a portable refrigeration system powered by exhaust heat of vehicle. They have incorporated the principle of thermoelectric effect. In this work, thermal energy was extracted from the waste exhaust heat. This was then directly converted into electrical energy. This electric energy was used to power the refrigeration system and stored for later use. Nohay et al. [12] designed and fabricated a portable solar-powered thermoelectric refrigerator for insulin storage. The designed refrigerator works on the principle of Peltier effect. The device operates with solar energy alone. It was reported that the device maintains lower temperature of 2–8. The average cop attained by the device always about 0.004. To reduce the power consumption and to increase the battery life, the device was designed to cut in at 7.2 and cut off at 2.

30.1.1 Thermoelectric Refrigeration

Thermoelectric refrigeration is a process in which temperature variation is created at the intersection of two dissimilar materials with the help of the Peltier effect [13]. It results in the generation of electric course. It makes one side of the module cool while the other side is heated.

30.1.1.1 Peltier Effect

A physicist, Jean Peltier came to know that an electrical course is able to produce a particular change in temperature at the intersection of the two unlike metals. According to the Peltier effect, if an electric course is passed through the two unlike conductors, then the intersection of the conductors will be able to intake or will be able to give away heat depending on the flow of the electric course that is given before. The heat that has been taken or given out at the intersection is proportional to the electric course that is given as input. At present, the Peltier effect is the most used principle for thermoelectric refrigeration. Peltier coefficient is the proportionality constant at the intersection.

30.1.2 Description and Specification of Components

See Fig. 30.1.

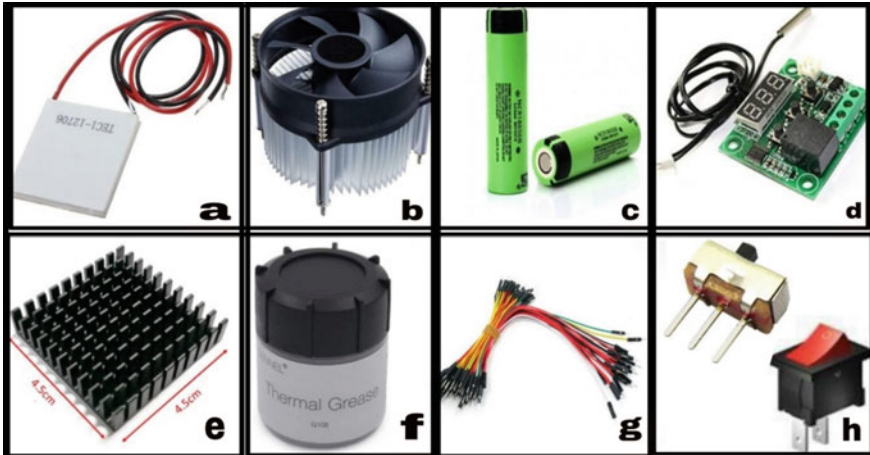


Fig. 30.1 Components used in the work

30.1.2.1. *Peltier Module*: The Peltier module used is TEC 12,706; the module's power is 92 watts with a 12-V power supply. A power supply of 11 V and 2.5 amps current is used here.

30.1.2.2. *Heat Sink Fan Setup*: It consists of one fan setup and a fin mounted on the stand. The fin made up of aluminum is used for a better heat transfer rate.

30.1.2.3. *Battery*: 3.7 V lithium-ion batteries were used. Six batteries were used for the Peltier module and two batteries for the heat sink fan setup [14].

- Battery capacity—3400mah
- Voltage—3.7 V
- Weight—45 gm
- Size—18 mm × 65 mm
- Resistance— ≤ 45 mohm
- Cut off voltage—2.75 V

30.1.2.1. *Internal Heat Sink*: An aluminum heat sink with extended rectangular fins made is used.

30.2 Description of Experimental Setup

A Peltier module is fixed at the bottom of the bottle by cutting operation. A steel plate of 2 mm thickness and 8 mm × 8 mm size is used. A hole is cut at the center of the plate of 4 mm × 4 mm to fix the internal fin by brazing. Holes are made in the plate to fix the heat sink fan setup and Peltier module. This plate is attached to

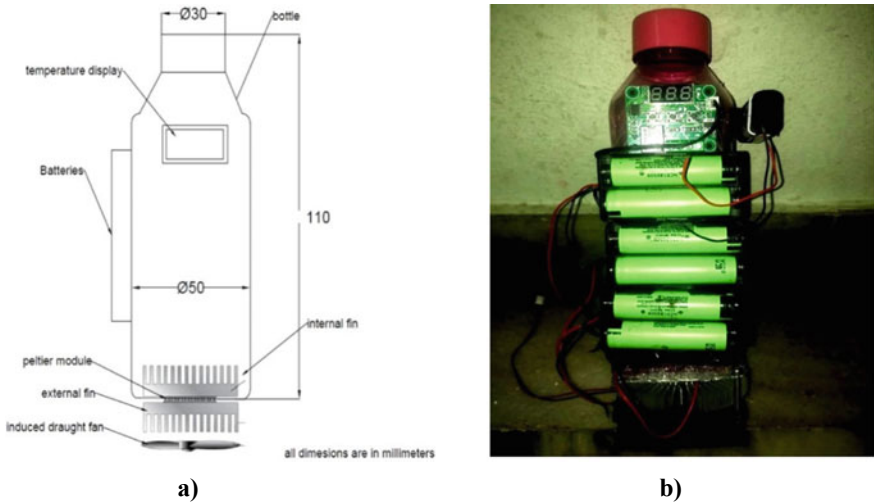


Fig. 30.2 a Schematic diagram of the experimental setup of Refrigeration bottle and b Experimental setup of refrigeration bottle

the base of the bottle using a glue stick. Thermopaste is used to fix the Peltier module to the external fin. The other side of the Peltier module is fixed to the internal fin. Screws are used to fix the assembly rigidly. The batteries are used for the Peltier module’s power is fixed onto the side of the bottle. A thermal display is mounted on the top of the bottle. The thermocouple is provided into the water—the two batteries to power the fan are power provided on the bottle. One switch is used in between the source and the Peltier module. The other switch is connected between the fan setup and display (Fig. 30.2).

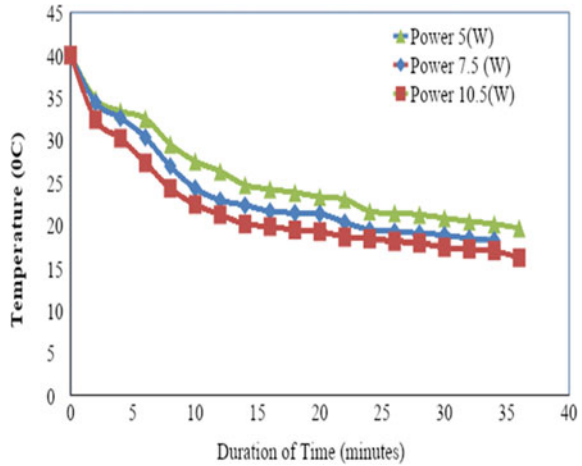
30.3 Results and Discussions

An experiment is conducted bottle for the refrigeration effect by using the Peltier module, and the flowing results are discussed.

30.3.1 Temperature Distribution

Figure 30.3 shows the distribution of temperature with operating time. The experiment is repeated for variable power inputs to the Peltier module. The variation of temperature with respect to time is studied. A sudden decline in the temperature of refrigerator space is observed at the start of the experiment. It is the result of a more significant temperature difference between refrigeration space and the Peltier

Fig. 30.3 Temperature distribution with time



module. As time passed, the decline in temperature is lowered. It is due to that the heat release rate is being slower relatively. When the power is 10 kW (5V, 2.1 amps), the lowest temperature is obtained. The increased power supply results in increased efficiency, up to 12W. However, the device has a limitation that it not exceed the 12 W. Figure 30.4 shows Carnot efficiency with time. It is observed that the trend of the curve is the same as the temperature distribution curve. It is due to that the Carnot efficiency is the function of temperatures only should.

30.3.2 Heat Absorbed from a Refrigerated Space and COP

Figure 30.5 shows that the heat absorption rate with respect to time. It is reported that heat absorption increased with increasing time continuously. As time is passed,

Fig. 30.4 Carnot efficiency with time

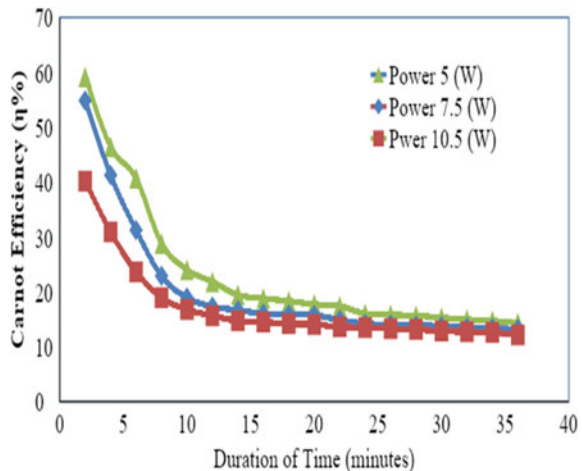


Fig. 30.5 Heat absorption with time

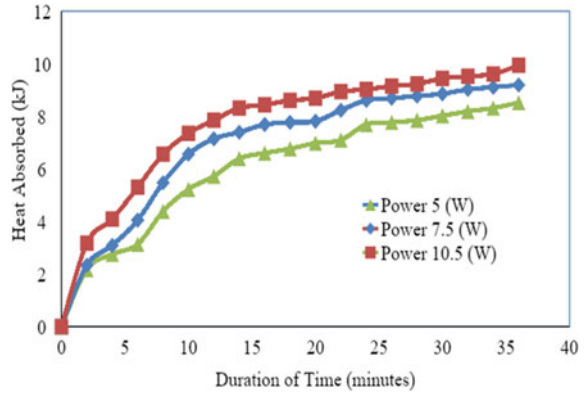
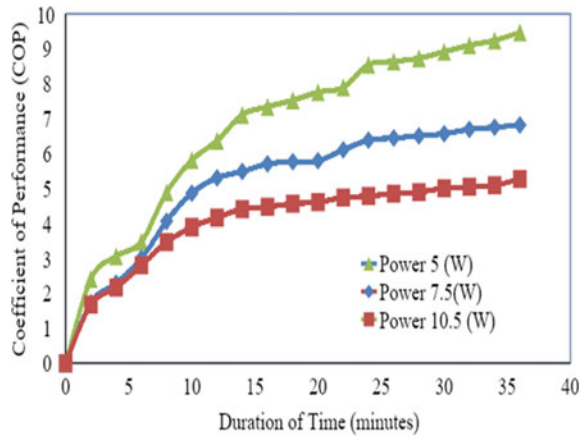


Fig. 30.6 COP with respect to time



the heat absorption rate is decreased due to the temperature differences with respect to time. The heat absorption is maximum when the power supply was 10.5 W.

Figure 30.6 shows the variation of COP of refrigeration with respect to time. It is noticed that COP increased continuously with time. It is also observed that the maximum COP is obtained for a power supply of 5 W. It is also observed that the minimum COP for a power supply of 10.5 W.

30.4 Conclusions

An experiment is conducted with one liter of water in a bottle, which is attached Peltier module. The below outcomes are drawn:

- It is observed that the lower temperature is achieved the power supply of 10.5 W, and the value of temperature is 16.2 °C.
- It is noticed that the COP is maximum for a power supply of 5 W and minimum for 10.5 W.
- It is observed that the heat absorption is maximum for a power supply of 10.5 W to the device.
- It is seen that the COP of refrigeration is minimum for a power supply of 10.5 W.

It is concluded that superior and improved performance is obtained when the device is supplied with 10.5 W power.

References

1. Patil, R.P., Suryawanshi, P., Pawar, A., Pawar, A.: Thermoelectric refrigeration using Peltier Effect. *Int. J. Eng. Sci. Res. Technol.* **6**, 614–618 (2017)
2. Chavan, R.S., Dhawde, M.: Review on performance and analysis of thermoelectric cooling in various applications. *Int. J. Adv. Res. Sci. Eng.* **4**, 1–7 (2015)
3. Rakesh, B.K., Shayan, A., Mithun Sharma, M. N., Mohan, M., Karthik, V.: Study, analysis and fabrication of thermoelectric cooling system. *IJSDR* **1**, 332–338 (2016)
4. Totala, N.B., Desai, V.P., Singh, R.K.N., Gangopadhyay, D., Yaqub, M.S.M., Jane, N.S.: Study and fabrication of thermoelectric air cooling and heating system. *Int. J. Eng. Inventions* **4**, 20–30 (2014)
5. Chang, Y.-W., Cheng, C.-H., Wu, W.-F., Chen, S.-L.: An experimental investigation of thermoelectric air-cooling module. *Int. J. Mech. Mechatron. Eng.* **1**, 1–6 (2007)
6. Maaspuro, M.: Experimenting and simulating thermoelectric cooling of an LED module. *IJOE* **11**, 47–54 (2015)
7. Shah, S., Bhatt, V., Shah, J., Sheladiya, M.K., Kikani, P.: Study of thermal insulating materials and costing of economic thickness of insulation. *Indian J. Appl. Res.* **3**, 77–80 (2013)
8. Lavanya, N., Ravalika, R.E., Dharani, V.: Design and fabrication of a portable refrigerator based on peltier effect. *Int. J. Mech. Eng. Technol.* **9**, 242–247 (2018)
9. Gokcek, M., Sahin, V.: Experimental performance investigation of minichannel water cooler thermoelectric refrigerator. *Case Stud. Thermal Eng.* **10**, 54–62 (2017)
10. Fadzly, M.K., Aqilah, S.N., Farizuan, Amarul, T., Irfan, A.R.: Portable water cooler with water heater using thermoelectric and arduino uno and powered using power bank. In: *IOP Conference Series: Materials Science and Engineering*, p. 864 (2020)
11. Chinguwa, S., Musormusora, C., Mushiri, T.: Design of portable automobile refrigerator powered by exhaust heat using thermoelectric. In: *15th global conference on sustainable manufacturing, procedia manufacturing*, vol. 21, pp. 741–748 (2018)
12. Nohay, J.A.D., De Belen, J.K.H., Claros, J.V.B., Lupo, R.B.P., Barrato, A.B., Dela Cruz, J. C., Amado, T.M., Manuel, M.C.E.: Design and fabrication of a portable solar powered thermoelectric refrigerator for insulin storage. In: *11th IEEE Control and System Graduate Research Colloquium (ICSGRC 2020)* (2020)
13. Yadav, R.K., Basak, R., Pandey, K.M.: Review on heat transfer from fins. *ICMAEM* **225**, 3–4 (2017)
14. Iclodean1, C., Varga, B., Burnete, N., Cimerdean, D., Jurchiş, B.: Comparison of different battery types for electric vehicles. *ICMAEM* **252**, 1–11 (2017)

Chapter 31

Challenges of Introducing Lean Six Sigma, IoT in Industry 4.0, and Supply Chain Management: A Review



Vedant Kale, Chetan Katke, Shailendra Dayane,
and Prashant Thakar

Abstract Since the first Industrial Revolution, the focus has shifted from mechanical production to smart manufacturing. The revolutionary term Industry 4.0 introduced in twenty-first century has still not been adopted worldwide due to various challenges in the manufacturing and production industries. There are concepts like lean and Six Sigma which have been introduced in the industry which helps to reduce waste and remove the unwanted processes. The Internet of things (IoT) with supply chain management (SCM) helps in building relations with suppliers as well as with other industries worldwide. Implementation of concepts like lean, Six Sigma, IoT in SCM, and Industry 4.0 will be helpful to industry to rely on technology rather than human work, production can be fast, and the ongoing processes can be upgraded. This paper gives a brief insight about the challenges and advantages of implementing these concepts in SCM and Industry 4.0.

31.1 Introduction

“Industry 4.0” (I4.0), this word was introduced by the leading industries in Germany in the year 2011. I4.0 aims for automation and globalization of all the manufacturing and production industries with assistance from technologies like Internet of things (IoT) and cyber-physical system (CPS). Smart factory, the other term for I4.0, is the technological amalgamation of CPS into production and logistics. It emphasizes the use of the IoT and related facilities in the enterprises for various processes [1, 2]. The IoT archetype connects all physical attributes in a universal Internet-based structure to share data and for communication. IoT

V. Kale (✉) · C. Katke

School of Mechanical Engineering, Dr. Vishwanath Karad, MIT World Peace University,
Pune 38, India

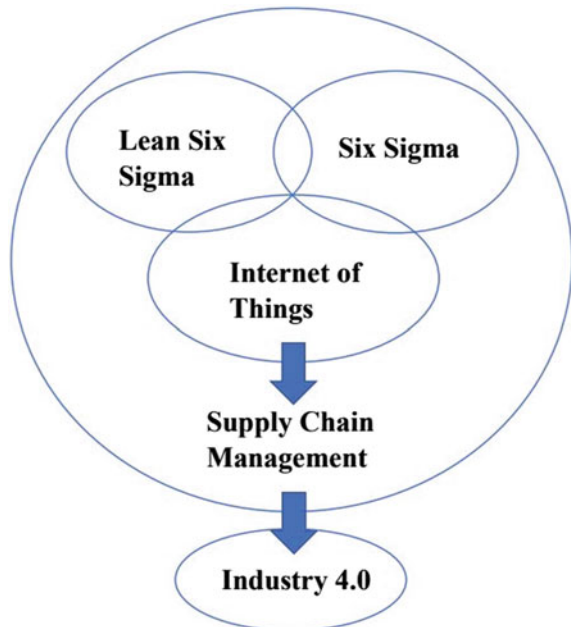
S. Dayane · P. Thakar

Faculty of Mechanical Engineering, Dr. Vishwanath Karad, MIT-World Peace University,
Pune 38, India

provides assistance in the supply chain management (SCM) by introducing intelligent identification, location, real-time tracking, controlling, and management [3]. Real-time data from smart technologies can help in connecting customer's demands and product queries. I4.0 technologies assist in operative and efficient life cycle management of the products. Industrial processes will be more efficient and resourceful due to implementation of Lean Six Sigma (LSS) for better quality control tools, manufacturing efficiency, process novelties, and sustainability [4].

One of the important areas that should be focused in I4.0 is the interdisciplinary collaboration between manufacturing and maintenance planning which can adopt a faster and effective maintenance service; it allows organizations to execute a cost-efficient manufacturing [5]. I4.0 allows to collect and analyze information effortlessly across machines, permitting quicker, flexible, and more effective processes to make efficient goods at decreased inventory. This leads to modification of the face of workforce which will change the competitiveness of enterprises and markets [6]. Various components of I4.0 such as IoT and SCM are interdependent on one another. With the introduction of new reforms such as Lean Sigma, Six Sigma and IoT as shown in Fig. 31.1, will surely help the I4.0 to surge productivity, decrease wastage, change economy and boost industrial development.

Fig. 31.1 Introduction of concepts like LSS, SS, and IoT in SCM and I4.0



31.2 Principles of Six Sigma, Lean Six Sigma, and IoT

31.2.1 Six Sigma (SS)

SS is a well-defined management approach that emphasizes on enhancing the standard of goods by measuring defects and reducing variation in processes and services [7]. Implementing SS leads to enhancement and improvement of various aspects such as profitable business objectives, performance of processes, flow of materials and information and product quality. This also leads to decrease the waste and cycle time and helps to gain reliability in deliveries with reduction in number of defective products [8].

The prime objective of SS is to cut the discrepancies in the goods and processes to gain quality stages of less than 3.4 defects per million opportunities (DPMO). Often, to check the quality of product sigma quality level is used as an indicator (Eq. 31.1). The lesser the value of sigma level (Eq. 31.2), the bigger is the likelihood of defective products and vice versa [9].

$$\text{DPMO} = (\text{Total No. of defects} / \text{Total No. of opportunities}) \times 10^6 \quad (31.1)$$

$$\text{Sigma level} = 0.841 + \sqrt{[29.37 - 2.221 \times \text{Ln}(\text{DPMO})]} \quad (31.2)$$

In order to initiate SS, certain conditions should be satisfied by an organization or industry which are visible management commitment and involvement, strong classification of the client requirements, sharing the considerate fundamentals of commercial processes and their crucial features, encouraging and appreciating the team mates, leadership, developing and improving proficiency of skills and ethics [10]. If these conditions are satisfied and SS is implemented into the industry, many reformations and benefits can be exercised throughout the organization. Hence, with implementation of SS, total quality management can be achieved.

31.2.2 Lean Six Sigma (LSS)

Lean manufacturing was introduced in the 1930s by the Toyota Group. Lean manufacturing is adopted by companies in order to keep a cutting edge over their competitors by improving the manufacturing system's efficiency and quality enrichment of the product [11]. The most significant attribute of the 4th Industrial Revolution is automation, and also lean automation aims to combine the lean production with automation technology [12]. Combining lean manufacturing with Six Sigma has many benefits as shown in Fig. 31.2. The various forms of waste or barriers that are detected in industry are excessive manufacturing, faults, hyped costs, unsuitable processing, unnecessary transport and waiting. This residue can be

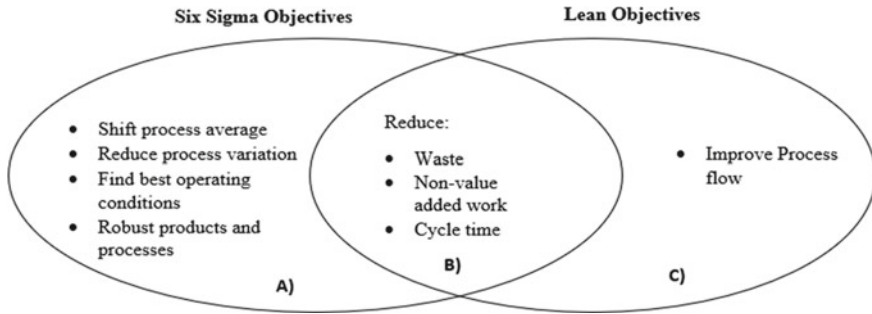


Fig. 31.2 A Objectives of Six Sigma, B objectives of lean, and C integrating Six Sigma and lean objectives [8]

removed by combining the lean with Six Sigma which can also be termed as Lean Six Sigma (LSS) [13]. It calculates the number of “imperfections” present in a process and professionally removes them to achieve customer loyalty and advantage.

Every LSS project follows a practical roadmap called DMAIC, which is the classical and cyclic process of five phases which include define, measure, analyze, improve, and control. Every stage has its own importance such as define—the business problems as well as the targets of the enterprise and the clients are recognized. Measure—It measures or calculates the efficiency of a process with a scope for betterment. Analyze—Primary reasons of faults are identified in detail. Improve—Answers to eliminate the faults are analyzed. Control—For supporting the improvements made in the process, control is applied [14, 15].

31.2.3 *Cyber-physical System (CPS) and Internet of Things (IoT)*

CPS promotes the powerful computation ability, high bandwidth for information exchange, and also the real-time decision making [5]. CPS comprises devices or objects that take local decisions. Sensors supply CPS with the required information. The system technologies like multi-agent system and machine learning confirm the effective execution of CPS in industrial and logistics applications [16]. The information flow of the visual programming models can allow the programmers to selectively create new techniques utilized for the collection of real-time data [17]. A CPS is expected to provide the outputs like condition monitoring (CM) for the previous and present gathered data controller parameters, digitized machine performance (measurement of the product quality), machine and component configuration and model information with the utilization history [18].

IoT is the combination of various communications solutions, detection and real-time tracking technologies, sensor, actuator networks, and divided smart objects [2]. Industry cloud or cloud computing is a significant part of I4.0 and IoT. In order to implement cloud computing, requirements should be supported by rapid on-boarding of customer goods and capability to find out various types of analytical solutions [19]. A novel computing concept, known as fog computing, is evolving to expand cloud capabilities, such as storage, computation, and networking. This highlights the need of fog-based architecture for I4.0 applications to reduce the energy usage of IoT nodes, which are battery inhibited. The fog uses the computational abilities to forecast upcoming information measurements and decrease the loop from IoT devices to the control unit [20]. Moreover by collaborating CPS with manufacturing, logistics and services in today's manufacturing practices will change industries into an I4.0 with major financial capacity [21].

31.3 Supply Chain Management (SCM)

SCM is the unification of the important commercial processes from the end consumer through the main suppliers that delivers goods, services, and information [22] as shown in Fig. 31.3.

SCM comprises of the suppliers, the vendors, the factory, the distribution channels, and primarily the consumers [15]. Logistics is that important part of the supply chain that strategizes, executes, and controls the efficient, effective flow and storing of products, services, and other related information from the source of origin to the source of consumption in terms of meeting customer's necessities [22, 24]. SCM focuses on process management, strategic planning, information and analysis, improving supplier relationships, and speed of product delivery and also aims to improve the quality of service increasing customer satisfaction and reducing non-conformity costs [25, 26]. Competitiveness is enhanced in various ways by lowering costs and higher flexibility with respect to changes in the client needs or by giving an excellent quality of goods and amenities [27, 28]. Supply chain management focuses on the selective companies that function together, trust each other, cooperate harmoniously, and share interests [29].

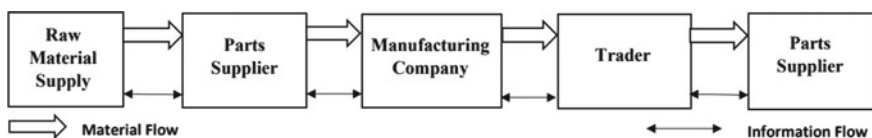


Fig. 31.3 A basic layout of a supply chain [23]

31.4 Challenges in IoT, Six Sigma, and SCM

Even though these principles help in increasing the speed of bringing Industry 4.0 into existence, there are many barriers and challenges at organizational level which should be addressed properly. These challenges are discussed in this section.

31.4.1 Six Sigma

Maximum producers focus on making products that are “good enough,” having an admissible number of flaws and fine acceptable range of quality goods. To improve, they give reason that it will cost additional expenditure and can surpass human capacity [30]. In general, SS is discriminated for its ability toward complications of a different technique and analysis and lean is discriminated for its capable clarity. Systematically executed SS should function well as a solution for a problem that is analyzed and try to figure out better working of process with the available resources.

31.4.2 Lean Six Sigma

Lean concept is not intended for analysis of problems but most probably focuses on waste management [30]. Lean execution is not successful in many organizations due to various barriers. One of them is product constraints, and the other barrier is differences in resources between small-scale and large-scale firms [31].

31.4.3 Challenges in Implementing IoT

There are various problems in evolution of IoT that are both technical and non-technical which are discussed in this section.

31.4.3.1 Security

Encryption has helped making wireless communication to assure data privacy, but still many IoT devices are not strong enough to provide robust encryption as it requires various codes and algorithms. Effective number of keys should be distributed for proper encryption and less time consumption. Identity management is one of the most crucial security factors of IoT devices. Thus, smart objects are what is required to ensure success in implementing IoT [32].

31.4.3.2 Privacy

As greater number of objects can be trackable through IoT, intimidation to the owner privacy has increased. Adding to this, ensuring information security does not fall into the wrong hands, the information owner must be assured that the information cannot be used without his/her permission, especially when the information is shared. Privacy policies can be one of the solutions to ensure the information security [33].

31.4.3.3 Legal/Accountability

As IoT is one of the global resources, therefore it will create new and different types of challenges. These challenges should not be governed by a single group but should be addressed by all important and responsible stakeholders [34]. In this case, global accountability can be helpful as it can help in improving the effectiveness of governance and reduced the threats that may occur.

31.4.4 Supply Chain Management (SCM)

Global SCM is quite difficult to execute due to lack of effective resources and low-cost management system and therefore cannot satisfy the need of customers [35]. One of the most important drawbacks of today's SCM model is lack of information sharing which has led to new phenomenon called "the bullwhip effect." Due to this, organizations have lost lots of opportunities in the market [36].

31.4.4.1 Demand Forecast and Price Variations

Estimation of demand of goods and products is one of the important factors in the SCM. But the upstream enterprises do not get the real demand information, and therefore, it is difficult for them to respond accurately which leads to insufficient production as well as insufficient supply. Variations in price lead to procurement in advance. Manufactures and vendors excite the consumers to buy more in advance due to which manufactures and vendors do not get the idea of present demand which leads to price variations [36].

31.4.4.2 Limited Supply and Short-Term Game

When there is supply shortage of products, suppliers try to supply less following the demand from buyers. But if the condition changes to vice versa, it is not possible for the suppliers to differentiate between the real demand and supply. Therefore,

this concept of limited supply and short-term game is not feasible [36]. The interruptions in SCM can impact the organization for more than one year, resulting in major drops in profits, sales, growth rate of the organization [37].

31.5 Implementation of Six Sigma, Lean Six Sigma, and IoT

31.5.1 *Six Sigma and Lean Six Sigma in Industry 4.0*

The main goal of SS is to improve the process till it produces 3.4 defects per million opportunities. This will help to exaggerate waste and save time as well as money while improving the customer satisfaction. After implementing the SS process, company should compare between SS way and previous way of working of the company [9] (Table 31.1).

Significance of combining lean and SS principles can eliminate waste and can help organizations to upgrade client contentment, raise procedure speed, and also improve the superiority of product and service, while compensating inventory and capital [41].

31.5.2 *Six Sigma and Lean Six Sigma in SCM*

When SS is implemented in SCM, the flaws are identified, and the information of the ongoing processes is assimilated and analyzed. Hence, scope of improvement in the quality of supply chain process is identified which is beneficial for the company [41] (Fig. 31.4).

Table 31.1 Smart variables and their functions

Smart variables	Function
Smart operator	Failure rate is predicted and notified to the machine operator with the help of smart watches [12, 38]
Smart product	Smart products can collect data at different stages of production for analysis and continuous improvement of the enterprise [39, 40]
Smart machine	With smart machines, the setup time required for conventional machine can be reduced significantly [39]
Smart planner	Smart planner focuses on decentralization, which helps in reducing cycle time, optimization, and proper utilization of working stations and maintain a continuous flow of products [12, 39]
Smart logistics	Smart logistics involves CPS for accomplishing the material flow in the factory and in the supply chain [40]

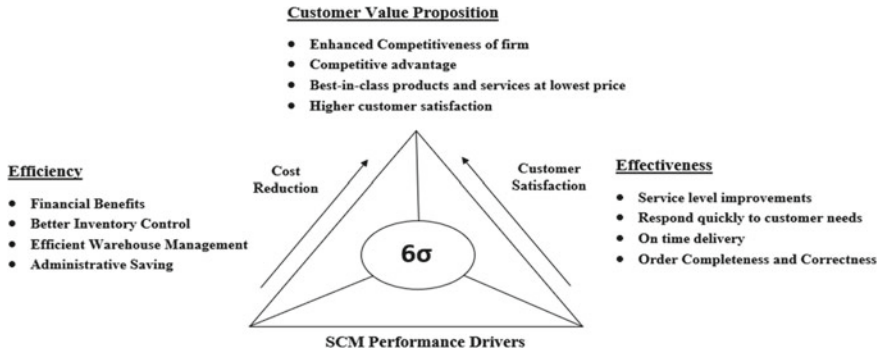


Fig. 31.4 Advantages of implementing Six Sigma and Lean Six Sigma in SCM [7]

Lean production can be beneficial for a company to progress in various aspects such as the supplier feedback, just-in-time (JIT) delivery by suppliers, supplier development, customer involvement, pull production, continuous flow, setup time reduction, total productive or preventive maintenance, statistical process control, and employee involvement [42]. Enterprises performing the combined approach will be benefited by becoming quicker and more responsive to customers, endeavor for SS capability level, and gain improved flexibility throughout the organization [43].

31.5.3 IoT in Industry 4.0

The I4.0 paradigm focuses on increased productivity, hence horizontal and vertical integration with physical interconnection of machines and newer intelligent technologies in the organization [44]. I4.0 involves autonomous production systems with the application of IoT, CPS, and AI [45]. There are various parameters where IoT can show better results in Industry 4.0 such as minimization of various resources like lead time, use of resources, storage costs, and mounting costs and can also maximize the performance and give adherence to delivery dates [16]. Fog computing has become an alternative to the cloud computing and can show better results than the cloud computing in Industry 4.0 with added advantages [20].

31.5.4 IoT in SCM

The objective of SCM is to manufacture and deliver goods through the integration and alliance among supply chain partners quickly and efficiently [46, 47]. With the help of IoT, combined flow and high traceability of materials and goods, enhanced

supplier performance because of real-time data exchange, integration with suppliers, smart warehousing, and vehicle routing systems can be achieved [48]. UHF band should be taken into consideration as it has primary advantages like the ability to permit multiple consecutive reading of tags, increased read rates, and allowing long-distance communication between the reader and tag [49]. Sensors are being implemented in assembly lines and production facilities. RFID is often used to track products through the supply chain controlled by a certain department [32]. It increases supply chain prominence, tracks deliveries in real time, enhances data accuracy, and increases capability of faster situation management. Hybrid RFID sensor network is vital in implementing Who, What, When, and Where (4Ws) data to the IoT for SCM [35]. The versatile applications of RFID technology and IoT to SCM will not only help companies exchange data, but also will help companies get out of the SCM “bullwhip effect” trouble [50].

31.6 Conclusion

Industry 4.0 aims to implement the latest methods and technologies in order to make manufacturing, production, and logistic industries more fast, efficient as well as more customer-centric. The various methodologies such as lean, Six Sigma, and Lean Six Sigma have their own way of working, but all of them focus on the same principles such as reduction of cost, time, wastage, and enhanced productivity. IoT can be the main pillar of Industry 4.0 because it can reduce the dependency on the manual work such as tracking of production status, machine health, and real-time information. In Industry 4.0, SCM plays an important role in the manufacturing industries from the start point to the end point of production. Implementation of IoT in SCM can help tracking packages and products as well as help in maintenance of warehouses. Therefore, introducing technologies and processes such as IoT, Six Sigma, and Lean Six Sigma can help industries to adopt automation and improve the SCM competently. This can help the adoption of Industry 4.0 worldwide.

References

1. Stentoft, J., Aadsbøll Wickstrøm, K., Philipsen, K., Haug, A.: Drivers and barriers for Industry 4.0 readiness and practice: empirical evidence from small and medium-sized manufacturers. *Prod. Plan. Control* **0**(0), pp. 1–18 (2020). <https://doi.org/10.1080/09537287.2020.1768318>
2. Chen, B., Wan, J., Shu, L., Li, P., Mukherjee, M., Yin, B.: Smart factory of industry 4.0: key technologies, application case, and challenges. *IEEE Access* **6**(c), 6505–6519 (2017). <https://doi.org/10.1109/ACCESS.2017.2783682>
3. Karakostas, B.: A DNS architecture for the internet of things: A case study in transport logistics. *Procedia Comput. Sci.*, **19**(Ant), 594–601 (2013). <https://doi.org/10.1016/j.procs.2013.06.079>

4. Kumar, R., Singh, R.K., Dwivedi, Y.K.: Application of industry 4.0 technologies in SMEs for ethical and sustainable operations: Analysis of challenges. *J. Clean. Prod.* **275**, 124063 (2020). <https://doi.org/10.1016/j.jclepro.2020.124063>
5. Silvestri, L., Forcina, A., Introna, V., Santolamazza, A., Cesarotti, V.: Maintenance transformation through Industry 4.0 technologies: A systematic literature review. *Comput. Ind.* **123**, 103335 (2020). <https://doi.org/10.1016/j.compind.2020.103335>
6. Rüßmann Philip Gerbert, M.M.L., Waldner, M., Justus, J., Engel, P., Harnich, M.: Industry 4.0: the future of productivity and growth in manufacturing industries. *Bost. Consult.*, 1–14 (2015) [Online]. Available: https://www.bcg.com/publications/2015/engineered_products_project_business_industry_4_future_productivity_growth_manufacturing_industries
7. Madhani, P.M.: Application of six sigma in supply chain management: evaluation and measurement approach. *IUP J. Supply Chain Manag.* **13**(3), 34–53 (2016) [Online]. Available: <http://ssrn.com/abstract=2851301>
8. Snee, R.D.: Lean Six Sigma—getting better all the time. *Int. J. Lean Six Sigma* **1**(1), 9–29 (2010). <https://doi.org/10.1108/20401461011033130>
9. Yadav, A., Sukhwani, D.V.: Quality improvement by using six sigma in an automotive industry: a case study. *Ind. Eng. J.* **11**(2), 41–46 (2018). <https://doi.org/10.26488/iej.11.2.1044>
10. Jeyaraman, K., Teo, L.K.: A conceptual framework for critical success factors of lean Six Sigma: implementation on the performance of electronic manufacturing service industry. *Int. J. Lean Six Sigma* **1**(3), 191–215 (2010). <https://doi.org/10.1108/20401461011075008>
11. Palange, A., Dhatrak, P.: Lean manufacturing a vital tool to enhance productivity in manufacturing. *Mater. Today Proc.* **46**, 729–736 (2021). <https://doi.org/10.1016/j.matpr.2020.12.193>
12. Kolberg, D., Zühlke, D.: Lean automation enabled by industry 4.0 technologies. *IFAC-PapersOnLine* **28**(3), 1870–1875 (2015). <https://doi.org/10.1016/j.ifacol.2015.06.359>
13. Pepper, M.P.J., Spedding, T.A.: The evolution of lean Six Sigma. *Int. J. Qual. Reliab. Manag.* **27**(2), 138–155 (2010). <https://doi.org/10.1108/02656711011014276>
14. Arcidiacono, G., Pieroni, A.: The revolution Lean Six Sigma 4.0. *Int. J. Adv. Sci. Eng. Inf. Technol.* **8**(1), 141–149 (2018). <https://doi.org/10.18517/ijaseit.8.1.4593>
15. Jayaram, A.: Lean six sigma approach for global supply chain management using industry 4.0 and IIoT. In: *Proceedings of 2016 2nd International Conference Contemporary Computing Informatics, IC3I 2016*, pp. 89–94 (2016). <https://doi.org/10.1109/IC3I.2016.7917940>
16. Böckenkamp, A., Mertens, C., Prasse, C., Stenzel, J., Weichert, F.: A Versatile and Scalable Production Planning and Control System for Small Batch Series, pp. 541–559 (2017). https://doi.org/10.1007/978-3-319-42559-7_22
17. Gokalp, M.O., Kayabay, K., Akyol, M.A., Eren, P.E., Kocyigit, A.: Big data for Industry 4.0: A conceptual framework. In *Proceedings—2016 International Conference on Computer Science and Computational Intelligence CSCI 2016*, pp. 431–434 (2017). <https://doi.org/10.1109/CSCI.2016.0088>
18. Lee, J., Kao, H.A., Yang, S.: Service innovation and smart analytics for Industry 4.0 and big data environment. *Procedia CIRP* **16**, 3–8 (2014). <https://doi.org/10.1016/j.procir.2014.02.001>
19. Kushida, T., Pingali, G.S.: Industry cloud—Effective adoption of cloud computing for industry solutions. *IEEE Int. Conf. Cloud Comput. CLOUD* **1**, 753–760 (2014). <https://doi.org/10.1109/CLOUD.2014.105>
20. Peralta, G., Iglesias-Urkia, M., Barcelo, M., Gomez, R., Moran, A., Bilbao, J.: Fog computing based efficient IoT scheme for the Industry 4.0. In: *Proc. 2017 IEEE International Workshop of Electronics, Control, Measurement, Signals their Application to Mechatronics, ECMSM 2017* (2017). <https://doi.org/10.1109/ECMSM.2017.7945879>
21. Lee, J., Bagheri, B., Kao, H.A.: A cyber-physical systems architecture for industry 4.0-based manufacturing systems. *Manuf. Lett.* **3**, 18–23 (2015). <https://doi.org/10.1016/j.mfglet.2014.12.001>

22. Cooper, M.C., Douglas, J.D.P., Lambert, M.: Supply Chain Management: Implementation Issues and Research Opportunities, vol. 9, no. 2 (1998). <https://www.ingentaconnect.com/content/mcb>
23. Skapinyecz, R., Illés, B., Bányai, A.: Logistic aspects of Industry 4.0. IOP Conference Series: Materials Science and Engineering, vol. 448, no. 1, pp. 0–11, (2018). <https://doi.org/10.1088/1757-899X/448/1/012014>
24. Bechtel, C., Jayaram, J.: Supply Chain Management: A Strategic Perspective, pp. 15–34 (1997). <https://www.ingentaconnect.com/content/mcb;jsessionid=g5mmki32prij.x-ic-live-02>. <https://doi.org/10.1108/09574099710805565>
25. Kuei, C.H., Madu, C.N., Lin, C.: Developing global supply chain quality management systems. *Int. J. Prod. Res.* **49**(15), 4457–4481 (2011). <https://doi.org/10.1080/00207543.2010.501038>
26. Yildirim, M.B., Barut, M., Kilic, K.: A global learning experience in supply chain logistics management. In: Proceedings of Fifth International Conference on Information Technology Based Higher Education Training, ITHET 2004, pp. 263–268 (2004). <https://doi.org/10.1109/ithet.2004.1358175>
27. Stadler, H.: Supply chain management—An overview. *Supply Chain Management and Advanced Planning* (Fourth Ed. Concepts, Model. Software, Case Stud.), pp. 9–36 (2008). https://doi.org/10.1007/978-3-540-74512-9_2
28. Beamon, B.M.: Measuring Supply Chain Performance, vol. 19, no. 3 (1999)
29. Liu, S., Wu, B.: Study on the supply chain management of global companies. In: Proceedings of International Conference on E-bus, E-Government, ICEE 2010, pp. 3297–3301 (2010). <https://doi.org/10.1109/ICEE.2010.829>
30. Bendell, T.: A review and comparison of six sigma and the lean organisations. *TQM Mag.* **18** (3), 255–262 (2006). <https://doi.org/10.1108/09544780610659989>
31. Bamber, L., Dale, B.G.: Lean production: A study of application in a traditional manufacturing environment. *Prod. Plan. Control* **11**(3), 291–298 (2000). <https://doi.org/10.1080/095372800232252>
32. Whitmore, A., Agarwal, A., Da Xu, L.: The Internet of Things—A Survey of Topics and Trends. *Inf. Syst. Front.* **17**(2), 261–274 (2015). <https://doi.org/10.1007/s10796-014-9489-2>
33. Lopez, J., Roman, R., Najera, P.: Securing the internet of things. *Smart Cards, Tokens, Security and Applications*, Second Ed., no. September, pp. 445–468 (2017). https://doi.org/10.1007/978-3-319-50500-8_16
34. Weber, R.H.: Internet of things—Need for a new legal environment? *Comput. Law Secur. Rev.* **25**(6), 522–527 (2009). <https://doi.org/10.1016/j.clsr.2009.09.002>
35. Xu, R., Yang, L., Yang, S.H.: Architecture design of internet of things in logistics management for emergency response. In: Proceedings of 2013 IEEE International Conference on Green Computing Communications and IEEE Internet Things IEEE Cyber, Physical and Social Computing GreenCom-iThings-CPSCOM 2013, pp. 395–402 (2013). <https://doi.org/10.1109/GreenCom-iThings-CPSCOM.2013.85>
36. Bo, Y., Guangwen, H.: Supply chain information transmission based on RFID and internet of things. In: 2009 Second ISECS International Colloquium on Computing, Communication, Control, and Management, CCCM 2009, vol. 4, pp. 166–169 (2009). <https://doi.org/10.1109/CCCM.2009.5267755>
37. Hendricks, K.B., Singhal, V.R.: The Effect of Supply Chain Disruptions on Shareholder Value, vol. 19, no. 7–8 (2008)
38. Shrouf, F., Ordieres, J., Miragliotta, G.: Smart factories in Industry 4.0: A review of the concept and of energy management approached in production based on the Internet of Things paradigm. In: IEEE International Conference on Industrial Engineering and Engineering Management, vol. 2015-Janua, pp. 697–701 (2014). <https://doi.org/10.1109/IEEM.2014.7058728>
39. Roblek, V., Meško, M., Krapež, A.: A Complex View of Industry 4.0. *SAGE Open*, vol. 6, no. 2 (2016). <https://doi.org/10.1177/2158244016653987>

40. Stock, T., Seliger, G.: Opportunities of Sustainable Manufacturing in Industry 4.0. *Procedia CIRP* **40**(Icc), 536–541 (2016). <https://doi.org/10.1016/j.procir.2016.01.129>
41. Christopher, M., Rutherford, C.: Supply Chain Six Sigma. *CriticalEYE*, no. August, pp. 24–28 (2004) [Online]. Available: www.criticaleye.net
42. Sanders, A., Elangeswaran, C., Wulfsberg, J.: Industry 4.0 implies lean manufacturing: Research activities in industry 4.0 function as enablers for lean manufacturing. *J. Ind. Eng. Manag.* **9**(3), 811–833 (2016). <https://doi.org/10.3926/jiem.1940>
43. Antony, J., Banuelas, R.: Key ingredients for the effective implementation of Six Sigma program. *Meas. Bus. Excell.* **6**(4), 20–27 (2002). <https://doi.org/10.1108/13683040210451679>
44. Hofmann, E., Rüsçh, M.: Industry 4.0 and the current status as well as future prospects on logistics. *Comput. Ind.* **89**, 23–34 (2017). <https://doi.org/10.1016/j.compind.2017.04.002>
45. Pacaux-Lemoine, M.-P., Trentesaux, D.: Cognitive Work Analysis vs. Human-Machine Cooperation in HUMANISM project. *Hum. Ind. 4.0* (2019)
46. Ping, L., Liu, Q., Zhou, Z., Wang, H.: Agile supply chain management over the Internet of Things. In: *International Conference of Management Service Science MASS 2011* (2011). <https://doi.org/10.1109/ICMSS.2011.05998314>
47. Wang, S., Wan, J., Li, D., Zhang, C.: Implementing Smart Factory of Industrie 4.0: An Outlook. *Int. J. Distrib. Sens. Netw.* **2016** (2016). <https://doi.org/10.1155/2016/3159805>
48. Ghadge, A., Er Kara, M., Moradlou, H., Goswami, M.: The impact of Industry 4.0 implementation on supply chains. *J. Manuf. Technol. Manag.* **31**(4), 669–686 (2020). <https://doi.org/10.1108/JMTM-10-2019-0368>
49. Stefanizzi, M.L., De Blasi, M., Mighali, V., Patrono, L.: Performance Evaluation of UHF RFID Tags in the Pharmaceutical Supply Chain M. In: *Internet of Things 20th Tyrrhenian Workshop on Digital Communications*, pp. 283–291 (2010). <https://doi.org/10.1007/978-1-4419-1674-7>
50. Susana Duarte, B., Cruz-machado, V.: *Proceedings of the Eleventh International Conference on Management Science and Engineering Management* (2018). <https://doi.org/10.1007/978-3-319-59280-0>

Chapter 32

Development of Novel Concrete for Recharging the Ground Water Levels in the Rocklands of Urban Areas



Venu Malagavelli, A. Jagadish Babu, S. Siva Rama Krishna, and V. Suryaprakash Reddy

Abstract Pervious concrete is a material developed from ancient history but was not in use because of strength issues. Pervious concrete is also determined as gap graded concrete, permeable concrete and no fines concrete. It is a type of concrete with greater porosity and is used for concrete flat work applications. This type of concrete allows the water to percolate in to the ground by reducing the storm water runoff and also recharges the ground water levels. Pervious concrete has found to be an authentic tool for storm water management. It is a compound made by blending concrete which is a coupling material with cement, coarse aggregates and water in required extents. Pervious concrete is generally low in strength but high in permeability. To increase compressive strength, several fibres are added.

32.1 Introduction

Pervious concrete is a creative approach as it is mostly used for controlling the storm water drainage and storm water runoff. When this pervious concrete used for pavement applications, this concrete can percolate the storm water and runoff into the ground. So, this concrete will help the recharge the ground water table, and it will improve the groundwater levels. Pervious concrete is made with coarse aggregate and binding material like cement. Fine aggregate can also be used, but very little amounts. The main aim of this concrete is to improve the ground water levels; i.e., the permeability of this concrete should be very good, then only we will be able to say this concrete is pervious concrete. The aim of this paper is to improve the strength characteristics and permeability of pervious concrete. Weichung et al. [1] conducted the experiments on pervious concrete made with electric arc furnace slag aggregates. They found that the pervious concrete with slag aggregate is the good strength properties and better permeability than the normal pervious concrete. Gesoglu et al. [2] investigated properties of the pervious concrete

V. Malagavelli (✉) · A. Jagadish Babu · S. Siva Rama Krishna · V. Suryaprakash Reddy
Department of Civil Engineering, Institute of Aeronautical Engineering, Dundigal,
Hyderabad, Telangana 500043, India

made using waste tire rubber. They partially replaced the aggregates with rubber to form a rubberized plain pervious concrete. They found that the rubberized pervious concrete improves the mechanical and permeability properties compared to normal concrete. Ravindrarajah and Yukari [3] kept their efforts in studying the porous concrete to make the construction sustain for longer period. They came to know the porosity, unit weight, weight loss on drying, shrinkage and compressive strength of the porous concrete. They tested three concrete mixers by replacing 0%, 20% and 50% of fly ash by cement and noticed the respective properties. By the end of the tests, they identified that porous concrete enables a porosity range of 12–30% and also found that there is no significant effect on water permeability by the addition of 50% fly ash. Patil et al. [4] studied the performance of pavement using pervious concrete as the land area was covering with cement material day by day, and they came to know that temperature and humidity was increasing and could not be adjustable. So, then the utilization of porous concrete in the construction of pavements began to improve the above factors. Porous concrete pavements have been using by many developed countries for 30 years. Hung et al. [5] worked on the difference between porosity and permeability of porous concrete by different aggregate sizes. They found that the porosity and permeability have been decreased as the fine aggregate content is increased. The permeability of porous concrete can be found by using falling head method and constant head method. Some of the researches [6] shows that the permeability is less if falling head method is used for the experiments compared to constant head method. Even though the above said two methods are used to know the permeability of pervious concrete. A new method had developed by Lin et al. [7] to know the permeability of pervious concrete including clogging in the concrete. The results of coefficient of permeability are quite impressive. The aggregate size and binding materials of pervious concrete are also playing very important role on permeability of this type of concrete [8]. As the amount of binder material and aggregate increases, the coefficient of permeability is decreasing as other strength properties are increasing. Researchers are developed the relations for compressive responses and understand the structure of materials in porous concrete [9]. Gersson et al. [10] conducted to experiments on clogging effect in pervious concrete with recycled aggregates. The results show the maintenance of pervious concrete at every five years would improve the performance. The behavior of pervious concrete with recycled asphalt aggregate studied by Susana et al. [11]. They found the modified pervious concrete can be used where the strength is not the criterion. Aggregate size also places very important role in the previous concrete [12]. If large size of the aggregate is used for making pervious concrete, then the permeability is also very good and vice versa.

In the present investigation, three types of concretes, i.e., M30, M40 and M50 considered to know the coefficient of permeability of these concrete, so that it can used as the load bearing material. For improving the tensile properties, polyethylene terephthalate fibres are introduced in the concrete.

32.2 Materials and Mix Proportions

Cement: Ordinary Portland cement of grade 43 is used.

Aggregate: The size of coarse aggregates used is less than 20 mm in size. Fine aggregates can be either natural or manufactured. The size of fine aggregates used are 90 microns.

Plastic fibres: Polyethylene terephthalate—PET is used (Fig. 32.1).

Compressive strength: The compressive strength of concrete (Fig. 32.3) is determined by subjecting gradual compressive load on the concrete surface. The concrete cube is of size 15 × 15 cm (Fig. 32.2) 3 samples of different grades of concrete. In this test, when load is applied if the specimen shows more cracks and deflections, the strength is lower. Whereas if there are a smaller number of cracks and deflection, then the strength of concrete specimen is increased. The concrete specimen gains strength gradually from the day of curing itself. We cannot determine at which period the concrete gains 100% strength because after 7 days the concrete attains 60–65% strength, and even after 28 days, the concrete specimen attains only 98% compressive strength; even after 28 days, the concrete specimen attains strength but at a slower rate.

Table 32.1 denotes the strength of concrete attains at the respective days.

Permeability test on concrete: Permeability of concrete (Fig. 32.4) structure shows the resistance of the concrete structure under hydrostatic pressure. The amount of water that seeps through the concrete structure in to the ground is known

Fig. 32.1 Polyethylene terephthalate (PET)



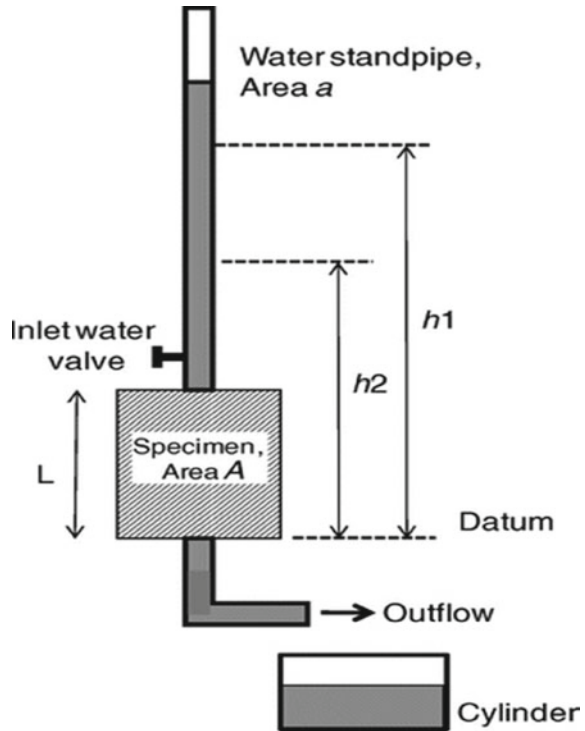
Fig. 32.2 Concrete specimen**Fig. 32.3** Compressive strength testing machine

as the permeability of the concrete. The pervious concrete permeability is determined by two methods, falling head method and variable head method. We use variable head method for our project as it is more suitable for pervious concrete.

Table 32.1 Attainment of concrete strength

Age of concrete in days	Strength of concrete (%)
1	15
3	35–40
7	65
14	90
28	98

Fig. 32.4 Permeability by variable head test



The above Table 32.2 shows the quantities of materials that are taken for grade of concrete for 7 and 28 days without using fibres. These quantities are for one concrete cube specimen. Water-cement ratio is reduced as the concrete grade is higher. For this porous concrete, fine aggregate is used are very minimal when compared to coarse aggregate.

The above Table 32.3 shows the quantities of materials that are taken for all grades of concrete for 7- and 28-days using fibres. For all three grades of concrete, the percentage of fibres is kept constant as 2%. The main idea behind this is to use the plastic waste into the concrete.

Figures 32.5 and 32.6 represent the compressive strength development from 7 to 28 days of M30, M40 and M50 concrete. It is over served that the strength of

Table 32.2 Mix proportions of grades of concrete for one specimen (15 × 15 × 15 cms) without using fibres

Materials used	M30	M40	M50
Cement	2.25 kg	2.45 kg	2.65 kg
Fine aggregate	0.25 kg	0.25 kg	0.25 kg
Coarse aggregate	7.05 kg	7.25 kg	7.35 kg
Water-cement ratio (%)	0.45 (1100 ml)	0.4 (900 ml)	0.3 (687 ml)

Table 32.3 Mix proportions of grades of concrete for one specimen (15 × 15 × 15 cms) with fibres

Materials used	M30	M40	M50
Cement	2.25 kg	2.45 kg	2.65 kg
Fine aggregate	0.25 kg	0.25 kg	0.25 kg
Coarse aggregate	7.05 kg	7.312 kg	7.25 kg
Water-cement ratio (%)	0.45	0.4	0.3
PET fibres	2%	2%	2%

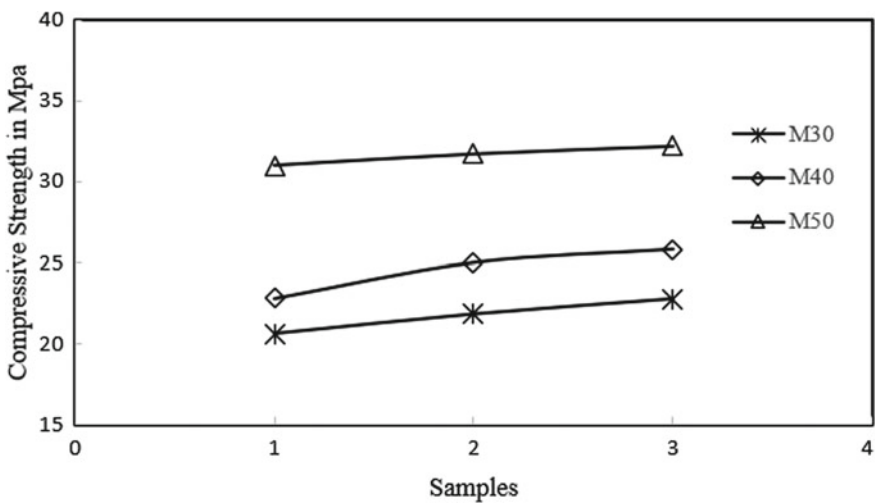


Fig. 32.5 Compressive strength (MPa) of concrete at the age of 7 days

concrete is more than the characteristic compressive strength of concrete. The percentage increase in the strengths of three samples are 7.23, 11.27 and 16.57 for M30 concrete, 13.3, 17.4 and 19.6 for M40 concrete and 2.6, 4.48 and 7.6 for M50 concrete.

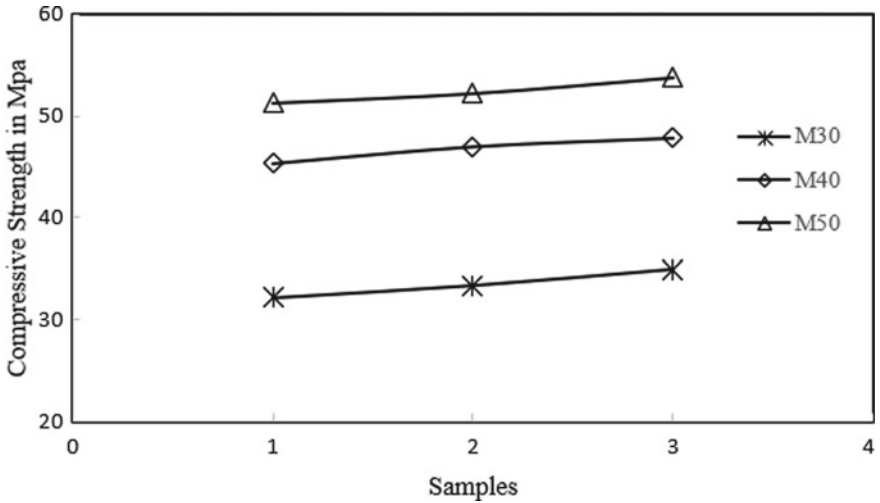


Fig. 32.6 Compressive strength (MPa) of concrete at the age of 28 days

The fibres are kept constant in the concrete for all three grades. Figure 32.7 represents the compressive strength of pervious concrete with fibres for both 7 and 28 days. From the figure, it is evident that the fibres can contribute the strength improvement in concrete. The percentage increase in the strengths is 5.15, 1.1 and 0.85 at the age 7 days, 5.16, 4.73 and 3.94 at the age 28 days for M30, M40 and M50 concretes, respectively.

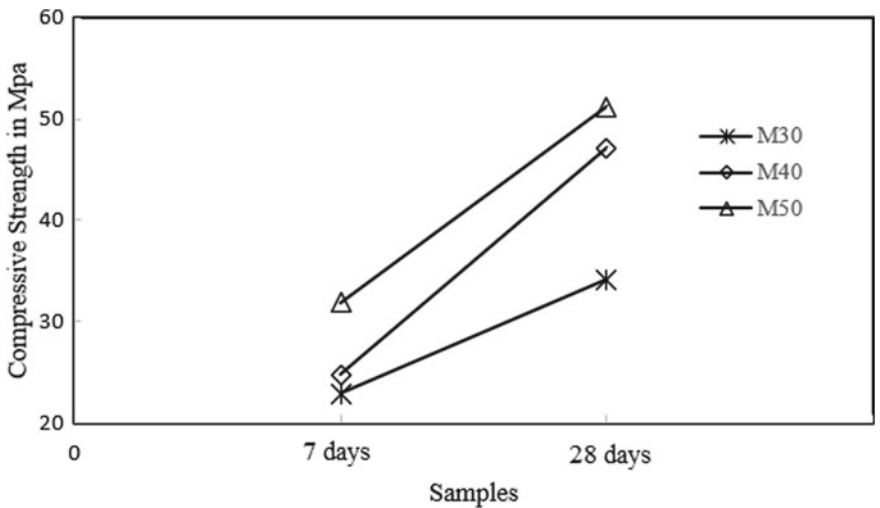


Fig. 32.7 Compressive strength (MPa) of concrete at the age of 7 and 28 days with fibres

This pervious concrete mainly used to recharge the ground water, so that the ground water table can be improved. This type of concrete can be used in the parking lots, foot paths, etc., where strength is the criterion. So, the coefficient permeability (k) of this concrete can be found by using falling head method.

$$k = \frac{2.303AH}{a(T_2 - T_1)} \left(\log \frac{L_1}{L_2} \right) \quad (32.1)$$

where

- A Cross-sectional area of sample.
- A Area of stand pipe = 0.95cm^2 .
- H Pervious concrete sample height.
- $(T_2 - T_1)$ Difference in time for water to fall from one level to another level.
- L_1 upper water level.
- L_2 lower water level.

Table 32.4 shows the rate of flow of water through the specimen for M30, M40 and M50 grade of concrete with and without using fibres. Permeability of concrete has been decreased as the fibres are used in the concrete. The percentage reduction in the permeability if fibres are used in the concrete are 31.37, 40.78 and 34.69 for the grades of M30, M40 and M50, respectively. This may due to the voids occupied by the fibres as well as the more cement and coarse aggregate content used as the grade of concrete is increases.

32.3 Conclusions

The key factor for porous concrete is the balance between permeability and strength of the concrete. The strength of pervious concrete is created by the bonding between the cementitious paste and aggregates. The size of aggregates, water to cement ratio and aggregate to cement ratio plays a vital role in strength of concrete. Among the two types of compressive strength of pervious concrete, the addition of fibres has given more value when compared to normal pervious concrete. The addition of fibres or fines with replacement to cementitious materials will reduce the permeability capacity of pervious concrete to drain water. Even though the

Table 32.4 Permeability of pervious concrete without fibres

Mix	Coefficient of permeability, k (cm/sec)	
	Without fibres	With fibres
M30	1.02	0.70
M40	0.76	0.45
M50	0.49	0.32

compressive strength is low for a pervious concrete, we can use it for several applications where load is not the main factor like footpaths, swimming pool decks, driveways, parks, etc., as permeability of pervious concrete is more.

References

1. Weichung, Y., Fu, T.C., Chang, J.J., Huang, R.: Properties of pervious concrete made with air-cooling electric arc furnace slag as aggregates. *Constr. Build. Mat.* **93**, 737–745 (2015)
2. Gesoğlu, M., Güneyisi, E., Khoshnaw, G., İpek, S.: Investigating properties of pervious concretes containing waste tire rubbers. *Constr. Build. Mat.* **63**, 206–213 (2014)
3. Ravindrarajah, R.S., Yukari, A.: Environmentally friendly pervious concrete for sustainable construction. In: 35th “CORAL” Conference on OUR WORLD IN CONCRETE & STRUCTURES, pp. 1–7, Singapore (2010)
4. Patil, V.R., Gupta, A.K., Desai, D.B.: Use of pervious concrete in construction of pavement for improving their performance. *IOSR J. Mech. Civ. Engg.* **4**, 54–560 (2010)
5. Hung, V.V., Seo, S.Y., Kim, H.W., Lee, G.C.: Permeability and strength of pervious concrete according to aggregate size and blocking material. *Sustainability* **13**(426), 1–13 (2021)
6. Qin, Y., Yang, H., Deng, Z., He, J.: Water permeability of pervious concrete is dependent on the applied pressure and testing methods. *Adv. Mat. Sci. Eng.* **2015**, 1–6 (2015)
7. Lin, W., Park, D.G., Ryu, S.W., Lee, B.T., Cho, Y.H.: Development of permeability test method for porous concrete block pavement materials considering clogging. *Constr. Build. Mat.* **118**, 20–26 (2016)
8. Fu, T.C., Yeih, W., Chang, J.J., Huang, R.: The influence of aggregate size and binder material on the properties of pervious concrete. *Adv. Mat. Sci. Eng.* **2014**, 1–17 (2014)
9. Deo, O., Neithalath, N.: Compressive behavior of pervious concretes and a quantification of the influence of random pore structure features. *Mat. Sci. Eng. A* **528**, 402–412 (2010)
10. Sandoval, G.F.B., Galobardes, I., De Moura, A.C., Toralles, B.M.: Hydraulic behavior variation of pervious concrete due to clogging. *C. Stud. Constr. Mat.* **13**, 1–11 (2020)
11. Bittencourt, S.V., da Silva Magalhães, M., da Nóbrega Tavares, M.E.: Mechanical behavior and water infiltration of pervious concrete incorporating recycled asphalt pavement aggregate. *C. Stud. Constr. Mat.* **14**, 1–10 (2021)
12. Yu, F., Sun, D., Wang, J., Hu, M.: Influence of aggregate size on compressive strength of pervious concrete. *Constr. Build. Mat.* **209**, 463–475 (2019)

Chapter 33

Vision-Based Real-Time Hand Wash Accuracy Prediction



C. Kavinkumar, S. Tony Geefus, and Prashant R. Nair

Abstract Hands are the primary means of germ transmission, which results in the transmission of deadly diseases. Hand hygiene is thus an important measure to prevent the spread of harmful diseases. The World Health Organization (WHO) has recommended seven steps for proper handwashing hygiene. However, not everyone adheres to the WHO's handwashing guidelines of seven steps. A proper hand wash is an important factor in protecting people's health during the corona virus disease (COVID-19) pandemic, especially for healthcare workers who are exposed to bacteria, influenza, and other infectious diseases. There are technologies available like ultraviolet (UV) images to check a person's hand hygiene. However, there is no real-time system to monitor how efficiently a person makes his or her hand wash. A real-time monitoring system is needed to check people's hand wash hygiene in public places and hospitals, reducing the risk of spreading communicable diseases. In this paper, we have discussed predicting the accuracy of handwashing actions performed by humans using a deep learning model with transfer learning (VGG16).

33.1 Introduction

Hand hygiene is one of the most effective actions we can take to reduce the spread of pathogens and prevent infections, including the COVID-19 virus. People are concerned about hand hygiene only when there is a spread of harmful disease like COVID-19. Washing our hands is one of the most effective ways to prevent the spread of germs. Clean hands can prevent germs from spreading from person to

C. Kavinkumar (✉) · S. Tony Geefus · P. R. Nair
Department of Computer Science and Engineering, Amrita School of Engineering,
Amrita Vishwa Vidyapeetham, Coimbatore, India
e-mail: cb.en.u4cse17428@cb.amrita.students.edu

S. Tony Geefus
e-mail: cb.en.u4cse17464@cb.amrita.students.edu

P. R. Nair
e-mail: prashant@amrita.edu

person and across an entire community, from your home and workplace to childcare facilities and hospitals.

A study by the CDC has estimated that if everyone routinely washed their hands, a million deaths in a year could be prevented [1]. According to a Portable Sinks company survey, only about 5% of people wash their hands correctly. The WHO has prescribed seven steps for good hand wash hygiene. However, not all people follow the seven steps of handwashing according to WHO's regulations. A real-time monitoring system is needed to check people's hand wash hygiene in public places and hospitals, reducing the risk of spreading communicable diseases. Current hand hygiene performance is evaluated through human sight, which is less effective. Later a research paper has proposed a new auditing algorithm for hand hygiene evaluation by applying image processing on the blue (B) component of an image which is greatly influenced by the effect of ultraviolet (UV) light [2]. Our work aims to propose a new hand wash evaluation system by evaluating the steps done in a hand wash by comparing it with the WHO prescribed steps using deep learning models. This step reduces the error caused by the traditional method, and it will also reduce the cost of the hand wash monitoring system by leaving the UV rays machine cost in the later algorithm.

Machine learning and deep learning techniques are used to provide advanced solutions to various problems. They have been applied to education [3], smart buildings [4], waste management [5], healthcare [6], and biometrics [7]. We have used a deep learning approach by using a pre-trained neural network model VGG16 with ImageNet weights and transfer learning techniques to train the model. By tracking each step using our model (deep learning model) and the time taken in each step, we have predicted the efficiency of a hand wash.

33.2 Related Work

33.2.1 Feature Extraction Using VGG16

Features are properties of the whole image. Therefore, feature extraction is an important step in performing computational operations on images relevant to specific applications [8]. Features and classifiers are important in performing high-level image classification [9]. Traditional feature-based image processing algorithms have some drawbacks because they are greatly influenced by noise [10] (Fig. 33.1).

Feature extraction in traditional Convolutional Neural Network (CNN) models gives lower performance than CNN architectures like Visual Geometry Group 16 (VGG16), ResNet, and AlexNet which are trained on large datasets. By using transfer learning, we can extract important features by using these architectures [12]. Most of the object/action detection datasets like ImageNet, COCO, etc., are highly broad in nature. So, we cannot use only that architecture to predict narrow datasets, so on top of this architecture, we can include some CNN layers which detect appropriate features from a narrow dataset like the hand wash dataset

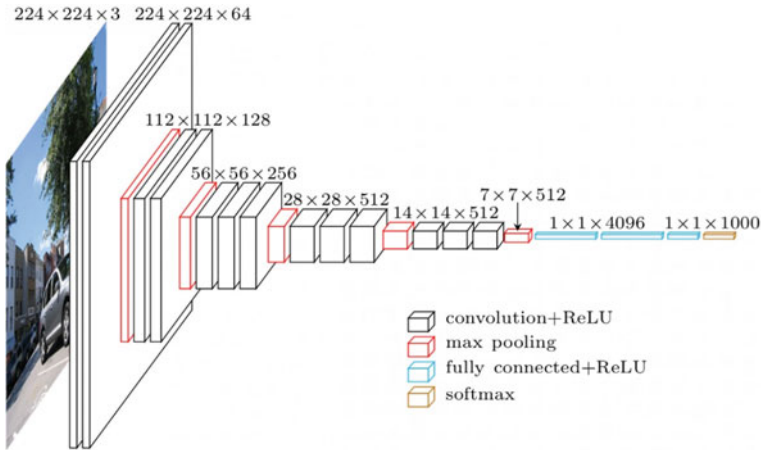


Fig. 33.1 VGG16 architecture [11]

effectively. We use this architecture to extract important features since in most cases, it outperforms ResNet and Visual Geometry Group (VGG) by a handsome degree [13]. VGG16 is built by VGG and trained on a huge dataset using the Nvidia Graphical User Interface (GPU) for weeks [14]. VGG16 architecture is an ultra-fine CNN architecture with excellent performance in image classification. The input of VGG16 architecture is a fixed-size 224×224 image.

33.2.2 Methodology

The process of building a real-time hand wash accuracy prediction system using deep learning has the following stages.

Challenges with training neural networks on massive video datasets.

The development of a network architecture allows for the classification of video clips solely with Red Green Blue (RGB) input image frames.

Creating a Flask Application Programming Interface (API) with appropriate parameters to classify the image frames.

Lastly, the steps necessary to make the neural network run in real-time on applications by integrating with Flask and deploying it (Fig. 33.2).

The implementation is performed in two stages, namely the training and testing phase.

33.2.3 Data Set

We have used the “hand wash dataset” from Kaggle. The dataset contains the video clips of the WHO prescribed seven-step hand wash procedure. Five of the seven

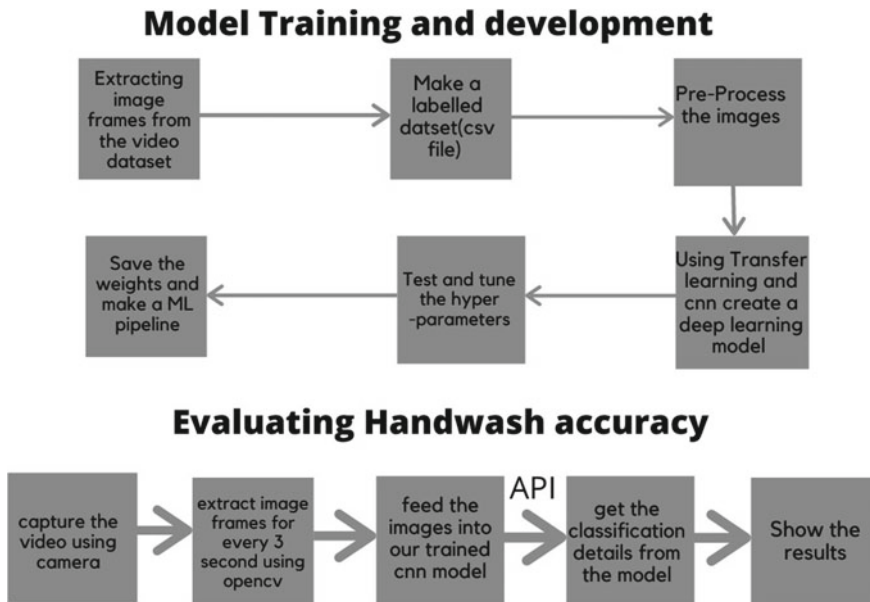


Fig. 33.2 Model flow diagram

steps are further divided into two steps (left and right hands) Thus, 12 steps are present in the dataset. The hand wash dataset consists of 292 individual videos of hand washes (with each hand wash having 12 steps, for a total of 3504 clips), in different environments to provide as much variance as possible (Fig. 33.3).

33.2.4 Training Phase

Extracting frames from the video dataset

The dataset contains each of the seven steps of the proper hand wash procedure in separate folders. In the model training phase, the frames are first extracted from the video dataset at the rate of 5 frames per second using OpenCV. An object detection algorithm like Fast Recurrent Neural Network (F-RNN) or You Look Only Once (YOLO) is used to detect the hand (object) in the video dataset. Once the hand is detected, the frame extraction process starts. The frames are generated at a rate of 10 frames per second. YOLO performs better than other object detection algorithms and can process up to 45 frames per second [15]. It uses the bounding boxes technique to detect objects. The input dimensions for YOLO are $608 \times 608 \times 3$. Then images are passed to a CNN, whose output is in the dimension $19 \times 19 \times 5 \times 8$. The last two dimensions are flattened to get output in $19 \times 19 \times 425$ dimensions. Finally, intersection over union and non-max suppression techniques are applied.

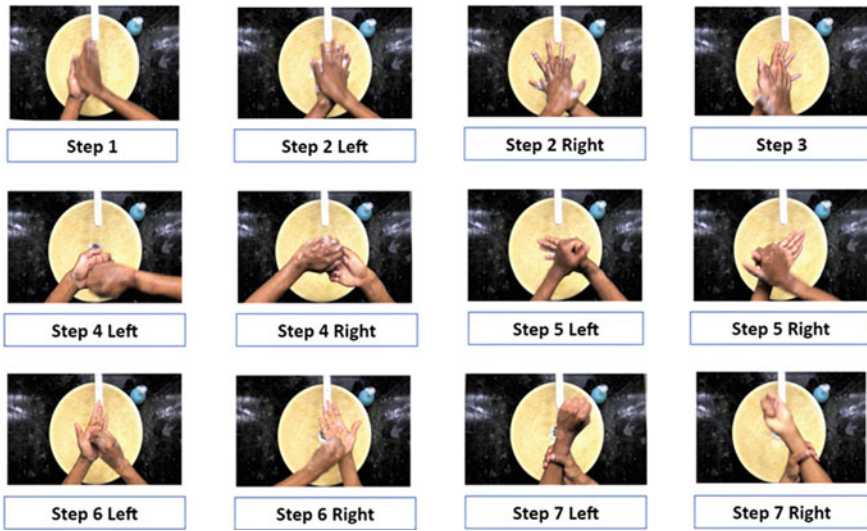


Fig. 33.3 Hand wash steps as per WHO guidelines

Labeling the image frames

After the frames were extracted from the training data's video files in the training phase, those frames are stored in a folder. During frame extraction, the number of frames obtained for each handwashing step is monitored and is used to label the image frames. A Comma Separated File (CSV) is used to store the image frame's name, and it is the corresponding hand wash step (label).

Splitting into training and testing data

After the frames were labeled, they are split into training and validation data. In our dataset, the number of frames for each step is different. Splitting the frames randomly in a specific ratio will result in poor training of the neural network model. So, the frames in each step are split in the ratio of 75:25 and grouped into training and validation data.

Preprocessing

The image frames in the training and validation data are then resized into 224×224 , which is the required input size for the first layer of the VGG16 model. The resized images are then converted into a NumPy array. Then `preprocess_input()` which is an inbuilt application of VGG16 is used to normalize the data. It accepts a NumPy array as input and gives the normalized values as output. The mean RGB channels are subtracted from the image data and normalized in the range $[-1, 1]$. The preprocessed image frames are then split into training and validation data.

Model training

A neural network sequential model is built using the Keras framework. Here, the VGG16 model is used, a pre-trained very deep convolutional neural network model containing 16 convolutional layers that help large-scale image classification. The VGG16 model uses the weights of ImageNet. The data stored in TrainX is given as input to the vgg16 model, and the model returns the top 1000 features in the image in the form of a single-dimensional array. This process of feature extraction helps to train the model based on the features of the image. The output from the VGG16 model is then passed as an input to a small neural network model capable of performing multi-class classification. Dense layers are added to the model with rectified linear units (ReLU) as the activation function for hidden layers and softmax for the output layer, which is used to classify images into multiple classes.

33.2.5 Testing Phase

Capturing the data

The high-resolution camera is placed in the handwashing area. The camera is placed approximately 6 feet above the surface level and at an angle, so that the handwashing video captured appears to be captured from the person's point of view. Sensors are used to detect humans, and the camera starts to capture video only if a person's hand is detected. There are technologies available such as light pulses, thermal measurements, and radio waves. Here, we use the concept of heat vision and detect human beings by using passive infrared (PIR) sensors. If there is a movement of human beings (warm objects) or a difference between an object and background temperatures, the sensor signals the camera to start recording.

Usage of YOLO results in optimal use of available resources. YOLO algorithm is used to detect hand objects in the video in real-time. If the hands are detected in the video, then frame extraction is performed at 10 frames per second using OpenCV (Fig. 33.4).

Preprocessing and prediction

The image frames are preprocessed and resized to 224×224 . These frames are normalized and fed into the VGG16 model for feature extraction. The output obtained is then resized to $7 \times 7 \times 512$, and then, the images are made zero centered by dividing each of the image frames by the maximum of testing data. The label encoder is used to convert categorical values to a series of integers representing multiple classes. The image frames are then subjected to our trained model for classification. The prediction results are used to calculate the screen time of each step involved in the handwashing action.

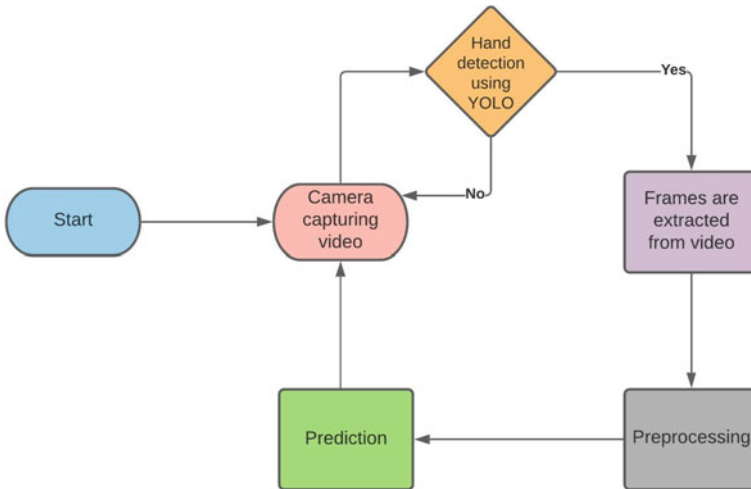


Fig. 33.4 Model with object detection

Model evaluation

The metrics used for evaluating our model are confusion matrix, f1-score, and classification report.

$$\text{Accuracy} = \frac{tp+fn}{tp+fp+tn+fn}$$

$$\text{Precision} = \frac{tp}{tp+fp}$$

$$\text{Recall} = \frac{tp}{tp+fn}$$

$$f1 = 2 * (\text{precision} * \text{recall}) / (\text{precision} + \text{recall})$$

We have achieved training accuracy of 89.9% and validation accuracy of 93.7%. A sample handwashing video is captured and subjected to our model for classification. We have obtained an accuracy of 79% with precision and recall values of 0.97 and 0.67, respectively. The f1-score obtained is 0.79.

33.2.6 Client-server Architecture.

For supervised learning system, prediction requested from the client-side can be processed in a server or client side. However, processing on the server-side has many advantages like version control. We can quickly release an updated machine learning model, and an API will make cross-platform integration easier. This model allows the server for serving multiple API requests in parallel (Fig. 33.5).

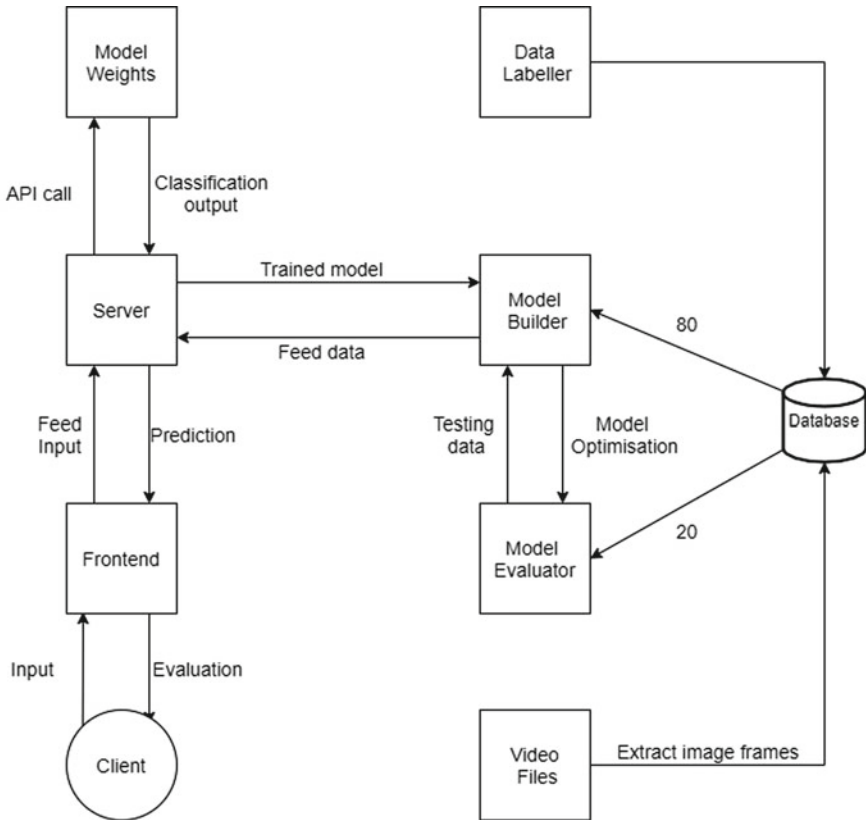


Fig. 33.5 Architecture diagram

33.2.7 Model Deployment

Deploying the model is one of the last stages of any machine learning project. TensorFlow Serving is a flexible, high-performance serving system for machine learning models, designed for production environments. TensorFlow Serving makes it easy to deploy new algorithms and experiments while keeping the same server architecture and API. TensorFlow Serving provides out-of-the-box integration with TensorFlow models but can be easily extended to serve other types of models and data. TensorFlow Serving provides solutions for the following post-deployment challenges.

- If a person wants to change the model in production with minimal downtime.
- If a person wants to roll back to the previous stable version.
- If a person wants to test multiple models or serve different models to different types of clients (Fig. 33.6).

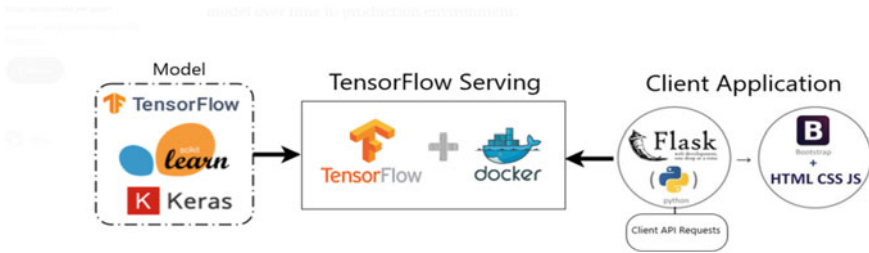


Fig. 33.6 Model deployment with TensorFlow Serving

33.3 Conclusion

We have proposed a client–server architecture system in predicting the efficiency of hand wash performed by people in public places. This system uses transfer learning techniques to extract the image’s features using the VGG16 model, and our deep neural network model classifies the images. Then the accuracy of the hand wash performed is calculated. We have tested our model with real-time testing data, and we achieved remarkable accuracy, thus suggesting that our model can be deployed in a real-time application. It can be installed in hospitals, restaurants, and other public places. This system aims at improving the hand hygiene of the people, which is an important health hygiene routine to be maintained during a pandemic like COVID-19.

33.4 Future Enhancements

Installing cameras will be very extortionate in public places and its maintenance will be tough. An algorithm should be found for using the number of cameras optimally to capture the video to reduce the expenses. The current model is trained using image frames generated from the video captured from only one angle. Image augmentation concept can be used here to train the model using the video captured at different angles. For making the model more effective, the model can also be trained with video in which maximum parts of the hands are covered by soap lather.

We need to concentrate on attaining high accuracy with low-resolution videos. Most data (video) gathered would be from low light-exposed areas like washrooms. This issue can be resolved by increasing the intensity of images while preprocessing the image frames. It would be better to capture and predict many hands using one camera rather than installing one camera per washbasin to capture every hand. Detection of multiple hands in a single camera can be done using object detection algorithms like YOLO.

Face recognition can be included in this project to detect and identify the people in an organization who does not perform their hand wash action as per the

guidelines. The same can be implemented in public places where face recognition based on government ID's like Aadhaar, voter id, etc., can be used to track people. However, this requires permission from the government, as well as people's consent to access their database.

References

- Curtis, V., Cairncross, S.: Effect of washing hands with soap on diarrhoea risk in the community: a systematic review. *The Lancet* **3(5)**, 275–281 (2003)
- Srisomboon, K., Malathum, K., Skuntaniyom, S., Duangthongkham, J., Phanthuna, N.: Hand hygiene auditing algorithm using image processing for hand hygiene evaluation machine. In: 16th International Conference on Electrical Engineering/Electronics, Computer, Telecommunications and Information Technology (ECTICON), 649–652 (2019)
- Thangavel, S.R., Rajevan, T.: Deep learning based emotion analysis approach for strengthening teaching-learning process in schools of tribal regions. *J. Adv. Res. Dyn. Control Syst.* **11**, 621–635 (2019)
- Paresh, P.A., Latha, P.: Vision-based algorithm for fire detection in smart buildings. In: *Lecture Notes in Computational Vision and Biomechanics*, vol. 30, Springer, Netherlands, pp. 1029–1038 (2019)
- Kambam, L.R., Aarathi, R.: Classification of plastic bottles based on visual and physical features for waste management. In: *IEEE International Conference on Electrical, Computer and Communication Technologies (ICECCT)*, Coimbatore, India, 2019, pp. 1–6 (2019)
- Sundara, S.M., Aarathi, R.: Segmentation and evaluation of white blood cells using segmentation algorithms. In: 3rd International Conference on Trends in Electronics and Informatics (ICOEI), Tirunelveli, India, 2019, pp. 1143–1146 (2019)
- Lalithamani, N.: Finger Knuckle biometric authentication using convolution neural network. *Int. J. Pure Appl. Math.* **117(10)**, 31–35 (2017)
- Pali, V., Goswami, S., Bhaiya, L.P.: An extensive survey on feature extraction techniques for facial image processing. In: *International Conference on Computational Intelligence and Communication Networks*, pp. 142–148 (2014)
- Wei, P., Zhou, Z., Li, L., Jiang, J.: Research on face feature extraction based on k-mean algorithm. *EURASIP J. Image Video Process.* **2018(1)**, 83 (2018)
- Ramani, S.K.: Facial expression detection using neural network for customer based service. In: *International Conference on Computer, Communication, and Signal Processing (ICCCSP)*, pp. 1–4 (2018)
- Loukadakis, M., Cano, J., O'Boyle, M.: Accelerating deep neural networks on low power heterogeneous architectures. In: *Eleventh International Workshop on Programmability and Architectures for Heterogeneous Multicores (MULTIPROG-2018)*, Manchester, UK (2018)
- Pan, S.J., Yang, Q.: A survey on transfer learning. *IEEE Trans. Knowl. Data Eng.* **22(10)**, 1345–1359 (2010)
- Das, P.P., Acharjee, A., Marium-E-Jannat: Double coated vgg16 architecture: An enhanced approach for genre classification of spectrographic representation of musical pieces. In: 22nd International Conference on Computer and Information Technology (ICCIT), pp. 1–5 (2019)
- Simonyan, K., Zisserman, A.: Very deep convolutional networks for large-scale image recognition. In: *International Conference on Learning Representations* (2015)
- Geethapriya, S., Duraimurugan, N., Chokkalingam, S.P.: Real-time object detection with Yolo. *Int. J. Eng. Adv. Technol. (IJEAT)* **8(3)**, 578–581 (2019)

Chapter 34

Development and Analysis of Efficient Dispatching Rules for Minimizing Flow Time and Tardiness-Based Performance Measures in a Job Shop Scheduling



S. Ashwin, V. Shankaranarayanan, Damien lamy,
S. P. Anbuudayasankar, and M. Thenarasu

Abstract Scheduling of jobs has a significant contribution to the improved performance of the job shop production system. This study is aimed at developing efficient priority dispatching rules (PDRs) for scheduling in a job shop to improve the tardiness and flow time performance measures. The selection of PDRs depends on the scheduling criteria and job shop conditions. LEKIN software can be used for a variety of well known job shop conditions and varying flexibility. Different schedules are derived using the LEKIN scheduling software for different PDRs such as earliest due date and shortest processing time. In this work, seven static dispatching rules have been taken from the literature study, and four new priority dispatching rules have been proposed and compared to schedule two formal job shop problems under four objective functions, whose aim is to improve the performance measures. The results show that the proposed PDRs are very effective in minimizing various performance measures.

S. Ashwin · V. Shankaranarayanan ·
S. P. Anbuudayasankar · M. Thenarasu (✉)
Department of Mechanical Engineering, Amrita School of Engineering, Amrita Vishwa
Vidyapeetham, Coimbatore, India
e-mail: m_thenarasu@cb.amrita.edu

S. P. Anbuudayasankar
e-mail: sp_anbu@cb.amrita.edu

D. lamy
Mines Saint-Etienne, Univ Clermont Auvergne, CNRS, UMR 6158 LIMOS, Institut Henri
Fayol, Saint-Etienne, France
e-mail: damien.lamy@emse.fr

34.1 Introduction

Scheduling is required for all types of environments, whereas in a job shop environment, it is of much importance as it involves a much more complex production system compared to the traditional manufacturing system. Job shop always consists of the allotment of shared resources to jobs over a period of time. This is an m machine and n job scenario where ' m ' jobs compete for ' n ' machines. It is not necessary that either all jobs get processed by all machines or all machines have to process all jobs. Each job type has its own predefined sequence in which it undergoes the production process in a group of machines designated on the basis of various job and machine parameters. Multiple job types in a job shop arrive based on the demand which is to be processed in parallel using the available resources in the facility. Proper dispatching of jobs, i.e., right quantity and time, is essential to achieve better performance to cater to the requirements of the customer. There are several sets of priority dispatching rules (PDRs) that are used for the sequencing of jobs based on the objective function that is of more importance to the company. Therefore, analyzing the viability as well as the scope of improvement of PDRs is essential.

34.2 Literature Review

Scheduling remains a largely used decision-making process on a regular basis in industries worldwide. Various factors of an industrial environment affect the performance and output, and as such scheduling will maintain its significance even in the future. Every industry is different from every other industry in multiple ways, and thus, it is impossible to have a universally applicable scheduling rule [1]. However, many industrial problems can be modeled using job shop scheduling. Hence, the selection of appropriate performance measures is important for optimizing the job shop, depending on the performance measure used, the level and type of optimization varies [2]. Using the available resources subjected to constraints effectively, maximum performance can be ensured. Ineffective scheduling means to under-utilize the available resources, which results in increased idleness of physical resources such as machines and jobs, which in turn leads to the under-utilization of manpower, thus incurring major losses to any company. All these issues lead to an increase in the overall cost of the product. Scheduling in JSSP is a typical combinatorial NP-Hard optimization problem.

A comprehensive discussion on various dispatching rules and procedures has been developed to rank the job processing order. There is a variety of dispatching rules categorized on the basis of different performance measures, for instance, processing time based, due date based, and combination of more than one rule and some which are not based on processing time or due date. Researchers found that all the performance measures can be combined into a single rule; hence, the

combination of rules had been proposed [3]. Researchers have proposed rules that effectively minimize various performance measures. The shortest processing time (SPT) rule can effectively minimize the percentage of tardy jobs, while the mean tardiness can be minimized using the effectiveness of RR [4].

Job shop scheduling is found to be more complicated compared to flow shop problems as there are no technical orderings [5]. From the earlier researches, some of the best-performing existing rules are SPT rule, process time combined with work in the next queue (PT+WINQ) rule, apparent tardiness cost (ATC) rule, modified operational due date (MOD), earliest due date (EDD), operational due date (ODD) rule, and RR rule [6]. The experimentation and analysis of dynamic JSSP having the operation of a variety of characteristics, for instance, job arrival rates, various levels of flexibility of machines, due date assignment methods are necessary due to its significance in different types of industries [7]. For efficient operation of job shops, dispatching rules have been developed.

Developing perfect dispatching is impractical; hence, researchers have been attempting to design dispatching rules which can provide a near-perfect solution that produces favorable output for the user. The key aspects of designing dispatching rules are selecting the attributes and how these attributes can be combined [8]. The simulation model is a set of instructions and programs which illustrate the working of a real-world system. With this model, various operational, transportation, scheduling, manufacturing, and other business problems can be analyzed and can be optimized later [9]. The simulation model was created using Arena software where it was found that it helps to evaluate a wide variety of performance measures of the system and also helps to identify the bottlenecks in the shop floor [10–12].

Many researchers have developed and analyzed various PDR and have obtained positive results for their respective objectives. Among these rules, an efficient dispatching rule was developed to reduce tardiness and flow time. However, the shortest processing time priority rule remains the most efficient in decreasing the number of tardy jobs [13]. AHP-based PDR was proposed [14] by considering real-time criteria such as production volume, due date, and cycle time with an objective of minimizing lead time of large-scale job shops. The heuristic algorithm can be used to optimize complex, powerful, and relatively large scheduling problems based on dispatching rules in a real-life production as they are simple, efficient, and flexible to the uncertainties of a workplace [15]. The experimentation and analysis of dynamic JSSP having operation of a variety of characteristics, for instance, job arrival rates, various levels of flexibility of machines, due date assignment methods. This paper proposed seven scheduling rules and claims that proposed rules based on due date based rules improves the flow time and tardiness based measures [16].

The classification of dispatching rules is as follows: due-date-based rules, combination rules, processing-time-based rules, and the rules which do not belong to processing time based and due date based [17]. PDRs are developed for finding the rank of the alternatives for the processing. The highest priority job will be sent to processing when the machine is free [18]. Cost-based scheduling rules that assume equal penalties for tardiness-based measures are inadequate in most real-

world scenarios due to the variance in holding costs for different items. Therefore, it is imperative to consider different weights that include tardiness-based penalties for each criterion [19]. MCDM-based PDR was proposed [20] by considering various real-time criteria such as customer due date and customer segment importance to reduce the customer defection rate.

Simulation models for dynamic JSSP that incorporate sequence-dependent setup time exhibit better performance when compared to simulation models having normal dispatching rules [21]. The majority of the dynamic JSSP studied have not researched assembly job shops where the usage of multi-level jobs is involved. For a large assembly job shop, maximum tardiness, as well as its standard deviation, plays an important role. The proposed due-date-based and lead-time-based rules have performed well for a simulated assembly job shop [22].

Many researchers have proposed exact and heuristic procedures for solving JSSP with many objectives such as minimizing makespan, completion time variance, and the number of tardy jobs. Extensive research is being done in this field. There are infinite ways to schedule problems based on objective functions. It has also been observed that there is always room for improvement in scheduling problems based on the objective. The purpose of this project is to find efficient dispatching rules to generate a schedule sequence in the job shop scheduling using LEKIN scheduling software to minimize the makespan and tardiness-based performance objectives.

34.3 Development of Composite Dispatching Rule

The optimum performance of PDRs for each of the four objective functions, such as maximum makespan, maximum delay, total flow time, and total delay, is combined into hybrid dispatch rules so that different objectives can be simultaneously improved. Four new PDRs were presented for scheduling in a workshop based on the results obtained.

34.3.1 Proposed Dispatching Rules

EDD+MS: The rule is the combination of the minimum slack of jobs (MS) and the earliest due date (EDD). This rule seeks to take advantage of the EDD and MS rules for minimizing flow time and tardiness of jobs.

MS+FCFS: This rule is the combination of the minimum slack of jobs and jobs which get served first (FCFS—first come first served). This rule is favorable for minimizing the makespan of jobs.

EDD+MS+FCFS: This rule is the combination of the EDD, MS, and FCFS rules. This rule is expected to perform efficiently in the makespan, and total tardiness objectives, when compared to other combined rules due to a combination of the best performing static rules, are chosen.

EDD+MS+FCFS+SPT: This rule is the combination of Rule 3 and SPT in order for minimizing the flow time and total tardiness of jobs. The advantage of this particular rule is that the shortest processing time rule delays the completion time and gives a large value of maximum makespan and tardiness as the outcome.

34.3.2 Sequence of Jobs on Machines

The job priority order on each machine for the proposed dispatching rules can be found out by the weighted average method.

34.4 Computational Experiments

34.4.1 Experimental Evaluations of Proposed Dispatching Rules

The two job shop problems taken from the literature for bench-marking are Muth and Thompson 6×6 and 10×10 problems. The 6×6 problem as shown in Table 34.1 consists of six jobs and six machines with each job consisting of six operations present on the shop floor in a determined order.

Table 34.1 Machine requirement for the Muth and Thompson 6×6 problem

Task No.	Job number					
	1	2	3	4	5	6
	Machine number (process time)					
1	1 (29)	1 (43)	2 (91)	2 (81)	3 (14)	3 (84)
2	2 (78)	3 (90)	1 (85)	3 (95)	1 (6)	2 (2)
3	3 (9)	5 (75)	6 (39)	1 (71)	2 (22)	6 (52)
4	4 (36)	10 (11)	3 (74)	5 (99)	6 (61)	4 (95)
5	5 (49)	4 (69)	9 (90)	7 (9)	4 (26)	9 (48)
6	6 (11)	2 (28)	6 (10)	9 (52)	5 (69)	10 (72)

Table 34.2 Muth and Thompson 10×10 problem

Task No.	Job number									
	1	2	3	4	5	6	7	8	9	10
	Machine number (process time)									
1	1 (29)	1 (43)	2 (91)	2 (81)	3 (14)	3 (84)	2 (46)	3 (31)	1 (76)	2 (85)
2	2 (78)	3 (90)	1 (85)	3 (95)	1 (6)	2 (2)	1 (37)	1 (86)	2 (69)	1 (13)
3	3 (9)	5 (75)	6 (39)	1 (71)	2 (22)	6 (52)	4 (61)	2 (46)	4 (76)	3 (61)
4	4 (36)	10 (11)	3 (74)	5 (99)	6 (61)	4 (95)	3 (13)	6 (74)	6 (51)	7 (7)
5	5 (49)	4 (69)	9 (90)	7 (9)	4 (26)	9 (48)	7 (32)	5 (32)	3 (85)	9 (64)
6	6 (11)	2 (28)	6 (10)	9 (52)	5 (69)	10 (72)	6 (21)	7 (88)	10 (11)	10 (76)
7	7 (62)	7 (46)	8 (12)	8 (85)	9 (21)	1 (47)	10 (32)	9 (19)	7 (40)	6 (47)
8	8 (56)	6 (46)	7 (89)	4 (98)	8 (49)	7 (65)	9 (89)	10 (48)	8 (89)	4 (52)
9	9 (44)	8 (72)	10 (45)	10 (22)	10 (72)	5 (6)	8 (30)	8 (36)	5 (26)	5 (90)
10	10 (21)	9 (30)	5 (33)	6 (43)	7 (53)	8 (25)	5 (55)	4 (79)	9 (74)	8 (45)

The 10×10 problem is shown in Table 34.2 with ten machines, ten jobs, and each job consisting of ten operations. The selected priority rules were applied to the given benchmark problems using LEKIN scheduling software.

34.4.2 Experimental Evaluations of Proposed Dispatching Rules

The best-performing dispatching rules are merged into hybrid dispatching rules in order to enhance the four objective functions simultaneously. Using these proposed hybrid dispatching rules, the sequence of jobs on machines for 6×6 and 10×10 problems was found and simulated in LEKIN scheduling software. The sequence of jobs on machines for hybrid priority rules was found using the weighted average method.

34.5 Results and Discussions

The model developed was helpful in determining the performance measures of the job shop based on the existing sequencing technique and other PDRs. The model may help to compare various results and choose the suitable PDR for the job shop that would yield better results based on the required objective function. Results of various performance measures for Muth and Thompson 6×6 are presented in Table 34.3.

Table 34.3 Performance measures of various dispatching rules for Muth and Thompson 6×6

Dispatching rules	Max. makespan	Mean flow time	Mean. tardiness	Max. tardiness
EDD	63	321	63	264
FCFS	65	329	65	229
LPT	67	354	67	254
MS	67	354	67	283
SPT	73	292	73	211
WSPT	73	292	73	218
CR	81	317	81	217
EDD+MS	62	310	62	210
FCFS+MS	62	312	62	212
EDD+FCFS+MS	61	318	61	217
EDD + FCFS + MS + SPT	60	321	60	219

The results obtained from Muth and Thompson 6×6 problem support the idea of using proposed hybrid priority rules. The hybrid rules have a significant impact on makespan and tardiness when compared to priority rules. Rule 4 (EDD+MS+FCFS+SPT) resulted in having the least maximum makespan and tardiness for Muth and Thompson 6×6 problems. As for reducing the total flow time and tardiness, Rule 1 (EDD+MS) and Rule 2 (MS+FCFS) emerge to have the best outcome of the combined dispatching rules. Rule 3 (EDD+MS+FCFS) has performed averagely well in all the performance measures. The results of the simulation on objective functions for Muth and Thompson 10×10 are presented in Table 34.4

Table 34.4 Performance measures in time units of various dispatching rules for Muth and Thompson 10×10

Dispatching rules	Max. makespan	Mean flow time	Mean. tardiness	Max. tardiness
LPT	1168	10,257	1168	10,887
MS	1168	10,687	1168	10,264
FCFS	1184	10,254	1184	10,582
EDD	1246	10,703	1246	10,703
SPT	1338	11,245	1338	10,109
WSPT	1338	10,564	1338	10,209
CR	1411	10,854	1411	10,182
EDD+MS	1255	10,191	1205	11,471
MS+FCFS	1189	10,057	1189	10,057
EDD+MS+FCFS	1180	10,154	1180	10,154
EDD + FCFS + MS + SPT	1134	10,175	1134	10,245

The results obtained from Muth and Thompson 10×10 problems also support the idea of using proposed hybrid priority rules. Rule 2 (MS+FCFS) and Rule 3 (EDD+MS+FCFS) have proven to be the best to minimize the mentioned performance objectives. Rule 4 (EDD+MS+FCFS+SPT) gave an average performance on the above-mentioned performance measures. As a whole, it can be observed that Rule 2 (MS+FCFS) performed efficiently in both the benchmark problems. In Muth and Thompson 6×6 , here we can see that the performance of hybrid priority rules is higher when compared to the Muth and Thompson 10×10 problem. The hybrid priority rules performance on maximum makespan and tardiness were reasonable but certainly not the least.

34.6 Conclusion

New hybrid dispatching rules were proposed for job shop scheduling. The rules are made on the basis of merging the processing time, due date, no of operation, and slack time of jobs. It has been shown that developed composite dispatching rules prove to be better on the four objective functions as opposed to the single dispatching rules separately. The results also show that no individual rule is optimum in reducing all objective functions. It was found that Rule 2 (MS+FCFS) is found to be quite significant in minimizing all the mentioned performance objectives. Rule 3 (EDD+MS+FCFS) reduced the maximum makespan and maximum tardiness-related objectives as mentioned. Rule 4 (EDD+MS+FCFS+SPT) performs well in smaller problems when compared to a larger problem. However, for minimizing total flow time and tardiness, the shortest processing time rule continues to be competent. The results convey that subsequent research could lead to the generation of rules for dispatching jobs on the basis of process time, due date, demand, setup, batch quantity, dynamic arrival, and no of operation in order to minimize as many performance measures as possible.

References

- Blackstone, J.H., Phillips, D.T., Hogg, G.L.: A state-of-the-art survey of dispatching rules for manufacturing job shop operations. *Int. J. Prod. Res.* **2**(1), 27–45 (1982)
- Ramasesh, R.V.: Dynamic job shop scheduling: a survey of simulation research. *Omega* **18**(1), 43–57 (1990)
- Oliver, H., Rajendran, C.: Efficient dispatching rules for scheduling in a job shop. *Int. J. Prod. Eco.* **48**(1), 87–105 (1997)
- Oliver, H.: Design of efficient job shop scheduling rules. *Comp. Ind. Eng.* **33**(1–2), 249–252 (1997)
- Ferrell, W., Jr., Sale, J., Sams, J., Yellamraju, M.: Evaluating simple scheduling rules in a mixed shop environment. *Comp. Ind. Eng.* **38**(1), 39–66 (2000)
- Jayamohan, M.S., Rajendran, C.: New dispatching rules for shop scheduling: a step forward. *Int. J. Prod. Res.* **38**(3), 563–586 (2000)

- Vinod, V., Sridharan, R.: Simulation-based meta-models for scheduling a dynamic job shop with sequence-dependent setup times. *Int. J. Prod. Res.* **47**(6), 1425–1447 (2009)
- Chiang, T.C., Fu, L.C.: Rule-based scheduling in wafer fabrication with due date-based objectives. *Comp. Oper. Res.* **39**(11), 2820–2835 (2012)
- Gupta, S., Starr, M.: *Production and operations management systems*. CRC Press (2014)
- Sathish Kumar, V.R., Anbuudayasankar, S.P., Thenarasu, M.: Design and development of simulation based model to rank job flow strategies. *ARPN J. Eng. Appl. Sci.* **11**(9), 6082–6086 (2016)
- Thenarasu, M., Rameshkumar, K., Anbuudayasankar, S.P., Arjunbarath, G., Ashok, P.: Development and selection of hybrid dispatching rule for dynamic job shop scheduling using multi-criteria decision making analysis (MCDMA). *Int. J. Qua. Res.* **14**(2) (2020)
- Neeraj, R.R., Nithin, R.P., Niranjhan, P., Sumesh, A., Thenarasu, M.: Modelling and simulation of discrete manufacturing industry. *Mater. Today Proc.* **5**(11), 24971–24983 (2018)
- Rameshkumar, K., Rajendran, C.: A novel discrete PSO algorithm for solving job shop scheduling problem to minimize makespan. In: *IOP Conference Series: Materials Science and Engineering*, vol. 310, issue 1, pp. 012143 (2018)
- Mohanavelu, T., Krishnaswamy, R., Marimuthu, P.: Simulation modelling and development of analytic hierarchy process-based priority dispatching rule for a dynamic press-shop. *Int. J. Ind. Sys. Eng.* **27**(3), 340–364 (2017)
- Sels, V., Gheysen, N., Vanhoucke, M.: A comparison of priority rules for the job shop scheduling problem under different flow time-and tardiness-related objective functions. *Int. J. Prod. Res.* **50**(15), 4255–4270 (2012)
- Vinod, V., Sridharan, R.: Simulation modeling and analysis of due-date assignment methods and scheduling decision rules in a dynamic job shop production system. *Int. J. Prod. Eco.* **129**, 1127–1146 (2011)
- Raghu, T.S., Rajendran, C.: An efficient dynamic dispatching rule for scheduling in a job shop. *Int. J. Prod. Eco.* **32**(3), 301–313 (1993)
- Thenarasu, M., Rameshkumar, K., Anbuudayasankar, S.P.: Multi-criteria decision making approach for minimizing makespan in a large scale press-shop. *Int. J. Ind. Eng.* **26**(6) (2019)
- Mohanasundaram, K.M., Natarajan, K., Viswanathkumar, G., Radhakrishnan, P., Rajendran, C.: Scheduling rules for dynamic shops that manufacture multi-level jobs. *Comp. Ind. Eng.* **44**(1), 119–131 (2003)
- Sidhartha, S., Thenarasu, M.: Customer-centric prioritization using multi-criteria decision-making method. *Int. J. Emerg. Technol.* **11**(3), 26–32 (2020)
- Vinod, V., Sridharan, R.: Simulation-based meta models for scheduling a dynamic job shop with sequence-dependent setup times. *Int. J. Prod. Res.* **47**(6), 1425–1447 (2009)
- Jayamohan, M.S., Rajendran, C.: Development and analysis of cost-based dispatching rules for job shop scheduling. *Eur. J. oper. Res.* **157**(2), 307–321 (2004)

Chapter 35

Vibration Measurement Using a Low-Cost MEMS Accelerometer Kit for the Education



Syed Faizan Shah and Skylab Paulas Bhore

Abstract The paper is based on the vibration measurement using a low-cost MEMS accelerometer kit. The MEMS accelerometer kit is developed using an open-source literature. The main components of the kit are ADXL 355 MEMS accelerometer, microcontroller, SD card and the batteries. The vibration measurement test on the electrical cooler is performed using the developed kit. It measures the acceleration in three axes x , y and z . The measured vibration response is validated with the phyphox application available for the smartphone with inbuilt accelerometer. The time domain responses acquired from both MEMS acceleration kit and the smartphone are analyzed using fast Fourier transform (FFT). The results are in good agreement. The developed kit can be used for measuring vibrations in the various applications. The cost of the kit is significantly lower than the conventional piezoelectric accelerometer.

35.1 Introduction

Microelectromechanical systems (MEMS) accelerometer is popular due to its reliability, small size and low cost. It is widely used in industrial, automotive and consumer applications [1]. Albarbar et al. [2] have studied the suitability of MEMS sensor with different specifications for the condition monitoring of the CNC machine. They found the potential in MEMS sensor with minor errors in phase shift and amplitude variation as compared to conventional one. Jimenez et al. [3] presented the mathematical formulation and the experimental test with the embedded MEMS sensor on the rotor. It finds the stator-based virtual displacement response of rotor using the sensor data. Lu et al. [4] presented test results on the condition monitoring of the motor bearings with wireless MEMS sensor. They show that the undersampled vibration signals are effective to handle the large data. Varanis et al.

S. F. Shah (✉) · S. P. Bhore

Product Development Lab, Department of Mechanical Engineering, Motilal Nehru National Institute of Technology Allahabad, Prayagraj, Uttar Pradesh, India
e-mail: skylabpbhore@mnnit.ac.in

[5] reviewed the use of MEMS sensor in different applications and presented the two case studies on vibration measurement and analysis using MEMS sensor. Recently, Koene et al. [6] presented a research on versatile wireless MEMS sensor with Internet of things. The sensor unit is tested for linear and rotating vibration applications. Wang et al. [7] presented an algorithm for the reduction of the data in MEMS sensor with Internet of things. The experimental tests are carried out, and significant improvement in the performance with 95% data reduction is achieved.

The MEMS sensor with Internet of things (IoT) feature is a promising solution for remotely monitoring and diagnosing the health of the industrial machineries. To demonstrate the MEMS sensor with IoT to engineering students is little challenging. Therefore, there is a need of MEMS accelerometer kit for effective teaching and learning. In this paper, a MEMS accelerometer kit is developed using the open-source literature. The procedure and the online resources are discussed. The vibration test is carried out on electric cooler. The vibration responses are analyzed using fast Fourier transform (FFT), and detail discussions are presented.

35.2 Methodology

The methodology involves the sensing of the mechanical vibrations, transduces them to electrical signals, stores these signals, retrieves back the data, performs further signal processing, and applies analysis algorithm. For this, the hardware and software requirements are [6]:

1. A sensor: ADXL355 by analog devices is chosen due to its high resolution.
2. A microcontroller or a microprocessor: ESP32-WROOM (a dual-core 32-bit microcontroller development board).
3. A data storage device: A micro-SD card.
4. Auxiliary components involved a micro-SD card reader module, some connecting wires (jumper wires), a USB type-B cable.
5. Software: Arduino IDE.

Figure 35.1 shows the main hardware components.

The bill of material is shown in Table 35.1. After following Ref. [6], the wired setup is prepared and programmed (see Fig. 35.2).

35.3 Tests and Results

The vibration measurement test is performed on the electric cooler using the developed MEMS accelerometer kit. The setup is made as shown in Fig. 35.3. The measured vibration response is validated with the phyphox application available for the smartphone with inbuilt accelerometer [8]. The time domain responses acquired from both MEMS acceleration kit and the smartphone are compared and analyzed

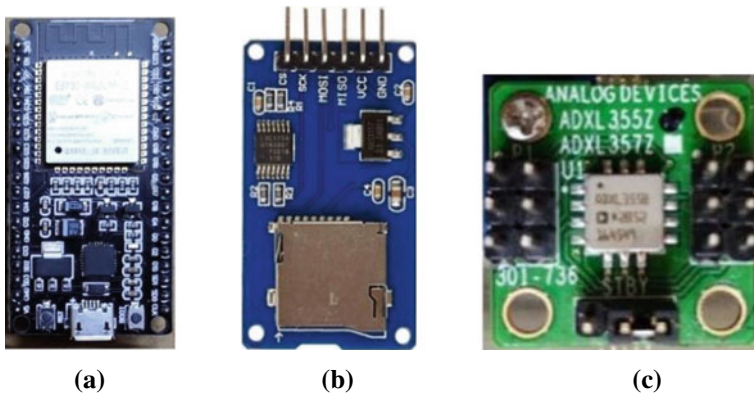


Fig. 35.1 Main hardware components. **a** Microcontroller ESP32-WROOM, **b** SD Card Reader Module, **c** Accelerometer ADXL355

Table 35.1 Bill of materials

S. no.	Component name		Quantity	Price (in INR)	Source
1	ESP-32 WROOM Development Board		1	750	Mouser.in
2	EVAL-ADXL355Z	Hardware	1	~ 2600 (35 USD)	Digikey.in
3		Shipping charges		~ 1490 (20 USD)	
4		Custom Duty charges		~ 2330 (31 USD)	
5	Jumper wires (female to female type)		1 set (20 pcs)	80	Robu.in
6	Micro-SD card reader module		1	80	Robu.in
7	8 GB micro-SD card (Class 10)		1	400	Amazon.in
8	USB-A to micro-USB-B cable		1	300	Amazon.in
9	Rechargeable 18,650 1300 mAh cell		2	600	Robu.in
10	Cell holder		1	90	Robu.in
11	Small container box (as housing)		1	150	Local market

using fast Fourier transform (FFT). The sampling rate of the phyphox [8] is restricted to a maximum of 410 Hz. However, the MEMS accelerometer kit has a maximum sampling rate of 4000 Hz. For the sake of making comparisons even, we set the MEMS accelerometer kit at a 500 Hz sampling rate (nearest possible setting to 410 Hz). The program for FFT was written in Python using Pandas, NumPy and Matplotlib modules.

The cooler is initially switched off. The MEMS accelerometer kit setup along with the smartphone is put over the cooler body as shown in Fig. 35.3. The cooler is

Fig. 35.2 Wired setup

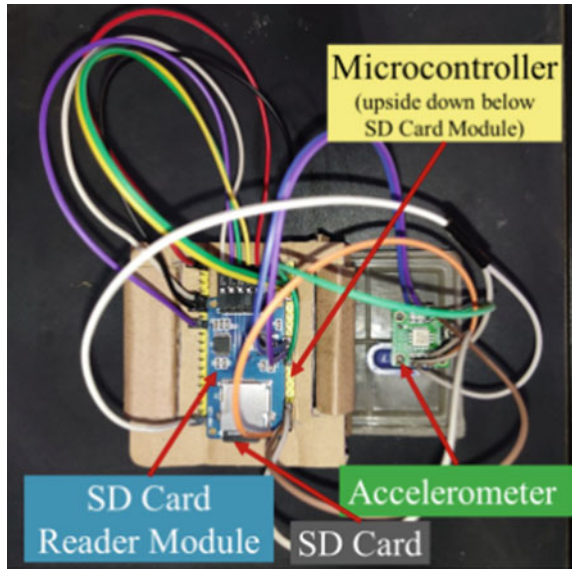
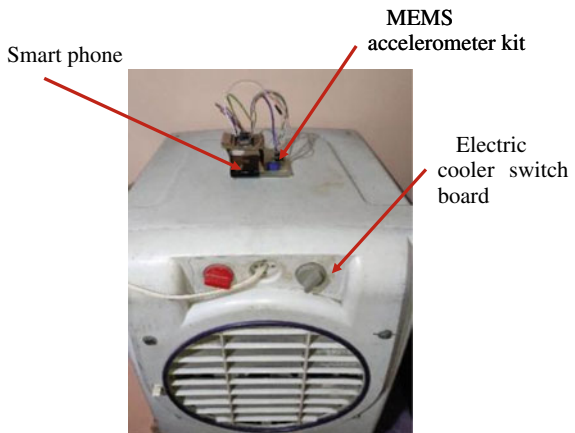


Fig. 35.3 Setup placed over cooler



switched ON. The measurements are taken for a period of 15 s from both the MEMS accelerometer kit and the smartphone as shown in Fig. 35.4. The time domain responses (data) acquired from both the devices are converted into the frequency domain using fast Fourier transform (FFT) as shown in Fig. 35.5.

From Fig. 35.4, it is observed that the acceleration responses along x -, y - and z -axes obtained using MEMS accelerometer kit and the smartphone application (phyphox) are similar and confirm the correctness of the developed kit. There is a little variation in amplitude along y -axis. It may be due to the difference in the sensor characteristics in both the devices.

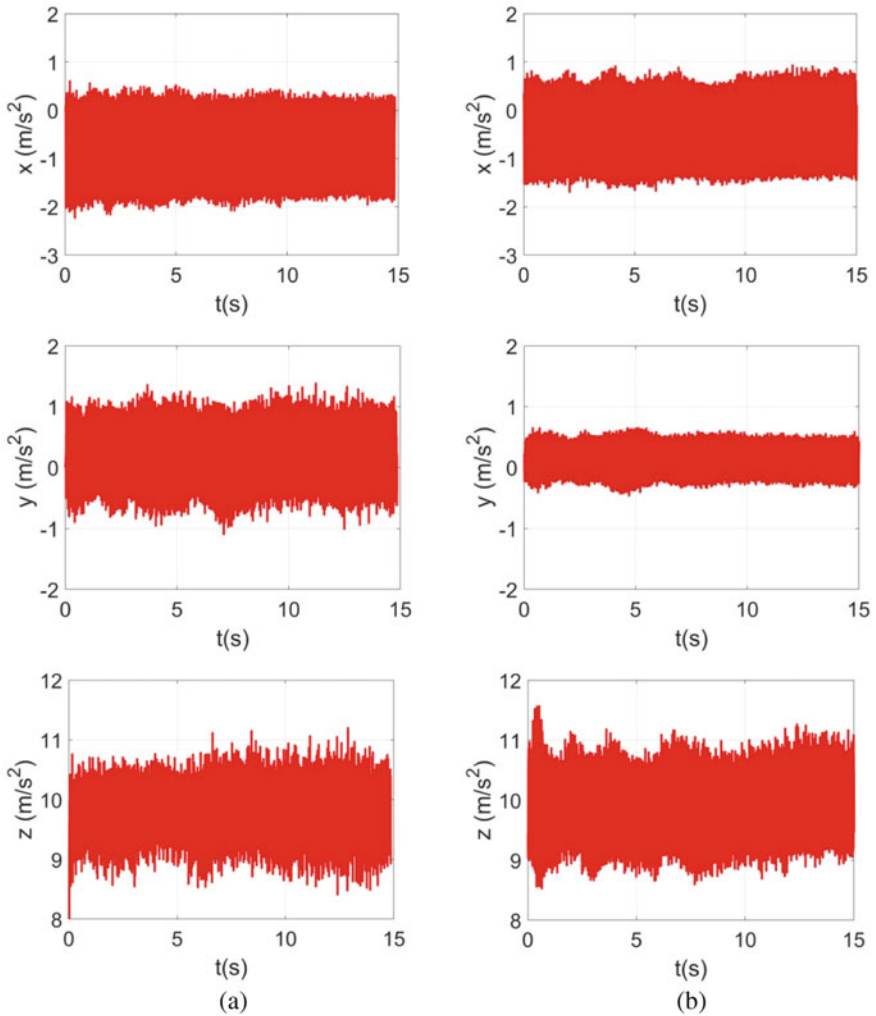


Fig. 35.4 Time domain vibration responses of cooler along x -, y - and z -axes obtained **a** using accelerometer kit and **b** using smartphone

The FFTs of the acceleration responses along x -, y - and z -axes obtained using MEMS accelerometer kit and the smartphone show multiple harmonics ($1X$, $2X$, ... nX) of the excitation frequency (see Fig. 35.5). The $1X$ frequency component is prevalent in all the directions (x -, y - and z -axes) in both the devices. The excitation frequency ($1X$) of the cooler using accelerometer kit and the smartphone is 19.8 Hz and 20 Hz, respectively. The frequency measurement error in both the devices is 1%.

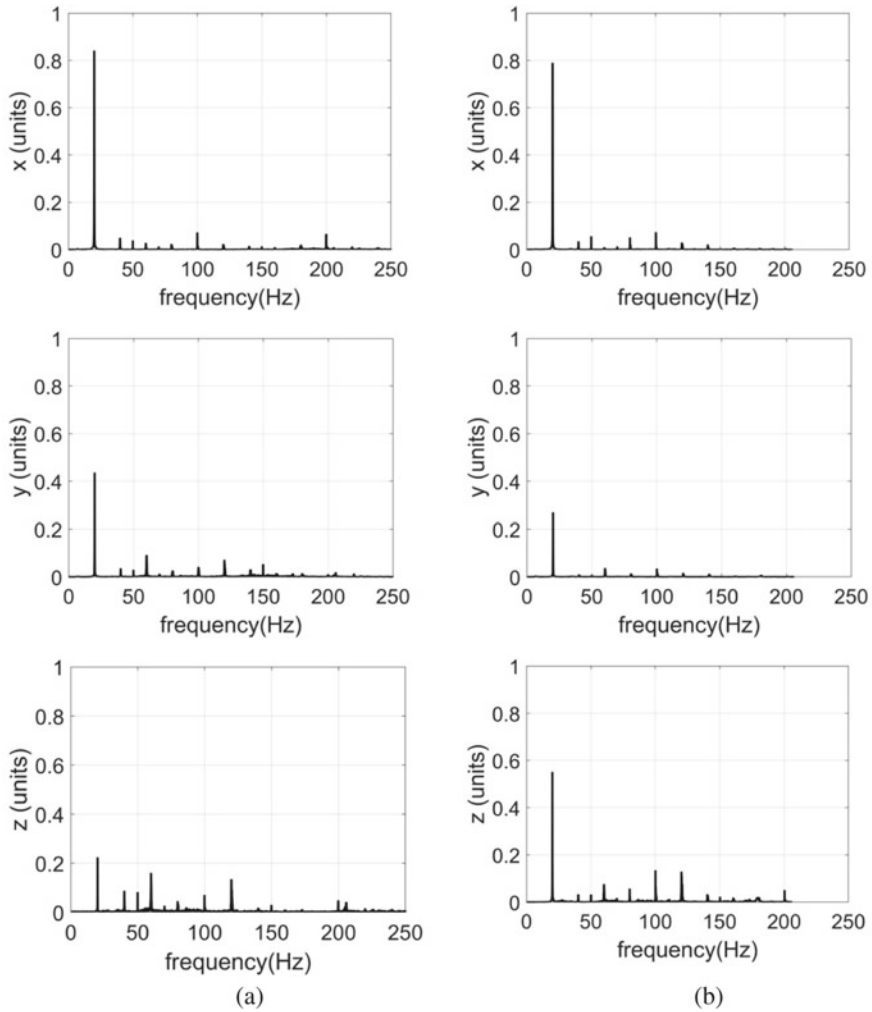


Fig. 35.5 Frequency domain vibration responses of cooler along x -, y - and z -axes obtained **a** using accelerometer kit and **b** using smartphone

35.4 Conclusions

A low-cost MEMS accelerometer kit for the education is developed using the open-source literature. The kit can be used for the vibration measurement in various applications. The vibration measurement in the electric cooler is recorded and validated with the smartphone application (phyphox). The vibration responses are further analyzed using fast Fourier transform. The error in the excitation frequency

measurement using both the devices is found to be 1%. The developed MEMS accelerometer kit can be used in the technical institute for the effective teaching and learning.

References

1. Hsu, T-R.: MEMS and Microsystems: Design, Manufacturing and Nanoscale Engineering. Wiley Publications (2008)
2. Albarbar, A., Mekid, S., Starr, A., Pietruszkiewicz, R.: Suitability of MEMS accelerometers for condition monitoring: an experimental study. *Sensors* **2008**(8), 784–799 (2008)
3. Jiménez, S., Cole, M.O.T., Keogh, P.S.: Vibration sensing in smart machine rotors using internal MEMS accelerometers. *J. Sound Vib.* **377**, 58–75 (2016)
4. Lu, S., Zhou, P., Wang, X., Liu, Y., Liu, F., Zhao, J.: Condition monitoring and fault diagnosis of motor bearings using undersampled vibration signals from a wireless sensor network. *J. Sound Vib.* **414**, 81–96 (2018)
5. Varanis, M., Silva, A., Mereles, A., Pederiva, R.: MEMS accelerometers for mechanical vibrations analysis: a comprehensive review with applications. *J. Braz. Soc. Mech. Sci. Eng.* **40**, 527 (2018)
6. Koene, I., Klar, V., Viitala, R.: IoT connected device for vibration analysis and measurement. *HardwareX* **7**, e00109 (2020)
7. Wang, X., Lu, S., Huang, W., Wang, Q., Zhang, S., Xia, M.: Efficient data reduction at the edge of industrial internet of things for PMSM bearing fault diagnosis. *IEEE Trans Instrum. Measur.* **70**, 3508612 (2021)
8. Stampfer, C., Heinke, H., Staacks, S.: A lab in the pocket. *Nat. Rev. Mater.* **5**, 169–170 (2020)

Chapter 36

Disease Prediction by Stacking Algorithms Over Big Data from Healthcare Communities



M. Hema Latha, A. Ramakrishna, B. Sudarsha Chakravarthi Reddy, Ch. Venkateswarlu, and S. Yamini Saraswathi

Abstract In the present society, everyone is busy in their work-life and other activities without having time to consult doctors which they treat as simple issues during the initial stages but as time passes these may convert into life risk parameters. So for the early prediction and prevention of diseases, the proposed system maintains a public cloud that stores the information about different patients along with various symptoms and probable diseases as a matrix. For predicting the type of disease, symptoms are collected from the user and passed as input to the stacking algorithm. The patient's records are collected from different hospitals, and this acquired huge amount of data cannot be handled using a local server so to provide a solution. A big data framework integrated with machine learning algorithms is deployed in the cloud. In the existing systems, big data tools like Hadoop, Apache Spark, and others are popular implementations at the same time the potential risk factors with these tools.

36.1 Introduction

Big data analytics has received prominent recognition for its implications in many of the industrial sectors, especially from the healthcare [1] industry. The health industry is popular for its numerous volumes of data that is one of the main reasons for the healthcare industry to choose big data analytics for solving its issues. The strength of big data lies in its five V's notation which can be described as follows:

- (a) Big data analytics can make huge “**volumes**” of data available to the users dynamically in different formats.

M. Hema Latha (✉)
Department of IT, Lakireddy Bali Reddy College of Engineering, Mylavaram 521230, India

A. Ramakrishna · B. Sudarsha Chakravarthi Reddy · Ch.Venkateswarlu · S. Yamini Saraswathi
Lakireddy Bali Reddy College of Engineering, Mylavaram 521230, India

- (b) It can operate on the data with a good “**velocity**” even though it collects data from different sources like smartphones, social media networks, survey forms, and others.
- (c) There is no guarantee that the data available is in good quality format; sometimes, it may exist in an unreadable format and at the same time, it is variable because it receives its dimensions from multiple sources. This form of inconsistency and uncertainty among the data is referred to as “**veracity**.”
- (d) The data collected from data sources should be converted into consistent and useful format; i.e., the data should be in a readable format as well as it should generate “**valuable**” information for the organizations.
- (e) It is widely accepted because of its existence in “**variant**” formats. These variant formats are categorized into three types. They are:
 - 36.1.1. **Structured data:** The data stored efficiently which can define the relationship between the various columns that are present in the table or database is referred to as “structured data.” The best example for these types of data is tables stored in SQL databases or data present in RDBMS.
 - 36.1.2. **Semi-structured data:** The data does not define the relationship among their columns, but still they can organize the data in good format and they can also analyze the data to provide some useful information. eXtensible Markup Language (XML) is a good tool to represent the semi-structured data.
 - 36.1.3. **Unstructured data:** The data which does not have any proper format to organize the data and which provides the information in messy format is known as “unstructured data.” This type of data neither analyzes nor generates good reports to the organizations. The good examples are the data stored in any type of text editors.

The healthcare industry has changed its direction very effectively to save the lives of people with the help of big data [2], which is now trending as “healthcare analytics.”

36.2 Related Work

In [3], **Chen et al.** proposed CNN-based imputation mechanism to predict a disease by designing a unimodal decision system. In this model, the system has utilized hospital data for predicting the risk associated with a disease. In this model, there is a lot of scopes to have either missing data or erroneous in the hospital data, which is referred to as “data imputation”; this can be handled by using a popular neural network mechanism known as “SGD” with good hyperparameters passed as estimators to the algorithm. Later, the textual data in the medical records is preprocessed using the word embedding technique to remove and handle the impure

sentences. To predict the disease, pure sentences are passed as input to the CNN with random weights, and the output is represented as a $50 * 50$ row vector. All the words generated may not have an equal role in the prediction, so a maximum pooling layer is applied to reduce and extract important features from the neural networks. So in this layer, a $100 * 1$ vector is produced as output. Finally, a softmax associated with fully connected neural network is used as an output layer to predict the risks. At last, to enhance the model, the system has implemented multi-model-based CNN to find more risks associated with different diseases. The purpose of this work is to determine if a patient is a highly risk population based on their history of hip fracture. In this research, the dataset of the hospital contains real-life data from the hospital and is stored in the data center. So, this hospital data is available in semi-structured data format because the medical data of a person includes both genetic and image data. To provide security for these health records, it also implements some security mechanisms to encrypt the patient's records.

In [4], **Nair et al.** designed a framework using Apache Spark integrated with machine learning algorithms to predict the health status of a person. In Spark, the availability of data is a continuous data stream and is represented by **Discrete Streams (DStreams)** which constitute an RDD sequence. This model collects the data from the Twitter social network where the user tweets his/her health attributes, namely age, blood pressure, heartbeat rate, and sugar levels from this framework; it extracts the attributes and notifies the user about his health status directly by applying machine learning algorithms. This model has chosen Twitter as a third-party platform as a communication channel because it provides security to the user's information by implementing OAuth authorization protocol. In this model, to train the model has utilized the heart dataset from the UCI repository by splitting the data into 70% training and 30% validation. In Apache Spark, there exists a predefined machine learning library called "MLlib," which integrates with the decision tree algorithm. This designed model is deployed in the amazon Web service known as "Elastic Compute Cloud," popularly known as EC2. This remote model helps the user to know about his health status with low cost and more security.

In [5], **Mehta et al.** concluded that there is currently no generic "big data" system analytical architecture available. However, various organizations have proposed several small-scale architectures to meet their requirements. The architecture is only developed for certain purposes where the applications deal with encryption and decryption algorithms, multitasking processors, and a huge amount of data. This product-focused architecture limits the scope of a company's specific products. The previous studies focused on the functionality aspects and budget-related requirements. Big data requirement analysis architecture lambda. Lambda architecture was implemented for Twitter data analysis on distributed data processing systems. It consists of three layers: batch, speed, and a portion layer. The big data reference architecture (NBDRA) is being developed for data-related issues to be addressed by data scientists, developers of software, data architects, technical engineers, and senior decision-makers. It describes an ecosystem of big data consisting of different operational layers interconnected by surfaces of interconnection.

NBDRA consists of five layers: system controller, data supplier, a data consumer, data application provider, and large data framework provider.

In [6], **Manogaran et al.** proposed a framework to collect relevant literature from different sources, and a chronic evaluation was carried out, with a focus on the following goals:

- Analysis of different perspectives of the users regarding the health predictions and their implementation in the cloud environment.
- Exploring big data predefined tools that support machine learning algorithms, especially clustering and graph mining algorithms, made their remarkable research in the healthcare industry.
- Identifying big data analysis technologies and medical technology.
- It addresses the problems associated with the information-sharing mechanisms over social media networks.
- Present strategies to address the challenges of large data health applications.

This review has concluded that the predictive nature of learning algorithms and pattern recognitions helped the healthcare industry to enter into a new era called “evidence-based medication” for saving the lives of many people at cost-effective prices.

In [7], **Palanisamy et al.** designed a framework for an implication of health analysis using big data. The data integration tools efficiently perform the knowledge discovery process. It also involves the decision-making process especially by highlighting the uncovered patterns in the manual process so that the patient can be provided medication with keen observation and care. A perspective analyzer of integration tool extracts information from big data platforms by taking smart decisions, and it works rapidly by pipeline with architectures that support cloud computing platforms. The searching tools integrated with map-reduce algorithms help to search in different platforms with low latency. These act as very scalable and good concurrent systems. The stream data processing tool checks the fault tolerance by internally creating distributed systems in the data centers. The data visualization tools provide a very friendly user interface to update clinical reports and generate their insights in user understandable format. Further care for details of health information is a security mechanism. This diversity feature demonstrates the availability of health data in different forms including textual, graphical, image, and others also.

36.3 Proposed System

In the proposed paper, the dataset contains class labels for 42 types of diseases varying from AIDS to allergy by taking 132 symptoms as features into account. The dataset contains a total of 4920 instances of various persons. All the previous studies have applied individual traditional machine learning algorithms, but the

proposed paper wants to implement the stacking of multi-classification algorithms since the class labels of the given dataset contain more than two class labels.

The dataset contains no missing data, as well as all the values in the feature vectors are represented either with 1 if the person is suffering from symptom; otherwise it is 0. The dataset does not contain any categorical data or nominal data. So, there is no need to apply a data preprocessing model for this data. In general, the reduced feature set improves the efficiency of the model but since it is a healthcare dataset and it wants to predict the class label out of 42 diseases, the model has decided to ignore the feature engineering step. So, the dataset is directly fed as input to the stacking models as shown in Fig. 36.1.

The stacking ensemble machine learning algorithm is a meta-learning algorithm which combines the best-predicted class labels, which are generated by the different traditional machine learning algorithms. This algorithm is a two-folded approach that is performed incrementally, the first fold is known as “level 0,” and all the selected algorithms are appended to level 0 and are known as “base classifiers.” The second fold is known as “level 1,” and the algorithm used in this level is “meta-classifier.” Decision tree, support vector machine, and KNN algorithms are used as a basic implementation classifier, which compiles the predictions by training the model, and logistic regression is used as the meta-classifier, which combines the best predictors obtained in the first fold. In the first fold, all the models work on the training data alone by splitting the test data separately and it uses 5-folded cross-validation so that it can randomly train the data, which helps in covering different types of disease records. In the second fold, the meta-classifier interprets the predictions made by the base classifiers and finds the best-predicted label based on the accuracy values.

Decision tree classifier is a tree-based learning model that constructs a tree with features as internal nodes and class labels as leaf nodes. The splitting of the tree is

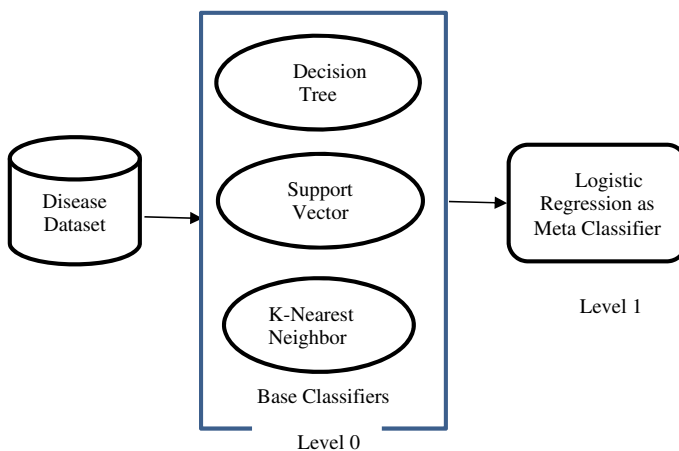


Fig. 36.1 Stacking implementation for disease prediction application

based on the entropy calculated for each feature to check the impurity of the node. This process of splitting the tree continues until all the nodes in the considered subset are pure. Based on the entropy, the information gain value is computed, and the higher the entropy value higher will be the probability of a node to be selected. Decision trees are simple nonparametric algorithm which does not need any additional effort for checking the hyperparameter values. The decision tree generates simple if and else rules to infer the variables and generate the target values.

Support vector machine is linear algorithm that can be used for both classification and regression. It is the best geometrical model that can plot data as points on the coordinate system. The major objective of SVM is to define a right hyperplane that precisely predicts the class label. The SVM algorithm in the proposed paper uses a nonlinear kernel, which is a mathematical function used to manipulate the data points since the dataset is imbalanced and multi-classification problem dataset. In this paper, SVM uses a nonlinear kernel function known as ‘‘Gaussian radial basis.’’ The power of GRB lies in its exponential equation which can be computed as shown in Eq. 36.1.

$$\text{GRBK}(Y, f(Y)) = e^{\frac{-(Y-f(y))^2}{2\gamma^2}} \quad (36.1)$$

where $(y, f(y))$ represents data points in the n-dimensional space.

γ is a constant value that should be supplied by the programmer based on the application. K-nearest neighbor is nonparametric algorithm that is suitable for constructing both classification trees and regression trees. The algorithm searches the entire dataset, predicts the class label by computing the distance, and assigns rank based on the distance. The algorithm considers the points that are less than or equal to K value. In this paper, the Minkowski distance is computed as shown in Eq. 36.2

$$\text{Mink}(D) = \left(\sum_{i=1}^n (X_i - Y_i)^p \right)^{\frac{1}{p}}. \quad (36.2)$$

where X_i and Y_i are a set of data points and $p \geq 1$.

36.3.1 Algorithm for KNN

Input: Disease Prediction Dataset, D, and Test data, t

Output: Predict the class label of test data

Begin:

1. Load the dataset D.
2. Input the number of neighbors, K.

3. Compute the Minkowski distance in between the neighbors.
4. Sort the first K neighbors which are nearer to the data point.
5. For each similar cluster, count the number of instances and assign the new data points.
6. Input the test data whose value has to be predicted.
7. Print the class label for the test data.

End.

36.4 Experimental Results

The proposed system uses a stacking mechanism and obtains the value as represented in Fig. 36.2, which represents the confusion matrix [8]. The accuracy of the model is determined by dividing all the true positive values by total number of records which represents the relation between the values predicted by the system and actual system. The results have shown that model has obtained 100% accuracy which means that the system has predicted all the values exactly similar to the actual values in the test data passed as input to the training model. Since the system supports multi-classification, the accuracy has computed per each class against the other classes available. Since the model has achieved 100% accuracy, the precision and recall also almost reached to 100%.

In this paper, the model has compared individual algorithm accuracies with the stacking algorithm and the results are plotted in Fig. 36.3. From this figure, it has observed that traditional approaches are performing less in terms of all metrics.

```

accuracy score of Stacked model: 100.0
The Output of the Confusion Matrix is:
[[18  0  0 ...  0  0  0]
 [ 0 22  0 ...  0  0  0]
 [ 0  0 31 ...  0  0  0]
 ...
 [ 0  0  0 ... 20  0  0]
 [ 0  0  0 ...  0 28  0]
 [ 0  0  0 ...  0  0 24]]

```

Fig. 36.2 Confusion matrix for stacked algorithm

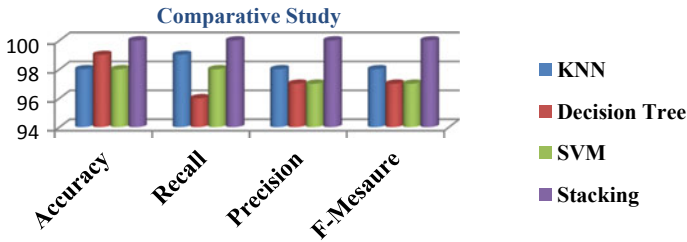


Fig. 36.3 Comparative study between individual algorithms and stacking algorithms

36.5 Conclusion

In the proposed paper, the stacking algorithm is implemented because it is considered a greedy technique, and in every cross-folded validation it picks only the best-predicted class label, and even the class label exists in different forms of data. The comparative study represented in figure Z clearly says that the stacking algorithm has received good accuracy when compared to the individual algorithm implementations. The proposed algorithm has achieved 100% accuracy, which represents an overfitting problem. So in further studies, mechanisms that handle the overfitting problem can be incorporated along with stacking algorithm and achieve accurate predictions so that it helps the patients not to enter into panic situations.

References

1. Prospero, M., Min, J.S., Bian, J., et al.: Big data hurdles in precision medicine and precision public health. *BMC Med Inform Decis Mak* **18**, 139 (2018). <https://doi.org/10.1186/s12911-018-0719-2>
2. Papineni, S.L.V., Yarlagadda, S., Akkineni, H., Mallikarjuna Reddy, A.: Big data analytics applying the fusion approach of multicriteria decision making with deep learning algorithms. *Int. J. Eng. Trends Technol.* **69**(1), 24–28. <https://doi.org/10.14445/22315381/IJETT-V69I1P204>
3. Chen, M., Hao, Y., Hwang, K., Wang, L., Wang, L.: Disease prediction by machine learning over big data from healthcare communities. *IEEE Access* **5**, 8869–8879 (2017). <https://doi.org/10.1109/access.2017.2694446>
4. Nair, L.R., Shetty, S.D., Shetty, S.D.: Applying spark based machine learning model on streaming big data for health status prediction. *Comput. Electr. Eng.* **65**, 393–399 (2018). <https://doi.org/10.1016/j.compeleceng.2017.03.009>
5. Mehta, N., Pandit, A.: Concurrence of big data analytics and healthcare: a systematic review. *Int. J. Med. Informatics* **114**, 57–65 (2018). <https://doi.org/10.1016/j.ijmedinf.2018.03.013>
6. Manogaran, G., Lopez, D.: A survey of big data architectures and machine learning algorithms in healthcare. *Int. J. Biomed. Eng. Technol.* **25**(2/3/4), 182 (2017). <https://doi.org/10.1504/ijbet.2017.087722>
7. Palanisamy, V., Thirunavukarasu, R.: Implications of big data analytics in developing healthcare frameworks—A review. *J. King Saud Univ. Comput. Inf. Sci.* (2017). <https://doi.org/10.1016/j.jksuci.2017.12.007>

8. Disease Dataset: <https://www.kaggle.com/kaushil268/disease-prediction-using-machine-learning>
9. Shaik, R., Padmanabhuni, S.S.: Heart disease prediction using machine learning techniques. *Int. J. Recent Technol. Eng.* **7**(5C), 101–104. <https://doi.org/10.35940/ijrte.d4537.118419>
10. Usama, M., Ahmad, B., Xiao, W., Shamim Hossain, M., Muhammad, G.: Self-attention based recurrent convolutional neural network for disease prediction using healthcare data. *Comput. Methods Prog. Biomed.* **190**, 105191 (2020). ISSN 0169-2607. <https://doi.org/10.1016/j.cmpb.2019.105191>
11. Lin, R., Ye, Z., Wang, H., Wu, B.: Chronic diseases and health monitoring big data: a survey. *IEEE Rev. Biomed. Eng.* **11**, 275–288 (2018). <https://doi.org/10.1109/RBME.2018.2829704>

Chapter 37

Experimental Investigation on Performance and Emission Characteristics of Mixture of Sunflower and Soybean Biodiesels



Shiva Kumar Reddy Devasani and K. Krishna Murthy

Abstract Performance and emission characteristics of various biodiesel blends prepared in a ratio by volume from a mixture of sunflower and soybean biodiesels are studied. It was found that the engine's performance characteristics like indicated power, indicated mean effective pressure, and the volumetric efficiency of the blend D70X15Y15 are higher than the other blends (16.75, 1.3, and 0.77%). It was also found that the blend D40X40Y20 has a significant effect on the break thermal and mechanical efficiencies than the other blends (23.32 and 17.83%). The air/fuel ratio is decreased with the increased load of all blends. The percentage of decrease in A/F is about 0.24–4.3%. And for all other blends, there is an increase in the A/F ratio. The emission characteristics of all blends are presented for the load. A significant decrease in CO and CO₂ emissions for the biodiesels D50X25Y25, D70X15Y15, D40X30Y30 up to 7.96–15.74% and 1.26–12.94% than that of diesel, respectively. The nitrogen oxides are decreased up to 4.8–18.2% with blends D70X25Y5, D40X30Y30, and X100 Y100. The smoke opacity for all blends X100 and Y100 are decreased up to 11.7–20.6%.

37.1 Introduction

The energy which is using today is mostly produced from fossil fuels such as coal and petroleum [1]. But with the increased usage of fossil fuels, these fuels are going to extinct in a few years. Along with this problem, with the use of fossil fuels, there is another major environmental degradation problem [2]. Biofuels have the potential to supply the required energy and overcome the difficulties of air pollu-

S. K. R. Devasani (✉)

Mechanical Engineering Department, Bachelor of Technology, VNR VJIET,
Hyderabad, India

K. K. Murthy

Mechanical Engineering Department, VNR VJIET, Hyderabad, India
e-mail: krishnamurthy_k@vnrvjiet.in

tion, price hikes, global warming, and sustainability [3]. The biodiesels produce very few pollutants as compared to fossil fuels and are non-hazardous [4]. Biodiesel is nothing but mono-alkyl esters of long-chain fatty acids. These are made from natural triglycerides, which are present in vegetable oils. This production is done with a process of transesterification along with a catalyst [5].

A lot of research has also been carried out to improve the biodiesel yield from transesterification. Many researchers are conducting analytical and experimental investigations on the performance of biodiesels on the engine and their emissions [6]. Elkelawy et al. conducted test on soybean and sunflower biodiesel performance on a diesel engine, combustion and emission analysis. It was found that biodiesel of the volumetric percentage of 30, 50, and 70% showed a decrease in CO, HC, and CO₂ emissions about 2.54–10.15%, 1.83–4.18%, and 6.06–14.17%, respectively. BSFC increased by approximately 2.44–11.43% [7]. Lahane et al. done an investigation on the effect of different blends of biodiesel and diesel on the performance and emission characteristics of a diesel engine. There was a decrease in CO, HC, and smoke emissions, increasing the biodiesel ratio to B100. Brake-specific. But it was observed that it decreased at a load of 50, 75, and 90% [8]. Patil et al. did investigations of the effect of mixed blends of biodiesel. The brake-specific fuel consumption and mechanical efficiencies were higher than that of diesel by 3.62 and 4.63% at rated load. Exhaust gas temperature was 14.70% higher at the no-load condition and 6.03% higher at the rated load condition than diesel [9]. Mubarak et al. had evaluated *Salvinia molesta* oil biodiesel blends on combustion, performance, and emissions of the diesel engine. The maximum brake thermal efficiency BTE of 29.51% and minimum brake-specific fuel consumption BSFC of 0.3081 kg/kWh with a B20 biodiesel blend was observed. The emission analysis for this blend on the same engine showed that the maximum reductions of CO, CO₂, UBHC, NO emissions, and smoke were 14%, 3.38%, 20.83%, 12.86%, and 10.99%, respectively, relative to that of diesel [10].

Many works which were done can be inferred from the above literature review, but further more works need to be done on mixtures of biodiesels. The investigation needs to be done on the mix of two biodiesels, and their characteristics are being studied.

37.2 Experimental Setup

37.2.1 *Experimental Setup and Significant Components*

An experimental investigation is carried out on a single-cylinder four-stroke water-cooled VCR multi-fuel engine. The setup having a power of 3.50 kW at 1500 rpm, which is constant speed, with cylinder bore 87.50 (mm), stroke length 110.00 (mm), connecting rod length 234.00 (mm), compression ratio 18.00, swept volume 661.45 (cc), and orifice diameter (20.00 mm) (Fig. 37.1).



Fig. 37.1 a Engine setup and b smoke meter and gas analyzer

The setup consists of various instruments and sensors to measure engine parameters like pressure, temperature, fuel consumption, coolant water flow rate into the engine and calorimeter, speed of the engine, brake power, etc. The test is conducted with all the blends at constant speed by varying load on the engine.

37.2.2 Blend Preparation

The transesterification process prepares pure sunflower biodiesel (100%) and pure soybean biodiesel (100%). Ten samples are prepared for the investigation, including diesel. These blends are prepared and stirred with the help of a stirrer. Out of them, three samples were 100% pure diesel, 100% pure soybean biodiesel, and 100% pure sunflower biodiesel. The other seven samples are prepared by mixing the sunflower and soybean biodiesels with diesel in different proportions by volume. One blend is prepared by mixing soybean and sunflower biodiesels in equal ratios by volume (50 + 50%). Out of the other six blends, three blends are prepared by mixing biodiesels in equal amounts and diesel. Those three blends are: D50B50 (diesel 50% + sunflower 25% + soybean 25%), D70B30 (diesel 70% + sunflower 15% + soybean 15%), and D40B60 (diesel 40% + sunflower 30% + soybean 30%) (Fig. 37.2 and Table 37.1).



Fig. 37.2 a Bomb calorimeter and b prepared biodiesel samples

Table 37.1 Thermal properties of fuel samples

Property	Diesel (D100)	Soybean oil	Sunflower oil	Sunflower (X100)	Soybean (Y100)	D0 + X50 + Y50
Density (gm/cm ³)	838	910	920	705	822	899
Calorific value (kJ/kg)	45,000	32,900	32,600	40,891	40,565	38,235
Property	D50 + X25 + Y25	D70 + X15 + Y15	D40 + X30 + Y30	D50 + X35 + Y15	D70 + X25 + Y5	D40 + X40 + Y20
Density (gm/cm ³)	943	950	956	895	898	896
Calorific value (kJ/kg)	40,396	41,820	39,430	41,422	40,059	38,056

The other blends are prepared by varying the ratios of both biodiesels. The mixing ratio is determined by studying their calorific values. It is observed that the calorific value of sunflower biodiesel is found to be higher than that of soybean biodiesel. Hence, the amount of sunflower biodiesel is taken in higher amounts than that of soybean in the remaining three blends. Those blends are as follows: diesel 50% + sunflower 35% + soybean 15%, diesel 70% + sunflower 25% + soybean 5%, and diesel 40% sunflower 40% + soybean 20%.

37.3 Results and Discussions

37.3.1 Performance Test of an Engine

The performance test is conducted on a single-cylinder four-stroke water-cooled VCR multi-fuel computerized engine at various loads, and the following observations are drawn.

Figures 37.3 and 37.4 show the variation of indicated power and frictional power with loads. It is observed that the indicated power increases with the increase of load on the engine. Also, friction power decreases concerning load. It is observed that the indicated power of diesel is more than that of all the biodiesel blends except one blend, D70X15Y15. It shows that these blends generate more energy than diesel for the same amount of fuel. The average increase in the indicated power of D70X15Y15 than diesel is 5.43%. Figures 37.5 and 37.6 indicate the variation of the specific fuel consumption and air–fuel ratio of various samples concerning load or brake power. It shows that the SFC and air–fuel ratio decreases with an increase in brake power. It is due to SFC depending on the brake power and A/F as the fuel's function. It is observed that the SFC for X100, Y100, and X50Y50 blends have an average increase of about 2.12%, 3.73%, 0.91%, respectively. Also shows an average decrease in the specific fuel consumption for all the other blends D50X25Y25, D70X15Y15, D40X30Y30, D50X35Y15, D70X25Y5, D40X40Y20 of 3.87%, 3.78%, 3.11%, 4.6%, 7.9%, and 4.79% respectively. Figures 37.7 and 37.8 represent the indicated and brake thermal efficiencies of all the blends for various brake power. It is found that the indicated thermal efficiency of D50X25Y25 is higher at the no-load condition, and it is decreased as the load increases. But the indicated thermal efficiency of D70X15Y15 is higher than that of all the blends as the load increases. The BTE of blend D40X40Y20 is higher than that of all other fuels, including diesel. It is due to factors like proper atomization, the formation of the air–fuel mixture. Figures 37.7 and 37.8 indicate the variation of mechanical and volumetric efficiency of an engine at different load conditions. It is observed that the mechanical efficiency increases with increase in brake power. It is notified that the friction power and indicated power are higher for the blend D70X15Y15. The mechanical efficiency is found to be higher for the blend D40X30Y30 than that of other fuels. It is because the frictional power for this blend

Fig. 37.3 Variation of indicated power

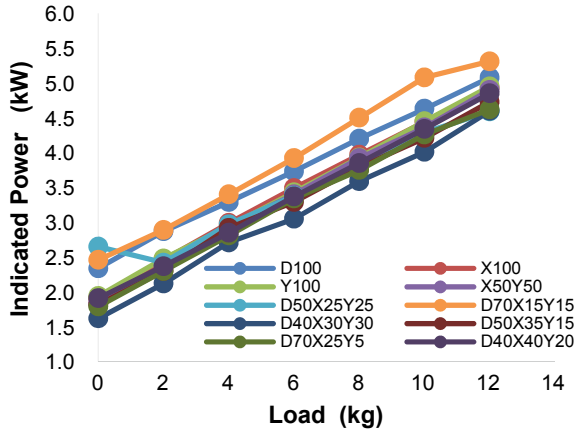


Fig. 37.4 Variation of frictional power

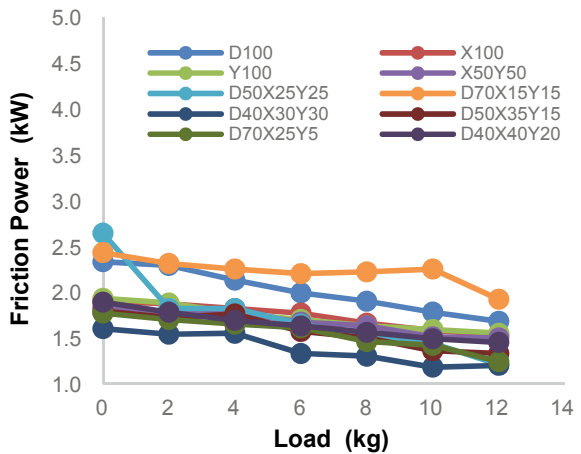


Fig. 37.5 Variation of SFC

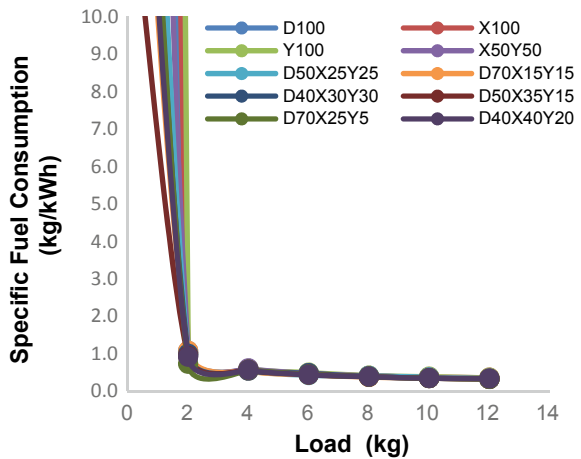


Fig. 37.6 Variation of air/fuel ratio

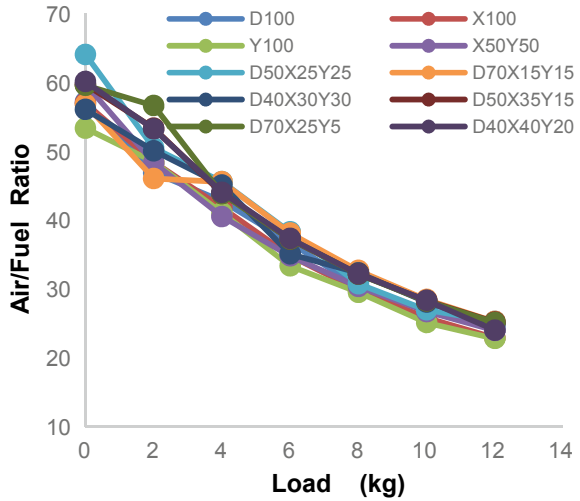
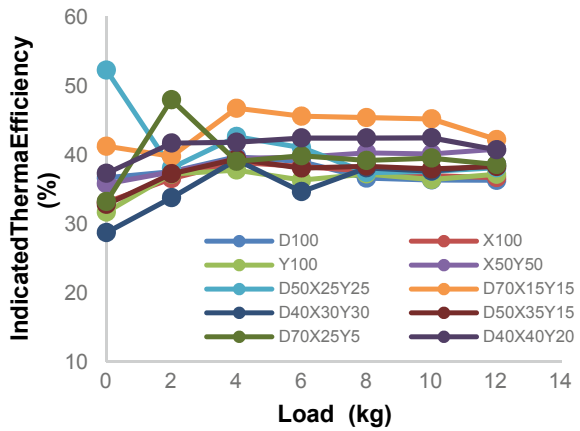


Fig. 37.7 Variation of ITE



is less compared to all other fuels. Also, the volumetric efficiency decreases with increase in brake power. It is due to less ram effect at higher load. Figures 37.11 and 37.12 show the variation of indicated mean effective pressure for various blends at different load and peak pressure in the cycle concerning crank angle. The trend of indicated mean effective pressure is similar to the indicated power trend. It is found that the imep of D70X15Y15 is higher than that of all the blends and diesel. The maximum pressure is 65.17 bar, 65.45 bar, 65.09 bar, 65.17 bar, 64.90 bar, 66 bar, 64.52 bar, 65.73 bar, 64.74 bar, and 65.19 bar for the fuel samples D100, X100, Y100, X50Y50, D50X25Y25, D70X15Y15, D40X30Y30, D50X35Y15, D70X25Y5, and D40X40Y20, respectively. X100, D70X15Y15, D40X30Y30, D50X35Y15, and D40X40Y20 biodiesel/diesel blends have achieved a little higher maximum pressure than diesel. However, all the fuel samples have shown a similar

Fig. 37.8 Variation of BTE

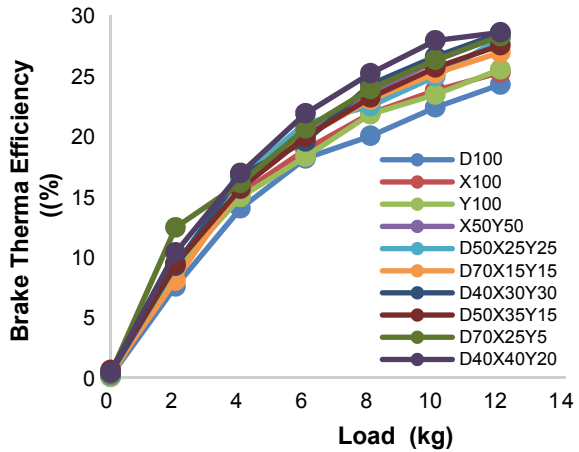
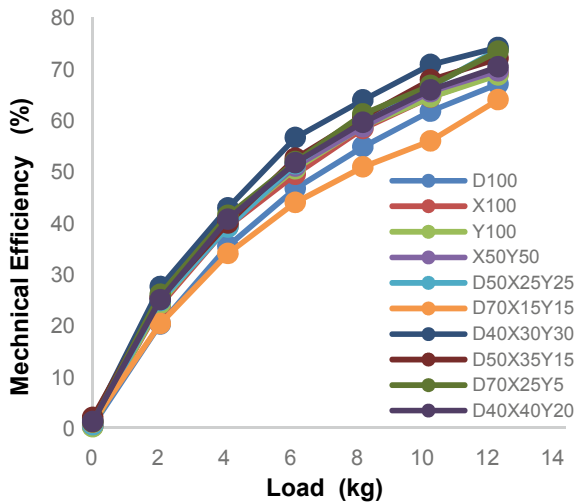


Fig. 37.9 Variation of mechanical efficiency



trend for pressure variation for a load. The start of combustion (SOC) of diesel is earlier than that of biodiesels except for D50X25Y25. It is due to that the diesel possesses a higher cetane number than that of those biodiesels except D50X25Y25. The slight increase or decrease in maximum pressure for biodiesel blends relative to diesel is due to the variation in ignition delay compared to diesel. Figures 37.13 and 37.14 indicate the effect of the heat release rate in a combustion and heat balance sheet of various samples. The study of heat release rate helps to analyze the rate of conversion of chemical energy of the fuel to the heat energy. In this work, all the blends' heat release rate is decreased insignificantly compared to diesel except for three blends D50X25Y25, D40X30Y30, and D70X15Y15. These three blends have

Fig. 37.10 Variations of volumetric efficiency

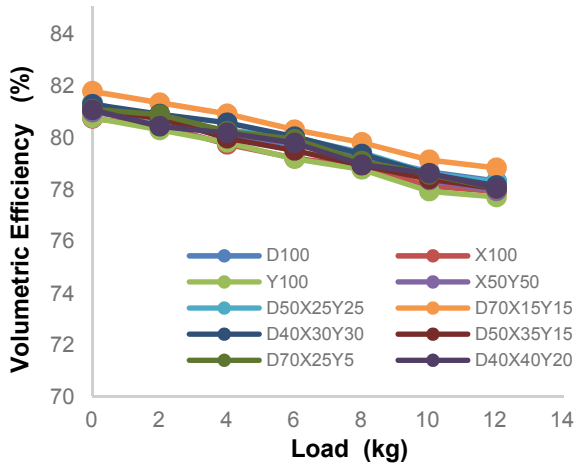
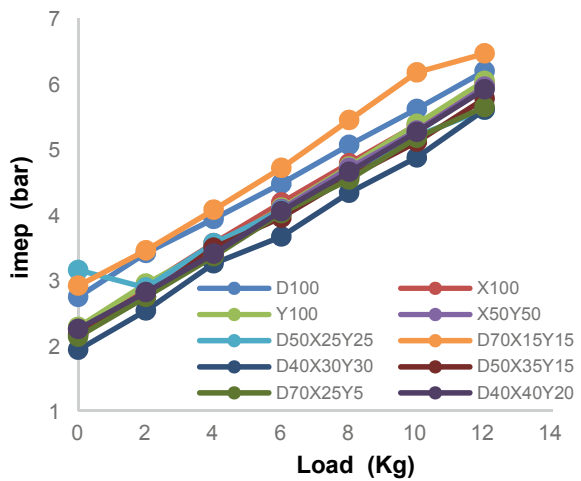


Fig. 37.11 Variation of imep



a very slight increase in HRR. The decrease of HRR in other blends indicates that the ignition lag is more and the combustion is more progressive than diesel (Figs. 37.9 and 37.10).

37.3.2 Emission Characteristics Analysis

Figure 37.15 shows the emission characteristics of smoke opacity for various loads on the engine of different blends. It is observed that the percentage of smoke increases with increasing load. It is due to incomplete combustion at higher loads.

Fig. 37.12 Variation of cylinder pressure

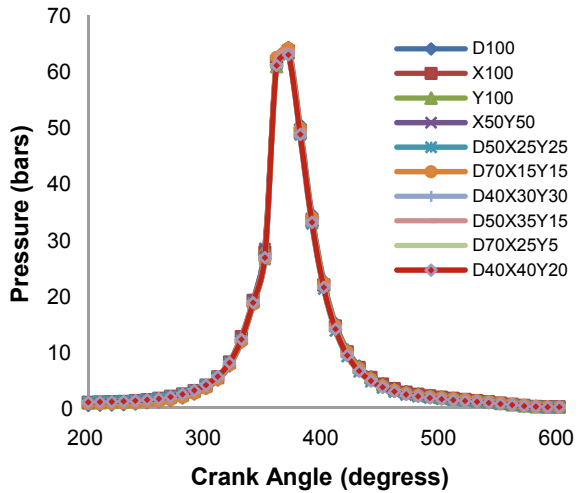
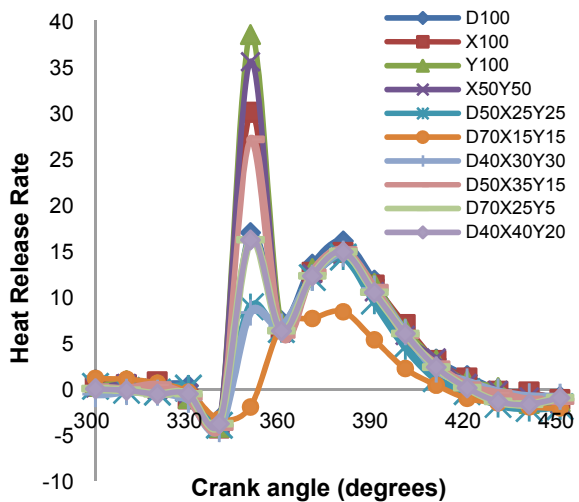


Fig. 37.13 Variations of heat release rate



When the biodiesels are blended with diesel, the smoke content is reduced. It is also observed that for two pure biodiesels, X100 and Y100, the smoke produced is more than diesel. The smoke opacity is less for the remaining blends. It is due to the oxygen content in biodiesels. The average decrease in smoke opacity for the blends X50Y50, D50X25Y25, D70X15Y15, D40X30Y30, D50X35Y15, D70X25Y5, and D40X40Y40 are 11.7%, 13.5%, 20.5%, 14.8%, 33.5%, 19.5%, and 20.63%, respectively. Figure 37.16 indicates the emission characteristics of carbon monoxide for various loads of different blends. It is seen that the CO emissions decreased with respect to load. It is due to incomplete combustion at higher loads. It is also observed that the CO emissions are decreased for the blends D50X25Y25,

Fig. 37.14 Heat balance sheet

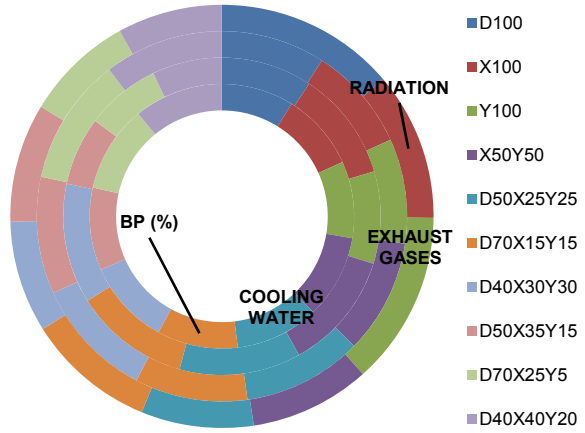


Fig. 37.15 Emission characteristics of smoke

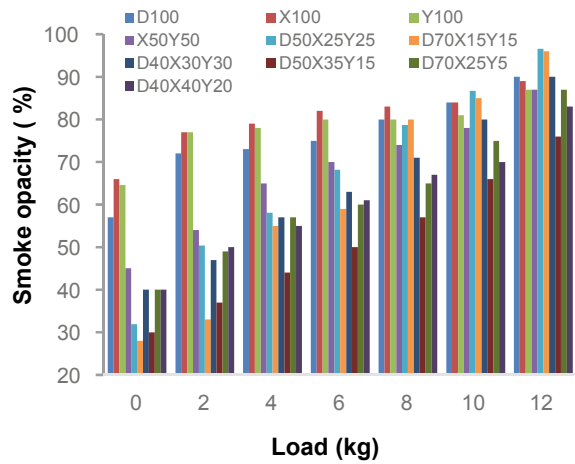


Fig. 37.16 Emission characteristics of CO

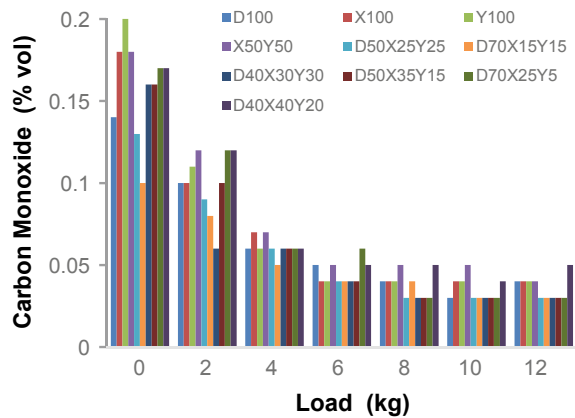


Fig. 37.17 Emission characteristics of HC

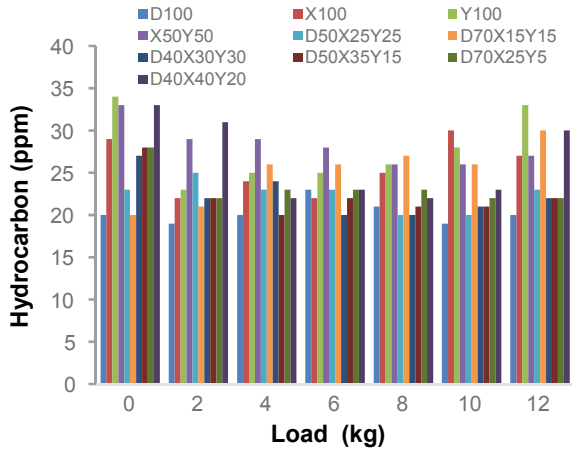
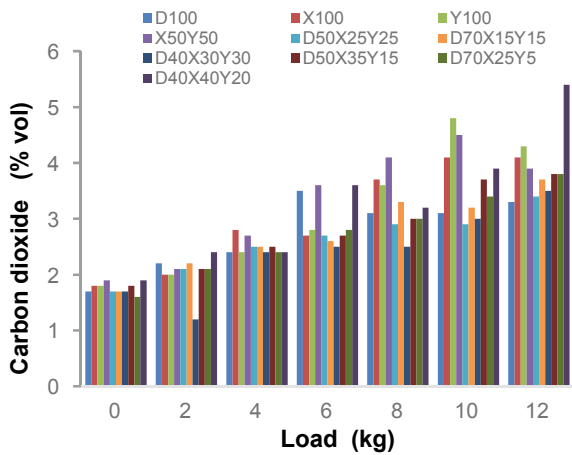


Fig. 37.18 Emission characteristics of CO₂



D70X15Y15, D40X30Y30, and D50X35Y15 relative to diesel, and the average decrease in CO emissions for these blends are 12.45%, 15.75%, 13.67%, and 7.96%, respectively. CO of the following blends, X100, Y100, X50Y50, D70X25Y5, and D40X40Y20 are increased insignificantly.

Figure 37.17 shows the emission characteristics of hydrocarbons of different blends at various loads. It is observed that the hydrocarbon emissions are mainly due to incomplete combustion. It is found that there is an increase in the hydrocarbon emissions for the blends compared to diesel. It is due to the rapid and incomplete combustion of the fuel. Figure 37.18 signifies the percentage of the volume of CO₂ of samples for different loads. It shows a decrease in CO₂ emissions for some of the biodiesel blends than the diesel. These blends X100, Y100, D70X15Y15, D50X35Y15, and D40X40Y20 showed an unnoticeable increase in the CO₂ emissions compared with the diesel. It also observed that these blends

Fig. 37.19 Emission characteristics of O₂

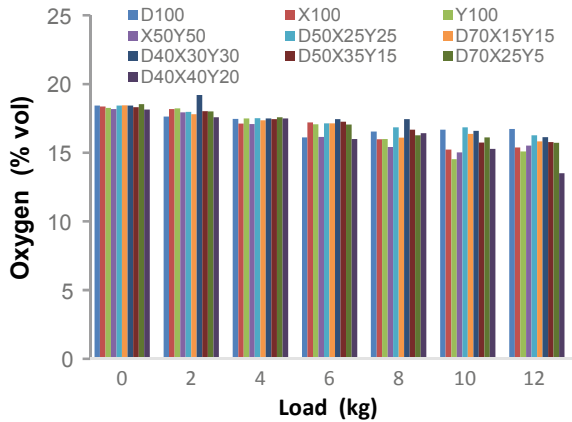
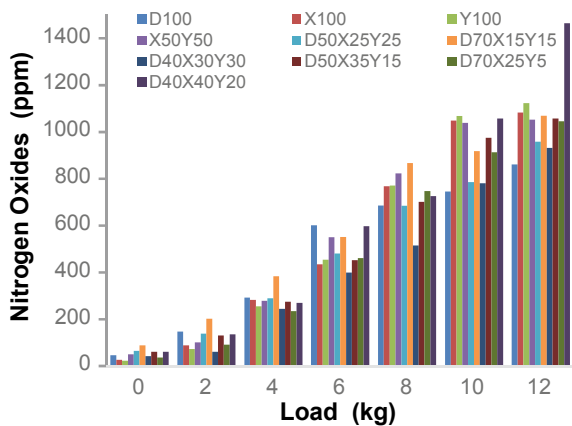


Fig. 37.20 Emission characteristics of NO_x



D50X25Y25, D40X30Y30, and D70X25Y5 are shown an average decrease in CO₂ emissions of 4.73%, 12.94%, and 1.26%, respectively. It is due to incomplete combustion and the lower carbon to hydrogen ratio. Figures 37.19 and 37.20 indicate the oxygen rate and emission characteristics of NO_x at various loads of different blends. It is observed that the percentage of oxygen decreases with increasing load. It is also observed that the NO_x emissions increase with increasing load. It is noticed that the NO_x emissions are more than that of diesel due to more oxygen content for biodiesel blends, generally. These blends X100, Y100, D40X30Y30, and D70X25Y5 decrease trend emissions characteristics in NO_x than the diesel. The average decrease in NO_x emissions for the blends is 4.8%, 7.8%, 18.2%, and 7%, respectively. It is observed that the following blends X50Y50, D50X25Y25, D70X15Y15, D50X35Y15, and D40X40Y20 are having an increase in NO_x emissions with an average increase of 6.5%, 4.5%, 32.5%, 6.6%, and 19.2%, respectively.

37.4 Conclusions

An experimental investigation is carried out on a single-cylinder four-stroke water-cooled VCR multi-fuel engine test rig, and the following observations are drawn:

- It is observed that the indicated power is decreased for all the blends except for blend D70X15Y15. It is also notified that the average increase in indicated power is about 5.43% compared to diesel. And also, this blend is achieved higher imep than other blends, including diesel.
- It shows that the blend D70X15Y15 has higher indicated thermal efficiency, which is about 16.75% higher than that of diesel. It is also identified that the brake thermal efficiency is found to higher for the blend D40X40Y20. The value of the percentage increase of brake thermal efficiency is 23.32% relative to diesel.
- It is noted that the blend D70X15Y15 has less mechanical efficiency, and D40X30Y30 has more mechanical efficiency. The percentage increase in efficiency for this blend is 17.83% compared to diesel.
- It observed that the heat release rate of all the blends was decreased insignificantly compared to diesel except for three combinations D50X25Y25, D40X30Y30, and D70X15Y15.
- It has shown a significant decrease in CO and CO₂ emissions of biodiesels D50X25Y25, D70X15Y15, and D40X30Y30 up to 7.96–15.74% and 1.26–12.94% than that of diesel, respectively. It is observed that there is a slight increase in hydrocarbon emissions as compared to diesel.
- It is observed that for the blends D70X25Y5, D40X30Y30, X100 Y100, the nitrogen oxides decreased up to 4.8–18.2%, and it is increased up to 4.5–32.5% for the remaining blends.
- The smoke opacity for all combinations except X100 and Y100 decreased up to 11.7–20.6%.

It is concluded that biodiesels have a solid potential to use as an alternative fuel. The mixture of biodiesels produces excellent results that are very promising to use as fuel for diesel engines. It is observed that the blend D70X15Y15 (diesel 70% + sunflower 15% + soybean 15%) shows superior performance and emission characteristics than the other blends and diesel.

References

1. Efe, Ş., Ceviz, M.A., Temur, H.: Comparative engine characteristics of biodiesels from hazelnut, corn, soybean, canola and sunflower oils on di diesel engine. *Renew. Energy* **119**, 142–151 (2017)
2. Bora, D.K., Baruah, D.C., Das, L.M., Babu, M.K.G.: Performance of diesel engine using biodiesel obtained from mixed feedstock. *Renew. Sustain. Energy Rev.* **16**, 5479–5484 (2012)

3. Gad, M.S., El-Shafay, A.S.: Assessment of diesel engine performance, emissions and combustion characteristics burning biodiesel blends from jatropha seeds. *Process Saf. Environ. Prot.* **147**, 518–526 (2020)
4. Sudalaiyandi, K., Alagar, K., Vignesh Kumar, R., Manoj Praveen, V.J., Madhu, P.: Performance and emission characteristics of diesel engine fueled with ternary blends of linseed and rubber seed oil biodiesel. *Fuel* **285**, 1–9 (2020)
5. Pramanik, K.: Properties and use of jatropha carcass oil and diesel fuel blends in compression ignition engine. *Renew. Energy* **28**(2), 239–248 (2003)
6. Shenawy, E.A., Elkelawy, M., Bastawissi, Ha, E., Panchal, H.: Comparative study of the performance, and emission characteristics of a direct injection diesel engine with a partially premixed lean charge compression ignition diesel engines. *Fuel* **249**, 277–285 (2019)
7. Elkelawy, M., et al.: Experimental studies on the biodiesel production parameters optimize sunflower and soybean oil mixture and DI engine combustion, performance, and emission analysis fueled with diesel/biodiesel blends. *Fuel* **255**, 1–12 (2019)
8. Lahane, S., Subramanian, K.J.F.: Effect of different percentages of biodiesel-diesel blends on injection, spray, combustion, performance and emissions characteristics of a diesel engine. *Fuel* **139**, 537–545 (2015)
9. Patil, S.D., Pawar, R.V., Sha, A.P.: Experimental analysis of effect of mixed biodiesel blends on performance, combustion, and emission of variable compression ratio engine. *mmc_c* **80**, 24–31 (2019)
10. Mubarak, M., Shaija, A., Suchithra, T.V.: Experimental evaluation of *Salvinia molesta* oil biodiesel/diesel blends fuel on combustion, performance and emission analysis of diesel engine. *Fuel* **287**, 1–8 (2020)

Chapter 38

Experimental Study of Nano Additive-Added Biodiesel Blend to Improve the Engine Performance Characteristics



B. Jayakrishnan and D. Senthilkumar

Abstract Biodiesel is the most promising alternative source to petroleum fuel which reduces emissions as well as the dependence on fossil fuels. Nanoparticles are used as combustion catalysts to improve performance characteristics and to reduce emissions. In this experiment, copper oxide (CuO) nanoparticle are added to the Jatropha biodiesel B10 and B20 blends for this study. Jatropha biodiesel is used in the blend of B10 and B20. Copper oxide is added in 50 and 100 ppm to the Jatropha biodiesel blend. The experimental results show that the performance and emission characteristics have been improved by adding copper oxide to the Jatropha biodiesel blends. BSFC reduces by 9.2%, brake thermal efficiency increases by 10.2%, and NO_x, CO, HC, and smoke emissions are reduced by 17%, 25%, 20%, and 11.5%, respectively for B20 with 100 ppm of CuO nanoparticles.

38.1 Introduction

Among India's transportation, about 95% heavily relies on petroleum-based fuel. Petroleum has been widely used and has a lot of advantages. However, it has an undesirable impact on the environment, cost, and availability. Biodiesel is one of the most promising alternative fuels that can be used as diesel alternative. The Jatropha biodiesel has similar properties to diesel. The expenses to cultivate the Jatropha are very less when compared with other biodiesel and the cost of Jatropha seed is also very low. Jatropha biodiesel has a higher flash point and calorific value than any other biodiesel. The nano additives added in fuel blends act as a catalyst

B. Jayakrishnan

PG Automotive Engineering Student, Amrita School of Engineering,
Amrita Vishwa Vidyapeetham, Coimbatore, India

D. Senthilkumar (✉)

Department of Mechanical Engineering, Amrita School of Engineering,
Amrita Vishwa Vidyapeetham, Coimbatore, India
e-mail: d_senthilkumar@cb.amrita.edu

that promotes combustion which in turn results in the complete burning of fuels. Nano additives vary the fuel chemical composition which leads to improved emission characteristics.

Perumal et al. [1] investigated the performance and emission characteristics of a diesel engine-fueled CuO nanoparticles-added Pongamia biodiesel blends. The results indicate that BSFC reduces by 1.0%, BTE improves by 4.01%. For B20 biodiesel blends, CO, HC, smoke, and NO_x emissions reduce by 29%, 7.9%, 12.8%, and 9.8%, respectively. Soner Gumus et al. [2] investigated the effect of aluminum oxide and copper oxide nanoparticles-blended diesel fuel on engine performance and emissions characteristics. This study uncovers that nanoparticle expansion within the diesel blends does not result in any complications within the physicochemical properties and creates great stability. CO, NO_x, and HC emissions reduces with the addition of nano additives to neat diesel and also reduces BSFC.

Amit et al. [3] investigated the performance of CI engine fueled with Jatropha biodiesel blended cobalt oxide and iron oxide nano molecule. The result appears to higher brake thermal efficiency of 32.5%, which is more prominent than brake thermal efficiency, 32% of neat diesel and BSFC around 0.270 kg/kWh as compared to 0.280 kg/kWh of neat diesel. Kalaimurugan et al. [4] conducted the study on the impact of blending copper dioxide (CuO₂) nanoparticles to Neochloris oleoabundans methyl ester-diesel-blended fuel on CI engine. Nanoparticles-added biodiesel blends improves brake thermal efficiency, brake-specific fuel consumption and exhaust gas temperature. CO, HC and smoke opacity reduces when CuO₂ nanoparticle-added to biodiesel blends.

Gada et al. [5] researched the performance and exhaust emission characteristics of a diesel engine fueled with Jatropha biodiesel blend with the nano-added substances such as carbon nanotubes (CNTs), titanium dioxide (TiO₂), and aluminum oxide (Al₂O₃) at 25 ppm, 50 ppm and 100 ppm, individually. The results show that when the Jatropha biodiesel blends are added with Al₂O₃, it improves performance parameter and also reduces the specific fuel consumption. When CNTs are added to Jatropha biodiesel blends, CO, NO_x, and smoke emissions reduces compared to other nano additives. Najafi et al. [6] researched the impact on the combustion parameters of a CI engine using CNT and Ag nanoparticles. When 120 ppm of carbon nano tubes are added with biodiesel blends, the peak pressure increases up to 15.38%. Ignition delay reduces by 8.98% with 120 ppm of carbon nano tubes added biodiesel blends compared to neat diesel.

Several studies [7, 8] show that adding nano additive to biodiesel blends results in improved performance and emission parameters. Nano additive has the property to alter the chemical composition of the fuel, which results in an improved performance and emission characteristics. The nano additive will act as the combustion catalyst due to its higher surface area, even at a low mass fraction. Several studies [9] are conducted using carbon nano tubes (CNT), silver oxide (AgO), titanium oxide (TiO₂), copper oxide (CuO), zinc oxide (ZnO), aluminum oxide (Al₂O₃), cobalt oxide (CoO), iron oxide(FeO) and cerium oxide(CeO) are the nano additives which can be added to biodiesel blends. Copper oxide nanoparticle has been used because the copper oxide nanoparticle acts as a combustion catalyst for hydrocarbon fuels.

38.2 Methodology

38.2.1 Preparation of Nano Additives-Added Biodiesel Blend

The biodiesel is prepared from the *Jatropha carcus* using the transesterification process [10]. The B10 and B20 blends are prepared by adding 10% biodiesel and 20% biodiesel with diesel, respectively. The nano additives have a purity of 99.9% with an average particle size of 30–50 nm. The nano additive is completely dispersed in the biodiesel blend using the ultrasonicator. The copper oxide nanoparticle of 0.1 and 0.05 g/l are added to biodiesel blends. Span 80 is used as a surfactant. The nano additive with biodiesel blend is agitated for 30 min by using the ultrasonicator which disperse the copper oxide nanoparticles and biodiesel blends completely. The properties of diesel, B10, B20 and B10 and B20 with 50 and 100 ppm CuO nanoparticles are given in Table 38.1.

38.2.2 Experiment Setup

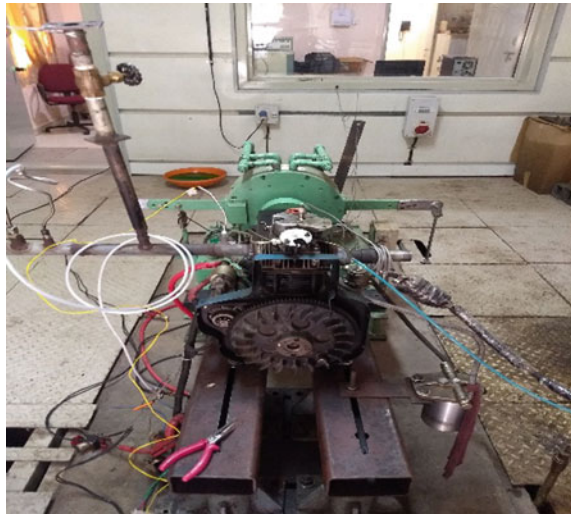
The experiment is performed on a single-cylinder air cooled four-stroke CI engine. The engine is loaded with an eddy current dynamometer. Engine specifications are shown in Table 38.2. The experiment is conducted for all loads at 2300 rpm. Figure 38.1 shows the engine in a test bed with sensors attached to it. The engine is tested with different blends with and without CuO nanoparticles. The engine is tested using diesel, B10, B20, and B10 with 50 and 100 ppm CuO, B20 with 50 and 100 ppm of CuO. The fuel consumption is measured by using the time taken for 10 cc of fuel. The emission analyzers are connected to the exhaust manifold. HC, CO, and NO_x are measured using the Horiba Automotive emission analyzer and smoke concentration are obtained using AVL 415 S smoke analyzer. Horiba emission analyzer and smoke meter specifications are mentioned in Table 38.3. The uncertainties of measured parameters are given in Table 38.4.

Table 38.1 Biodiesel blend properties

Properties	Diesel	B10	B20	B10 CuO50	B20 CuO50	B10 CuO100	B20 CuO100
Density (kg/m ³)	814	820	829	826	833	830	835
Calorific value (MJ/kg)	42.7	40.38	40.1	40.47	40.66	40.84	41.12
Kinematic viscosity (cSt)	4.83	5.48	5.73	5.97	6.2	6.34	6.56
Flash points (°C)	55	63	65	60	61	58	59

Table 38.2 Engine specifications

Parameter	Specifications
Model	Greaves GL-400
Maximum power output	5.5 kW
Bore	63 mm
Stroke	86 mm
Displacement	395 cm ³
Compression ratio	18:1
Rated speed	3600

Fig. 38.1 Engine in the test bed with sensor connected**Table 38.3** Emission measuring instruments

Model	Pollutant	Range	Resolution
MEXA 584L	NO _x	0–5000 ppm vol	1 ppm vol.
MEXA 584L	HC	0–20,000 ppm vol	1 ppm vol.
MEXA 584L	CO	0–20% vol	0.02% vol.
Smoke Meter AVL 415S	Smoke	0–10 FSN	0.001 FSN

Table 38.4 Parameters with percentage uncertainty

S. No.	Parameter	Percentage uncertainty (%)
1	BP	±1.00
2	SFC	±1.00
3	BTE	±1.45

38.3 Experimental Results

38.3.1 Brake Specific Fuel Consumption

Figure 38.2 shows the brake specific fuel consumption of various test fuels. It is observed that the brake specific fuel consumption of CuO nanoparticle-added biodiesel blend reduces when compared with biodiesel blends and diesel. The brake-specific fuel consumption reduces by 7.1% for B10 with 100 ppm nanoparticles, and it reduces by 9.2% for B20 with 100 ppm nanoparticles, respectively. The brake-specific fuel consumption reduces due to the higher calorific value of the nano additives-added biodiesel blends. When compared with existing literature based on different biodiesel blends with CuO, there is also an improvement in BSFC.

38.3.2 Brake Thermal Efficiency

Figure 38.3 shows the brake thermal efficiency of various test fuels. The result indicates that the brake thermal efficiency is higher for CuO nanoparticle-added biodiesel blends than biodiesel blends and diesel. The brake thermal efficiency increases by 8.5% for B10 with 100 ppm nanoparticles, and it increases by 10.2% for B20 with 100 ppm nanoparticles, respectively. The increase in the brake thermal efficiency is due to the increase in the calorific value of nanoparticle-added biodiesel blends.

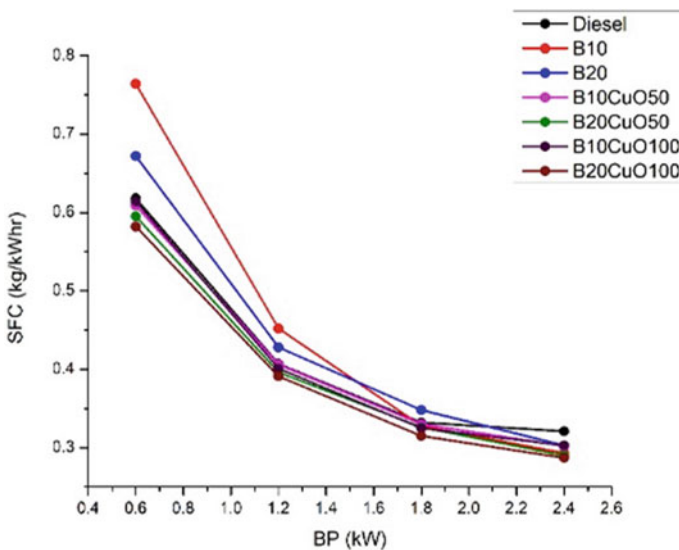


Fig. 38.2 Brake power versus brake specific fuel consumption

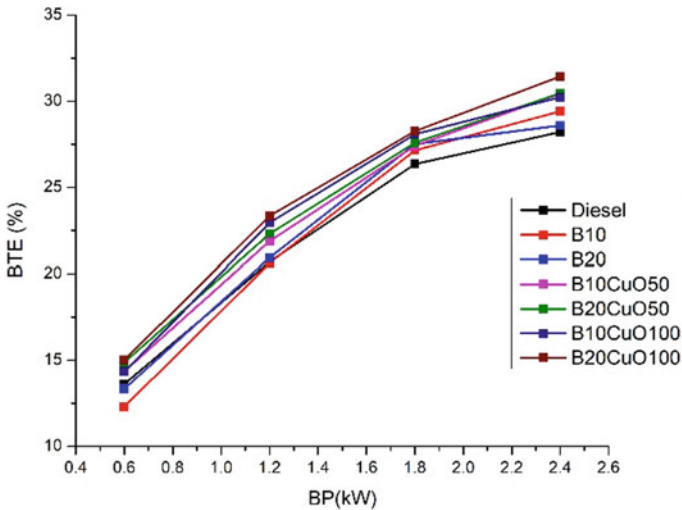


Fig. 38.3 Brake power versus brake thermal efficiency

38.3.3 Emissions

Figure 38.4 shows the NO_x emission of various test fuels. It is observed that the NO_x emission reduces when CuO nanoparticle are added to biodiesel blend when compared to biodiesel blends and diesel. NO_x emission reduces by 15.2% for B10 with 100 ppm nanoparticles, and it reduces by 17% for B20 with 100 ppm nanoparticles, respectively. The CuO nanoparticles being thermally stable promotes the nitrogen oxide reduction process which causes the reduction in the NO_x emission.

Figure 38.5 shows the CO emission of various test fuels. It is observed that the CO emission of CuO nanoparticle-added biodiesel blend reduces when compared with biodiesel blends and diesel. CO emission reduces by 20.4% for B10 with 100 ppm nanoparticles, and it reduces by 25% for B20 with 100 ppm nanoparticles, respectively. The addition of CuO nanoparticles increases oxygen content in fuel which oxidizes CO to CO_2 which causes reduction in CO emission.

Figure 38.6 shows the HC emission of various test fuels. It is observed that the HC emission of CuO nanoparticle-added biodiesel blend reduces when compared with biodiesel blends and diesel. HC emission reduces by 12% for B10 with 100 ppm nanoparticles, and it reduces by 20% for B20 with 100 ppm nanoparticles, respectively. The addition of CuO nanoparticles reduces the ignition delay as a result of complete burning which causes the reduction in the HC emission.

Figure 38.7 shows the smoke emissions of various test fuels. It is observed that the smoke emissions of CuO nanoparticle-added biodiesel blend reduces when compared with biodiesel blends and diesel. Smoke emission reduces by 10.5% for B10 with 100 ppm nanoparticles, and it reduces by 11.5% for B20 with 100 ppm

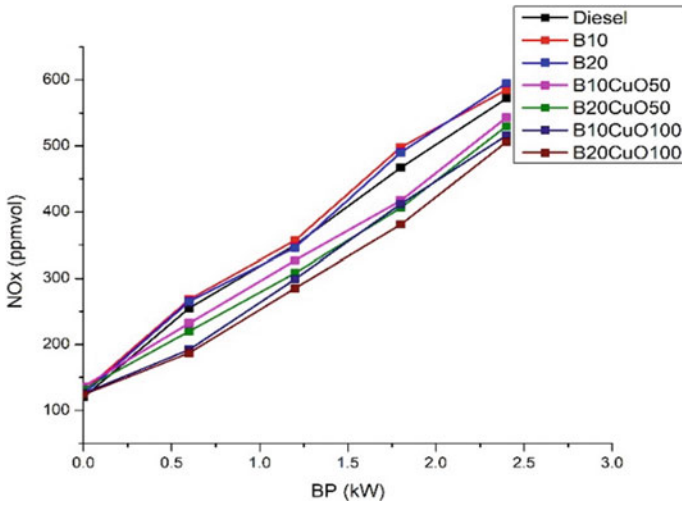


Fig. 38.4 Brake power versus NO_x emissions

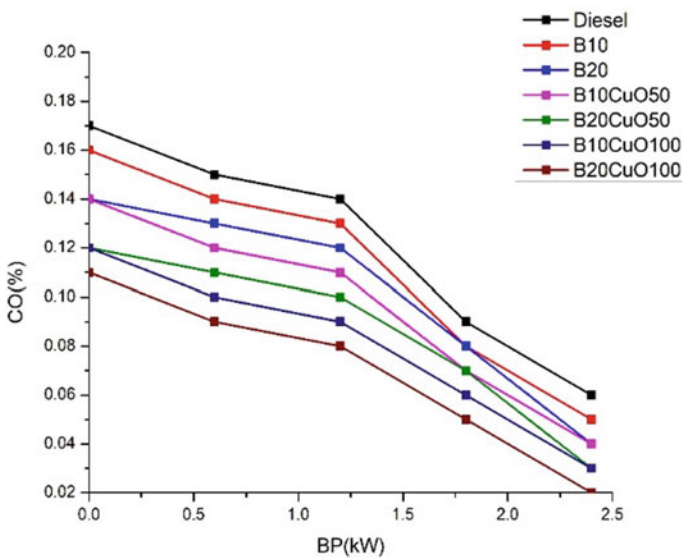


Fig. 38.5 Brake power versus CO emissions

nanoparticles, respectively. CuO nanoparticles act as combustion catalyst to accelerate the burning rate which as a result reduces ignition delay which causes the reduction of the smoke emissions.

When compared with existing literature based on different biodiesel blends with CuO, there is also a reduction in CO, HC, NO_x, and smoke emissions.

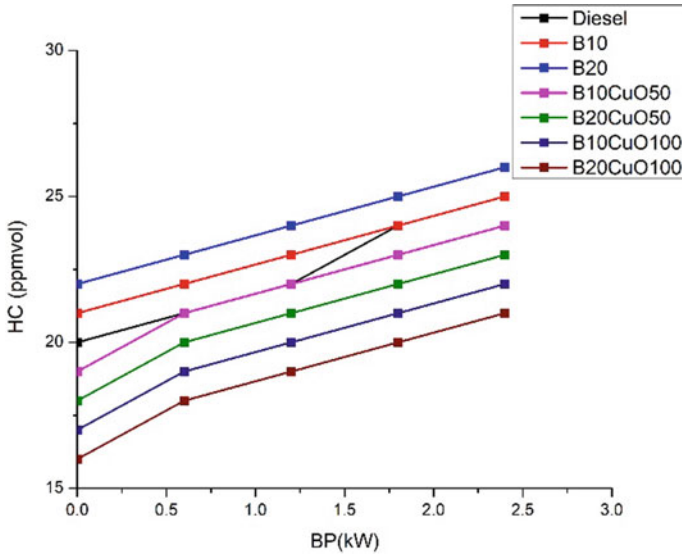


Fig. 38.6 Brake power versus HC emissions

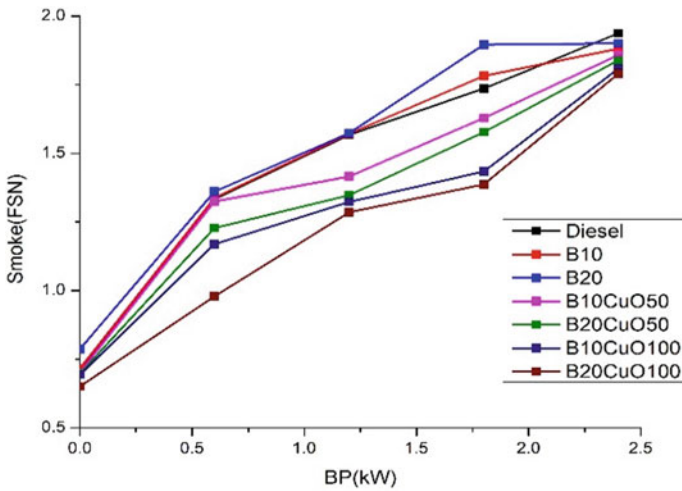


Fig. 38.7 Brake power versus smoke emissions

38.4 Conclusions

This experimental result shows that there is an improvement in the engine performance characteristics and also reduce in emission level when copper oxide nanoparticle is added with biodiesel blends. The BSFC and brake thermal efficiency are improved when nanoparticle has been added to the biodiesel blends. There is also a reduction in CO, HC, NO_x, and smoke emissions when B10 and B20 biodiesel blend is added with the copper oxide nanoparticle. B20 biodiesel blend with 100 ppm of CuO shows more improved performance and emission characteristics when compared with other test fuel blends.

- Brake-specific fuel consumption reduces by 9.2% for B20 with 100 ppm of CuO nanoparticles.
- Brake thermal emission increases by 10.2% for B20 with 100 ppm of CuO nanoparticles.
- NO_x, CO, HC, and smoke emissions reduce by 17, 25, 20, and 11.5% for B20 with 100 ppm of CuO nanoparticles.

References

1. Perumal, V., Ilangkumaran, M.: The influence of copper oxide nano particle added pongamia methyl ester biodiesel on the performance, combustion and emission of a diesel engine. *Fuel* **232**, 791–802 (2018)
2. Gumus, S., Ozcan, H., Ozbey, M., Topaloglu, B.: Aluminum oxide and copper oxide nanodiesel fuel properties and usage in a compression ignition engine. *Fuel* **163**, 80–87 (2016)
3. Amit, S.K.: Impact on the performance of direct compression ignition engine by adding nano-particle in biodiesel. *J. Mater. Sci. Mech. Eng. (JMSME)* **2**(7), 7–9 (2015)
4. Kalaimurugan, K., Karthikeyan, S., Periyasamy, M., Mahendran, G., Dharmaprabhakaran, T.: Experimental studies on the influence of copper oxide nanoparticle on biodiesel-diesel fuel blend in CI engine. *Energy Sources Part A Recovery Utilization Environmental Efficiency*. ISSN: 1556–7036 (2019)
5. Gad, M.S., Jayaraj, S.: A comparative study on the effect of nano-additives on the performance and emissions of a diesel engine run on *Jatropha* biodiesel. *Fuel* **267**, Article 117168 (2020)
6. Najafi, G.: Diesel engine combustion characteristics using nano-particles in biodiesel diesel blends. *Fuel* **212**, 668–678 (2018)
7. Reddy, V.P.K., Kumar, D.S., Thirumalini, S.: Effect of antioxidants on the performance and emission characteristics of a diesel engine fuelled by waste cooking sunflower methyl ester. *IOP Conf. Ser. Mater. Sci. Eng.* **310**, 012116 (2018)
8. Vishnu Varthan, R., Senthil Kumar, D.: Emission characteristics of turbocharged single cylinder engine. *Indian J. Sci. Technol.* **9** (2016)
9. Senthil Kumar, D., Thirumalini, S., Praveen, H.S.S.K.: Experimental investigation to improve performance and emission characteristics of a diesel engine by using n-butanol as additive to the biodiesel-diesel blends. *IOP Conf. Ser. Mater. Sci. Eng.* **577**, 012102 (2019)
10. Srihari, S., Thirumalini, S.: Investigation on reduction of emission in PCCI-DI engine with biofuel blends. *Renew. Energy* **114**, 1232–1237 (2017)

Chapter 39

Detection of Fake and Clone Accounts in Twitter Using Classification and Distance Measure Algorithms



S. Siva Rama Krishna, K. Umakanth Reddy, T. Anji Reddy, A. Saiteja, and R. Sumanjali

Abstract The social media applications like Facebook, Twitter, and others have gained a lot of name and fame and are represented as “Online Social Networks” (OSN). These networks are similar in their usage and can access with ease. With this popularity, people are sharing their personal sensitive information without checking any privacy policies, which made cyber-attacks easier nowadays. Most teenagers and women are getting affected by these cyber-attacks. Hackers take away the profile information of existing users in a profile cloning attack to create duplicate profiles, which are then used to compromise the identity of the original profile owners. This process is known as “Profile Cloning,” this cloning can be created on the same site or another site. Nowadays, hackers are creating fake profiles in cross-site, i.e., other social networks which are rare from the popular OSN walls. So, the users do not have any clue about their accounts on other platforms. Moreover, to simplify the registration process, the OSNs are not asking for authorization details which became an advantage for hackers to create millions of fake accounts. The proposed KNN algorithm is compared with the probability algorithm naïve Bayesian.

39.1 Introduction

In the world of social networking platforms, a few people are trying to do cyber-crimes by cheating the people with fake accounts. To identify the fake accounts in the OSN platforms, the proposed system wants to classify the real and fake or cloned accounts with the help of machine learning model by performing the NLP operations. Sentiment analysis is famous among the text data classifiers. To work with the

S. Siva Rama Krishna (✉)
Department of AI&DS, Lakireddy Bali Reddy College of Engineering,
Mylavaram 521230, India

K. Umakanth Reddy · T. Anji Reddy · A. Saiteja · R. Sumanjali
MCA Department, Lakireddy Bali Reddy College of Engineering,
Mylavaram 521230, India

Twitter data, the sentiment analysis marks the tweets as positive and negative by calculating the polarity of the tweet. Twitter API presents the data in the form of two datasets namely, historical and current tweets. The historical tweets analyze the patterns associated with the data in a period. The current tweets simplify the searching process by making use of hashtags. Twitter data takes the help of the NLTK library of NLP to perform the data cleaning and to explore the data. The entire quality of the proposed model is based on the cleaning step; if it is not performed accurately, it leads to machine learning algorithms to work with inconsistent and uncertain data. Then, a feature space is created only with numeric and unique data with their occurrences stored in the matrix format. The most complicated sentiment analysis case study is working with financial stock data. This financial stock data is getting more complicated if the system is based on keyword searches.

Word sense disambiguation (WSD): In natural language processing, there is a lot of scope for the word to be in an ambiguous state. So, to resolve this issue, the system extracts the context in which the word is used and the meaning is interpreted by the NLTK. There are three types of ambiguities namely lexical, syntax, and semantics. The syntactic is handled by generating the “Parts of Speech” tags and semantic is handled by “Word Sense Disambiguation.” This mechanism dictionary and test corpus as input, and it use either dictionary-based or knowledge-based methods to extract the context of utilization. There is a novel approach for this approach which is known as “**Twitter Financial Disambiguation (TFD)**,” which works on financial data to make working with these types of data simple.

39.2 Related Work

In [1], Sowmya et al. mentioned that profile cloning has become common but a serious threat among social networking sites. So, there is a need for designing a framework that can automatically detect fake account users. The author of this paper has discussed various approaches to create these sorts of models.

- a. A prototype is designed based on the user similarity score in which user information is extracted from social media and compared against other profiles by using all the attributes of the user. The prototype has statistically fixed some threshold value, and if the calculated score is greater than the threshold value, then that particular user account is declared, they seem to be exactly the same as them.
- b. The second model is based on the relationship among the various networks, i.e., this type of model detects the clone profiles in cross-site areas. To detect, it uses the name as the primary key for the search mechanism. All the retrieved profiles are assumed as a potential clone and are compared with original use details based on the similarity index. The novelty in this approach is it uses a decision tree classifier to generate the rules for training.

In [2], Zola designed a framework for performing sentiment analysis on alloy steel data of Twitter. In the current scenario, the financial products are analyzed by

quality and price rather than the reviews provided by the other users. The reason for implementing numerical data analysis in the models is due to the complicating process involved in text processing. The proposed paper collects some set of tweets based on the search query passed by the user from Twitter API, and then it retrieves all the records that match with the product based on the frequency of the term. It uses the word to vector technique to convert textual data into numerical data. In a single classification process, it measures the distance between the tweets and reduces the dimensions if required; it applies statistical measures to extract the important features based on the correlation vector, and finally, a new algorithm is known as “OneCSVM” to classify the tweets.

In [3], Ruz proposed multiple detection strategies that have been developed to address the spam problem in social networks. The paper address the Sybil attack, which creates an exact image of the profile and makes the network comprise with fake IP address created. The proposed model extracts the social relationships and is stored in the form of graphical representation. This type of attack is very critical to solving because it creates the fake profile along with the same background information, and the communicators are also created in replica to the original profile. These technographic techniques have complex efforts to detect, and new spam-recognition approaches need to be developed.

In [4], Gurajala mentioned characteristics of fake profile accounts. This model uses the Web crawling technique to get user profile information from the API. In this API, the social network data is stored in the form of graphical representation, so it becomes a complicated process to extract the information. This model extracts the information based on the concept of seeding and extracts the information about the user with 33 important attributes but it implements a map-reduce algorithm to further reduce these 33 attributes into 8 attributes. A pattern recognition algorithm is implemented to identify the common properties in displaying their screen names based on these, a pattern list is prepared. To identify the cloned profiles, it uses Shannon entropy to remove the less likely patterns.

In [5], Mateen et al. proposed that online websites are based on trust principles and attracted several researchers because of their popularity. An experiment conducted on a Facebook dataset found several unknown friend requests being accepted by 41% of users. According to the available Research users can click on the links of unknown individuals. They may give a detailed analysis of the tactics used by spammers on evasion [6, 10]. Analyzed the extent to which social networking sites have entered spam. This model is deployed in social network platforms like Twitter and Facebook, and it identified the accounts which are irregular to log in and whose accounts are more sensitive to compromise with attacker data [11, 15].

39.3 Proposed Methodology

The proposed algorithm consists of six modules which are illustrated as follows.

39.3.1 *Cleaning of Text*

The dataset contains nine categorical attributes. The class labels contain six multiple values, which is the case study for a multi-classification problem. The descriptions of all columns are represented in Table 39.1.

In this cleaning step, first, the most important categorical data like statements, subjects, and context are majorly cleared by removing the special characters. Next, all the sentences are transformed into words by recognizing the tabs and converting all the words into lower case. Then, all the words are passed to the nltk corpus to remove all the stop words like a, an, the, etc. These words are considered as stop words in corpus because the frequency of these words is more than the specific words which are more relevant to the context. So, during the training phase, machine learning algorithms may produce the wrong output if frequency the considered as the calculating estimator. Later, Porter stemming [6] predefined function is applied to convert the prefix and suffix word transformation into proper word. This helps in the removal of adverb, adjective, and plural forms of words.

39.3.2 *Bag of Words (BOW) Model*

Before this bag of words model, the word embedding techniques have achieved good attention in natural language processing. But, to simplify and handle the disadvantages in the word embedding technique, the bag of words model is proposed in three different mechanisms. In this paper, the count vectorization, which counts the occurrences of words in the sentences, is implemented. This process can be illustrated as follows:

Sentence: “All the researchers want to learn NLP. This is the right time to start learning NLP”

After pre-processing of the data, the remaining words in the above sentence with their respective occurrences are represented in Table 39.2.

Table 39.1 Dataset representation

S. No.	Feature name	Description
1	Statement ID	Unique number for each statement
2	Statement	Twitter post statements
3	Subjects	Twitter subject statements
4	Speaker	Account holder name
5	Job title	Designation of speaker
6	State info	State name
7	Party affiliation	Name of the political party
8	Context	Name of the topic
9	Label	Class label

Table 39.2 Occurrence table

S. No.	Name	Count
1	Research	1
2	Want	1
3	Learn	2
4	Right	1
5	Time	1
6	Start	1
7	NLP	2

This occurrence may suffer from high bias because few words may high occurrences, but they may not be relevant to the context. So, this can be handled by using the normalization of counting vectors.

39.3.3 *Training and Testing Datasets*

The most common problem that many of the machine learning algorithms may suffer due to excessive training is overfitting issues or underfitting. This can be handled by splitting the data into the training dataset and testing dataset. Again, this training dataset undergoes cross-folded validation to repeat the training process iteratively for the “K” number of times, in each iteration a single fold is maintained as a holdout set and remaining folds are passed as training data to the model that is developed.

39.3.4 *Feature Scaling*

All the machine learning models are known for their fast computations. This fastness of the algorithm is achieved by converting the data into numerical form. But still, if the range of values is high, then again, the computation process becomes slow. So, the normalization process converts all the possible values into the range of 0 and 1. This conversion process is known as “Feature Scaling.” In this paper, the min–max normalization is implemented.

39.3.5 *KNN Algorithm*

The KNN is a simple and non-parametric machine learning algorithm that can be computed using hamming distance. This paper is implemented using hamming

distance because most of the data in the given dataset exist in the categorical format. The hamming distance can be computed as shown in Eq. 39.1.

$$\text{Hamming_Distance}(A, B) = \sum_{i=1}^n (A_i - B_i) \tag{39.1}$$

If $A_i = B_i$ then $\text{Hamming_Distance}(A, B) = 0$ else $\text{Hamming_Distance}(A, B) = 1$.

39.3.6 Prediction

Finally, all the test dataset values, which are separated from the complete dataset are passed as a parameter to the predict function, on which the fit and transformation function applied using the KNN classifier. It computes the predicted class labels, and it further sends to the evaluation metrics to measure the quality or accuracy. The true positive rate and misclassification rate for the proposed model are reported as “74.5%” and “26.3%,” respectively. The overall architecture of the proposed algorithm can be represented in Fig. 39.1.

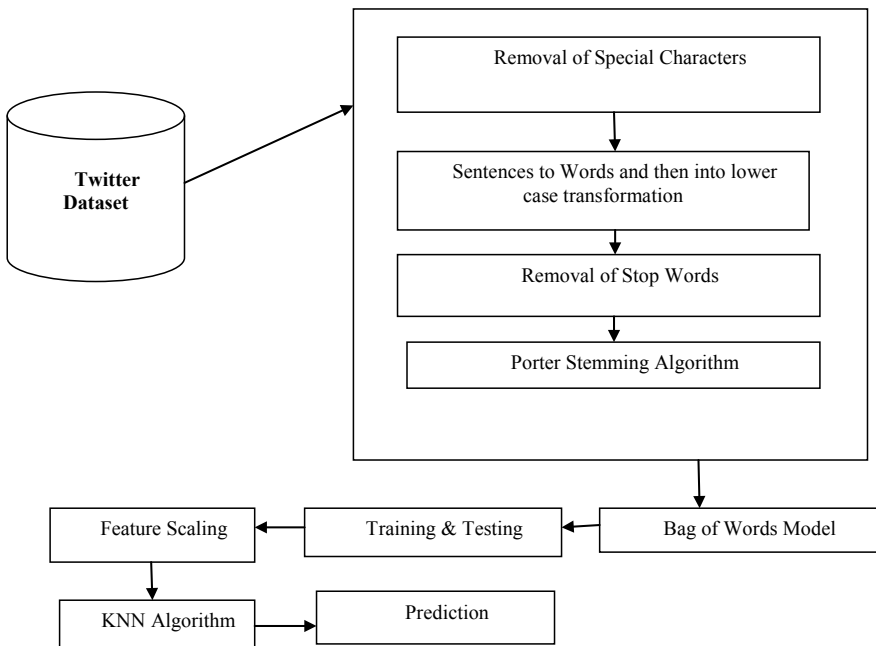


Fig. 39.1 Overview of the KNN classification model over Twitter data clone

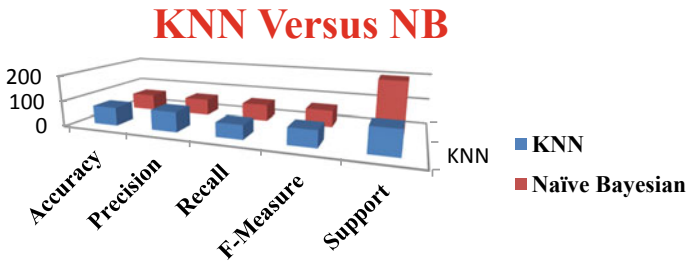


Fig. 39.2 Comparative study on KNN and NB

Table 39.3 Performance metrics of KNN and NB

	Accuracy	Precision	Recall	F-Measure	Support	Confusion matrix
KNN	70.5	77	56	65	97	[[54 43] [16 87]]
Naïve Bayesian	65.0	66	65	65	200	[[75 22] [48 55]]

39.4 Experimental Results

The proposed algorithm uses a distance metric to find the similarity characteristics. In the KNN algorithm, the distance parametric as “Hamming Distance,” then results are compared with naïve Bayesian as shown in Fig. 39.2, and the performance metrics are illustrated in Table 39.3.

From the above table, it is observed that in terms of all evaluation metrics, the KNN algorithm has performed well when compared to the naïve Bayesian. For clear understanding of the results, it has been represented as graphical representation in Fig. 39.2.

39.5 Conclusion

All the previous mechanisms used “TF-IDs” [6] mechanisms for finding the relevance between the tweets. This proposed model focuses only on filtering the users based on the tweets posted by the user and a novel evaluation measure known as “TUR,” is computed to find the user relevance concerning a particular tweet. The proposed system identifies the fake accounts using KNN with an accuracy of **70.5%** accuracy. But with the advancement of machine learning techniques, the obtained accuracy is not satisfactory, so in further research, it is better to offer an automated transfer-learning approach where labeled tweet data is available to train

the text classifiers with a good amount of data. There are three other approaches where distance measures like cosine and sine are dynamically wrapped and can be integrated with one or two classes with the help of autoencoders. In the future studies, the system can be incorporated with pretrained models, and the last layers of the model can be customized with text classification algorithms so that the computation becomes efficient in handling the categorical data.

References

1. Sowmya, P., Chatterjee, M.: Detection of fake and clone accounts in twitter using classification and distance measure algorithms. In: 2020 International Conference on Communication and Signal Processing (ICCSP) (2020). <https://doi.org/10.1109/iccsp48568.2020.9182353>
2. Zola, P., Cortez, P., Brentari, E.: Twitter alloy steel disambiguation and user relevance via one-class and two-class news titles classifiers. *Neural Comput. Appl.* (2020). <https://doi.org/10.1007/s00521-020-049918>
3. Ruz, G.A., Henríquez, P.A., Mascareño, A.: Sentiment analysis of Twitter data during critical events through Bayesian networks classifiers. *Future Gener. Comput. Syst.* (2020). <https://doi.org/10.1016/j.future.2020.01.005>
4. Gurajala, S., White, J.S., Hudson, B., Voter, B.R., Matthews, J.N.: Profile characteristics of fake Twitter accounts. *Big Data Soc.* **3**(2), 205395171667423 (2016). <https://doi.org/10.1177/2053951716674236>
5. Mateen, M., Iqbal, M.A., Aleem, M., Islam, M.A.: A hybrid approach for spam detection for Twitter. In: 2017 14th International Bhurban Conference on Applied Sciences and Technology (IBCAST) (2017). <https://doi.org/10.1109/ibcast.2017.7868095>
6. Padmanahuni, S., Hima Bindu, T.: Search results clustering: comparison of Lingo and K-Means. *Int. J. Adv. Res. Comput. Sci. Manage. Stud.* **1**(5), 70–83. <http://www.ijarcsms.com/docs/paper/volume1/issue5/V1I5-0009.pdf>
7. Sravya, G.S., Pradeepini, G.: Mobile Sms spam filter techniques using machine learning techniques. *Int. J. Sci. Technol. Res.* **9**(3), 384–389 (2020)
8. Mallikarjuna Reddy, A., RupaKinnera, G., Chandrasekhara Reddy, T., Vishnu Murthy, G., et al.: Generating cancelable fingerprint template using triangular structures. *J. Comput. Theoret. Nanosci.* **16**(5–6), 1951–1955(5) (2019). <https://doi.org/10.1166/jctn.2019.7830>
9. Mallikarjuna Reddy, A., Krishna, V.V., Sumalatha, L., Obulesh, A.: Age classification using motif and statistical features derived on gradient facial images. *Recent Adv. Comput. Sci. Commun.* **13**, 965 (2020). <https://doi.org/10.2174/2213275912666190417151247>
10. Ayaluri, M.R., Reddy, S., Konda, S.R., Chidirala, S.R.: Efficient steganalysis using convolutional auto encoder network to ensure original image quality. *Peer J. Comput. Sci.* **7**, e356 (2021). <https://doi.org/10.7717/peerj-cs.356>
11. Papineni, S.L.V., Yarlagadda, S., Akkineni, H., Reddy, A.M.: Big data analytics applying the fusion approach of multicriteria decision making with deep learning algorithms. *Int. J. Eng. Trends Technol.* **69**(1), 24–28. <https://doi.org/10.14445/22315381/IJETT-V69I1P204>
12. NagaSanthosh Kumar, C.H., Reddy, K.S.: Effective data analytics on opinion mining. *Int. J. Innovative Technol. Exploring Eng.* **8**(10), 2073–2078
13. Sirisha, C.R.T.G., Reddy, A.M.: Smart healthcare analysis and therapy for voice disorder using cloud and edge computing. In: 2018 4th International Conference on Applied and Theoretical Computing and Communication Technology (iCATccT), Mangalore, India, pp. 103–106 (2018). <https://doi.org/10.1109/iCATccT44854.2018.9001280>

14. Mallikarjuna Reddy, A., Venkata Krishna, V., Sumalatha, L.: Face recognition approaches: a survey. *Int. J. Eng. Technol. [S.l.]* **7**(4.6), 117–121 (2018). ISSN 2227–524X. <https://doi.org/10.14419/ijet.v7i4.6.20446>
15. Santhosh Kumar, C.N., Pavan Kumar, V., Reddy, K.S.: Similarity matching of pairs of text using CACT algorithm. *Int. J. Eng. Adv. Technol.* **8**(6), 2296–2298

Chapter 40

Review of Recent Developments in Sustainable Traffic Management System



Bhawini Sharma and Jai Kumar Maherchandani

Abstract Nowadays, rapid growth in vehicles on the road causes traffic congestion, a considerable problem. Accidents, noise, long lines at intersections, health damage, and other facets of the transportation sector of modern society are all impacted by this problem. A reliable traffic management system (TMS) is needed in the contemporary world to resolve traffic-related issues and improve the transportation systems' safety and overall efficiency. TMS collects data from various sources and analyses it using various techniques like artificial intelligence, optimization, data analysis etc., to identify hazards and then provides services to mitigate them. In light of this, this article reviews the recent developments, challenges, and potential prospects of implementing a traffic management system.

40.1 Introduction

In today's society, moving fast is everyone's goal. Everybody wants to find the fastest way to reach their destination and, in that transportation, plays an important role. People use the vehicle of every form to reach their destiny.

Rapid growth in the number of vehicles due to population increases causes a severe problem in the transportation system, and traffic congestion will have become a pressing issue. This problem will need a very efficient traffic management system to manage vehicles to reduce congestion, waiting time on lights, efficient fuel consumption, etc.

Bad weather, work zones, accident events, and poor traffic signal scheduling are examples of direct traffic influencing events. In contrast, lack of efficient transportation facilities, such as poor road conditions, are indirect traffic influencing events [1]. As a result, large cities with heavy traffic depend on TMS to solve their traffic management problems and ensure smooth city transportation.

Along with long queues at intersection and traffic jams, weather conditions like fog, snow, and rainfall are significant problems for a driver. These factors affect

B. Sharma · J. K. Maherchandani (✉)
College of Technology and Engineering MPUAT, Udaipur, India

traffic flow, speed etc.; intelligent traffic management addresses issues like water logging, narrow roads, and weak drainage systems [2, 3]. Another major issue in developing countries is toll booths. A manual toll system results in slow speed, jams, and lengthy queues [4]. So, an automated toll system is also a part of the intelligent traffic management system. This paper presents a brief review of some recent TMS approaches.

The remainder of the paper is as follows. Section 40.2 gives a brief idea of the concept of TMS with an explanation of its three phases. Section 40.3 reviews some of the traffic management systems found in the literature, explaining each type of technique in brief. Section 40.4 gives the idea of various challenges that remain to be addressed in traffic management systems. And lastly, Sect. 40.5 concludes the article.

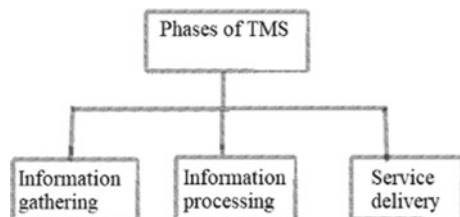
40.2 Traffic Management System

A traffic management system is a platform to solve traffic-related problems. TMS defines various algorithms and models related to traffic issues. The main problems concerning increasing traffic for which we need TMS include traffic congestions and long traffic jams, providing a smooth path for medical emergencies, reducing waiting time at intersections, and reducing fuel consumption and lane management [5]. Over time, various TMSs have been introduced and implemented. TMSs consist of mainly three phases. First is the information gathering step in which different information related to traffic is gathered and collected. In the second step of information processing, the traffic hazard is identified, and the data collected is used accordingly. Lastly, the third step of service delivery solutions is given for the identified problem [6]. Figure 40.1 shows the three phases of the traffic management system, and a brief about all three steps are given as follow.

Information gathering: This phase collects data from different traffic-related sources like roadside units, traffic lights, roadside sensors, etc., as in vehicles, various inbuilt sensors like speedometer, GPS, etc., provide traffic-related data. Then, the data is sent to the information processing unit to process it.

Information processing: Following the information gathering process, the data must be effectively used to predict various traffic-related hazards. The data must be aggregated in the information processing phase to enhance data quality and provide services as required.

Fig. 40.1 Phases of traffic management system



Service delivery: This phase provides services related to the hazard identified in the information processing phase. The service provided by this phase helps in controlling hazards and improving overall traffic efficiency.

40.3 Recent Traffic Management Systems

This section contains a summary and qualitative study of some of the literature-based TMSs. Figure 40.2 shows the different techniques used by researchers in the area of the traffic management system.

40.3.1 Artificial Intelligence (AI)-Based Models

AI-based solution for traffic management problems is presented in [7]. A design is produced for variable signal timing and special requirement for medical emergencies. It is proposed that signal timing be adjusted based on density and traffic

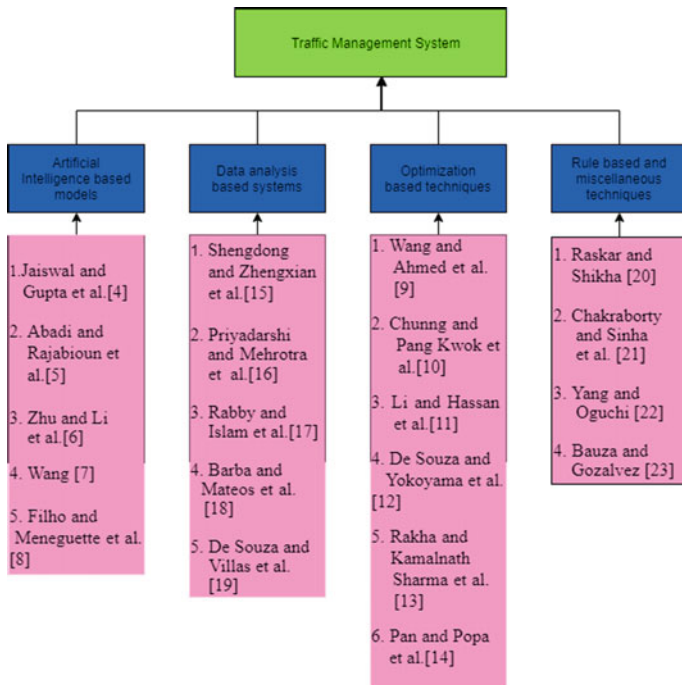


Fig. 40.2 Techniques for traffic management system

demands. In medical emergencies, traffic from the corridor should be diverted to provide a smooth path for ambulances. A technique for predicting traffic flow for all connections in a transportation network over a limited time horizon is proposed in [8]. The first step is to produce traffic flow data at all links using a dynamic origin–destination matrix, and then future traffic flow is projected using the collected data.

A new generation of intelligent transportation systems (ITS) based on parallel transportation management and control systems (PIMS) is proposed in [9]. Existing transportation systems and artificial transportation systems are linked in PIMS, and experiments are carried out on the latter. It is a simple way to apply optimization and evaluation. The public may use a crowdsourcing platform for transportation to obtain or release travel-related information anytime they need it. Lastly, the MapReduce framework technique is used to predict traffic flow.

Three major techniques for the ITS are presented in [10]. First, hierarchical intelligent control systems were used to decompose complex issues in traffic networks. Second, networked traffic controllers of street intersections and freeway entry and exit, the agent-based control (ABC) system, and the concept of “local easy, remote complex” were used to provide a low-cost, high-performance, and intelligence method. Finally, the artificial transportation systems (ATS) idea was implemented to provide an in-the-loop emulation of real-time traffic information to support traffic decision making.

An inter-vehicular solution is developed in [11] to help during vehicle traffic congestion problems in cities. To minimise congestion problem, qualitative and quantitative data is obtained to gather knowledge. Then, vehicle to vehicle (V2V) communication is established to determine which vehicle should change its route to avoid congestion.

40.3.2 Optimization-Based Techniques

A discrete-time stochastic dynamic model is proposed in [12] to explain urban traffic dynamics. The term “congestion broadcast stage” (CBL) is used for the first time. As soon as CBL exceeds the prescribed limit, congestion will be announced. An objective function is made of throughput and waiting time. An optimization problem is formulated and solved by dynamic programming to describe the effectiveness of the mathematical model.

A hybrid intelligent traffic light system for Hong Kong is presented in [13]. The aim is to dynamically monitor the traffic light system by measuring vehicles and pedestrians at the intersection using object recognition. A simulator is formed to demonstrate the effectiveness of road users for fixed cycle traffic light systems and intelligent traffic light systems. The parameter collection is optimized using an evolutionary algorithm to reduce the average waiting time for all road users.

A traffic control mechanism is devised in [14] that is responsible for intersection congestions. A hierarchical framework for optimizing traffic signal setting based on a multi-agent system was proposed. The work creates an intelligent real-time traffic

management mechanism that incorporates online changes and offline optimization to customize traffic signal settings.

In [15], an intelligent traffic system is proposed that detects when a congestion is forming and systematically manages traffic to distribute the density of vehicles so that congestion in the near future is avoided. A framework based on vehicle to infrastructure (V2I) communication is proposed in [16], which enhances fuel consumption. The driver is assumed to follow instructions thoroughly to get optimum fuel consumption. Through optimization, the algorithm system computes the maximum acceleration level from net force computation. The work presented in [17] gives five different rerouting algorithms and compared them with a standard algorithm to check their efficiency levels.

40.3.3 Data Analysis-Based Management System

Designing an intelligent transportation cyber-physical cloud control system is presented in [18]. The data is first collected and sent to a cloud control platform, after which it is intelligently processed to produce prediction results and control schemes, which are then sent to an intelligent traffic system for tracking, management, and decision making.

Issue of rapid transit of vehicles, emergency vehicles and stolen vehicle recovery are dealt in [19]. The concept of roadside unit (RSU) and on-board unit (OBU) was used. It is assumed that every vehicle is attached with an RFID tag, which contains all its information to help retrieve the vehicle if it is stolen. The reader reads the RFID tag and displays vehicle density on LCD to make traffic flow management smart. Every emergency vehicle will have a transmitter through which its arrival will be detected, and the lane will be cleared.

An IoT-based intelligent traffic management system is explored in [20] by considering sensor fusion techniques and image data streaming from multiple cameras installed on different traffic system parts. The cameras and sensors work as eye and ear for the car. The system is based on the attainment of traffic information from various sources, analysis of traffic data, monitoring and proper control of traffic operation and data storage, and information presentation.

In [21], a framework has been developed where intelligent traffic light (ITL) system gathers information from passing vehicles and update traffic information of city and report strategies to vehicles. It also sends warning messages to vehicles to avoid any further collisions in case of accidents.

40.3.4 Rule-Based and Miscellaneous Techniques

A new traffic management system using an intelligent barricade system is proposed in [22]. The idea is to make the extra lane available dynamically in such situations,

such as traffic congestion or an accident. In this work, the barricade movement is decided by a rule-based system. A communication system consisting of the V2I and V2V communication is used.

An algorithm that determines the green light duration and handles emergency vehicle management is proposed [23]. The algorithm uses a wireless sensor network (WSN) for input. The algorithm works in four steps that decide queue length, determine if an ambulance or priority vehicle is present, assign green light to the most appropriate phase, and calculate green light time.

A multilevel integrated TMS manages large scale on the road-connected vehicles to reduce road congestion and vehicle travel time proposed in [24]. The system divides the entire network into three levels to gather traffic data and monitor individual vehicles with three vehicle control systems: lane shifting assistance during road collisions, optimum lane selection, and dynamic routing with turning cost estimation. The system also gives different instructions to linked vehicles at different levels, such as route and lane choices, to reduce individual vehicle travel times. Furthermore, the system is tested at a city-level road network with the integration of microscopic traffic assignment and simulation tools to understand its effects on individual vehicles at various levels.

40.4 Challenges and Future Perspective

Despite the introduction of so many traffic management systems, some challenges remain to be stated. Figure 40.3 shows the different challenges in the traffic management system.

Some of the challenges are listed below.

40.4.1 Security and Privacy

Data generation is the fundamental step in any TMS. Data regarding vehicles contain much personal information about the vehicle as well as the owner. So, the security of data gathered from different sources is one of the major challenges in the

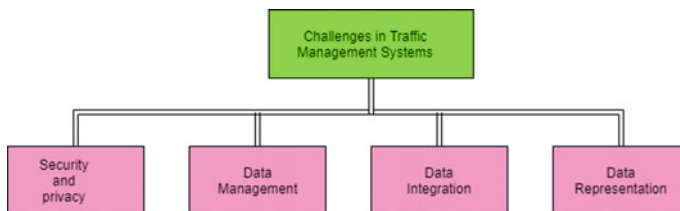


Fig. 40.3 Challenges in traffic management system

TMS. Several requirements need to be satisfied to assure safety and privacy to the vehicular ad hoc networks (VANETs) [25]. To prevent messages containing malicious data, data integrity verification tests the legality and consistency of messages. In [26, 27], various issues related to information privacy and security in intelligent traffic management system are discussed.

40.4.2 Data Representation

After gathering data from different sources, it is accumulated and studied to gather knowledge. The knowledge gathered should be represented in proper form to make it easy to understand. This defined data is used to identify many of the hazards. Accurate representation makes identifying hazards easy and helps to stop them in time.

40.4.3 Data Management

Since TMS must deal with many data, data representation standardization is critical to the system's efficiency. Some of the challenges faced in data management are:

- (a) Each source may have different measurements and formatting.
- (b) Asynchronous data reporting from many sources.
- (c) Data flow to different systems from the same source.

TMSs must have efficient mechanisms to fuse, aggregate, and exploit data to deal with various data types generated from heterogeneous sources.

40.4.4 Data Integration

Acquiring data from sources that are not integrated is a significant challenge in TMS. The biggest issue is figuring out how to achieve this integration. Many different systems and sources can exist with no integration, resulting in a massive amount of data with no standardization.

40.5 Conclusion

Improving transportation efficiency is still a significant research area and needs study. Traffic management system mainly relies on the data collection and data management system. Collecting data from a wide variety and number of sources is

a huge problem that still needs some work. The same can be said for data management; using data, gathering information from collected data requires a systematic and efficient system. These issues still need to be explored more to make TMS efficient and reliable.

This article has explored the various aspects of the traffic management system. First, it gives a brief idea about the traffic management system and related critical issues. A review of the various works done by researchers in this area is organized by the technique used. Finally, the challenges faced by TMS and possible solutions are discussed.

New techniques can be explored for traffic management during bad weather conditions. Research on traffic management with automatic vehicles can be done as unmanned vehicles are the new future of the transport sector. Accidents due to the same lane for heavy vehicles and cars is a major issue to be acknowledged. More advanced techniques can be explored for systematic lane management to reduce travel time as well as accidents.

References

1. U.S Department of transportation. Traffic congestion and reliability: trends and advanced strategies for congestion mitigation (2012)
2. Nigam, A., Chaturvedi, M., Srivastava, S.: Impact of rainfall and waterlogging on traffic stream variables in developing countries. In: 2021 International Conference on COMMunication Systems & NETworkS (COMSNETS), pp. 728–735 (2021)
3. Shevtsova, A.G., Novikov, A.N., Silyanov, V.V.: Method of urban traffic management. In: 2021 Systems of Signals Generating and Processing in the Field of on Board Communications, pp. 1–4 (2021)
4. Design and development of lane management and automatic toll collection system. In: 2021 2nd International Conference on Robotics, Electrical and Signal Processing Techniques (ICREST), pp. 629–634 (2021)
5. de Souza, A.M., Brennand, C.A.R.L., Yokoyama, R.S., Donato, E.A., Madeira, E.R.M., Villas, L.A.: Traffic management systems: a classification, review, challenges, and future perspectives. *Int. J. Distrib. Sens. Networks* **13**(4) (2017)
6. Majeed, F.A., et al.: Smart traffic management system for foggy weather conditions. In: 2019 Advances in Science and Engineering Technology International Conferences, ASET 2019. (2019)
7. Jaiswal, M., Gupta, N., Rana, A.: Real-time traffic management in emergency using artificial intelligence. In: ICRITO 2020—IEEE 8th International Conference on Reliability, Infocom Technologies and Optimization (Trends and Future Directions), pp. 699–702 (2020)
8. Abadi, A., Rajabioun, T., Ioannou, P.A.: Traffic flow prediction for road transportation networks with limited traffic data. *IEEE Trans. Intell. Transp. Syst.* **16**(2), 653–662 (2015)
9. Zhu, F., Li, Z., Chen, S., Xiong, G.: Parallel transportation management and control system and its applications in building smart cities. *IEEE Trans. Intell. Transp. Syst.* **17**(6), 1576–1585 (2016)
10. Wang, F.Y.: Integrated intelligent control and management for urban traffic systems. In: IEEE Conference on Intelligent Transportation Systems, Proceedings, ITSC, vol. 2, pp. 1313–1317 (2003)
11. Wang, S., Ahmed, N.U., Yeap, T.H.: Optimum management of urban traffic flow based on a stochastic dynamic model. *IEEE Trans. Intell. Transp. Syst.* **20**(12), 4377–4389 (2019)

12. Rocha Filho, G.P., et al.: Enhancing intelligence in traffic management systems to aid in vehicle traffic congestion problems in smart cities. *Ad Hoc Networks* **107** (2020)
13. Ng, S.C., Kwok, C.P., Fung, Y.C., So, C.Y., Lam, Y.H.: A Hybrid intelligent traffic light system for solving traffic congestion in Hong Kong. In: 10th International Conference on Information Science and Technology, ICIST 2020, pp. 258–265 (2020)
14. Li, Z., Al Hassan, R., Shahidehpour, M., Bahramirad, S., Khodaei, A.: A hierarchical framework for intelligent traffic management in smart cities. *IEEE Trans. Smart Grid* **10**(1), 691–701 (2019)
15. De Souza, A.M., Yokoyama, R.S., Maia, G., Loureiro, A., Villas, L.: Real-time path planning to prevent traffic jam through an intelligent transportation system. In: 2016 IEEE Symposium on Computers and Communication (ISCC), Messina, 27–30 June 2016, pp. 726–731. IEEE, New York (2016)
16. Rakha, H., Kamalanathsharma, R.: Eco-driving at signalised intersections using v2i communication. In: 2011 14th International IEEE Conference on Intelligent Transportation Systems (ITSC), Washington, DC, 5–7 October 2011, pp. 341–346. IEEE, New York (2011)
17. Pan, J., Popa, I.S., Zeitouni, K., Borcea, C.: Proactive vehicular traffic rerouting for lower travel time. *IEEE Trans. Veh. Technol.* **62**(8), 3551–3568 (2013)
18. Shengdong, M., Zhengxian, X., Yixiang, T.: Intelligent traffic control system based on cloud computing and big data mining. *IEEE Trans. Ind. Inform.* **15**(12), 6583–6592 (2019)
19. Priyadarshi, S., Mehrotra, R., Shekhar, S.: Self control monitoring traffic management system. In: 2019 2nd International Conference on Power Energy Environment and Intelligent Control, PEEIC 2019, pp. 366–370 (2019)
20. Rabby, M.K.M., Islam, M.M., Imon, S.M.: A review of IoT application in a smart traffic management system. In: 2019 5th International Conference on Advances in Electrical Engineering, ICAEE 2019, pp. 280–285 (2019)
21. Barba, C., Mateos, M., Soto, P., Mezher, A., Igartua, M.: Smart city for vanets using warning messages, traffic statistics and intelligent traffic lights. In: 2012 IEEE Intelligent Vehicles Symposium (IV), Alcalá de Henares, 3–7 June 2012, pp. 902–907. IEEE, New York (2012)
22. Raskar, C., Shikha, N.: A Prototype of the dynamic traffic management: smart barricade system. In: International Symposium on Advanced Networks and Telecommunication Systems, ANTS, 2019, vol., December 2019
23. Chakraborty, P.S., Sinha, P.R., Tiwari, A.: Real time optimised traffic management algorithm for intelligent transportation systems. In: Proceedings—2015 IEEE International Conference on Computational Intelligence and Communication Technology, CICT 2015, pp. 744–749 (2015)
24. Yang, H., Oguchi, K.: Integrated traffic management system under connected environment. In: 2019 IEEE Intelligent Transportation Systems Conference, ITSC 2019, pp. 3379–3386 (2019)
25. Namazi, E., Holthe-Berg, R.N., Lofsberg, C.S., Li, J.: Using vehicle-mounted camera to collect information for managing mixed traffic. In: Proceedings—15th International Conference on Signal Image Technology and Internet Based Systems, pp. 222–230 (2019)
26. Fries, R.N., Gahroei, M.R., Chowdhury, M., Conway, A.J.: Meeting privacy challenges while advancing intelligent transportation systems. *Transp. Res. Part C Emerg. Technol.* **25**, 34–45 (2012)
27. Yan, G., Wen, D., Olariu, S., Weigle, M.C.: Security challenges in vehicular cloud computing. *IEEE Trans. Intell. Transp. Syst.* **14**(1), 284–294 (2013)

Chapter 41

Automatic Machine for Round Welding Using Programmable Logic Controller (PLC)



Gautam Gupta, Rajanpreet Singh, and Anant Kumar Singh

Abstract The proposed research paper is to illustrate the execution of the round seam welding machine based on the programmable logic controller (PLC) automation. This machine aspires to increase the production rate of the product that requires welding on the circumference. It is an innovation from manual welding to automatic welding for any rounded border welding industrial part. For a worker, it is very difficult to rotate and weld the product simultaneously. This modernization shifts the arduous task to surveillance work for the labor. Panel designing and wiring of PLC with the welding machine was simulated in “SolidWorks Electrical.” “DELTA” PLC was used to move the pneumatic cylinder that holds the welding torch, and it also helps to rotate the plate using the AC motor where a product is placed. The PLC was encrypted with ladder logic programming using the “ISP Soft” software.

41.1 Introduction

The development has brought many powerful changes in the industry. Automation has become a pivotal part of every industry. It predominantly mainly centers on mechanization having minimum cost, less maintenance, high durability, and making user-friendly systems as possible. This paper aims at the problem solving for the welding at the ends of any circular surface or to the circumference of a surface with other products. The current scenario of productivity is not as fast as demand due to high cycle time and squander in non-valuable activities. Welding is followed by the tacking of the product, which is done with eight points through the fence that is equidistant from each other. The welder has to place the product on the table and rotate the product many times to weld a limited part or reachable region of

G. Gupta (✉) · R. Singh · A. K. Singh
Department of Mechanical Engineering, Thapar Institute of Engineering and Technology,
Patiala, Punjab 147004, India
e-mail: ggupta2_be15@thapar.edu

the circumference. This manual intervention of rotating is highly non-valuable and squanders activity that hinders the production.

This scenario is experimented on the welding of “Rim” to “Funnel” of the “Union,” a head of grain unloader used in combine harvester. The unloading system has a pivoting unloading tube assembly movable between a storage position and an unloading position. The unloading tube assembly has an inner riser section and a variable-length outer transport section. The unloading tube located at bottom of the grain container. To power the bin unloading system, power heads is manufactured to meet the bin unload requirements. This system is known as tube and union system.

Notwithstanding, utilizing innovation and legitimate insurance incredibly lessens dangers of injury for a welding operator. A welding line operator has to rehash a similar process throughout the day, about a thousand times. This obviously, will lead to early mileage of body parts in the long run. To conquer this issue, a table is modified to around seam welding machine that helps to reduce the non-valuable activity and reduce the operator’s risk during welding. The automated machine was designed in the software—SolidWorks, and the machine is coded using PLC.

A 3D panel is designed in SolidWorks Electrical with all the required electrical components. A panel is also installed along with the table that contains PLC and other electrical components used to control the machine. The wiring of PLC with motor and pneumatic cylinder of the panel in round seam welding machine is simulated and wired in the SolidWorks electrical software. The machine mainly consists of a rotating plate that is controlled with the paddle and a torch holder is established near the plate that helps to hold the welding torch.

41.2 Literature Review

Manufacturing industries has gone through improvements of robotization. To date, PLC stays the most ideal alternative for modern mechanization [1]. In this paper introduced the study and practices of ladder logical programming and utilization of library [2]. This report has examined the job that PLC does with effective plan and control of mechanical cycles [3]. In this paper, an occasion-driven methodology is proposed to improve the plan of mechanical control frameworks utilizing PLCs.

Automation centers on creating development having minimal expense [4]. This work portrays forging machine coded by PLC that supplants manual feed [5]. This directed the design of out diameter finish machine using PLC to lessen events time [6]. This has upgraded the paper machine by installing PLC that helps to control synchronization, reduce wear and tear [7]. This improves the plant’s sludge dewatering cycle by using PLC to build the proficiency [8]. This shows sorting using PLC that separates the product based on properties like size, height, and color [9]. This paper planned to monitor and control the interaction at the wastewater treatment plant by adding sensors and actuators with PLC [10]. This planned the bottle container filling with PLC, which gets the sensor input and controls the solenoid valve timing.

The automobile industry is no more unusual to mechanization [11]. This research applies PLC for light hybrid electric vehicle power train to control the two drive power sources [12]. In this, an automatic parking for car is framed with PLC that can guide to space for the transports to the park [13]. This project highlights an automatic car washing, which is controlled using PLC that work to use less water [14]. This executes the smart traffic light framework based on PLC innovation.

There are several applications to automate from diurnal tasks to focus on even small critical issues [15]. The proposed model of cooking machine is fully automated based on PLC, in this recipe with required ingredients [16]. This paper depicts plant water siphoning control framework that is planned utilizing PLC [17]. This paper primarily centers to control the circuit to fabricate the elevator model utilizing PLC [18]. This paper targets automizing any home appliances.

41.3 Methodology

The productivity is not as fast as demand, due to high cycle time and waste of time in non-valuable activities. To exile the unproductivity, the time analysis has been done on the old manual method of welding. Time study is the first step to improvement in assembly line engineering. This can be done by watching the process repeatedly and making list of time needs to complete each section. This is done on welding of the tube and union part, to joint two parts of “Funnel” and “Rim.” This phenomenon helps us to understand how much time is to be allocated to each station.

It is observed that time taken for final welding process of the entire process of production too long. The non-valuable activity seen during the process are rotating the work-piece to weld it in sections and hammering on funnel and rim to sync the both, which got dislocated during rotating the work-piece. It is seen noted that overall time taken to complete the welding included non-valuable activities are 240 s. Hence, to increase the efficiency, the automation setup has to be designed that makes the process of final welding faster. The welding process of the work-piece that been conducted by operator has been shown in Figs. 41.1 and 41.2 performing welding at different position of position A and position B of work-piece, respectively.

41.3.1 *Design of Automatic Machine*

The idea is to implement the automated machine that rotate the work-piece and reduce the time and effort of the operator. The machine can also be added with the welder torch holding stand that moves with the pneumatic cylinder actuator to weld the work-piece. The 3D-model machine is designed in the SolidWorks. The plate and welder holder stand are designed as shown in Figs. 41.3 and 41.4, respectively.

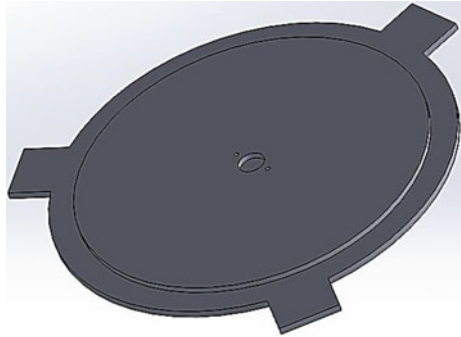
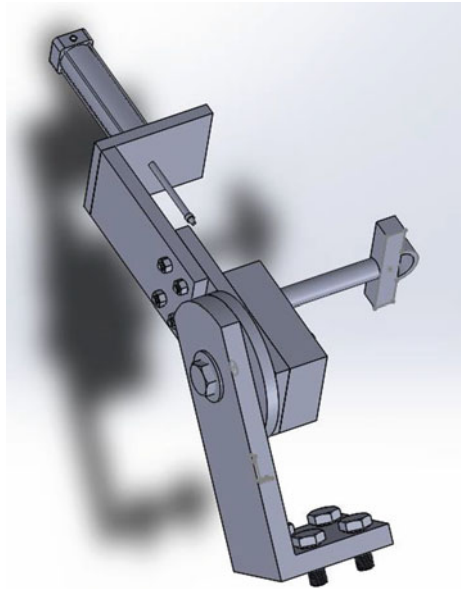
Fig. 41.1 Manual welding
(Position A)



Fig. 41.2 Manual welding
(Position B)



The diameter of plate is taken 460 mm decided by examine the maximum diameter of the union which is 443 mm. The parts are then assembled together on the table to complete the required machine as shown in Figs. 41.5 and 41.6 captured at different position A and position B, respectively. The top of the table frame has dimensions as 750 mm \times 480 mm i.e. the area being 3600 cm².

Fig. 41.3 Design of plate**Fig. 41.4** Design of holder

41.3.2 Panel of Automatic Machine

The table is then equipped with the electrical panel containing electrical components that control and run the machine. As per the requirement, one programmable logic controller (PLC), three relays, and two contractors are needed.

PLC: DELTA's PLC DVP-16ES2 was used, as it comes with the in-built SNMP card. DVP-16ES2 is in-built with one RS-232 port and two RS-485 ports.

Relay: A relay is use an electromagnet to accurately work as a switch. An electromagnetic relay comprises a curl of collapsed over a sensitive iron.

Fig. 41.5 3D model of machine (Position A)

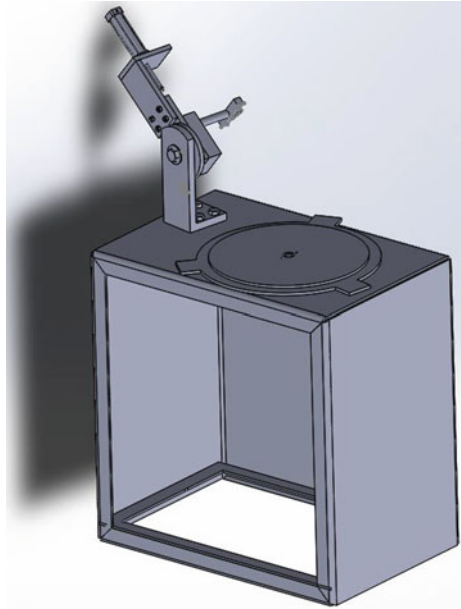
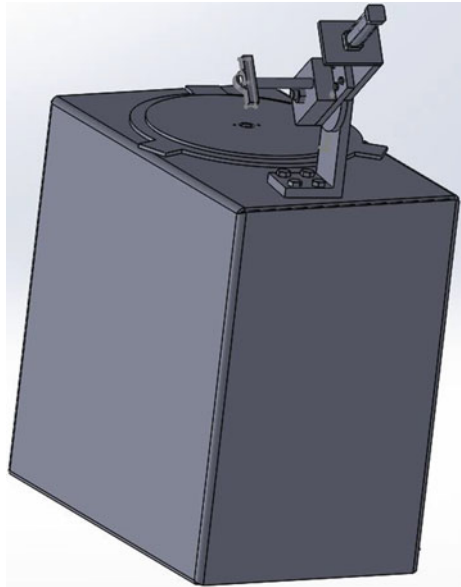


Fig. 41.6 3D model of machine (Position B)



Contactor: A contactor is an electrically controlled switch for exchanging a force circuit. A contactor is constrained by lower power level than the exchanged circuit.

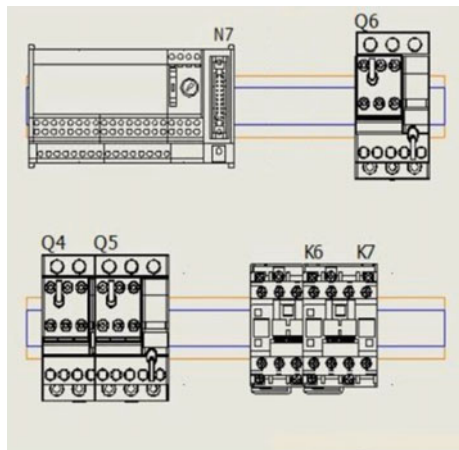
The panel was designed in the SolidWorks Electrical in 2D and 3D model by selecting the components from the list of the medley of items in the SolidWorks Electrical. The vital components were placed on the duct inside the panel as per the selection to complete the needed panel. 2D and 3D designing of the panel in SolidWorks are shown in Figs. 41.7 and 41.8, respectively.

Apart from the panel, other electrical components are AC motor, pneumatic cylinder, and welding torch machine performing MIG welding. The circuit was designed in SolidWorks Electrical as showed in Fig. 41.9. Firstly, on the left-hand side, first switch is to turn ON/OFF the machine which can be shown through the indicator on the other hand followed by the relay. Secondly, two colored buttons are placed: green to ON and red to OFF; the pneumatic cylinder that is shown on the right side is followed by relay and contactor. Thirdly, a button to turn ON/OFF the motor is placed along with a paddle to control the motor. The motor is attached with the relay, contactor, and motor drive. At the last, an emergency STOP button is situated at the bottom left to stop all the working of the machine.

41.3.3 Code of Automatic Machine

Ladder logic is a graphical way of a programming language used to program PLC. These logic operations express with symbolic representations. Ladder logic forms with rungs of logic, and is written, by vertical connections between two lines. Each of the connection line is called a rung. The PLC performs operation on one rung at a time, and then the next. Each symbol in ladder logic is an instruction.

Fig. 41.7 2D model of panel



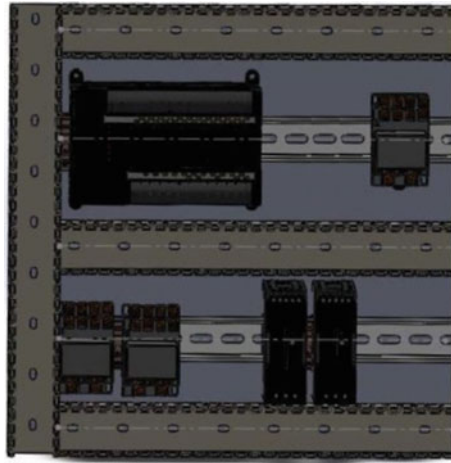


Fig. 41.8 3D model of panel

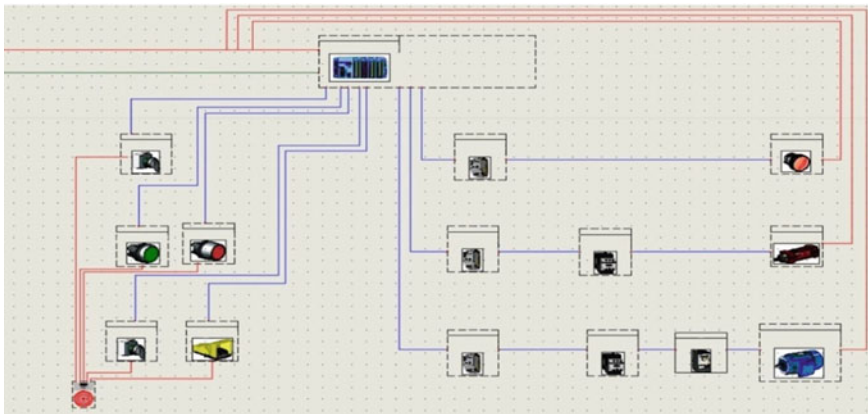


Fig. 41.9 Wiring of the panel in SolidWorks electrical

Normally Open (NO) -| |:- If input condition is TRUE then the circuit is CLOSED and output of the system starts working.

Normally Closed (NC) -| |:- If input condition is TRUE then the circuit is OPEN and output of the system stops working.

Output Coil -():- Output of system remains ON, if input condition is TRUE. Output of the system remains OFF, if the input condition is FALSE.

Output Latch (self-hold): The latching is used where the output must be activated even after the entry ceases.

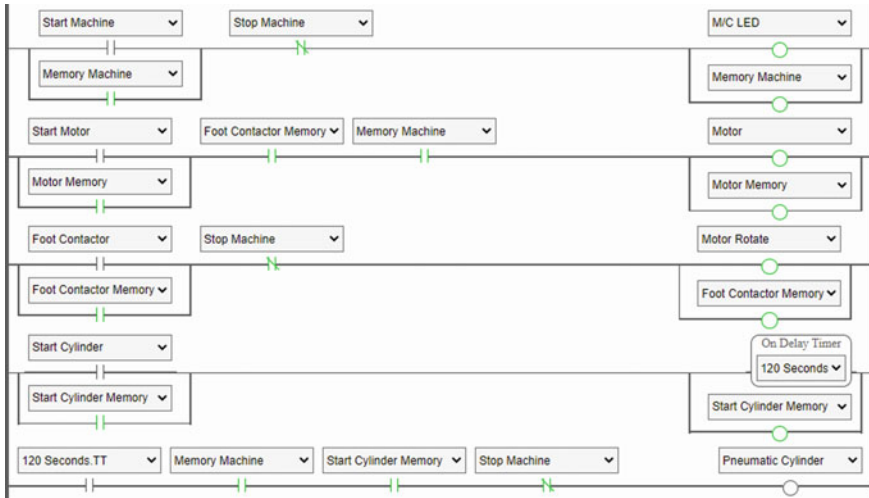


Fig. 41.10 Coding on PLC using ladder logic programming

The ladder logic programming for the PLC is shown in Fig. 41.10. The code was written with five rungs of ladder. Starting from top to bottom, each rung has been explained meticulously. The first rung is to start the machine will start using NO button “Start Machine” that use latch memory of the output “Machine” and will keep run the output “Machine” and LED. In the second rung, NO button “Start Motor,” a memory latch is created with output “Motor” that will keep run the motor, when the output “Machine” was running. Third rung, the NO button “Foot Contactor” uses to rotate the motor by latching the output “Motor Rotate” when the output “Machine” and output “Motor” was running. The second-last rung is to latch memory of the cylinder using NO button “Start Cylinder.” The reverse timer of 120 s has been added with the output “Start Cylinder Memory.” In the last rung, the output “Start Cylinder Memory” helps to run the NO button “Start Cylinder Memory” that is attached to run the cylinder when output “Machine” was running. This helps to compress the pneumatic cylinder piston, which moves the welding torch downwards and the get in contact with the work-piece. After 120 s, rotation of motor will be complete when running 0.5 RPM. Thus, the welding of the work-piece throughout the circumference will be completed. When the timer will come to 0 s, it will turn off the cylinder and helps to expand the piston of the cylinder. This leads release the contact of welding torch with the work-piece. All the arrangements of the machine were fabricated to provide a safe and hassle-free task to the welding operator. A stop button was also placed to avoid any accident during the welding. It is added as NC button “Stop machine” in three rungs adjacent to all outputs “Machine,” “Motor,” and “Pneumatic Cylinder”. This button helps to stop each component of the machine.

41.4 Results

This paper discussed an automated machine for doing welding operations of round seam products at the circumference. The automated machine for round welding has covered many aspects. Time study and analysis plays an important factor in the research. This helps to analyze and work on the non-valuable aspects. The manual welding on the circumference of the product was completed in 240 s. However, the welding machine has reduce affords and time to 120 s. Thus, it reduces the 50% of the time use to complete the work-piece and increase the production rate of the product for the industry. The implementation of machine can be seen in Figs. 41.11 and 41.12 for different position of work-piece at position A and position B, respectively. This helps to change the vision of the industry from manual tasks to automated machines. The machine copes up with the industrial environment.

Fig. 41.11 Automated welding (Position A)



Fig. 41.12 Automated welding (Position B)



References

1. Ljungkrantz, O., Åkesson, K.: A study of industrial logic control programming using library components. In: Proceedings 3rd IEEE International Conference Automation Science and Engineering IEEE CASE 2007, pp. 117–122 (2007). <https://doi.org/10.1109/COASE.2007.4341783>
2. Nandgave, A., Deshbhratar, H., Khandare, S., Heda, L.: Industrial Drives & Automation Using PLC, vol 3, no 2, pp 2228–2233 (2014)
3. Basile, F., Chiacchio, P., Gerbasio, D.: On the implementation of industrial automation systems based on plc. IEEE Trans. Autom. Sci. Eng. **10**(4), 990–1003 (2013). <https://doi.org/10.1109/TASE.2012.2226578>
4. Prajapati, M., Deivanathan, D.R.: Automatic Pneumatic Forging Machine Using PLC (2018)
5. Ardi, S., Ponco, A., Kurnia, A.F.: Design control systems of the out diameter finish machine based on programmable logic controller. In: Proceedings 2013 3rd International Conference Instrumentation, Communications, Information Technology and Biomedical Engineering Science Technology Improvement Healing Safety, Environment, ICICI-BME 2013, pp. 307–312 (2013). <https://doi.org/10.1109/ICICI-BME.2013.6698514>
6. Kaur, A.: Paper Machine Automation Using PLC, VFD's and HMI, vol 6, no 05, pp. 590–594 (2017)
7. Rahim, A.A.A., Shah, M.H.M., Halim, I.S.A., Hassan, S.L.M.: Programmable Logic Controller (PLC) for polymer mixing tank. In: ISCAIE 2012–2012 IEEE Symposium on Computer Applications and Industrial Electronics Iscaie, pp. 136–141 (2012). <https://doi.org/10.1109/ISCAIE.2012.6482084>

8. Thirumurugan, P.: Automatic sorting in process industries using PLC. *GRD J. Glob. Res. Dev. J. Eng.* **3**(3), 8–13 (2018)
9. Ardi, S., Fairus, S., Sukmaningrum, S.: Design control and monitoring system for boiler wastewater treatment process using programmable logic controller and Hmi (human machine interface). *Sinergi* **24**(2), 133 (2020). <https://doi.org/10.22441/sinergi.2020.2.007>
10. Baladhandabany, D., Gowtham, S., Kowsikkumar, T., Gomathi, P., Vijayasalini, P.: International journal of computer science and mobile computing PLC based automatic liquid filling system. *Int. J. Comput. Sci. Mob. Comput.* **4**(3), 684–692 (2015)
11. Nallamothu, R.B., Science, A.: (Plc) Application for Hybrid Electric Vehicle (Hev) Simulator. no. September, 2017
12. Al Mamun, M.A., Rahman, S.A.M.M., Ahamed, N.U., Ahmed, N., Hassnawi, L.A., Yusof, Z. B.M.: Automatic car parking and controlling system using programmable logic controller (PLC). *Int. J. Appl. Eng. Res.* **10**(1), 69–75 (2015)
13. Gaikwad, R., Kharat, S.M.M., Thakur, J.: PLC based automatic car washing system using proximity sensors. In: *IEEE International Conference Power Control Signals Instrumentation Engineering ICPCSI 2017*, pp. 1875–1878 (2018). <https://doi.org/10.1109/ICPCSI.2017.8392041>
14. Dev Srivastava, M., Sachin, S., Sharma, S., Tyagi, U., Professor, A.: Smart traffic control system using PLC and SCADA. *Int. J. Innov. Res. Sci. Eng. Technol.* **1**(2), 2319–8753 (2012)
15. Patel, R., Shewale, A.N., Patil, C.S.: Automated cooking machine using programmable logic controller (PLC). *Int. J. Comput. Sci. Trends Technol. (IJCS T)* **4**(4), 16–18 (2013)
16. Bayindir, R., Cetinceviz, Y.: A water pumping control system with a programmable logic controller (PLC) and industrial wireless modules for industrial plants—an experimental setup. *ISA Trans.* **50**(2), 321–328 (2011). <https://doi.org/10.1016/j.isatra.2010.10.006>
17. Htay, S., Mon, S.S.Y.: Implementation of PLC based elevator control system. *Int. J. Electron. Comput. Sci. Eng.* **3**(2), 91–100 (2014)
18. Deshpande, V.S., Vibhute, A.S., Choure, A.K., Smitha, P.: Home automation using PLC and SCADA. *Multidiscip. J. Res. Eng. Technol.* **5**(1), 86–90 (2016)

Chapter 42

Road Surface Quality Monitoring Using Machine Learning Algorithm



Prabhat Singh, Abhay Bansal, Ahmad E. Kamal, and Sunil Kumar

Abstract Nowadays, analyzing the road surface conditions is one of the most important aspects of road infrastructure which in turn leads to the better driving conditions and minimizes the risk of road accident. Traditional road condition monitoring systems falls short of collecting real-time update about the road conditions. In earlier models, road surface condition monitoring is done for the fixed roads and static speed of the vehicles. Various systems have proposed approaches of utilizing the sensors mounted in the vehicles. But this approach will not help in predicting the exact location of the potholes, speed breakers and staggered roads. Therefore, smartphone-based road condition assessment as well as the use of the navigation has gained a great existence. We propose to analyze different machine learning approaches to effectively classify the road conditions using accelerometer, gyroscope and GPS data collected from smartphones. In order to avoid noise in the data, we also captured the videos of the roads. This dual technique to data collection will help in providing a more accurate location of potholes, speed breakers and staggered roads. This way of data collection using machine learning algorithms will help in the classifications of roads conditions into various features such as smooth roads, potholes, speed breakers and staggered roads. This information will be provided to the user through the map by classifying the various road conditions. Accelerometers and Gyroscope sensors will investigate various features from all the three axis of the sensors in order to provide a more accurate location of classified roads. Investigate the performance using SVM, random forest, neural network and

P. Singh (✉)
ABES Engineering College, Ghaziabad, India
e-mail: Prabhat.singh@abes.ac.in

P. Singh · A. Bansal · S. Kumar
Amity University, Noida, India
e-mail: abansal1@amity.edu

S. Kumar
e-mail: skumar58@amity.edu

A. E. Kamal
IOWA State University, AMES, IA, USA
e-mail: kamal@iastate.edu

deep neural network to classify the road conditions. Hence, our results will show that the models trained with the help of the dual technique of data collection will provide the more accurate results. By using neural networks will provide significantly more accurate data classification. The approaches discussed here can be implemented on a larger scale to monitor road for defects that present a safety risk to commuters as well as provide maintenance information to relevant authorities.

42.1 Introduction

Smartphones and tablets have become an important aspect of modern society. In recent years, the smartphone market has seen substantial increases in the number of shipments all over the world [1]. Furthermore, mobile Internet use has also seen steady growth in the last few years and has recently surpassed desktop Internet usage for the first time worldwide [2]. The popularity of mobile devices, coupled with their increasing computing power, means that smartphones are performing an increasingly wide range of functions. Applications on mobile platforms such as Google Android and Apple iOS can also take advantage of devices internal sensors, which open up new ways to utilize these smart devices [3, 4]. Sensors can be leveraged for different tasks, such as detecting the orientation of the device or for more complex problems, such as human activity detection [5]. Road infrastructure is another important part of modern society. A large number of people frequently use roads, whether it be in a personal car, on a bike, on foot, or in public transport. Many public services and businesses also depend on the road network in one way or another. As the motorization rate continues to grow [6], a well-maintained and safe road network is beneficial for everybody involved. The monitoring of roads became the challenging worldwide problem in the field of transportation [7, 8]. Bad road conditions lead to large number of accidents and maintenance costs as well it is also a developmental issue of the country. Good roads are the essential part of a developing country like India. In India, road accidents kill almost 1.5 lakh people annually (Table 42.1).

Table 42.1 Comparative analysis of last 5 years road accidents due to road condition

Year	Total number of road accidents	% Change	Total numbers of person killed	% Change	Total number of person injured	% Change
2014	4,89,400	2.21	1,39,671	4.21	4,93,000	4.41
2015	5,02,321	2.46	1,46,133	4.63	5,00,278	1.38
2016	4,80,652	-4.14	1,50,785	3.18	4,95,294	-1.13
2017	4,64,910	-3.28	1,47,913	-1.9	4,75,274	-4.78
2018	4,67,044	0.46	1,51,417	2.37	4,69,297	-0.33
2019	5,10,000	2.41	1,64,418	2.51	4,88,212	-2.21
2020	5,15,000	3.21	1,68,413	3.12	4,76,298	-2.25

Hence, good road quality became major in order to prevent the road accidents which are increasing day by day. Also, the maintenance of the road is one of the challenging tasks due to high rush on the road and weather conditions. There are so many methods which have been used for the road conditions surveyed in [9, 10]. But, the limitation to these several methods is that these are costly due to which they cannot use on the large scale for the monitoring of the roads conditions. There are so many factors due to which pavement failure occurs. Some of them are:

1. Potholes
2. Depression
3. Rutting
4. Raveling
5. Alligator cracking.
 - a. **Patholes:** Potholes are small, deep depressions in the roads that penetrate all the way to the depth of the surface. It generally causes a large number of accidents because those holes are not seen easily. Some form of filling can be used to cover the potholes (Fig. 42.1).
 - b. **Depression:** Depression is the failure in which the surface is slightly lower along with the surrounding pavement surface. It can be easily seen after a rain because water became filled in these depressions due to which other issues also rises (Fig. 42.2).
 - c. **Rutting:** Rutting is a depression of the surface which forms over a large amount of time, and it generally occurs by the load and heavy vehicles. It must be recovered as early as possible in order to prevent the accidents by heavy vehicles (Fig. 42.3).
 - d. **Raveling:** Raveling is generally caused due to the removal of top pavement surface of the road. Another reason for raveling is continuous intrusion of water. It also requires early treatment because it can also cause harmful incidents in the future (Fig. 42.4).
 - e. **Alligator cracking:** Alligator cracking is the problem where the surface begins to compress from bearing the load and heavy traffic on the roads. It generally found where vehicles stopped for a large amount of time frequently (Fig. 42.5).

Fig. 42.1 Potholes



Fig. 42.2 Depression

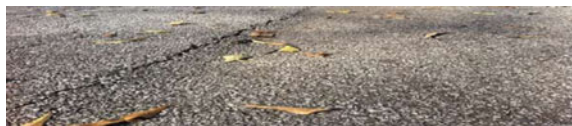


Fig. 42.3 Rutting**Fig. 42.4** Raveling**Fig. 42.5** Alligator cracking

42.2 Literature Review

For classification, Seraj et al. [11] used support vector machines with RBF kernel. Features were extracted from time domain, frequency domain and wavelet decomposition. Frequency domain representation of the signal was computed using a FFT algorithm with a Hamming window function, and the signal decomposition was done using stationary wavelet transform [12, 13]. Time domain features included: standard deviation, mean, variance, root mean square, peak to peak, mean of absolute values, zero-crossing rate, correlation between all axes, tilt angles, signal magnitude area and waveform length. Hoffmann et al. [14] also uses machine learning for classification. Two types of road surface classification processes were carried out: direct road surface classification and bump detection-based classification. Direct road surface classification consisted of classifying a road surface as one of three categories: *smooth*, *bumpy* or *rough*. Eriksson et al. [15] used a signal processing and machine learning approach to detect and classify several specific road anomalies. The paper describes the issue of having other unwanted anomalies manifest in the accelerometer signal, for instance abrupt turning or stopping. Different characteristics, such as speed, and filters, such as a high-pass filter, were used to reject such events.

For various types of roads conditions, multiclass classification techniques have not been explored which can produce huge changes in the output of the data. There are some applications like potholes Marker and More “[16] and Fill That Hole” [17] where we can submit the images of potholes to their central server. However, those applications are not so efficient on the large scale.

Sensor Technology: Sensors are the parameters which can provide us various information of road by which we can provide an efficient solution or the betterment of roads. There are various types of sensors like static sensors and mobile sensors. Let us see various types of sensors:

(a) Static Sensors

Static sensors are those sensors which are statically placed on the roads, i.e., once they are placed, their position cannot be changed. Every year, government spends a huge amount of money on infrastructure of roads but due to heavy traffic rush on the roads, their condition becomes damage easily [18–20]. Today, various automobile industries also use various sensors even in the vehicles to detect the conditions so that they can improve their technologies and functions. Static sensors collect real-time data from environment which helps to monitor condition of roads in an efficient manner [21] (Fig. 42.6).

(b) Mobile Sensors

Mobile sensors become very popular as the installation of these types of sensors does not need huge maintenance and installation cost; on the other hand, these types of sensors are efficient as they generally do not get affected by the climatic and environmental conditions. It is because as these types of sensors are generally wireless, so also provide faster and prominent output. There are some other sensors which also installed in the devices like laser node, Bluetooth node, gas node, GPS and Wi-Fi setting [14] was the first who proposed an idea that we can add sensors in the moving vehicles in the road in order to monitor the condition of road along with the static sensors. It results that this proposal becomes popular for the sensing technology as it reduces the installation cost which was so huge in the static sensors [22, 23].

42.3 Proposed Work

There are so many reasons like potholes, depression, etc. as discussed in introduction part which causes the abnormal vibration in the vehicles on the roads. Due to the presence of these vibrations, different sensors also collect the data along with vibration disturbance which does not give accurate results. We have made two assumptions in our research. We assume that value of acceleration is similar to that of accelerometer as the coordinate system of the accelerometer is fixed. Another assumption is that the suspension system of the vehicle is in the good condition.

Fig. 42.6 Static sensor



Firstly, we have to examine the road condition and categorize it in the particular category, then only we can evaluate the condition of the road. With the help of acceleration data analysis, we have to focus on locating the problem of road. Now, the condition of the road can be evaluated with the help of data collected in the first step. Generally, there are two types of road surfaces, i.e., smooth and rough surfaces. A smooth surface is that on which traveling is very smooth as it provides high-quality driving surface which the rough surface is completely vice versa. Road surface quality is to examine the function with the model of smooth surface. According to the definition of International Roughness Index [24], roughness in the road can be evaluated on the basis of the vertical deviations on the surface of the road. To determine the results, accelerometer and gyrosensor has been set up on the front bumper of the vehicle (Fig. 42.7).

42.3.1 *Process Flow of Data Preprocessing*

The categorization or labeling of the roads is very typical task in this research as there are so many vibrations and environmental errors due to which it becomes difficult to take the accurate readings. Also, it leads to the problem in finding the exact position of the potholes present on the pavement surface. In order to overcome this problem, the process of labeling is performed again. It is because as if the result of labeling would be more accurate, then it would be easy for finding the anomaly detection (Fig. 42.8).

Fig. 42.7 Setup of sensors in a vehicle



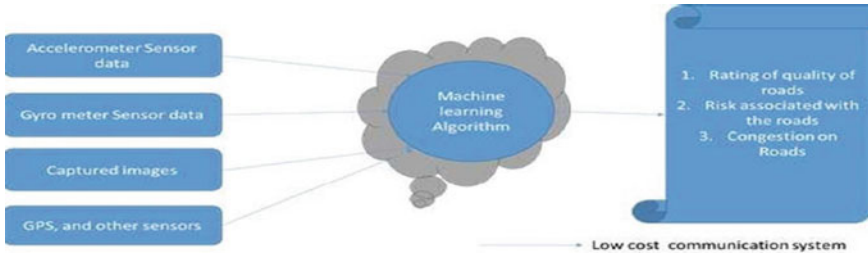


Fig. 42.8 Data preprocessing using mobile sensors

42.3.2 Model Building and Algorithm

After gathering all the required features of the data, further processing of data takes place. Now, the process of training begins in which we make use of LIBSVM, a library package of Support Vector Machine Classification [25]. By using the SVM, when we give the training data as input to the model, it divides the data into partitions via hyperplane into desired categories. Hence, model would learn for the future unknown data by using this method. Apart from supervised classification technique, we have also used an unsupervised learning method for the model of the smooth surface. The proposed method for the smooth surface would be as follows:

Algorithm for constructing the model of smooth surface: Input: A is the set of Input data segment, and B is a smooth surface model.

1. For each $X \in B$
2. do For each $\epsilon \in B$
3. do If Speed ($X_s = \epsilon$)
4. Then M_s . Add(X_s)
5. End
6. End
7. End
8. For each $M^\epsilon \in M_s$
9. do HC= Hierarchical Cluster(M^ϵ)
10. do $M^\epsilon =$ Filter Majority(HC)
11. End

42.4 Result

In the proposed model, the simple support vector machine was implemented with one hundred iterations, where every iteration uses different groupings of occurrences for the testing and training. It also maintains the same ratio every time for all

Table 42.2 Implemented results of smooth surface algorithm on simple SVM

Parameter (AVG)	All axis (ms)		Y axis (ms)	
Training loss	0.0154		0.0657	
Fivefold loss	0.081		0.0924	
Sevenfold loss	0.086		0.0956	
Tenfold loss	0.0898		0.094	
Leave one out loss	0.081		0.092	
Parameter (AVG)	All axis (ms)		Y axis (ms)	
Training loss	0.0281		0.0762	
Test accuracy	0.879		0.912	
	Not smooth	Smooth	Not smooth	Smooth
Precision	0.451	0.921	0.431	0.941
Recall	0.473	0.934	0.456	0.956

classes. The generalized performance of the algorithm is evaluated using the average values of evaluation parameters. The calculated results are being enlisted in Table 42.2 having the training loss, accuracy of testing, correctness and recall rates.

Through the analysis of Table 42.2 shows that SVM classifier is trained using structures which has lower loss and performs better on all three axes in comparison to the only one axis.

42.5 Conclusion and Future Work

In this paper, various types of road surface were analyzed. After analyzing the road surface conditions, various methods for detecting the road surface conditions were discussed such as deploying sensors road side or in the vehicle to obtain the information about the road. Working model is being proposed for the collection of the data from the mobile sensors and then applying machine learning algorithms in order to classify the road surface conditions based on their quality.

It is also observed that the machine learning approaches implemented are quite effective in classifying road anomalies such as cracks and potholes. Classifiers trained using features from all axes proved to be more accurate when compared to features from only one axis. Since our approach of extracting large number of features from all three axes to train multiclass machine learning classifiers was a novel approach, our results are independent from those in current literature.

There are certain limitations in our current work that can be overcome in future works by addressing certain challenges. The relatively small size of our training dataset can cause loss of accuracy and precision. The disproportional distribution of instances of cracks, potholes and smooth road conditions introduces a bias and may have affected the individual precision and recall rates. Since neural networks generally require a very large dataset to accurately train itself using direct data, results can be improved by addressing our shortage of data.

References

1. Bajpai, P.: The evolution of smartphone markets: where growth is going (2016). <http://www.nasdaq.com/article/the-evolution-of-smartphone-markets-where-growth-is-going-cm619105> (10.05.2017)
2. StatCounter press release. Mobile and tablet internet usage exceeds desktop for first time worldwide (2016). <http://gs.statcounter.com/press/mobile-and-tablet-internet-usage-exceeds-desktop-for-first-time-worldwide> (10.05.2017)
3. Proceedings—2015 5th International Conference on Communication Systems and Network Technologies, CSNT 2015, pp. 194–200 (2015)
4. Kumar, S., Ranjan, P., Ramaswami, R.: Energy optimization in distributed localized wireless sensor networks. In: Proceedings of the International Conference on Issues and Challenges Intelligent Computing Technique (ICICT). <https://doi.org/10.1109/ICICT.2044.678130>
5. Anguita, D., Ghio, A., Oneto, L., Parra, X., Reyes-Ortiz, J.L.: Human activity recognition on smartphones using a multiclass hardware-friendly support vector machine. In: International Workshop on Ambient Assisted Living, pp. 216–223. Springer, Berlin, Heidelberg (2012)
6. Tonde, V.P., Jadhav, A., Shinde, S., Dhoka, A., Bablade, S.: Road quality and ghats complexity analysis using android sensors. *Int. J. Adv. Res. Comput. Commun. Eng.* **4**(3), 101–104 (2015)
7. Seraj, F., van der Zwaag, B.J., Dilo, A., Luarasi, T., Havinga, P.: Roads: a road pavement monitoring system for anomaly detection using smart phones. In: International Workshop on Modeling Social Media, pp. 128–146. Springer International Publishing (2014)
8. Alessandrini, G., Klopfenstein, L.C., Delpriori, S., Dromedari, M., Luchetti, G., Paolini, B. D., Seraghiti, A., Lattanzi, E., Freschi, V., Carini, A., Bogliolo, A.: SmartRoadSense: collaborative road surface condition monitoring. In: Proceedings of UBIComm-2014. IARIA., pp. 210–215 (2014)
9. Astarita, V., Caruso, M.V., Danieli, G., Festa, D.C., Giofrè, V.P., Iuele, T., Vaiana, R.: A mobile application for road surface quality control: UNIquALroad. *Procedia Soc. Behav. Sci.* **54**, 1135–1144 (2012)
10. Kumar, S., Ranjan, P., Ramaswami, R., Tripathy, M.R.: EMEEDP: enhanced multi-hop energy efficient distributed protocol for heterogeneous wireless sensor network
11. Eriksson, J., Girod, L., Hull, B., et al.: The Pothole patrol: using a mobile sensor network for road surface monitoring. In: 6th International Conference on Mobile Systems, Application, and Services (MobiSys 2008), Breckenridge, USA, June, 2008, pp. 29–39.1
12. Bishop, R.: A survey of intelligent vehicle application worldwide. In: IEEE Intelligent Vehicles Symposium (IV 2000), Dearborn, MI, USA, May 2000, pp. 25–30
13. Kumar, S., Ranjan, P., Ramaswami, R., Tripathy, M.R.: A utility maximization approach to MAC layer channel access and forwarding. In: Progress in Electromagnetics Research Symposium, 2015 Jan, pp. 2363–2367 (2015)
14. Sanwal, K., Walrand, J.: Vehicles as probes. Paper ucb-its-pwp-95-11. California Partners for Advanced Transit and Highways (PATH) (1995)
15. Gillespie, T.: Everything you always wanted to know about the IRI, but were afraid to ask! In: Road Profile Users Group Meeting, Lincoln, Nebraska (1992)
16. Smith, S.: Digital Signal Processing: A Practical Guide for Engineers and Scientists. Newnes (2003) [Online]. Available: <http://www.dspguide.com/pdfbook.htm>
17. Chang, C.-C., Lin, C.-J.: LIBSVM: A Library for Support Vector Machines, 2001, Software. Available at <http://www.csie.ntu.edu.tw/~cjlin/libsvm>
18. Singh, P., Bansal, A., Kumar, S.: Performance analysis of various information platforms for recognizing the quality of Indian roads. In: Proceedings of the Confluence 2020–10th International Conference on Cloud Computing, Data Science and Engineering, pp. 63–76, 9057829 (2020)

19. Reghu, S., Kumar, S.: Development of robust infrastructure in networking to survive a disaster. In: 2019 4th International Conference on Information Systems and Computer Networks, ISCON 2019, pp. 250–255, 9036244 (2019)
20. Kumar, S., Ranjan, P., Ramaswami, R., Tripathy, M.R.: An NS3 implementation of physical layer based on 802.11 for utility maximization of WSN. In: Proceedings—2015 International Conference on Computational Intelligence and Communication Networks, CICN 2015, pp. 79–84, 7546060 (2016)
21. Kumar, S., Ranjan, P., Ramaswami, R., Tripathy, M.R.: Energy efficient multichannel MAC protocol for high traffic applications in heterogeneous wireless sensor networks. *Rec. Adv. Elect. Electron. Eng. (Formerly Recent Patents on Electrical & Electronic Engineering)* **10**(3), 223–232 (2017)
22. Sunil Kumar, et al.: *Evolution of Software-Defined Networking Foundations for IoT and 5G Mobile Networks*, 2020/10, p. 350, IGI Publisher. ISBN 9781799846857
23. Kumar, S., Ranjan, P., Ramaswami, R., Tripathy, M.R.: Energy aware distributed protocol for heterogeneous wireless sensor network. *Int. J. Control Autom.* **8**(10), 421–430 (2015). <https://doi.org/10.14257/ijca.2015.8.10.38>
24. Kumar, S., Ranjan, P., Ramaswami, R., Tripathy, M.R.: Resource efficient clustering and next hop knowledge based routing in multiple heterogeneous wireless sensor networks. *Int. J. Grid High Perform. Comput. (IJGHPC)* **9**(2), 1–20 (2017)
25. Dubey, G., Kumar, S., Navaney, P.: Extended opinion lexicon and ML based sentiment analysis of tweets: a novel approach towards accurate classifier. *Int. J. Comput. Vis. Robot. (IJCVR) (Inderscience Publishers)* **10**(6), 505–521 (2020)

Chapter 43

Optimization of Electric Vehicle Ladder Frame Chassis Based on Material and Thickness Parameter Variation Using FEA



Yash Keskar, Sourabh Damkale, and Pankaj Dhattrak

Abstract A Go-Kart is a four-wheeled vehicle having low ground clearance and does not involve a differential and suspension. The present study focuses on the analysis of an electric Go-Kart chassis frame based on proper material selection and optimized chassis thickness. To find the optimum material and thickness, a comparative analysis was conducted with three different materials, namely AISI 1018, AISI 1020 and AISI 4130, which were selected based on their yield tensile strength values. Similarly, the effect of stress on thickness variation of the chassis is analysed by varying the thickness values between 1.4 and 2 mm in a step of 0.2 mm. From the numerical studies, the results show that the AISI 1018 is the suitable material based on the factor of safety, weldability and machinability. Optimizing the thickness of the chassis helps chassis weight and cost reduction.

43.1 Introduction

A Go-Kart is a vehicle consisting of four non-aligned wheels without any suspension having a very low ground clearance which is used mainly for racing purposes and recreation [1]. The chassis of an electric Go-Kart is designed by taking into account the several factors such as the location of the subsystems, weight reduction and the stiffness, and it should be able to withstand both static loading and dynamic loading [2]. Chassis is one of the fundamental units of any vehicle and acts as the backbone of the vehicle. The shape of the vehicle depends on the chassis structure, and it also absorbs energy from the side, rollover and frontal impacts [3]. The greater the absorption of energy on impact by the chassis,

Y. Keskar (✉) · S. Damkale
School of Mechanical Engineering, Dr. Vishwanath Karad, MIT World Peace University,
Pune, India

P. Dhattrak
Faculty of Mechanical Engineering, Dr. Vishwanath Karad, MIT-WPU, Pune, India
e-mail: pankaj.dhattrak@mitwpu.edu.in

the lower are the levels of energy transmitted to the occupants of the vehicles and its surroundings, thereby also reducing the probabilities of injury [4]. The two main functions of the chassis are to provide a support to the components and the mounted payload which includes the body, passengers, engine, and luggage and to sustain the relationship which is desired between the mounting points of steering mechanism and suspension if any. A ladder frame type of chassis with tubular cross section is usually preferred for a Go-Kart [3].

A ladder frame chassis offers superior beam resistance, but poor resistance to warping and torsion [5, 6]. Efficient and effective performance of chassis depends on sustaining the rigidity in torsion and bending, proving competent load absorption and decreasing the total weight of the chassis. The material of the chassis plays a vital role in determining the endurance, strength, weight, safety, reliability and thus the overall performance of the chassis [7].

Generally, steel is used as the material for the ladder frame chassis of a Go-Kart. To be more specific, the AISI 1018, AISI 1020 and AISI 4130 grades of steel are used for the Go-Kart chassis [1]. Because of the strength, stiffness, endurance and durability offered by steel, it is therefore a desirable material to be used in the chassis of a Go-Kart. Also AISI 1018 offers high machinability and high tensile strength and is thus a suitable material for a Go-Kart chassis [8]. For a chassis material, especially steel, a variation in the subsystems and its location plays a vital role as it is correlated with the static failure [9, 10]. Also, the thickness of the tubular chassis members and the position of the cross members are important factors affecting the failure of the chassis. It is therefore necessary to figure out the best suitable material and thickness of the tubular chassis members so as to design a strong chassis, thus avoiding the failure. This study intends to give a comprehensive understanding about the design and the static analysis of an electric Go-Kart chassis. A thorough comparison between the standard materials of AISI 1018, AISI 1020 and AISI 4130 has been carried out having variable thickness of 2 mm, 1.8 mm, 1.6 mm and 1.4 mm. It will help in optimizing both the material and thickness parameters of the chassis.

43.2 Materials and Methods

43.2.1 Material Selection and Thickness Variation

The process of selection of a material for a chassis is an important and a tedious task as it involves dealing with several constraints of structural resilience and weight which are subjected to different types of forces, factor of safety and torsional rigidity when various loads are applied, and the material selection also depends on the cost and pricing constraints and the availability of material in the market [11]. Generally, the material having high rigidity and high weight to strength ratio is selected as it leads to reduction in weight. Hence, carbon fibre is one of the

materials used for chassis building nowadays. This also includes materials like molybdenum and chromium steel [12]. Sometimes, a composite or hybrid material is also used for building up of a chassis, provided it shows better performance and results. S235 steel has also been used in the construction of a Go-Kart chassis owing to its good material and mechanical properties [9, 13].

In the present study, three grades of steel are the material for our chassis, namely AISI 1018, AISI 1020 and AISI 4130. AISI 1018 was chosen, the reason being its high strength to weight ratio, high yield strength, good manufacturability and weldability and because it is relatively soft. AISI 1020 was chosen owing to its good weldability and machinability properties. AISI 4130 was selected because of its high strength to weight ratio and high yield strength. The thickness directly impacts the strength and weight of the chassis, thus optimization of the thickness parameter is crucial. The selected chassis cross section was a circular with an outer diameter of 25.4 mm, and thickness values selected were from 1.4 to 2 mm in steps of 0.2 mm. The material properties of the selected three grades are given in Table 43.1.

43.2.2 3D Modelling of Chassis

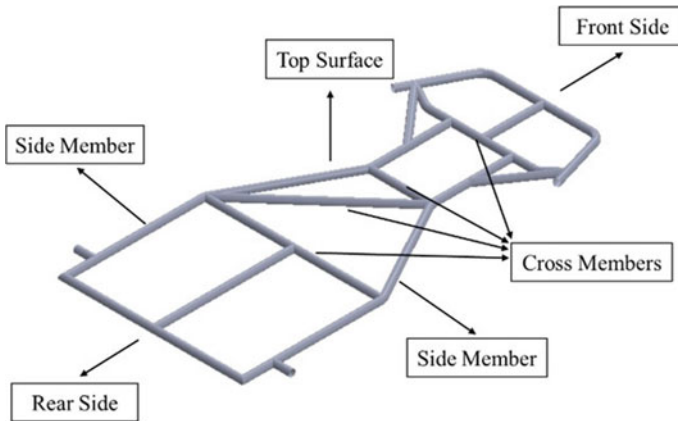
For a Go-Kart, a simple design is preferred in order to ease the manufacturing process of the chassis [14]. There are different types of chassis which are classified based on body style, each of them having different applications, construction and functionality. Ladder frame, monocoque, tubular, rolling frame, etc., are some of the types of chassis [15]. The ladder frame type of chassis having circular cross section was chosen for the Go-Kart, and the use of software like CATIA, Pro E and Creo was suggested for designing of the chassis [13, 16]. However, Patil et al. [17] and Bopaiah et al. [18] have used the roll cage type of chassis for designing and analysis of the Go-Kart chassis. While designing, the chassis factors that we focused on were driver ergonomics and the structural integrity. Table 43.2 represents the vehicle design specifications. 3D CAD model of chassis (Fig. 43.1) was designed in SolidWorks software.

Table 43.1 Material properties of AISI 1018, AISI 1020 and AISI 4130 [12]

Sr. No.	Properties	AISI 1018	AISI 1020	AISI 4130
1.	Density (gm/cc)	7.87	7.83	7.85
2.	Young's modulus (GPa)	205	200	210
3.	Bulk modulus (GPa)	159	140	140
4.	Elongation at break (%)	15	36.5	28.2
5.	Ultimate tensile strength (MPa)	440	394.72	560
6.	Poisson's ratio	0.29	0.29	0.27
7.	Yield strength (MPa)	370	294.74	435
8.	Machinability (%)	70	65	70

Table 43.2 Vehicle design specifications for electric four-wheeler Go-Kart

Sr. No.	Parameter	Specification
1	Gross vehicle weight	180 kg
2	Payload	Single seater (70 kg)
3	Track width	864–965 mm
4	Wheelbase	1067 mm
5	Top speed	60 km/h

**Fig. 43.1** Isometric view of the CAD model of the electric Go-Kart chassis

43.3 Analysis of Chassis

43.3.1 Meshing

The chassis is divided very finely into a large number of finite elements, and then each of these elements undergoes a very critical analysis [8]. The tetrahedral-shaped mesh is generally used in analysis since it gives best results [2]. Patil et al. [17] used ANSYS 14.5 software for meshing and also stated the number of nodes and elements in the meshed model of the Go-Kart chassis. Bopaiah et al. [18] used ANSYS 16.0 software for meshing of the chassis and also reported the number of nodes and elements. The chassis was meshed using the tri/quad elements of average size 3 mm using HyperMesh. The chassis was fine meshed at the joints and constraint locations to obtain the accurate stress distribution. Figure 43.2 represents the FE meshed model of the Go-Kart chassis.

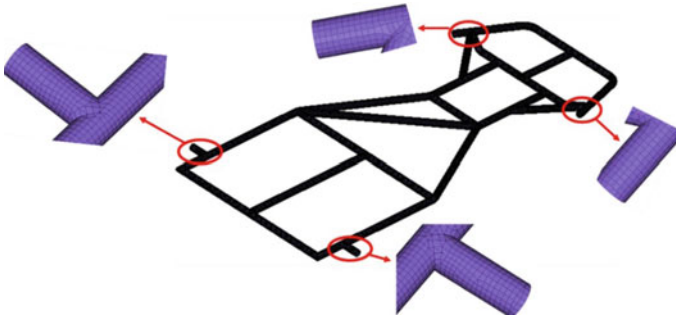


Fig. 43.2 Isometric view of the meshed model of chassis with zoom views at four constraints

43.3.2 Load and Boundary Conditions

The forces are primarily the reason behind the deformation and crack initiation in the vehicle, thus making it vital to determine the maximum stress areas [19]. Jafri et al. [14] stated that the average weight of a male and the engine is to be considered during the Go-Kart chassis analysis study. Kumar et al. [16] have stated the different loads acting on a frame. In the present study, a set of nodes was selected, followed by creation of master node with a spider of 1D elements at each of the four locations, master nodes 1, 2, 3 and 4 (Fig. 43.3). Each of these master nodes was then constrained in all degrees of freedom.

Master node 5 (Fig. 43.3) was generated by selecting slave nodes in the centre according to location of the load. The vertical load was applied after considering the overall weight of the Go-Kart and the weights of the major components. A load of 180 kg was applied on the top surface of the chassis which included the weight of the driver (70 kg), chassis and mounts (10 kg), battery (25 kg), motor (15 kg) and miscellaneous (60 kg) which adds up to sum of 180 kg. The force of 1765.8 N was applied on the master node created, in the negative Y direction (Fig. 43.4).

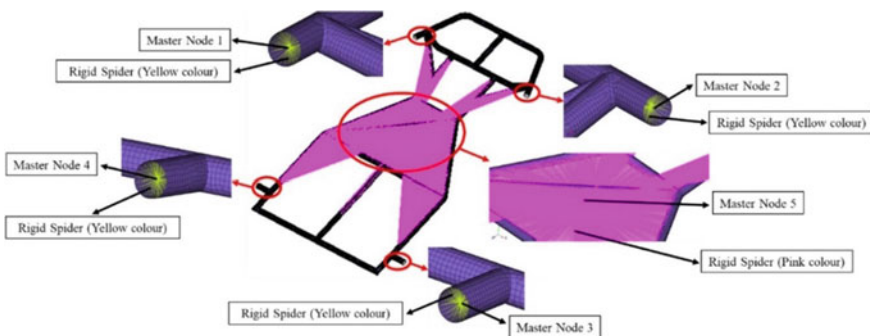


Fig. 43.3 Rigid RBE2 elements at four constraints and rigid RBE3 element for load application

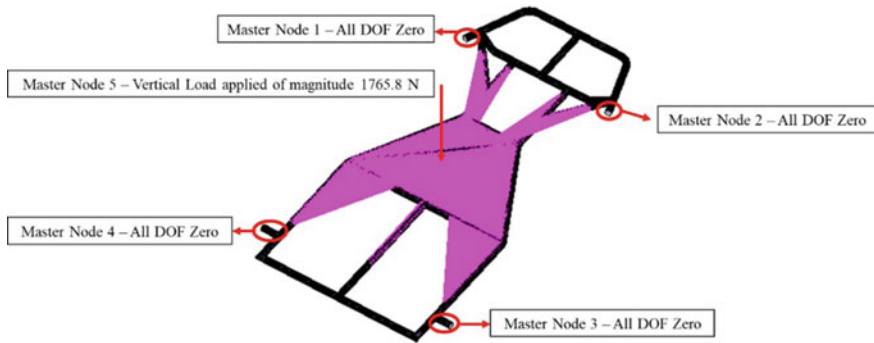


Fig. 43.4 Boundary conditions—master nodes 1, 2, 3 and 4 are constrained with all DOF zero, and vertical load of 1765.8 N is applied on master node 5

43.4 Results and Discussion

The results displayed maximum deformation for AISI 1020 and least deformation for AISI 4130. For each of the material, the trend read least values of deformation for 2 mm thickness, and then there was a gradual increase in the value of deformation with the decrease in thickness, where 1.4 mm thickness witnessed maximum deformation. Amongst the twelve iterations, the highest value of deformation (4.09 mm) was recorded for AISI 1020 having 1.4 mm thickness, and the least value of deformation (2.49 mm) was recorded for AISI 4130 having 2 mm thickness. Hence, the results conclude that AISI 4130 material having a thickness of 2 mm underwent the least deformation.

The analysis included computing the von Mises stress which is generally used for determining the yielding or fracture in a material. AISI 4130 generated higher values of von Mises stress as compared to AISI 1018 and AISI 1020 (Fig. 43.6). The von Mises stress generated in AISI 1018 and AISI 1020 was observed to be the same for each of the corresponding thickness values. Within each material, the trend read least values of von Mises stress for 2 mm thickness, and then the value went on increasing gradually with decrease in thickness. Within the set of twelve iterations, the highest value of stress (388.9 MPa) was generated in AISI 4130 having 1.4 mm thickness, and the least value of stress (227.12 MPa) was generated by AISI 1018 and AISI 1020 having 2 mm thickness.

Later, the factor of safety (FoS) was computed for each of the twelve iterations. The variation in the factor of safety and the deformation observed after the analysis is depicted in Fig. 43.5 according to the different materials along with the various thickness values. Nawade et al. [20] discussed the FEA results and stated that by using FEA, they were successfully able to conclude that their chassis design was safe. Raghunandan et al. [8] stated that with the help of analysis they were able to rectify the weak points and hence modify the chassis by strengthening the weak areas which would eventually bear the weight of 120 kg successfully concluding

their design to be safe. Sannake et al. [21] highlighted the importance of determining the best suitable material for building up the Go-Kart chassis with the help of the analysis carried out using FEM. Their chassis design was safe since the factor of safety obtained was greater than 1. Viswanadh et al. [22] discussed the analysis results obtained from FEM and concluded that they were able to locate the areas of maximum deflection which eventually helped them to produce a safe chassis design. Jafri et al. [14] concluded that the analysis carried out using FEM helps in cost reduction by minimizing the amount of material used and also helps in optimizing the overall performance of the chassis.

Nawade et al. [20] conducted a computational and numerical analysis for AISI 4130 material for front, side and rear impact and concluded that AISI 4130 can be used for a Go-Kart chassis similar study conducted by Saini et al. [1] and Attarde et al. [12]. They also stated that a further study is required on the performance of advanced material like carbon fibre as the chassis material. Kumar et al. [16] presented a comparative FEA study and concluded that carbon fibre material is the best suitable material based on strength to weight ratio, rigidity, corrosion resistance, von Mises stress and the total deformation achieved. Boddepalli et al. [23] selected the material of AISI 1020, amongst AISI 4130, AISI 1026 and AISI 1020 for Go-Kart chassis, concluded that the chassis designed with AISI 1020 is safe and bears good strength. Kumar et al. [24] and Quazi et al. [25] performed FEA with chassis material AISI 1018 and concluded that the designed chassis is safe and has good strength to weight ratio and is easy to manufacture.

The FoS of 1.3 and above was safe as it ensures that the chassis can sustain loads well above the defined loading conditions and ensures that the chassis is not over designed, which would increase the overall weight and hamper the performance otherwise. There were six cases (Fig. 43.5) which satisfied this criterion. All the deformation values observed are well below the maximum allowable deformation, based on the ground clearance. The density of all the materials is the same; thus, the weight varies with the change in thickness values. The weight of the chassis for a thickness of 2 mm was calculated to be 7.81 kg. The weight reduction for 1.8 mm

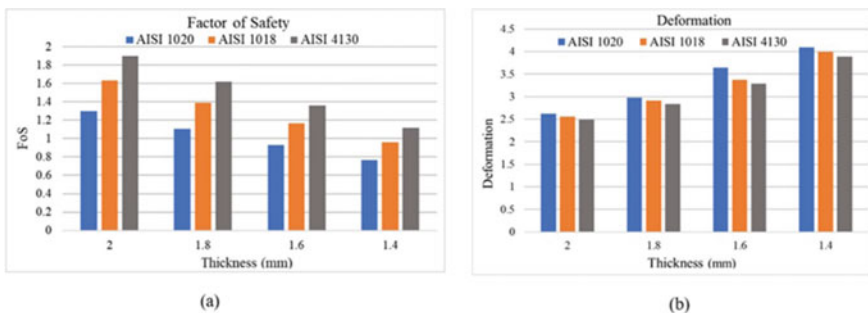


Fig. 43.5 Variation in **a** factor of safety and **b** the deformation in the chassis observed by varying the materials along with the different thickness values

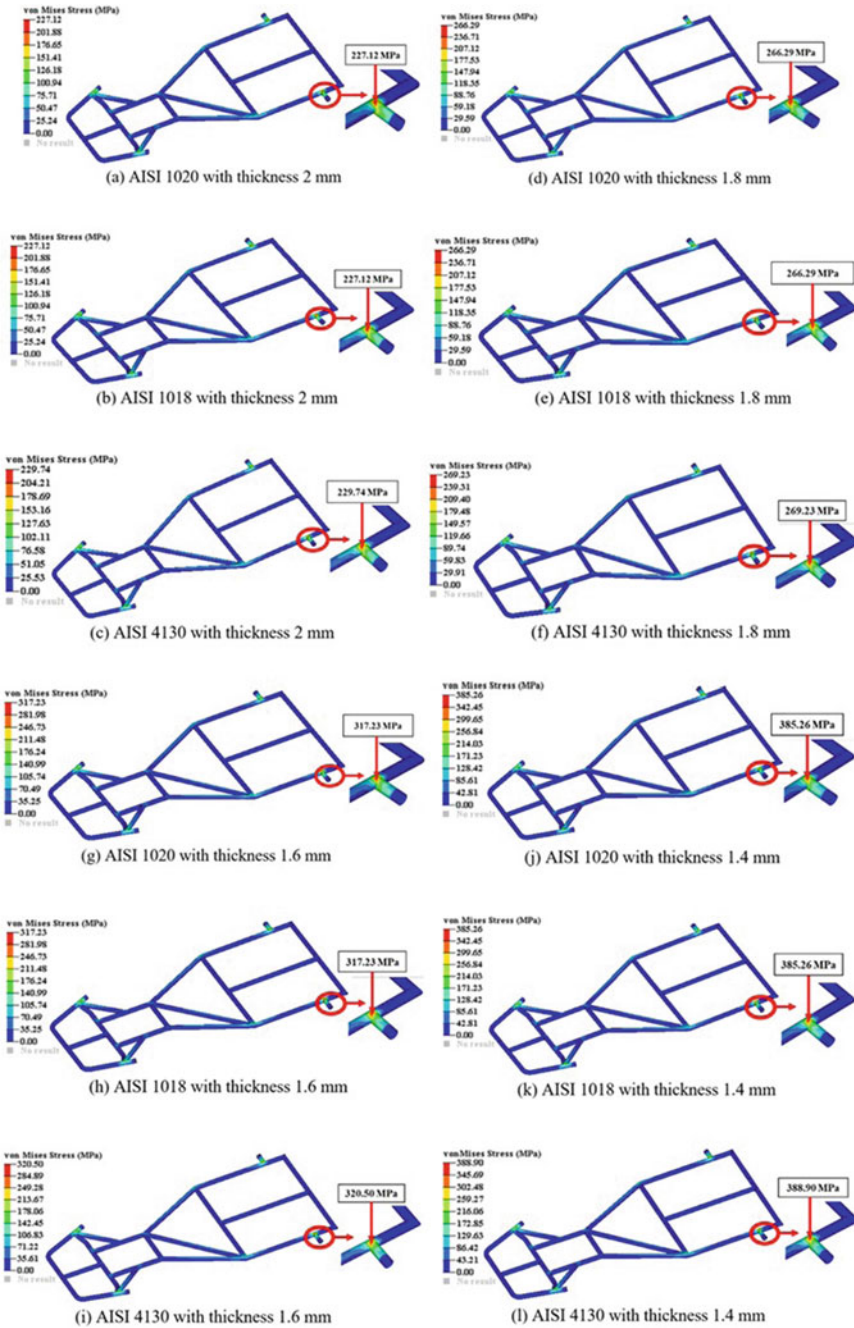


Fig. 43.6 von Mises stress in the chassis for different materials and varying thickness

thickness was 9.22%, and similarly for 1.6 and 1.4 mm thickness chassis was 18.56% and 28.17%, respectively. The machinability of AISI 1018 and AISI 4130 is greater than that of AISI 1020. AISI 1018 and AISI 1020 have better weldability as compared to AISI 4130 (Fig. 43.6).

43.5 Conclusion

The FEA of a chassis is vital as it helps in determining both the weakness and the strength of the design. The present study deals with the comparison of three materials for the Go-Kart chassis AISI 1018, AISI 1020 and AISI 4130 with thickness variation 1.4–2 mm. Using finite element method, static analysis of the chassis was carried out by applying vertical loads to compute the maximum deformation and the equivalent stress. On the basis of parameters like FoS, deformation, weight, cost, weldability and machinability, it is concluded that the suitable material is AISI 1018 and the suitable thickness is 1.8 mm. The FoS of chassis with material AISI 1018 and having thickness 1.8 mm is 1.39, which serves as an optimum FoS as it can sustain loads well above the loading conditions. AISI 1018 has both good machinability and weldability and thus makes it easier to manufacture the chassis. A thickness of 1.8 mm also ensures that there a proper optimization of the weight and thus the cost of the chassis. The selected material AISI 1018 with 1.8 mm thickness has shown deformation which is well under the maximum allowable deformation. From the results, it can be concluded that the Go-Kart chassis designed is safe, and the material and the thickness parameters are optimized. This work is intended for helping the designers in designing a safe chassis and to improve the overall performance of the Go-Kart.

References

1. Saini, N.K., Rana, R., Hassan, M.N., Goswami, K.: Design and impact analysis of Go-kart chassis. *Int. J. Appl. Eng. Res.* ISSN 0973–4562 **14**(9) (2019)
2. Kondala Rao, P., Jagadish, Ch., Abhishek, P., Mutra, R.R.: Design and static analysis of chassis used in Go-kart. *Int. J. Eng. Res. Technol. (IJERT)* ISSN: 2278–0181 **7**(03) (2019)
3. Kanade, P., Mankar, R.: Finite element analysis of automobile chassis. *Glob. Res. Dev. J. Eng.* **2**(7), 4
4. Nega, H.F., Hui, Y.: Study of fatigue analysis of vehicle truck chassis, *Int. J. Sci. Res. (IJSR)* **4**(5), 5, Corpus ID: 47006678 (2013)
5. Mishra, Y.: Design & analysis of ladder frame chassis. *Int. Res. J. Eng. Technol. (IRJET)* **07** (08), 10 (2020)
6. Darlong, O.L., Reddy, B., Dadapeer, B.: Design and analysis of a ladder frame chassis for static and dynamic characteristics. *Int. J. Latest Trends Eng. Technol.* **6**(1), 14 (2015)
7. Denny, J., Veale, K., Adali, S., Leverone, F.: Conceptual design and numerical validation of a composite monocoque solar passenger vehicle chassis. *Eng. Sci. Technol. Int. J.* **21**(5), 1067–1077 (2018). <https://doi.org/10.1016/j.jestch.2018.07.0149>

8. Raghunandan, D., Pandiyan, A., Majeed, S.: Design and analysis of Go-kart chassis. *IJESRT* **5**(11) (2016). <https://doi.org/10.5281/zenodo.164912>
9. Ramli, A.S., Said, A.Y.B., Chalons, E.: Design and analysis of chassis for Go-kart using finite element. *Eng. Technol.* **01**, 5 (2016)
10. Thangarasu, V.S., Dhandapani, N.V., Sureshkannan, G.: A study on fatigue failure analysis of an off-highway vehicle chassis rear rail structure using finite element approach. *Int. J. Appl. Eng. Res.* ISSN 0973-4562 **10**(71) (2015)
11. Bhadang, S.J., Pimpalgaonkar, S.M., Masurkar, N., Gabne, S., Rane, N., Rathi, S.: Design and analysis of go kart chassis. *Int. J. Curr. Eng. Sci. Res. (IJCESR)* **6**(3), 4 (2019)
12. Attarde, R., Chougule, A., Magdum, R.: Material based FEA analysis of a Go-kart chassis: a comparative study. *Adv. Eng. Forum* **31**, 10-25 (2019). <https://doi.org/10.4028/www.scientific.net/AEF.31.10>
13. Bhosale, N.B., Deshmukh, M.B., Darandale, G.N., Fadale, J.L.: Design and FEA of Go kart chassis. *Int. J. Eng. Res. Technol. (IJERT)* **6**(6) (2017). <https://doi.org/10.17577/IJERTV6IS060402>
14. Jafri, M.A., Marwan, S.H., Lazim, M.K., Anuar, N.D.: Finite element analysis of Go-kart chassis TeMCI (2019)
15. Prashant, A., Suresh, D., Sivaramakrishna, V.: Design and analysis of automobile chassis by using composite material E-glass epoxy. *Int. J. Innovative Res. Sci. Eng. Technol. (IJIRSET)* **6**(10) (2017). <https://doi.org/10.15680/IJIRSET.2017.0610060>
16. Kumar, M.D., Naryan, K.L., Choudary, P.S., Ganapathi, A.S.: Design and analysis of Go-kart chassis using CATIA and ANSYS. *Int. J. Res.* **5**(7) (2018)
17. Patil, H.D., Bhange, S.S., Deshmukh, A.S.: Design and analysis of Go-kart using finite element method. *Int. J. Innovative Emerg. Res. Eng.* **3**(1) (2016)
18. Bopaiah, K.: Design and analysis of Go-kart using finite element method. *Int. J. Sci. Technol. Eng.* **4**(8) (2018)
19. Manikanta, P.C., Ram, P.J.: Design and analysis of Go kart chassis using FEA. *Int. J. Sci. Res. Dev.* **6**(2) (2018)
20. Nawade, S., Pathan, D., Bawane, A., Baitule, S., Shende, O., Birkurwar, R., Sabnis, T.V.: Design and analysis of Go-kart chassis **3** (2018)
21. Sannake, S.A., Shaikh, R.S., Khanfare, A.S., Nehatrao, S.A.: Design and analysis of GO-kart chassis. *IJARIE* **2**(2) (2017)
22. Viswanadh, P.K., Kakarla, S., Komali, K.: Design and static analysis for Go-kart chassis. *Anveshana's Int. J. Res. Eng. Appl. Sci. (AIJREAS)* **3**(2) (2018)
23. Boddepalli, A., Sankar, N.M., Chaitanya, G., Mallampalli, V.A., Teja, P., Kaki, G.K., Vyas, G.: Design of Go Kar frame chassis and steering system for computational impact load analysis. *Int. J. All Res. Educ. Sci. Methods* **9**(5) (2021)
24. Kumar, N., Mishra, S., Mishra, S.: Design and analysis of electric Go kart. In: *Conference 2nd Virtual National Conference on Advancement in Materials Processing Technology* (2020)
25. Quazi, T.Z., Jalvi, O., Shinde, S., Kamble, R., Sagar, T.: *Int. J. Res. Eng. Sci. Manage.* **1**(10) (2018)

Chapter 44

Smart Personal Task Scheduler



N. Sai Swaroop Krishna, A. Krishna Tej, and M. Suchithra

Abstract Meeting our daily scheduled events in time has always been a challenging task to be accomplished. The recent advancements in the NLP area developed many general-purpose personal assistants like Google Assistant, Alexa, Siri, etc., that can perform a vibrant range of tasks and remind the user about various tasks. The existing schedulers have not taken the real-world factors like traffic, the current location of the user into consideration while managing the user schedule and reminding the user about an event. Thus, the development of an efficient task scheduler is still a challenging problem. This paper proposes a personal task scheduler to assist the user by considering both event time and current user location. We used technologies like Dialogflow and Google Maps APIs for developing a web application prototype for our reminder system that reminds the user dynamically without having a preset time.

44.1 Introduction

Every day people have to perform a variety of tasks in their day-to-day life from meetings at work to non-daily tasks such as buying groceries after work. We use reminders to schedule and manage our tasks. Paper-based reminders including notes and memos are beneficial to a certain extent, but these methods are difficult to effectively organize. With the advancements in technology, we are equipped with many assistants like Google, Alexa, Siri, etc., [1] and mobile apps like Todoist, TickTick which help us set and manage our schedule. The common features of any

N. Sai Swaroop Krishna (✉) · A. Krishna Tej · M. Suchithra
Department of Computer Science and Engineering, Amrita School of Engineering,
Amrita Vishwa Vidyapeetham, Coimbatore, India
e-mail: cb.en.u4cse17237@cb.amrita.students.edu

A. Krishna Tej
e-mail: cb.en.u4cse17402@cb.amrita.students.edu

M. Suchithra
e-mail: m_suchithra@cb.amrita.edu

task scheduler include the creation of a task list, scheduling of a task list and notifications regarding the tasks [2, 3].

When we consider a task like “buying groceries at 6 pm” which needs to be performed at a specific location at the desired time, time-based task schedulers [4] might fail to help the user to reach his event in time. One of the reasons is the timing of the reminder, and existing schedulers would be reminding based on user customization. When there is a change in plan or due to user unawareness of real-time factors like travel time between the scheduled events, it could lead to scenarios where it reminds user 1 h before the event but the event location is 2 h far away from the current location which results in event not being attended in time. Another reason would be wrong allocation of the event, for instance an event “Movie at 3 pm, duration of 2 h 30 min” at location B has already been scheduled and user is trying to set an event at 6 pm which is at location A, and the time-based schedulers would allocate the event as there is not any overlap with the scheduled events but the travel time between the two locations is 1 h which is greater than interval between the events which eventually leads to the user not reaching the event in time.

The above problems are being met by our task scheduler by taking both location and time factors into consideration. Instead of having preset reminder time by user, we continuously monitor user location and compute the travel time between the current location and the upcoming events and remind the user when he should start his journey toward the upcoming event location [5, 6]. While setting up the schedule, our bot would consider the travel time between the current event and previous event and also current event and next event to check the possibility of allocating the event in the schedule. Our bot also assists the user in scheduling by providing smart suggestions while allocating an event when there is a clash with other events by considering factors of the events and the clash impact on schedule. We also developed a web application prototype for the proposed smart personal task scheduler with the help of technologies like Dialogflow [7] and Google Map APIs [8, 9].

The rest of this paper is structured as follows. Section 44.2 explains the detailed description of the data sets. Section 44.3 explains the proposed dynamic reminder system. Section 44.4 explains the results and discussion. Section 44.5 explains the conclusion and Sect. 44.6 future work.

44.2 Materials

44.2.1 Data Set

Train Data Set

The bot is trained with different sentences for each intent and entity cases so that it would be able to classify the user request into right intent and identify the entities in the request. The following is the sample for training set schedule intent.

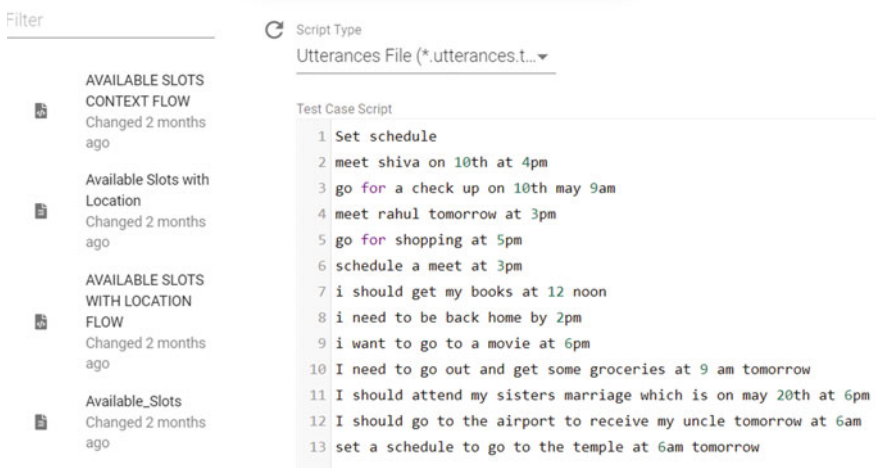


Fig. 44.1 Botium box test sample data set

Test Data Set

See Fig. 44.1.

44.3 Proposed System

44.3.1 System Modules

Our proposed system consists of mainly four modules.

44.3.1.1 Web Site Setup

This module presents the user interface (UI) and server-related parts for the proposed system. The first part of this module is the UI design. We used HTML to create pages individually and ensuring the pages are loosely coupled. We used JavaScript and jQuery to make the pages responsive and applied CSS and Bootstrap for better appearances. The second part of this module is setting up the development server which consists of downloading various software, node modules and configuring APIs to make use of them. The third part of the module is about setting up the database. We used the MySQL database server for storing the conversations.

44.3.1.2 Data Parser Algorithm

In this module, we processed the user text and retrieved useful information like time and location for scheduling the event. This is done with Dialogflow which helps in finding the intents of the user, retrieves the entities and also maintains the dialog context flow to gather the required information from the user. Intent classification [10] is used to categorize the sentence entered by the user. We used different intents for different scenarios. Each intent is fed with examples so that chatbot gets trained to identify the intent for a new scenario. Entity recognition [11] is used to extract the attribute values in the user's sentence. Each training example is marked with entities so that the chatbot can be trained to extract entities in the new scenario. We used Google Map API to get addresses of the user's intended location and Geocoding API to get the coordinates of those locations.

44.3.1.3 Commute Reminder Algorithm

In this module, we developed an algorithm which helps to find the accurate time to remind the user. We initially recorded scheduled destination location and time. The algorithm would constantly monitor the location and find the distance between the current location of the user and the scheduled location of user using API and calculate the commute distance. When the commute distance exceeds the time interval between the source and destination along with buffer time, then the reminder would be triggered.

44.3.1.4 Schedule Clash Detection

In this module, we developed an algorithm which helps to find the clash between the user scheduled events and scheduling event and assist the user by providing alternative schedule plans. We calculated the travel duration between the scheduling location with the other events and check the possibility of making up the event in time. If there is a clash between the events, then different alternatives for the events are checked based on stay duration, priority and impact on other events. If there is no clash, the event is recorded in database.

44.3.2 System Architecture

This section presents the proposed system architecture. The user has to enter a query in the user interface, and the text will get into the model. Then the model will perform intent classification and entity recognition simultaneously. Dialogflow context tracking is done for slot filling. These results will be sent to the server which consists of pipeline flow. The server will make necessary requests to the

database and calendar. Then these will provide information or store information as requested by the server. The server will generate responses that have to be given to the user. Finally, these responses will be displayed on user interface. The server also sends notifications to the user before the prescribed time. The workflow of the proposed method is given in Fig. 44.2.

44.3.3 Notification Algorithm

This algorithm will be continuously running in the backend which constantly monitors the schedule of the user and performs the triggering of notification based on the user's current location where the travel time would be computed to check whether he would be able to reach the upcoming scheduled event in time.

There are three types of notifications that would be triggered by the algorithm:

Reminder Notification: This is triggered when the threshold, i.e., interval time < buffer time (set by the user to intimate in prior for the journey) + travel time is reached between the current location and next scheduled event.

Event Delayed Notification: This is triggered when the current location of the user is met with the event location within interval time, i.e., the current time is between the event start time and end time. Here it would be checking if there are any clashes to the upcoming events due to delay in the time if so, they would be noted down to inform the user. Reached time and status are updated in the database. In the delayed notification, the following details would be displayed:

- The time he reached, actual time and the amount of time delay.
- If there are clashes then,
- The duration he can spend in the current event as he reached late.

The schedules would be affected and the delay that they have if they stay for the same amount of time that he committed earlier.

Event Missed Notification: This is triggered if the current location of the user did not match with the event location within the event time. Status as the missed event is updated in the database. This algorithm would run for multiple users asynchronously and deal with their schedules, respectively.

44.3.4 Schedule Algorithm

This algorithm helps in monitoring clashes for the user's requested slot with the scheduled events for the day and provides a suggestion if there is a clash.

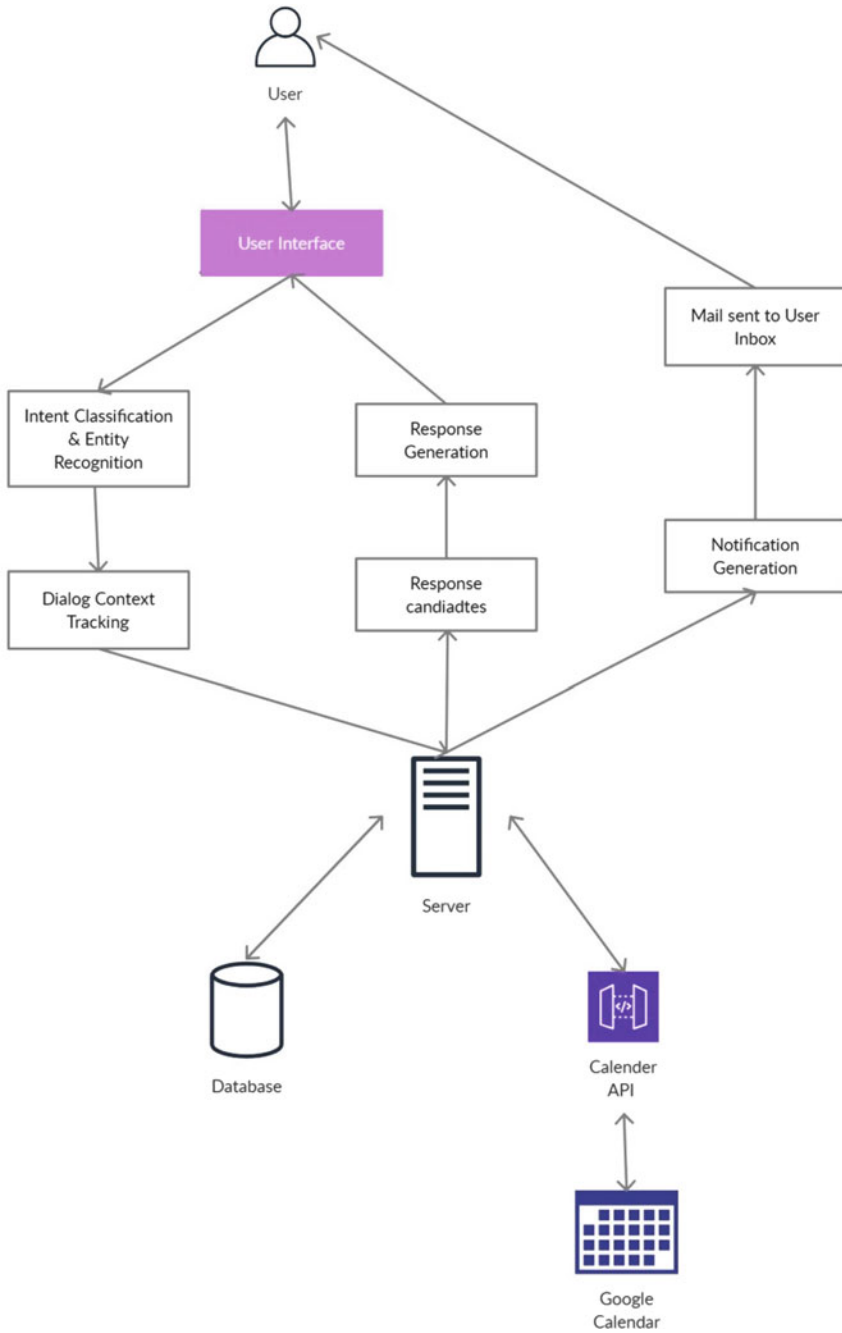


Fig. 44.2 Architecture of the proposed system

Types of Clashes:

- 1. **Clash with the upcoming event:** This is caused when the interval time between the event’s start times is less than the travel time.
- 2. **Clash with the previous event:** This is caused when the interval time between the event’s start times is less than the travel time.
- 3. **Clash with the upcoming event due to duration:** This is caused when the interval time between the current event end time and the next event start time is less than the travel time.
- 4. **Clash with both upcoming event and previous event:** This is caused when the interval time between the events start times is less than the travel time with next event as well as previous event.
- 5. **Clash due to over lapping:** This is caused if the current event is overlapped with already existing schedules.

Types of suggestions:

The suggestions proposed would be different for each clash case. The algorithm smartly proposes a suggestion by considering different probabilities of overcoming the clash and choosing the best-case possibility for the user by taking factors like the priority of events (assigned by the user) and the scale of impact on the existing schedule of change into consideration.

44.4 Results and Discussion

We used the Botium Box tool to test the intent classification ability of the chatbot, and our proposed system could achieve 90% accuracy. Figure 44.3 shows the chatbot accuracy.

Based on the Botium Box tool which is a widely used tool to perform testing automation for chatbots, the agent picks up the user utterances that are syntactically correct and of specific purposes and marginally ambiguous. For example, the agent understands better if the user says, “I want to go for a boat ride,” the purpose is not

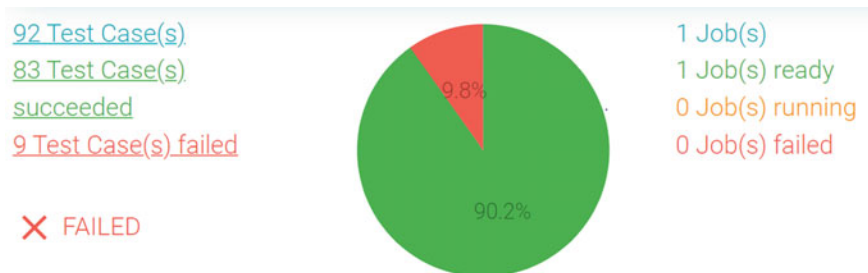


Fig. 44.3 Chatbot accuracy

picked up because boat ride is not included during the training of our custom entity, so if all the purposes are included for training, then the bot could recognize boat ride as an entity. The agent successfully recognizes the intent and entities which are passed on to the backend form where the respective operation is performed. The scheduling algorithm can successfully monitor schedule clashes and provide appropriate suggestions to the user and has passed all the test cases which were written in the jasmine tool, but there is a lag in presenting the output as it requires better computation powered resources and a high-speed connectivity as it needs to process multiple API requests and comes to an appropriate suggestion. Notification algorithm has also been able to trigger notifications accurately for multiple users based on the logic discussed earlier, but the parallel handling of multiple users has not been met as we implemented a single-threaded approach (default Node.js approach) for the system as it is for prototype purpose, but it could be extended for handling multiple users parallel by introducing a multi-threaded approach to the algorithm.

44.5 Conclusion

We successfully built up a Web site prototype where the user can manage his schedule and perform different operations on it using the smart chatbot which can detect schedule collision while setting up a schedule and suggest the best alternative for the event timings, and it can perform various other operations like viewing schedule, showing available slots based on users request type and can help you to find the amount of duration you can spend in a particular location at a particular time. Chatbot has an accuracy of 90%. The notifications are accurately being triggered based on the user's current location and the schedule. And if the user delayed the event, it notifies the amount of modified duration he can stay so that there would not be a clash with upcoming events and also the clashed events if he stays for the same initial amount of time. In the future, this project can be extended to suggesting the best means of transport for the user to commute between the locations.

44.6 Future Enhancements

In the future, this work can be extended to suggesting the best means of transport for the user to commute between the locations, and it could be extended for handling multiple users parallelly by introducing a multi-threaded approach to the algorithm.

References

1. Tulshan, A.S., Dhage, S.N.: Survey on virtual assistant: Google assistant, Siri, Cortana, Alexa. In: Thampi, S., Marques, O., Krishnan, S., Li, K.C., Ciuonzo, D., Kolekar, M. (eds.) *Advances in Signal Processing and Intelligent Recognition Systems. SIRS 2018. Communications in Computer and Information Science*, vol. 968. Springer, Singapore
2. Dalvi, A., Siddavatam, I.: Snoopme-interactive task scheduler mobile application related first developed for students. In: *2019 International Conference on Nascent Technologies in Engineering (ICNTE)*, IEEE, pp. 1–6 (2019)
3. Bhaskar, L., Ranjith, R.: Robust text extraction in images for personal event planner. In: *2020 11th International Conference on Computing, Communication and Networking Technologies (ICCCNT)*, pp. 1–4 (2020)
4. Graus, D., Bennett, P.N., White, R.W., Horvitz, E.: Analyzing and predicting task reminders. In: *Proceedings of the 2016 Conference on User Modeling Adaptation and Personalization (UMAP '16)*. Association for Computing Machinery, New York, NY, USA, 7–15 (2016)
5. Larsen, G.H., Yoshioka, L.R., Marte, C.L.: Bus travel times prediction based on real-time traffic data forecast using artificial neural networks. In: *2020 International Conference on Electrical, Communication, and Computer Engineering (ICECCE)*, pp. 1–6 (2020)
6. Anudeep, P., Krishna Prakash, N.: Intelligent passenger information system using IoT for smart cities. In: Tiwari, S., Trivedi, M., Mishra, K., Misra, A., Kumar, K. (eds.) *Smart Innovations in Communication and Computational Sciences. Advances in Intelligent Systems and Computing*, vol. 851. Springer, Singapore (2019)
7. Salvi, S., Geetha, V., Sowmya Kamath, S.: Jamura: a conversational smart home assistant built on Telegram and Google Dialogflow. *TENCON 2019—2019 IEEE Region 10 Conference (TENCON)*, pp. 1564–1571 (2019)
8. Kumar, P., and Raghul, M.: Location based parental control-child tracking app using android mobile operating system. In: *2018 4th International Conference on Computing Communication and Automation (ICCCA)*, pp. 1–4 (2018)
9. Prathilothamai, M., Nair, P.R., Alakh, R., Singh, P., Aditya, P.N.S.: Offline navigation: GPS based location assisting system. *Indian J. Sci. Technol.* **9**(45), 1–6 (2016)
10. Purohit, H., Dong, G., Shalin, V., Thirunarayan, K., Sheth, A.: Intent classification of short-text on social media. In: *2015 IEEE International Conference on Smart City/SocialCom/SustainCom (SmartCity)*, pp. 222–228 (2015)
11. Guo, J., Xu, G., Cheng, X., Li, H.: Named entity recognition in query. In: *Proceedings of the 32nd International ACM SIGIR Conference on Research and Development in Information Retrieval (SIGIR '09)*. Association for Computing Machinery, New York, NY, USA, pp. 267–274 (2009)

Chapter 45

Employee Attrition Prediction Using Machine Learning Comparative Study



Shobhit Aggarwal, Manik Singh, Shivam Chauhan, Mugdha Sharma, and Deepti Jain

Abstract When you think about the global situation, there is a sea of opportunity for skilled people all over the globe, and for a given opportunity, the workers shift from one company to other that leads to a high attrition rate within the company. Nowadays, employee attrition is treated as a severe problem by all the companies due to the negative impact on productivity at work and on completing company goals and vision in time. To deal with this problem, companies are now relying on machine learning methods to predict employee attrition rate. These methods work on products based on employee data analysis and the degree of prediction by the models. With accurate results, all the companies may take necessary actions in a timely manner for retaining or dismissing the staff. The system currently in use is the human resource's data system which does not work well in predicting how efficient the worker will be to the institution in future. These models that are used by the companies are now outdated and do not help them in successfully making decisions; in this paper, we have used modern machine learning algorithm models for predicting employee attrition that is employee's plan to either leave or continue working within the organization based on available huge data set to give more close results.

45.1 Introduction

In current times, all sorts of companies have become increasingly secular, and they are curious and cautious about their reputation in the market and to have an upper hand in order to earn big profits and get all kinds of benefits. Companies focus on a variety of HR-related problems and habits. Companies view workers as the central service of all, so workers must be treated with great care. It is the responsibility of all the companies to solve any kind of personal or professional problem and provide

S. Aggarwal · M. Singh · S. Chauhan · M. Sharma (✉) · D. Jain
Bhagwan Parshuram Institute of Technology, Guru Gobind Singh Indraprastha University,
Delhi 110085, India
e-mail: deeptijain@bpitdelhi.com

© The Author(s), under exclusive license to Springer Nature Singapore Pte Ltd. 2022
A. N. R. Reddy et al. (eds.), *Intelligent Manufacturing and Energy Sustainability*,
Smart Innovation, Systems and Technologies 265,
https://doi.org/10.1007/978-981-16-6482-3_45

the correct solution and maintain proper relationship with the workers to grow a strong workplace. The worst concern affecting the companies and even disrupting their efficiency is attrition. Attrition is considered as reduction in the number of workers due to death, retirement or another natural or conventional method.

Earlier when a worker used to join a company, he or she was fully committed to the work and did not leave, but now the faces of the companies have changed, especially in the information technology sector. The staff of these times is very large and flexible compared with older staff. Whenever a new opportunity comes, they leave the company leading to higher attrition rate. Attrition creates endless problems in the company which has been realized by companies recently. It also contributes to the competitive power of the company due to the constant demand for technical staff. With the recent emergence of new IT companies and start-ups, many have shown interest in the acquisition of learning new skills. In the eyes of managers, attrition is a very expensive and challenging problem to find accurate solutions too. Now companies are also considering changing various HR policies and practices to decrease their attrition rate, and to some extent they are successful, but however at the same time, rate of attrition rises quarterly.

45.1.1 Attrition-Definition

According to the Barron Business Dictionary, “attrition” is defined as “Normal and Uncontrollable reduction of a workforce because of retirement, death, sickness and relocation” [1].

According to the Longman Dictionary of Contemporary, “Attrition occurs when people leave a company or course of study and are not replaced” [2].

According to the American Heritage Dictionary of English, “Attrition is a gradual, natural reduction in membership or personnel, as through retirement, resignation or death” [3]. According to Investopedia, “Attrition in business can mean the reduction in staff and employees in a company through normal means such as retirement and resignation, the loss of customer or clients to old age or to growing out of a company’s target demographic” [4].

45.1.2 Causes of Attrition

Misconduct: Many studies have proved that misconduct creates a negative impact on production by leading workers quitting the companies. Immorality, back biting and being biased are all reasons for lack of code of conduct, thereby forcing workers to resign from the company in search of better opportunities [5].

Occupational Health Inequality: Company’s purpose is to get a job of three or more people done by a single person, forming excessive work pressure on an

individual that results in removing inspiration and will carry out the work in the company [6].

Staff Inefficiency: Sometimes, companies hire people who are not qualified for that particular work which leads to incompatibility of the workers in terms of their personnel growth as well as the growth of the company, therefore leading to a feeling of dissatisfaction among the staff ultimately leading to attrition [7].

Lack of Decision-Making Power: Staff at times feel very insecure about their inability to make or contribute to a decision. Companies need workers who display ownership and power, confident workers that have complete freedom of action, suggestion, ideas and decisions. And if the companies do not increase the power sharing and decision-making policies, all this feeling of not being a part of the company at work will lead to attrition [8].

Professional Skills Not Enough: Sometimes, promotions come to those workers who lack the skills and affect the efficiency and results of the company. These types of workers cannot do the job well and force the workers to stop the work which results in their termination from the company, thus attrition rate is higher in the company [9].

Freeze Incentives and Salary Increases: Over the years, research has proven that suspending the promotion and not giving compensation against overtime done by the worker also result in attrition. Companies sometimes hold salary hikes and suspend incentives, therefore workers consider this as poverty of employment and less chances of financial growth within the company, which in turn forces workers to look for other opportunities and increases attrition in the company [10].

45.2 Literature Review

Employee attrition can be considered as a factor which defaces the cognitive capital of the company. Literature review focuses on strategies which are proposed to predict the recruitment of several employees. Cotton and Tuttle [11] suggested that the strongest possible factors that are considered while recruitment are age, salary, job fulfilment and ideas for the future. Others also added important parameters such as gender, race, education, salary, technical skills development and marital status [12]. With the increase in the number of workers, companies face negative consequences in achieving their goals. It also affects the current work on existing products and ongoing projects. Recruitment of new staff also destroys the organization's financial resources as new staff requires training, rent allowance and travel allowance.

Ozolina-Ozola et al. [13] suggest that work benefits are defined by employees' work ethic, job fulfilment and commitment to the company or either of these attributes. Workers benefits and attrition generate unpredictability among other workers. The effect of attrition and profit has an impact on senior executives as well.

Hoffman et al. [14] used surveys of workers with responses in relation to the manager to estimate skills of the worker. The conclusion of this study was that workers with excellent skills should be praised, which will lead to a reduction in workers attrition. Ideally, better human resources managers should reap the benefits which will help ensure corporate governance success. Also, a consistent response regarding staff performance is required, which keeps workers engaged. Research has shown that a job that requires less skill (e.g. truck drivers, etc.) is much easier to do as compared to tasks which requires high skill set [15].

Ongori et al. [16] said companies should pay workers on the basis of their performance and various incentives as per total amount bonus, profit sharing and other benefits. Research also suggested that the information as well as the views of the company must be made available to the workers which provide workers the satisfaction and reason to stay in the current organization and have a strong commitment to staff performance. Excellent performance can lead to organizational success by getting a job done in the right way with excellent quality products. Also, a good working environment will also lead to lower attrition rate. The conclusion of this study was that employee empowerment can contribute to a company's success. [17]

O'Halloran et al. [18] evaluated different performance-related pay (PRP) plans affecting workers benefits. The study tried out whether profit sharing was effective in comparison with different PRP. It has shown that there is a bad connection between integrated PRP and profit measures.

45.3 Classification of ML Techniques

Machine learning is a very important technology in relation to quality forecasting, data analysis and testing. There are different algorithms for machine learning that are used for predicting the category of new or unexplored information. In our system, we have used different machine learning algorithms to find out the different factors that result in attrition. The algorithms used in the project are defined below.

45.3.1 *Decision Tree*

As the name implies, all the alternating remedies for decision-making divide the visibility into branches to form a tree aimed at improving predictive accuracy. The decision tree is the standard algorithm used to perform tasks in stages on the basis of decisions made in a single section. This gives tree provision made with decision sets. The decision tree is a tree-like flow chart, in which each internal node defines a test in the attribute, each branch represents the test result, and each leaf node (terminal node) holds a section label.

45.3.2 *Random Forest*

The random forest is used for regression and classification problems in ML which is based on the concept of integration of learning, which is the process of combining multiple divisions to solve complicated problems and improve performance of a model. Instead of relying on a single tree of decision, the random forest makes a prediction on each tree. The forecast with the most votes is the final output. Accuracy increases as the number of trees increases and prevents it from having more relevant problems. In classification problem, the end result is determined by using a majority vote classifier, and in regression problem, the end result is the mean of all outcomes.

45.3.3 *XGBoost*

XGBoost runs on the principle of gradient boosting and belongs to a boosted tree algorithm. As compared to others, it is accustomed to reinforce the standard model controlling excess and thus improving performance. It is a quick method that involves the construction of similar trees as well as being set to tolerate errors under the shared setting. The classifier captures information in the form of D-Matrix [19]. It is considered an internal data structure used by XGBoost for memory efficiency and speed performance. XGBoost uses a gradient boosting (GBM) framework as core. Some of the features of XGBoost included while using ML are as follows:

1. Parallel computing.
2. One of the benefits of XGBoost is regularization [20]. Regularization is the method which is used to avoid overspending on linear and tree-based models.
3. Cross Permission Allowed: Scale file for performance of the model in new data sets based on certain methods.
4. Lost Values: XGBoost can handle lost values as if there is already a tendency for the model with lost values.
5. Adaptability: Define support for the purpose of user-created tasks without backtracking, in stages, etc.
6. Save and Reload: XGBoost has its own feature avoiding counting over and over that way saving the data model and utilizing time by reloading it in future.
7. Pruning of a Tree [21]: It generates a tree to the maximum depth and does backward pruning such that loss performance becomes lower than the threshold, therefore, different from GBM.

45.4 Proposed Approach

45.4.1 Data Sets

The whole data set has been explained with its description in Table 45.1.

Table 45.1 Explanation of data set

Name	Description
Id	Integer value
Age	Integer value
Attrition	Employee leaving the company (0 = No, 1 = Yes)
Business travel	(1 = No Travel, 2 = Travel Frequently, 3 = Travel Rarely)
Department	(1 = HR, 2 = R&D, 3 = Sales)
Distance from home	Integer value
Education	Integer value
Education field	Integer value—education field
Employee number	Integer value—employee id
Gender	(1 = Female, 2 = Male)
Environment satisfaction	Integer value—environmental satisfaction
Job involvement	Integer value—job involvement
Job satisfaction	Integer value—job satisfaction
Marital status	(1 = Married, 2 = Single, 3 = Divorce)
Monthly income	Integer value—monthly salary
Number of companies worked in	Integer value—no. of companies worked in
Overtime	(1 = No, 2 = Yes)
Percentage salary hike	Integer value
Performance rating	Integer value—performance rating
Stock options level	Integer value
Total working years	Integer value
Training times last year	Integer value—training hours
Years at company	Integer value—total years at the company
Years in current role	Integer value
Years since last promotion	Integer value—year since last promotion
Years with current manager	Integer value
Behaviour	(1 = Good, 2 = Bad, 3 = Not Rated)
Communication skills	(1 = Bad, 2 = Average, 3 = Good, 4 = Better, 5 = Best)

45.4.2 *Data Pre-processing*

To do research, a database contains many attributes that affect recruitment of employees directly or indirectly. In fact, we have identified and trimmed the attributes in a database with a few numbers of signs which were appropriate. We have trained the model and then validated the test set. We did all our analysis on the training set, and it was validated on our test set. We split our database into training (80%) and testing (20%).

45.4.3 *Correlation of Attributes*

The data set has a wide range of symbols, but we have considered some great symbols in acquisition of attrition rate. We found a lot of interesting things in the relationship between the qualities that have led us to our aim of receiving the attrition rate. We have shown relationships among different symbols such as education, environment satisfaction, total working years and performance rating. We have shown a correlation between the level of activity or work and salary of the worker. We are also looking at the relationship between attributes such as percentage increase and performance rate of the worker. We also looked at the relation between parameters such as the age vs monthly income, level of work and salary increase percentages. So, we used a number of parameters and their relations to find the company's profit margin over a period of time.

Figure 45.1 shows how one parameter is affecting other parameters positively or negatively. Consider the value for "YearsAtCompany" and "YearsInCurrentRole" that is 0.77. This means there is a 77% chance that "YearsInCurrentRole" will increase if "YearsAtCompany" increases.

45.4.4 *Analysis*

The study concluded that there are certainty variables that affect the level of profits of the company.

Figure 45.2 shows that all the variables affect the profit levels of an organization more in comparison with other variables in the data set on the basis of results generated after applying Chi-square test.

The variables that have a major impact on capture are registered as follows:

1. Overtime

Figure 45.3 shows that the employees who are doing overtime almost 67% of them are leaving, whereas the employees who are not doing overtime around 36% of them are leaving. So, the respective attrition rate is 67.66 and 36.43%.

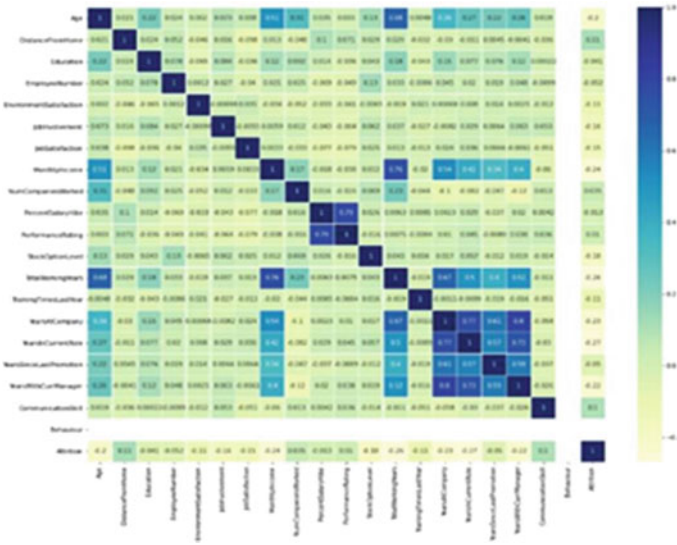
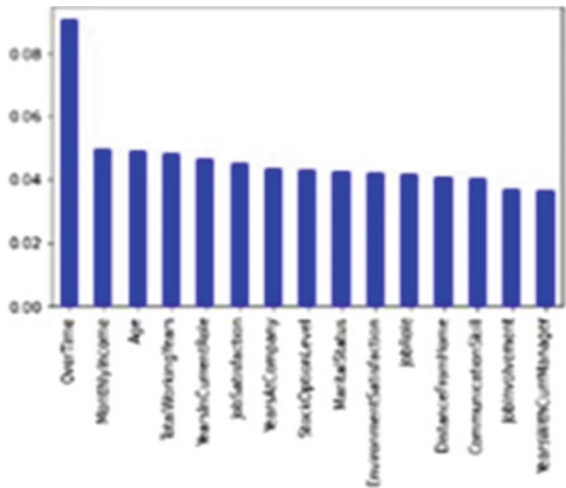


Fig. 45.1 Correlation matrix

Fig. 45.2 CHI square test results



2. Marital Status

Figure 45.4 shows that the employees who are divorced almost 38% of them are leaving, the employees who are married almost 37% of them are leaving, and the employees who are single more than 60% of them are leaving. So, the attrition rate is 38%, 37.44% and 62.11%, respectively.

Fig. 45.3 Attrition % versus overtime

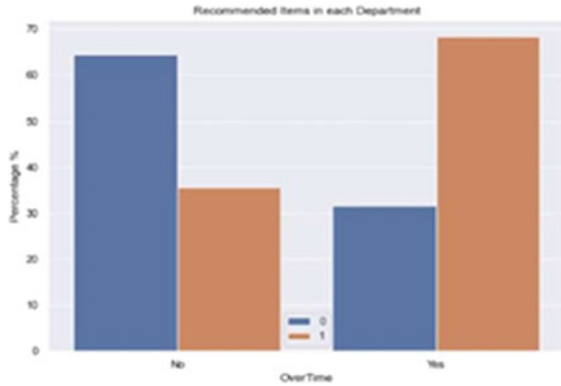
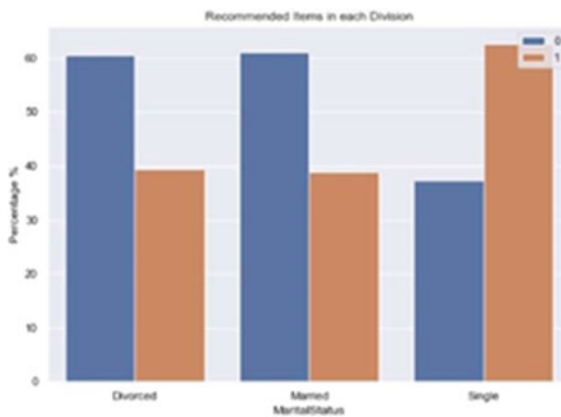


Fig. 45.4 Attrition % versus marital status



3. Monthly Income

Figure 45.5 shows the relation of age with respect to the employee’s monthly income. The slope of the above graph is positive that shows that as age increases, there is a chance that the monthly income also increases.

- 4. Job Role
- 5. Age
- 6. Total Working Years
- 7. Distance from Home
- 8. Stock Options Level
- 9. Job Satisfaction
- 10. Years at Company.

Fig. 45.5 Scatter plot of age versus monthly income



45.5 Results and Discussions

In the data set above, there are various features such as age, attrition, education and marital status. Based on these values, a model is developed with the help of different machine learning algorithms which will predict whether employees will stay in the company or not. Predicted values are compared with test values to calculate the accuracy of each algorithm. The table given below describes the various factors, so we can easily determine which algorithm is best for our model. From the table, we can see that random forest provides the highest accuracy, and the logistic regression provides the lowest accuracy for the same data set.

45.5.1 *Random Forest Classifier*

See Fig. 45.6.

45.5.2 *XGBoost*

See Fig. 45.7.

```
In [99]: pred = rf_random.predict(X_test)
print("randomforest confusion matrix with randomsearchCV: \n",confusion_matrix(pred,y_test))
print("\n")
print("randomforest test accuracy score with randomsearchCV: ",accuracy_score(pred,y_test))
print("\n")
print("randomforest classification report with randomsearchCV: \n",classification_report(pred,y_test))

randomforest confusion matrix with randomsearchCV:
[[165  0]
 [  7 154]]

randomforest test accuracy score with randomsearchCV: 0.9785276073619632

randomforest classification report with randomsearchCV:
      precision    recall  f1-score   support

 0         0.96      1.00      0.98       165
 1         1.00      0.96      0.98       161

 accuracy          0.98
 macro avg         0.98      0.98      0.98       326
 weighted avg     0.98      0.98      0.98       326
```

Fig. 45.6 Random forest classifier results

```
In [63]: import xgboost
xgb=xgboost.XGBClassifier()
xgb.fit(X_train ,y_train)
pred = xgb.predict(X_test)
print("confusion matrix: \n",confusion_matrix(pred,y_test))
print("\n")
print("accuracy score: ",accuracy_score(pred,y_test))
print("\n")
print("classification report: \n",classification_report(pred,y_test))

confusion matrix:
[[159  0]
 [ 13 154]]

accuracy score: 0.9601226993865031

classification report:
      precision    recall  f1-score   support

 0         0.92      1.00      0.96       159
 1         1.00      0.92      0.96       167

 accuracy          0.96
 macro avg         0.96      0.96      0.96       326
 weighted avg     0.96      0.96      0.96       326
```

Fig. 45.7 XGBoost results

45.5.3 Logistic Regression

See Fig. 45.8.

45.5.4 SVM

See Table 45.2 and Figs. 45.9 and 45.10.


```
In [39]: from sklearn.linear_model import LogisticRegression

from sklearn.metrics import confusion_matrix, accuracy_score, classification_report

lr = LogisticRegression()
lr.fit(X_train_scl, y_train)

pred = lr.predict(X_test_scl)

print("confusion matrix: \n", confusion_matrix(pred, y_test))
print("\n")
print("accuracy score: ", accuracy_score(pred, y_test))
print("\n")
print("classification report: \n", classification_report(pred, y_test))

confusion matrix:
[[128  37]
 [ 44 117]]

accuracy score: 0.7515337423312883

classification report:
              precision    recall  f1-score   support

     0       0.74      0.78      0.76       165
     1       0.76      0.73      0.74       161

   accuracy: 0.75
  macro avg: 0.75      0.75      0.75
 weighted avg: 0.75      0.75      0.75       326
```

Fig. 45.8 Logistic regression results

Table 45.2 Comparison of different models

Model attribute	Random forest	XGBoost	Logistic regression	SVM
Accuracy	0.9785	0.9601	0.7515	0.877
<i>Precision</i>				
0	0.96	0.92	0.74	0.82
1	1.00	1.00	0.76	0.94
<i>Recall</i>				
0	1.00	1.00	0.78	0.94
1	0.96	0.92	0.73	0.82
<i>F1-score</i>				
0	0.98	0.96	0.76	0.88
1	0.98	0.96	0.74	0.88

45.6 Conclusion

The main purpose of this paper is to do a comparative study on modern classification models for predicting the attrition of the employee. We have applied four such optimal models, namely random forest classifier, XGBoost, logistic regression and SVM, for common data set and attributes, and an important observation came out that random forest classifier-based model poses to be best predictive model as per our selected metric of performance.

```
In [42]: from sklearn.svm import SVC
svc = SVC(kernel='rbf')
svc.fit(X_train_scaled,y_train)
pred = svc.predict(X_test_scaled)
print("confusion matrix: \n",confusion_matrix(pred,y_test))
print("\n")
print("accuracy score: ",accuracy_score(pred,y_test))
print("\n")
print("classification report: \n",classification_report(pred,y_test))

confusion matrix:
[[141  9]
 [ 31 145]]

accuracy score: 0.8773006134969326

classification report:
      precision    recall  f1-score   support
0         0.82     0.94     0.88       150
1         0.94     0.82     0.88       176

 accuracy
macro avg     0.88     0.88     0.88       326
weighted avg   0.89     0.88     0.88       326
```

Fig. 45.9 SVM results

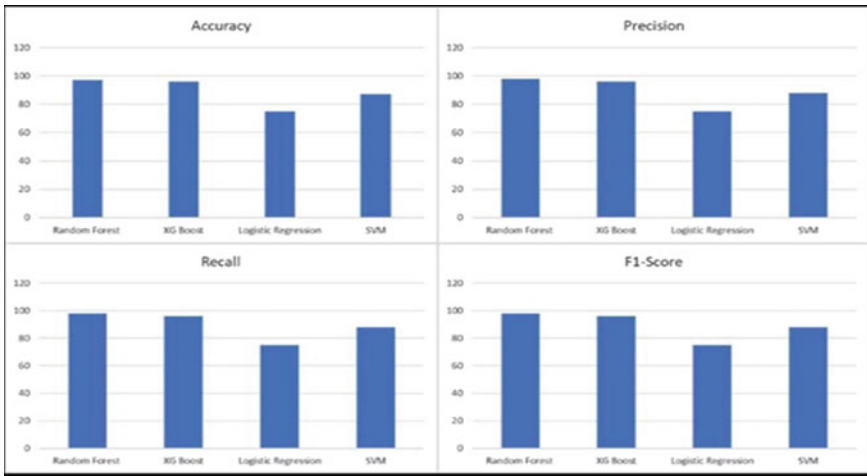


Fig. 45.10 Comparison of ML techniques used

45.7 Future Work

Data mining and machine learning are developing at a rapid pace with many new techniques being developed and old techniques being improved to enhance the performance, and keeping this in mind, our work can be further expanded to incorporate new methods of classification for outcome prediction. With enhanced methods and more research, our model can be changed into “predictive mode” which solves various kinds of issues that are not yet handled and thus, making the model more accurate, more convenient and easier to use.

References

1. Latha, K.L.: A study on employee attrition and retention in manufacturing industries. *BVIMSR's J. Manage. Res. (BJMR)* **5**(1), 1–23 (2013)
2. Ajit, P.: Employee turnover prediction in organizations using ML. *Int. J. Adv. Res. Artif. Intell.* **4**(5), C5 (2016)
3. Jahan, S.S.: Human resources information system (HRIS): a theoretical perspective. *J. Hum. Resour. Sustain. Stud.* **2**(02), 33 (2014)
4. Alao, D., Adeyemo, A.B.: Analysing employee attrition using decision tree algorithms. *Comput. Inf. Syst. Dev. Inf. Allied Res. J.* **4**(1) (2013)
5. Aliaga, O., Shuck, B., Young, J.A., Stone, J.: Job embeddedness theory: can it help explain employee retention among extension agents? *J. Extension* **51**(4), 4FEA7
6. Goud, P.V.: Employee retention for sustainable development. *IJITAM* **1**(5), 10–16 (2013)
7. Zhang, Y.: Research of employee retention on job embeddedness perspective, pp. 343–346. *ICASM*, Atlantis Press (2013)
8. Shubhada Kulkarni, P.S.J.: A study of talent management strategies in I.T. sector of India. *IJMMS* **2**(1), 1–8 (2015)
9. Sultana, N., Bushra, B.: A study of select MNCs. *IJEMS* **4**(3), 361–368 (2013)
10. Mohan, S., Muthuswamy, P.R.: *CIJIFR*, vol. 2, no. 6
11. Cotton, J.L., Tuttle, J.M.: Employee turnover—a meta-analysis and review with implications for research. *Acad. Manage. Rev.* **11**(1), 55–70 (1986)
12. Young, M.: *The technical writer's handbook*. University Science, Mill Valley, CA (1989)
13. Ozolina-Ozola, I.: *Reducing Employee Turnover in Small Business* (2015)
14. Hoffman, M., Tadelis, S.: *People Management Skills, Employee Attrition, and Manager Rewards: An Empirical Analysis*, (No. w24360), NBER (2018)
15. Bidyut, B.N., Mukulesh, B.: An empirical study on automobile service workshops of Assam. *IFBM* **3**(1) (2015)
16. Ongori, H.: *A Review of the Literature on Employee Turnover* (2007)
17. Karatepe, O.M.: Effects on job embeddedness and turnover intentions due to high performance work practices. *IJCHM*, **25**, 903–909 (2013)
18. O'Halloran, P.L.: Performance pay and employee turnover. *J. Econ. Stud.* **39**(6), 653–674 (2012)
19. Saradhi, V.V., Palshikar, G.K.: Employee churn prediction. *Expert Syst. Appl.* **38**(3), 1999–2006 (2011)
20. Glu, Z.Ö.K.: *Employee turnover prediction using ML based methods*. Doctoral Dissertation, Middle East Technical University
21. Srivastava, D.K., Nair, P.: Employee attrition analysis using predictive techniques. In: *International Conference on Information and Communication Technology for Intelligent Systems*, pp. 293–300 (2017, March)

Chapter 46

Optimising Effect of Resonance by Harmonic Analysis of Ethylene Propylene Diene Monomer (EPDM) Engine Mount



Tripti Khulbe and Vikas Rastogi

Abstract In this work, it is aimed to find and analyse natural frequencies and optimise resonance conditions of roll cage of an All-Terrain Vehicle. The analysis is done to predict failure modes of the frame of the vehicle under harmonic analysis. Further investigations are made to minimise the resonance and effect of engine vibrations on roll cage by using dampers such as ethylene propylene diene monomer (EPDM) rubber engine mount. ANSYS workbench is used for simulations and modelling.

46.1 Introduction

Frame of an All-Terrain Vehicle (ATV) is the main structural component which is subjected to all the static and dynamic loads. Apart from this, it also responds to the various vibrational loads. Noise reduction is a technique opted by engineers to optimise performance of vehicle. Main component in the vehicle which is responsible for imparting oscillatory motion is the engine which is mounted on the rear part of the roll cage. The internal combustion engine is a concentrated mass in the vehicle which will cause vibrations and transfer to the supporting structures, effecting ride comfort, driving stability and drivability. Failure due to weaknesses caused in structure because of vibrational loads is a major concern in the industry and is just not limited to vehicle but is omnipresent from turbines to aeroplanes to any other device which is in motion. Trying to eliminate this failure is the need of the hour, and we try to explore that in this paper.

Vibrations in a structure occur due to the presence of a compelling force that acts as the source and due to which the structure tends to vibrate. A major source of

T. Khulbe (✉)
Delhi Technological University, Delhi, India
e-mail: triptikhulbe_2k17ae59@dtu.ac.in

V. Rastogi
Department of Mechanical Engineering, Delhi Technological University, Delhi, India

vibration in the vehicle is the engine. Failure of structures occurs due to effect of resonance. Resonance occurs when natural frequency modes of the structure coincide with the frequency of excitation of the source. Due to this, the roll cage becomes structurally weak. To avoid this, it becomes of paramount importance that situations like these must be avoided. Other sources of vibration can be from tyre and suspension system. Finding modes of vibration could be well used to understand the dynamic behaviour of a structure.

46.2 Effect of Engine Vibrations

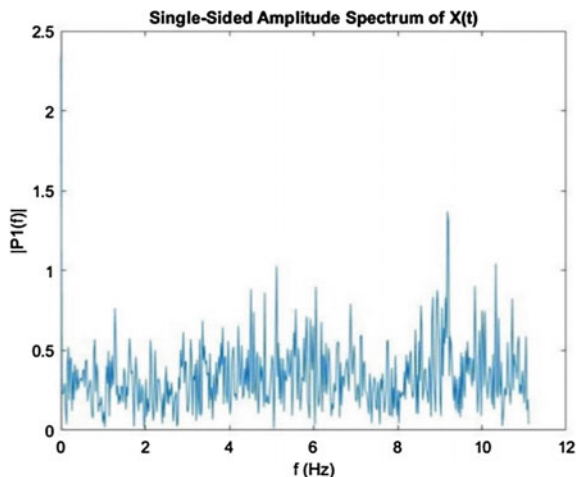
To evaluate the effect of vibrations on roll cage, power spectral density (PSD) curve frequency acceleration is plotted in Random Vibration Suite of ANSYS.

Engine provided in this vehicle has a governor setting fixed at 3800 RPM. After much deliberation, MEMS accelerometer (MPU 9250) was chosen to fulfil the need and technicalities of the project for its high accuracy, precision and low cost. Using MPU 9250, we measure the acceleration of engine vibration. To calculate the frequency, fast Fourier transformation (FFT) is used [1–3], Fig. 46.1.

46.3 Roll Cage

The structure which envelops and ensures driver safety and supports all other vehicle components such as electrical system, power and transmission system, suspension, wheels and axles, braking system is the roll cage of the vehicle [4–6]. All these components are mounted on the frame. All-Terrain Vehicle, as the name tells, is required to perform in hilly, mountainous, rugged and rough terrains.

Fig. 46.1 Power spectral density (PSD) curve frequency acceleration



46.3.1 Material, Components and Dimensions

AISI 4130 is a medium to low carbon alloy steel classified by American Iron and Steel Institute according to the content of the material. It is chosen because of its good weight-to-strength ratio, toughness, weldability and machinability (Fig. 46.2 and Tables 46.1, 46.2).

46.4 Analysis and Simulations

Basic procedure to reduce the effect of resonance and making the vehicle more driver friendly is to begin with finding the natural frequencies of the roll cage structure through modal analysis. The base of the roll cage is fixed since tyres and springs are mounted on axle which is not a part of roll cage; hence, the degree of freedom will be 0 as there is no motion [7]. Afterwards, harmonic response of roll cage is seen along with working condition of engine with ethylene propylene diene monomer (EPDM) rubber mounts.

$$w_n = \sqrt{\frac{k}{m}}$$

where w_n is natural frequency. k , m are stiffness to weight and mass, respectively.

Fig. 46.2 Roll cage

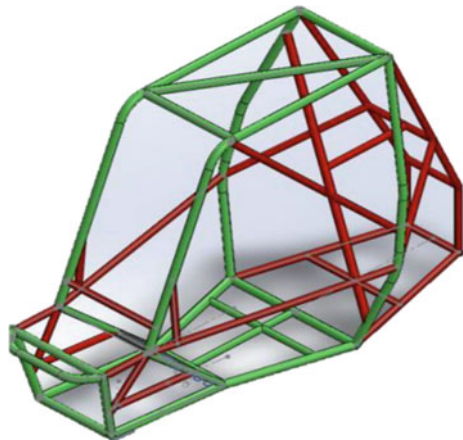


Table 46.1 Mechanical properties of AISI 4130

Mechanical properties	AISI 4130
Ultimate tensile strength	821 MPa
Yield tensile strength	736 MPa
Stiffness to weight	72–130 kNm/kg
Elongation at break	21.5%

Table 46.2 Dimensions of roll cage

Type of tube	Outer diameter	Wall thickness
Primary	31.75 mm	1.675 mm
Secondary	25.4 mm	1 mm

Table 46.3 Natural frequencies of roll cage

	Mode	Frequency (Hz)
1	1	33.412
2	2	64.560
3	3	72.639
4	4	121.38
5	5	144.77

46.4.1 Modal Analysis

Extended structures have various mode shapes and accordingly corresponding frequencies. This is due to the many different ways a body can vibrate and have dissimilar deformations. Natural frequencies of roll cage are calculated in five different mode shapes. At various points of nodes, longitudinal, torsional and transverse vibrations occur in the roll cage. Modal analysis was done on ANSYS to calculate the natural frequencies (Table 46.3).

Corresponding to lowest mode is the natural frequency 33.412 Hz. This is way below 40 Hz. The highest natural frequency is 144.77 Hz. All of this is done under no pre-stress conditions and just under self-weight of roll cage.

Since the lowest natural frequency is way low, there is a chance that resonance occurs. For eliminating this, we choose ethylene propylene diene monomer (EPDM) rubber mounts to be used for mounting engine on rear roll cage.

46.4.2 Harmonic Responses

While ethylene propylene diene monomer (EPDM) rubber mounts in place with working condition of engine, harmonic analysis is done on ANSYS with input of harmonic displacements (input), pressure and loads [8–10].

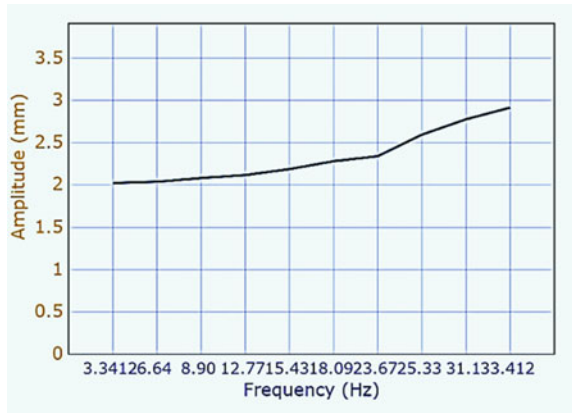
Harmonic analysis is done to know how a body would respond to sinusoidal loads in steady state of frequencies which were found out earlier. This process is used in almost all bodies in motion with source imparting sinusoidal forces. By knowing the response, it can always be made out if there is a decrease in resonance and in turn drivability is improved. The damping process helps in reduction of transfer of vibrations from engine to the body via rubber mounts.

EPDM is known to have damping ratio of 0.03 and modulus of storage to be around 4.2 MPa. This information is used to feed into ANSYS settings to perform the analysis with a load of 220 N [11–14] (Table 46.4).

Table 46.4 Settings in ANSYS software

State	Steady, fully defined
Range maximum	33.412 Hz
Range minimum	0 Hz
Solution intervals	10
Solution method	Mode superposition

Fig. 46.3 Amplitude spectrum



The output that we get includes the displacement at every degree of freedom with its amplitude. Stress and strains are also determined.

46.5 Results

The table shows the result with amplitude of displacement within 10 solution intervals when an EPDM elastomer is used to dampen vibrations from engine (Fig. 46.3, Table 46.5).

46.6 Conclusions

The engine is set at a governor setting of 3800 RPM and hence is a major source of vibrations. The frequency of excitation is 40 Hz. The lowest mode natural frequency of the roll cage of material AISI 4130 found out by modal analysis is 33.412 Hz which is below excitation frequency resulting in resonance. To counter that, harmonic analysis of EPDM mount is done to dampen the vibrations. It is noted after the analysis that with a damping ratio of 0.03, the elastomer produces a lower amplitude of displacement at 33.412 Hz.

Table 46.5 Harmonic analysis with ethylene propylene diene monomer rubber mount

Frequency (Hz)	Amplitude
3.3412	2.0212E-02
6.6459	2.0352E-02
8.9076	2.0796E-02
12.7765	2.1149E-02
15.4356	2.1856E-02
18.0987	2.2789E-02
23.6754	2.3386E-02
25.3345	2.5937E-02
31.1267	2.7761E-02
33.412	2.9144E-02

Hence, after analysing the damping behaviour of ethylene propylene diene monomer used as engine mount, it is considered a viable option for isolation of engine from rest of the body.

Acknowledgements This paper was supported by Design Lab, Department of Mechanical Engineering, Delhi Technological University and we would like to extend our gratitude for the same. We would like to thank Shaswat Garg for his extended help in analysing effect of engine vibrations.

References

1. Santana, C., et al.: Analysis of vibration and noise of an internal combustion engine by application of test and experimental analysis of the frequency spectrum. In: XXI Simpósio Internacional de Engenharia Automotiva (2014)
2. Ahirrao, N., Bhosle, S., Nehete, D.: Dynamics and vibration measurements in engines. *Procedia Manuf.* **20**, 434–439 (2018). <https://doi.org/10.1016/j.promfg.2018.02.063>
3. Brunton, S.L.: *Data-Driven Science and Engineering: Machine Learning, Dynamical Systems, and Control*, 1st edn. Cambridge University Press (2019)
4. Mahadik, S.S.: Design and ANSYS analysis of components of wheel assembly of SAE car. *Int. J. Curr. Eng. Technol.* **8**(02), 407–438. (2018). <https://doi.org/10.14741/ijcet/v.8.2.36>
5. Budynas, R., Nisbett, K.: *Shigley's Mechanical Engineering Design*, 11th edn. McGraw-Hill Education (2019)
6. Milliken, M.F., Milliken, D.W., Metz, L.D.: *Race car vehicle dynamics*. SAE International (1994)
7. Tsongas, K., Mansour, G.: Optimization of the Vibration Isolation Performance of an Impact-testing Machine Using Multi-walled Carbon Nanotubes Reinforced Elastomeric Machine Mounts (2019)
8. Szabo, J.P.: *Characterization of Engine Mount Elastomers* (2005)
9. Mansour, M., Tsongas, K., Tzetzis, D.: Measurement of the mechanical and dynamic properties of 3D printed polylactic acid reinforced with grapheme. *Polym.-Plast. Technol. Eng.* **58**(11), 1234–1244. (2019). <https://doi.org/10.1080/03602559.2018.1542730>
10. Karaagac, B., Bayram, T., Konyali, H.: Evaluating Ethylene Propylene Diene Rubber for Dynamic Applications Instead Of Natural (2019)

11. Mao, X., Xu, S.-A., Wu, C.: Dynamic mechanical properties of EPDM rubber blends. *Polym.-Plast. Technol. Eng.* (2008)
12. Robertson, C.G.: Dynamic mechanical properties. *Encycl. Polym. Nanomater.* (2014). https://doi.org/10.1007/978-3-642-36199-9_317-1
13. Jiang, L., Polack, M., Chernuka, M.W.: Improvement of the vibration isolation system model generation and visualization code-VIMGEN. 2003, DRDC Atlantic Contract Report (2003)
14. Zhang, F., Guo, M., Xu, K., Guo, S.: Multilayered damping composites with damping layer/ constraining layer prepared by a novel method (2014)

Chapter 47

Design and Analysis of Multi-Tool Light Agricultural Vehicle



K. Vijay Kumar, Ismail Kakaravada, and Y. Dilip Kumar

Abstract Agricultural automation is an important subject for high production yield of crops and minimizing work time on farms, and multipurpose vehicles can be utilized for agricultural work to address financial issues. Purchasing of three different vehicles for farming activities is not affordable for small-scale farmers in Asian and African countries. To overcome this problem, a new multi-specialty vehicle combining the three fundamental farming activities of tilling, plowing, and reaping was designed. The multi-tool light agricultural vehicle (MTLAV) is advantageous for small to medium farms and hill areas. The whole design was carried out in CATIA, and analysis was done using Ansys. Structural analysis was performed for the plow and tiller. This work aims to provide a cost-effective solution for agricultural problems that plague farmers in Asia.

47.1 Introduction

Farm mechanization increases the crop productivity with least amount labor. The huge amount of work in farm operations can be reduced through mechanization with advanced features like remote control operating mechanisms, navigation sensors, and image sensing mechanisms [1–4]. The mechanization in processes industry impacted with the factors such as demand for agricultural food products and land-labor ratio. Common farm equipment are divided into two categories: conventional and conservative agriculture systems. In the conventional agriculture systems such as animal traction units which are manually operated units, like two or four-wheeled tractors [5]. Labor and animal-drawn operated are extensively used. These tools involve a significant amount of fatiguing work. This equipment is used

K. Vijay Kumar (✉) · Y. Dilip Kumar
Department of Mechanical Engineering, Mallareddy College of Engineering, Secunderabad,
Telangana 500100, India

I. Kakaravada
Department of Mechanical Engineering, Prasad V. Potluri Siddhartha Institute
of Technology, Vijayawada, Andhra Pradesh 520007, India

due to a lack of technology and poor economical backgrounds. Naturally, animal and manual traction units are confined to use in small farms and hilly areas; on other hand, agricultural activities are vulnerable because of nature abnormality [6–8]. Currently, the acceptance of agricultural automation technology is escalating because of fast and reduces in fatigue work of labor. The demand for agricultural tractors with farm equipment has been growing remarkably. Nowadays, more than 250,000 tractors are manufactured every year with different power ranges (25–54 horsepower) in India according to power requirement of farm equipment. However, there is lagging in acceptance of conservative agriculture equipment by the farmers due to the lack of technical knowledge and manufacturing facility of equipment for small to medium farms in Asia. In the latest decades, irrigation pumps, tillage equipment, chaff cutters, tractors, and threshers have been gradually introduced in the farm mechanization. Machinery for sowing, tillage, and threshing was significantly received by the farmers when it was introduced [9, 10]. Small-scale farmers are utilizing developed machinery to provide the service on other farmer on payment basis. In the current era, the new trend in rent farming machinery with high capacity to the fieldwork can be done very easily. For various crop productions, farmers have opted to use conservative machinery high production yield with less amount of time. All farmers cannot afford the farm machinery due to the variation in farm holdings and economic inequalities. For example, Indian agriculture continues to be dependent upon human power (the agricultural worker population was around 324 million in 2009–10) and draft animal power (27 million pairs) [7]. In the year of 1961, the production of power tillers began with twelve rudimentary models. These were marketed in various states across the country with appropriate farming conditions for the machinery to cultivate the land. The mechanization for harvesting equipment is very expensive, and this may be due to updated technology and complicated designs and the cost of fabricating materials for the usage of crop cutting. To the best of knowledge, there is no inexpensive, low-power agricultural equipment put into operations that can perform multiple tasks. The market share of power tillers is small as compared with expensive tractors. This might be cause of deficient in multitasking ability of tractors and power tillers and which also creates a dusty environment to the operator. This has to be overcome to provide a non-tiresome work environment. There is diminishing in sales of tractors noticed during the floods and irregular monsoons. In this crucial times, farmer thinks about them as an extravagance because of that they cannot afford. The cost of harvesters is too high for a small-farm farmer which led to minimal usage machinery [11, 12]. Low-cost alternatives need to be developed for progress in mechanization for harvesting. The government has taken certain steps to improve the usage of mechanized machinery in harvesting which is developed at lower cost with improved mechanization. The developed machinery makes availability to the famers at subsidized prices. Biodiversity-friendly agricultural practices with multi-functional machinery hike agriculture profitability with reduction contribution such as labor, fuel, and fertilizer. A multi-specialty vehicle was designed to combine three fundamental farming activities: tilling, plowing, and reaping. The MTLAV is lightweight, affordable, and

suitable to all kinds of farmers. The MTLAV reduces labor costs and speeds up tasks compared to larger tractors. The current work discloses the modern agriculture machine tool strategy that has been designed for the small to medium landscape of the farmers which is helpful to make multiple tasks in less time.

47.2 Design of MTLAV

47.2.1 Chassis

The chassis design is a primitive longitudinal frame with lateral reinforcement based on a ladder chassis format. Aspects of low-cost production, easy maintenance, and reduced curb weight are taken into account in the design of the chassis because the MTLAV will not encounter high speeds. The chassis is constructed with consideration of the structural rigidity demands that arise through the prerequisites of powerfully heavy-duty agricultural work. The MTLAV will not encounter high speeds, so a simplistic chassis is sufficient. The total length of the chassis is 2250 mm, the engine is mounted at 926.15 mm, and the seat is mounted at 1150 mm, as shown in Fig. 47.1.

47.2.2 Transmission

The transmission is designed to transfer power from the torque converter to the engine smoothly. After considering constraints and calculations, a final drive ratio of 1:42 was determined. Several transmission systems available in the market are also compatible with the MTLAV, so it is possible to retrofit an aftermarket transmission to the engine and still obtain a good performance level. The major

Fig. 47.1 Design of the chassis

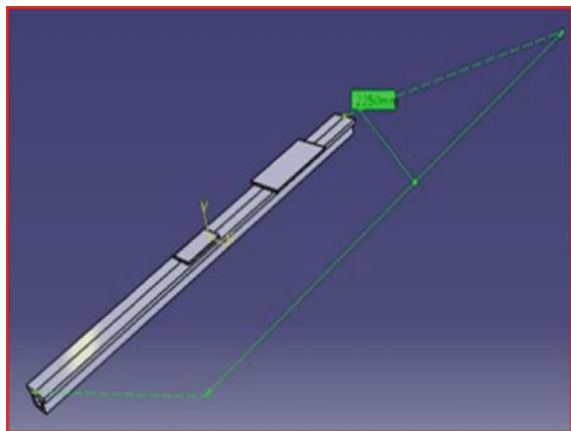
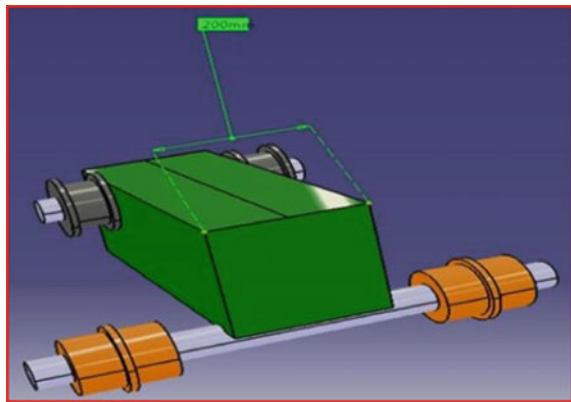


Table 47.1 Dimensions of transmission components

Name of component/name of measurement	Magnitude (mm)
Axle length	670
Axle radius	25.4
Clutch length	120
Length of a groove in clutch	10
Radius of clutch	50
Groove radius	60
Length × height × width of gearbox	600 × 200 × 200
Height from base of the gearbox to pulley center	150
Height from base of the gearbox to pulley center	150
The thickness of the belt connecting engine and drive pulleys	4
The total radius of the gearbox pulley	65
The inner radius of the gearbox pulley	50
Shaft radius	25.4
The radius of the engine pulley (total)	42.5
Inner radius	30

Fig. 47.2 Design of the transmission system



dimensions of the transmission are presented in Table 47.1, and the design is shown in Fig. 47.2.

47.2.3 Tires and Seat

The design of the tires is crucial for rough terrain. The MTLAV is expected to surmount hard surfaces. The tires need to be equipped to handle slush and bumpy surfaces where traction is limited. ATV radials were chosen for their pretension

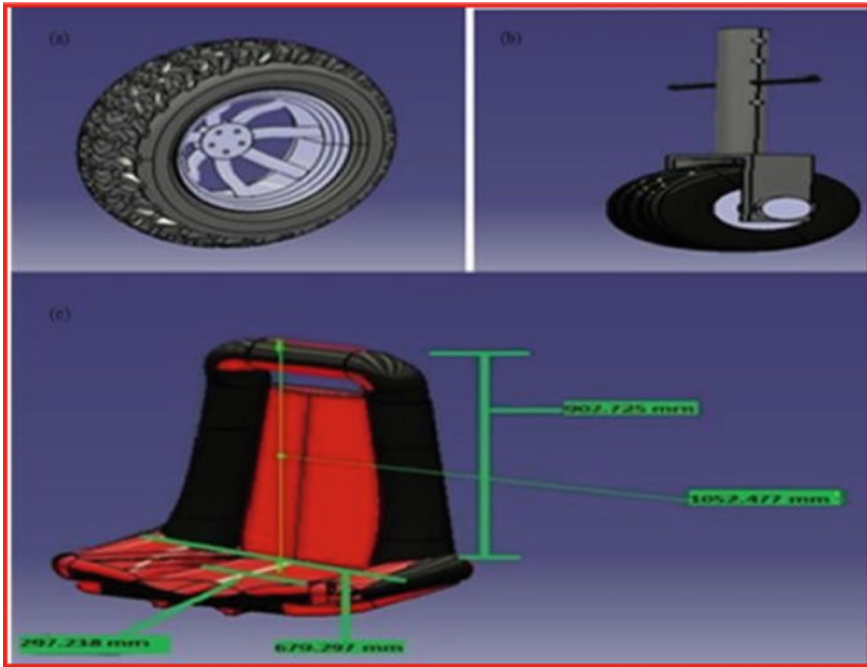


Fig. 47.3 Design of **a** main wheel, **b** supporting wheel, and **c** seat construction

levels and lightweight. The opposing V-tread pattern eliminates the likelihood of mud retention on the tire surface and ensures maximum grip even over marshy terrain. Two different sizes of tires for the front wheels and rear fortifying wheels were designed, which are shown in Fig. 47.3. The front-wheel width is 152.4 mm, and the total radius is 304.8 mm, as shown in Fig. 47.3a. The rear wheel radius is 104.7 mm, and the shaft radius is 25.4 mm, as shown in Fig. 47.3b. The seat was designed to provide good lumbar support for long work shifts. Lower height support was provided for the operator to maintain an upright position without any kind of effort, as shown in Fig. 47.3c.

47.2.4 Reaper

The reaper setup was designed to provide a compact yet effective collecting attachment to the MTLAV, as shown in Fig. 47.4a–c. The amassing system was designed based on the size of the reaper and the likely size of the harvested crops. Conventionally, there are “ $n + 1$ ” spikes on a reaper for every “ n ” teeth to ensure smooth harvesting. The design was made with 16 teeth and 17 spikes for the reaper. Figure 47.4a–c show the MTLAV with the reaper attachment to the front side of the

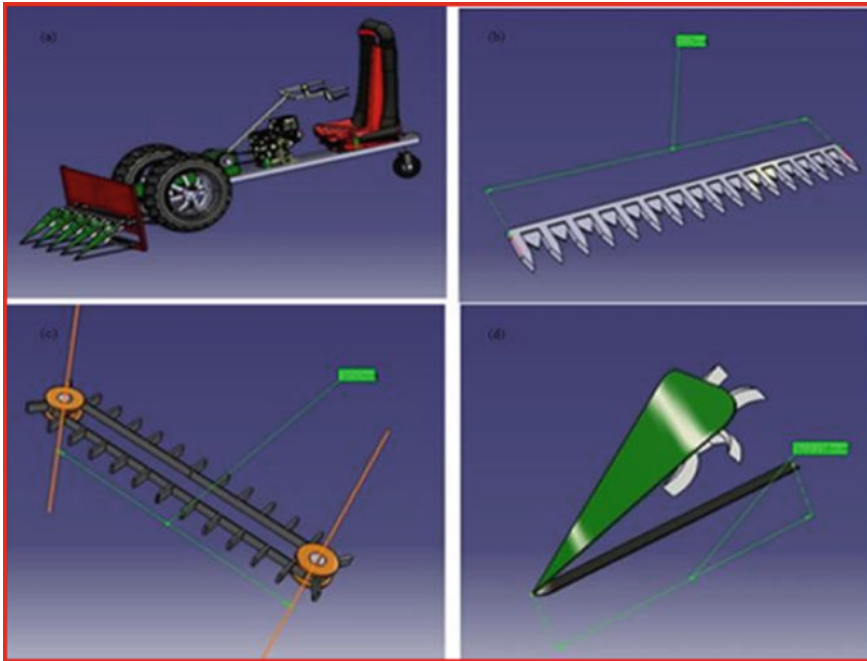


Fig. 47.4 a 3D model of MTLAV with reappear, b Blades, c Conveyer belt, and d Gathering plate attachment

vehicle, the geometry of the reaper blades, and the model of the conveyer belt, which is 1010 mm in length and 10 mm in width, with 4-mm belt thickness, 26 lugs, and 1220-mm minimum clearance required between two adjacent lugs. Figure 47.4d shows the model of the amassing plate. The plate length is 450 mm, the plate thickness is 3 mm, and the total length of the fortification rod is 552 mm.

47.2.5 Tiller

Tilling is the most useful tool for cultivating soil and makes it ready for planting. Tilling is the first stage of cultivating the land. Weeds and rocks in the soil are removed by tilling. If the soil is full of weeds and rocks, then the condition of the soil is not good for fruit, flower, and vegetable production. Hence, it is necessity to prepare the soil for planting by tilling it and add fertilizers or compost if needed with lawn and rotary tillers, and this can be done easily. The finalized tiller design features a 120° angle between successive blades for rapid completion of de-weeding and tilling. Figure 47.5a shows the tiller for the MTLAV, and b shows the simple tiller assembly and the corresponding dimensions; the shaft length is 700 mm, the blade spacing is 20 mm with a 120° angle, the blade thickness is

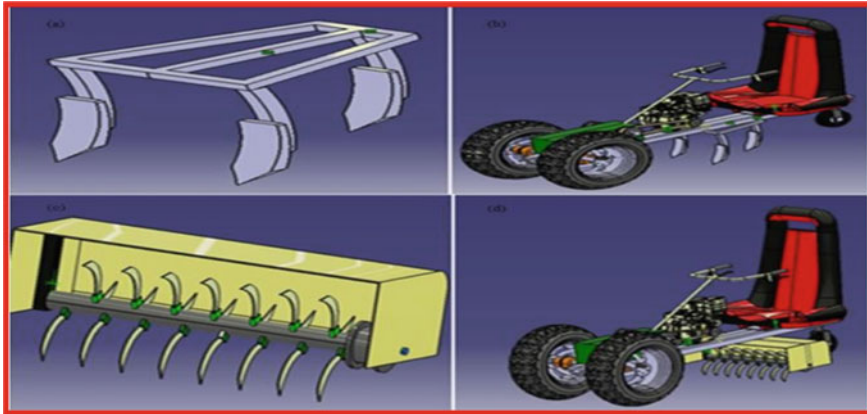


Fig. 47.5 Three-dimensional models of a Tiller model, b MTLAV with tiller attachment, c Plow assembly, and d MTLAV with plow attachment

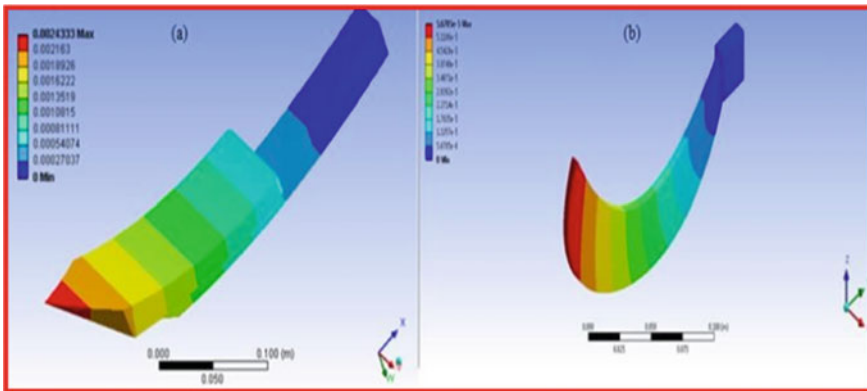


Fig. 47.6 Structural analysis of a Plow and b Tiller element

5 mm, and the blade length is 178 mm. The plow blades were designed to maximize plowing capacity while minimizing the horsepower so that the plow can move in a typical field. The design uses a 3-furrow setup with 2 furrows in the front with a distance of 175 mm between them and a third furrow placed centrally behind the two furrows. Two furrows were integrated in the front with a trailing furrow behind them for plowing the land with good results. The plow assembly is shown in Fig. 47.5c, d. The dimensions of the plow are as follows: The length of the blade is 242 mm, the width is 76 mm, the thickness is 14.484 mm, the total length of the plow is 369 mm, and the thickness of the rod is approximately 30 mm.

47.3 Analysis of MTLAV

Analysis has been performed on the plow and tiller blades with Ansys since these components should work reliably under the heavy wear from unforgiving soil. Based on the real conditions, the interaction of test soil-bottom surfaces of both plow and tiller components and boundary conditions was applied. These components passed the test, yielding a factor of safety (FOS) over 5.71 (the minimum accepted FOS is 3). The analysis was carried out by meshing the attachment with 2686 nodes and 1286 elements. The analysis of the plow and tiller is shown in Fig. 47.6a, b. The considered properties of plow and tiller elements for structural and thermal analysis are shown in Table 47.2.

47.4 Results and Discussion

The three-dimensional (3D) model of each component was designed with consideration of various aspects such as operating parameters, materials, soil conditions, and optimum weight reduction taken into account. Structural analysis and optimization of the plow and tiller were obtained through computations through Ansys software. Simulation results show that multi-task of agriculture operations can perform at a time; these features of the MTLAV are to attract the farmers. The maximum stress intensities occurred at the bottom tip of the plow and tiller with negligible deformation. According to simulated results, it is noticed that no need of complementary support under the bottom of the tip region, which leads to reduce the weight and cost of these components, and these are suitable for real field conditions even in hill areas. Estimation of soil force acting on either plow or tiller is crucial due to wear rate depends upon the soil condition, and soil type is varying

Table 47.2 Properties of plow and tiller were used in Ansys analysis

Property	Value
Young's modulus	2.e + 005 MPa
Poisson's ratio	0.3
Density	7.85e-006 kg/mm ³
Thermal expansion	1.2e-0051/°C
Tensile yield strength	560 MP
Compressive yield strength	250 MPa
Tensile ultimate strength	660 MPa
Thermal conductivity	6.05e-002 W/mm°K
Specific heat	434 J/Kg°C
Relative permeability	10,000
Resistivity	1.7e-004 Ω*mm

in different regions. The soil force acting on the plow (K_e) is 4.7 kg, which is calculated using the following equation [7]:

$$K_e = \frac{K_s C_p}{i Z_e N_e} \tag{47.1}$$

Where K_s is the maximum tangential force (kg), C_p is the coefficient of tangential force, Z_e is the total numbers of elements (i.e., plow or tiller) on flange, knee is the ratio of a number of the contact point on the soil into the total number of elements, and i is the number of flanges. The seat was designed while keeping the rigors of agricultural toil in mind. The seat continues to support the driver through volatile changes in terrain and work surfaces. The seat is designed to first and foremost provide an upright seating position. This ensures clear vision and minimizes the risk of back problems due to prolonged exposure to rough terrains. The estimated values of the design and Ansys analysis of the MTLAV are presented in Table 47.3. The seat also has cushions to provide lumbar support, unlike most tractor seats on the market. Thigh support has also been deemed crucial, given the absence of a floor board in the MTLAV. The pedals, the handle, and every controller have been designed to be within the reach of an average Asian. The statistics of the average Asian farmer was analyzed, and a mannequin was designed. Based on the mannequin in the seat, a sphere was constructed so that the mannequin could freely reach any point within the sphere drawn around him without any stretching of the arms or getting up. All the controls needed to operate the MTLAV, including the

Table 47.3 Estimated calculations according to the design and Ansys analysis of MTLAV

<i>Engine</i>	
Type	Four stroke single cylinder (petrol)
Displacement	338 cc
Compression ratio	16:1
Power	10 hp @ 3700 rpm
Torque	19 Nm @ 2500 rpm
<i>Chassis type</i>	
Chassis	Ladder frame
Overall length	2250
Overall width	1100
Ground clearance	330.2 mm
<i>Tires</i>	
Front	304.8/56/R10
Rear	104.68/56R8
Turning radius	1.8 m
<i>Performance</i>	
Top speed	8.7 km/hr
Working speed	6 km/hr

pedals and the handlebar, were designed to fall within this sphere. Another sphere was obtained for the driver's vision from the driving position to prevent vision obstruction. Emphasis was placed on the driver having an uncluttered view of the surface that lay ahead of him.

47.5 Conclusions

The equipment sold is highly specialized and provides only one or two implements needed for cultivation. These principle points are kept in the mind, and the MTLAV was conceptualized to combine the features of three different types of agricultural equipment. The MTLAV can be sold at cheaper costs as compared to commercial tractors. The developed MTLAV will be more appealing to farmers due to the low cost and simplicity of the design and operation. MTLAV conceptualized design is a great opportunity for manufacturers to work out for the agricultural needs.

References

1. Jorge, T.S., Francisca, L.P.G., Ana, I.D.C., Jose, M.P.B.: Configuration and specifications of an unmanned aerial vehicle (UAV) for early site-specific seed management. *Plos One* **8**(3), 1–15 (2013)
2. Ming, L., Kenji, I., Katsuhiko, W., Shinya, Y.: Review of research on agricultural vehicle autonomous guidance. *Int. J. Agri. Bio. Engg.* **2**(3), 1–26 (2009)
3. Bechar, A., Edan, Y.: Human-robot collaboration for improved target recognition of agricultural robots. *Indus. Robot.: An Int. J.* **30**(5), 432–436 (2003)
4. Xiao, B., Wang, CH., Guo, X., Wu, SH.: Image acquisition system for agricultural context-aware computing. *Int. J. Agri. Bio. Engg.* **7**(4), 75–80 (2014)
5. Amarjit, S.N., Toshihiko, N.: Role of buffalo in the socioeconomic development of rural Asia: current status and future prospectus. *Anim. Sci. J.* **74**, 443–45. (2003)
6. United Nations Population Fund. www.unfpa.org/swp/2007/. Accessed on 13 Oct 2014
7. Mandal, S.K.R., Bhattacharya, B., Mukherjee, S.: Optimization of design parameters for rotary tillers blade. In: Proceedings of the 1st International and 16th National Conference on Machi and Mechas (iNaCoMM2013), IIT Roorkee, India (2013)
8. Jat, M.L., Gathala, M.K., Ladha, J.K., Saharawat, Y.S., Jat, A.S., Sharma, S.K.: Evaluation of precision land leveling and double zero tillage systems in the rice-wheat rotation: water use, productivity, profitability and soil physical properties. *Soil. Till. Reserv.* **105**, 112–121 (2009)
9. Chauhan, B.S., Mahajan, G., Sardana, V., Timsina, J., Jat, M.L.: Productivity and sustainability of the rice-wheat cropping system in the Indo-Gangetic plains of the Indian subcontinent: problems, opportunities, and strategies. *Adv. Agron.* **117**, 23–34 (2012)
10. Devendra, C., Thomas, D.: Smallholder farming systems in Asia. *Agri. Syst.* **71**, 17–25 (2002)
11. Esdaile, R.J.: Two Wheel Tractor Newsletter. <http://conservationagriculture.mannlib.cornell.edu/pages/resources/twowheel.html>. Accessed on 7 Oct 2014
12. Haque, M.E., Bell, R.W., Islam, A.K.M.S., Sayre, K., Hossain, M.M.: Versatile multi crop planter for two-wheel tractors: an innovative option for small holders. In: Proceedings of 5th World Congress Conservation Agriculture Brisbane, pp 102–103 (2011)

Chapter 48

Identification of Alzheimer’s Disease Using Various Deep Learning Techniques—A Review



Ragavamsi Davuluri and Ragupathy Rengaswamy

Abstract Effective identification of Alzheimer’s disease (AD) becomes primary importance in biomedical research. Recently, deep models have reported with high accuracy for AD detection compared to general machine learning (ML) techniques. Nevertheless, identifying brain disorder like AD and tumor is still challenging, and for classification, it requires a highly discriminative feature representation to separate similar brain patterns. Present state of AD detection techniques using various deep learning (DL) models is studied here. Features of personal data, genetic information, and brain scans were focused. This includes required preprocessing steps with neuro-imaging data that extracted from single and multiple modalities. Performance of deep learning mechanisms and their accuracy values obtained are described. Although deep learning has achieved notable performance in detecting AD, there are several limitations, especially regarding the availability of datasets and training procedures.

48.1 Introduction

For detecting neuro-degeneration, many powerful tools are used in medical imaging, and examination has been delivered, and imaging information is mostly used in the detection of disease. Recently, it is shown that computer-aided detection can make the results more effective and accurate [1]. A neuro-degenerative disorder is a disease that gradually destroys memory that leads in communication difficulties also that might cause speaking and walking inabilities and affects daily activities and sometimes results in fatal.

Alzheimer’s disease (death of brain cells) affects the significant brain functionalities that lead to memory loss for the patient. Brain cell connected to the body parts and the cells connected themselves may degenerate and sometimes die, and

R. Davuluri (✉) · R. Rengaswamy
Department of Computer Science and Engineering, Annamalai University, Chidambaram,
Tamil Nadu, India

that causes gradual memory loss and significant cerebral functions destroying. No cure exists, but medication and management strategies may temporarily improve symptoms.

AD is commonly recognized as dementia that estimates 60–80% of all dementia cases. This disease normally affects the people who are in middle age or old age, potentially started by amassing the neurons protein present in and around, and prompts a consistent memory (reminiscence) decay (related with brokenness of synaptic, shrinkage, and brain cell demise) [2].

Deep learning is a subset of AI that mirrors the activities of processing of brain and prototype detection for solving intricate executive issues. Effective deep learning in 2D images classification has benefited medical imaging deep learning techniques [3]. Recently, deep learning models were developed in specific convolutional neural networks (CNNs) which combine both 2D and 3D CNN's and perform better in disease detection field using medical imaging [4].

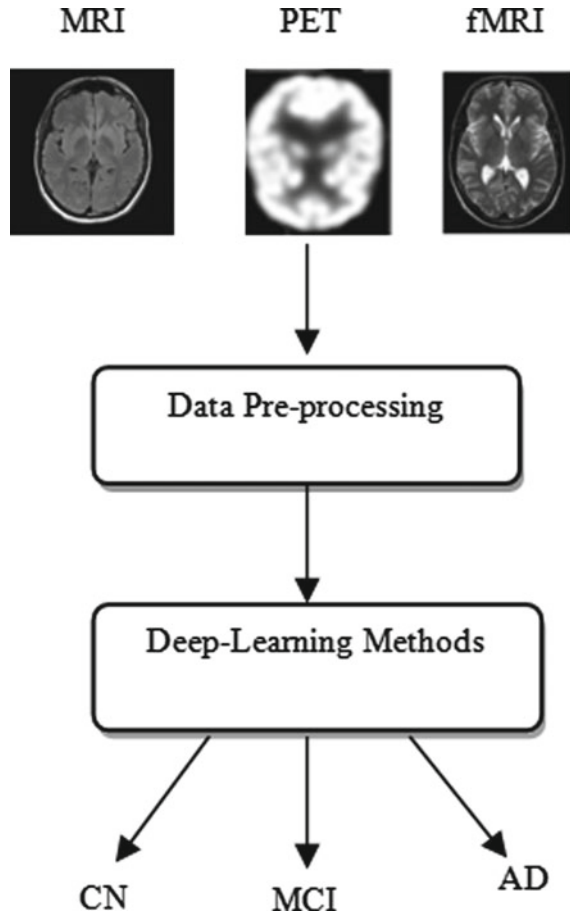
The perspective here is to perceive what sort of biomarkers and components can be utilized in AD diagnosis, which preprocessing technique is required to deal with biomarkers and what type of datasets are available (specifically for neuro-imaging). It also confronts what deep model mechanism can be used to capture exact disease-oriented patterns from single features of brain MRI's also how to deal with multi-modal information. Figure 48.1 shows the block diagram for detection of AD using deep learning methods.

Feature extraction, dimension decrease, and classification are three main components in machine learning algorithm. Precise detection of Alzheimer's at an early stage requires some quantitative biomarkers evaluation and automatic classification of AD carried out through magnetic resonance image (MRI) [5]. Numerous neuro-imaging modalities like MRI, fMRI, and positron emission tomography (PET) were investigated for the diagnosis of AD. Mostly, MRI is used to detect AD since it has high accuracy [6]. Magnetic field and radio frequency pulses are used for creating 3D representation of images for various parts in the human body like brain, lungs, hands, and bones. Patch, ROI, voxel are the data management methods that handle with brain which is carried out with necessary preprocessing steps. The functional MRI reflects the modifications that are related with blood flow. Metabolism processes are observed using PET which is a functional scan technique on basis of nuclear.

48.2 Preprocessing

Once neuro-imaging modalities are taken, then the process of detecting AD is initiated with preprocessing steps. The required steps for preprocessing should be recognized, more specifically in machine learning, the data is manipulated before preprocessing. The effective preprocessing makes more effective results in

Fig. 48.1 Diagnosis of AD using DL methods



obtaining accuracy in DL models, and some preprocessing steps are less critical compared to other techniques [7]. Tissue segmentation, skull stripping, intensity normalization, etc. are the preprocessing techniques used to preprocess the raw data. Deep learning methods propose advanced preprocessing techniques [8]. Intensity charts of all the pixels or voxels with respect to its reference scale are said to be intensity normalization. Therefore, the resultant structures have same intensities [9]. N3 non-parametric is the commonly used non-uniform IN algorithm for preprocessing the data. For improving peaks of histogram, N3 algorithm is established well, and hence, any non-uniformity intensity is reduced [10]. The other IN method is shifting the voxel intensity distribution about zero (i.e., zero-centred).

Grad warp is the one more preprocessing method; here, geometrical distortions are adjusted with respect to gradient nonlinearity. The tissue segmentation plays a major role in measuring the tissue volume in each region. In the initial stage of neuro-degeneration, the temporal region of lobe (a part of gray matter (GM)) gets affected [11], and GM is the common input given for classification problems, and

the input is termed as GM; a probability map which is contrasted to white matter (WM). A quantitative image of spatial distribution of brain tissue is obtained through GM probability maps; here, voxel brightness represents GM quantity. Hence, various models are used for non-WM which is extracted from brain medical imaging using GM mask with consequent FDG-PET scan [12]. Skull stripping is one of the preprocessing methods in which the skull bones are removed from the images, and this can be used together with cerebellum removal or can be used alone. The other preprocessing method is motion rectification; here, motion artifacts are suppressed.

Voxel-based tissue segmentation is not the complete part of full brain image analysis since it works only a part of the brain. In general, feature dimension reducing technique is applied for voxel-based ML methods, and it is not essentially functional in deep structures. However, a voxel pre-selection method can be applied autonomously to each neuro-imaging modality in order to conquer high feature dimensionality; as an example, t-test algorithm is used for removal of unnecessary voxels in an ROI-based study and also decreases the load of computation [13]. Voxel-based morphometry is developed from structural MRI in order to obtain significant volumes of interests (VoIs) in relation to GM damage. A CNN was trained using a series of convolutional feature detectors acquired by a patch-based auto-encoder (AE) training to extract prognostic features from MRI [14].

Certain properties of slice-based architectures are minimized into two-dimensional (2D) images, and hyper-parameters reduction of slice-based methods is generally done in the mid-part of the brain. In slice-based axial scans, no information is available from starting slice to ending slice which is used for dissection of GM volumes [15]. Some examples are given for MRI in which median axial slices are used, and some of the axial slices are given 166 of GM, fMRI slices is 43, and 3 for MRI. In fMRI data, the axial slices of images were used in [16], but due to the absence of information, first ten slices are removed of each scan slices. An identical trial was considered in [17]; here, three slices were used in the MRI axial plane, and the anatomical regions reported as RoI which is correlated with the detection of AD. A method was adopted [18] in which three slices are combined to form RGB color so that the requirements of CNN architectures are met. To select the most informative slices, an entropy-based sorting method [19] was used as of the available axial slices of MRI scan. Image entropy was computed for each of the slices using histogram info of each slice through its obtained variation measure, and the slices with high entropy values are considered to be most informative slices. The decomposed slices of image scans are segmented into small groups with periodic intervals without or with some overlap but without segmentation.

ROI methods particularly focused on affected parts of the brain without considering the whole brain in order to identify the Alzheimer's in its early stages. ROI usually needs the information of previous anomalous regions and a brain chart of anatomical region [20] or the orientation area. Eighty-three functional regions of GM are considered from MRIs [21]. After the extraction of 93 MRI features (ROI-based volumetric features), PCA was applied for the similar number of PET features [22]. In [23], among brain region pairs, the correlation coefficient is

computed for the extracted 90 ROIs from fMRI images. Fractal measurement (FM) surface features were extracted together with texture feature areas, volumetric, and cortical thickness of the divided MRIs, and the geometric properties of the image are calculated for feature pattern description. AD diagnostics is based on CNN and structural MRI and DTI modalities fusion on hippocampal ROI using data from the ADNI database [24], the right lobe and left lobe of the hippocampus were selected, and a deep model for each region was designed.

Morphological estimations are utilized for various pieces of MRI checks, volumes, normal thickness, surface region, and deviation. The two hippocampi are the another MRI analysis [25]; here, hippocampi are portioned, and a neighborhood pixel of 3D image is separated from the focal point of each; a profound model was then utilized for grouping. Nearly, 440 features are chosen like thickness, curve, skewness, energy, surface area, mean, and volume just like hippocampus analysis along with the benchmark of minimum mean square error and absolute score. Features exception is highly correlated and was then taken out to create autonomous features. At last, an irregular forest classifier was utilized for determination of features to recognize the 20 most significant features.

A patch is characterized as a three-dimensional (3D) cuboid. This approach-based methodologies can catch infection-related examples by separating features from patches. The fundamental test in fix-based strategies is to pick the most useful patches for catching both patch level and image level features. This methodology has been utilized in various examinations for AD identification [26]. For instance, 27 uniform inflexible sizes nearby fixes of voxels are separated with half-image. Comparable methodology is enclosed with multi-methodology review [27]. Milestone-based techniques have been utilized to consequently separate discriminative anatomical landmark spots of AD from MRIs by means of gathering correlation of subjects; initially, the best discriminative Alzheimer's landmark areas are distinguished utilizing a milestone disclosure calculation.

MRI of brain was constantly segmented to different number of regions of similar size, and numerous pixels of 3D were taken to identify the most affected part of the brain cells from each segmented part. Then, patches are grouped into various clusters that exist in each region by applying k-means clustering model before doing classification procedure [28]. For high-level feature demonstration, a class discriminative patch can be applied in single multi-modality examination.

Hippocampus presented in the temporal lobe is a complex brain structure, and it is useful in identifying Alzheimer's. In initial stage of Alzheimer's, the hippocampus's shape and volume are already affected, and it is the sign or marker of earlier detection of AD [29]. The texture investigation can perform well in both shape and volumetric examinations in characterization exactness. Some studies include shape, volume, power, and surface attributes in assessing AD [30] that might bring good achievement in classification performance. The locales are mostly damaged because of AD, and it must be recollected in the analysis of AD or initial stage of AD since other regions of brain may also get affected due to AD in any case, their commitment is as yet not investigated fully.

48.3 Materials

The data used in our study is from two public datasets: the Alzheimer's disease neuro-imaging initiative (ADNI) study and the open access series of imaging studies (OASIS). The ADNI (<http://www.loni.ucla.edu/ADNI>) was launched in 2003 as a public-private partnership, led by Principal Investigator Michael W. Weiner, MD. ADNI is a longitudinal multicenter study designed to develop clinical, imaging, genetic, and biochemical biomarkers for the early detection and tracking of Alzheimer's disease (AD). And, the OASIS is a project aimed at making neuro-imaging datasets of the brain freely available to scientific community accessible at (<http://www.oasisbrains.org>). OASIS provides two types of data: cross-sectional and longitudinal for the identification of AD.

48.4 Deep Learning Techniques

Deep learning techniques are usually classified into supervised learning and unsupervised learning methods. This is again classified into auto-encoder (AE), deep neural network (DNN), restricted Boltzmann machine (RBM), recurrent neural network (RNN), deep polynomial network (DPN), and convolutional neural network (CNN). CNN is further divided into 2D CNN and 3D CNN. Deep supervised feature extraction mechanism utilizing common stochastic system was projected throughout learning methods called supervised and unsupervised.

48.4.1 Supervised Deep Learning

Supervised methods are mainly used and have higher popularity in deep learning; here, feature extraction process and classification process are combined and done in single process. Some of the supervised models for detection of Alzheimer's are explained below.

DNN has a similar arrangement compared to conventional multi-layer perceptron (MLP) organization, yet consolidates with numerous stacked layers. DNNs are absolutely managed and generally utilized in various examination zones to find previous conceptual correlations and patterns. Nonetheless, the preparation cycle of DNNs not ideal, in any event contrasted with SVMs, and its learning cycle is additionally extremely moderate. Deep NN with one concealed layer was proposed after a component extraction venture with an adjusted sparse AE [31]. Deep learning framework with modified K-sparse auto-encoder (m-KSA) classification is used to collect neutrally affected areas of the brain MRI, low amyloid beta 1–42 imaging in cerebro-spinal fluid (CSF), and PET imaging of amyloid; here, a sample of 150 images is taken. KSA method is highly used in detection of AD for the consequences of producing good classification results.

DPN is one of the supervised DL algorithms. When compared with deep belief network (DBN) and stacked AE, DPN may have same or even better performance [32]. DPN is stacked with deep configuration for improving the performance further. A multi-modal stacked DPN (SDPN) with bi-level SDPN's was proposed for extracting the features from neuro-imaging multi-modal data for Alzheimer's classification [33].

CNN: Convolutional neural networks (CNNs) are more popular and come under the category of DNN that is effective in the area of image classification. Also, it is a type of ANN which learns image features by its own in the convolutional layers. CNNs are inspired by brain's visual cortex. This mechanism has gaining high accuracy in DL model in image examination and also designed efficiently for using spatial data by taking respective inputs of 2D or 3D images, then the features get extracted from the respective image by stacking many convolutional layers; resultant is the hierarchy of more abstract features [34]. The major advantage and main characteristics of CNN are to combine both the process of feature extraction and classification. In deep models, the inputs are mostly considered in vector form.

2D-CNN: In general, deep model techniques are followed by fully connected layers, CNN layers get paired with clustered layer, and it called as softmax layer. Example, 2D CNNs with 2, 3, or 5 convolutional layers are considered in single-modality model, or multi-modality with 4 convolutional layers had taken and examined [35]. More examples such as two-dimensional image with 2 convolutional layers in both slices of MRI; 6 layers on 1 sagittal slice of MRI slice which include hippocampus, together with 1 convolutional layer; here, CNN filters are provided by a sparse AE along with polynomial kernel SVM. Seven 2D CNNs of slices of seven groups comprise of three convolutional layers [36]; this indicates that if one of the classifier or more than one classifier resultant the subject as Alzheimer's, then definitely the resultant subject is classified as AD. Two convolutional layers in 2D CNN were used for weak learners, for predicting response values from $m \times n$ models of regression [37]. The spectral CNN framework is carried out by taking common CNN that comprised with sub sampling layers, connected, and convolutional layers.

The CNN input layer is represented in spectral domain of neuro-data, where the connections between regional pairs and node location are represented by a set of eigen values. Conversely, there is no third dimension for sharing the kernel, and hence, 2D CNNs seem to be inefficient to encode the spatial data obtained from 3D images. Therefore, 3-2D CNNs were projected to attain various views for an MRI [38]. Each CNN (3D CNN) comprises of 4 layers and 4 blocks (i.e., each block has 12 layers), and hence, finalized result was made on basis of consequences of majority voting. The approach of CNN and RNN is used together to capture the spatial data in a 3D image. Here, 2D CNNs were utilized to confine the intra-slice features (single slice with similar structure), while RNN is utilized for extracting adjacent slice features for concluding process of classification.

3D CNN: A 3D CNN is popular for their spatial relationship since neuro-imaging provides 3D images for examination. The entire image or some region of brain lobe should be taken as input for the identification of Alzheimer's

disease in spite of its complexity. However, it is in need of more parameters even for a small training dataset which might result in over-fitting. In other methods of CNN; 3D CNNs with 12, 5, and 4 convolutional layers were used. Various feature combinations are utilized from 3D CNN along with six convolutional layers and 3D convolutional auto-encoders and softmax layer for the purpose of classification [39].

By applying 1 or 3 convolutional layers along with AE, the 3D CNNs were pre-trained. In [40], two convolutional layers from 3D CNNs were used, and each convolutional layer was pre-trained using sparse AE, which connects the two modalities in order to make them as a fully connected layer. Some other 3D CNNs models might proceed with 5 or 7 convolutional layers and fused with deep neural network in the final step to create fully connected layer. Medical image data or some genetic data is used as input for DNN and 3D CNN for MRI.

In many local image patches, multi-3D CNNs along with 4 convolutional layers are used [41]. On basis of data validation and classification accuracy, the CNNs for the assembly were selected and jointly fine-tuned in some upcoming final layers, and this seems to be more adaptable for task of global classification. A 3D CNN was used in multi-modality examination with three convoluting layers to predict MCI conversion. Feature extraction is a labor-intensive and time-consuming process. During the pre-diagnosis of Alzheimer's illness, the 3D CNN, on the other hand, spontaneously learns the features from images [42].

Cascading 2D/3D CNN: CNN cascading was built mainly to study the characteristic of MRI and PET learning features from brain image [43]. Multiple CNNs like four layers deep 3D CNN were built on various regions for transforming the image to the compact high-level features. Similarly, high-level 2D-CNN (2-convoluting layers) is cascaded to combine high-level features.

RNNs have lower number of layers that might cause memory insufficient problems for long input image or data. It requires large datasets for processing. Provisionally, proxy the perceptron hidden units help in memory overloading issues. Long short-term memory (LSTM) function is used as storing unit to avoid over usage of memory. The LSTM comprises three gate units and one memory cell unit, and it is considered highly risk during arrangement when compared with conventional RNN, though valuable information can be captured effectively in a sequence [44].

48.4.2 Unsupervised Deep Learning

Unsupervised DL tries to get hold task-related operations from neuro-imaging information. Advancement from ML into DL was initially taken by utilizing an unsupervised DNN for extracting features. An approach was developed in such a way that the features are iteratively discarded from the uninformative features in a hierarchical manner for selecting the high-level features from the input data of MRI, PET, and CSF biomarkers [45].

Auto-encoder is a particular type of neural network that comprises two modules such as an encoder and a decoder. By reducing the error rates caused because of reconstruction among the input and output network values, an AE can get a compressed depiction or resultant value from the given input data. Various variations of AEs are sparse AE, convolutional AE, denoising encoder, and changing encoder. Stacked AEs with hidden layers (2 or 3) and one softmax layer are trained and finely tuned finally in modalities [46]. The features learned in the middle layer of auto-encoder are extracted for the purpose of classification also used in pre-training phase feature extraction and reduction.

Stacked denoising AE with two hidden layers is used for extracting the regional abnormalities. It was proposed by combining AEs such as denoising and sparse. This approach uses hidden layers of three together with support vector machine (SVM) for during the process of classification. Concatenating stacked AE from MRI and images with inventive low-level features, feature vector was constructed and given as input to multi-kernel SVM. With respect to 2D CNN or deep neural network sparse, AE is used to extract the features used a sparse AE for classification. Deep dictionary learning platform was proposed using clean as well as noisy filter samples; finally, classification is done through NN.

RBM is designed using a one-layered undirected chart replica with one visible layer and one hidden layer. There exists a symmetric links among noticeable and concealed (hidden) layers; however, there is no connection between units within the equivalent layer. Input data is generated from hidden representations like AE, a deep model consists of RBM stack which is used for feature extraction process [47], and a linear SVM classification is done finally. For transforming the features of functional MRI, multiple RBMs are stacked with one another into a low-dimensional space through detection of nonlinear relations between ROIs. Initially, relational nonlinearity function is identified, then hidden Markov mechanism (HMM) has been used to estimate the fMRI features which is given as input; then, classification is done at last, and equivalent diagnostic of disease was done using linear SVM.

DBN has indirect links to the top presented two layers also direct link to the bottom presented layers. Three concealed layers of DBN for pixel and voxel values of MRI (taken from gray matter tissue) are considered for detecting AD with a linear classifier SVM, and it was given in [48].

48.5 Comparative Analysis of DL Models

Unsupervised deep models seem to be better for utilizing feature extraction and then given as input for the classifier. Stacked AE model can be improved significantly with respect to the considered nonlinear power and difficult patterns. Other benefit of AEs is a good initialization parameters that can be found for CNNs. However, by taking suitable initialization models such as transfer learning and Xavier, this model gains an advantage of AEs have certain limits. Supervised

Table 48.1 Pros and cons of DL models used to detect AD

DL models	Advantage	Limitations
Auto-encoder	Initializes CNNs and represents complex pattern	Captures all information
DNN	Used for vector-based problems and able to identify nonlinear complex relationships	Not apt for images with generalization issues
RBM	Patterns can be created if data found to be missed	High computation cost in training process
DPN	Can be able to learn feature representation from small datasets	Performance rate is low due to simple concatenation
RNN	Highly suitable for sequential 2D images	Training process issues occur due to exploding gradients
2D CNN	Training process is ease, and feature extraction has good results	Spatial encoding of 3D images is not so easy
3D CNN	From 3D volume of MRI, 3D information can be fetched easily	High computation cost

methods were explained well in this survey, and feature extraction process and classification process are enabled into a single model. Results are analyzed and compared for AE and DPN and show better performance than DPN or a stacked DPN. Table 48.1 shows the pros and cons of DL models for detection of Alzheimer's disease.

DNN is more suitable for solving vector-based problems compared to SVMs; when comparing with DNN, SVM has minimum optimality for the training process, and learning process is also slow. The most significant process for detection of AD in DL models is 2D CNNs and 3D CNNs which are highly optimized for data or image-based issues. From 3D volume of brain scan, the former can capture 3D information and shows better performance while comparing with 2D CNNs. However, training process is more complex, and it is considered an issue here, although patch-based or ROI-based methods are used to resolve the issue instead of using voxel-based methods. Although in 2D CNNs, training process is easy to carry. However, a scheme that uses 2D CNNs is not more efficient for spatial information encoding process of 3D images since kernel sharing is absent across the third dimension. Henceforth, the schemes which consider all three views of a brain scan in adjacent image slice in an image sequence give better resultant. The CNN effect has been examined, and results are reported, and therefore, highly, DNN does not necessarily give optimal results.

Table 48.2 gives the accuracy, sensitivity, and specificity values for some DL models. The performance of Alzheimer's disease detection depends on neuro-imaging quality measurements. Finally, registration and intensity normalization are done. Results from balanced and unbalanced dataset are suggested with accuracy, the accuracy results slightly, and dataset balancing can improve the performance of accuracy results.

Table 48.2 Result comparison of deep learning techniques

S. No.	DL model	Accuracy	Sensitivity	Specificity
1	Multi-modal DBM with an SVM [49]	95.36	94.65	95.2
2	Multi-modal stacked DPN with SVM [50]	97.2	95.6	98.6
3	2D CNN [51]	97.7	98	97.36
4	2D CNN with sparse regression model [37]	91.02	92.8	90
5	A 3D CNN models with landmark concatenation at final stages [52]	91.10	88.1	93.5
6	A multi-modal 3D CNN [53]	84.2	81	87
7	3D CNN pre-trained with stacked 3D convolutional AEs [54]	97.6	–	–
8	3D CNN based on ResNet and VGGNet [55]	88	–	–
9	Multi-modal and multi-scale DNNs consist of 7 DNNs [56]	84.7	80	91.9
10	Google Net and LeNet-5 [57]	98.7	–	–

48.6 Conclusion

Alzheimer disease is the leading disease that affects the mental health for the patients and at sometimes even causes death. Therefore, early diagnosis of Alzheimer's is mandate. Earlier diagnosis of Alzheimer's is a tough task with the use of computer-based systems, which is highly recommended in Alzheimer's diagnosis. To perform this task, deep learning models are highly attracted in recent years also gather strong intention for implementing since it performs well and has good accuracy. Here, how DL models have enabled the development of Alzheimer's recognition systems review is carried out. The biomarkers including MRI, PET, and fMRI models are also explained in brief together with how they are used for the detection of AD with its symptoms. Thereby, combining the neuro-imaging modalities can aid AD identification along with few factors like genetic information and memory test scores to deliver more accurate results of diagnosis.

Many DL models have been discussed here, and in terms of the stage like classification process, CNNs have been used popularly for its outcome in terms of accuracies compared to other models. Automatic multi-modal approach is preferred for AD diagnosis, but issues of over-fitting related to dataset can be resolved further.

References

1. Ilias, M., Lazaros, I., Elias, P.: Applying deep learning to predicting. *Artif. Intell. Appl. Innovations* **584**, 308–319 (2020)
2. William, T.: 2018 Alzheimer's disease facts and figures. *Alzheimers Dement* **14**(3), 367–429 (2018)
3. Ker, J., Wang, L.: Deep learning applications in medical image analysis. *IEEE Access* **6**, 9375–9389 (2017)

4. Litjens, G., Kooi, T., Ehteshami, B.: A survey on deep learning in medical image analysis. *Med. Image Anal.* **42**, 60–88 (2017)
5. Ragavamsi, D., Ragupathy, R.: A survey of different machine learning models for Alzheimer disease prediction. *Int. J. Emerg. Trends Eng. Res.* **8**, 3328–3337 (2020)
6. Liu, J., Pan, Y., Li, M.: Applications of deep learning to MRI images: a survey. *Big Data Mining Analytics* **1**(1), 1–18 (2018)
7. Lu, D., Karthik, P., Rakesh, B.: Alzheimer’s disease neuroimaging initiative multimodal and multiscale deep neural networks for the early diagnosis of Alzheimer’s disease using structural MR and FDG-PET images. *Sci. Rep.* **8**, 5697 (2018)
8. Akkus, Z., Hoogi, A., Rubin, D.L.: Deep learning for brain MRI segmentation: state of the art and future directions. *J. Digit. Imag.* **30**, 449–459 (2017)
9. Liu, M.: Deep multi-task multi-channel learning for joint classification and regression of brain status. In: *International Conference on Medical Image Computing and Computer-Assisted Intervention, LNCS*, pp 3–11. Springer (2017)
10. Sled, J.G., Zijdenbos, A.P., Evans, A.C.: A nonparametric method for automatic correction of intensity nonuniformity in MRI data. *IEEE Trans. Med. Imaging* **17**, 87–97 (1998)
11. Jack, C.R., Jr., Wiste, H.J., Prasanthi, V.: Brain beta-amyloid measures and magnetic resonance imaging atrophy both predict time-to-progression from mild cognitive impairment to Alzheimer’s disease. *Brain* **133**, 3336–3348 (2010)
12. Vu, T.D., Ho, N.H., Yang, H.J.: Non-white matter tissue extraction and deep convolutional neural network for Alzheimer’s disease detection. *Soft. Comput.* **22**, 6825–6833 (2018)
13. Ortiz, A., Gorriz, J.M.: Ensembles of deep learning architectures for the early diagnosis of the Alzheimer’s disease. *Int. J. Neural Syst.* **26**, 1650025 (2016)
14. Çitak-ER, F., Goularas, D., Ormeci, B.: A novel convolutional neural network model based on voxel-based morphometry of imaging data in predicting the prognosis of patients with mild cognitive impairment. *J. Neurol. Sci.* **34**, 52–69 (2017)
15. Farooq, A., Awais, M.: A deep CNN based multi-class classification of Alzheimer’s disease using MRI. In: *2017 IEEE International Conference on Imaging systems and techniques (IST)*, IEEE, China, pp 1–6 (2017)
16. Sarraf, S., Tofighi, G.: Classification of Alzheimer’s disease using fMRI data and deep learning convolutional neural networks. *arXiv preprint*
17. Sarraf, S., Tofighi, G.: Deep learning-based pipeline to recognize Alzheimer’s disease using fMRI data. In: *2016 Future Technologies Conference (FTC)*, pp 816–820, USA (2016)
18. Wu, C., Guo, S., Hong, Y.: Discrimination and conversion prediction of mild cognitive impairment using convolutional neural networks. *Quant. Imaging Med. Surg.* **8**, 992–1003 (2018)
19. Hon, M., Khan, N.: Towards Alzheimer’s disease classification through transfer learning. In: *2017 IEEE International Conference on Bioinformatics and Biomedicine (BIBM)*, pp 1166–1169 (2017)
20. Tzourio-Mazoyer, N., Landeau, B., Crivello, F.: Automated anatomical labeling of activations in SPM using a macroscopic anatomical parcellation of the MNI MRI single-subject brain. *Neuroimage* **15**, 273–289 (2002)
21. Liu, S., Cai, W., Che, H.: Multimodal neuroimaging feature learning for multiclass diagnosis of Alzheimer’s disease. *IEEE Trans. Biomed. Eng.* **62**, 1132–1140 (2014)
22. Li, F., Tran, L., Ji, S.: A robust deep model for improved classification of AD/MCI patients. *IEEE J. Biomed. Health Inf.* **19**, 1610–1616 (2015)
23. Ju, R., Pan Zhuo, C., Li, Q.: Early diagnosis of Alzheimer’s disease based on resting-state brain networks and deep learning. *IEEE/ACM Trans. Comput. Biol. Bioinf.* **16**, 244–257 (2017)
24. Khvostikov, A., Aderghal, K., Benois-Pineau, J.: 3D CNN-based classification using sMRI and MD-DTI images for Alzheimer disease studies, *arXiv preprint*
25. Cui, R., Liu, M.: Hippocampus analysis based on 3D CNN for Alzheimer’s disease diagnosis. In: *Tenth International Conference on Digital Image Processing (ICDIP 2018)*, International Society for Optics and Photonics, pp 108065 (2018)

26. Gupta, A., Anthony, S.M., Ayhan, S.: Natural image bases to represent neuroimaging data. In: International Conference on Machine Learning, pp 987–994, USA (2013)
27. Liu, M., Cheng, D., Wang, K.: Multi-modality cascaded convolutional neural networks for Alzheimer's disease diagnosis. *Neuroinformatics* **16**, 295–308 (2018)
28. Li, F., Liu, M.: Alzheimer's disease diagnosis based on multiple cluster dense convolutional networks. *Comput. Med. Imaging Graph.* **70**, 101–110 (2018)
29. Shakeri, M., Lombaert, H., Shashank, T.: Deep spectral-based shape features for Alzheimer's disease classification. In: International Workshop on Spectral and Shape Analysis in Medical Imaging. LNCS, pp 15–24 (2016)
30. Wolz, R.: Multi-method analysis of MRI images in early diagnostics of Alzheimer's disease. *PloS one* (2013)
31. Bhatkotli, P., Paul, M.: Early diagnosis of Alzheimer's disease: a multi-class deep learning framework with modified k-sparse auto encoder classification. In: 2016 International Conference on Image and Vision Computing New Zealand (IVCNZ). IEEE, New Zealand, pp 1–5 (2016)
32. Livni, R., Shalev-Shwartz, S., Shamir, O.: An algorithm for training polynomial networks, arXiv preprint
33. Zheng, X., Shi, J., Li, Y., Liu, X.: Multi-modality stacked deep polynomial network based feature learning for Alzheimer's disease diagnosis. In: 2016 IEEE 13th International Symposium on Biomedical Imaging (ISBI), IEEE, Czech Republic, pp 851–854 (2016)
34. Razzak, M., Naz, S., Zaid, A.: Deep learning for medical image processing: overview, challenges and the future. *Classif. BioApps* **26**, 323–350 (2017)
35. Danni, C., Manhua, L.: CNNs based multi-modality classification for AD diagnosis. In: 2017 10th international congress on image and signal processing, biomedical engineering and informatics (CISP-BMED), IEEE, pp 1–5 (2017)
36. Luo, S., Li, X., Li, J.: Automatic Alzheimer's disease recognition from MRI data using deep learning method. *J. Appl. Math. Phys.* **5**, 1892–1898 (2017)
37. Suk, H.I., Lee, S.W., Shen, D.: Deep ensemble learning of sparse regression models for brain disease diagnosis. *Med. Image Anal.* **37**, 101–113 (2017)
38. Islam, J., Zhang, Y.: Brain MRI analysis for Alzheimer's disease diagnosis using an ensemble system of deep convolutional neural networks. *Brain Inf.* **5**, 2 (2018)
39. Liu, M., Li, F.: Alzheimer's disease classification based on combination of multi-model convolutional networks. In: 2017 IEEE International Conference on Imaging Systems and Techniques (IST), IEEE, China, pp 1–5 (2017)
40. Payan, A., Montana, G.: Predicting Alzheimer's disease: a neuroimaging study with 3D convolutional neural networks, arXiv preprint
41. Cheng, D., Liu, M., Fu, J., Wang, Y.: Classification of MR brain images by combination of multi-CNNs for AD diagnosis. In: Ninth International Conference on Digital Image Processing (ICDIP 2017), International Society for Optics and Photonics, p 1042042 (2017)
42. Karasawa, H., Liu, C., Ohwada, H.: Deep 3d convolutional neural network architectures for Alzheimer's disease diagnosis. In: Asian Conference on Intelligent Information and Database System, LNCS, pp 287–296. Springer (2018)
43. Liu, S., Cheng, D., Wang, K.: Multimodal neuroimaging feature learning for multiclass diagnosis of Alzheimer's disease. *IEEE Trans. Biomed. Eng.* **62**, 1132–1140 (2014)
44. Cui, R., Liu, M., Li, G.: Longitudinal analysis for Alzheimer's disease diagnosis using RNN. In: 2018 IEEE 15th International Symposium on Biomedical Imaging (ISBI 2018), IEEE, USA, pp 1398–1401 (2018)
45. Suk, H.I., Lee, S.W., Shen, D.: Deep sparse multi-task learning for feature selection in Alzheimer's disease diagnosis. *Brain Struct. Funct.* **221**, 2569–2587 (2016)
46. Lu, D., Kartek, P., Ding, G.W.: Multiscale deep neural network based analysis of FDG-PET images for the early diagnosis of Alzheimer's disease. *Med. Image Anal.* **46**, 26–34 (2018)
47. Li, F., Tran, L., Thung, K.H.: A robust deep model for improved classification of AD/MCI patients. *IEEE J. Biomed. Health Inform.* **19**, 1610–1616 (2015)

48. Faturrahman, M., Hanifah, N., Wasito, I.: Structural MRI classification for Alzheimer's disease detection using deep belief network. In: 2017 11th International Conference on Information and Communication Technology and System (ICTS), IEEE, Indonesia, pp 37–42 (2017)
49. Suk, H.I., Lee, W., Shen, D.: Hierarchical feature representation and multimodal fusion with deep learning for AD/MCI diagnosis. *Neuroimage* **101**, 569–582 (2014)
50. Shi, J., Zheng, X., Li, Y.: Multimodal neuroimaging feature learning with multimodal stacked deep polynomial networks for diagnosis of Alzheimer's disease. *IEEE J. Biomed. Health Inform.* **22**, 173–183 (2017)
51. Wang, S.H., Phillips, P., Sui, Y.: Classification of Alzheimer's disease based on eight-layer convolutional neural network with leaky rectified linear unit and max pooling. *J. Med. Syst.* **42**, 85 (2018)
52. Liu, M., Zhang, J., Adeli, E., Shen, D.: Landmark-based deep multi-instance learning for brain disease diagnosis. *Med. Image Anal.* **43**, 157–168 (2018)
53. Choi, H., Jin, K.H., Kyong, C.: Predicting cognitive decline with deep learning of brain metabolism and amyloid imaging. *Behav. Brain Res.* **344**, 103–109 (2018)
54. Hosseini-Asl, E., Keynton, R., El-Baz, A.: Alzheimer's disease diagnostics by adaptation of 3D convolutional network. In: 2016 IEEE International Conference on Image Processing (ICIP), IEEE, pp 126–130 (2016)
55. Korolev, S., Safiullin, A., Belyaev, M., Dodonova, Y.: Residual and plain convolutional neural networks for 3D brain MRI classification. In: 2017 IEEE 14th International Symposium on Biomedical Imaging (ISBI 2017), IEEE, Australia, pp 835–838 (2017)
56. Lu, D., Karteek, P., Ding, G.W.: Multimodal and multiscale deep neural networks for the early diagnosis of Alzheimer's disease using structural MR and FDG-PET images. *Sci. Rep.* **8**, 1–13 (2018)
57. Sarraf, S., DeSouza, D., Anderson, J., Tofighi, G.: DeepAD: Alzheimer's disease classification via deep convolutional neural networks using MRI and fMRI, *BioRxiv*

Chapter 49

UPQC with AI Techniques for Power Quality Improvement



M. Sharanya, Basavaraja Banakara, and M. Sasikala

Abstract Unified power quality conditioner (UPQC) is a custom power device (CPD) which can be used for voltage quality (VQ) and current quality (CQ) improvement. In this paper, the working of UPQC is given with AI techniques like “fuzzy logic controller” (FLC), “artificial neural networks” (ANN), and “adaptive neuro-fuzzy-inference system” (ANFIS). MATLAB software is used for simulation, and Simulink results are verified. Total harmonic distortion (THD) of source current and load voltage of system are calculated with each of these three methods, and the results are compared.

49.1 Introduction

Electrical system has serious problem of increasing number of electronic components that are used by industry and domestic consumers. The harmonic-related problems are increasing in utility load interface due to the use of nonlinear loads such as power converters in industry and domestic applications. These loads are generators of current harmonics and tend to distort supply current. Apart from this, supply volt is distorted. Attempts are made to isolate volt-sensitive loads from a supply system experiencing unwanted disturbance. Even though utility voltage is not distorted initially, it is nonlinear load current which is responsible for harmonic voltage drop across impedance of utility, thereby introducing harmonic distortion in voltage. Therefore, the voltage is distorted at the utility end. The supply system treats converter fed load as nonlinear, and load current exhibits a non-sinusoidal shape with different harmonics. Therefore, devices which reduce this drawback

M. Sharanya (✉)

Malla Reddy College of Engineering and Technology (MRCET), UGC Autonomous, Maisammaguda, Secunderabad, Telangana, India

B. Banakara

Davangere University, Davangere, Karnataka, India

M. Sasikala

GECW, Sharnbasava University, Kalaburigi, Karnataka, India

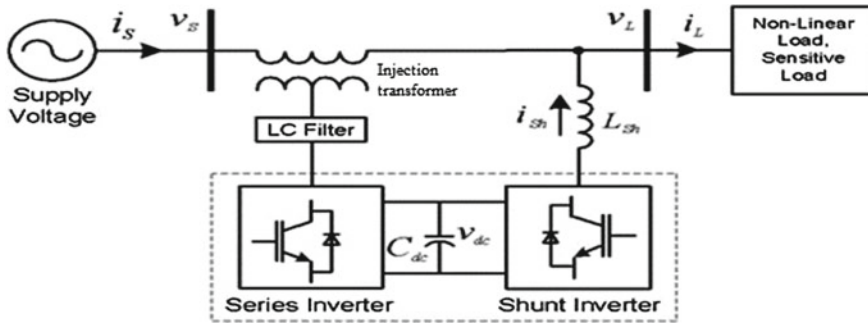


Fig. 49.1 Basic circuit of UPQC

have been developed, and one among them is the unified power quality conditioner (UPQC). UPQC consists shunt active power filter (APF) and series APF. VSI with IGBT-based and with back-back DC link is UPQC as shown in Fig. 49.1 [1, 2]. VSI connected in shunt injects compensating current, i_{sh} . Supply side inverter connected in series with load acts as voltage source feeding compensating voltage, V_{sc} through an insertion transformer [3].

49.1.1 UPQC Series Control

Series inverter operates in current control mode by introducing voltage of source between load and supply. Voltage disturbances like swell and sag are compensated. To obtain the 3ph ref volt, 3ph load volt are subtracted from 3ph supply volt. These volts are injected at PCC [4]. PWM current controller is fed with ref currents. Volt is given to load by volt injection in series with source volt. So, reliability of supply volt at load is increased by series VSI [5].

Injected voltage is:

$$\overline{V_{inj}} = V_s - V_l \tag{49.1}$$

Injected voltage magnitude is

$$\overline{V_{inj}} = |\overline{V_{inj}}| = V_{inj} \tag{49.2}$$

Injected voltage phase is

$$\delta_{inj} = \tan(\text{Re}[V_{pq}]/\text{Im}[V_{pq}]) \tag{49.3}$$

3ph ref values of injected volt

$$\begin{aligned}
 V_{la}^* &= \sqrt{2}V_{inj} \sin(\omega t + \delta_{inj}) \\
 V_{lb}^* &= \sqrt{2}V_{inj} \sin\left(\omega t + \frac{2\Pi}{3} + \delta_{inj}\right) \\
 V_{lc}^* &= \sqrt{2}V_{inj} \sin\left(\omega t + \frac{2\Pi}{3} + \delta_{inj}\right)
 \end{aligned} \tag{49.4}$$

3ph ref currents of series inv

$$\begin{aligned}
 i_{sea}^* &= V_{la}^*/Z_{se} \\
 i_{seb}^* &= V_{lb}^*/Z_{se} \\
 i_{sec}^* &= V_{lc}^*/Z_{se}
 \end{aligned} \tag{49.5}$$

49.1.2 UPQC Shunt Control

$$v_{sm} = \left[\frac{2}{3} (v_{sa}^2 + v_{sb}^2 + v_{sc}^2) \right]^{1/2} \tag{49.6}$$

3ph per unit current vectors are given as:

$$u_{sa} = \frac{v_{sa}}{v_{sm}}; \quad u_{sb} = \frac{v_{sb}}{v_{sm}}; \quad u_{sc} = \frac{v_{sc}}{v_{sm}}; \tag{49.7}$$

Ref supply current is obtained by multiplying supply current (i_{sp}) with 3ph per unit current vectors (u_{sa}, u_{sb}, u_{sc}).

$$i_{sa}^* = i_{sp}u_{sa}; \quad i_{sb}^* = i_{sp}u_{sb}; \quad i_{sc}^* = i_{sp}u_{sc}; \tag{49.8}$$

$$i_{sha}^* = i_{sa}^* - i_{la}; \quad i_{shb}^* = i_{sb}^* - i_{lb}; \quad i_{shc}^* = i_{sc}^* - i_{lc}; \tag{49.9}$$

Actual currents and ref currents i_{ref} of shunt VSI are compared.

49.2 Controllers

49.2.1 Fuzzy Logic Controller

This is algorithm of processing fuzzy logic or fuzzy interference. Fuzzy control of adaptive or nonlinear control gives better performance for linear or nonlinear plant with varying parameters [6]. To implement this strategy, 49 rules are selected. Steps involved are:

1. 7 fuzzy sets are used for each of 2 inputs.
2. 7 fuzzy sets are also used for output.
3. Membership functions (MF) triangular is considered.
4. Fuzzification is done with “continuous universe of discourse.”
5. Implication is carried out using “min” operator.
6. Interference mechanism is carried by fuzzy implications.
7. “Centroid method” is used for defuzzification [7].

49.2.2 ANN Controller

Architecture of ANN consists of three layers, namely input, hidden, and output layers. ANN has to be trained to perform a function and is done using “Levenberg Marquardt back propagation (LMBP) algorithm.” Harmonics extracted and signal from feedback are the two inputs of ANN. These are then compared. By comparing ref signal from ANN to triangular wave, gating signals are produced for the VSI.

49.2.3 ANFIS Controller

In ANFIS, FLC and ANN are hybridized to get prior knowledge, good interpretation, and learning capabilities. ANN does the decision logic by fuzzy membership values. Least square estimation and back propagation algorithm tune ANFIS. Good PQ control is possible with this technique due to its robustness to parameter variation [8]. Improvement of PQ is done with this algorithm by controlling various parameters. TS-FLC model is the architecture of ANFIS model which has five interconnected layers.

Table 49.1 UPQC test parameters

Parameters	Value
Supply voltage	380 V
DC link capacitor	2000 μ F
DC link voltage	600 V
Filter inductor	50 mH
Filter resistance	1 Ω

49.3 Simulation Results

To validate the proposed controllers, UPQC simulations are run with various case studies using MATLAB-Simulink. Parameters of UPQC are given in Table 49.1. During all simulations, power from the source is unvarying. The simulation results are grouped as waveforms of the concerned parameters and then its corresponding THD value.

49.3.1 With Fuzzy Logic Controller

UPQC is considered with FLC. UPQC consists of series APF and shunt APF. During 0.15–0.25 s interval, 1-phase fault is created due to which sag is observed. THD of this source voltage with sag is 18.15%. Voltage is injected during the interval 0.15–0.25 s which leads to the mitigation of sag. THD of load voltage after sag mitigation with FLC is reduced to 4.47%.

The current at nonlinear loads is distorted and not sinusoidal. THD of load current is 28.47%. With shunt APF, harmonics in load current is mitigated, and hence, current drawn from source is sinusoidal. As harmonics is mitigated with FLC, THD of source current is reduced to 4.21%.

49.3.2 With ANN Controller

To improve the PQ and avoid the drawbacks of FLC, UPQC is controlled with ANN. The THD values of source voltage and load voltages of series APF are verified with ANN. Also, the THD of load and source current of shunt APF is verified. Source voltage and load voltage THD of series APF are 15.13% and 3.44%, respectively. Load current and source current THD of shunt APF are 26.58% and 3.8%, respectively. ANN training is difficult.

49.3.3 With ANFIS Controller

Hence, ANFIS controller is used for UPQC. The voltage compensation is done with series APF. Series APF working is considered with ANFIS controller. The source voltage consists of distortions due to nonlinear loads and faults. Sag is created from 0.1 s to 0.2 s, and swell is created between 0.2 s and 0.3 s. Due to the presence of harmonics and distortions, THD of source voltage is 22% as shown in Fig. 49.2. The series APF injects voltage to compensate for voltage sag and swell. THD of load voltage after compensation with ANFIS is reduced to 1.24% as shown in Fig. 49.3.

The shunt APF simulation is carried out with ANFIS controller. Due to nonlinear load, harmonics is present in the load current, and current drawn is distorted and not sinusoidal in nature. About 29.49% THD of load current is given in Fig. 49.4. Shunt APF with ANFIS controller can effectively mitigate the current harmonics. As the harmonics in the current waveforms is mitigated, THD is reduced to 3.06% as shown in Fig. 49.5. Load volt and source current THD with UPQC and with different controllers is compared in Table 49.2. UPQC gives better voltage profile and current profile with reduced THD values with ANFIS controller.

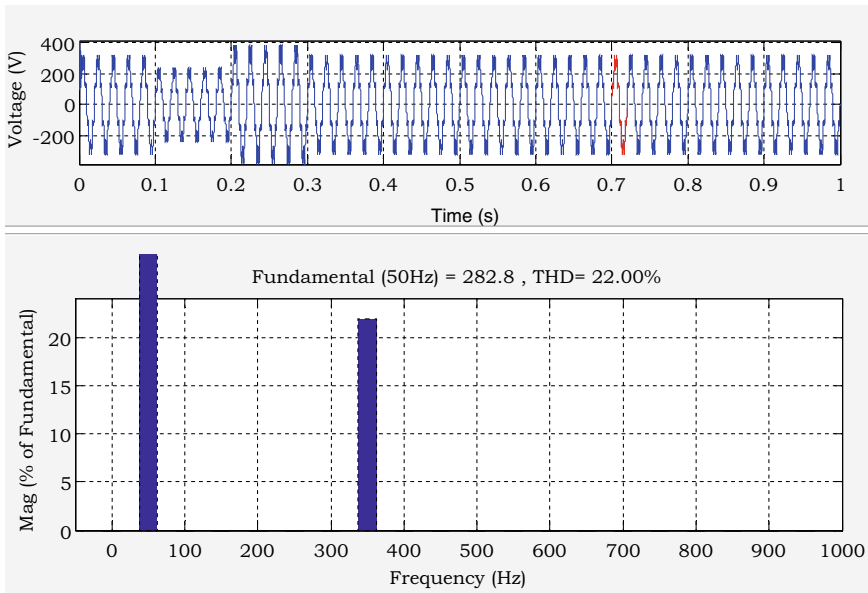


Fig. 49.2 Source voltage THD without ANFIS

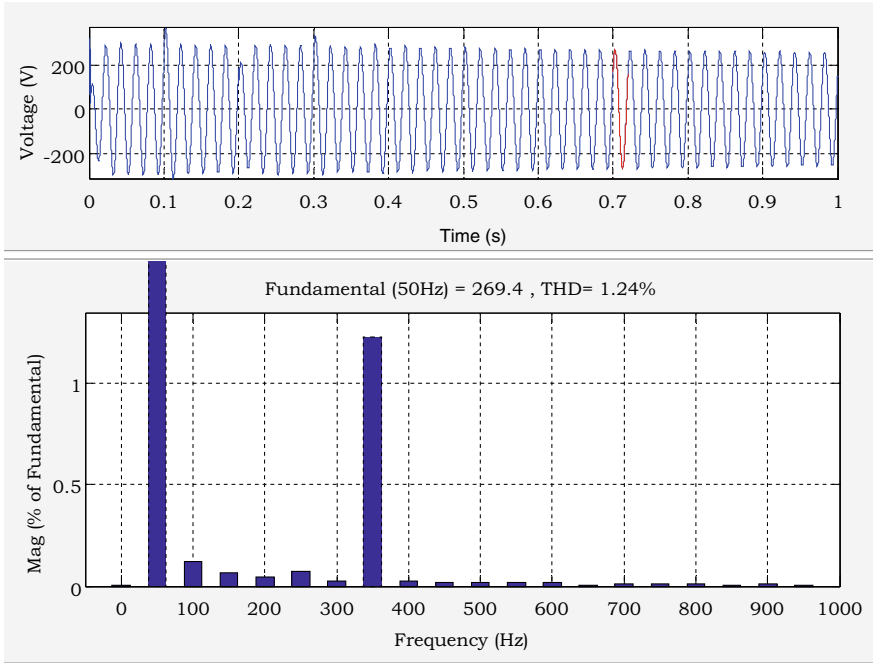


Fig. 49.3 Load voltage THD with ANFIS

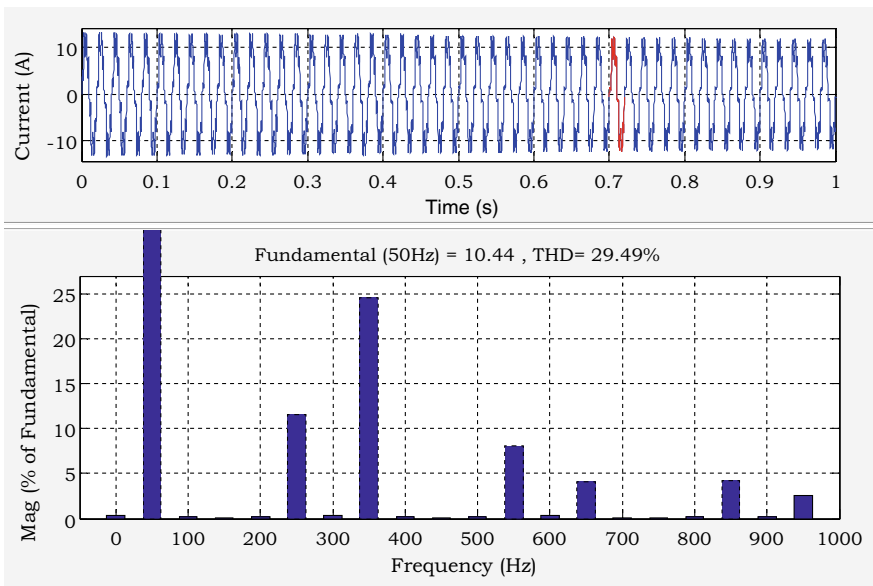


Fig. 49.4 Load current THD without ANFIS

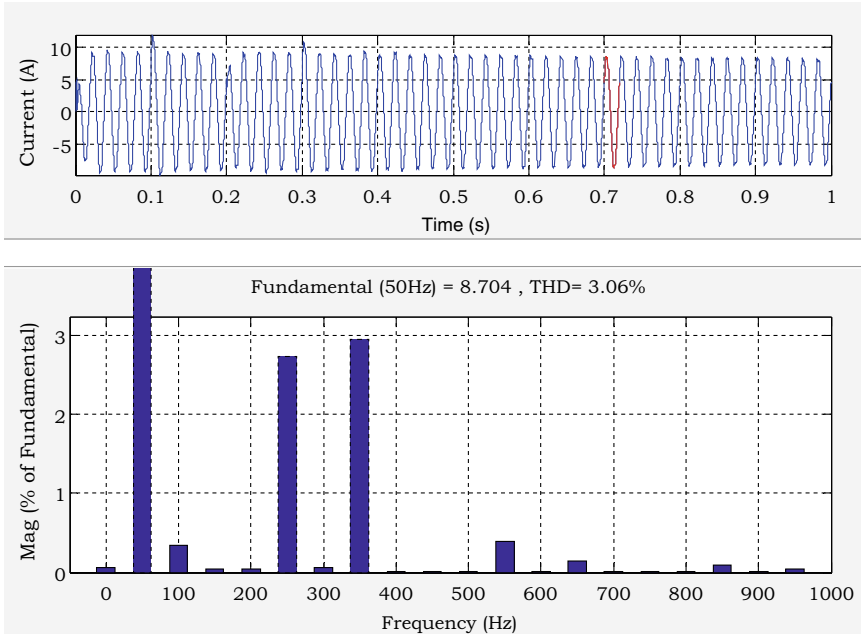


Fig. 49.5 Source current THD with ANFIS

Table 49.2 Comparison of THD values of voltage and current with UPQC with different controllers

Heading	Load voltage measured in % THD	Source current measured in % THD
Fuzzy logic controller	4.47%	4.21%
ANN controller	3.44%	3.80%
ANFIS	1.24%	3.06%

49.4 Conclusion

UPQC consists of shunt and series APF connected back-back with DC link capacitor. “Fuzzy logic controller,” ANN, and ANFIS controller are used with UPQC. THD of source and load voltage of series APF and source and load current of shunt APF is calculated with these controllers. ANFIS gives better results compared to other controllers with source current THD reduced to 3.06% and load volt THD to 1.24%. Hence, UPQC is able to improve voltage quality and current quality.

References

1. Akagi, H.: New trends in active filters for power conditioning. *IEEE Trans. Ind. Appl.* **32**(6), 1312–1321 (1996)
2. Fujita, H., Akagi, H.: The unified power quality conditioner: the integration of series and shunt active filters. *IEEE Trans. Power Electron.* **13**(2), 315–322 (1998)
3. Ghosh, A., Ledwich, G.: Unified power quality conditioner. In: *Power Quality Enhancement Using Custom Power Devices*. The Springer International Series in Engineering and Computer Science (Power Electronics and Power Systems). Springer, Boston, MA (2002). https://doi.org/10.1007/978-1-4615-1153-3_10
4. Singh, B.N., Chandra, H., Al-Haddad, K., Singh, B.: Fuzzy control algorithm for universal active filter. In: *IEEE International Conference on Power Quality, India*, pp 73–80 (1998)
5. Jayalakshmi, D., Sankar, S., Venkateshkumar, M.: An analysis of load management system by using unified power quality conditioner for distribution network. In: Rathore, V., Worring, M., Mishra, D., Joshi, A., Maheshwari, S. (eds.) *Emerging Trends in Expert Applications and Security*. *Advances in Intelligent Systems and Computing*, vol. 841. Springer, Singapore (2019). https://doi.org/10.1007/978-981-13-2285-3_32
6. Dhurvey, S.N. Chandrakar, V.K.: Improvement of power system performance using fuzzy logic based interline power flow controller [IPFC]. *J. Power Energy Eng.* **4**, 67–77 (2016)
7. Rama Rao, R.V.D., Dr. Dash, S.S.: Enhancement of power quality by using unified power quality conditioner with PID and fuzzy logic controller. *Int. J. Comput. Appl.* **5**(7), 21–27 (2010)
8. Roshan, S, Dr. Kusagra, A.: Improvement of power quality using a hybrid UPQC with ANFIS controller. *Int. J. Sci. Res. (IJSR)* **7**(5), 1448–1453 (2018)
9. Vinnakoti, S., Kota, VR.: Implementation of artificial neural network based controller for a five-level converter based UPQC. *Elsevier, Alexandria Eng. J.* **57**, 1475–1488 (2017)

Chapter 50

Field Investigation of Fundamental Frequency of Structures Using Frequency Domain Vibration Analysis



Saugato Dey, Saikat Kr Shome, and Kalyan Kr Mistry

Abstract The transient nature of forces produced in the system requires vibration analysis to determine their behavior patterns accurately. Modal analysis represents the dynamic response of the bridge structure via modal descriptive terms: natural frequencies, mode shapes, and damping ratios. Accurate measurement of these dynamic characteristics for structures allows for better evaluation of structural stability and structural health monitoring of such systems. It is time-saving as well as useful to use force vibration analysis to approximate modal parameters. Natural frequencies are derived from the observations of force vibration analysis techniques. Modified power spectral analysis and cross-power spectral analysis are carried out to identify the structure's resonant frequency. From the experimental analysis, the range of resonant frequencies observed is 0.9766–4.8828 Hz in longitudinal direction, 1.9531–4.8828 Hz in transverse direction, and 2.9297–4.8828 Hz in vertical direction. Accurate modal parameters estimation of the structures allows better evaluations of structural stability and structural health monitoring.

50.1 Introduction

Structures like barriers, constructions, dams, highways, airplanes, and vehicles are complex engineered systems that assure the nation's economic and technological development. Unfortunately, these structures are subject to extreme loading situations and severe environmental factors such as constant traffic flows, varying wind forces, thunderstorm strikes, and temperature effects, which are not anticipated during design that will result in long-term structural deterioration causing severe harm to the structure's safety operation which results in catastrophic accidents and fatalistic casualties [1–3]. Observing vast-span tunnels and bridges in actual envi-

S. Dey · S. K. Shome (✉) · K. K. Mistry
CSIR-Central Mechanical Engineering Research Institute, Durgapur 713209, India
e-mail: saikatshome@cmeri.res.in

K. K. Mistry
e-mail: kalyan@cmeri.res.in

ronments, detecting the system's defect level in real-time, forecasting the system's performance level, and trying to take the efficient solution to make a diagnosis of the structures have become the primary challenges that should be addressed immediately in large-scale projects. In various structures, including aircraft, ships, and civilian structures, structural monitoring systems can be found. SHM can appropriately analyze the stress situation and damage evolution law of bridge and tunnel system throughout the construction and maintenance [4]. Methods of damage detection are used to recognize structural distress. A significant number of damage detection methods have been implemented and developed during the past decade [5]. Methods of damage detection can usually be defined in two types: local-based and global-based damage detection methods. Local-based methods of identification of damage aim to determine damage based on structure scanning. In contrast, global detection of damage applies the computational methods of the structure's global vibration characteristics (e.g., mode shapes, natural frequencies) to recognize the damage [6]. Experimental modal analysis is implemented from the measurement response to determine the dynamic characteristics of vibrating systems. This analytical approach has been carried out globally. Until today, numerous studies and analytical approaches have been developed for SHM mechanisms in various civil structures [7, 8]. To support the dynamic structures' response monitoring, a range of modern sensors and methods was established [9–13]. Real-time vibration-based SHM have been carried out using frequency domain analysis technique to identify the track and monitor the status of the bridge. Testing and statistical treatment analysis suggest the effectiveness of frequency domain analysis in real-time application [14]. The transient existence of seismic forces caused in civil structures needs dynamic modeling to analyze their responses. The modal analysis defines a structure's dynamic response form of modal descriptors: natural frequencies, mode shapes, and damping ratios. For accurate and efficient structural evaluations for bridges, it is essential to formulate specific modal parameters effectively.

This paper deals with different spectral analysis techniques on the field measurement linear acceleration data to identify the model parameters. Modal parameter estimation in frequency domain techniques such as Fourier spectrum analysis, power spectral analysis, and cross-power spectral analysis is carried out to identify the structure's resonant frequency. The experimental results of different estimation techniques are compared to determine the resonant frequency of the structure accurately.

50.2 Vibration Analysis

The implementation of vibration-based monitoring (VBM) systems is a promising way of determining fragile structures' safety. SHM has proven to be especially suitable for the process whose structural behaviors are severely influenced by their geometric complexity or the homogeneity of their constituent components. SHM

has proven to be especially suitable for the process whose structural behaviors are severely influenced by their geometric complexity or their constituent components' homogeneity. Thus, the modal behavior analysis can reveal structural weaknesses or deficiencies amplified or induced by unforeseen events.

50.2.1 Modal Parameter Estimation in Frequency Domain

The vibrating system's dynamic characteristics include its natural frequencies, mode shapes, and damping constant. Each structure vibrates as per its vibration modes.

Power Spectral Density analysis: When the dynamic response function $x(t)$ is taken as a random vibration, the statistical expectation or average value of the product $x(t) \cdot x(t + \tau)$ yields the auto-correlation function $R_{xx}(\tau)$.

If the transient response function $x(t)$ is considered as a spontaneous vibration, the product's statistical assumption or average value $x(t) \cdot x(t + \tau)$ yields the auto-correlation function $R_{xx}(\tau)$,

$$R_{XX} = E[x(t) \cdot x(t + \tau)] \tag{50.1}$$

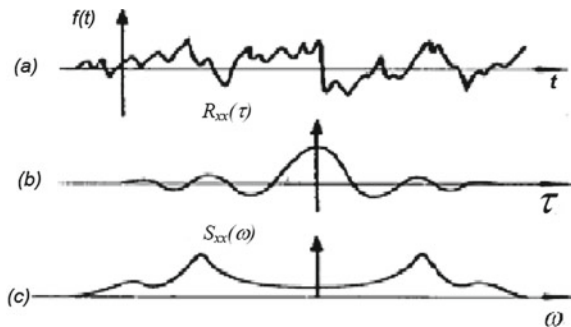
Since this function obeys the Dirichlet condition, a frequency description of the original signal $f(t)$ is estimated from the Fourier transformation of $R_{xx}(\tau)$ as the power spectral density (PSD) or auto-spectral density (ASD) $S_{xx}(\omega)$.

As this function with the Dirichlet condition, a frequency representation of the original signal $f(t)$ is calculated as the power spectral density (PSD) or auto-spectral density (ASD) $S_{xx}(\omega)$, from the Fourier transform of $R_{xx}(\tau)$,

$$S_{xx}(\omega) = \frac{1}{2\pi} \int_{-\infty}^{\infty} R_{xx}(\tau) e^{-j\omega\tau} d\tau \tag{50.2}$$

Figure 50.1 illustrates the time history, auto-correlation function, and PSD of a random signal [11].

Fig. 50.1 a Signal $x(t)$;
b Auto-correlation function $R_{xx}(\tau)$; c PSD $S_{xx}(\omega)$



Cross-power spectral density analysis: When applied to a pair of simultaneous functions $y(t)$ and $x(t)$, cross-correlation $R_{xy}(\tau)$ and cross-spectral density (CSD) $S_{xy}(\omega)$ functions will be generated. The cross-correlation function is defined as: If extended to the set of simultaneous functions $y(t)$ and $x(t)$, functions can produce cross-correlation $R_{xy}(\tau)$ and cross-spectral density (CSD) $S_{xy}(\omega)$ function. The feature cross-correlation is represented as,

$$R_{xy} = E[x(t) \cdot y(t + \tau)] \tag{50.3}$$

And, the CSD is defined by its FT as,

$$S_{xy}(\omega) = \frac{1}{2\pi} \int_{-\infty}^{\infty} R_{xy}(\tau) e^{-j\omega\tau} d\tau \tag{50.4}$$

Welch PSD/CSD analysis: Welch’s PSD/CSD analysis strategy appeared in the 1960s [13] splits time history into the overlapping segments, calculates the power spectrum for each segment, and produces an average power spectrum. The principal of the Welch PSD/CSD analysis concept had proved effective by increasing the S/N ratio of power spectra despite the decrease of frequency resolution.

50.3 Schematic Diagram of Vibration Analysis

The schematic block diagram is shown in Fig. 50.2 has strategies of vibration analysis. Initially, the bridge structure is perturbed with an excitation signal. The bridge acceleration signal is measured with a linear accelerometer attached to the surface of the structure. The noise from the sensor data is eliminated by using a noise removal moving average median filter.

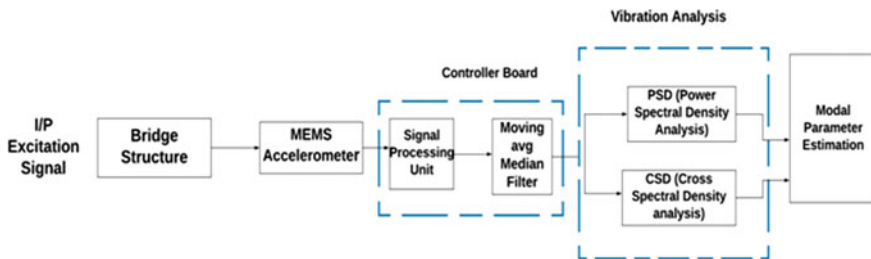


Fig. 50.2 Schematic block diagram of proposed vibration analysis for bridge prototype

50.4 Analysis on Experimental Results

Experimental modal analysis (EMA) is performed with the force vibration analysis techniques. The MATLAB platform is used to process the data files and execute spectral analyses. Figure 50.3 shows the experimental setup. The bridge structure is perturbed with the help of the exciter. Excitation of the structure is provided by chirp signal of 5 amplitude and 0.5-15 Hz frequency (sample time 0.001 s). The structure's response is a linear combination of inputs due to system linearity corresponding to linear acceleration data taken from MEMS accelerometer placed on the top of the structure. Two analysis methods were used and compared: (1) Welch's PSD spectral approach; (2) Welch's CSD spectral approach.

Experimental Setup:



Fig. 50.3 Experimental setup

50.4.1 Frequency Domain Analysis

The force vibration tests were carried out with experimental modal analysis (EMA).

Welch's PSD method

Firstly, with a 50% variation between overlapping samples, the time duration is divided into eight parts of a similar duration. To attenuate the noise in the overlapping portions, a Hamming window is added to each section. Windowing eliminates spectral leakage from the analyzes that occur when the sections are expected to be periodic. FFT is applied to each section, and the corresponding periodograms have been generated. Finally, the average of the periodograms is calculated from all sections. This periodogram defines the power spectral densities in terms of power/frequency.

Welch’s CSD Method

Welch’s modifications calculate the cross-spectral intensity estimation of simultaneous readings. Every record was initially split into eight equal segments, with a 50% overlap between neighboring segments. A Hanning window is added to each segment. In order to obtain the approximate cross-spectral density range in terms of power per density, an average periodogram was built after applying an FFT to each section and determining the respective periodograms. Resonant frequencies are measured from the spectra directly.

The full set of response spectra is scrutinized within the range of 0.5 Hz up to 15 Hz to identify the bridge’s fundamental frequency. Resonant frequencies are identifiable in all orthogonal directions. The directional components for each measurement are aligned with the principal axes of the bridge. The X-component is aligned with the bridge’s longitudinal axis, the Y-component with the bridge’s transverse axis, and the Z-component is aligned with the vertical axis of the bridge.

The Welch’s PSD (abbreviated by PSD) method produced three resonant frequencies in the output spectra (Fig. 50.4) and Table 50.1. Similar to the Fourier method results, these values occur solely in one of the orthogonal directions. In the longitudinal axis, resonance peaks are observed in the range between 2.9297 and 4.8828 Hz. In the transverse axis, resonance peaks are observed in 2.9297–4.8828 Hz. The vertical axis of the bridge resonance peaks is observed in the range between 3.9063 and 4.88 Hz.

The Welch’s CSD (abbreviated by CSD) method produced three resonant frequencies (Fig. 50.5) and Table 50.2. In the longitudinal axis, resonance peaks are observed in the range between 0.9766 and 2.92 Hz. The transverse axis resonance

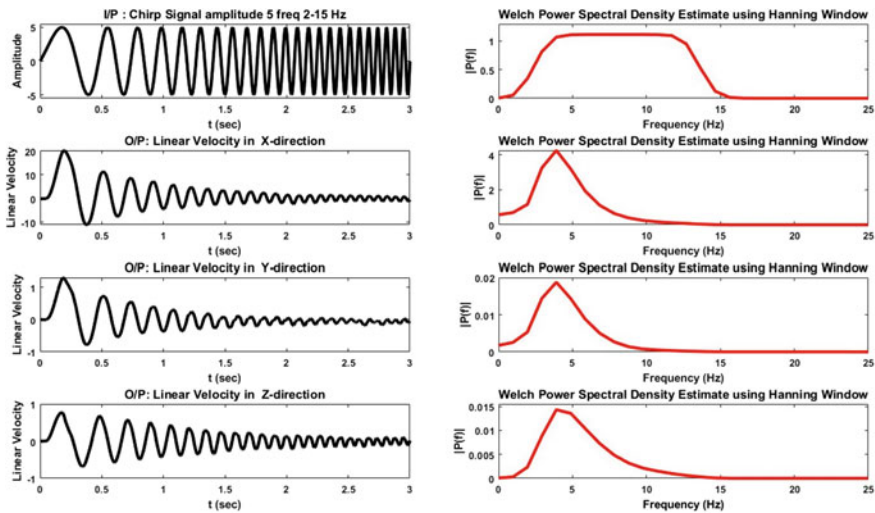


Fig. 50.4 Frequency response spectra using Welch’s PSD method

Table 50.1 Resonance peak and corresponding frequencies using Welch’s PSD method

Signal	Longitudinal axis	Transverse axis	Vertical axis
Peak of first mode of vibration	5.4487	0.0238	0.0157
Freq. of first mode of vibration	2.9297	2.9297	3.9063
Peak of second mode of vibration	4.9656	0.0214	0.0133
Freq. of second mode of vibration	3.9063	3.9063	2.9297
Peak of third mode of Vibration	2.9632	0.0133	0.0127
Freq. of third mode of vibration	4.8828	4.8828	4.8828

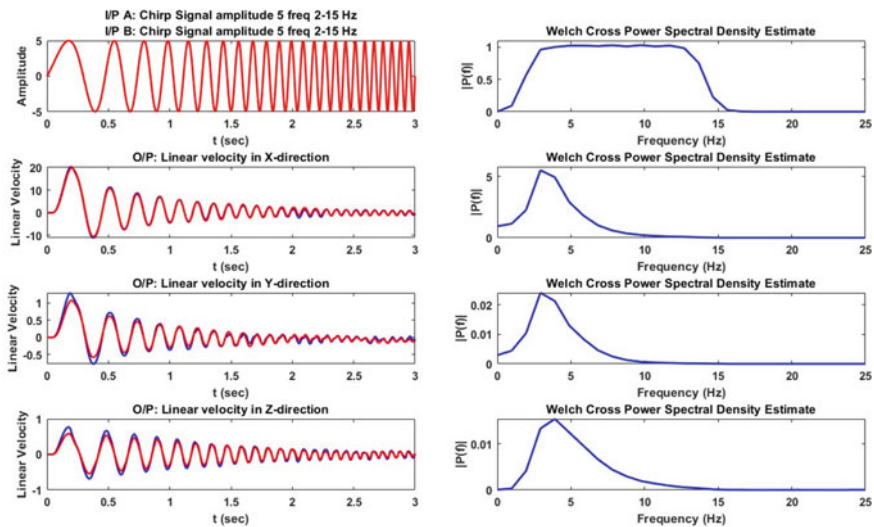


Fig. 50.5 Frequency response spectra using Welch’s CSD method

Table 50.2 Resonance peak and corresponding frequencies using Welch’s CSD method

Signal	Longitudinal axis	Transverse axis	Vertical axis
Peak of first mode of vibration	6.0638	0.0323	0.0026
Freq. of first mode of vibration	2.9297	2.9297	2.9297
Peak of second mode of vibration	4.8566	0.0262	0.0018
Freq. of second mode of vibration	1.9531	1.9531	4.8828
Peak of third mode of vibration	2.8056	0.0130	0.0016
Freq. of third mode of vibration	0.9766	3.9063	3.9063

peaks are observed in 1.9531–3.9063 Hz, and the vertical axis of the bridge resonance peaks is observed in the range between 2.92 and 4.88 Hz.

Table 50.3 displays the comparative assignment of response spectra for two different frequency response techniques. From this comparative assignment, the

Table 50.3 Comparative assignment between PSD and CSD analysis techniques

Signal	Frequency domain techniques	Frequency of first mode of vibration	Frequency of second mode of vibration	Frequency of third mode of vibration	Range of resonance frequency (Hz)
X-axis	PSD	2.9297	3.9063	4.8828	0.9766– 4.8828
	CSD	2.9297	1.9531	0.9766	
Y-axis	PSD	2.9297	3.9063	4.8828	1.9531– 4.8828
	CSD	2.9297	1.9531	3.9063	
Z-axis	PSD	3.9063	2.9297	4.8828	2.9297– 4.8828
	CSD	2.9297	4.8828	3.9063	

range of resonant frequency in the longitudinal axis is 0.9766–4.8828 Hz. In the transverse axis, the range of resonance peaks is observed in the range 1.9531–4.8828 Hz, and in the vertical axis of the bridge, resonance peaks are observed in the range between 2.9297 and 4.8828 Hz. In all three direction for both the techniques, resonant peak is observed at 2.9297 Hz.

50.5 Conclusion

In this paper, different model parameter estimation techniques have been discussed and implemented to identify the structure's resonant frequency. The system perturbed with chirp signal of the 0.5–15 Hz frequency. Two modal parameter estimation techniques are implemented to identify the dynamical properties of the frequency response function. Natural frequency is estimated from the peak amplitude in the longitudinal, transverse, and vertical direction. We can effectively identify the system's modal parameters from the frequency estimation techniques and the repeatability of occurrence of resonance peaks in all three directions. The accurate modal parameters estimation of the structures allows better evaluations of structural stability and structural health monitoring of such systems.

Acknowledgements The authors thank the Director, CSIR-Central Mechanical Engineering Research Institute (CMERI), Durgapur, for providing necessary infrastructure and support. Authors thank to the Department of Science and Technology (DST), New Delhi, for funding the research grant in the field of structural health monitoring project.

References

1. Chan, M., Poon, W.K., Leung, Y.W., Sai ho Chan, D., Premaud, V., Rialland, Y.: Challenges in Hong Kong–Zhuhai–Macao Bridge (Hzmb) Hong Kong Link Road Project. In: IABSE Symposium Report; International Association for Bridge and Structural Engineering: Zurich, Switzerland, pp 797–804 (2016)
2. Chen, Z.-S., Zhang, C., Wang, X., Ma, C.-M.: Wind tunnel measurements for flutter of a long-after body bridge deck. *Sensors* **17**, 335 (2017)
3. Sharma, R.C., Tateishi, R., Hara, K., Nguyen, H.T., Gharechelou, S., Nguyen, L.V.: Earthquake damage visualization (EDV) technique for the rapid detection of earthquake induced damages using SAR data. *Sensors* **17**(2), 235 (2017)
4. Wardhana, K., Hadipriono, F.C.: Analysis of recent bridge failures in the United States. *J. Perform. Constructed Facil.* **17**(3) (2003)
5. Chen, Z., Zhou, X., Wang, X., Dong, L., Qian, Y.: Deployment of a smart structural health monitoring system for long-span arch bridges: a review and a case study. *Sensors* **17**(9), 2151 (2017)
6. Yi, T.-H., Li, H.-N., Gu, M.: Recent research and applications of GPS-based monitoring technology for high-rise structures. *Struct. Control. Health Monit.* **20**(5), 649–670 (2013)
7. Wang, H., Li, A.Q., Hu, R.M.: Comparison of ambient vibration response of the Runyang suspension bridge under skew winds with time-domain numerical predictions. *J. Bridg. Eng.* **16**(4), 513–526 (2011)
8. Yi, T.-H., Li, H.-N., Gu, M.: Experimental assessment of high-rate GPS receivers for deformation monitoring of bridge. *Measurement* **46**(1), 420–432 (2013)
9. Wang, H., Li, A., Hu, R., Li, J.: Accurate stress analysis on steel box girder of long span suspension bridges based on multi-scale sub modeling method. *Adv. Struct. Eng.* **13**(4), 727–740 (2010)
10. Zhou, Y., Sun, L.: Effects of high winds on a long-span sea crossing bridge based on structural health monitoring. *J. Wind Eng. Ind. Aerodyn.* **174**, 260–268 (2018)
11. Ewins, D.J.: *Modal Testing: Theory, Practice and Application*, 2nd edn. Research Studies Press Ltd. (2000)
12. Liu, W., Wu, X., Zhang, L., Wang, Y., Teng, J.: Sensitivity analysis of structural health risk in operational tunnels. *Autom. Constr.* **94**, 135–153 (2018)
13. Trauth, M.H.: *MATLAB Recipes for Earth Sciences*, 2nd edn. Springer (2007)
14. De La Torre, R.D., Pasobillo, G.A.E., Rebueno, M.F., Donnabel, P.: Vibration based structural health monitoring system for bridges using ADXL345 accelerometer with MATLAB standalone application. In: 2020 IEEE 12th International Conference on Humanoid, Nanotechnology, Information Technology, Communication and Control, Environment, and Management (HNICEM) (2020)

Chapter 51

On the Study and Analysis of Automated Aquaponics System Using AVR Microcontroller



Alka Sathyan, Senthil Arumugam Muthukumaraswamy,
and Habibur Rahman

Abstract With exponential increases in population, the need for water has equally gone up. Water resources are rapidly drying up, whether it is used for drinking or agricultural and industrial purposes. The main aim is to study aquaponics systems that would efficiently use water and analyze methods of monitoring and controlling the parameters concerning water quality. This paper focuses on the study and analysis of different techniques to enhance aquaponics systems' efficiency through IoT-supported automation techniques. AVR microcontroller is interfaced with aquaponics systems through IoT to obtain readings to monitor the system parameters remotely. With this automation process, it can be more convenient to maintain an environment optimal for both the plants and fish. The results reveal methods used to balance the water quality conditions and how automation increases system efficiency.

51.1 Introduction

The recorded population in the year 2020 is 7.8 billion [1]. This number is projected to go up to 10 billion by 2050, with demand for water increasing by 70% [2]. To keep up with the demand for food, the production in the agriculture sector would have to increase by about 60%, of which 50% is irrigated agriculture [1]. Due to the water stress that this will cause, experts predict that about 6 billion people will experience clean water shortages by 2050 [1]. On average, one person drinks 2–4 L of water, but it takes almost 5000 L to produce one person's food intake for a day [3]. Currently,

A. Sathyan (✉) · S. A. Muthukumaraswamy
Heriot-Watt University, Dubai, United Arab Emirates
e-mail: as905@hw.ac.uk

S. A. Muthukumaraswamy
e-mail: m.senthilarumugam@hw.ac.uk

H. Rahman
University of Oslo, Oslo, Norway
e-mail: habibur.rahman@fys.uio.no

there is insufficient supply to keep up with the demand, and 2 billion people live underwater scarcity conditions [1]. Along with population increase, there is also the concern of climate change where countries that rely on “seasonal” sources of water, like rain, might go through more water stress than others [1].

Many solutions have been presented to ensure food and water security. One of these solutions is aquaponics [4]. Aquaponics describes a closed-loop system wherein the fish and plant species exist symbiotically [5]. The uneaten food and excretion from the fish breaking down by “nitrogen-fixing” bacteria convert the ammonia in the excretion to nitrates [6]. These nitrates, which is essential to plant growth, flow through the system to the plants, thus delivering nutrient-rich water for successful plant growth. The plants are essentially “purifying” the water by absorbing the nitrates before re-entering the fish environment [4].

There are many advantages to use an aquaponics system [5]:

- A significant advantage of the system is that it reuses 98% of the water, where the only water exiting the system is through evaporation.
- The lower susceptibility to pests and diseases due to the soil-less nature of the system; thus, little to no chemicals are used to treat the plants.
- The use of an aquaponics system also gives way to a secondary supply line by way of fish farming.
- It is also a great way to grow crops in areas where the soil is too salty.

51.1.1 Types of Aquaponics

There are three types of aquaponics systems in practice: nutrient film technique (NFT), media-based systems, and deep water culture (DWC). The apt method can be chosen by how complex a system is being built.

51.1.1.1 Nutrient Film Technique (NFT)

The “film” of this system is the water that delivers nutrients to the roots of the plants. This system works best with plants with a smaller root network, leafy greens, for example [6]. One of its significant advantages is that it is cost-effective in terms of the labor needed and installation and taking up little space [6]. Another significant advantage is that the system has the lowest rate of evaporation [6]. However, the disadvantage of the system is that it is susceptible to clogging, resulting in reduced filtration of nitrates that are toxic to the fish [6]. The clogging also leads to stagnation of the water in parts of the pipes, increasing the water’s temperature used by the plants unbalancing the system. The NFT method [7] is seen in Fig. 51.1.

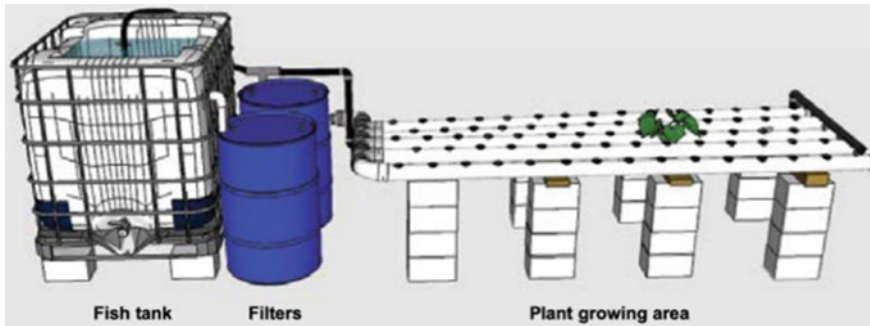


Fig. 51.1 Nutrient film technique

51.1.1.2 Media-based System

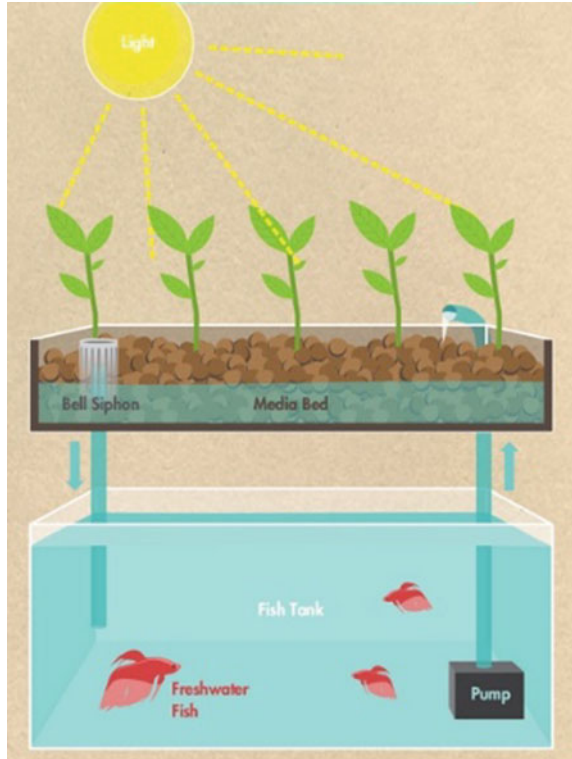
As shown in Fig. 51.2, the plants are placed in a “media bed” consisting of gravel or hydrostones or similar rock media [6]. The presence of the media keeps the roots of the plants in place while also acting as a filter. The water in this system is “flooded and drained,” typically using a bell siphon to drive as much oxygen and nutrients to the plants. This system is better suited for small-scale purposes [4]. Since the rock media imitates soil-based agriculture, it is a versatile system that can grow different types of plants, especially plants that bear fruits, such as tomatoes [6]. With the rock media being porous, it can absorb nutrients and oxygen. This system is disadvantageous due to the weight of the bed, making it unsuitable when scaling for a large-scale project [6]. This method also requires much maintenance, thus, increasing labor costs.

51.1.1.3 Deep Water Culture (DWC)

Deep water culture system is also known as the raft system and is shown in Fig. 51.3. It is defined as “systems with a water level generally more than 5 cm deep, with the water kept in circulation, while plants float on the water in Styrofoam plates or otherwise held in position for the crop production” [8]. It is the most popular method for commercial aquaponics [6]. This technique is known for its maintenance costs, commercial scalability, and the root-to-water exposure [6]. This exposure, however, has a couple of drawbacks as this method requires constant aeration, and large in weight [6].

In an international survey [9], it was noted that at least 43 countries actively engage in aquaponics. The majority of respondents did aquaponics as a hobby and had less than three years of experience in the field but knew how to maintain their system. Other respondents used the system as a teaching tool for primary, secondary, and university students and were also used in vocational courses. The survey also noted that the size of the system ranged from small indoor systems to larger commercial builds.

Fig. 51.2 Media bed system



51.1.2 Automation of System

To understand the automation process of this system, the parameters that need monitoring are to be looked at first. Table 51.1 consists of the studies analyzed based on parameters to be monitored and controlled.

51.2 Methodology

51.2.1 Parameters and Components for Automation

A large part of the aquaponic system becoming successful relies on the nitrification of the bacteria being processed correctly. To ensure, the correct processing of the bacteria is ensured by setting components/parameters of the system certain to the appropriate levels. From Table 51.1, it can be noticed that the three most importantly monitored parameters are water pH, water temperature, and water level.

Fig. 51.3 Deep water culture system



Table 51.1 Analysis of parameters to be monitored

Study used	Parameters considered
Nagayo et al. [10]	(a) Air temperature humidity, (b) light, (c) water temperature (d) pH, (e) dissolved oxygen, (f) water level, and (g) EC, TDS, and salinity
Mamatha and Namratha [11]	(a) Water temperature, (b) light, (c) water level, and (d) pH
Pasha et al. [12]	Water temperature, water level, and pH
Riansyah et al. [6]	pH and total dissolved solids

51.2.1.1 Water pH

Maintaining the appropriate level of pH is crucial for the water being circulated to the plants and essential to the rate of nitrification [6]. The pH of the system can be tested either using test strips or pH meters [4]. A third option is available, automatic probes in controllers, i.e., the water is tested against a set pH level and is dosed with a balancing agent if needed [13]. The pH required varies depending on the plant and fish species used. The PH0-14 pH sensor module has high accuracy, fast response time and is relatively cost-effective. It can be connected to pH probes with BNC connectors.

51.2.1.2 Water Temperature

Optimizing temperature control is dependent on the species of plant and fish used. The most common type of fish used in an aquaponic system is Tilapia that thrives in water temperature of 22–29 °C [6]. Maintaining optimal temperatures ensures fast growth and lower stress levels which leads to fewer diseases [4]. It is crucial to select appropriate sensors that can stay submerged underwater for long periods of time and produce high enough resolution [13]. While the DHT11 is used for ambient temperatures, the DS18B20 is used to measure the temperature in the fish tank. The sensor uses the one-wire protocol. Hence, it can be configured using just one pin. It directly converts the digital output received to a temperature value by toggling its bits based on temperature information.

51.2.1.3 Air Temperature and Humidity

Ambient temperature and humidity are factors that affect the plants more than the fish. The more crucial of the two is humidity, as moisture levels in the air affect the growth of the plants. Seedlings need to have a 60–70% humidity range since the younger leaves need more water to grow [5]. As the plants develop, they require less moisture and settle at around 40% [5]. DHT11 is a temperature and humidity sensor, that is, for ambient temperature and humidity. It has high accuracy, fast response and is cost-effective. The sensor can send signals up to 20 m in low power. It has a temperature range of 0–50 °C and a humidity range of 20%–90%.

51.2.1.4 Water Level

As the aquaponics system is a closed-loop system, the only way water leaves the system is through evaporation. Hence, the water level is determined and affected by other factors such as fish stocking density and the size of the tank containing the fish [6]. Low water levels cause fish stress which leads to lower growth and decline in health [12]. HC-SR04 is an ultrasonic sensor usually used to measure distance with no contact between the sensor and water. There are two parts to the sensor, one part that converts the electric signal to ultrasonic waves, and another part that converts it back. It has a detection range of 2–400 cm. Also, the sensor needs to be placed away from the water.

Atmega32 is the microcontroller that powers this setup. The microcontroller is a low power, 8-bit microcontroller CMOS that is based on AVR RISC architecture. This architecture allows the user to attain the most out of a single clock cycle. One of the main advantages of the Atmega32 is its serial programmable USART. The microcontroller also has the capability for ADC conversion. The ESP8266 module is a Wi-Fi transceiver that is mainly used for IoT applications. In this case, it is used to transmit information from the sensor to a mobile application and receives any information to adjust the parameters or simply to monitor the system (Fig. 51.4).

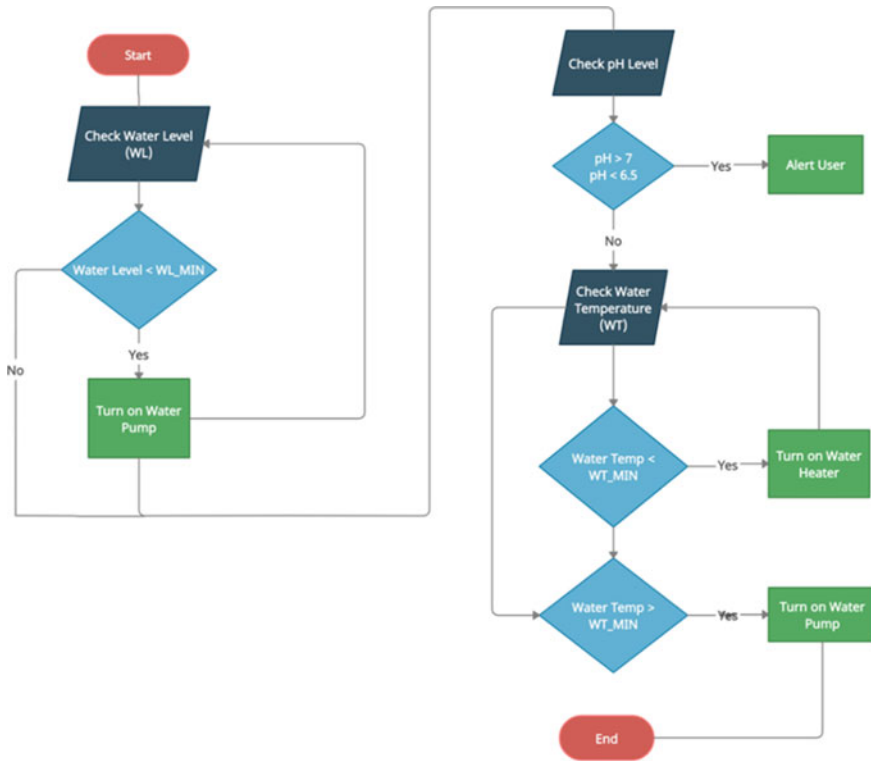


Fig. 51.4 Parameters logic flowchart

51.2.2 Mechanical Build of the System

The proposed mechanical build of this system shown in Fig. 51.5 consists of 2-inch PVC pipes drilled with holes that can fit 2-inch net cups. These net cups will hold the seedling of the plant required. The pipes are placed at a slight angle (approximately 5°), allowing water to flow and not stagnate in one area since stagnation could deprive the roots of oxygen and increase the temperature of the water.

In the hydroponics section of the NFT system, the water moves through the pipes that hold the plants is supplied from a sump tank. This sump tank is filled with water from the fish tank that contains the nutrients required for plant growth. Using gate valves and a submersible pump, with a flow rate of 100 gallons per hour, to regulate water flow. The water then exits the system and directly falls into the fish tank. Three different species of plants, namely—lettuce (*Lactuca sativa*), basil (*Ocimum basilicum*), and mint (*Mentha*) —are used to investigate the efficiency of the system.

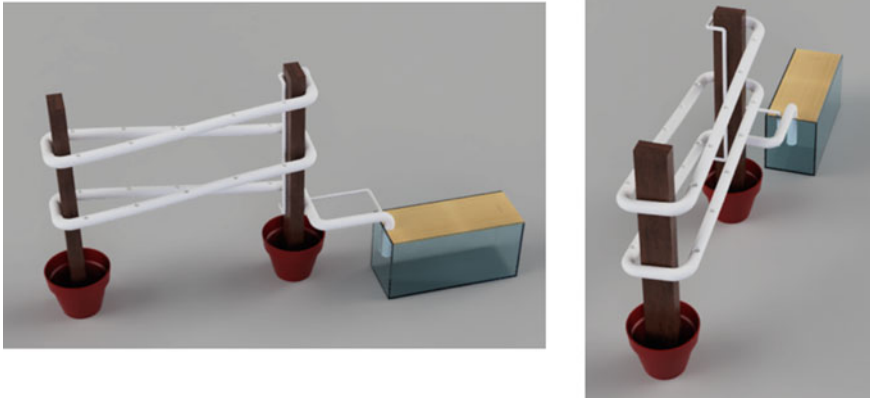


Fig. 51.5 Proposed system design

In the aquaculture section, the fish tank is connected to a filter which is then connected to the sump tank. In the tank, an air stone is attached to provide sufficient oxygen for the fish. There are three 2-inch holes for the net cups. The fish used will be Tilapia, as they are easy to maintain and can adapt to survive if the pump stops operating long enough for repairs to be conducted.

51.3 Results and Observation

The user can access the readings obtained from the sensors by uploading the data to the cloud or interface the system to a mobile application. Another method is to interface the system to a global system for mobile communication (GSM) module, where messages are sent to the user about the system's condition or an imbalance in the system.

51.3.1 Water pH

Due to the formation of carbonic acid from the carbon dioxide produced upon fish respiration, pH value lowers and, hence, become more acidic during the night [4]. In an uncontrolled environment, this is dangerous and requires the water to be cycled regularly [5]. The measurement was done using a pH sensor, pH meters, and pH-ISFETs. On comparing these methods, pH sensors were said to have lower percentage error, thus providing more accurate readings [6].

51.3.2 Water Temperature

Water temperature was set between 25 and 30 °C on average. When temperatures were found to be lower than 30 °C, warmer lamps or water heaters were turned on, and if the temperature was too high, then fans and the water pump were turned on [14]. The temperature was tested using a sensor and a thermometer to test accuracy [10].

51.3.3 Water Level

Float probes used were set as “up,” “medium,” and “low” to indicate water level. When in “medium” and “low” states, the pump is turned off. In the “up” state, the water is pumped from the tank to the grow bed [5]. When ultrasonic sensors were used, on the other hand, it was seen that the water pump would be turned on to restore 25% of the water [4].

51.4 Conclusion

Aquaponics as a solution to water scarcity and its ability to be installed in small areas with poor access to constant irrigation as one of its most significant advantages is clear, as evidenced through this study. It has also elucidated that a large part of the system depends on proper maintenance, and an understanding of how the system works was demonstrated. The proposed aquaponics system was streamlined with automation techniques using an AVR microcontroller and interfacing with IoT. Arrangement of the system was seen to be very successful as a significant amount of workload was controlled remotely or automated by setting sensors to desired values which would then control actuators or simply alert them in case manual intervention was required. Maintaining the pH value and temperature level of water at regular intervals guaranteed the optimal stress level for both the plant and fish. This research can be extended by using solar power for the aquaponics system as part of the future work.

References

1. Corporate author: UNESCO World Water Assessment Programme.: The United Nations world water development report 2021: valuing water. United Nations Educational, Scientific and Cultural Organization, France (2021)
2. Water in Agriculture.: World Bank [Online]. Available: <https://www.worldbank.org/en/topic/water-in-agriculture#1>. Accessed on 11 Apr 2021

3. Manju, M., Karthik, V., Hariharan, S., Sreekar, B.: Real time monitoring of the environmental parameters of an aquaponic system based on Internet of Things. In: 2017 Third International Conference on Science Technology Engineering and Management (ICONSTEM), 23–24 March 2017, pp 943–948 (2017). <https://doi.org/10.1109/ICONSTEM.2017.8261342>
4. Bernstein, S.: Aquaponic gardening: a step-by-step guide to raising vegetables and fish together (in English) (2011) [Online]. Available: <https://www.deslibris.ca/ID/439361>
5. What Is The Aquaponics System? Definition, Benefits, Weaknesses.: Youmatter, 16 May 2020 [Online]. Available: <https://youmatter.world/en/definition/aquaponics-sustainable-benefits-system/>
6. Pasha, A.K., Mulyana, E., Hidayat, C., Ramdhani, M.A., Kurahman, O.T., Adhipradana, M.: System design of controlling and monitoring on aquaponic based on internet of things. In: 2018 4th International Conference on Wireless and Telematics (ICWT), 12–13 July 2018, pp 1–5 (2018). <https://doi.org/10.1109/ICWT.2018.8527802>
7. Somerville, C., Cohen, M., Pantanella, E., Stankus, A., Lovatelli, A.: Small-scale Aquaponic food production: integrated fish and plant farming. FAO Fisheries and Aquaculture Technical Paper, pp 1–262 (2014)
8. Vermeulen, T., Kamstra, A.: The need for systems design for robust Aquaponic systems in the urban environment. In: International Society for Horticultural Science (ISHS), Leuven, Belgium, 1004 edn., pp 71–77 (2013). <https://doi.org/10.17660/ActaHortic.2013.1004.6> [Online]. Available: <https://doi.org/10.17660/ActaHortic.2013.1004.6>
9. Love, D. et al.: An international survey of aquaponics practitioners. PloS One **9**, e102662 (2014). <https://doi.org/10.1371/journal.pone.0102662>
10. Mandap, J.P., Sze, D., Reyes, G.N., Dumlao, S.M., Reyes, R., Chung, W.Y.D.: Aquaponics pH Level, temperature, and dissolved oxygen monitoring and control system using raspberry Pi as network backbone. In: TENCON 2018–2018 IEEE Region 10 Conference, 28–31 Oct 2018, pp 1381–1386 (2018). <https://doi.org/10.1109/TENCON.2018.8650469>
11. Mamatha, M.N., Namratha, S.N.: Design and implementation of indoor farming using automated aquaponics system. In: 2017 IEEE International Conference on Smart Technologies and Management for Computing, Communication, Controls, Energy and Materials (ICSTM), 2–4 Aug 2017, pp 396–401. (2017) <https://doi.org/10.1109/ICSTM.2017.8089192>
12. Ong, Z.J., Ng, A.K., Kyaw, T.Y.: Intelligent outdoor aquaponics with automated grow lights and internet of things. In: 2019 IEEE International Conference on Mechatronics and Automation (ICMA), 4–7 Aug 2019, pp 1778–1783 (2019). <https://doi.org/10.1109/ICMA.2019.8816577>
13. Yanes, A.R., Martinez, P., Ahmad, R.: Towards automated aquaponics: a review on monitoring, IoT, and smart systems. J. Cleaner Prod. **263**, 121571 (2020). <https://doi.org/10.1016/j.jclepro.2020.121571>
14. Montesines-Nagayo, A., Mendoza, C., Vega, E., Izki, R., Jamisola, R.: An automated solar-powered aquaponics system towards agricultural sustainability in the Sultanate of Oman, pp 42–49 (2017)

Chapter 52

Stack-based Outbound Operation Method for Steel Plate Yard in Shipbuilding



Lebao Wu and Zuhua Jiang

Abstract The outbound operation of steel plate yard is a time-consuming job in shipbuilding. Crane should retrieve outbound plates from different stacks. If the outbound plates are blocked by other plates, relocation is required in advance to replace blocking plates to other stacks. To reduce the unproductive relocation, the retrieval and relocation operation should be well-planned. In this paper, we proposed a stack-based outbound operation method. Outbound plates are retrieved based on a specific stack sequence and blocking plates are relocated as much as possible to stacks without outbound plates. We proposed the mathematical model of this method, and a heuristic algorithm is introduced. The computational experiment shows that our method can get good results in a short time.

52.1 Introduction

As the main material of shipbuilding, steel plates should be first preprocessed before sending to work shop. Limited by the pretreatment capacity, plates should be temporarily stored in the steel plate yard which is made up by stack. A rolling plan is made for pretreatment process. This plan determines the plates to be preprocessed in the following three days. However, the preprocess plan is not formulated when plates enter the yard. As a result of random inbound operations, steel plates to be preprocessed in the same day are located in different stacks. Some of them may be piled in the middle of stack. In yard, crane is responsible for plate movement, and it can only move plates in the top slot due to the last-in-first-out (LIFO) policy. Crane needs to retrieve plates from different stacks to implement outbound operation. Since the pretreatment process of plates is the same, there is no requirement for

L. Wu (✉) · Z. Jiang
School of Mechanical Engineering, Shanghai Jiao Tong University, Shanghai 200240, China
e-mail: awkwar@sjtu.edu.cn

Z. Jiang
e-mail: zhjiang@sjtu.edu.cn

plates' outbound order. Meanwhile, if a plate is blocked by other plates, blocking plates should be first relocated to other stacks.

It is clear that the outbound efficiency has a great impact on the subsequent processes. Relocation, the unproductive move, takes up too much time in the operation. The main job of this paper is to determine the retrieve order of outbound plates and the relocation strategy for blocking plates, so that the relocation number is minimized, and the outbound efficiency can be improved.

Relocation problem arises a great attention in the past two decades. This problem occurs in storage place where items are stored in pile. The typical occasion including container terminal, railway terminal, and steel plate yard in shipbuilding and steel industry. The block relocation problem (BRP) is the widely studied relocation problem, which is first introduced by Kim et. al. [1] in 2006. The job of this problem is reducing by choosing the relocation places for blocking plates when the outbound order is given. Caserta et al. [2] proved that this problem is NP-hard and proposed a mathematical model. Kim et. al. [1] introduced an ENAR heuristic rule to select the relocation place. By calculating the expected number of additional relocations, the relocated stack of blocking plates is determined. Caserta et al. [2] introduced "look-ahead" algorithm by considering the impact of relocation move on the next retrieval move. This method is improved by Jin et al. [3] and Jovanovic et al. [4] by considering more subsequence plate retrieval. Since the heuristic method may not obtain optimal result, other researchers using exact methods to solve this problem. Tanaka et al. [5] use branch-and-bound algorithm to solve this problem. Several dominance properties are added to accelerating the algorithm. Bacci et al. [6] proposed another BRP mathematical model so that branch-and-cut algorithm can be used to deal with this problem. The problem studied in this paper is called the block retrieval problem (BRTP), which is introduced by Marcos et al. [7] in 2017. In addition to selecting the relocation place for blocking plates, outbound order is required to be determined in BRTP. It is also a NP-hard problem. Marcos et al. [7] proposed branch-and-bound algorithm to deal with it. Due to the high time complexity of exact method, meta-heuristic algorithm is used to get good results in short time. Zhang [8] introduced a two-stage method combining dynamic programming and local search algorithm. Wang et al. [9] applied nested heuristic algorithm.

The relocation problem in shipbuilding is a BRTP problem. From the literature review, it seems that solutions of this problem are either time-consuming or cannot guarantee the effect of results. In this paper, we introduce a stack-based outbound operation method that can obtain good results in short time.

52.2 Problem Modeling

A typical steel plate yard outbound problem can be described given the following information. A yard with $S \geq 2$ stacks. Each stack has H slots so that each stack can store at most H plates. Some plates distributed in different stacks are about to be

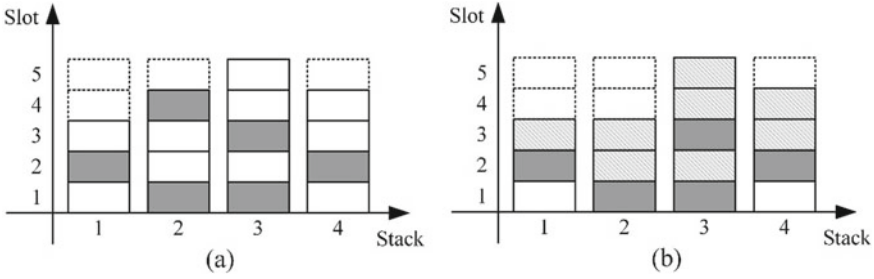


Fig. 52.1 **a** Storage configuration and corresponding **b** Problem instance. The target plates are colored in black, and the blocking plates are colored in gray. The top target plates in Stack 2 is eliminated because it is not blocked by non-target plates

taken out of yard, and they are called target plates. Since the crane can directly move the topmost plates in stack, we assume that target plates located in the top slot have been retrieved, the remaining target plates are blocked by at least one non-target plates. These non-target plates are called blocking plates. Figure 52.1 shows an example of outbound problem. Due to the LIFO policy, blocking plates should be relocated other stack in advanced so that hindered target plates can be retrieved out of yard. The aim of this problem is reducing relocation movement by determining target plates' outbound order and blocking plates' relocation strategy.

The configuration of stack i can be described by a three-element set (w_i, u_i, e_i) . w_i is the number of target plates. $w_i \geq 1$ means that stack i has target plates. Such stack is called target stack. W is used to present the number of target stack. Conversely, stack with $w_i = 0$ is called non-target stack. u_i is the number of blocking plates. To retrieve all target plates in a stack, blocking plates should all be relocated. Since non-target stack has no blocking plates, so the total relocation number is at least $\sum_{i=1}^W u_i$. e_i is the empty slot number in one stack. To ensure that the outbound operation can be processed normally, there are at least $H - 1$ empty slots in yard, i.e.,

$$\sum_{i=1}^S e_i \geq H - 1 \tag{52.1}$$

We define $h_i = w_i + u_i + e_i$ as the valid height of stack i . $h_i \leq H$ because there exist non-target plates buried in the bottom of stack. These plates will not be moved in the outbound operation.

Non-target stack has no outbound plates, and plates in this stack will not be moved during the whole operation. As a result, the empty slot of non-target stack is the priority choice for blocking plates' relocation. We use ps as the total number of empty slots in the non-target stack. ps is dynamically changing during the operation. ps decreases when those slots are used, ps increases when target plates in a stack have been all retrieved, and the stack is changed to a non-target stack.

52.3 Stack-based Outbound Operation Method

In this section, we proposed a structured outbound operation method. This method is mainly divided into two parts. First of all, relocate a number of blocking plates to the initial non-target stacks. This process is call pre-relocation process because we have not retrieved target plates. Then, retrieve target plates based on a given stack sequence. Before all target plates in one stack are retrieved, plates in other stack cannot be moved. This process is called retrieval process. Since, non-target stack is the priority choice for relocation, and ps increases when a target stack is converted to a non-target stack, and a proper stack sequence should be considered so that blocking plates can be relocated to non-target stack as many as possible.

52.3.1 Retrieval Process Based on Stack Sequence

Consider a retrieval process based on target stack sequence $P = (p_1, p_2, \dots, p_W)$, where p_i is the i th retrieval stack, $u_{p_i} \geq 1$. When p_1 is transformed to a non-target stack. It is sure that when we retrieve p_2 target plates, $ps \geq h_{p_1}$. If blocking plates in p_2 can all be relocated to non-target stack, $h_{p_1} \geq u_{p_2}$ should be satisfied. The same condition for p_3 is

$$(h_{p_1} - u_{p_2}) + h_{p_2} \geq u_{p_3}.$$

The left side of this formula represents the available empty slots in non-target stack, which consists of remaining slots in p_1 ($h_{p_1} - u_{p_2}$) and new generated p_2 empty slots (h_{p_2}). Generally, $\forall i \in \{2, 3, \dots, W\}$, if

$$(h_{p_1} - u_{p_2} + h_{p_2} - u_{p_3} + \dots + h_{p_{i-2}} - u_{p_{i-1}}) + h_{p_{i-1}} \geq u_{p_i},$$

i.e.,

$$\sum_{j=1}^{i-1} h_{p_j} \geq \sum_{j=2}^i u_{p_j} \tag{52.2}$$

holds blocking plates in p_i can all relocated to a non-target stack. Such stack sequence is called hindering-averse stack sequence. If the retrieval process is conducted based on a hindering-averse stack sequence, the relocation number can be reduced in maximum degree.

For p_1 blocking plates, the following strategy is used to choose the relocated place:

Step 1: $j = W$.

Step 2: Relocate $b_j = \max(e_{p_j}, u_{p_1})$ blocking plates to stack p_j .

Step 3: $u_{p_1} = u_{p_1} - b_j$. If $u_{p_1} = 0$, exit. Otherwise, $j = j - 1$, return to Step 2.

The main idea of this strategy is to place these plates to the last stack of the sequence so that the next relocation is deferred as possible. In conclusion, if the retrieval process is based on a hindering-averse stack sequence, only blocking plates in p_1 will be relocated twice. The total relocation number is

$$u_{p_1} + \sum_{i=1}^W u_i. \tag{52.3}$$

Formula (52.3) indicates that a proper stack sequence with minimum u_{p_1} value can reduce the relocation number.

52.3.2 Pre-relocation and Structured Outbound Operation

Since only p_1 blocking plates are relocated twice in the retrieval process, the pre-relocation strategy is moving as many p_1 blocking plates as possible to the initial non-target stack, so that u_{p_1} is minimum at the beginning of retrieval process. The complete outbound operation is shown as follows:

Step1: Separate non-target stack and target stack in the initial yard configuration.

Step2: Choose a hindering-averse target stack sequence $P = (p_1, p_2, \dots, p_W)$.

Step3: Relocate p_1 blocking plates to non-target stack until $u_{p_1} = 0$ or $ps = 0$.

Step4: Retrieve target plates based on stack sequence P .

An example of this operation is shown in Fig. 52.2. If $ps \geq u_{p_1}$, all blocking plates in p_1 can be moved to non-target stack in pre-relocation process, remaining totally $\sum_{i=2}^W u_i$ blocking plates and $u_{p_1} = 0$. According to formula (52.3), relocation

number of retrieval process is $0 + \sum_{i=2}^W u_i$. The total relocation of this operation is

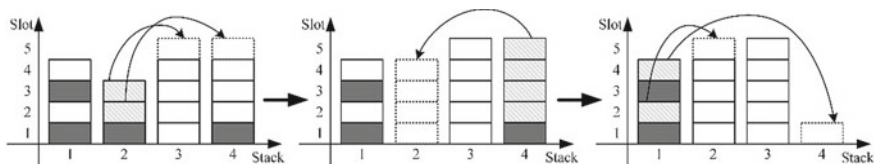


Fig. 52.2 Example of proposed outbound operation. Target plates are retrieved based on stack sequence $P = (2, 4, 1)$ and one blocking plate in Stack 2 is relocated to non-target Stack 3

$\sum_{i=1}^W u_i$, which is also the lower bound of relocation number. The result is optimal. Similarly, if $ps < u_{p_1}$, ps blocking plates are relocated to non-target stack. Relocation number of pre-relocation and retrieval process is ps and $(u_{p_1} - ps) + \left(\sum_{i=1}^W u_i - ps\right)$, resulting totally $(u_{p_1} - ps) + \sum_{i=1}^W u_i$ relocations. Combining these two situations, the relocation number of this operation can be expressed as

$$\max(u_{p_1} - ps, 0) + \sum_{i=1}^W u_i. \tag{52.4}$$

The mathematical model of this operation is shown below. We use R to represent u_{p_1} value after pre-relocation process. Use binary variable x_{ip} to illustrate stack sequence:

$$x_{ip} = \begin{cases} 1, & \text{if stack } i \text{ is the } p\text{th retrieval stack;} \\ 0, & \text{otherwise.} \end{cases}$$

The integer model (IP) is shown as follows:

$$\min f = R + \sum_{i=1}^W u_i \tag{52.5}$$

$$\text{s.t. } \sum_{i=1}^W x_{ip} = 1, \quad \forall p \in \{1, 2, \dots, W\} \tag{52.6}$$

$$\sum_{p=1}^W x_{ip} = 1, \quad \forall i \in \{1, 2, \dots, W\} \tag{52.7}$$

$$\sum_{p=1}^{j-1} \sum_{i=1}^W x_{ip} h_i \geq \sum_{p=2}^j \sum_{i=1}^W x_{ip} u_i, \quad \forall j \in \{1, 2, \dots, W\} \tag{52.8}$$

$$R \geq \sum_{i=1}^W x_{i1} u_i - ps \tag{52.9}$$

$$R \geq 0 \tag{52.10}$$

Formula (52.5) is equivalent to Formula (52.4). Formulas (52.6) and (52.7) ensure that each stack can only be placed in one position of the sequence. Formula (52.8) guarantees the chosen sequence is a hindering-averse stack sequence.

Formulas (52.9) and (52.10) illustrate the value of R . It is a non-negative value larger than $u_{p_1} - ps$.

52.4 Heuristic Algorithm

The difficulty of the proposed method is to find a hindering-averse stack sequence with minimum u_{p_1} value. In this section, we introduced a heuristic algorithm that a proper hindering-averse stack sequence can be found, and the relocation number can be calculated in the linear time of stack number S . The flowchart of this algorithm is shown in Fig. 52.3. First of all, construct an initial target stack sequence by sorting the stack sequence based on u_i value in non-decreasing order. For $\forall i \in \{1, 2, \dots, W - 1\}$, $h_{p_i} \geq u_{p_i} \geq u_{p_{i+1}}$, so the constructed stack sequence is a hindering-averse stack sequence. This process costs $O(S + H)$ time if counting sort is used. Then, starting from the second stack, if

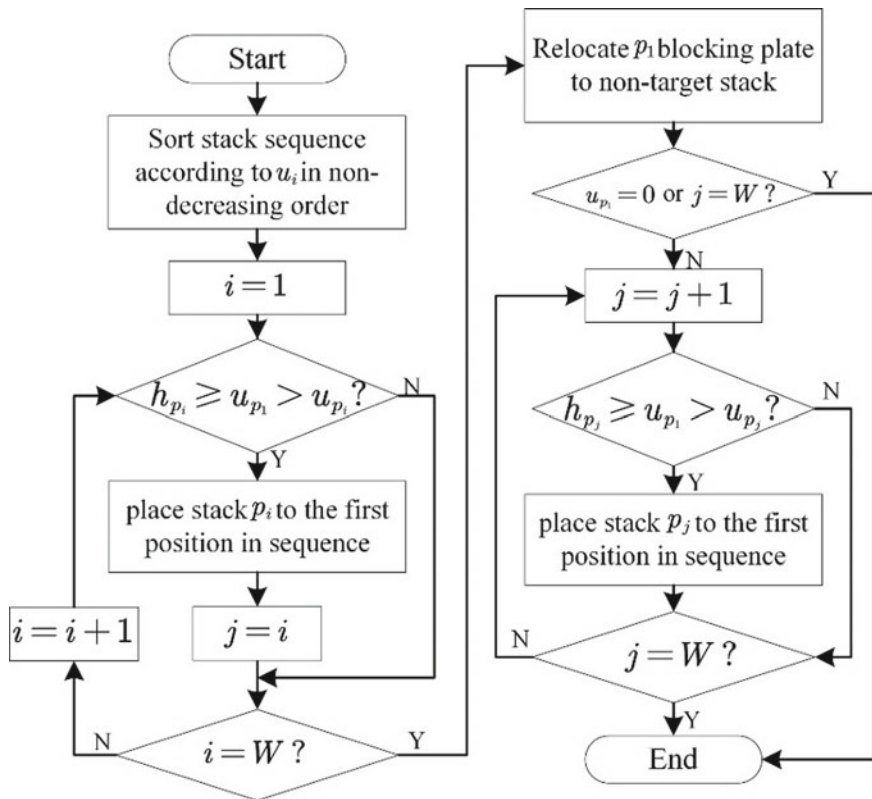


Fig. 52.3 Flowchart of algorithm

$$h_{p_i} \geq u_{p_1} > u_{p_i} \quad (52.11)$$

holds in stack p_i , update the sequence by putting this stack to the first place. Time complexity of this process is $O(S)$. After sequence update, pre-relocation is conducted, u_{p_1} is reduced until $u_{p_1} = 0$ or $ps = 0$. If $u_{p_1} = 0$, exit and output the solution because the result is optimal. Time complexity of this process is $O(1)$. If $u_{p_1} > 0$, conduct a second sequence update. The second update is similar to the first one. However, second update starts from the last update position because only stacks at the back of sequence have smaller u_i value. This process costs $O(S)$ time. The total time complexity of this algorithm is $O(S+H)$, which means that this algorithm can be finished in the linear time of stack number S .

52.5 Computational Experiment

In this section, we present the computational experiment results. The test instances are transformed from BRP instances provided by Caserta et al. [2]. The original BRP set has 21 classes with $S \in \{3, 4, 5, 6, 7, 8, 9, 10\}$ and $H \in \{5, 6, 7, 8, 12\}$. Each class has 40 instances. In the instance, each plate is provided a unique number starting from 1. We transform BRP instances into BRTP's by setting first S plates as target plates. The mathematical model (IP) is solved using CPLEX 12.6.3, and the heuristic algorithm (HA) is compiled in Python 3.8. Two methods are implemented in an Intel Core i7-7700 @ 3.4 GHz CPU with 8 GB memory.

Since the gap of these two methods is small when $H = 5$, only the relocation number and computing time in $H \geq 6$ cases are presented in Table 52.1. Column "Rel" and "Time" present the relocation number and calculating time of corresponding method. Column "Gap(%)" shows the relocation gap of these two methods. When $H = 7$, relocation number increases from 5.525 to 13.550 as S increases from 4 to 10. When $S = 7$, $H = 5$, the relocation number is 4.175, while this number increases four times when H increases to 12. The increase of H has greater impact on relocation number compared to stack number S .

Comparing the relocation number of two methods, there is no difference when $H \leq 8$. The only gap occurs when $H = 12$, $S = 10$, and the gap is only 0.31%. These two methods obtain similar result. However, the computing time of heuristic algorithm is faster than IP model. Although these two methods can all solve the problem within 1 s, heuristic algorithm can be finished within 0.01 s, while IP model requires about 0.06–0.08 s. This evident shows that compared to the IP model, heuristic algorithm can get close results in a short time.

Table 52.1 Computational result of the proposed method

H	S	Cplex (IP)		HA		Gap (%)
		Rel	Time (sec)	Rel	Time (sec)	
6	4	3.975	0.072	3.975	<0.010	0.00
	5	4.975	0.073	4.975	<0.010	0.00
	6	5.375	0.081	5.375	<0.010	0.00
	7	7.025	0.084	7.025	<0.010	0.00
7	4	5.525	0.071	5.525	<0.010	0.00
	5	6.225	0.072	6.225	<0.010	0.00
	6	8.325	0.072	8.325	<0.010	0.00
	7	9.525	0.071	9.525	<0.010	0.00
	8	11.325	0.071	11.325	<0.010	0.00
	9	12.875	0.072	12.875	<0.010	0.00
	10	13.550	0.071	13.550	<0.010	0.00
8	6	10.300	0.076	10.300	<0.010	0.00
	10	18.250	0.074	18.250	<0.010	0.00
12	6	19.450	0.069	19.450	<0.010	0.00
	10	32.050	0.069	32.150	<0.010	0.31

52.6 Conclusions

In this paper, we introduce a stack-based method for minimizing the relocation number in steel plate yard outbound operation. The method can be divided into pre-relocation and retrieval process. We introduce the retrieval process based on hindering-averse stack sequence, and the pre-relocation strategy that only blocking plates in the first stack is relocated. The complete process and the mathematical model of this method are proposed. In addition, we introduced a heuristic method which can solve this problem in a polynomial time in terms of stack number S . The hindering-averse stack sequence is searched by updating from a basic sequence. A computational experiment based on a public dataset is conducted. The results show that these two methods can obtain results in a short time.

Acknowledgements The authors acknowledge the funding support from China Ministry of Industry and Information Technology Project.

References

1. Kim, K.H., Hong, G.P.: A heuristic rule for relocating blocks. *Comput. Oper. Res.* **33**, 940–954 (2006)
2. Caserta, M., Schwarze, S., Voß, S.: A mathematical formulation and complexity considerations for the blocks relocation problem. *Eur. J. Oper. Res.* **219**, 96–104 (2012)

3. Jin, B., Zhu, W., Lim, A.: Solving the container relocation problem by an improved greedy look-ahead heuristic. *Eur. J. Oper. Res.* **240**, 837–847 (2015)
4. Jovanovic, R., Voß, S.: A chain heuristic for the blocks relocation problem. *Comput. Ind. Eng.* **75**, 79–86 (2014)
5. Tanaka, S., Mizuno, F.: An exact algorithm for the unrestricted block relocation problem. *Comput. Oper. Res.* **95**, 12–31 (2018)
6. Bacci, T., Mattia, S., Ventura, P.: A branch-and-cut algorithm for the restricted block relocation problem. *Eur. J. Oper. Res.* **287**, 452–459 (2020)
7. da Silva, M.M., Erdoğan, G., Battarra, M., et al.: The block retrieval problem. *Eur. J. Oper. Res.* **265**, 931–950 (2018)
8. Zhang, Z.Y., Wang, W.Z., Hou, J.: Optimization of multistage operation scheduling for a steel plate stockyard in shipbuilding (in Chinese). *J. Harbin Eng. Uni.* **36**, 638–643 (2015)
9. Wang, G., Jin, C., Deng, X.: Modeling and optimization on steel plate pick-up operation scheduling on stackyard of shipyard. In: *IEEE International Conference on Automation and Logistics*, pp 548–553. ACM Press, Qingdao (2008)

Chapter 53

Investigations on Microstructures by Using Friction Stir Processing



Bazani Shaik, G. Harinath Gowd, B. Durga Prasad, and P. Siddik Ali

Abstract The paper focuses on the processing of FSW and to have the position of conditions to improve the efficiency for welding of the materials to improve the strength. The research has taken place innovative manner for different input process parameters for significance taken place by studying and understanding of a lot of literature survey for different speeds and tool angles. The position of the tool takes a major role in the designing of the tooltip to have the particular position to weld today's scenario of the investigations. The experimental design and microstructural investigations were planned with the help of the Taguchi method. The responses are calculated based on experimental work to get the position of the optimal welding process of the technology to help the society satisfying environmental conditions. The responses are calculated and carried on the optimization techniques of multiple responses applicable and helpful for this method. It is quite possible to optimize the optimal conditions for the output responses more than one. So, this method is very helpful and proved to be very effective in finding the multiple responses which can yield the optimal results.

53.1 Introduction

The FSW process is very popular to have the working conditions for the controlling of parameters inexpensive. The direction of large welding joint composition [1] is available and due to external heating low power consumption and fine-grain size.

B. Shaik (✉) · P. S. Ali

Department of Mechanical Engineering, Ramachandra College of Engineering, Eluru
534007, India
e-mail: drbazanishaik@rcee.ac.in

G. H. Gowd

Department of Mechanical Engineering, Madanapalle Institute of Technology and Science,
Angallu 517325, India

B. D. Prasad

Department of Mechanical Engineering, JNTUA, Ananthapuramu, A.P. 515002, India

The similar and dissimilar metals can be weld and here not use filler metals, flux, etc. The main portion has no environmental pollution, and nowadays, joining process innovative methods prefer marine, automotive, and aerospace for particular properties. The working condition of this process having a controllable area with toll low plasticity. The workpieces and materials in between their generation of heat to get revolutionary weld non-consumable tool shown in Fig. 53.1.

Fallahi et al. [2] studied in detail the Taguchi modeling process with the investigated of acrylonitrile butadiene styrene and polypropylene is incorporated with copper powder at the weld zone of the heating temperature is 80 °C at rotational speed 1600 rpm, travel speed 16 mm/min. The joint weld on polypropylene hardness has 94.1%, and weld strength equal to 91.2% at welding condition optimum of tensile strength is 36%, and hardness is 30% by adding copper powder. Studied welding of butt on dissimilar joining [3] AA6061T6 and pure copper of laser power 700 W, tool speed 950 rpm, and travel speed 23.5 mm/min. The tool pin offset distances are having 0.2–2.1 mm. SEM and EDS, the microstructure of intermetallic compounds. AA1050 alloy and PM Al-Al₂O₃-SiC nanocomposite joints of rotational speed 1200 rpm and travel speed 50 mm/min and electron microscope formation have a three-grain structure of microscale >1 μm to nanoscale <100 nm in stir zone joint. By using FSW in air and underwater, aluminum alloy AA5052 of 6 mm thickness [4, 5] investigated is lower hardness at stir zone and HAZ, and the base metal has high microhardness and stir zone of voids size 0.00073 mm² and base metal of void size 0.0024 mm² and 0.0039 mm². Studied dissimilar joining of 304 austenite steel and SAF 2205 duplex stainless steel [6, 7] of damage is continuum mechanics used for residual stress, and fatigue life has 30% weld sample in residual stress concentration [8]. Studied the welding joint of AA2024T6 and AA6061T6 plates of 4 mm thickness and taper threaded tool were used, welding speed 100 mm/min, rotational speed 1000 rpm with [9]. Precipitation has taken place at heat treatment hardening effects at advancing side, and retreating side [10–15] microhardness of the different weld zone on parameters

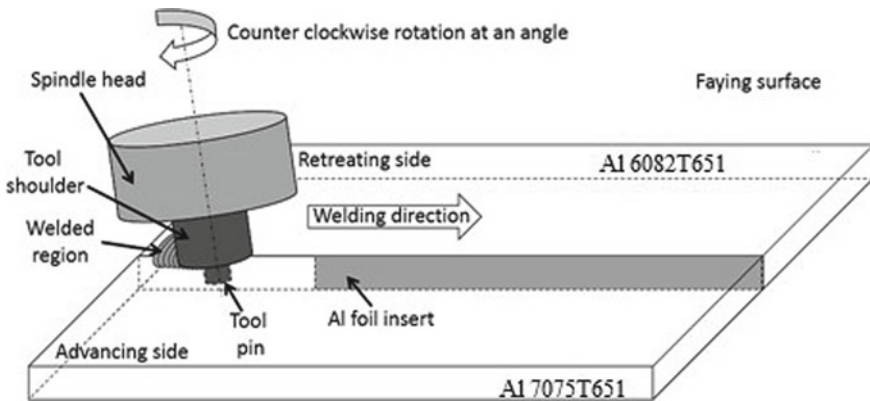


Fig. 53.1 Typical view of FSW setup

of tensile at different welded joints is fractured with the help of metallurgical properties.

53.2 Experimental Procedure and Operating Parameters

AA7075T651 and AA6082T651 plate of thickness 6 mm is used as workpiece material. The material is penetrated by friction stir processing. The experiments done on dissimilar AA7075T651 and AA6082T651 aluminum alloys having 6 mm thickness of each on a computer numerically controlled friction stir welding. It is an FSW setup done at Annamalai university. The chemical compositions of the base material are in Table 53.1. The specimens were taken in 100 mm × 50 mm × 6 mm. The joining is clamped AA 7075T651 and AA 6082T651 using M2 grade SHSS tool of shoulder dia 18 mm and probe length 6 mm. The test specimens are prepared according to the ASTM standards. The influences and coded actual values are in Table 53.2. The dissimilar welds of 7075 aluminum alloy and 6082 aluminum alloy were etched with hydro-fluoric solution. Microstructural examination and material mixing observation were carried out using an optical microscope for microstructural investigations.

Table 53.1 Chemical compositions of base material

Al alloy		
Elements	7075-T651	6082-T651
Si	0.12	1.05
Fe	0.2	0.26
Cu	1.4	0.04
Mn	0.63	0.68
Mg	2.53	0.8
Cr	0.2	0.1
Ni	0.004	0.005
Zn	5.62	0.02
Ti	0.03	0.01
Al	Bal	Bal

Table 53.2 Input variables and coded values

No	Parameters	Notation	Unit	Levels		
				1	2	3
1	Rotational speed	<i>RS</i>	rpm	1150	1250	1350
2	Welding speed	<i>WS</i>	mm/min	40	50	60
3	Tilt angle	<i>TA</i>	Degree	1	2	3

53.3 Microstructural Investigations of Friction Stir Processing for Samples

Figure 53.2 microstructural investigations done on $100\times$ and Keller's reagent are in the microstructure of parent metal AA6082 in the annealed condition with precipitated Mg_2Si particles in primary aluminum alpha solid solution. The grains of eutectics flow in a rolling direction. The primary grains are elongated, and the eutectics are precipitated.

Figure 53.3 the shoulder zone of dominant AA6082 constituents for taper-threaded tool sample with fine fragmented particles of dominant AA6082 constituents. The top layer shows a fusion of AA7075 materials.

Figure 53.4 shows the TMT zone of the retreating side of AA6082 for the taper-threaded tool sample shown AA6082 has a thermomechanical transformation zone with the directional flow of grains of primary and secondary phase grains. The direction of parent metal has changed.

Figure 53.5 shows AA6082 has a nugget and interface zone. Parent metal shows the vertical flow of grains, and the nugget zone at the left shows fragmented particles of the two-alloy used along the same vertical direction.

Figure 53.6 shows the nugget zone center with fragmentation and dynamic recrystallization. An alternate layer of both metals has formed shows the top zone of the FSW with fragmented grains and recrystallization, and the grain size is 10 microns. The constituents of the two alloys have undergone fragmentation and dynamic recrystallization.

Figure 53.7 shows alternate layers of both metals have formed with the effective plasticity of both the constituents of the alloys. Both the constituents show fusion

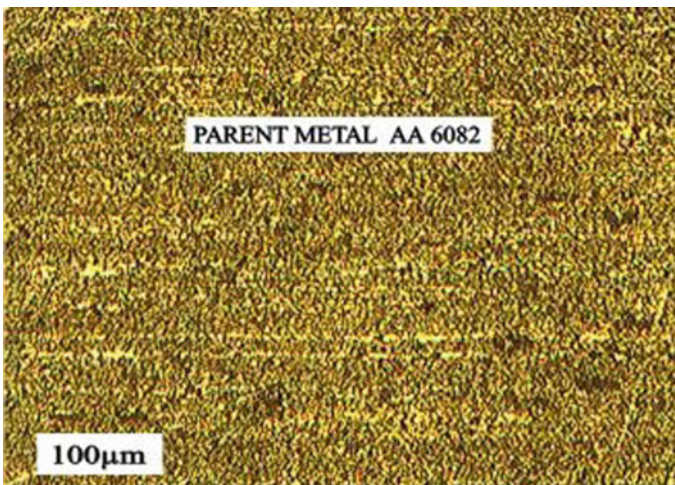


Fig. 53.2 Parent metal

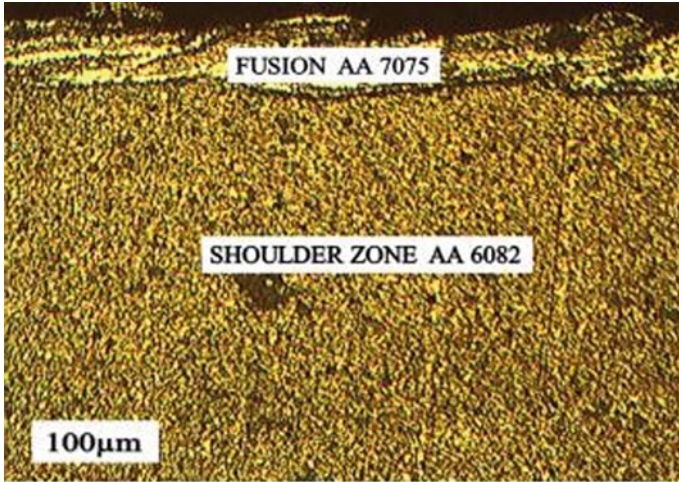


Fig. 53.3 Shoulder zone of dominant AA6082 constituents on FSW by using taper threaded tool for samples

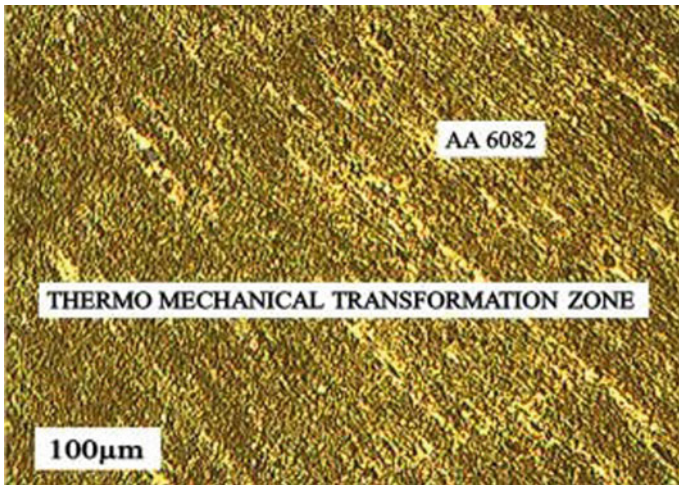


Fig. 53.4 TMT zone of the retreating side of AA6082 on FSW by using taper-threaded tool for samples

and uniform recrystallization to give a grain size of 15 microns of AA7075 and 5 microns of AA6082 as average as per grain size measurements.

Figure 53.8 AA7075 at left and the right side at advancing side process that shows the microstructure of the nugget very close to the interface zone AA7075 and nugget zone. The high-density fusion zone of the nugget with AA7075 at the bottom has taken place.

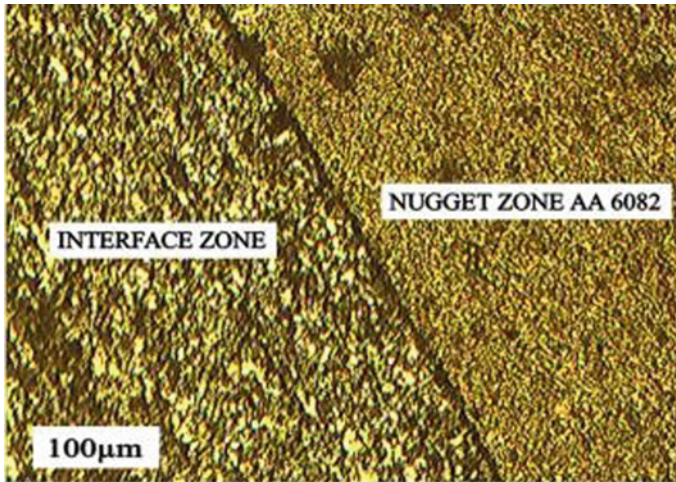


Fig. 53.5 Interface zone of AA6082 with nugget zone on FSW by using taper threaded tool for samples

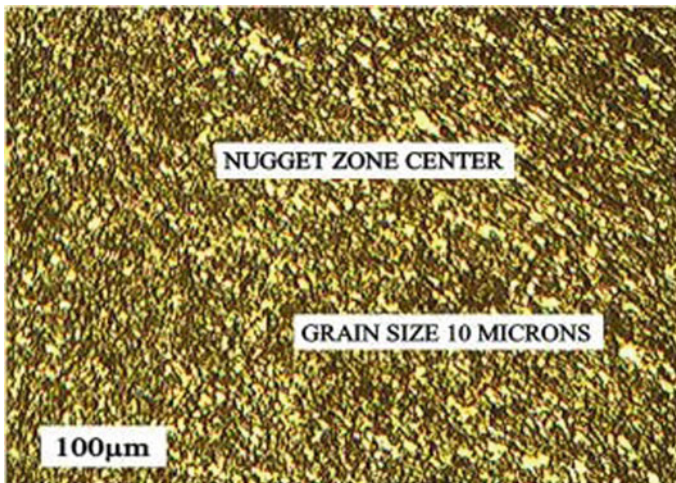


Fig. 53.6 Nugget zone center for on FSW by using taper-threaded tool for samples

Figure 53.9 shows AA7075 has a thermomechanical transformation zone that had undergone higher plasticity due to the heat and stress of the process. This has led to the thermomechanical transformation with the partial dissolution of the constituents of AA7075.

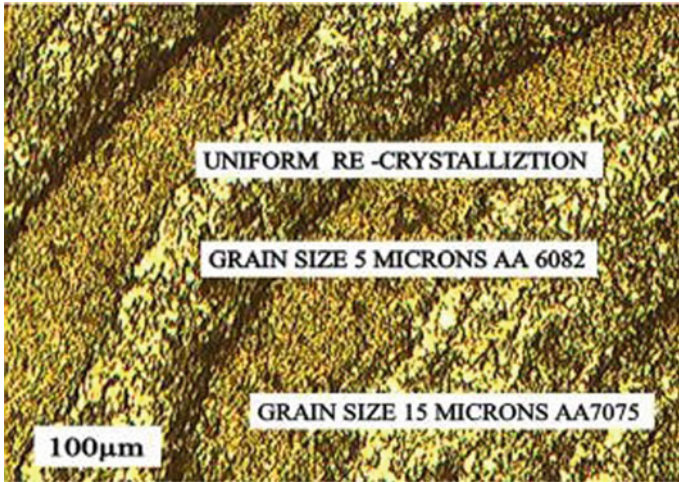


Fig. 53.7 Effective plasticity of both constituents on FSW by using taper-threaded tool for samples

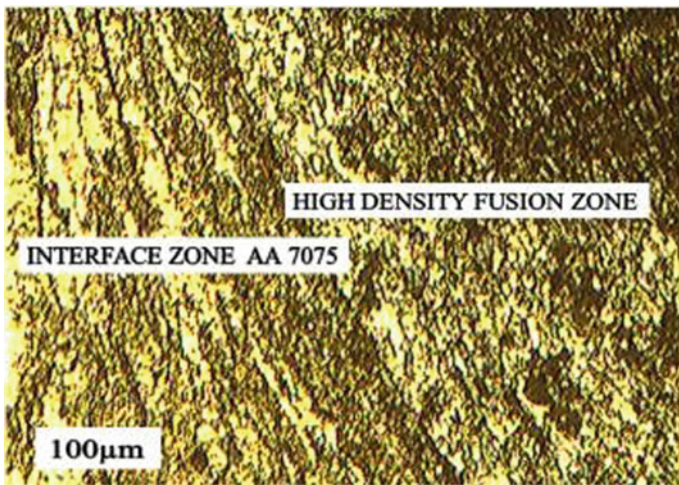


Fig. 53.8 Interface zone of AA7075 on FSW by using taper-threaded tool for samples

Figure 53.10 shows AA7075 the parent condition of the structure level of the rolled position in forming the different chemical reactions and composition are structured and mounted in elongated with rolling direction of precipitation.

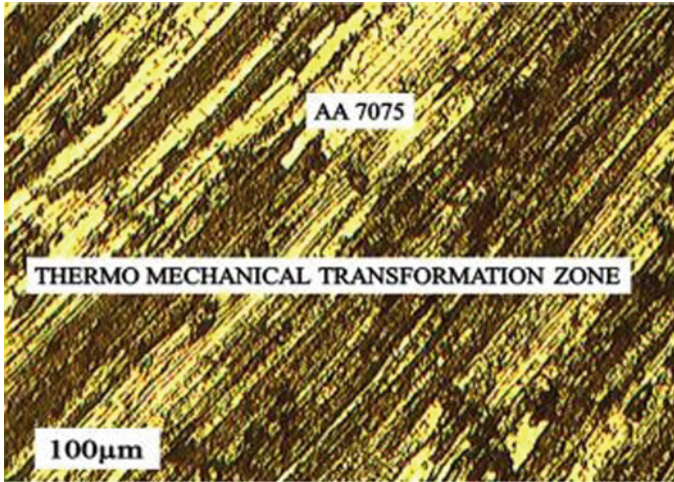


Fig. 53.9 TMT zone of AA7075 on FSW by using taper-threaded tool for samples

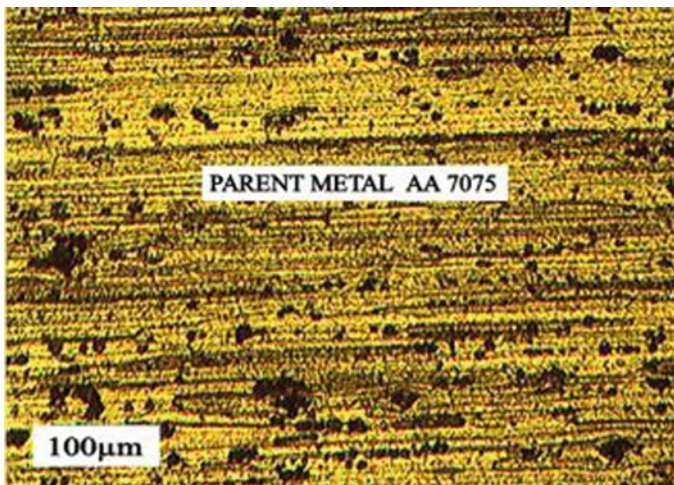


Fig. 53.10 AA7075 parent metal on FSW by using taper-threaded tool for samples

53.4 Conclusions

In this paper, friction stir processing of experiments based on central composite design and microstructural investigations are done led to the following conclusions.

The CNC-friction stir welding framework has proved to be efficient in performing welding operations. It can be inferred that the process parameters can be ideally controlled for attaining the better quality weld in the friction stir welding

process. The results presented in the work can be used for further analysis. Overall, this method proved to be very successful in optimizing the FSP process with the application of this method, and it is quite possible to optimize the output responses more than one. So, this method proved to be very effective in finding the multi-responses which can yield the optimal results.

References

1. Markopoulos, A.P., Habrat, W., Galanis, N.I., Karkalos, N.E.: Modelling and optimization of machining with the use of statistical methods and soft computing, Springer International Publishing Switzerland 2016. In: Davim, J.P. (ed.) Design of Experiments in Production Engineering, Management and Industrial Engineering. https://doi.org/10.1007/978-3-319-23838-8_2
2. Fallahi, A.A., Shokuhfar, A., Ostovari Moghaddam, A., Abdolazadeh, A.: Analysis of SiC nano-powder effects on friction stir welding of dissimilar Al-Mg alloy to A316L stainless steel. *J. Manuf. Process.* **30**, 418–430 (2017)
3. Tara, J., Mustapha, S., Fakir, M.A., Herb, M., Wang, H., Ayoub, G., Hamade, R.: Application of ultrasonic waves towards the inspection of similar and dissimilar friction stir welded joints. *J. Mater. Process. Technol.* <https://doi.org/10.1016/j.jmatprotec.2018.01.006>
4. Morgan, R., Thirumalaisamy, N.: Experimental and numerical analysis of friction stir welded dissimilar copper and bronze plates. *Mater. Today: Proc.* **5**, 803–809 (2018)
5. KepiGangwar, M.: Ramulu, frictionstir, welding of titaniumalloys. *Jade* (2017). <https://doi.org/10.1016/j.matdes.2017.12.033>
6. Moradi, M., Aval, H.J., Jamaati, R., Amirhanlo, S., Ji, S.: Microstructure and texture evolution of friction stir welded dissimilar aluminum alloys: AA2024 and AA6061. *J. Manuf. Process.* **32**, 1–10 (2018)
7. Abandon, H.K., Jashnani, H.R., Payday, M.: Effect of precipitation hardening heat treatment on mechanical and microstructure features of dissimilar friction stir welded AA2024-T6 and AA6061-T6 alloys. *J. Manuf. Process.* **31**, 214–220 (2018)
8. Hajideh, M.R., Farahani, M., Ramezani, N.M.: Reinforced dissimilar friction stir weld of polypropylene to acrylonitrile butadiene styrene with copper nanopowder. *J. Manuf. Process.* **32**, 445–454 (2018)
9. Fey, X., Ye, Y., Jin, L., Wang, H., Live, S.: Special welding parameters study on Cu/Al joint in laser-heated friction stir welding. *J. Mater. Process. Technol.* <https://doi.org/10.1016/j.jmatprotec.2018.02.004>
10. Zhou, L., Zhang, R.X., Hu, X.Y., Guo, N., Zhao, H.H., Huang, Y.X.: Effects of a rotation speed of assisted shoulder on microstructure and mechanical properties of 6061-T6 aluminum alloy by dual-rotation friction stir welding. *Int. J. Adv. Manuf. Technol.* **100**, 199–208 (2019)
11. Liu, F.J., Fu, L., Chen, H.Y.: Microstructure evolution and fracture behavior of friction stir welded 6061-T6 thin plate joints under high rotational speed. *Sci. Technol. Weld Join* **23**(4), 1–12 (2017)
12. Zhu, J., Jiang, W., Li, G., Guan, F., Yu, Y., Fan, Z.: Microstructure and mechanical properties of SiCnp/Al6082 aluminum matrix composites prepared by squeeze casting combined with stir casting. *J. Mater. Process. Tech.* **283**, 116699 (2020). <https://doi.org/10.1016/j.jmatprotec.2020.116699>
13. Veysel, E., Sezer, Ç., Oguzhan, S.: Investigation of the microstructure of aluminum-based composite material obtained by mechanical alloying. *Met. Mater. Int.* **139** (2020). <https://doi.org/10.1007/s12540-019-00583-x>

14. Erturun, V., Sahin, O.: Investigation of microstructural evolution in ball-milling of SiC reinforced aluminum matrix composites. *Powder Metall. Met. Ceram.* **57**(11–12), 687–696 (2019)
15. Sadooghi, A., Rahmani, K.: Experimental study on mechanical and tribology behaviors of Mg–SiC nano/micro composite produced by friction stir process. *J. Mech. Sci. Technol.* **35**, 1121–1127 (2021). <https://doi.org/10.1007/s12206-021-0225-9>

Chapter 54

Comparative Study of Plain and Twisted Ducts in Heat Transfer



M. Udaya Kumar and Gadi Karthik

Abstract The experimental and simulation investigations are meted out to review heat transfer, friction characteristics of twisted and plain ducts. In the present work, Reynolds number varied from 7000 to 40,000 the flowing fluid is considered as air. Twisted duct is a new invention to reduce pressure drop and also increases heat transfer. The practical work has meted out and also experimental setup depends on plan of investigations to induce the best possible warmth transmit and less significant in pressure fall. Then, numerous parameters are such as: hotness, flow rapidity, mass flux, inserts. Twisted ratio of the duct is considered as 6.12. All values and analysis are considered in terms of Nusselt number and Reynolds number and friction factor. The outcome of the experiment shows that twisted duct Nusselt number shows 1.90 times more than the plain duct and also thermal performance of the twisted duct is obtained as 1.43. In this current work, numerical simulations are performed by using ANSYS 18.2FLUENT. In the present work hotness transmit, statistical flow patterns like heat transmit, frictional resistance graphs of twisted and smooth ducts are studied.

54.1 Introduction

Heat exchangers are mechanical appliance to pass on warmth power from one section to a different one by the use of exterior region. Al Mudhafa et al. [1] numerically investigated about new modified webbed heat exchanger, and these

Please note that the LNCS editorial assumes that all authors have used the western naming convention, with given names preceding surnames. This determines the structure of the names in the running heads and the author index.

M. Udaya Kumar (✉) · G. Karthik
Department of Mechanical Engineering, Methodist College of Engineering and Technology,
Hyderabad, Telangana, India

results show that thermal performance of phase change material solidification process accelerates 41% more as compared to webbed tube heat exchanger.

Hajabdollahi et al. [2] explored that tube fitted with twisted tape fin-and-tube heat exchanger provides better results in terms of effectiveness (related to heat transfer), and annual cost is optimized (related to heat transfer area related to pressure drop). Stamation et al. [3] studied that latent heat energy storage using phase change material is considered as a promising thermal energy storage system.

Chang and Yu [4] explored the consequences of spiral-shaped coil springs in a heat exchanger. It has been observed that recital of heat exchanger is enhanced with spiral shaped coil inserts.

Khoshvght et al. [5] explained spiral-coil twist shaped duct has been utilized used and analysis was made by both experimental and numerical. The highest enhancement of Nusselt's numeral and frictional ratio are 1.87, 1.38 for nano fluid and H₂O... Xu et al. [6] analyzed that consequences of obstruction percentage, attack angle, pitch ratio of the vortex generators of the circular tube the maximum warmth performance was obtained at pitch ratio 2.40 obstruction ratio 0.10. Samruasin et al. [7] focused on pressure fall, heat transmit distinctiveness of rounded tube combined with usually spaced quadric type twisted tape element under turbulent flow situations. It has been observed that twisted ratio is equal to 0.5 thermal improvement is 27% is more. Hong et al. [8, 9] examined twisted with overlapped tapes inserted in the groove shaped tube. The results show that recital assessment criteria are approximately between 1.04 and 1.15 for a groove shaped tube. And also compound twisted tapes give maximum Nusselt's number.

Skullong et al. [10, 11] studied thermal uniqueness heat exchanger with winglet perforated tapes. The thermal efficiency is obtained as 1.70 for 30° horse shoe baffles good heat enhancement is achieved.

Promvong et al. [12] described mathematically and outcome of investigational result shows that finned type inserts are exhibit better arrangement, in square duct... Bhadouriya et al. [13] studied frictional resistance, warmth transmit distinctiveness were examined of twisted duct between the ratio of 11.49–16.50, Reynold's numeral is in the course 500–69,000. The resultant of the experiment gives prominent heat transfer improvement until Reynolds number is 9500.

54.2 Plain and Twisted Square Ducts Experimental Setup Procedure

The investigational working model has shown in Fig. 54.1. The equipment setup made up of blower with capacity of one kilowatt power, square duct, variable flow drive, dimmer start, heaters. In order to minimizing the errors, measuring devices like anemometer, thermocouples are calibrated. The arrangements square duct with

rope insulation, duct inside the casing, heaters are incorporated as shown in Fig. 54.1. Air is flowing fluid which is passing through inside the duct, to compute the capacity stream rate an Orifice meter is used, to get accuracy of pressure differential manometer is also presented in the experimental setup. The cross section of the duct is 65×65 mm, length is 1500 mm. The material of the duct is aluminum, K-type thermocouple resolution is 0.1° , and thermocouples are placed at appropriate location to compute inlet, outlet, and surface temperatures. In this present experimental work, constant speed air blower is used, after attaining steady state condition all readings are noted, the speed of the blower is controlled by variable flow drive. All readings are measured at a velocity of 2.2, 3.5, 4.4, 5.5, 6.4, 8.6, 9.5 m/s at constant heat flux condition and temperature at inlet is considered as 300 degree Kelvin. Then after calculate pressure drop, heat transfer coefficient, friction factor. After taking readings of plain square duct at different intervals, same procedure is adopted for twisted duct with 270° angle twisted ratio is equal to 6.12. Length, width, height, thickness as same as plain square duct. Twisted square duct as shown in Fig. 54.2.



Fig. 54.1 Experimental setup (1 air blower, 2 square duct test section with casing, 3 dimmer start, 4 control panel, 5 U-tube differential vertical manometer, 6 variable flows drive, 7 orifice setup and setting chamber)



Fig. 54.2 Twisted square duct

54.3 Simulations

54.3.1 Plain Square Duct Simulations

Figure 54.3 explained that air hotness is improved from entry to exit, it happens because of air flow is continuously rotate each corner of the duct. The difference of first in- last out temperatures are high and it has been observed that warmth transmit is amplified for the Velocity of 2.20 m/s. Nusselts number and frictional resistance are analyzed by using standard equations. Through square duct temperature of the air is initially considered and is temperature at beginning 300 degree Kelvin heat is deposited t from the surrounding walls. As velocity of air increased air remains

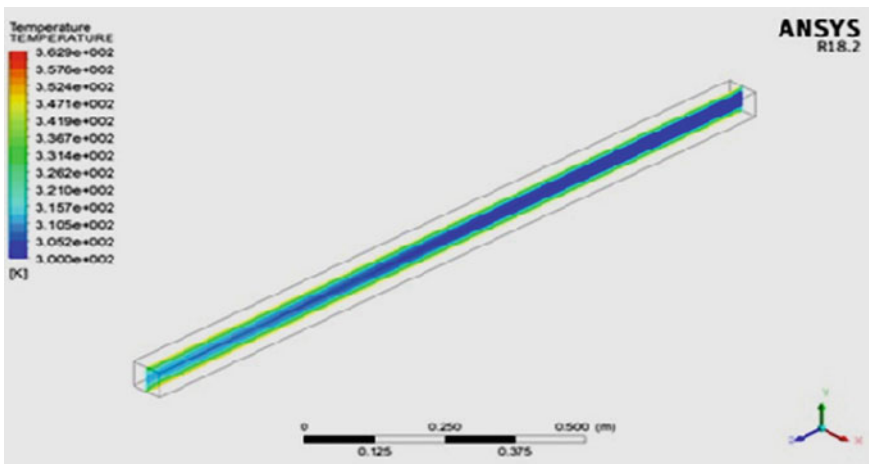


Fig. 54.3 Temperature profile of plain duct at velocity of flow 2.20 m/s

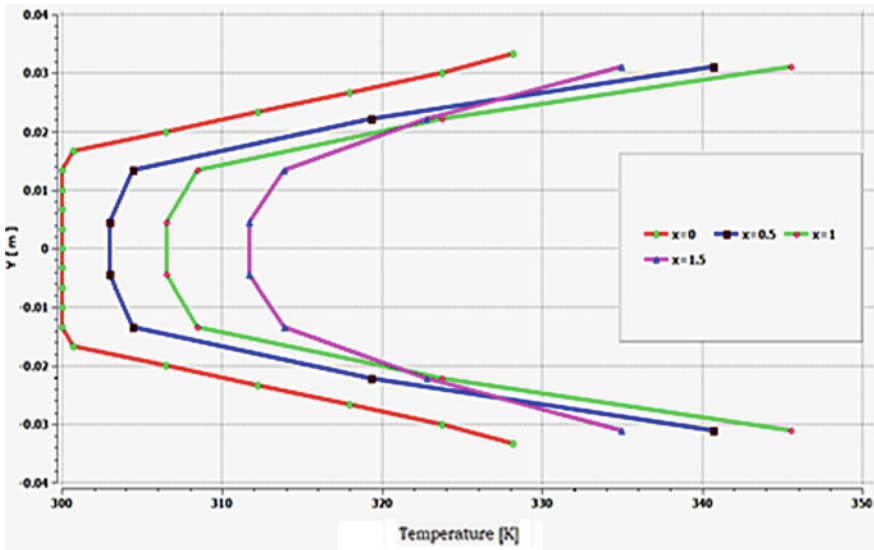


Fig. 54.4 Temperature contour of smooth square duct

inside the duct for less time, so it absorbs less heat from walls. Hence, common air temperature at exit is diminished as Reynolds number enhanced.

Figure 54.4 is explored the disparity of temperature in the plain or smooth duct at various interval like $X = 0$, $X = 0.5$ m, $X = 1$ m, $X = 1500$ mm. In the above graph shown that at $Y = 0.0250$ m space, air flow velocity is maximum. Because of flow obstruction is very minimum.

Figure 54.5 exhibits disparity of twisted duct temperature at air flow velocity 2.20 m/s. It has been identified variation of exit and entry temperature is maximum as compare to square duct, for the similar working circumstances. Because of swirl movement is formed by derived or secondary flow, which helps increases warmth difference between inlet and outlet, therefore, improve heat transfer rate and also increases heat transfer coefficient of heat transfer.

Figure 54.6 shows disparity of temperature of twisted duct. From the above graph explored that at $X = 0$ splitting up temperature is minimum. After that at $X = 1$ m it has been identified that disparity connecting exit and entry warmth is better. Because of velocity flow of air direction is warped in twisting mode.

54.4 Results and Discussions

Figure 54.7 shows variation of Nusselt number versus Reynolds number of square duct. And also, Nusselt numeral is gradually increasing with Reynolds number, because of declinment of thermal edge layer thickness. All values have taken with

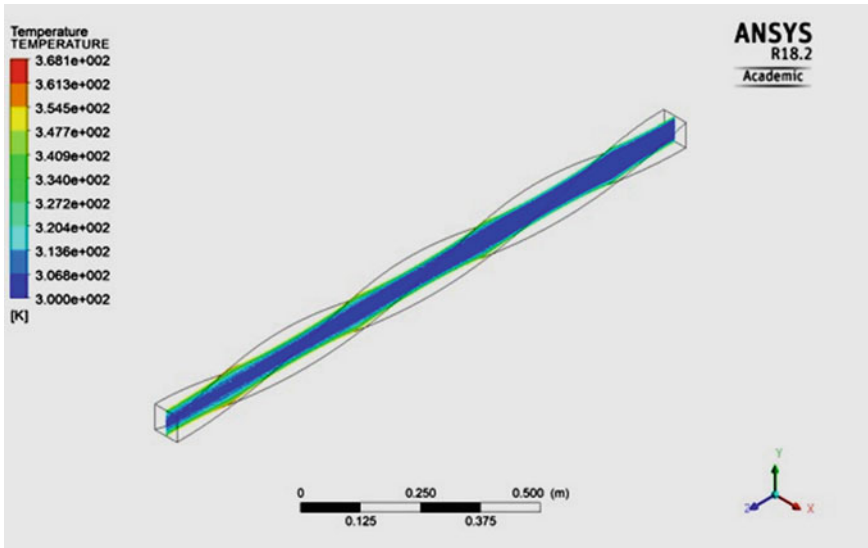


Fig. 54.5 Change of temperature for twisted duct velocity 2.20 m/s

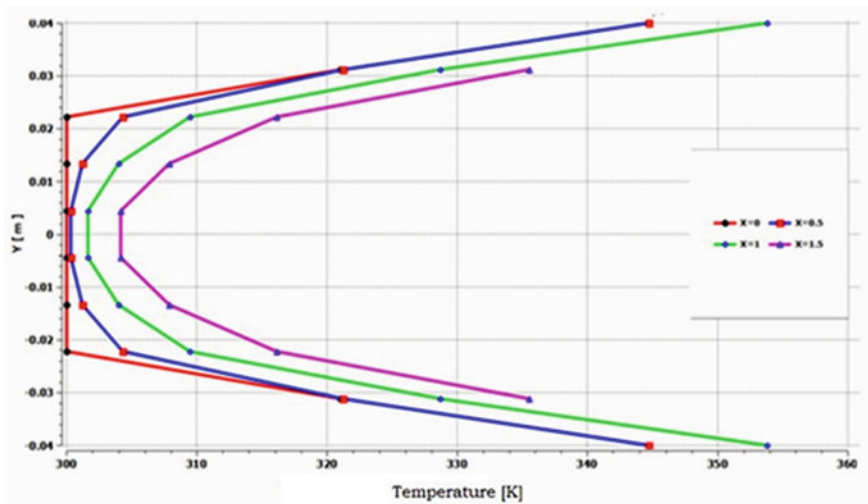


Fig. 54.6 Twisted square duct temperature contour at a flow velocity 2.2 m/s

starting velocity from 2.2 m/s in this process final velocity is considered as 9.5 m/s. Beyond the 8.6 m/s flow of velocity, a huge discrepancy in the practical Nusselt number. Therefore, the experimental flow velocity is constrained to 8.6 m/s.

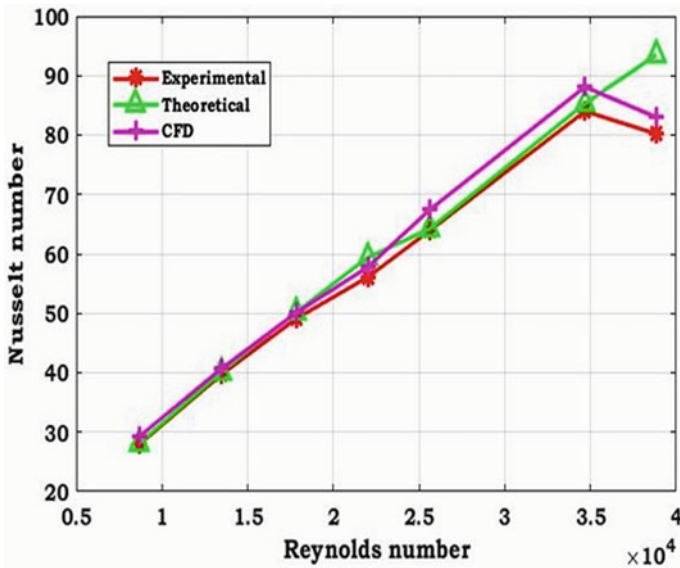


Fig. 54.7 Investigational, theoretical, CFD results of square duct

The cause may be due to prominent flow velocity less possibility for inclusion of fluid to pass on heat. Hence, all values are within the range. Consequently, investigational system is validated.

Figure 54.8 focused on hypothetical and practical results of smooth or plain square duct. It reveals that practical frictional factor data significantly concur with theoretical data, intended by applying Pethokova's correlation, as air flow velocity is higher since movement of solution is not in straight path, and then, it offers extra abode time in the square duct. For this reason, frictional factor data steadily diminished, while Reynolds number is augmented.

Figure 54.9 represents the upper most practical Nusselt number is obtained at Reynolds number = 34,937, at flow swiftness of 8.6 m/s, due to high-obstruction percentage, it produces flow swirl movement and severance. Hence, it increases turbulent flow of the fluid. Consequently, maximum heat transfer is observed in the twisted square duct.

Figure 54.10 gives comparison of plain and twisted ducts Nusselt number and Reynolds number. In the present analysis, twisted duct has got uppermost Nusselt number than smooth or plain square duct of the similar investigational conditions. Because at the twisted ratio of 6.12 inclined suitable mixing of liquefied molecules, and the highest instability is produced.

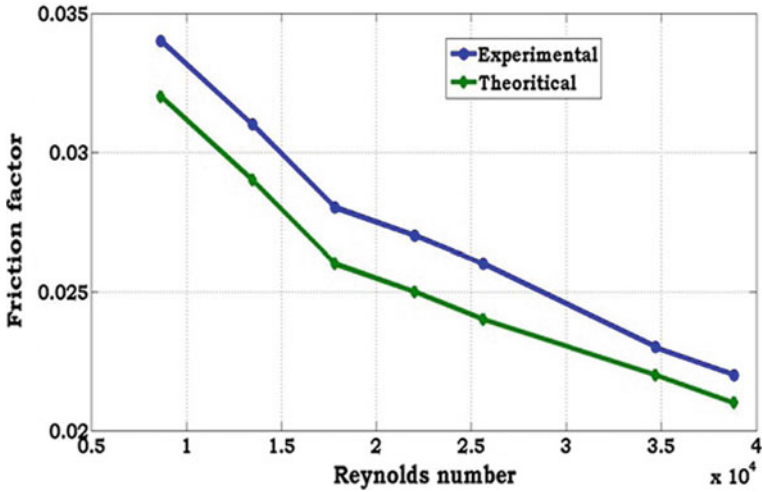


Fig. 54.8 Explores the disparity of frictional factor versus Reynolds number

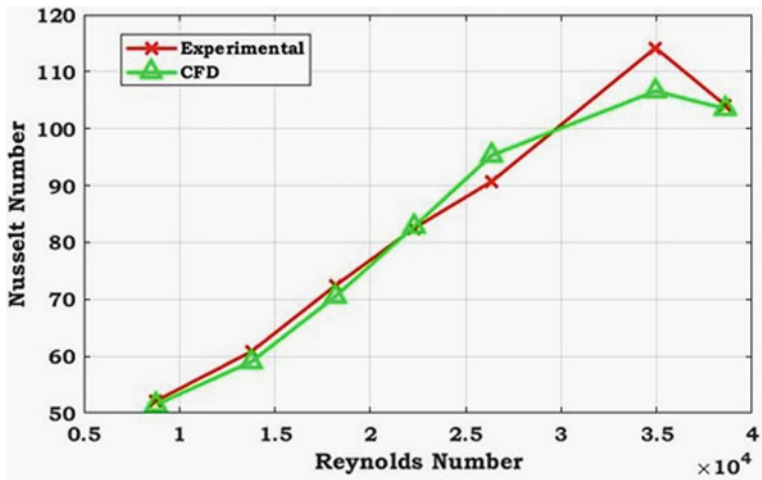


Fig. 54.9 Estimation of investigational replication result of square twisted duct

54.5 Conclusions

- The percentage variation of theoretical and experimental results for Nusselts number is ± 0.7 – 5.3% and frictional factor is ± 3.2 – 7.3% for the square duct. Hence, investigational working model is validated within the permissible limits.

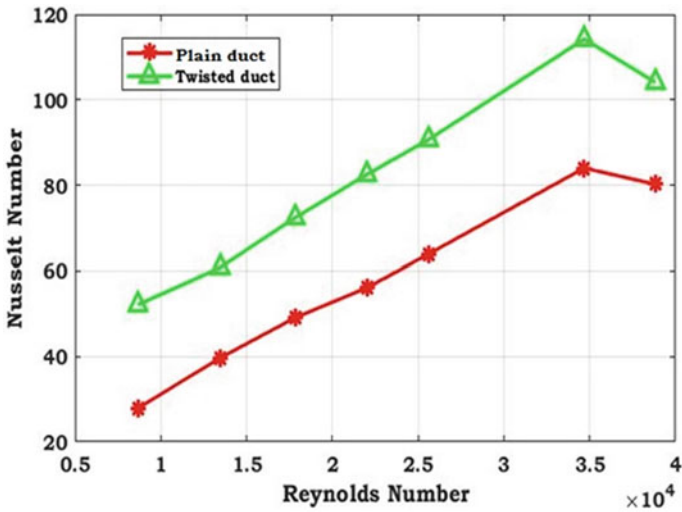


Fig. 54.10 Assessment of twisted square duct and plain square duct

- The investigational Nusselt number of twisted square duct is highest at a velocity of 8.60 m/s, i.e., 114.2. This happens to be because of larger blockage ratio provides maximum stream movement, which provide stronger turbulent flow concentration leads to devastation of thermal frontier layer, and it leads to augmentation of heat movement in the object.
- The practical results reveal that twisted square duct Nusselt number is 1.889 times more than of square duct.
- Thermal recital of the twisted square duct is equal to 1.419 at flow of velocity is 2.2 m/s. Because of the highest impasse percentage in the square twisted duct, the growth of pitch percentage is not as much of effectual to diminish gradually frictional thrashing in the duct.
- Finally, it is observed that twisted square duct gives better heat transfer enhancement than plain square duct.

References

1. Al Mudhafa, A.H.N., Nowakowski, A.F., Nicolleau, F.C.G.A.: Performance enhancement of PCM latent heat thermal energy storage system utilizing a modified webbed tube heat exchanger. *Energy Reports* **6**, 76–85 (2020)
2. Hajabdollahi, Z., Hajabdollahi, H., Kim, K.C.: Heat transfer enhancement and optimization of a tube fitted with twisted tape in a fin-and-tube heat exchanger. *J. Thermal Anal. Calorimetry* **140**, 1015–1027 (2020)
3. Stamation, A., Maranda, S., Waser, R., Worlitschek, J.: Comparison of heat transfer enhancement techniques in latent heat storage. *Appl. Sci.* **10**, 1–23 (2020)

4. Chang, S.W., Yu, K.-C.: Heat transfer enhancement by spirally coiled spring inserts with and without segmental solid cords. *Exp. Thermal Fluid Sci* **97**, 119–132 (2018)
5. Khoshvaght Aliabad, M., Khaligh, S.F., Tavassoli, Z.: An investigation of heat transfer in heat exchange devices with spirally-coiled twisted-ducts using nanofluid. *Appl. Thermal Eng.* **143**, 358–375 (2018)
6. Xu, Y., Islam, M.D., Kharoua, N.: Experimental study of thermal performance and flow behaviour with winglet vortex generators in a circular tube. *Appl. Thermal Eng.* **135**, 257–268 (2018)
7. Samruaisin, P., Changcharoen, W., Pimsarn, M., Thianpong, C., Chuwattanakul, V., Eiamsa-ard, S.: Influence of regularly spaced quadruple twisted tape elements on thermal enhancement characteristics. *Chem. Eng. Process. Intensification* **128**, 114–123 (2018)
8. Hong, Y., Du, J., Wang, S.: Experimental heat transfer and flow characteristics in a spiral grooved tube with overlapped large/small twin twisted tapes. *Int. J. Heat Mass Transfer* **106**, 1178–1190 (2017)
9. Hong, Y., Du, J., Wang, S.: Turbulent thermal, fluid flow and thermodynamic characteristics in a plain tube fitted with overlapped multiple twisted tapes. *Int. J. Heat Mass Transfer* **115**, 551–565 (2017)
10. Skullong, S., Promvong, P., Thianpong, C., Pimsarn, M.: Heat transfer and turbulent flow friction in a round tube with staggered-winglet perforated-tapes. *Int. J. Heat Mass Transfer* **95**, 230–242 (2016)
11. Skullong, S., Thianpong, C., Jayranaiwachira, N., Promvong, P.: Experimental and numerical heat transfer investigation in turbulent square- duct flow through oblique horseshoe baffles. *Chem. Eng. Process.* **99**, 58–71 (2016)
12. Promvong, P., Skullong, S., Kwankaomeng, S., Thiangpong, C.: Heat transfer in square duct fitted diagonally with angle-finned tape—part 2: numerical study. *Int. Commun. Heat Mass Transfer* **39**, 625–633 (2012)
13. Bhadouriya, R., Agrawal, A., Prabhu, S.V.: Experimental and numerical study of fluid flow and heat transfer in a twisted square duct. *J. Heat Mass Transfer* **82**, 143–158 (2015)

Chapter 55

Performance Evaluation of a Predictive and PID Control Applied to a Didactic Flow Regulation Process



Wilson Guambo, Byron P. Corrales, Luigi O. Freire,
and Mauro D. Albarracin

Abstract This work presents a comparison between a predictive control and a PID control applied to a flow process, covering technical and theoretical aspects that range from the acquisition and estimation of mathematical models, to the design and implementation of controllers using an OPC communication gateway. The evaluation of its performance is carried out based on the characteristic parameters of a transient response to a step-type signal, and additionally its behavior is also evaluated in the face of disturbances of external origin, thus allowing to establish causes for the implementation of one or another controller in the control of the flow variable.

55.1 Introduction

A control system is characterized by the presence of a series of elements that allow influencing the operation of the system, in order to achieve, through the manipulation of the control variables, a domain over the process variables making it remain in a value as close as possible to the set point.

Ideally, a control system should be able to achieve its objective by complying with requirements such as guarantee stability and, particularly, be robust against disturbances and errors in the models; be as efficient as possible, according to pre-established criteria; be easily implementable and comfortable to operate in real time with the help of a computer [1, 2].

W. Guambo · B. P. Corrales · L. O. Freire (✉) · M. D. Albarracin
Universidad Técnica de Cotopaxi, Latacunga, Ecuador
e-mail: luigi.freire@utc.edu.ec

W. Guambo
e-mail: wilson.guambo9721@utc.edu.ec

B. P. Corrales
e-mail: byron.corrales@utc.edu.ec

M. D. Albarracin
e-mail: mauro.albarracin@utc.edu.ec

Within this context, the proportional integral derivative (PID) controller has become the most widely used process variable regulation tool, and for this reason, it has been applied indiscriminately on linear and nonlinear dynamic systems, generating control problems in the industrial sector, producing a loss of efficiency in productivity and a decrease in the quality of manufactured products. Among the modern control techniques that have emerged to respond in applications in which the PID controller has not operated satisfactorily is model-based predictive control (MPC). This control algorithm has been characterized by its great response capacity; however, its expansion in the industrial sector has been slow, since it has been commercialized for particular applications [3].

55.2 System Description

The first part of the study consists of obtaining the mathematical model of the process, and for this purpose, a flow station shown below is used (Fig. 55.1).

For this particular case, the actuating element will be a frequency variator, because its control is more effective in ranges from 20 to 100% of the nominal flow, coinciding with the sensor's measurement range, which presents errors and instability in values lower than 25 LPM, and in addition, the control by frequency variator reduces the increase of pressure during the operation avoiding the leaks, vibrations, and overheating of the pump motor [4].

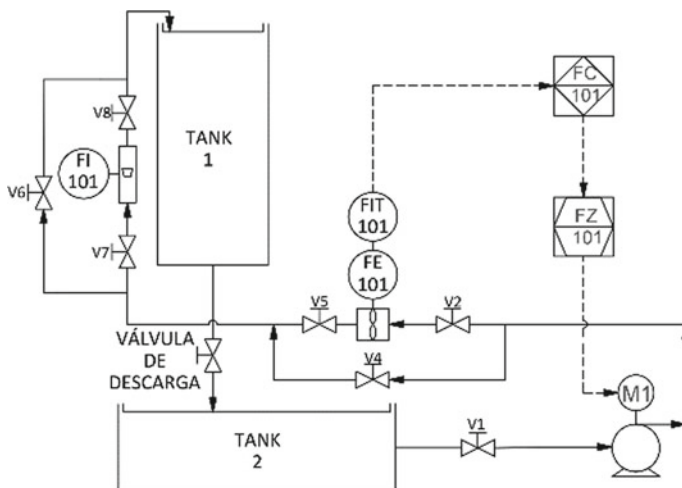


Fig. 55.1 Diagrama P&ID de la estación de caudal

55.2.1 Proportional Integral Derivative (PID)

It is the most common control algorithm, most of the feedback loops are controlled by this algorithm or another with small variations. The actions of the PID control are summarized as follows: the proportional action (Kc) reduces the rise time, but never eliminates the error in steady state. The integral action (Ki) eliminates the error in steady state, but worsens the transient response. Derivative action (Kd) increases system stability, reduces overshoot, and improves transient response [5].

55.2.2 Predictive Control (MPC)

Predictive control is not a specific control strategy, but rather a very broad field of control methods developed around certain common ideas. Its control strategy based on complex mathematical processes requires intense computational activity; however, with the processing capacity of current computers, this is not really an insurmountable difficulty and from this fact its applicability in various industrial processes has begun to give their first steps [6, 7].

- Control strategy (Fig. 55.2)

The predictive controller operates in two phases to calculate the next move: Estimation and optimization. Once these processes are finished, the controller applies the restricted control signal (uk) to the plant, which operates with this input until the next control interval, where the controller takes new measurements to repeat the processes, this process is known as sliding horizon [3].

Two fundamental parameters within the control strategy are the prediction horizon (H_p) and control horizon (H_c), the first refers to the future time interval that is considered in the optimization for the control signal and the second refers to the number of movements calculated for each manipulated variable, where the control horizon is less than the prediction horizon [8].

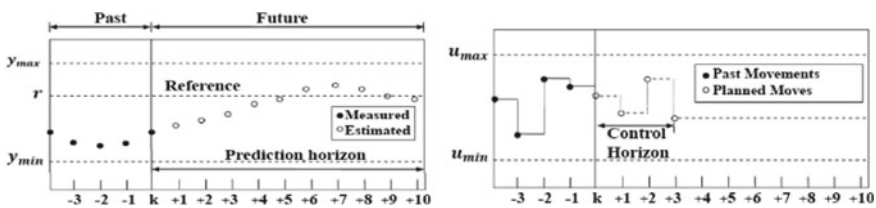


Fig. 55.2 Operación de un MPC

55.3 Data Acquisition and Model Estimation

55.3.1 Data Acquisition

The data acquisition corresponds to the registry of values of the input and output variable of the plant, whose units will be scaled to liters per minute (LPM) with the use of Eq. 55.1 to transform LPM to volts at the input of the drive and Eq. 55.2 to transform the sensor output voltage to LPM. These equations are unique to this flow station and respond only to the current plant configuration.

$$V = 0,0002Q2 + 0,0393Q + 1,7813. \quad (\text{Entrada}) \quad (55.1)$$

$$Q = 0,0785V2 + 19,829V - 19,144. \quad (\text{Salida}) \quad (55.2)$$

The diagram for data acquisition is shown in Fig. 55.3a or data acquisition, a NI myDAQ card from National Instruments is used, into which a virtual instruments (VI) is loaded with the programming blocks.

Because flow measurement signals are usually noisy from turbulent flow, a first-order low-pass filter is applied, specifically the exponential moving average (EMA). The result of applying this filter is shown in Fig. 55.3b where a smoother signal is observed in the process variable (PV). In [9] you can review important concepts about flow measurement and process pump control, useful information for data acquisition.

55.3.2 Model Estimation

The plant model is estimated using Matlab using its “systemIdentification” or “ident” tool. The system model will be represented in two different ways: Process model with transfer function and Model in state space (Fig. 55.4). It is worth mentioning that states cannot always be measurable or observable; For a better analytical understanding of the models in state spaces see [10, 11].

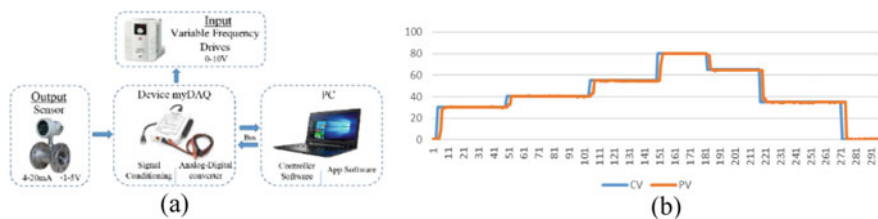


Fig. 55.3 Components of a data acquisition system (a), filtered database (b)

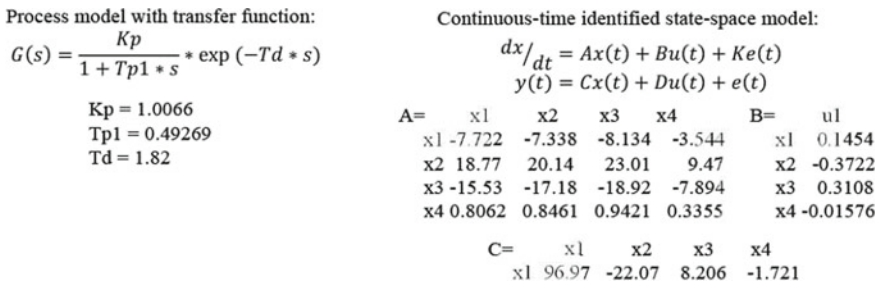


Fig. 55.4 FOTD model and estimated state space model of the plant

The validation of the estimated models is carried out using the “modelOutput” tool of the “systemIdentification” in which for the transfer function it amounts to 92.57% and for the case of the model in state space the degree of coincidence is 92.62% with a grade four model [12]. In chapter 2 of [13] foundations for the transformation of mathematical models with Matlab are described.

55.4 Design and Implementation

55.4.1 OPC Communication Structure

Figure 55.5 shows the structure to establish communication between the controllers design software (Matlab) and the real plant, where the S7-1200 PLC performs the function of a data acquisition card, that is, to receive and send signals from the real plant to the computer and vice versa through physical connection via Ethernet port. OPC communication acts as a gateway to read and write data from Simulink to the PLC.

55.4.2 Predictive Control Development

The tuning parameters for the predictive control are the result of an experimental process based on the theoretical foundations and the application of the physical restrictions of the plant [14]. The detail of all the tuning parameters of the predictive controller is shown below (Table 55.1).

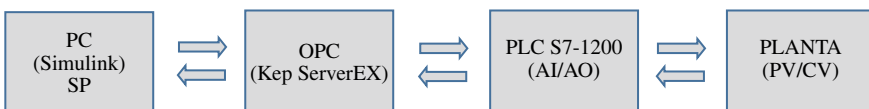


Fig. 55.5 Communication structure between the actual plant and the design software

Table 55.1 MPC tuning parameters

Forecast horizon	20 s	Control horizon	1 s
Restrictions		Min	Max
Input		0	62%
Output		0	80 LMP
Change in control signal		-1.4	1.4
Weights associated with input and output signals			
Input		5	
Output		5	

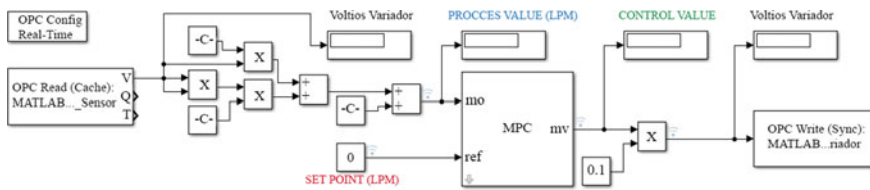


Fig. 55.6 Structure for the implementation of an MPC using OPC communication

The structure necessary for the implementation in a real plant is shown in Fig. 55.6, where the use of the OPC reading and writing blocks is observed, to establish communication between the input and output of the real system. Converting the voltage from the sensor to flow units in LPM is done using Eq. 55.2.

55.4.3 PID Control Development

For the calculation of the tuning constants, the lambda method is used because it makes use of the values given by the FOTD transfer function (Fig. 55.4a). The results of this process are given in Table 55.2. where:

Table 55.2 Lambda method equations

PI		PID	
Aggressive	Strong	Aggressive	Strong
$K = \frac{1}{K_p} \frac{T}{L+T} = 0.1998$	$K = \frac{1}{K_p} \frac{T}{L+3T} = 0.1484$	$K = \frac{1}{K_p} \frac{L/2+T}{L/2+T} = 0.9934$	$K = \frac{1}{K_p} \frac{L/2+T}{L/2+3T} = 0.5835$
$T_i = T = 0.49269$	$T_i = T = 0.49269$	$T_i = T + L/2 = 1.402$	$T_i = T + L/2 = 1.402$
-	-	$T_d = \frac{TL}{L+2T} = 0.3196$	$T_d = \frac{TL}{L+2T} = 0.3196$

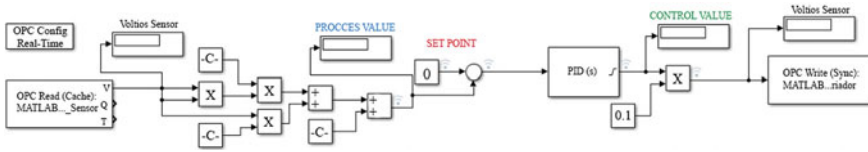


Fig. 55.7 Structure for the implementation of a PID controller using OPC communication

$$Kp = Kp; \quad T = Tp1; \quad L = Td$$

The programming structure for the implementation of the PID controller is similar to that used by the MPC controller, making use of the read and write OPC communication blocks. And in the same way, the input and output signals are transformed to their respective units and operating ranges in volts, as shown in Fig. 55.7.

55.5 Results

55.5.1 Experimental Results.

Figure 55.8 shows the response obtained in the control of the flow variable using a predictive control algorithm (a) and PID (b) in which the curve of the process variable is appreciated as well as the set point, in the case of the PID with a more aggressive response than the MPC, but without showing overshoots.

55.5.2 Results Comparison

Maximum Overshoot (Mp) and Peak Time (Tp)

The overshoots or overshoots are practically nil, as both controllers have a critically damped curve, and since there are no overshoots, there will be no peak times either, since these two for meters are closely related (Fig. 55.9a).

Delay Time (Td)

It is the time required for the variable to reach 50% of the final value, in the case of the MPC this time is 8 s and 4 s for the PID, reflecting a noticeable difference in favor of the PID controller in this parameter (Fig. 55.9b).

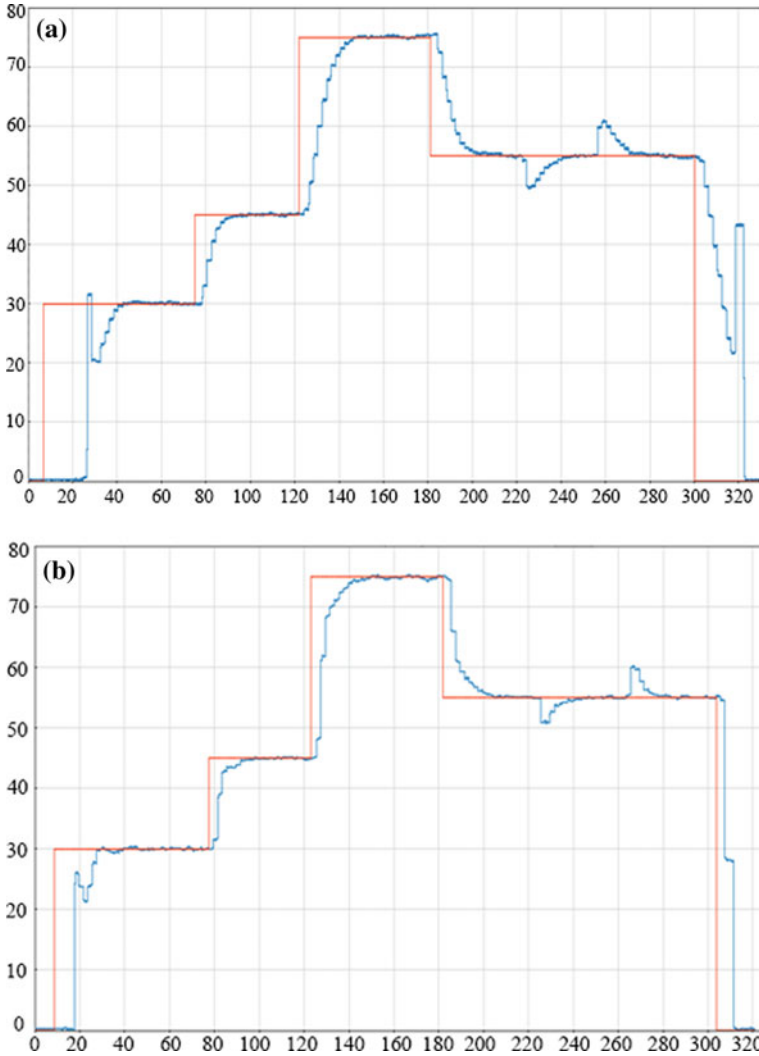


Fig. 55.8 Result of an implemented MPC control (a), Result of an implemented PID control (b)

Rising Time (T_r) and Settling time (T_s)

The rise time is the instant it takes for the variable to go from 10 to 90% of the final value, and this parameter clearly reflects the aggressive tuning with which the PID manipulates the control action and therefore its effect on the process variable, taking 4 s less than the MPC, which has a more gradual control action due to its restrictions (Fig. 55.10a).

By contrasting the time it takes for the variable to reach the reference end point in a step of 45–75 LPM, the MPC controller takes approximately 26 s to reach the

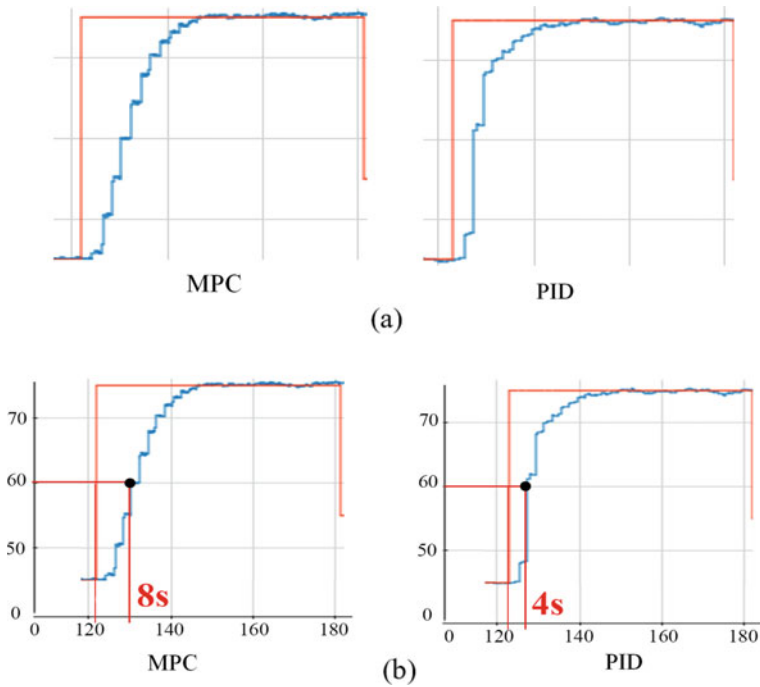


Fig. 55.9 Response to overshoot (a), Delay time analysis (b)

setpoint, while the PID in this parameter is one second slower, taking approximately 27 s (Fig. 55.10b).

Stability and Oscillations

When the controllers have brought the variable to 75 LPM, substantial differences are observed in terms of the stability of the process variable, marking a better stability with the MPC and with respect to the PID, it shows certain variations without straying too far from the set point. For lower ranges like 45 LPM both controllers keep the process variable totally stable (Fig. 55.11).

Response to Disturbances

In zone one, an external disturbance appears due to the throttling of the valve, generating a reduction in the flow of approximately 5 LPM, and therefore, the response of the controller is to increase the pump flow until the variable returns to the set point, delaying this action. Corrective time of 20 s for both controllers and for zone two with an overflow of approximately 5 LPM due to the total opening of the valve, the PID control has a faster response in 2 s with respect to the MPC. In general, both controllers have a good response to disturbances with quite similar times (Fig. 55.12), which reflects an even performance. This result supports other theses with similar results such as [3, 10, 15].

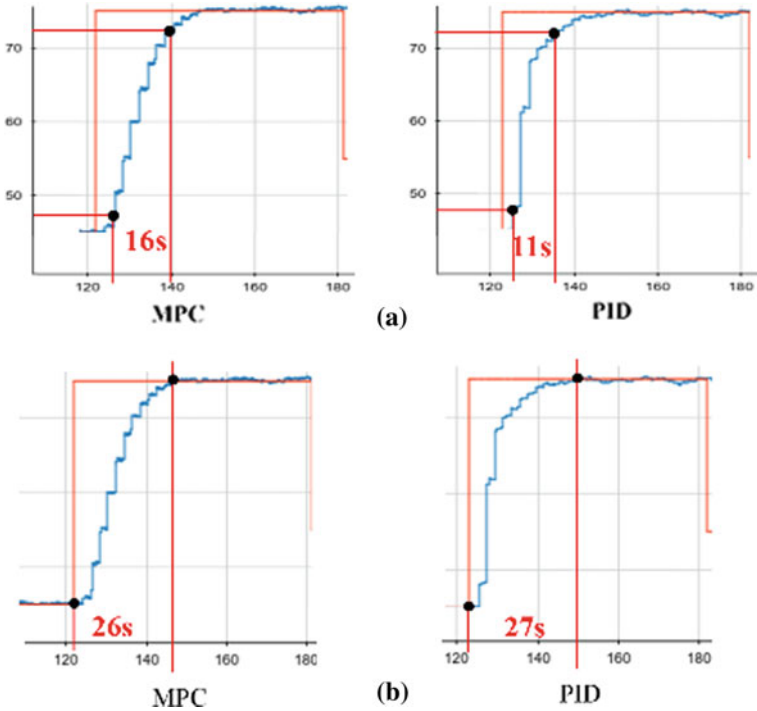


Fig. 55.10 Rise time between an MPC and PID control (a), Settling time for an MPC and PID control (b)

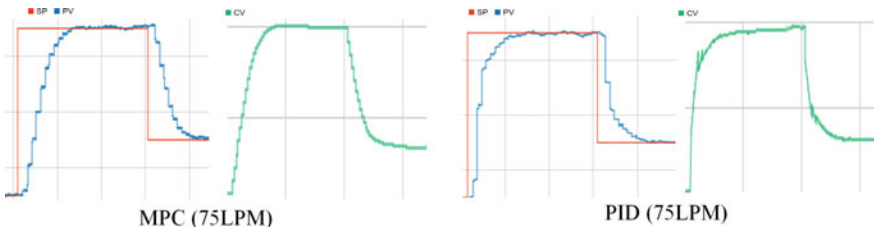


Fig. 55.11. Stability analysis of MPC and PID controllers at 75LPM

55.6 Conclusions

The mathematical tools involved in each of the controllers represent a turning point in favor of the PID control due to its simple and intuitive functions, while the MPC control requires complex mathematical tools, this being one of the causes of the massive use of the classical control compared to modern control.

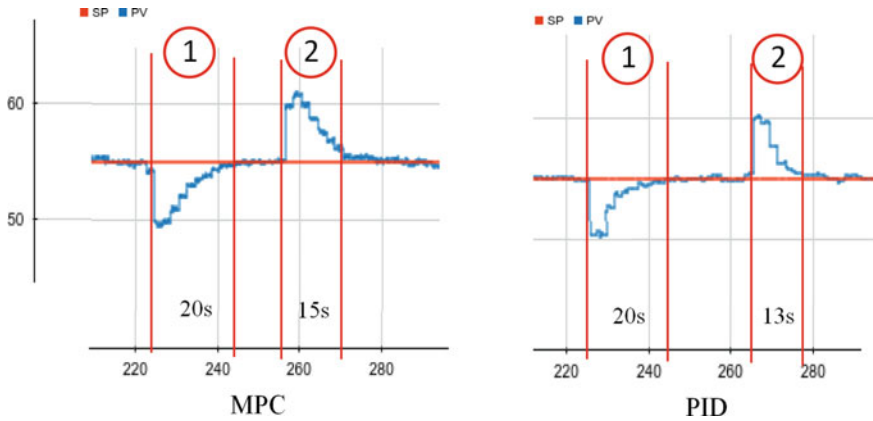


Fig. 55.12. Response to disturbances of an MPC and PID control

The parameters that evaluate the transient response of the MPC and PID mark a difference proportional to each other, that is, at larger steps, the greater difference between their times and at small steps the difference will be less; however, these differences are simplified by having a settling time and rejection of disturbances by the same practitioner, causing both controllers to take the same time to reach a set point.

In this particular case, given the results obtained with an equivalent performance in general terms for both controllers, the most viable option is the implementation of a PID control due to its simple and intuitive logic, easier tuning method, use of conventional control equipment and more economical; however, it should be taken into account that the performance of a predictive controller applied to a SISO process is being evaluated and compared, and it is worth mentioning that one of the strengths of this controller is in the management of the MIMO process.

By successfully implementing a predictive controller and comparing its performance with that of a PID controller in a simple input and output system, a basis has been established for future research that will allow us to achieve the implementation of controllers in multivariable systems in order to further explore the potential of controlling predictive.

References

1. Alvarez, X.: Control predictivo de canales de riego utilizando modelos de predicci3n de tipo Muskingum (primer orden) y de tipo Hayami (segundo orden). Universidad Polit3cnica de Catalu1a, Catalu1a (2004)
2. Roca, A.: Control Autom3tico de Procesos Industriales, Diaz de Santos (2014)

3. Lopera, E., Mejía D.: Implementación de un Control Predictivo Basado en Modelo Aplicado a un Sistema de Control de Caudal de Agua Didáctico. Instituto Tecnológico Metropolitano, Antioquia (2010)
4. TECNOLOGIAVAO, «Tecnología para la Industria». <https://tecnologiaparalaindustria.com/cual-es-el-mejor-metodo-de-control-de-flujo-de-bombas/>
5. Moncada, L.: Automatización y Control de Procesos. Universidad Nacional de Trujillo, Trujillo (2005)
6. Bordóns, C.: Control Predictivo: Metodología, Tecnología y Nuevas Perspectivas. Escuela Superior de Ingenieros, Sevilla (2000)
7. Lozoya, C.: Modelo de control predictivo aplicado a sistemas de riego de precisión. Tecnológico de Monterrey, Monterrey (2014)
8. Ortiz, J.M.: Diseño y Construcción de un Convertidor DC/DC Reductor Elevador con Control Predictivo Controlado por una Tarjeta FPGA. EPN, Quito (2011)
9. Acedo, J.: Control Avanzado de Procesos (Teoría y práctica). Diaz de Santos, Madrid (2003)
10. Aceros, E., Parabavire, O.: Comparación Cualitativa del Desempeño de la Aplicación del MPC y el PID para el Control de Nivel de Pozos. Universidad Central de Venezuela, Caracas (2016)
11. Domínguez, S., Campoy, P., Sebastian, J., Jiménez, A.: Control en el Espacio de Estados. Pearson, Madrid (2006)
12. Guambo, W.G.: Estudio comparativo de un control Predictivo y PID aplicado a un proceso didáctico de caudal. Universidad Técnica de Cotopaxi, Latacunga (2021)
13. Nise, N.: Sistemas de Control para Ingeniería. Compañía Editorial Continental, México (2006)
14. Ogata, K.: Ingeniería de Control Moderna. PEARSON EDUCACIÓN S.A, Madrid (2010)
15. Olídem, J.C.: Desarrollo de un Controlador Predictivo basado en Modelo para Plataforma Industrial. Universidad de Piura, Piura (2016)

Chapter 56

Analysis Factors in the Adoption of Digital Manufacturing Technologies in SMEs



Luisa Maria Tumbajoy and Mariela Muñoz-Añasco

Abstract Small and medium enterprises (SMEs) are investing in adoption of digital manufacturing technologies to scope system complexity, increase information visibility, improve production performance, and gain competitive advantages in the global market. This article presents an analysis of the technology adoption models for the implementation of digital manufacturing to identify which factors influence the implementation process. We discuss the methodology for using technology adoption models. We hope this work will help multidisciplinary research efforts to advance in the adoption of digital manufacturing technologies in SMEs.

56.1 Introduction

Technology adoption refers to incorporating technologies from outside a given system; it is a process of permanent change that unfolds under conditions of uncertainty and diversity of agents. This process is complex from a technical and social perspective because it involves contextual, emotional, and cognitive factors [1]. Thus, when a study focused on implementing one or more digital tools, it is generally done using some available technology adoption model or its adaptation. Each adoption model represents a framework to determine the critical factors influencing the adoption of technologies from users and the technologies' use and behavior within the organization [1].

Digital manufacturing technologies (DMT) belong to the Fourth Industrial Revolution Framework. These key technologies are based on the principles of connectivity, automation, integration, computing, and transforming traditional

L. M. Tumbajoy (✉) · M. Muñoz-Añasco
Department of Electronic, Instrumentation and Control, University of Cauca,
Popayán, Colombia
e-mail: ltumbajoy@unicauca.edu.co

M. Muñoz-Añasco
e-mail: mamunoz@unicauca.edu.co

factories into smart ones [2]. Nowadays, companies need to apply adoption models for embracing these technologies to remain competitive and active in the market. Thus, the implementation of DMT is a timely topic that requires attention.

This article uses technological adoption models available in the literature as analytical tools to understand the implementation process of DMT. The analysis is performed to determine how the technological adoption models can be used to adopt DMT, specifically in small and medium enterprises (SMEs). Furthermore, the analysis aims to establish the methodological steps and tools used to evaluate the relationship of the involved factors in adopting the technologies.

The remainder of the paper starts with identification of theoretical and conceptual elements of technology adoption models oriented to the adoption of DMT. Subsequently, a description of the methodology in the implementation of these models is presented. Finally, the article proposes reflections and conclusions about the study of the adoption of DMT in SMEs guided by the theoretical technology adoption models.

56.2 Methodology

Different stages have been proposed to analyze the technology adoption models reported in the literature regarding their application in the adoption of DMT:

- (i) A documentary search aimed at collecting information regarding studies related to the use of technology adoption models applied to the implementation process of DMT in SMEs, i.e., integrated engineering systems, digital automation with sensors, simulations, big data collection and analysis, digital product–service items, additive manufacturing, cloud services, and blockchain [3]. The construct used in the research engine was “smart manufacturing” OR “industry 4.0” AND “technology adoption models” AND “SMEs”.
- (ii) Information filtering by adjusting each database to the specific requirements, such as year of publication (between 2010 and 2021); type of publication (journal articles, conferences, and books); search by title, keyword, and abstract. The filtering allows obtaining highly relevant articles in broad access digital libraries such as Science Direct, IEEE, Taylor and Francis, and Google Scholar.
- (iii) The inclusion criteria include studies involving models of adoption of DMT and written in English. As exclusion criteria, non-relevant studies have been disregarded, namely studies that do not discuss the use of digital manufacturing technology adoption models.
- (iv) Identify the constructs employed within the proposed model. Then group constructs with similar characteristics and find out those constructs oriented to DMT technical characteristics and SME’s particular.

Initially, a total of 89 studies were obtained. An analysis of each of the selected studies was performed to determine the adoption model involved, the scope of application, and the results obtained. Then, by comparing the selected studies, it was possible to determine common stages, establish the tools used, and group them according to similar characteristics. Finally, the results of each study were considered to obtain the common factors involved in the process of implementation of DMT in SMEs.

Some general conclusions are presented in the following section regarding the scope of the models of adoption of DMT in SMEs.

56.3 Results and Discussion

Technology adoption is a complex process from a technical and social perspective that also involves contextual, emotional, and cognitive factors [1]. For this reason, when a study involving the implementation of a digital tool or several tools is conducted, it is generally done using some adoption model present in the literature or an adaptation of it. Technology adoption models have been applied in various fields to understand and determine which critical factors influence this process [4].

According to the selected studies, it must be highlighted that the implementation of a technology adoption model begins with selecting the model that fits the needs to be explored. Moreover, each model presents some constructs or main factors related to each other, and each construct could consist of more specific factors.

Regarding models and theories of technology adoption, the literature presents the following: Diffusion of Innovations Theory (DOI), Technology Organization Environment (TOE), Technology Acceptance Model (TAM), Theory of Planned Behavior (TPB), Theory of Reasoned Action (TRA), Theory of Interpersonal Behavior (TIB), Unified Theory of Acceptance and Use of Technology (UTAUT), among others [1].

Within the implementation process of DMT, technology adoption models allow identifying relationships between the technological tool and the process in which it is implemented. For example, authors in [5] identify blockchain's relationship with supply chain management, taking as an analysis tool an adaptation of the TOE model. Similarly, in [6], blockchain analysis in supply management systems is performed using an adaptation of the TOE and TPB models. Furthermore, in [7], an adaptation of TAM and ECM is presented to study the implementation of digital manufacturing.

The models of adoption of DMT can be used not only within industrial processes as discussed in [5–7] but also in non-industrial processes, as evidenced in [8], where a study is conducted through the theory of planned behavior (DTPB) model to analyze big data in disaster management.

The adoption models used in the analyzed studies are compiled in Table 56.1, differentiating those oriented toward SMEs.

Table 56.1 Adoption models used

ID	Author	SMS's	Model
1	Masood and Sonntag [9]	YES	TAM
2	Junior et al. [10]	YES	TOE—DOI
3	Khayer et al. [11]	YES	TOE
4	Mayaram et al. [12]	YES	TOE
5	Khayer et al. [13]	YES	UTAUT—TOE
6	Rababah et al. [14]	YES	TOE
7	Ghobakhloo and Ching [15]	YES	TOE
8	Awa and Ojiabo [16]	YES	TOE
9	Masood and Egger [17]	NO	TOE
10	Fosso Wamba et al. [5]	NO	TOE
11	Zaman et al. [8]	NO	DTPB
12	Kamble et al. [6]	NO	TAM—TPB
13	Sepasgozar [7]	NO	TAM—ECM

According to the analysis of the selected studies, the most widely applied model is the TOE and its implementation together with other adapted models. TOE is a classical framework that proposes a generic set of factors that influence the adoption and/or implementation of technological innovations: the organizational context, the environmental context, and the technological context [4].

The adoption models reported in the literature present some general constructs already established, on which specific characteristics of analysis are defined. Specifically, the general constructs of the adoption models mentioned in the studies analyzing SMEs are described as follows. In [9], the TAM model was used with the following general constructs: external factors, perceived challenges, and perceived benefits. Studies [10–12, 14–16] used the TOE model, with the following general constructs: organization context, technology context, and environment context. In [13], an adaptation of the TOE and UTAUT models is made, and the following constructs were defined: performance expectancy, effort expectancy, absorptive capacity, technology readiness, competitive pressure, regulatory support, data security and privacy, and perceived trust.

After selecting a model and defining the characteristics in each construct, possible relationships between them, known as hypotheses, are established. For example, in [9], the model used was the TOE. Within the general constructs (explained previously), the following specific characteristics were defined for the external factors construct: Company size, manufacturing complexity, and attitude toward Industry 4.0. Next, six hypotheses were defined, seeking to relate the constructs to each other, as shown in Fig. 56.1.

Once the theoretical model has been adapted to the particular problem, the validation process begins. Most studies use questionnaires or surveys as data collection tools to validate the hypotheses formulated. Usually, the Likert scale is used as a measurement tool in this type of questionnaire since the factors analyzed are

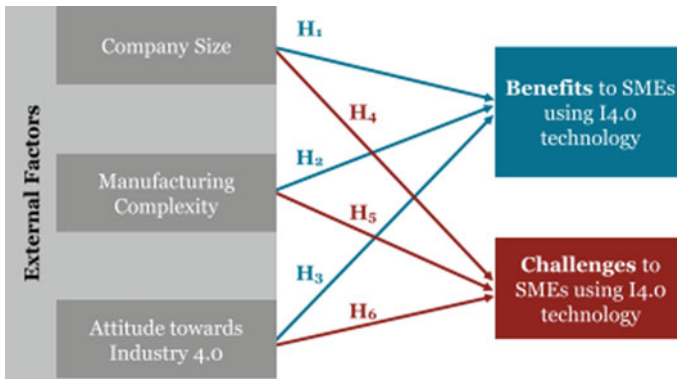


Fig. 56.1 Example of a proposed technology adaption model. Taken from [9]

generally qualitative. Moreover, with this scale, the answers can be offered at different levels of measurement from a quantitative point of view [18].

Initially, the data collected from the questionnaires were processed using statistical tools for reliability and data quality analysis. Next, the relationship modeling of the constructs evaluated was performed, i.e., the design of a formalism to evaluate the proposed hypotheses from the data based on construct relationship tools [19].

It can be seen that in the studies analyzed, a combination of these tools is used to validate data reliability. Table 56.2 contains a compilation of the statistical tools applied.

Table 56.2 Compilation of statistical tools

Reliability tools
Kaiser Meyer Olkin (KMO)
Mardia multivariable test of normality
Robust maximum likelihood MLM
Satorra–Bentler corrected
Cronbach’s Alpha
Dijkstra–Henseler’s rho
Average variance extracted (AVE)
Heterotrait-monotrait ratio of correlations (HTMT)
Fornell-Lacker criterion
Maximum Likelihood (ML) method
Importance–performance map analysis (IPMA)
Variance inflation factor (VIF)
Kaiser Normalization
The Exploratory Factor Analysis
Common Method Variance (CMV)

The tools used in the studies analyzed for construct relationship analysis are structural equation modeling (SEM), partial least square method (PLS-SEM), neural network analysis, technology adoption decision-making, and multiple regression analysis. Notice that from the total of the selected studies (13 studies), there is a preference for the SEM tool and its variant partial least square method (PLS-SEM) since nine of them apply it.

SEM is a set of multivariate statistical techniques, which establish the dependence relationship between variables. Within SEM, there are two types of approaches: covariance (CB-SEM) and the PLS-SEM, establishing the dependency relationship between the variables involved. When working with SEM, there is the advantage of testing all the hypotheses simultaneously since each variable's behavior is analyzed against the others [19].

Data interpretation through these tools helps establish whether the model is correct and the acceptance or rejection of the proposed hypotheses.

56.3.1 Methodological Application of Models in the Adoption of Digital Manufacturing Technologies in SMEs

Some studies in the literature identified the use of technology adoption models for adopting DMT in SMEs, taking into account some particular characteristics of SMEs, such as size, purchasing power, and the type of industry [12].

Authors in [9] use the TOE model to analyze the benefits and challenges of implementing DMT in SMEs. In [15], an analysis of the influence factors of technologies on DMT implementation in SMEs is presented. Similarly, in [10], the TOE model is used to adapt a tool of the technological pillars defined for Industry 4.0 as a vertically integrated enterprise resource planning (ERP) system applied to SMEs. In [11], a study of the implementation of cloud computing in SMEs is performed using SME and neural network analysis. Another tool analyzed with an adaptation of TOE is presented in [12], where the ERP integration tool in SMEs is examined. In [13], the TOE plus UTAUT model is adapted to evaluate the implementation of cloud computing technology in SMEs. Similarly, in [14], TOE is used to analyze cloud computing implementation in SMEs in Jordan.

From DMT are identified augmented reality, blockchain, and big data analyzed in the selected studies. And cloud computing and ERP analyzed in the selected studies about SMEs.

The impact of DTM adoption is highlighted in [7] since it improves the understanding of the digital technologies providers and improves the behavior of the customers toward their use, which increases the adoption rate. Authors in [5] indicate that knowledge sharing among stakeholders and pressure from partners in adopting blockchain technology are good predictors for technology implementation. Moreover, they also state that the type of manufacturing company does not

represent a determining characteristic for the implementation. In [17], the authors conclude that technological factors and organizational fit are critical for augmented reality adoption success. In [6], evidence is provided toward stating that the perceived usefulness, attitude, perceived behavioral control, and subjective norms are directly related to applying the blockchain technology tool. Notice that the studies mentioned above are applied to industry in general.

On the other hand, the finding for studies focused on the application and/or adoption of DMT, particularly in SMEs, is presented as follows. According to [9], most SMEs struggle with the abundance of available digital technologies, the time to learn about them, and the funding to implement them. Furthermore, the size and type of the company affect the benefits of implementing DMT. Similarly, [16] identifies that firm size is a determinant of ERP adoption, in addition to infrastructure, technical know-how, perceived compatibility, perceived values, and security. Thus, [16] highlights that ERP adoption is mainly driven by technological factors.

In [13], it follows that SMEs should focus their attention on developing technology infrastructure and ICT knowledge to get the maximum benefit from cloud computing adoption. Similarly, [14] proposes that technology availability and compatibility have the most significant influence on cloud computing adoption. In [15], the authors recognize that planning each step is necessary for SMEs, e.g., having a timeline and detailed costs and benefits associated with the adoption of DMT. The authors also state that the strategic path should address technology maturity, digitization maturity, organizational readiness, digitization knowledge, and integration capability. Hence, maturity models are proposed as an assessment tool.

Other studies, on the contrary, mention that the firm size variable is not important in the explanation of ERP adoption [10]. Authors in [11] also identify that firm size and type do not cause significant variation in the performance of cloud computing adoption.

It should be remarked that there are common analysis factors, such as technology compatibility, technological knowledge, company size, and implementation costs. However, although they are notable and relevant to be studied, these are not necessarily positively influencing variables.

56.4 Conclusion and Further Studies

From the information gathered, it can be inferred that it is necessary to examine the technical components of implementation as well as the social and administrative components involved to analyze the adoption of technologies within a system.

For this reason, the technology adoption analysis process is guided by theoretical technology adoption models. These models provide theoretical bases for the various components present in technology adoption. An analysis methodology is distinguished, beginning with selecting the theoretical adoption model, particularly

adapted to each case's needs. Then, the proposed model needs to be validated through statistical analysis of data collected through questionnaires. Finally, the components that are related to the implementation of the technology can be identified.

It was found that the theoretical technology adoption models have been used to project how the components involved in the implementation can respond to the original system's adoption of a particular technology. It was also shown that the technology adoption models are applied for analyzing the adoption of any technology into any enterprise or process, whether the process is industrial or not. This includes DMT and SMEs, taking into account the company size and the implementation costs.

As a result, in the analysis of the adoption of DMT in SMEs, the following components stand out as common: technological (e.g., technology compatibility, perceived compatibility, and technological readiness); social (e.g., attitudinal, perceived behavioral); and organizational (e.g., management support).

According to the results of analyzing the adoption models of DMT in SMEs, the authors proposed to examine their inclusion in a decision-making model to implement the studied technologies.

References

1. Taherdoost, H.: A review of technology acceptance and adoption models and theories. *Proc. Manuf.* **22**, 960–967 (2018)
2. Gillani, F., Chatha, K.A., Sadiq Jajja, M.S., Farooq, S.: Implementation of digital manufacturing technologies: antecedents and consequences. *Int. J. Prod. Econ.* **229**, 107748 (2020)
3. Dalenogare, L.S., Benitez, G.B., Ayala, N.F., Frank, A.G.: The expected contribution of Industry 4.0 technologies for industrial performance. *Int. J. Prod. Econ.* **204**, 383–394 (2018)
4. Lai, P.: The literature review of technology adoption models and theories for the novelty technology. *J. Inf. Syst. Technol. Manag.* **14**(1), 21–38 (2017)
5. Fosso Wamba, S., Queiroz, M.M., Trinchera, L.: Dynamics between blockchain adoption determinants and supply chain performance: an empirical investigation. *Int. J. Prod. Econ.* **229**, 107791 (2020)
6. Kamble, S., Gunasekaran, A., Arha, H.: Understanding the blockchain technology adoption in supply chains-Indian context. *Int. J. Prod. Res.* **57**(7), 2009–2033 (2019)
7. Sepasgozar, S.M.E.: Digital technology utilization decisions for facilitating the implementation of industry 4.0 technologies. *Constr. Innov.* (2020)
8. Zaman, U., Zahid, H., Habibullah, M.S., Din, B.H.: Adoption of big data analytics (BDA) technologies in disaster management: a decomposed theory of planned behavior (DTPB) approach. *Cogent Bus. Manag.* **8**(1), 1880253 (2021)
9. Masood, T., Sonntag, P.: Industry 4.0: adoption challenges and benefits for SMEs. *Comput. Ind.* **121**, 103261 (2020)
10. Junior, C.H., Oliveira, T., Yanaze, M.: The adoption stages (evaluation, adoption, and routinisation) of ERP systems with business analytics functionality in the context of farms. *Comput. Electron. Agric.* **156**, 334–348 (2019)

11. Khayer, A., Talukder, M.S., Bao, Y., Hossain, M.N.: Cloud computing adoption and its impact on SMEs' performance for cloud supported operations: a dual-stage analytical approach. *Technol. Soc.* **60**, 101225 (2020)
12. Mayaram, U., Dussoye, A., Cadessaib, Z.: ERP acceptance model for SMEs based on CSFs. In: *Proceedings of NextComp 2019*, pp. 1–6 (2019)
13. Khayer, A., Jahan, N., Hossain, M.N., Hossain, M.Y.: The adoption of cloud computing in small and medium enterprises: a developing country perspective. *VINE J. Inf. Knowl. Manag. Syst.* (2020)
14. Rababah, K.A., Al-nassar, B.A., Al-Nsour, S.N.: Factors influencing the adoption of cloud computing in small and medium enterprises in Jordan. *Int. J. Cloud Appl. Comput.* **10**(3), 96–110 (2020)
15. Ghobakhloo, M., Ching, N.T.: Adoption of digital technologies of smart manufacturing in SMEs. *J. Ind. Inf. Integr.* **16**, 100107 (2019)
16. Awa, H.O., Ojiabo, O.U.: A model of adoption determinants of ERP within TOE framework. *Inf. Technol. People* **29**(4), 901–930 (2016)
17. Masood, T., Egger, J.: Augmented reality in support of Industry 4.0—implementation challenges and success factors. *Robot. Comput. Integr. Manuf.* **58**, 181–195 (2019)
18. Chintalapati, N., Daruri, V.S.K.: Examining the use of YouTube as a learning resource in higher education: scale development and validation of TAM model. *Telemat. Inf.* **34**(6), 853–860 (2017)
19. Davvetas, V., Diamantopoulos, A., Zaefarian, G., Sichtmann, C.: Ten basic questions about structural equations modeling you should know the answers to—but perhaps you don't. *Ind. Mark. Manag.* **90**, 252–263 (2020)

Chapter 57

Analysis of Microstructural Features and Corrosion Resistance of Cryogenic Burnished and Hydroxyapatite Powder Burnished Titanium Alloy



Samatham Madhukar, Gyara Ajay Kumar, Dharamkar Sai Suman, Syed Azam Pasha Quadri, and U. Ashok Kumar

Abstract Titanium is one of the super-hard alloys and the fastest-growing materials used in defense, aerospace, and biomedical sectors due to its outstanding properties like high strength to weight ratio, better corrosion resistance, and good fatigue life. In traditional machining methods like turning, milling, and grinding, the required surface finish for biomedical and aerospace applications cannot be obtained for titanium alloys. To overcome these problems in aerospace and medical areas, one of the latest innovative methods employed is cryogenic burnishing and HA powder burnishing. In this work, surface characterization is studied using the scanning electron microscope and corrosion analysis is studied using an electrochemical corrosion test. SEM micrographs and corrosion analysis confirmed that better surface roughness is obtained in traditional burnishing and better corrosion resistance is obtained in the HA powder burnishing.

57.1 Introduction

Burnishing process is one of the fine surface finishing methods that is performed by applying an extremely polished tungsten carbide ball to roll against the metallic surface (Fig. 1a) under desired pressure depending on the type of material, which in turn helps in smoothing of the surface. (Fig. 1c) [1–6]. The combination of elements like equivalent compressive residual stress, reduced surface roughness, and micro-notches is the significant aspects of the burnishing process.

S. Madhukar (✉) · G. A. Kumar · D. S. Suman · S. A. P. Quadri
Department of Mechanical Engineering, Lords Institute of Engineering and Technology,
Osmania University, Hyderabad 50091, India

U. Ashok Kumar
Department of Mechanical Engineering, University College of Engineering, Osmania
University, Hyderabad 50091, India

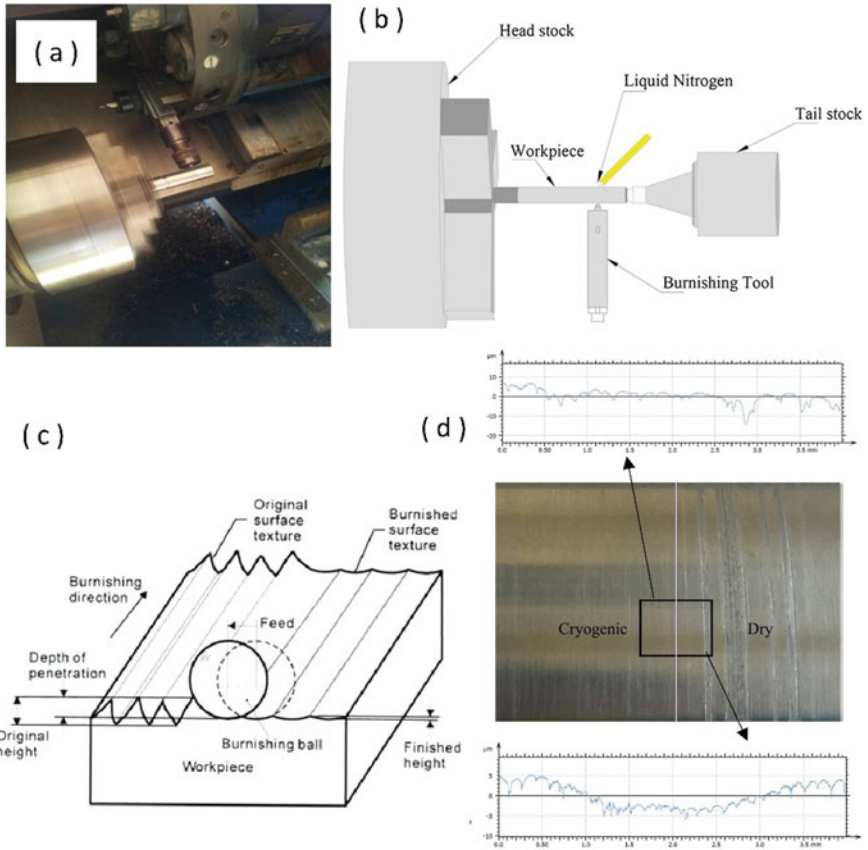


Fig. 57.1 a Burnishing operation, b cryogenic burnishing setup, c diagrammatic representation of burnishing operation, and d surfaces of HA powder and cryogenic burnished samples

Ti-6Al-4V is one of the complex to machine material and to overcome this disadvantage one of the recently developed surface engineering methods in mechanical surface treatment processes is cryogenic burnishing in which traditional oil coolant is replaced by liquid nitrogen which is dispensed either manually or automated and this process can be carried out on a conventional lathe machine [6–10]. Only a few researchers had worked on this type of method, but still, there are no clear conclusions on the effects of process variables during the burnishing of titanium alloys. In the current work, new method hydroxyapatite powder (HA) powder burnishing is used in which the traditional oil-based coolant is replaced by water-mixed HA powder. Surface microstructure analysis and corrosion analysis are carried for both burnished samples in this work.

57.2 Experimental

Titanium (Ti–6Al–4V) with a chemical combination of (wt%) of approximately 6.29 aluminum, 4.17 vanadium, 0.025 iron, 0.007 of carbon, 0.001 nitrogen, 0.0012 hydrogen, 0.14 oxygen, and the balance of titanium are selected for the experiment. Burnishing operations were performed on Hindustan Machine Tools (HMT) high-precision lathe NH22 which has spindle power of 11 kW making it capable of providing rotation speed range from 40 to 2040 rpm. A specially designed ball burnishing tool that has a spring attachment for the accurate surface contact of the material with the tungsten ball of diameter 19 mm is used for the entire experiment [1, 11–13].

The experiments were performed at cryogenic conditions as per the L9 orthogonal array with three levels and four factors. The proposed performance characteristics are determined using Minitab software by applying signal-to-noise ratio and using lower the best condition for surface roughness. The surface roughness of the burnished samples is measured by the Taylor Hobson S-100 series machine which can calibrate to ISO 4287 roughness standard. The Stylus tip radius of 5 μm , measuring the length of 4 mm and measuring the speed of 1 mm/s (0.04 in/s) with a gauge resolution of 6 nm, is used for the entire testing of eighteen samples. Microstructure at various regions of the burnished was captured using a scanning electron microscope (SEM) [14–16].

Electrochemical tests are performed by employing a conventional three-electrode cell in which the saturated calomel electrode was the reference electrode, selected titanium alloy was the working electrode, and a Pt wire was the counter electrode. All electrochemical experiments were performed using a SII287 model of Solartron Company controlled by a computer in Ringer's solution which composed of 8.62 g NaCl, 0.34 g KCl, 0.02 g NaHCO₃, and 0.35 g CaCl₂, with the remainder being distilled water. Electrochemical corrosion analysis was carried out at a temperature of 37 ± 1 °C. The samples which are having an exposed working surface area of nearly 1 cm² were prepared in epoxy resin providing a contact using copper wire. Before the tests, working electrode was kept in the Ringer's solution for 24 h to enable it to reach stable potential before the test. Then, cathodic pre-polarization was conducted at –0.8 V for 260 s for the removal of oxides, and an open circuit potential (OCP) test was performed. Electrochemical impedance spectroscopy analysis was performed at the OCP in an ample frequency range from 10 μHz to 32 MHz with 10 μHz resolution. The potentiodynamic polarization curves were obtained from –1.2 to +1.5 V at a scan rate of 1 mV/s. All the potentials reported in the present work are with reference to the SCE. To obtain accurate results, all the experiments were repeated minimum of three times using a fresh Ringer's solution every time.

57.3 Results and Discussion

The effect of the HA powder burnishing and cryogenic burnishing treatment on the microstructure of titanium alloy is evaluated using the Hitachi S 3400 N model scanning electron microscope with EDS attachment. Figure 57.2 a, c, e shows the micrographs of HA powder burnished samples, and Fig. 2b, d, f shows the micrographs of traditional burnished samples. The reduction in surface hardness in the HA powder burnished sample is due to the presence of material tearing which can be evaluated in the SEM image (Fig. 2c) where no material tearing is seen in the cryogenic burnished sample. More feed marks are visible in the SEM image (figure b) of the HA powder burnished sample which concludes that higher surface roughness values are obtained due to these feed marks. The 3D surface plots (Fig. 2h, g) generated by ImageJ software also show that the higher peaks are seen in traditional burnished samples as compared to the HA powder burnished samples.

Potentiodynamic polarization curves of the cryogenic and HA powder samples are represented in Fig. 57.3a, b. The significant change in the corrosion rate (mpy) for the samples is shown and presented in Table 57.1. Based on the previous works, it can be concluded that corrosion resistance is excellent (less than 1 mpy) for both samples and better of both is obtained for HA burnished sample.

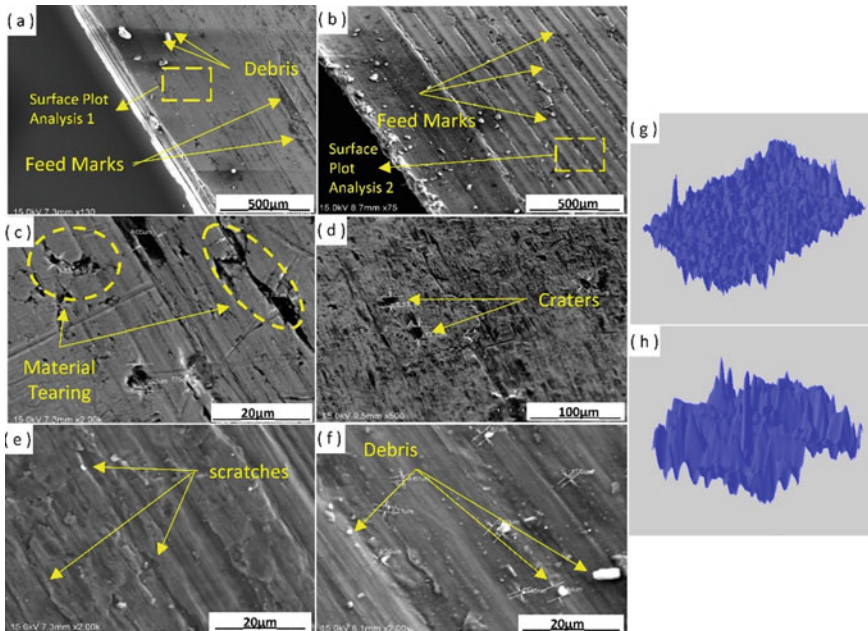


Fig. 57.2 a–c SEM images of dry burnished sample 4, d–f SEM images of cryogenic burnished samples 4, g 3D surface plot of dry burnished sample 4, and h 3D surface plot of a cryogenic burnished sample

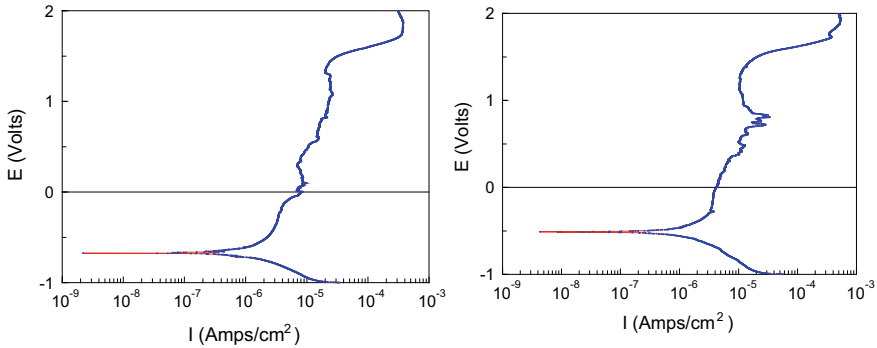


Fig. 57.3 Potentiodynamic polarization curves of Ti-6Al-4V of **a** cryogenic burnished sample and **b** HA powder sample

Table 57.1 Corrosion test result of Ti-6Al-4V cryogenic burnished sample and HA powder sample

Parameter	Cryogenic sample	HA powder sample
Corrosion rate (MPY)	0.43904	0.35079
Corrosion rate (mm/year)	0.011	0.009
Rp (Ohms/cm ² ~)	41,449	51,877
Io (Amp/cm ² ~)	6.2938E-7	5.0287E-7
Eo (Volts)	-0.51095	-0.51095

57.4 Conclusions

The electrochemical corrosion tests used in this work revealed that very low corrosion current densities were obtained for both cryogenic and HA powder burnished titanium alloy samples tested in Ringers’ solution showing that they are passive in this electrolyte. The improved corrosion performances of the HA powder burnished sample can be attributed to the formation of higher peaks in ImageJ microstructure analysis when compared with the traditional burnished sample. This conclusion shows a way for the use of HA powder as a coolant to manufacture human implants in traditional machining in the coming future which indirectly reduces the cost of an implant.

References

1. Surface modification of β-phase Ti implant by hydroxyapatite mixed.pdf, (n.d.)
2. Samatham, M., Kumar, A., Pappula, U.L.: Critical review on different burnishing processes of Ti-6Al-4V alloy. Int. J. Sci. Res. Sci. Eng. Technol. (2020). <https://doi.org/10.32628/ijrsret20721>

3. Sai, P.V., Madhukar, S., Krishna, M., Reddy, P., Rao, N.V.S.R.: A review on machinability aspects of titanium grade-2. *Ijrsret* (2017)
4. Revankar, G.D., Shetty, R., Rao, S.S., Gaitonde, V.N.: Wear resistance enhancement of titanium alloy (Ti-6Al-4V) by ball burnishing process. *J. Mater. Res. Technol.* (2017). <https://doi.org/10.1016/j.jmrt.2016.03.007>
5. Revankar, G.D., Shetty, R., Rao, S.S., Gaitonde, V.N.: Analysis of surface roughness and hardness in ball burnishing of titanium alloy. *Meas. J. Int. Meas. Confed.* (2014). <https://doi.org/10.1016/j.measurement.2014.08.043>
6. Yang, S., Puleo, D.A., Dillon, O.W., Jawahir, I.S.: Surface layer modifications in Co-Cr-Mo biomedical alloy from cryogenic burnishing. *Proc. Eng.* **19**, 383–388 (2011). <https://doi.org/10.1016/j.proeng.2011.11.129>
7. Madhukar, S., Shravan, A., Sai, P.V., Satyanarayana, V.V.: A critical review on cryogenic machining of titanium alloy (Ti-6Al-4V). *Int. J. Mech. Eng. Technol.* **7** (2016)
8. Tang, J., Luo, H.Y., Zhang, Y.B.: Enhancing the surface integrity and corrosion resistance of Ti-6Al-4V titanium alloy through cryogenic burnishing. *Int. J. Adv. Manuf. Technol.* (2017). <https://doi.org/10.1007/s00170-016-9000-y>
9. Wyrwas, R.B., Lamothe, M.E.: Report on electrochemical corrosion testing of 241-SY-102 Grab. (2013)
10. Yang, S., Umbrello, D., Dillon, O.W., Puleo, D.A., Jawahir, I.S.: Cryogenic cooling effect on surface and subsurface microstructural modifications in burnishing of Co-Cr-Mo biomaterial. *J. Mater. Process. Technol.* **217**, 211–221 (2015). <https://doi.org/10.1016/j.jmatprotec.2014.11.004>
11. Jawahir, I.S., Attia, H., Biermann, D., Duffou, J., Klocke, F., Meyer, D., Newman, S.T., Pusavec, F., Putz, M., Rech, J., Schulze, V., Umbrello, D.: Cryogenic manufacturing processes. *CIRP Ann. Manuf. Technol.* **65**, 713–736 (2016). <https://doi.org/10.1016/j.cirp.2016.06.007>
12. Studies, E.: Investigation of Sequential Cryogenic **53**, 521–525 (2014)
13. Caudill, J., Huang, B., Arvin, C., Schoop, J., Meyer, K., Jawahir, I.S.: Enhancing the surface integrity of Ti-6Al-4V alloy through cryogenic burnishing. *Proc. CIRP.* **13**, 243–248 (2014). <https://doi.org/10.1016/j.procir.2014.04.042>
14. Amini, C., Jerez-Mesa, R., Travieso-Rodríguez, J.A., Llumà, J., Estevez-Urra, A.: Finite element analysis of ball burnishing on ball-end milled surfaces considering their original topology and residual stress. *Metals (Basel)*. **10**, 1–16 (2020). <https://doi.org/10.3390/met10050638>
15. Silva-Álvarez, D.F., Márquez-Herrera, A., Saldana-Robles, A., Zapata-Torres, M., Mis-Fernández, R., Pena-Chapa, J.L., Moreno-Palmerín, J., Hernández-Rodríguez, E.: Improving the surface integrity of the CoCrMo alloy by the ball burnishing technique. *J. Mater. Res. Technol.* **9**, 7592–7601 (2020). <https://doi.org/10.1016/j.jmrt.2020.05.038>
16. Rotella, G., Caruso, S., Del Prete, A., Filice, L.: Prediction of surface integrity parameters in roller burnishing of ti6al4v. *Metals (Basel)*. **10**, 1–17 (2020). <https://doi.org/10.3390/met10121671>

Chapter 58

Detection of Micro-defects on Metal Screw Surfaces Based on Faster Region-Based Convolutional Neural Network



Mohd Nor Azmi Ab Patar, Muhammad Azmi Ayub,
Nur Aainaa Zainal, Muhammad Aliff Rosly, Hokyoo Lee,
and Akihiko Hanafusa

Abstract The detection of defects in a product is one of required production process for quality control. Currently, the quality control process of metal screws uses many manpower for manual inspection. Hence, this study about to implement faster region-based convolutional neural network (faster R-CNN) to detect the micro-defects on metal screw surfaces. The defects of surface damage, stripped screw, and dirty surface screw considered in this research. Raspberry Pi 3 with a camera module is used for image acquisition of the metal screws in determining various kinds of defects. The image is also acquired to be used for the training of the faster R-CNN. A testing is carried out to test the performance of the model. The experiment outcome shows that the detection accuracy of the model is 98.8%. The model also shows superiority in this project detection method compared with the traditional template-matching method and single-shot detector (SSD) model.

58.1 Introduction

Computer vision system can be described as a system that resembles the operation of a human eye. Computer vision generally enables the system to automatically see, identify, and understand the visual world automatically [1]. Many studies had been

M. N. A. A. Patar (✉) · M. A. Ayub · N. A. Zainal · M. A. Rosly
School of Mechanical Engineering, College of Engineering, Universiti Teknologi MARA,
Shah Alam, Selangor, Malaysia
e-mail: azmipatar@uitm.edu.my

H. Lee
Department of Mechanical and Control Engineering, Niigata Institute of Technology,
Kashiwazaki, Japan

A. Hanafusa
Department of Bio-Science and Engineering, Shibaura Institute of Technology, Tokyo, Japan
e-mail: hanafusa@sic.shibaura-it.ac.jp

done in computer vision, such as face detection [2], a sorting system of wheat [3], robot manipulator in the industry [4], waste recycling robot [5], and kiwifruits detection [6]. The application of computer vision in quality control of the production process is essential to maintain the quality of the products by detecting the defects on the surface of the products [7]. Currently, most manufacturers perform defect detection by using manual inspection. However, large production and small products such as metal screws will require many workforces and very time-consuming. Therefore, developing an automatic defect detection system is essential in the production process to increase productivity [8].

There were many studies had been done on the automatic defect detection system. The current research was utilizing a deep learning algorithm for the system. The work in [9] presented a defect detection system in metal casting. This research utilized convolutional neural networks (CNN) to identify defects of casting using X-ray images. The system has a high accuracy result with obtaining a mean average precision (mAP) of 0.957. The automatic defect detection system is also used to detect the fasteners' defects on catenary support device [10]. The system was applying deep convolutional neural networks (DCNN) to detect the defects on the fasteners. The proposed DCNN also gave high accuracy. DCNN was also applied on metal screws to detect micro-defects on its surface [11]. The experiment results show a detection accuracy of 98% that demonstrated the superiority compared to Le-Net 5. A faster R-CNN model was utilized to detect defects such as in wheel hubs [12] and irregular reflective surfaces [13]. The methods were compared with other deep learning methods and showed better detection performance. It is challenging to train deep learning algorithms from scratch because they are hard to optimize and require a powerful graphics processing unit (GPU)s. The usual method to solve the problems is transfer learning by using the pretrained model [14].

This project attempts to implement an object detection system for identifying metal screws with micro-defects. A platform for image acquisition is built to collect an image of defective and defect-free screws. The image datasets are rotated and exposed with different light intensities to increase the number of images. Then, the image datasets are put into the faster R-CNN network to train the model. The result is then compared with traditional template-matching techniques and single-shot detector (SSD).

58.2 Methodology

58.2.1 System Description

The platform system is designed for obtaining the screw images is shown in Fig. 58.1. The device used in the project is Raspberry Pi 3 Model B as the data processor. The processor for this device is a 64-bit quad-core that running at 1.4 GHz. The image is acquired by using Raspberry Pi camera module V2 with a resolution of 3280×2464 pixels. The distance from the camera to the object, h , is

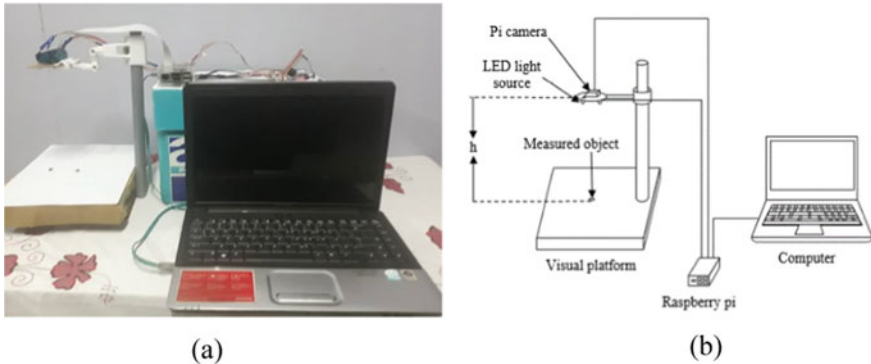


Fig. 58.1 Visual platform: **a** detection system and **b** system structure diagram

about 200 mm. Light-emitting diode (LED) is used as the light source for providing the lighting for the platform. The LED light source has an adjustable brightness programmed to control the intensity of the light. The image is captured on 24-bit with an image size of 1600×1200 pixels in JPEG format.

58.2.2 Data Preparation

This project used 6 mm diameter of M3 head screws with cross countersunk head. The defects such as surface damage stripped screw and dirty surface screw are considered in this project. Figure 58.2 shows the image captured by the visual platform system. The screw image sample size was resized to 640×480 that captured with various intensities of lights that can be changed by adjusting the brightness of the light source. When the training set is small, faster R-CNN is prone to overfitting. To avoid overfitting, the acquired sample was rotated and distorted to extend the samples. The results of changing the brightness of light and rotation of the screw image sample are shown in Figs. 58.3, 58.4, 58.5, and 58.6. Some defect-free image samples were randomly selected, as shown in Fig. 58.3, and some defective screw samples were shown in Figs. 58.4, 58.5, and 58.6.

After using the data enhancement method, the sample dataset has a total of 2454 images. The dataset was randomly divided into two classes: the training set and the test set. The dataset was divided into a ratio of 80:20 for the training set and test set. The training set was the input images of the training process where they were used to update the weight of the model. Then, the detection performance of the model will be evaluated by the test set.

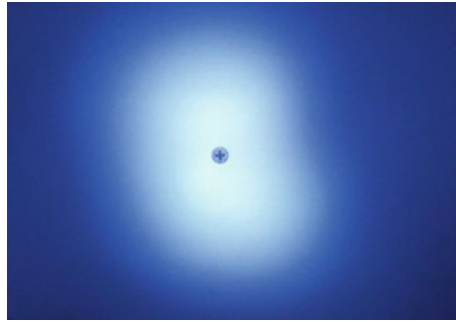


Fig. 58.2 Image acquired

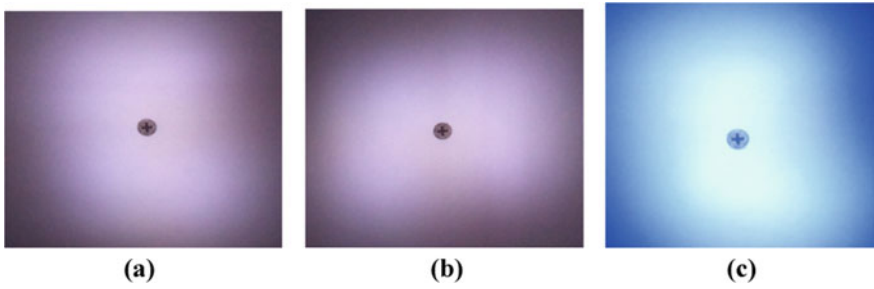


Fig. 58.3 Defect-free screw. **a** The low intensity of light, **b** rotated image, and **c** intensity of light image

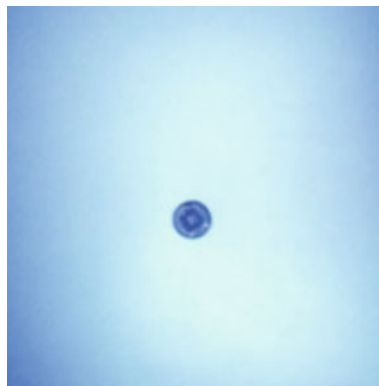


Fig. 58.4 Stripped screw

Fig. 58.5 Surface damaged screw

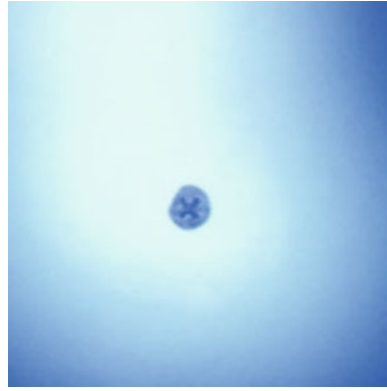
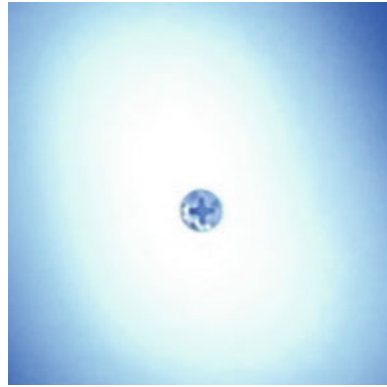


Fig. 58.6 Surface dirty screw



58.2.3 Neural Network Structure

The detection method in this project is implementing faster R-CNN with Inception V2 pretrained model from TensorFlow Object Detection API. The model is made up of two modules. The first module is used to propose the regions by using a fully convolutional neural network. The second module is used as a detector that uses fast R-CNN. Faster R-CNN replaced slow selective search algorithm with region proposal network (RPN) [15]. The faster R-CNN model's architecture is shown in Fig. 58.7.

RPN is a fully convolutional layer used for sharing the computing with the fast R-CNN network. The input is a received image to produce the output as a collection of rectangular object proposals. The last layer of the convolutional layer is mapped using a 3×3 sliding window to a smaller-dimension feature map. The feature map is inserted into two layers: the box regression layer (reg) and the box classification layer (cls). The highest achievable proposals for each location of the sliding window are identified as k . Reg layer produces $4k$ locations of k boxes, and Cls layer

Fig. 58.7 Faster R-CNN architecture [15]

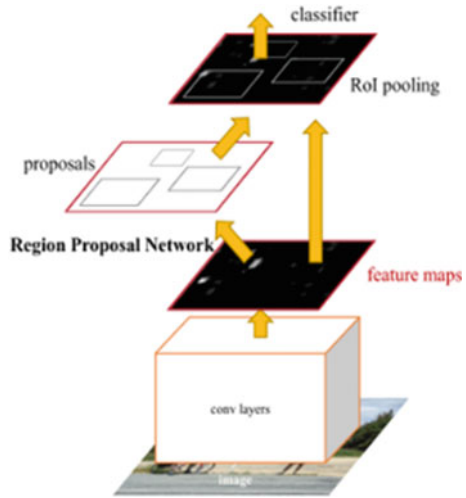
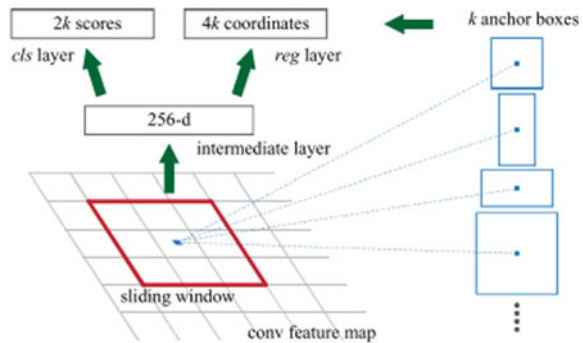


Fig. 58.8 Region proposal network (RPN) [15]



produces $2k$ scores to evaluate the object’s possibility as an object. Anchors are the k proposals in the middle of sliding window that are relative to k reference boxes. The intersection of union (IoU) will affect the label of the archors, which are positive label and negative label. The anchors are classified as a positive label if IoU is highest or greater than 0.7, whereas negative label if IoU is less than 0.3. The positive means that it is an object, while the negative label is background. The region proposal network is shown in Fig. 58.8.

Inception V2 is the CNN used in the model. It was designed to reduce the model’s computational complexity. The network becomes wider than deeper. The original Inception module has a convolution of 5×5 which is replaced by two successive 3×3 convolutions, as shown in Fig. 58.9. The replacement of the convolution layer resulted in an improved performance of the network [16].

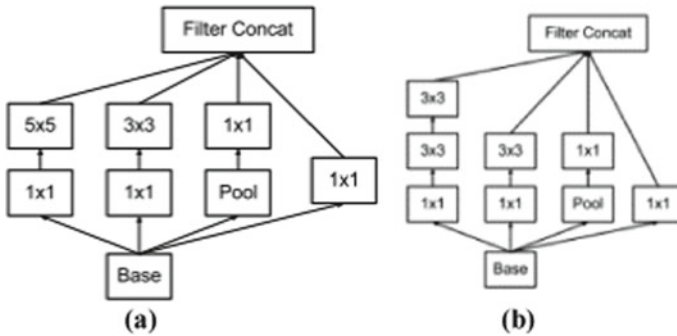


Fig. 58.9 Inception modules. **a** Inception V1 and **b** Inception V2 [16]

58.2.4 Detection Method

To identify the defect on the surface of the screws effectively, the screw surfaces are placed. The detection of screw surface defects process can be summarized as:

1. The metal screw image is captured by using the optical platform.
2. The grayscale processing is carried out that turns the image from three color channels to one gray channel image.
3. The contours of the screw surfaces are obtained by using the canny detection method [17]. The locations, heights, and widths of the screw are obtained based on the contour. It indicates the points at the left, top, bottom, and right of the contour.
4. The image acquired in Step 1 is adjusted to 640×480 to be the input image for the trained faster R-CNN model to detect the surface defects.
5. The position of the screws is obtained and labeled on the original image. The labels for different types of defects are indicated with different color borders.

58.3 Results and Discussion

The experimental detection result of faster R-CNN was compared with traditional template-matching methods and SSD MobileNet V1 model to determine which network is superior. The program was run on ASUS A450L computer. The computer configuration is core i7-4500U CPU, NVIDIA GEFORCE 820M GPU, 8 GB RAM, and Windows 10 operating system, as shown in Table 58.1. The training and testing of the faster R-CNN were using the TensorFlow framework.

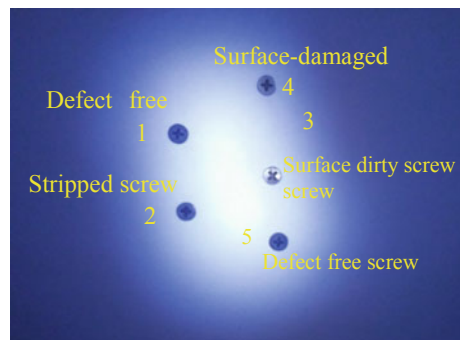
First of all, the traditional template-matching method was used for the detection of screw defects. The original image for the testing is shown in Fig. 58.10 that consists of five screws. The image is marked as numbers to ease the description of

Table 58.1 Configuration of the computer

CPU model	Intel core i7-4500U
Core/thread number	Two cores/four threads
Memory capacity	8 GB
Hard drive capacity	1 TB
Graphics chip	NVIDIA GEFORCE 820M GPU
Video memory	2 GB

the screw defects. Defect-free screws are indicated as 1 and 5, stripped screw as 2, surface-damaged screw as 3, and dirty surface screw as 4. A template image was selected as a defect-free image and tested on different template-matching methods to detect the defects. The template-matching methods that were used in the experiment were the normalized correlation matching method (NCMM), normalized correlation coefficient method (NCCM), correlation coefficient matching method (CCMM), square difference matching method (SDMM), and correlation matching method (CMM) [18]. The results of the various methods are shown in Fig. 58.11.

The results show that the NCMM, NCCMM, and CMM cannot detect screws based on the template image. CCMM and SDMM are only able to detect one defect-free screw. Therefore, the traditional template-matching base method can be seen as not the best method used in this experiment. At best, the methods only can detect one object at a time based on the template image. A faster R-CNN model was compared with the SSD model to verify the superiority of the models further. The two networks were trained with the same screw dataset. The loss value was studied in the first 10,000 iterations of the training. The loss value is very important and will affect the detection quality—the lower the loss value, the better the detection accuracy of the model. After finished the training of the two networks, the detection performance of the two models was tested to verify the models. The same test image (Fig. 58.10) was used. The detection results of the experiment are shown in Fig. 58.12. The test result indicates that the faster R-CNN has no detection error. On the other hand, SSD has three detection errors.

Fig. 58.10 Screws for testing

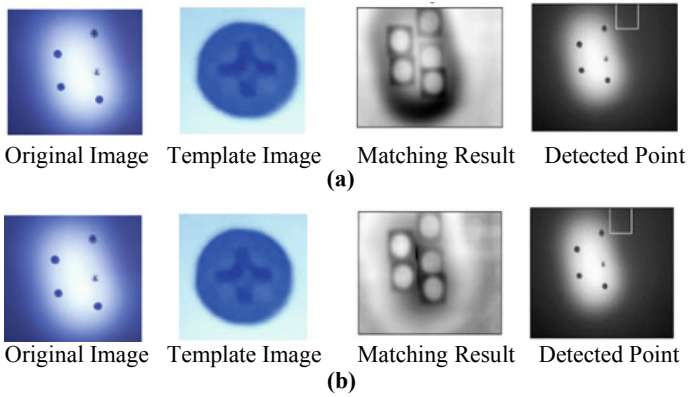


Fig. 58.11 Traditional template-matching-based methods. **a** Normalized correlation matching method and **b** normalized correlation coefficient matching method

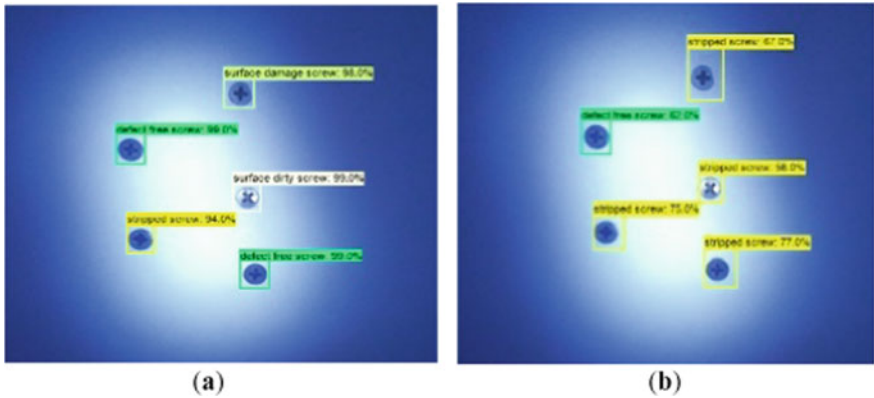


Fig. 58.12 Results of the test. **a** Test result of faster R-CNN and **b** test result of SSD

The performance on detection of the faster R-CNN model was further examined. The model was utilized to test the detection on a test set to obtain the accuracy of the model. The test set consists of 500 different types of images to evaluate the efficiency of the model’s detection by obtaining accuracy. The accuracy was calculated by dividing the no error detected images by the total number of images. The result of the test is tabulated in Table 58.2.

Table 58.2 Detection performance of the models

Model	Total number of images	No error	Error	Accuracy (%)
Faster R-CNN	500	494	6	98.8
SSD	500	139	361	27.8

The detection accuracy of faster R-CNN is very high that can achieve an accuracy as high as 98.8%. When compared to the SSD models, faster R-CNN clearly shows the superiority of the model. The drawback of faster R-CNN is the detection speed is slower when compared with SSD. This proves that better accuracy can be achieved by sacrificing the speed of the detection [19].

58.4 Conclusions and Recommendations

In this experiment, a faster R-CNN model has been implemented to detect the micro-defects of metal screw surfaces. The comparison with the traditional template-matching methods and SSD model shows the effectiveness of the faster R-CNN model on identifying micro-defects of the metal screws. The experiment results show that the accuracy of the faster R-CNN model's detection can achieve 98.8%. Other object detection applications to identify different objects can implement this model. It is also recommended to train the network using a high-end computer because it is very time-consuming for a medium specification computer. For future work, a pick and place robotic arm will be implementing the faster R-CNN model to sort the metal screws with different types of defects.

Acknowledgements The author would like to express sincere gratitude to the supervisor for the guidance in completing this project. The authors also gratefully acknowledge the Ministry of Education Malaysia (MOE) for the fund received through the Fundamental Research Grant Scheme (FRGS) [Project file: 600-IRMI/FRGS 5/3 (472/2019)].

References

1. Feng, X., Jiang, Y., Yang, X., Du, M., Li, X.: Computer vision algorithms and hardware implementations: a survey. *Integration* **69**(June), 309–320 (2019)
2. Hassanat, B.A., Alkasassbeh, M., Al-awadi, M., Alhasanat, E.A.A.: Color-based object segmentation method using artificial neural network. *Simul. Model. Pract. Theory* **64**, 3–17 (2015)
3. Kaya, E., Saritas, İ.: Towards a real-time sorting system: identification of vitreous durum wheat kernels using ANN based on their morphological, colour, wavelet and gaborlet features. *Comput. Electron. Agric.*, **166**(July), 105016 (2019)
4. Ali, M.H., Aizat, K., Yerkhan, K., Zhandos, T., Anuar, O.: Vision-based robot manipulator for industrial applications. *Proc. Comput. Sci.* **133**, 205–212 (2018)
5. Wang, Z., Li, H., Zhang, X.: Construction waste recycling robot for nails and screws: computer vision technology and neural network approach. *Autom. Constr.* **97**(March), 220–228 (2019)
6. Fu, L., et al.: Kiwifruit detection in field images using faster R-CNN with ZFNet. *IFAC-PapersOnLine* **51**(17), 45–50 (2018)
7. Bulnes, F.G., Usamentiaga, R., Garcia, D.F., Molleda, J.: An efficient method for defect detection during the manufacturing of web materials. *J. Intell. Manuf.* **27**(2), 431–445 (2016)

8. Yapi, D., Mejri, M., Allili, M.S., Baaziz, N.: A learning-based approach for automatic defect detection in textile images. *IFAC-PapersOnLine* **28**(3), 2423–2428 (2015)
9. Ferguson, M., Ak, R., Lee, Y.-T.T., Law, K.H.: Detection and segmentation of manufacturing defects with convolutional neural networks and transfer learning. *Smart Sustain. Manuf. Syst.* **2**(1), 20180033 (2018)
10. Chen, J., Liu, Z., Wang, H., Nunez, A., Han, Z.: Automatic defect detection of fasteners on the catenary support device using deep convolutional neural network. *IEEE Trans. Instrum. Meas.* **67**(2), 257–269 (2018)
11. Song, L., Li, X., Yang, Y., Zhu, X., Guo, Q., Yang, H.: Detection of micro-defects on metal screw surfaces based on deep convolutional neural networks. *Sensors (Switzerland)* **18**(11) (2018)
12. Sun, X., Gu, J., Huang, R., Zou, R., Palomares, B.G.: Surface defects recognition of wheel hub based on improved faster R-CNN. *Electron.* **8**(5), 1–16 (2019)
13. Zhou, Z., Lu, Q., Wang, Z., Huang, H.: Detection of micro-defects on irregular reflective surfaces based on improved faster r-cnn. *Sensors (Switzerland)* **19**(22), 1–15 (2019)
14. da Costa, Z., Figueroa, H.E.H., Fracarolli, J.A.: Computer vision based detection of external defects on tomatoes using deep learning. *Biosyst. Eng.* **190**, 131–144 (2020)
15. Ren, S., He, K., Girshick, R., Sun, J.: Faster R-CNN: towards real-time object detection with region proposal networks. *IEEE Trans. Pattern Anal. Mach. Intell.* **39**(6), 1137–1149 (2017)
16. Szegedy, C., Vanhoucke, V., Ioffe, S., Shlens, J., Wojna, Z.: Rethinking the inception architecture for computer vision. In: *Proceedings of the IEEE Conference on Computer Vision and Pattern Recognition*, vol. 2016, December 2016, pp. 2818–2826 (2016)
17. Ayub, M.A., Ab Patar, M.N.A., Zainal, N.A.: ‘AZ’ humanoid robot head with object and color tracking capabilities. *Int. J. Mech. Eng. Robot. Res.* **9**(6) (2020)
18. Vidhyapeeth Rajasthan Neelam Sharma, B., Banasthali Vidhyapeeth Rajasthan, A.: An overview of various template matching methodologies in image processing. *Int. J. Comput. Appl.* **153**(10), 975–8887 (2016)
19. Huang, J. et al.: Speed/accuracy trade-offs for modern convolutional object detectors. In: *Proceedings of 30th IEEE Conference on Computer Vision and Pattern Recognition, CVPR 2017*, vol. 2017, January 2017, pp. 3296–3305 (2017)

Chapter 59

Effects of Rotation Speeds on Electrical Submersible Pump Performance Under Two-Phase Flow



Abdulqader Hasan, Salman Shahid, Sharul Sham Dol,
Mohamed S. Gadala, Mohd Shiraz Aris, and Mohammed Alavi

Abstract Electrical submersible pumps (ESP) are a pump classification, which is typically connected to an application of transporting fluids located in submersible elevations into supply pipelines. These pumps type can be found in offshore oil and gas facilities and are often used as transfer pumps for liquefied natural gas (LNG) terminals. In multiphase applications such as in LNG transport, operational challenges from the presence of air pockets and bubbles present a cavitation and degradation risk to the pump components. This paper proposed a computer simulation model using CFD analysis in ANSYS Fluent to study the effects of multiphase flow (gas–liquid flow) on ESP while varying the rotational speed with constant flow rate and inlet gas volume fraction (IGVF). Flow rate and IGVF kept constant with 20 L/min and 1%, respectively, while rotation speed varied by 500, 900, 1500, 2000, and 2500 rpm. The CFD results show that at low rotation speeds a large gas pocket performed at impeller inlet. However, by increasing the rotation speed, this gas pocket collapses to bubbly flow at the impeller inlet which leads to losses in high kinetic energy and concentration of bubbles at the impeller outlet and volute.

A. Hasan · S. Shahid · S. S. Dol (✉) · M. S. Gadala · M. Alavi
Department of Mechanical Engineering, Abu Dhabi University,
Abu Dhabi, United Arab Emirates
e-mail: sharulsham.dol@adu.ac.ae

A. Hasan
e-mail: 1047456@students.adu.ac.ae

S. Shahid
e-mail: 1062192@students.adu.ac.ae

M. S. Gadala
e-mail: mohamed.gadala@adu.ac.ae

M. Alavi
e-mail: mohammed.alavi@adu.ac.ae

M. S. Aris
Tenaga Nasional Research Sdn. Bhd, Kajang, Malaysia
e-mail: Shiraz.aris@tnb.com.my

59.1 Introduction

The electrical submersible pump is a centrifugal pump type, the second most widely used artificial lift method in oil and gas sector. These pumps consist of many stages which are connected by single shaft, and each stage consists of impeller, diffuser, and sealing system. The impellers rotate to increase the kinetic energy of the fluid, and diffusers are a stationary part that diffuse the flow and guide it to the next stage as shown in Fig. 59.1. In oil and gas sector, ESP are utilized for boosting pressure and transferring fluids from underground to ground level. The aim of the paper is to investigate the effects of varying rotational speed while keeping the other parameters constant (model, mesh, liquid and gas flow rates, and time step). In addition, the behavior of the bubbles and gas pockets inside the pump will be discussed and compared for each case study. The effects of gas volume fraction were investigated and were currently considered for another publication.

Pumps convert electrical power to kinetic energy by rotating pump impeller. A pump performance curve consolidates the pressure head and flow range and is typically used by designers and operators to determine the operating region of the pump [2]. ESP have high efficiency and avoids cavitation, since water is pushed rather than pulled, and this reduces the casual of the negative pressure head in the system. The multistage ESP application in the oil and gas industry is found as main crude oil transfer pumps, LNG transport (shipment-regassification terminals), the adaptability of ESP in regardless of the application conditions (heavy oil or associated with solid particles and vertical or deviated wells). The pumping fluid undergoes pressure charging across the pump stages and, depending on the fluid type, may contain air pockets or bubbles. The multiphase fluid conditions are risk to

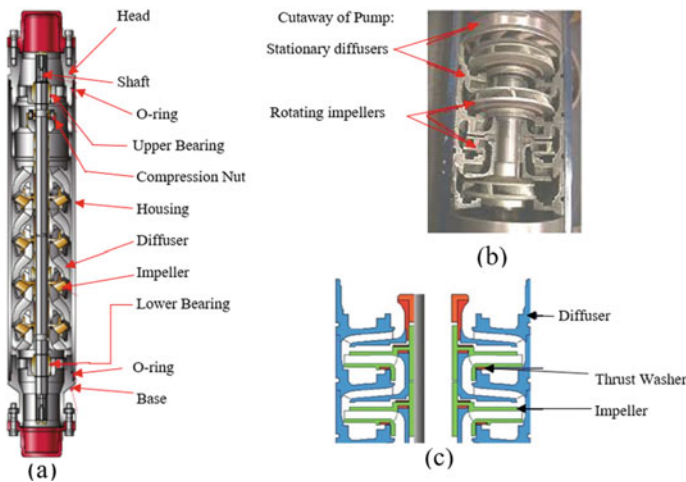


Fig. 59.1 Main parts of ESP: **a** multistage ESP components, **b** cutaway of pump, and **c** impeller and diffuser [1]

pumping components at the operating pump speeds as cavitation may be introduced to the rotating components. Corrections or operational limitation guidelines on the performance curves will therefore be a helpful reference to ESP operators [3].

59.1.1 Numerical Simulations of the ESP

ESP consist of rotating parts (impeller) and stationary (diffuser). In order to study the effects of differences in velocities and the interfaces between them, Gonzalez et al. [4] and Gonzalez and Santolaria [5] simulate a centrifugal pump in Fluent by using sliding mesh technique with unsteady flow to solve viscous incompressible Navier–Stokes equation. They observed that the model was able to predict the effects inside the pump, and a relationship was developed between global parameters (torque, flow volute, impeller relative position, etc.), in which the pressure forces are the main driven forces. The sliding mesh (Eqs. 59.1 and 59.2) and Navier–Stokes equation (Eq. 59.3) are represented as the form below [6]:

$$\frac{d}{dt} \int_V \rho \phi dV \int_{\partial V} \rho \phi (\vec{u} - \vec{u}_g) \cdot d\vec{A} = \int_{\partial V} \Gamma \nabla \phi \cdot d\vec{A} + \int_V S_\phi dV \quad (59.1)$$

where ρ is the fluid density, V is volume, ϕ is general scalar, \vec{u} is flow velocity vector, \vec{u}_g is mesh velocity vector for moving mesh, Γ is the diffusion factor, and S_ϕ is the source term of ϕ . Since the volume and the next volume are constant $V^{n+1} = V^n$, the material time derivative is shown in Eq. 59.2 as [7]:

$$\frac{d}{dt} \int_V \rho \phi dV = \frac{((\rho \phi)^{n+1} - (\rho \phi)^n) V}{\Delta t} \quad (59.2)$$

$$\rho \left\{ \frac{\partial u_i}{\partial t} + u_j \frac{\partial u_i}{\partial x_j} \right\} = - \frac{\partial p}{\partial x_i} + \rho \nu \frac{\partial^2 u_i}{\partial x_j \partial x_j} \quad (59.3)$$

where u_i and x_i are the velocity vector and position vector, respectively.

Huang et al. [8] simulate a transient single-stage centrifugal pump also by using sliding mesh technique, to study the effects of the interaction between the rotor and stator that occur due to pressure fluctuation and the transient flow. Zhu and Zhang [9] simulate TE 2700 three stages pump and were compared with Salehi [10] experiment. At first steady state of single phase was simulated by using sliding mesh technique to solve RANS equation to match the affinity law and manufacturer performance curves. Then by specifying three different bubbles diameters with 0.1, 0.2, and 0.3 mm, a two-phase flow (gas–water) was simulated to solve the Navier–Stokes equation by using the Eulerian–Eulerian approach and k -epsilon as turbulence model in ANSYS CFX. They observed that bubbles diameter plays dominant role in affecting performance curve in two-phase flow. Zhu et al. [11] investigated the flow patterns numerically by using advanced techniques in ANSYS Fluent.

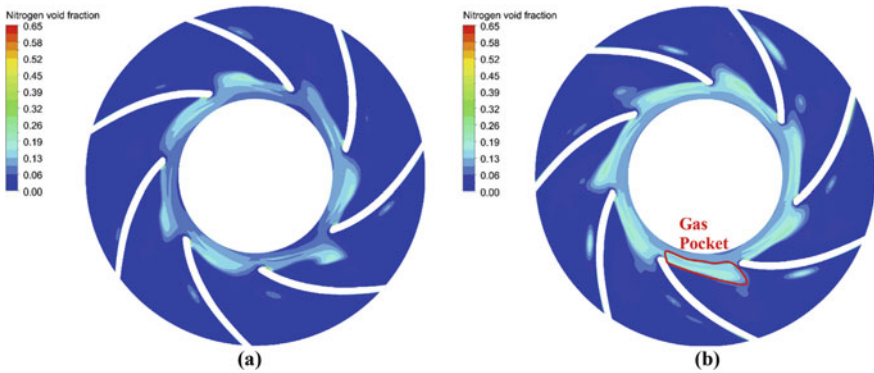


Fig. 59.2 In situ contour on second stage impeller, **a** case 2 $t = 7.956$ s and **b** case 3 $t = 15$ s, [11]

They compared the two approaches of multiphase flow (volume of fluid VOF and Eulerian–Eulerian) by using transient with sliding mesh technique and realizable k -epsilon model, and the code was successfully implemented. Their results show that the Eulerian approach was more superior than VOF approach in capturing the flow patterns and bubbles behavior for the three cases studied (case 1 $\lambda_G = 0.35\%$, case 2 $\lambda_G = 0.56\%$, and case 3 $\lambda_G = 0.69\%$). Figure 59.2 shows the distribution of gas in two-phase flow at the second stage impeller on half-span surface for case 2 and 3. Figure 59.2a represents case 2 at flow time of 7.956 s and at gas flow of 0.56%, and it was observed that bubbles accumulate at impeller pressure side to produce a behavior similar to agglomerated flow pattern. By increasing gas volume further, Fig. 59.2b represents case 3 $\lambda_G = 0.69\%$ and at flow time of 15 s, a gas pockets started to be produced due to coalescence of the bubbles.

59.2 Methodology

59.2.1 Geometry

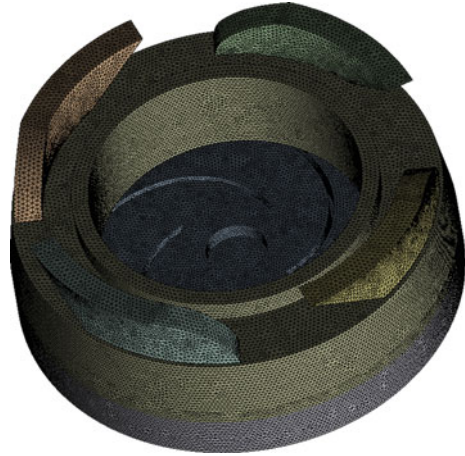
The geometry was created in ANSYS, and it consists of single stage of ESP pump. The dimensions and curves are designed accurately based on data provided from the manufacture. Figure 59.3 depicts pump impeller, diffuser, and fluid zone (volute). The pump impeller details are represented in Table 59.1.

59.2.2 Grid Independency Test

The grid independency test consulted to verify the results accuracy and the optimum element number that can provide accurate results as well as lower computing

Table 59.1 Pump impeller details

Parameters	Symbols	Values
Inlet diameter (mm)	D_1	42
Outlet diameter (mm)	D_2	140
Height of the blades (mm)	H	11
Number of blades	n	4
Impeller inlet angle ($^\circ$)	β_1	97
Impeller outlet angle ($^\circ$)	β_2	44

Fig. 59.3 Pump geometry and meshing

time. A tetrahedron mesh type was performed using 1.5, 3, 5, 7, and 9 million elements. Figure 59.3 shows a tetrahedrons mesh type using 3 million elements. To perform the grid test, a single-phase flow with constant flow rate and rotational speed were selected by 150 L/min and 2850 rpm, respectively, while the elements number varied as previous. The results obtained show that after 3 million elements the stability of the results was not varying much; however, at the same time the computing time increased to the double as the number of elements increased in order to solve the problem as shown in Fig. 59.4. The reduction of error from 1 to 3 million is almost 3%, although this percentage is almost constant for higher number of elements [12].

59.2.3 Setting up

The 3 million elements model was further used on two-phase flow simulations as the parameters varied. To model two-phase flow in ANSYS Fluent, various models are available to solve the Navier–Stokes equation. Some of the most commonly used models to handle multiphase flow are full-Eulerian, mixture, and volume of fluid

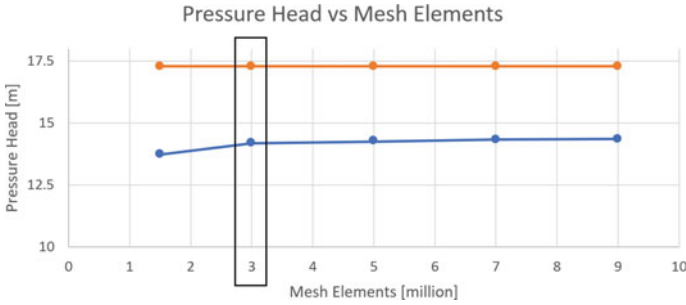


Fig. 59.4 Grid independency test

(VOF). The VOF model is multiphase model using the fraction of each phase to solve the momentum equation. Meanwhile, mixture model uses the summation of the momentum equation of all phases. The full Eulerian–Eulerian model is the most advanced model which solves n-terms of momentum equation parallel. In this research, the mixture model was used in order to find the pressure distribution over the pump. The equations and table below represent more details about the model used.

The continuity equation of the mixture model:

$$\frac{\partial}{\partial t} \sum_{k=1}^n (\alpha_k \rho_k) + \nabla \cdot \sum_{k=1}^n (\alpha_k \rho_k u_k) = 0 \tag{59.4}$$

where n is number of phases, α is the phase fraction, the subscript k is liquid or gas, and u_k is the velocity of the phase. Then the momentum equation can be represented as:

$$\begin{aligned} \frac{\partial}{\partial t} \sum_{k=1}^n \alpha_k \rho_k u_k + \nabla \cdot \sum_{k=1}^n \alpha_k \rho_k u_k u_k = & - \sum_{k=1}^n \alpha_k \nabla p_k + \nabla \cdot \\ & \cdot \sum_{k=1}^n \alpha_k (\tau_k + \tau_{TK}) + \sum_{k=1}^n \alpha_k \rho_k g + \sum_{k=1}^n M_k \end{aligned} \tag{59.5}$$

where τ_k is the stress tensor of the phase, τ_{TK} is turbulence stress tensor of the phase, and M_k is the surface tension force of the phase (Table 59.2).

59.3 Results and Discussion

Figure 59.5 shows the results of 20 L/min of water flow rate and 1% air volume fraction at 500 rpm and 900 rotational speeds. At Fig. 59.5a, the air volume fraction (AVF) presents a large gas pocket concentrated at the impeller inlet, and this gas

Table 59.2 Details of the CFD analysis model

Boundary conditions	Value
Velocity inlet	0.20938 m/s equivalent to 20 L/min
Outlet boundary	Pressure outlet (gauge pressure)
Rotational speed (impeller)	500, 900, 1500, 2000, 2500 rpm
Solids boundary	Stationary relative to adjacent, no-slip condition
Water density and fraction	998 kg/m ³ , 99%
Air density and fraction	1.225 kg/m ³ , 1%
Gravity	$g = -9.81 \text{ m/s}^2$ (y-direction)
Time step size	0.0001 s
Model	Method
Turbulence model	K-omega SST
Multiphase model	Mixture model (implicit)
Body forces formulation	Implicit body forces
Interface modeling	Sharp/dispersed
Water, Air	Primary phase, secondary phase

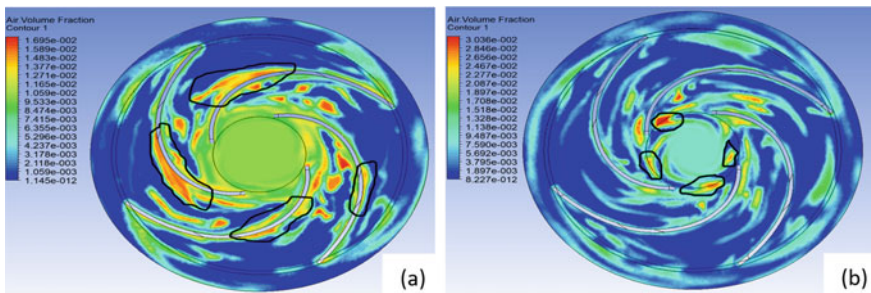


Fig. 59.5 AVF contour at: **a** 500 rpm and **b** 900 rpm

pocket chokes the flow inside the impeller. Meanwhile, the kinetic energy of the impeller goes to break down the gas pocket instead of accelerating the flow. In addition, a small gas pockets agglomerate at the impeller pressure side. These gas pockets blocking the adverse pressure gradient as well as it causes a head degradation. However, in Fig. 59.5b, at higher rotational speed, the large gas pocket at the impeller inlet starts to breakdown to smaller gas pockets as marked. These small pockets move as Taylor Bubble (slug flow as a coalescence of small bubbles in a series) toward the impeller outlet, although less concentration of the bubbles on the impeller pressure sides and unsteady flow between the passages were performed.

The results obtained from 1500 and 2000 rpm rotation speeds are almost identical in the flow path. However, Fig. 59.6 below illustrates that the large pocket collapsed totally (due to reduction in bubbles size as the rotation speed increased) to smaller gas pockets, and these pockets are accumulated at impeller outlet and the

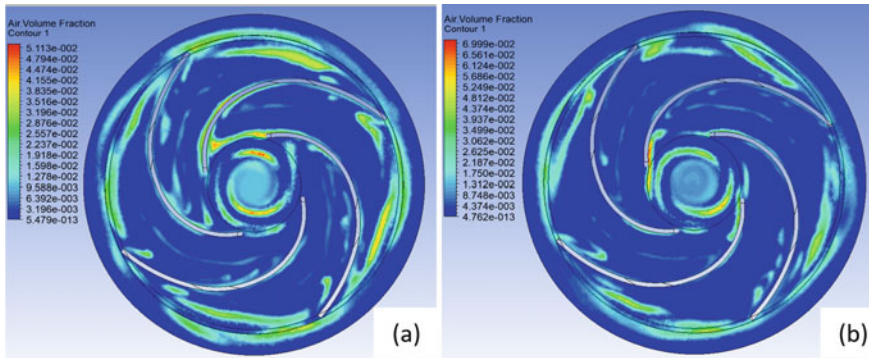
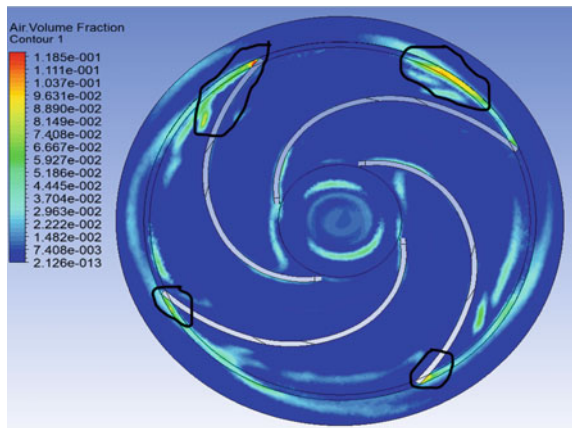


Fig. 59.6 AVF contour at: a 1500 rpm and b 2000 rpm

Fig. 59.7 AVF contour at 2500 rpm rotational speed



volute. The impeller passages are having less concentration of bubbles compared with lower rpm (500 and 900 rpm), but the bubbles accumulate with high GVF at the volute and impeller outlet with 2% fraction. This concentration of bubbles occurred due to the breakdown of gas pocket, and kinetic energy is lost in the form of drag force that acts on the bubbles and enforcing it to decelerate the relative fluid velocity [12, 13]. Figure 59.7 shows air fraction contour at maximum rotation speed 2500 rpm. The observed results show that at high rotation speeds the flow at inlet tends to become bubbly flow (small size of bubbles distributed uniformly). Due to the high kinetic energy that is produced from the rotated impeller, the gas pockets are moved to the volute, as well as less concentration of gas pockets at the impeller pressure side.

The pump performance degraded with the presence of gas bubbles. The two-phase flow performance curves are not provided by the manufacture, since the air bubbles risk the pump components and cavitation may be introduced. The pump head of two-phase flow simulated models deteriorates from the single-phase flow.

Table 59.3 Pump head comparison

Rotation speed (rpm)	Single-phase flow head (m)	Two-phase flow head (m)	Percentage of head reduction (%)
500	0.414	0.307	25.8
900	1.53	1.15	24.8
1500	4.6	3.94	14.3
2000	8.25	7.2	12.7
2500	13.11	11.9	9.2

Table 59.3 shows the percentage of head deterioration in two-phase flow from single-phase flow. Two-phase flow reduces the head generated of the pump. In addition, as the rotation speed increases further, the pump ability to handle gas increases [14].

59.4 Conclusion

The CFD model used was able to present the capacity of the pump on handling the two-phase flow accurately. As the rotation speed varied from 500, 900, 1500, 2000, and 2500 rpm, the less concentration of gas pocket in the inlet as well as the percentage of head reduction reduced, which the results can be significant in off-shore gas facilities.

Acknowledgements We would like to thank Abu Dhabi Award for Research Excellence (AARE) for the research funding.

References

1. Admin: Production Technology: 28 April 2017 [Online]. Available: <https://production-technology.org/pump-performance-curves/>
2. Shahid, S., Dol, S.S., Hasan, A.Q., Kassem, O.M., Gadala, M.S., Aris, M.S.: A review on electrical submersible pump head losses and methods to analyze two-phase performance curve. *WSEAS Trans. Fluids Mech.* **16**, 14–31 (2021)
3. Kassem, O.M., Abdullah, A.Q., Dol, S.S., Gadala, M.S., Aris M.S.: CFD analysis of electrical submersible pump handling single-phase flow. *Platform: J Eng* **4**(4), 26–34 (2020)
4. Gonzalez, J., Fernandez, J., Blanco, E., Santolaria, C.: Numerical simulation of dynamic effects due to impeller-volute interaction in a centrifugal pump. *J Fluid Eng* **124**, 348–355 (2002)
5. Gonzalez, J., Santolaria, C.: Unsteady flow structure and global variables in a centrifugal pump. *J Fluid Eng* **128**, 937–946 (2006)
6. Fluent, A.: ANSYS fluent theory guide 18.0. Ansys Inc., USA (2017)

7. Halawa, T., Alqaradawi, M., Badr, O., Gadala, M.: Numerical investigation of rotating stall characteristics and active stall control in centrifugal compressors. In: ASME 2014 Power Conference, Power2014–32052, Maryland, USA, 28–31 Jul 2014
8. Huang, S., Mohamad, S., Nandakumar, K.: Numerical simulation of unsteady flow in a multistage centrifugal pump using sliding mesh technique. *Progress Comput. Fluid Dyn.* **10** (2010)
9. Zhu, J., Zhang, H.-Q.: CFD simulation of ESP performance and bubble size estimation under gassy conditions. In: SPE Annual Technical Conference and Exhibition, Amsterdam, The Netherlands, 27–29 October 2014
10. Salehi, E.: ESP performance in two-phase flow through mapping and surging tests at various rotational speeds and intake pressures. Master's Thesis, The University of Tulsa, Tulsa, OK, USA, 2012
11. Zhu, J., Zhu, H., Zhang, J., Zhang, H.-Q.: A numerical study on flow patterns inside an electrical submersible pump (ESP) and comparison with visualization experiments. *J. Petrol. Sci. Eng.* **173**, 339–350 (2018)
12. Shahid, S., Hasan, A.Q., Dol, S.S., Gadala, M.S., Aris, M.S.: Effect of near-wall vortices on wall shear stress in a centrifugal pump impeller. *WSEAS Trans. Fluids Mech.* **16**, 37–47 (2021)
13. Wong, S.F., Dol, S.S.: Turbulence characteristics study of the emulsified flow. *WSEAS Trans. Heat Mass Transfer* **14**, 45–50 (2019)
14. Dol, S.S., Wee, S.K., Chan, H.B., Kumar, P.: Turbulence characteristics behind a flexible vortex generator. *WSEAS Trans. Fluids Mech.* **14**, 1–7 (2019)

Chapter 60

Design of Electrical Screwdriver Using Arduino and Planetary Gear System



Rajanpreet Singh, Gautam Gupta, and Gaganpreet Kaur

Abstract Screws are essential and widely used hardware because of their ease of use and very high joint force. A screwdriver is a device utilized for screwing and unscrewing the screws. For years, screwdriver somehow got very little attention, and hence, very little innovation in the designing and manufacturing took place within the years. This paper presents the design of the “pistol”-type VSR (variable speed reversible) electric screwdriver and an economical and effortlessly assembled open-source screwdriver based on the Arduino micro-controller chip platform. This design allows users to avoid using awkward wrist postures, attempting to fasten or unfasten screws with manual screwdrivers. The 3D model of electric screwdriver is designed and optimized in PTC Creo Parametric 3.0. The apparatus contains planetary gear system, a DC motor, optical groove coupler module, and a variety of sensors. Additional features, such as an LCD, are placed to display torque, and RPM is added to the screwdriver.

60.1 Introduction

Industrial screws are hardware that is used to hold materials together. This category is incredibly broad; some of the many workplaces in which screws are used include furniture, building construction, household appliances, military and defense, automotive manufacturing, HVAC, surgery, aerospace, and security. A screwdriver is a

R. Singh · G. Gupta (✉)

Department of Mechanical Engineering, Thapar Institute of Engineering and Technology, Patiala, Punjab 147004, India

e-mail: ggupta2_be15@thapar.edu

R. Singh

e-mail: rsingh16_be15@thapar.edu

G. Kaur

Department of Electronics and Communication Engineering, Thapar Institute of Engineering and Technology, Patiala, Punjab 147004, India

e-mail: gaganpreet.kaur@thapar.edu

device, electrical powered or manual, utilized for fastening or unfastening screws. A normal straightforward screwdriver constructs from a handle with a shaft. This type of screwdriver has been supplanted in numerous working environments and homes, and power drills are faster, simpler, and furthermore can bore openings. A few screwdrivers are available with exchangeable tips which fit into a connection on ending of shaft and are engaged in magnetically or mechanically. A wide assortment of force screwdrivers goes from a basic “handle”-type includes batteries, a tip holder, and motor, to incredible “pistol” form variable speed reversible (VSR) drills that likewise work as screwdrivers.

There are two types of tightening torque tools that are used, namely pneumatic and electric tools. The pneumatic tools require frequent inspecting after tightening and cost the companies a lot of energy as the compressor supplying the compressed air needs to remain ON continuously to supply air to the main air duct, uninformed of the number of tools being used or not. Thus, a lot of energy can be saved if industry switch to electric torque tools, but the electric tools cost a fortune to the companies. Hence, this makes forcing the companies to settle with pneumatic tools or a small number of electric tools. To diminish the intricacy and price of the electric screwdrivers, screws tighten and loosen torque varying electric screwdriver, based on the Arduino UNO that can also calculate RPM and torque.

60.2 Literature Review

The new design allows users to avoid using awkward wrist postures whenever attempting to fasten or unfasten screws. The ergonomics and forces associated with the working with screwdrivers have been studied in next three papers. These studies help us to work on the best design that is ergonomically effective [1]. This researched the attributes of electrical screwdrivers that influence the operator’s usefulness, well-being, and quality of working life [2]. This shows statics and dynamics forces of pneumatic power screwdriver [3]. This study shows the impacts of forces acting against the hand on lower arm muscle movement.

There are very few innovations that had applied on the screwdrivers. Next four papers show the ideas that are implemented to make the tool avant-garde [4]. The paper reports the plan of the screw fixing using the disturbance observer [5]. These designed screwdriver with star arrangement for gear train uses principles of TRIZ [6]. In this work, an electric screwdriver was made with a torque estimating gadget that controls the speed and the turning of screw and measures and shows the driving torque.

To make the low-cost effective tool with Arduino, studying the essence of the microcontroller and their applications is important [7]. This presents an Arduino-based framework to control the streetlamps dependent on solar rays [8]. This examination is the programmed automatic gadget for folding garments [9]. This paper has introduced to portable attendance system based on fingerprint

identification [10]. This paper created the smart stick for visually impaired persons using ultrasonic sensors.

Robots are adapted to do a far more prominent level of task-to-task variability. These three studies put light on how Arduino helps automation to grow that applied in this research paper [11]. This paper reports the design, construction, and control of a two-wheel self-balancing robot [12]. Five degree of freedom (DOF) robotic mechanical arm has been fostered that is constrained [13]. This article describes the development of a minimal expense data glove for use in virtual reality.

Moreover, there are numerous IoT applications based on Arduino in creating smart home and doing smart farming, which help this research to show vision toward IoT [14]. This paper offers a smart home system planned and made by using a WLAN [15]. This paper centers around the control part that helps the watering an outside ranch dependent on the measurable information detected from the sensors.

60.3 Methodology

The concept of an electric screwdriver gun was inspired by a hand drill machine. The difference between the two is that drilling machine only focuses on high RPM and does not need much precision for that, but a torque tool specializes in high torque with precision without compromising RPM. A torque tool needs to vary the torque and RPM along with measuring the torque and speed of the tool from time to time. To make an electric tightening torque tool, the major needs faced are a high torque and RPM motor, a torque transducer, for measuring torque, an RPM sensor, a torque altering system, a display to display the output torque and speed.

The major cost proportion of a tightening torque tool comes from the rotary torque transducer, which is used to measure the dynamic torque. Dynamic torque is the torque in continuous motion, rather than having one cycle and measuring the torque. A small rotary transducer with measuring capacity till 4 Nm costs around \$200. The aim is to make a tool which is low cost. Thus, an alternate for the transducer needs to be found. The alternative to this problem was to design a mechanism that would fulfill the same criteria, i.e., measure the force and then multiply it to the radius of the output shaft.

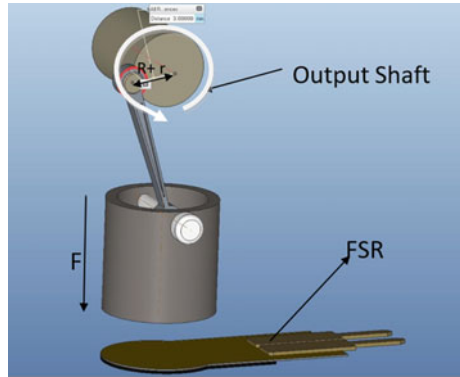
This mechanism works as the principle of a slider crank mechanism or a piston cylinder arrangement. The connecting rod will be connected to the output shaft of the tool, and the piston will transmit the rotary motion to linear motion. The force will be multiplied to radius of the shaft. Therefore, we can derive torque from the product of the force applied on a force sensor and the radius of the output shaft.

The sensor used for sensing force in this research is FSR-402. It has been shown below in Fig. 60.1. The torque sensor is basically a piston cylinder arrangement with the force sensor at the bottom dead center of the stroke of the piston. The piston will be connected to the output shaft of the device. The output shaft will be coupled with a shaft parallel to the main shaft which will be connected to the piston. Hence, we will get the force being exerted by the shaft which will then be

Fig. 60.1 FSR-402 sensor



Fig. 60.2 Torque sensor arrangement



multiplied to the shaft radius, eventually giving out the torque parameters of the tool. A 3D arrangement of the sensor has been shown in Fig. 60.2. It was designed in PTC Creo Parametric 3.0.

The force sensor then sends the force output to the Arduino where it is processed to give out the torque. The RPM sensor we have used needs to measure how many rotations the shaft make per minute. The concept of the speed sensor is that a velocity sensor will sense how many times an object pass through it. We are going to measure how many times a small attachment connected to the output shaft passes through the sensor in one second and then multiply it with 60 to find the RPM.

To vary the torque, we have used mechanical means instead of electrical means of varying torque as used in industrial screwdrivers. The best way of multiplying torque is gear reduction, but in this case, we have one constraint, which is lack of space inside the screwdriver housing. This leaves the option of using a planetary gear system. The chuck of the screwdriver gun will be removable containing with planetary gear set.

Table 60.1 Gear ratios according to different combinations

Case	Input	Output	Stationary	Gear ratio
A	Sun (S)	Planet carrier (C)	Ring (R)	$1 + R/S$
B	Planet carrier (C)	Ring (R)	Sun (S)	$1/(1 + S/R)$
C	Sun (S)	Ring (R)	Planet carrier (C)	$-R/S$

A planetary gear set has three main components: a sun gear, planet gears, and the ring gear. To find the number of teeth on each one of these, equation that followed is

$$R = (2 \times P) + S \quad (60.1)$$

where “ R ” is the number of teeth on the ring gear, “ P ” is the number of teeth on each planetary gear, and “ S ” is the number of teeth on the sun gear.

In Table 60.1, the first case (A) and the third case (C) are cases of reduction; i.e., the output torque will be more than the input torque. The second case (B) is a case of overdrive, meaning the output speed will be more, but the output torque will be lower.

Clearly, a case from A or C needs to choose. Now, it depends on what will be the input and what will be the output. Here, the sun gear is taken as the input because it will be directly connected to the motor shaft in the gun, transmitting the input torque to the output shaft through the ring gear.

According to the standards for tightening a self-tap screw on the tail cover sub-assembly of N251, the required range of torque is 1.8–4 Nm throughout the process. A gear system is designed according to the same. Assuming the nominal torque or input torque as 1.8 Nm and the nominal speed as 1778 RPM. In order to achieve an output torque of 3 Nm, the gear ratio (“output torque”/“input torque”) will come out to be 1.666 or 1.67. Hence, the gear ratio would be 1.67:1.

A model of the sun gear and three planet gears has been designed according to the motor shaft. So, the number of teeth came out to be 15 on the sun gear. For the number of planetary and ring gears, by using equation in Case C equation from Table 60.1, putting values as follows “gear ratio” as 1.67 and “ S ” as 15, “ R ” will be 25.05 or 25. Thus, the ring gear will have 25 teeth.

Similarly, by using Eq. (60.1), putting values as follows “ R ” as 25 and “ S ” as 15, “ P ” will be 5. Therefore, each of the planet gears will have nine teeth.

For Example, to obtain a torque of **3 Nm**, a new designed of a planetary gear set within the configuration **$R = 25$, $P = 5$, and $S = 15$** . The 3D model of the gear system is shown in Fig. 60.3.

A force sensitive resistor is a sensor of a material whose resistance changes as the force is applied on it. Here, it will be used to help measure the torque acting on the output shaft. For measuring the RPM, an optical groove coupler has been used. It deciphers how many times an object has passed between its poles and gives an output accordingly, which helps to measure RPM of the output shaft. Brushed DC

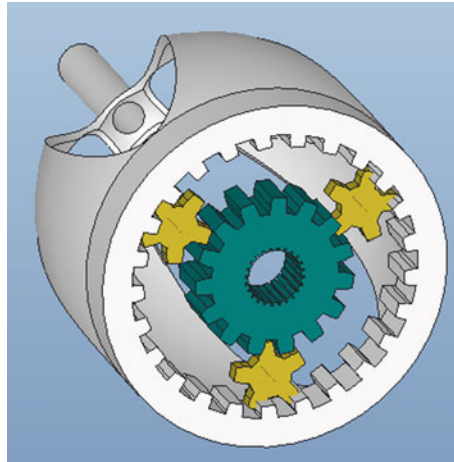


Fig. 60.3 Gear ratio for 3 Nm torque setting

motor is used with the nominal torque of 1.8 Nm and nominal speed of 1778 RPM. In addition to these, we have used a 16×2 LCD to display necessary parameters.

Also, a Wi-Fi ESP 8266-01 module is used to push all the parameters to a dedicated server for IOT if the using facility is IOT-enabled. The data can be pushed to a local server and eventually to cloud to use the parameters for quality

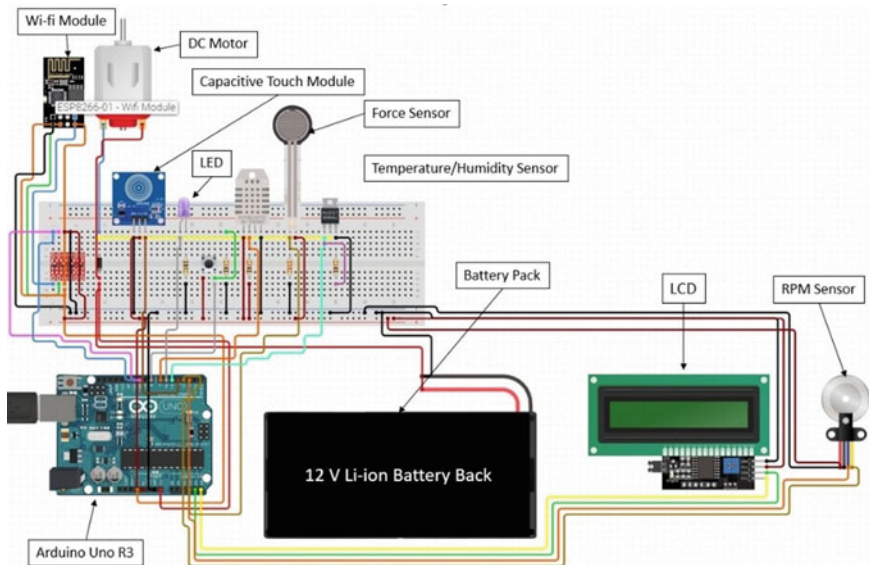
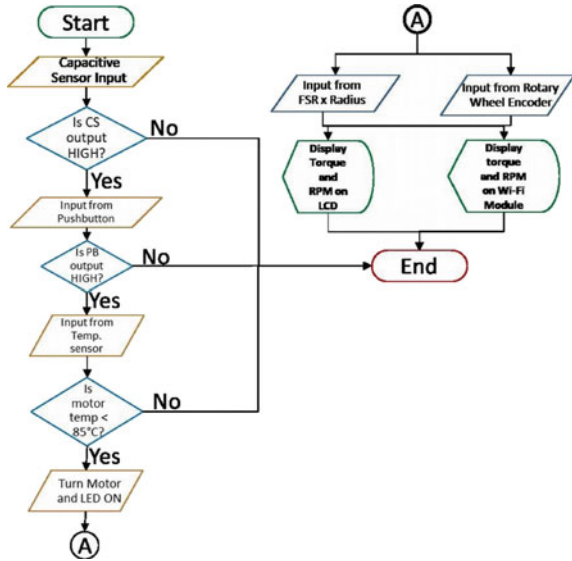


Fig. 60.4 Circuit diagram of screwdriver with Arduino UNO

Fig. 60.5 Logic flowchart of screwdriver



and Research & Development (R&D) purposes. The circuit in Fig. 60.4 shows the basic connections and sensors and actuators included in the circuit of the screwdriver.

The code to the tool has been designed based on the connection on the Arduino. As being an open-source microcontroller, working and coding with Arduino is the easy to use and implement. To write a program, a schematic diagram plays an important role that helps to follow the path to write the code. The working of sensors and other components can be evaluated using the schematic diagram. The schematic diagram of the electric screwdriver is shown in Fig. 60.5.

The 3D model of the electrical screwdriver has been designed in the software named—“PTC Creo Parametric 3.0” as shown in Figs. 60.6 and 60.7 with assembled view and the sectional view, respectively. All the components that are fitted in the electrical screwdriver can be seen in the sectional view of the model including the electronics and mechanical components used in the fabrication of the tool.

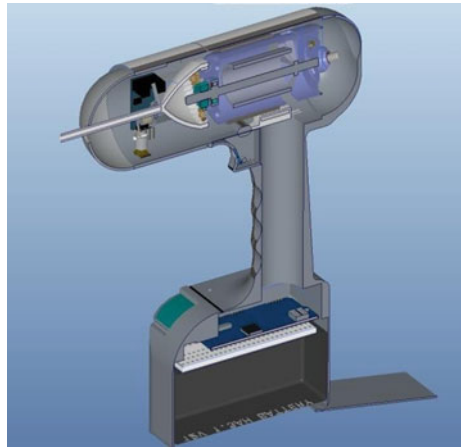
60.4 Results and Discussion

The resulting assembly can be seen in Fig. 60.8 with exploded view, which has been represented with labeling of all the components used in the fabrication of the electric tool. To test the results, time study has been compared on fastening the screw with manual screwdriver and with electrical screwdriver. The task is to

Fig. 60.6 Assembled 3D view



Fig. 60.7 Sectional 3D view



tighten the four screws at the four corners of rectangular wooden frame. The type of screw taken for the experimentation is “Steel Metal Screw (SMS)” with “Phillips Flats Head” of length 1 inch each. The experimentation has been repeated 20 times to come up with average time taken in both the cases. The time taken for an operator to tighten the four screws with manual screwdriver is 60 s, whereas the time taken with the new designed electrical screwdriver is 30 s. Clearly, it has been noted that with the innovation in new tool, it saves 50% time of the operator.

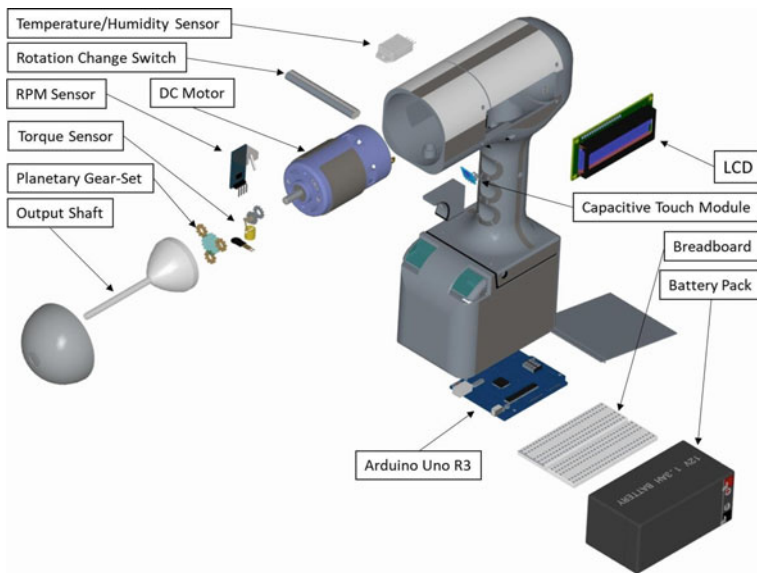


Fig. 60.8 Exploded view of screwdriver

60.5 Conclusion

The screwdrivers are effective and helpful to the operators as it prevents to use repeatedly wrist turning during use of manual screwdriver. It also observed with an experiment that the electric screwdriver saves 50% of the time for an operator that helps the industry to increase the production. The overall cost of the screwdriver will come out to be approximately \$350 including the whole circuit and housing as compared to the price of other industrial screwdrivers which come in the same torque range starting from \$1300 for the basic ones to \$5500 for premium make. In addition to cost benefits, the screwdriver gives a major advantage over pneumatic screwdrivers which are commonly used in the industry in terms of quality, fatigue, and delivery time.

References

1. Johnson, S.L.: Evaluation of powered screwdriver design characteristics. *Hum. Factors* **30**(1), 61–69 (1988). <https://doi.org/10.1177/001872088803000106>
2. Lin, J.H., Radwin, R.G., Fronczak, F.J., Richard, T.G.: Forces associated with pneumatic power screwdriver operation: statics and dynamics. *Ergonomics* **46**(12), 1161–1177 (2003). <https://doi.org/10.1080/0014013031000139518>

3. Radwin, R.G., VanBergeijk, E., Armstrong, T.J.: Muscle response to pneumatic hand tool torque reaction forces. *Ergonomics* **32**(6), 655–673 (1989). <https://doi.org/10.1080/00140138908966140>
4. Chen, C.H., Der Chong, W.: Fastening torque control for robotic screw driver under uncertain environment. In: *International Conference on Control, Automation and Systems*, no. Iccas, pp. 814–818, 2014. <https://doi.org/10.1109/ICCAS.2014.6987891>
5. Ng, P.K., Jee, K.S., Choong, B.S.: Design innovation of a manual screwdriver using the inventive principles of TRIZ. *Middle East J. Sci. Res.* **24**(2), 372–378 (2016). <https://doi.org/10.5829/idosi.mejsr.2016.24.02.23028>
6. Okiy, S., Emagbetere, E., Oreko, B.U.: Development of an electric screwdriver with incorporated torque measuring device. *Int. J. Eng. Technol.* **7**(3), 1198 (2018). <https://doi.org/10.14419/ijet.v7i3.12295>
7. Mumtaz, Z., et al.: An automation system for controlling streetlights and monitoring objects using arduino. *Sensors (Switzerland)* **18**(10), 1–14 (2018). <https://doi.org/10.3390/s18103178>
8. Irawan, Y., Wahyuni, R., Fonda, H.: Folding clothes tool using arduino uno microcontroller and gear servo. *J. Robot. Control* **2**(3), 170–174 (2021). <https://doi.org/10.18196/jrc.2373>
9. Zainal, N.I., Sidek, K.A., Gunawan, T.S., Manser, H., Kartiwi, M.: Design and development of portable classroom attendance system based on arduino and fingerprint biometric. In: *2014 5th International Conference on Information and Communication Technology, Muslim World, ICT4M 2014*, pp. 3–6, 2014. <https://doi.org/10.1109/ICT4M.2014.7020601>
10. Gbenga, D.E., Shani, A.I., Adekunle, A.L.: Smart walking stick for visually impaired people using ultrasonic sensors and arduino. *Int. J. Eng. Technol.* **9**(5), 3435–3447 (2017). <https://doi.org/10.21817/ijet/2017/v9i5/170905302>
11. Juang, H.S., Lurr, K.Y.: Design and control of a two-wheel self-balancing robot using the arduino microcontroller board. In: *IEEE International Conference on Control Automation ICCA*, pp. 634–639, 2013. <https://doi.org/10.1109/ICCA.2013.6565146>
12. Bhargava, A., Kumar, A.: Arduino controlled robotic arm. In: *Proceedings of International Conference on Electronics, Communication and Aerospace Technology, ICECA 2017*, vol. 2017, pp. 376–380, January 2017. <https://doi.org/10.1109/ICECA.2017.8212837>
13. Silva, L., Dantas, R., Pantoja, A., Pereira, A.: Development of a low cost dataglove based on arduino for virtual reality applications. In: *2013 IEEE Proceedings of International Conference on Computational Intelligence and Virtual Environments for Measurement Systems and Applications, CIVEMSA 2013*, pp. 55–59, 2013. <https://doi.org/10.1109/CIVEMSA.2013.6617395>
14. Adriansyah, A., Dani, A.W.: Design of small smart home system based on Arduino. In: *Proceedings of 2014 Electrical Power, Electronics, Communications, Control and Informatics Seminar, EECCIS 2014*, Conjunction with 1st Jt. Conference on UB-UTHM, pp. 121–125, 2014. <https://doi.org/10.1109/EECCIS.2014.7003731>
15. Putjaika, N., Phusae, S., Chen-Im, A., Phunchongarn, P., Akkarajitsakul, K.: A control system in an intelligent farming by using arduino technology. In: *Proceedings of 2016 5th ICT International Student Project Conference (ICT-ISPC)*

Author Index

A

Abdelrahman, Hazem, 95
Abidin, Ana Sakura Zainal, 21
Adithya, Pitala, 185
Agarwal, Shubham, 199, 227
Aggarwal, Shobhit, 453
Alavi, Mohammed, 599
Albarracin, Mauro D., 559
Ali Akbar, N., 77
Ali, Siddik P., 539
Anbuudayasankar, S.P., 337
Anji Reddy, T., 391
Anu, K.A., 77
Aris, Mohd Shiraz, 599
Ashok Kumar, U., 581
Ashwin, S., 337
Ayub, Muhammad Azmi, 11, 587

B

Baini, Rubiyah, 21
Banakara, Basavaraja, 499
Bansal, Abhay, 423
Bhardwaj, Ankur, 217
Bhore, Skylab Paulas, 209, 347

C

Cardona, Luisa Tumbajoy, 571
Chaudhary, Priya, 67
Chauhan, Shivam, 453
Chippe, Vineela, 277
Corrales, Byron P., 559

D

Damkale, Sourabh, 433
Davuluri, Ragavamsi, 485

Dayane, Shailendra, 303
Dennis, Bino Prince Raja, 107
Devasani, Shiva Kumar Reddy, 295, 365
Dey, Saugato, 509
Dhatrak, Pankaj, 433
Dilip Kumar, Y., 475
Dol, Sharul Sham, 599

E

Esanakula, Jayakiran Reddy, 199, 227

F

Freire, Luigi O., 559

G

Gadala, Mohamed S., 599
Gopalakrishnan, Ramanan, 107
Gour, Sonam, 67
Gowd, Harinath G., 539
Guambo, Wilson, 559
Gupta, Abhishek, 115
Gupta, Gautam, 411, 609

H

Hanafusa, Akihiko, 21, 587
Haque, Nawshad, 115
Hasan, Abdulqader, 599
Hema Latha, M., 355
Ho, Jeng-Rong, 147
Huynh, Quoc-Khanh, 147

J

Jagadish Babu, A., 317
Jain, Anuj, 115
Jain, Deepti, 453

Jamalpur, Gurunandan, [199](#), [227](#)
 Jaswanth Raju, J., [277](#)
 Jayakrishnan, B., [381](#)
 Jiang, Zuhua, [529](#)

K

Kakaravada, Ismail, [475](#)
 Kale, Vedant, [303](#)
 Kamal, Ahmad E., [423](#)
 Karthik, Gadi, [549](#)
 Karthikkumar, M., [249](#)
 Katepalli, Manikanta S. B., [167](#)
 Katke, Chetan, [303](#)
 Kaur, Gaganpreet, [609](#)
 Kaur, Sanmukh, [217](#)
 Kavinkumar, C., [327](#)
 Keskar, Yash, [433](#)
 Khan, Mohammed Abdul Hameed, [95](#)
 Khulbe, Tripti, [467](#)
 Krishnamurthy, K., [295](#)
 Krishna Tej, A., [443](#)
 Kumar, Alok, [257](#)
 Kumar, Arvind, [115](#)
 Kumar, Labesh C., [185](#)
 Kumar, Gyara Ajay, [581](#)
 Kumar, Laxman K., [167](#)
 Kumar, Sunil, [423](#)
 Kurian, James, [285](#)
 Kuzhanthai, Anton Savio Lewise, [107](#)

L

Lamy, Damien, [337](#)
 Lee, Hokyoo, [587](#)
 Leman, Muhammad Naim, [21](#)

M

Madhukar, Samatham, [581](#)
 Maherchandani, Jai Kumar, [401](#)
 Malagavelli, Venu, [317](#)
 Manikanta Katepalli, S.B., [277](#)
 Manoj, Aluri, [135](#)
 Mathur, Tanishi, [157](#)
 Mazni, Mazleenda, [11](#)
 Mboreha, Chanfiou Ahmed, [95](#)
 Midhun, M.S., [285](#)
 Mishra, Saurabh, [267](#)
 Mistry, Kalyan Kr, [509](#)
 Mohamaddan, Shahrol, [21](#)
 Mohan, Navya, [285](#)
 Muñoz-Añasco, Mariela, [571](#)
 Muhammad, Norhafiza, [11](#)
 Murthy, Krishna K., [365](#)
 Murugesan, Sivanesan, [239](#)

Muthukumaraswamy, Senthil Arumugam, [157](#),
[519](#)

N

Nair, Prashant R., [327](#)
 Nguyen, Chi-Ngon, [147](#)
 Nguyen, Van-Cuong, [147](#)

P

Pandurangadu, V., [177](#)
 Panneerselvam, Balamurugan, [125](#)
 Patar, Mohd Nor Azmi Ab, [587](#)
 Patel, Satyanarayan, [57](#)
 Paul, Akshoy Ranjan, [115](#)
 Poojitha, Vindala, [177](#)
 Prasad, Durga B., [539](#)
 Prasanth, P. P., [285](#)
 Premchandran, V., [249](#)

Q

Quadri, Syed Azam Pasha, [581](#)

R

Raghu, T., [177](#)
 Rahman, Habibur, [519](#)
 Ramakrishna, A., [355](#)
 Ramakrishnan, Neela Rajan Rajadurai, [107](#)
 Rao, Chandra Sekhara P. V., [135](#)
 Rao, Veeredhi Vasudeva, [1](#)
 Rastogi, Ujjwal, [267](#)
 Rastogi, Vikas, [467](#)
 Rathi, Amit, [67](#)
 Ravichandran, Nagananthini, [125](#)
 Ravichandran, Nagavinothini, [125](#)
 Reddy, A.N.R., [85](#)
 Rengaswamy, Ragupathy, [485](#)
 Rosly, Muhammad Aliff, [587](#)

S

Sai Swaroop Krishna, N., [443](#)
 Saiteja, A., [391](#)
 Samaddar, Siddharth, [267](#)
 Sasikala, M., [499](#)
 Sathish, E., [249](#)
 Sathyan, Alka, [519](#)
 Satish Kumar, N., [33](#)
 Saurabh, Nishchay, [57](#)
 Senthilkumar, D., [381](#)
 Shahid, Salman, [599](#)
 Shah, Syed Faizan, [347](#)
 Shaik, Bazani, [539](#)
 Shankaranarayanan, V., [337](#)
 Sharanya, M., [499](#)

Sharma, Bhawini, 401
 Sharma, Mugdha, 453
 Shome, Saikat Kr, 509
 Shukla, Anand Prakash, 217
 Shukla, Manoj, 217
 Singh, Anant Kumar, 411
 Singh, Manik, 453
 Singh, Prabhat, 423
 Singh, Rajanpreet, 411, 609
 Sithebe, Thembelani, 1
 Siva Rama Krishna, S., 317, 391
 Sozhamannan, G.G., 33
 Sreedhar, C., 45
 Suchithra, M., 443
 Sudarsha Chakravarthi Reddy, B., 355
 Sudheer Kumar Reddy, G., 277
 Suffian, Mohamad Syazwan Zafwan
 Mohamad, 21
 Suman, Dharamkar Sai, 581
 Sumanjali, R., 391
 Sunil, B.D.Y., 185
 Sunil Kumar Reddy, S., 45
 Suresh, S., 45
 Suryaprakash Reddy, V., 317
 Swathi, Renuka B., 135

T

Tamrin, Khairul Fikri, 21
 Thakar, Prashant, 303
 Thallapalli, Nagaveni, 167, 277
 Thamizharasan, V., 249
 Thenarasu, M., 337

Thomas, Athul, 285
 Tony Geefus, S., 327
 Tuljapurkar, Nikhil, 199, 227
 Tyagi, Soham, 267

U

Udaya Kumar, M., 549
 Umakanth Reddy, K., 391

V

Vadhera, Shelly, 257
 Vaisnav, Mithun S., 239
 Venkatachalapathy, V.S.K., 33
 Venkata Subba Reddy, O.Y., 85
 Venkatesh, V., 85
 Venkateswarlu, Ch., 355
 Verma, Shalini, 115
 Vijay Kumar, K., 475
 Vodnala, Sudeshna, 295
 Vo-Nguyen, Hong-Phuc, 147

W

Wu, Lebao, 529

Y

Yamini Saraswathi, S., 355
 Yede, Rushikesh Hanuman, 209

Z

Zainal, Nur Aainaa, 587